AD 219 958

UNITED STATES AIR FORCE
SUMMER FACULTY RESEARCH PROGRAM
1989
PROGRAM TECHNICAL REPORT
UNIVERSAL ENERGY SYSTEMS, INC.
VOLUME III of IV

Program Director, UES
Rodney C. Darrah

Program Administrator, UES
Susan K. Espy

Program Manager, AFOSR
Lt. Col. Claude Cavender

Submitted to

Air Force Office of Scientific Research

Bolling Air Force Base

Washington, DC

December 1989

Accesion For	
NTIS CRA&I	☑
DTIC TAB	☐
Unannounced	☐
Justification	
By	
Distribution /	
Availability Codes	
Dist	Avail and / or Special
A-1	

SECURITY CLASSIFICATION OF THIS PAGE

REPORT DOCUMENTATION PAGE

1a. REPORT SECURITY CLASSIFICATION: UNCLASSIFIED	1b. RESTRICTIVE MARKINGS
2a. SECURITY CLASSIFICATION AUTHORITY	3. DISTRIBUTION/AVAILABILITY OF REPORT: APPROVED FOR PUBLIC RELEASE; Distribution Unlimited
2b. DECLASSIFICATION/DOWNGRADING SCHEDULE	
4. PERFORMING ORGANIZATION REPORT NUMBER(S)	5. MONITORING ORGANIZATION REPORT NUMBER(S): AFOSR-TR-90-5368
6a. NAME OF PERFORMING ORGANIZATION: Universal Energy Systems, INc; 6b. OFFICE SYMBOL (If applicable)	7a. NAME OF MONITORING ORGANIZATION: AFOSR/XOT
6c. ADDRESS (City, State and ZIP Code): 4401 Dayton-Xenia Road, Dayton, OH 45432	7b. ADDRESS (City, State and ZIP Code): Building 410, Bolling AFB, DC 20332
8a. NAME OF FUNDING/SPONSORING ORGANIZATION: AFOSR; 8b. OFFICE SYMBOL (If applicable): XOT	9. PROCUREMENT INSTRUMENT IDENTIFICATION NUMBER: F49620-85-C-0013
8c. ADDRESS (City, State and ZIP Code): Building 410, Bolling AFB, DC 20332	10. SOURCE OF FUNDING NOS.

PROGRAM ELEMENT NO.	PROJECT NO.	TASK NO.	WORK UNIT NO.
61102F	3396	D5	

11. TITLE (Include Security Classification): USAF Summer Faculty Research Program - Management Report - Vol 3 of 4

12. PERSONAL AUTHOR(S): Rodney C. Darrah, Susan K. Espy

13a. TYPE OF REPORT	13b. TIME COVERED	14. DATE OF REPORT (Yr., Mo., Day)	15. PAGE COUNT
Annual	FROM _____ TO _____	Dec 89	

16. SUPPLEMENTARY NOTATION

17. COSATI CODES			18. SUBJECT TERMS (Continue on reverse if necessary and identify by block number)
FIELD	GROUP	SUB. GR.	

19. ABSTRACT (Continue on reverse if necessary and identify by block number)

See Attached

20. DISTRIBUTION/AVAILABILITY OF ABSTRACT: LASSIFIED/UNLIMITED XX SAME AS RPT. ☐ DTIC USERS ☐	21. ABSTRACT SECURITY CLASSIFICATION: UNCLASSIFIED

22a. NAME OF RESPONSIBLE INDIVIDUAL	22b. TELEPHONE NUMBER (Include Area Code)	22c. OFFICE SYMBOL
Lt. Col Claude Cavender	202-767-4970	XOT

TABLE OF CONTENTS

Section	Page
Preface	i
List of Participants	ii
Participant Laboratory Assignment	xxx
Research Reports	xxxiv

PREFACE

The United States Air Force Summer Faculty Resarch Program (USAF-SFRP) is designed to introduce university, college, and technical institute faculty members to Air Force research. This is accomplished by the faculty members being selected on a nationally advertised competitive basis for a ten-week assignment during the summer intersession period to perform research at Air Force laboratories/centers. Each assignment is in a subject area and at an Air Force facility mutually agreed upon by the faculty members and the Air Force. In addition to compensation, travel and cost of living allowances are also paid. The USAF-SFRP is sponsored by the Air Force Office of Scientific Research, Air Force Systems Command, United States Air Force, and is conducted by Universal Energy Systems, Inc.

The specific objectives of the 1989 USAF-SFRP are:

1) To provide a productive means for U.S. faculty members to participate in research at Air Force Laboratories/Centers;

2) To stimulate continuing professional association among the faculty and their professional peers in the Air Force;

3) To further the research objectives of the United States Air Force; and

4) To enhance the research productivity and capabilities of the faculty especially as these relate to Air Force technical interests.

Keywords: reports, abstracts. (KR)

During the summer of 1989, 168-faculty members participated. These researchers were assigned to 23 USAF laboratories/centers across the country. This four volume document is a compilation of the final reports written by the assigned faculty members about their summer research efforts.

LIST OF 1989 PARTICIPANTS

NAME/ADDRESS	DEGREE, SPECIALTY, LABORATORY ASSIGNED
Thomas Abraham Instructor Saint Paul's College Sci. & Math. Dept. Lawrenceville, VA 23868 804\848-3111	Degree: MS Specialty: Mathematics Assigned: School of Aerospace Medicine
Charles Alajajian Assistant Prof. West Virginia University PO Box 6101 Morgantown, WV 26506 304\293-6371	Degree: PhD Specialty: Electrical Eng. Assigned: Rome Air Development Center
Barbara Alvin Associate Prof. Eastern Washington Univ. Math Dept. #32 Cheney, WA 99004 509\359-2203	Degree: PhD Specialty: Biostatistics Assigned: Occupational & Environmental Health Laboratory
Jon Anderson Assistant Prof. Texas Tech. University PO Box 4200 Lubbock, TX 79409 806\742-3533	Degree: PhD Specialty: Civil Engineering Assigned: Engineering & Services Center
Peter Armendarez Professor Brescia College 7th at Frederica Owensboro, KY 42301 502\686-4285	Degree: PhD Specialty: Physical Chemistry Assigned: Armament Laboratory
Pradip Bakshi Professor Boston College Physics Dept. Chestnut Hill, MA 02167 617\552-3585	Degree: PhD Specialty: Theoretical Physics Assigned: Geophysics Laboratory

NAME/ADDRESS	DEGREE, SPECIALTY, LABORATORY ASSIGNED
William Bannister Professor Lowell, University of Dept. of Chemistry Lowell, MA 01854 508\452-5000	Degree: PhD Specialty: Organic Chemistry Assigned: Engineering & Services Center
Beryl Barber Assistant Prof. Oregon Institute of Tech. 3201 Campus Dr. Klamath Falls, OR 97601 503\882-3899	Degree: MS Specialty: Electronic Engineering Assigned: Electronic Systems Division
Brian Beecken Assistant Prof. Bethel College 3900 Bethel Dr. St. Paul, MN 55112 612\638-6334	Degree: PhD Specialty: Physics Assigned: Arnold Engineering Development Center
Christopher Bell Assistant Prof. Illinois State Univ. 133 Stevenson Normal, IL 61761 309\438-8338	Degree: PhD Specialty: Psychology Assigned: Human Resources Laboratory: Manpower & Personnel Div.
Kevin Bennett Assistant Prof. Wright State University 309 Oelman Hall Dayton, OH 45435 513\873-2444	Degree: PhD Specialty: Applied Psychology Assigned: Human Resources Laboratory: Logistics & Human Factors
Emerson Besch Professor Florida, University of Box J-144 JHMHSC Gainesville, FL 32610 904\392-1841	Degree: PhD Specialty: Animal Physiology Assigned: Engineering & Services Center

NAME/ADDRESS	DEGREE, SPECIALTY, LABORATORY ASSIGNED
Robert Blystone Professor Trinity University 715 Stadium Dr. San Antonio, TX 78284 512\736-7231	Degree: PhD Specialty: Zoology Assigned: School of Aerospace Medicine
Karren Brito Research Chem. Dayton, University of 300 College Park Dayton, OH 45469 513\229-3118	Degree: PhD Specialty: Chemistry Assigned: Materials Laboratory
Lee Britt Instructor Grambling State University Dept. of Physics Grambling, LA 71245 318\274-2575	Degree: MS Specialty: Physics Assigned: Arnold Engineering Development Center
Joseph Brown Professor Mississippi State Univ. PO Brawer ME Mississippi State, MS 39762 601\325-7310	Degree: PhD Specialty: Mechanical Engineering Assigned: Armament Laboratory
Roger Bunting Professor Illinois State University Dept. of Chemistry Normal, IL 61761 309\438-7661	Degree: PhD Specialty: Inorganic Chemistry Assigned: Armament Laboratory
Larry Byrd Assistant Prof. Arkansas State University PO Box 1080 State University, AR 72467 501\972-2088	Degree: PhD Specialty: Mechanical Engineering Assigned: Flight Dynamics Laboratory

NAME/ADDRESS	DEGREE, SPECIALTY, LABORATORY ASSIGNED
Anthony Carlisle Assistant Prof. Huntingdon College 1500 E. Fairview Ave. Montgomery, AL 36194 205\265-0511	Degree: MS Specialty: Computer Science Assigned: Engineering & Services Center
Carolyn Caudle-Alexander Assistant Prof. Tennessee State University 3500 John A. Merritt Blvd. Nashville, TN 37209 615\320-3115	Degree: PhD Specialty: Microbiology Assigned: School of Aerospace Medicine
James Chambers Associate Prof. Texas-San Antonio, Univ. Brain Research Lab. of Biochemistry San Antonio, TX 78285 512\691-5477	Degree: PhD Specialty: Biochemistry Assigned: School of Aerospace Medicine
Satish Chandra Assistant Prof. Kansas State Univ. Dept. of Elec. and Comp. Eng. Manhattan, KS 66506 913\532-5600	Degree: PhD Specialty: Electrical Engineering Assigned: Armament Laboratory
Chi Chen Professor Southeastern Mass. Univ. Dept. of Elect. & Comp. Eng. North Dartmouth, MA 02747 508\999-8475	Degree: PhD Specialty: Electrical Engineering Assigned: Geophysics Laboratory
David Choate Assistant Prof. Transylvania University Dept. of Mathematics Lexington, KY 40508 606\233-8237	Degree: PhD Specialty: Mathematics Assigned: Avionics Laboratory

NAME/ADDRESS	DEGREE, SPECIALTY, LABORATORY ASSIGNED
Ajit Choudhury Associate Prof. Howard University Dept. of Electrical Eng. Washington, DC 20059 202\636-6593	Degree: PhD Specialty: Electrical Engineering Assigned: Electronic Systems Division
Derald Chriss Assistant Prof. Southern University PO Box 10572 Baton Rouge, LA 70813 504\771-3990	Degree: MS Specialty: Chemistry Assigned: Engineering & Services Center
Donald Chung Associate Prof. San Jose State Univ. Dept. of Mat. Eng. San Jose, CA 95192 408\924-3873	Degree: PhD Specialty: Material Science Assigned: Materials Laboratory
Mingking Chyu Assistant Prof. Carnegie Mellon University Dept. of Mechanical Eng. Pittsburgh, PA 15213 412\268-3658	Degree: PhD Specialty: Mechanical Engineering Assigned: Aero Propulsion Laboratory
David Cicci Assistant Prof. Auburn University 162 Wilmore Laboratories Auburn, AL 36849 205\826-4874	Degree: PhD Specialty: Aerospace Engineering Assigned: Armament Laboratory
Brian Circelli Assistant Prof. Mississippi, Univ. of Dept. of Chemical Eng. University, MS 38677 601\232-5347	Degree: PhD Specialty: Chemical Engineering Assigned: Arnold Engineering Development Ctr.

NAME/ADDRESS	DEGREE, SPECIALTY, LABORATORY ASSIGNED
Jerry Clark Assistant Prof. Wright State Univ. Dept. of Physics Dayton, OH 45435 513\873-2954	Degree: PhD Specialty: Physics Assigned: Aero Propulsion Laboratory
Stephen Cobb Assistant Prof. Murray State University Dept. of Physics Murray, KY 42071 502\762-6186	Degree: PhD Specialty: Physics Assigned: Arnold Engineering Development Ctr.
Kathryn Cochran Assistant Prof. Northern Colorado, University Div. of Res., Eval., & Devel. Greeley, CO 80639 303\351-2807	Degree: PhD Specialty: Educational Psychology Assigned: Human Resources Laboratory: Manpower & Personnel Division
R. H. Cofer Professor Florida Institute 150 W. University Blvd. Melbourne, FL 32901 407\984-5689	Degree: PhD Specialty: Electrical Eng. Assigned: Avionics Laboratory
George Coleman Instructor Elizabeth City St. University Dept. of Mathematics Elizabeth City, NC 27909 919\335-3487	Degree: MS Specialty: Applied Mathematics Assigned: Armament Laboratory
Kenneth Cornelius Assistant Prof. Wright State Univ. Dept. of Mechanical Eng. Dayton, OH 45435 513\873-3682	Degree: PhD Specialty: Fluid Mechanics Assigned: Flight Dynamics Laboratory

NAME/ADDRESS	DEGREE, SPECIALTY, LABORATORY ASSIGNED
Mark Cornwall Assistant Prof. Northern Arizona Univ. POB 15105 Flagstaff, AZ 86011 602\523-1606	Degree: PhD Specialty: Human Performance Assigned: School of Aerospace Medicine
Larry Crum Professor Wright State University Dept. of Comp. Sci. & Eng. Dayton, OH 45435 513\259-1342	Degree: PhD Specialty: Electrical Engineering Assigned: Avionics Laboratory
Kenneth Currie Assistant Prof. Kansas State Univ. 228 Durland Hall Manhattan, KS 66506 913\532-5606	Degree: PhD Specialty: Industrial Engineering Assigned: Materials Laboratory
Phanindramohan Das Professor Texas A&M University Dept. of Meteorology College Station, TX 77843 409\845-0633	Degree: PhD Specialty: Geophysical Science Assigned: Geophysics Laboratory
Vito DelVecchio Chairman Scranton, University of Biology Dept. Scranton, PA 18510 717\961-6117	Degree: PhD Specialty: Biochemical Engineering Assigned: School of Aerospace Medicine
Avery Demond Assistant Prof. Massachusetts, University of Dept. of Civil Eng. Amherst, MA 01003 413\545-0685	Degree: PhD Specialty: Civil Engineering Assigned: Engineering & Services Center

NAME/ADDRESS	DEGREE, SPECIALTY, LABORATORY ASSIGNED
Walter Drost-Hansen Professor Miami, University of Dept. of Chemistry Coral Gables, FL 33124 305\284-5842	Degree: PhD Specialty: Physical Chemical Assigned: Wilford Hall Medical Center
Thomas Dwyer Professor Illinois, University of 104 South Mathews Ave. Urbana, IL 61801 217\244-0720	Degree: PhD Specialty: Mathematics Assigned: Weapons Laboratory
Wayne Eckerle Associate Prof. Clarkson University MIE Dept. Clarkson University, NY 13676 315\268-2203	Degree: PhD Specialty: Fluid Mechanics Assigned: Aero Propulsion Laboratory
Dennis Farrell Associate Prof. Cincinnati, University of Mail Location 103 Cincinnati, OH 45210 513\556-6558	Degree: MS Specialty: Electrical Engineering Assigned: Flight Dynamics Laboratory
William Filippone Associate Prof. Arizona, University of Group X6, MS B226 Los Alamos, NM 87545 505\665-2307	Degree: PhD Specialty: Nuclear Engineering Assigned: Weapons Laboratory
John Francis Professor Oklahoma, University of 865 Asp, Room 210 Norman, OK 73019 405\325-5011	Degree: PhD Specialty: Mechanical Engineering Assigned: Arnold Engineering Development Ctr.

NAME/ADDRESS	DEGREE, SPECIALTY, LABORATORY ASSIGNED
Frank Gerner Assistant Prof. Cincinnati, University of 756 Baldwin Hall Mail Loc. #72 Cincinnati, OH 45221 513\566-2646	Degree: PhD Specialty: Mechanical Engineering Assigned: Aero Propulsion Laboratory
Robert Granger Professor US Naval Academy Dept. of Mechanical Engineering Annapolis, MD 21402 301\267-3186	Degree: PhD Specialty: Mechanical Engineering Assigned: Frank J. Seiler Research Lab.
William Grissom Assistant Prof. Morehouse College 830 Westview Dr. SW Atlanta, GA 30314 404\681-2800	Degree: MS Specialty: Mechanical Eng. Assigned: Weapons Laboratory
Ian Grosse Assistant Prof. Massachusetts, University of ELAB 213 Amherst, MA 01003 413\545-1350	Degree: PhD Specialty: Mechanical Eng. Assigned: Rome Air Development Center
John Hadjilogiou Professor Florida Instit.Tech. 150 West University Blvd. Melbourne, FL 32901 407\768-8000	Degree: PhD Specialty: Electrical Eng. Assigned: Rome Air Development Center
Ernest Hallford Assistant Prof. Moorhead State Univ. Dept. of Psychology Moorhead, MN 56560 218\236-4077	Degree: PhD Specialty: Psychology Assigned: Aerospace Medical Research Lab.

NAME/ADDRESS	DEGREE, SPECIALTY, LABORATORY ASSIGNED
Orlando Hankins Assistant Prof. North Carolina State Univ. NCSU Box 7909 Raleigh, NC 27695 919\737-3292	Degree: PhD Specialty: Nuclear Eng. Assigned: Arnold Engineering Development Center
Patrick Hannon Associate Prof. Northern Arizona University Box 6012 Flagstaff, AZ 86011 602\523-4331	Degree: PhD Specialty: Exercise Science Assigned: School of Aerospace Medicine
Cynthia Hardy Associate Prof. Jackson State Univ. 1400 Lynch St. Jackson, MS 39217 601\968-2371	Degree: PhD Specialty: Education Psychology Assigned: School of Aerospace Medicine
Kirk Hatfield Assistant Prof. Florida, University of 346 Weil Hall Gainesville, FL 32611 904\392-0956	Degree: PhD Specialty: Civil Engineering Assigned: Engineering & Services Center
Kim Hayes Assistant Prof. Michigan, University of Dept. of Civil Engineering Ann Arbor, MI 48109 313\763-9661	Degree: PhD Specialty: Environmental Eng. Assigned: Engineering & Services Center
Henry Helmken Professor Florida Atlantic University PO Box 3091 Boca Raton, FL 33431 407\367-3452	Degree: PhD Specialty: Physics Assigned: Rome Air Development Center

NAME/ADDRESS	DEGREE, SPECIALTY, LABORATORY ASSIGNED
Peter Henriksen Associate Prof. Akron, University Dept. of Physics Akron, OH 44325 216\375-6054	Degree: PhD Specialty: Physics Assigned: Materials Laboratory
Lloyd Hillman Assistant Prof. Cornell University 215 Phillips Hall Ithaca, NY 14853 607\255-8212	Degree: PhD Specialty: Optical Engineering Assigned: Frank J. Seiler Research Lab.
Jeffrey Himm Assistant Prof. North Dakota State University Dept. of Physics Fargo, ND 58105 701\237-7048	Degree: PhD Specialty: Physics Assigned: School of Aerospace Medicine
Stuart Hirshfield Associate Prof. Hamilton College Dept. of Math. & Comp. Sci. Clinton, NY 13323 315\859-4136	Degree: PhD Specialty: Computer Science Assigned: Rome Air Development Center
Harry Hogan Assistant Prof. Texas A&M University Eng./Physics Bldg. College Station, TX 77843 409\845-1538	Degree: PhD Specialty: Mechanical Eng. Assigned: Weapons Laboratory
Gwendolyn Howze Associate Prof. Texas Southern Univ. 3100 Cleburne Houston, TX 77004 713\527-7095	Degree: PhD Specialty: Molecular Biology Assigned: School of Aerospace Medicine

NAME/ADDRESS	DEGREE, SPECIALTY, LABORATORY ASSIGNED
Carl Ingling Associate Prof. Ohio State Univ. 1314 Kinnear Rd. Columbus, OH 43212 614\292-6424	Degree: PhD Specialty: Psychology Assigned: Aerospace Medical Research Lab.
Alan Kafka Associate Prof. Boston College Weston Observatory Weston, MA 02193 617\899-0950	Degree: PhD Specialty: Geophysics Assigned: Geophysics Laboratory
Mohammad Karim Associate Prof. Dayton, University of 300 College Park Dayton, OH 45469 513\229-3611	Degree: PhD Specialty: Electrical Eng. Assigned: Avionics Laboratory
John Kenney Assistant Prof. Eastern New Mexico University Station #33 Portales, NM 88130 505\562-2152	Degree: PhD Specialty: Physical Chemistry Assigned: Astronautics Laboratory
M. Kenney Instructor Eastern New Mexico University Station #33 Portales, NM 88130 505\562-2152	Degree: MS Specialty: Physical Chemistry Assigned: Astronautics Laboratory
Charles Kincaid Lecturer Florida, University of 477 Little Hall Gainesville, FL 32611 904\392-1941	Degree: MS Specialty: Statistics Assigned: Aerospace Medical Research Lab.

NAME/ADDRESS	DEGREE, SPECIALTY, LABORATORY ASSIGNED
Lynn Kirms Assistant Prof. Southern Oregon St. College Chemistry Dept. Ashland, OR 97520 503\482-6471	Degree: PhD Specialty: Organic Chemistry Assigned: Astronautics Laboratory
Mark Kirms Assistant Prof. Southern Oregon St. College Dept. of Chemistry Ashland, OR 97520 503\482-6471	Degree: PhD Specialty: Organic Chemistry Assigned: Astronautics Laboratory
Michael Klein Professor Worcester Poly Inst 100 Institute Rd. Worcester, MA 01609 508\831-5527	Degree: PhD Specialty: Physics Assigned: Rome Air Development Center
Faysal Kolkailah Professor California Polytec. Dept. of Aero. Eng. San Luis Obispo, CA 93407 805\786-2393	Degree: PhD Specialty: Mechanical Eng. Assigned: Astronautics Laboratory
William Kuriger Professor Oklahoma, University of EECS Dept. Norman, OK 73019 405\325-4721	Degree: PhD Specialty: Electrical Eng. Assigned: Rome Air Development Center
Thomas Lalk Associate Prof. Texas A&M Univ. Dept. of Mechanical Eng. College Station, TX 77843 409\845-4734	Degree: PhD Specialty: Mechanical Eng. Assigned: Aero Propulsion Laboratory

NAME/ADDRESS	DEGREE, SPECIALTY, LABORATORY ASSIGNED
John Lanning Asscciate Prof. Colorado-Denver, University Box 144, 1200 Larimer St. Denver, CO 80204 303\556-2557	Degree: PhD Specialty: Analytical Chemistry Assigned: Frank J. Seiler Research Lab.
Jay Lee Assistant Prof. Syracuse University Link Hall Syracuse, NY 13244 315\443-4395	Degree: PhD Specialty: Electrical Engineering Assigned: Rome Air Development Center
Lang-Wah Lee Professor Wisconsin-Plattevil. Dept. of Mechanical Eng. Platteville, WI 53818 608\342-1534	Degree: PhD Specialty: Mechanical Eng. Assigned: Arnold Engineering Development Center
Tze San Lee Assistant Prof. Western Illinois University Dept. of Mathematics Macomb, IL 61455 309\298-1485	Degree: PhD Specialty: Applied Mathematics Assigned: School of Aerospace Medicine
Baruch Lieber Assistant Prof. New York, State Univ. of Dept. of Mech. & Aero. Eng. Buffalo, NY 14260 716\636-2391	Degree: PhD Specialty: Aerospace Engineering Assigned: Aero Propulsion Laboratory
Charles Lishawa Assistant Prof. Utica College Burstone Rd. Utica, NY 13502 315\792-3139	Degree: PhD Specialty: Physical Chemistry Assigned: Geophysics Laboratory

NAME/ADDRESS	DEGREE, SPECIALTY, LABORATORY ASSIGNED
Dar-Biau Liu Professor California State University Dept. of Comp. Sci. and Eng. Long Beach, CA 90840 213\985-1594	Degree: PhD Specialty: Applied Math Assigned: Avionics Laboratory
Thomas Lockwood Associate Prof. Wright State Univ. 3640 Col. Glenn Hwy. Dayton, OH 45435 513\873-3060	Degree: PhD Specialty: Toxicology Assigned: Aerospace Medical Research Lab.
Harold Longbotham Assistant Prof. Texas-San Antonio, University 7000 Loop 1604 NW San Antonio, TX 78285 512\691-5518	Degree: PhD Specialty: Electrical Eng. Assigned: School of Aerospace Medicine
Lewis Lutton Associate Prof. Mercyhurst College Glenwood Hills Erie, PA 16546 814\825-0372	Degree: PhD Specialty: Envir. Physiology Assigned: Aerospace Medical Research Lab.
Ethel Matin Professor Long Island Univ. CW Post Campus/LIU Brookville, NY 11548 516\299-2063	Degree: PhD Specialty: Exper. Psychology Assigned: Aerospace Medical Research Lab.
Stewart Maurer Associate Prof. New York Inst. Tech. 1855 Bway New York, NY 10023 212\399-9698	Degree: PhD Specialty: Electrical Eng. Assigned: Occupational and Environmental Health Laboratory

NAME/ADDRESS	DEGREE, SPECIALTY, LABORATORY ASSIGNED
Amy Miller Assistant Prof. Oklahoma, Univ. of 620 Parrington Oval Norman, OK 73019 405\325-4836	Degree: PhD Specialty: Chemistry Assigned: Geophysics Laboratory
Thomas Miller Professor Oklahoma, Univ. of Dept. of Physics & Astronomy Norman, OK 73019 405\325-3961	Degree: PhD Specialty: Physics Assigned: Geophysics Laboratory
Deborah Mitta Assistant Prof. Texas A&M Univ. Dept. of Industrial Eng. College Station, TX 77843 409\845-3299	Degree: PhD Specialty: Industrial Eng. Assigned: Human Resources Laboratory: Logistics & Human Factors
Augustus Morris Assistant Prof. Central State Univ. Dept. of Manufacturing Eng. Wilberforce, OH 45384 513\376-6435	Degree: PhD Specialty: Biomedical Engineering Assigned: Flight Dynamics Laboratory
Rex Moyer Professor Trinity Univ. 715 Stadium Dr. San Antonio, TX 78284 512\736-7242	Degree: PhD Specialty: Microbiology Assigned: School of Aerospace Medicine
Sundaram Natarajan Associate Prof. Tennessee Tech Univ. Box 5004 Cookeville, TN 38505 615\372-3450	Degree: PhD Specialty: Electrical Eng. Assigned: Electronic Systems Division

NAME/ADDRESS	DEGREE, SPECIALTY, LABORATORY ASSIGNED
Henry Nebel Associate Prof. Alfred University Physics Dept. Alfred, NY 14802 607\871-2208	Degree: PhD Specialty: Physics Assigned: Geophysics Laboratory
Joseph Newkirk Assistant Prof. Missouri-Rolla, University 282 McNutt Hall Rolla, MO 65401 314\341-4725	Degree: PhD Specialty: Materials Science Assigned: Materials Laboratory
Duc Nguyen Assistant Prof. Old Dominion Univ. Civil Eng. Dept. Norfolk, VA 23529 804\683-3761	Degree: PhD Specialty: Civil Engineering Assigned: Weapons Laboratory
James Noyes Associate Prof. Wittenberg Univ. Box 720 Springfield, OH 45501 513\327-7858	Degree: PhD Specialty: Computer Science Assigned: Avionics Laboratory
Hugh Nutley Professor Seattle Pacific University 3307 3rd Ave. W. Seattle, WA 98119 206\281-2954	Degree: PhD Specialty: Physics Assigned: Geophysics Laboratory
Robert O'Connell Associate Prof. Missouri, Univ. of ECE Dept. Columbia, MO 65211 314\882-8373	Degree: PhD Specialty: Electrical Eng. Assigned: Rome Air Development Center

NAME/ADDRESS	DEGREE, SPECIALTY, LABORATORY ASSIGNED
Bipin Pai Associate Prof. Purdue Univ. Dept. of Eng. Hammond, IN 46323 219\989-2694	Degree: PhD Specialty: Mechanical Eng. Assigned: Astronautics Laboratory
Harvey Paige Associate Prof. Alfred University PO Box 546 Alfred, NY 14802 607\871-2[illegible]1	Degree: PhD Specialty: Inorganic Chem. Assigned: Materials Laboratory
Arnold Polak Professor Cincinnati, University of M.L. #70 Cincinnati, OH 45221 513\556-3550	Degree: PhD Specialty: Aerospace Eng. Assigned: Flight Dynamics Laboratory
Randy Pollack Assistant Prof. Wright State Univ. Computer Sci. Dept. Dayton, OH 45435 513\873-2491	Degree: PhD Specialty: Anthropology Assigned: Aerospace Medical Research Lab.
Raymond Quock Professor Univ. of Illinois at Rockford 604 N. 16th St. Milwaukee, WI 53233 414\224-7251	Degree: PhD Specialty: Pharmacology Assigned: School of Aerospace Medicine
Vittal Rao Professor Missouri-Rolla, University Dept. of Electrical Eng. Rolla, MO 65401 314\341-4508	Degree: PhD Specialty: Control Systems Assigned: Astronautics Laboratory

NAME/ADDRESS	DEGREE, SPECIALTY, LABORATORY ASSIGNED
Craig Rasmussen Assistant Prof. Utah State Univ. CASS UMC 4405 Logan, UT 84322 801\750-2967	Degree: PhD Specialty: Physics Assigned: Geophysics Laboratory
Michael Resch Assistant Prof. Nebraska-Lincoln, University of 212 Bancroft Hall Lincoln, NE 68588 402\472-2354	Degree: PhD Specialty: Materials Science Assigned: Materials Laboratory
Richard Robertson Professor California State Univ. 3801 W. Temple Ave. Pomona, CA 91768 714\869-3488	Degree: MS Specialty: Mathematics Assigned: Astronautics Laboratory
Larry Roe Assistant Prof. Virginia Poly Institute Dept. of Mech. Eng. Blacksburg, VA 24061 703\231-7295	Degree: PhD Specialty: Mechanical Eng. Assigned: Aero Propulsion Laboratory
Deborah Ross Assistant Prof. Indiana-Purdue, University of 2101 Coliseum Blvd. East Fort Wayne, IN 46805 219\481-6313	Degree: PhD Specialty: Microbiology Assigned: Engineering & Services Center
Duane Sanders Assistant Prof Texas A&M Univ. Dept. of Civil Eng. College Station, TX 77843 409\845-9566	Degree: PhD Specialty: Civil Engineering Assigned: Weapons Laboratory

NAME/ADDRESS	DEGREE, SPECIALTY, LABORATORY ASSIGNED
John Sanders Assistant Prof. Northwestern State University Fournet Hall Natchitoches, LA 71497 318\357-5501	Degree: PhD Specialty: Chemistry Assigned: Frank J. Seiler Research Lab.
Paul Scheie Professor Texas Lutheran Coll 1000 West Court Seguin, TX 78155 512\379-4161	Degree: PhD Specialty: Biophysics Assigned: School of Aerospace Medicine
William Schulz Professor Eastern Kentucky University Moore 337 Richmond, KY 40475 606\622-1463	Degree: PhD Specialty: Analytical Chemistry Assigned: Aero Propulsion Laboratory
Ronald Seaman Associate Prof. Louisiana Tech University PO Box 3185 Ruston, LA 71272 318\257-4562	Degree: PhD Specialty: Biomedical Eng. Assigned: School of Aerospace Medicine
Sally Sedelow Professor Arkansas-Little Rock, Univ. 33rd and University Little Rock, AR 72204 501\569-8130	Degree: PhD Specialty: Computer Science Assigned: Rome Air Development Center
Nisar Shaikh Assistant Prof. Nebraska-Lincoln, University 212 Bancroft Hall Lincoln, NE 68588 402\472-6692	Degree: PhD Specialty: Applied Math. Assigned: Flight Dynamics Laboratory

NAME/ADDRESS	DEGREE, SPECIALTY, LABORATORY ASSIGNED
Clay Sharts Professor San Diego State University Dept. of Chemistry San Diego, CA 92182 619\594-5576	Degree: PhD Specialty: Chemistry Assigned: Frank J. Seiler Research Lab.
Edmund Shearer Professor Fort Hays State University 600 Park St. Hays, KS 67601 913\628-4506	Degree: PhD Specialty: Chemistry Assigned: Occupational and Environmental Health Laboratory
James Sherwood Assistant Prof. New Hampshire, University of Kingsbury Hall Durham, NH 03824 603\862-2624	Degree: PhD Specialty: Aero. Mechanics Assigned: Materials Laboratory
Robert Shock Associate Wright State Univ. Dept. of CEG and CS Dayton, OH 45435 513\259-8402	Degree: PhD Specialty: Mathematics Assigned: Avionics Laboratory
Hugh Siefken Chairman Greenville College Dept. of Physics Greenville, IL 62246 618\664-4081	Degree: PhD Specialty: Nuclear Physics Assigned: Weapons Laboratory
John Silvestro Assistant Prof. Clemson Univ. Riggs Hall Clemson, SC 29634 803\656-5921	Degree: PhD Specialty: Electrical Eng. Assigned: Weapons Laboratory

NAME/ADDRESS	DEGREE, SPECIALTY, LABORATORY ASSIGNED
Miles Simpson Associate Prof. North Carolina Cent. Univ. Dept. of Sociology Durham, NC 27707 919\560-6420	Degree: PhD Specialty: Sociology Assigned: Human Resources Laboratory: Manpower and Personnel Division
Boghos Sivazlian Professor Florida, Univ. of 303 Weil Hall Gainesville, FL 32611 904\392-1464	Degree: PhD Specialty: Operations Research Assigned: Armament Laboratory
William Smith Associate Prof. Pittsburgh, Univ. of 526 C.L. Pittsburgh, PA 15260 412\624-6559	Degree: PhD Specialty: Linguistics Assigned: Human Resources Laboratory: Training Systems
Michael Stanisic Assistant Prof. Notre Dame, University of Dept. of Aero/Mech Eng. Notre Dame, IN 46556 219\239-7897	Degree: PhD Specialty: Robotics Assigned: Aerospace Medical Research Lab.
Stanley Stephenson Associate Prof. Southwest Texas State University CIS/ADS Dept. San Marcos, TX 78666 512\245-2291	Degree: PhD Specialty: Psychology Assigned: Human Resources Laboratory: Training Systems
Chun Fu Su Assistant Prof. Mississippi State University Dept. of Physics Mississippi State, MS 39762 601\325-2931	Degree: PhD Specialty: Physics Assigned: Arnold Engineering Development Center

NAME/ADDRESS	DEGREE, SPECIALTY, LABORATORY ASSIGNED
Khaja Subhani Associate Prof. Lawrence Tech. Univ. 21000 West Ten Mile Southfield, MI 48075 313\356-0200	Degree: PhD Specialty: Electrical Eng. Assigned: Rome Air Development Center
Larry Swanson Assistant Prof. Denver, Univ. of 2390 S. York St. Denver, CO 80208 303\871-3816	Degree: PhD Specialty: Mechanical Eng. Assigned: Astronautics Laboratory
Michael Sydor Professor Minnesota-Duluth, University of Dept. of Physics Duluth, MN 55812 218\726-7205	Degree: PhD Specialty: Physics Assigned: Materials Laboratory
Joseph Szucs Associate Prof. Texas A&M Univ. GACD PO Box 1675 Galveston, TX 77553 409\740-4463	Degree: PhD Specialty: Functional Analytics Assigned: Aerospace Medical Research Lab.
Chi-Ming Tang Associate Prof. New York, State Univ. of Dept. of Math Geneseo, NY 14454 716\245-5386	Degree: PhD Specialty: Mathematics Assigned: Aerospace Medical Research Lab.
Richard Tankin Professor Northwestern Univ. Mechanical Eng. Dept. Evanston, IL 60201 312\491-3532	Degree: PhD Specialty: Mechanical Eng. Assigned: Aero Propulsion Laboratory

NAME/ADDRESS	DEGREE, SPECIALTY, LABORATORY ASSIGNED
Teresa Taylor Assistant Prof. Missouri-Columbia, University of 600 West Mechanic Independence, MO 64050 816\276-1285	Degree: PhD Specialty: Civil Eng. Assigned: Engineering & Services Center
Ebo Tei Professor Arkansas-Pine Bluff, Univ. of Social & Behavioral Sci. Pine Bluff, AR 71601 501\541-6787	Degree: PhD Specialty: Psychology Assigned: Aerospace Medical Research Lab.
Roger Thompson Assistant Prof. Pennsylvania St. University 233 Hammond Bldg. University Park, PA 16802 814\863-0968	Degree: PhD Specialty: Eng. Mechanics Assigned: Astronautics Laboratory
Richard Tipping Professor Alabama, University Dept. of Physics Tuscaloosa, AL 35487 205\348-3799	Degree: PhD Specialty: Physics Assigned: Arnold Engineering Development Ctr.
Phillip Tomporowski Assistant Prof. Alabama, University of Box 870348 Tuscaloosa, AL 35487 205\348-1936	Degree: PhD Specialty: Psychology Assigned: Human Resources Laboratory: Operations Training Division
Ram Tripathi Professor Texas-San Antonio, Univ. of Dept. of Mathematics San Antonio, TX 78285 512\691-5549	Degree: PhD Specialty: Statistics Assigned: School of Aerospace Medicine

NAME/ADDRESS	DEGREE, SPECIALTY, LABORATORY ASSIGNED
Steven Trogdon Associate Prof. Minnesota-Duluth, University of 108 Heller Hall Duluth, MN 55812 218\726-6173	Degree: PhD Specialty: Mechanics Assigned: Armament Laboratory
Timothy Troutt Associate Prof. Washington State University of Mech. & Mat. Eng. Dept. Pullman, WA 99164 509\335-4375	Degree: PhD Specialty: Mechanical Eng. Assigned: Frank J. Seiler Research Lab.
Donald Ucci Associate Prof. Illinois Inst.Tech. 3300 S. Federal St. Chicago, IL 60616 312\567-3405	Degree: PhD Specialty: Electrical Eng. Assigned: Rome Air Development Center
George Veyera Assistant Prof. Rhode Island, University of Dept. of Civil Eng. Kingston, RI 02881 401\792-2692	Degree: PhD Specialty: Civil Eng. Assigned: Engineering & Services Center
Hung Vu Assistant Prof. California State University Mech. Eng. Dept. Long Beach, CA 90840 213\985-1524	Degree: PhD Specialty: Applied Mechanics Assigned: Frank J. Seiler Research Lab.
Bonnie Walker Assistant Prof. Central State Univ. Psychology Dept. Wilberforce, OH 45384 513\376-6516	Degree: PhD Specialty: Experimental Psychology Assigned: Aerospace Medical Research Lab.

NAME/ADDRESS	DEGREE, SPECIALTY, LABORATORY ASSIGNED
William Wallace Professor Rensselaer Poly. Inst CII Room 5117 Troy, NY 12180 518\276-6452	Degree: PhD Specialty: Management Science Assigned: Rome Air Development Center
Ji Wang Professor San Jose State Univ. S. 7 St. San Jose, CA 95192 408\924-4299	Degree: PhD Specialty: Mechanical Eng. Assigned: Astronautics Laboratory
Phillip Wapner Associate Prof. Southern Illinois University Dept. of Mech. Eng. Carbondale, IL 62901 618\453-7021	Degree: PhD Specialty: Chemical Eng. Assigned: Astronautics Laboratory
Robert Wheasler Professor Wyoming, Univ. of Box 3295 University Station Laramie, WY 82071 307\766-5126	Degree: PhD Specialty: Engineering Assigned: Aero Propulsion Laboratory
D. Wilkes Assistant Prof. Vanderbilt Univ. Box 1649 Station B Nashville, TN 37235 615\343-6016	Degree: PhD Specialty: Electrical Eng. Assigned: Arnold Engineering Development Center
Robert Willis Associate Prof. Mercer University 1400 Coleman Ave. Macon, GA 31207 912\744-2704	Degree: PhD Specialty: Physics Assigned: Geophysics Laboratory

NAME/ADDRESS	DEGREE, SPECIALTY, LABORATORY ASSIGNED
John Wills Professor Indiana Univ. Physics Dept. Bloomington, IN 47405 812\855-1479	Degree: PhD Specialty: Physics Assigned: Geophysics Laboratory
David Woehr Assistant Prof. Texas A&M Univ. Dept. of Psychology College Station, TX 77843 409\845-2097	Degree: PhD Specialty: Industrial Psychology Assigned: Human Resources Laboratory: Manpower and Personnel Division
Michael Wolfe Assistant Prof. West Virginia Univ. PO Box 6025 Morgantown, WV 26506 304\293-4495	Degree: PhD Specialty: Management Science Assigned: Human Resources Laboratory: Logistics & Human Factors
William Wolfe Associate Prof. Ohio State Univ. 470 Hitchcock Hall Columbus, OH 43210 614\292-0790	Degree: PhD Specialty: Engineering Assigned: Flight Dynamics Laboratory
James Wolper Assistant Prof. Hamilton College Dept. of Math. & Comp. Sci. Clinton, NY 13323 315\859-4417	Degree: PhD Specialty: Mathematics Assigned: Rome Air Development Center
Asad Yousuf Assistant Prof. Savannah State College PO Box 20089 Savannah, GA 31404 912\356-2154	Degree: MS Specialty: Electrical Eng. Assigned: Armament Laboratory

NAME/ADDRESS	DEGREE, SPECIALTY, LABORATORY ASSIGNED
Juin Yu Professor West Virginia Tech. Mechanical Eng. Dept. Montgomery, WV 25136 304\442-3248	Degree: PhD Specialty: Mechanical Engineering Assigned: Flight Dynamics Laboratory
Gregory Zagursky Assistant Prof. Morris College Div. General Studies Sumter, SC 29150 803\775-9371	Degree: MS Specialty: Biology Assigned: Occupational and Environmental Health Laboratory
Lawrence Zavodney Assistant Prof. Ohio State Univ. 209 Boyd Lab. Columbus, OH 43210 614\292-2209	Degree: PhD Specialty: Mechanical Eng. Assigned: Flight Dynamics Laboratory
Yehoshua Zeevi Professor Harvard Univ. Applied Sciences Cambridge, MA 02138 617\495-2850	Degree: PhD Specialty: Electrical Eng. Assigned: Human Resources Laboratory: Operations Training Division
Robert Zerwekh Assistant Prof. Northern Illinois University Dept. of Comp. Sci. DeKalb, IL 60115 815\753-6949	Degree: PhD Specialty: Philosophy Assigned: Human Resources Laboratory: Training Systems
Henry Zmuda Assistant Prof. Stevens Inst Tech Dept. of Electrical Eng. Hoboken, NJ 07030 201\420-5507	Degree: PhD Specialty: Electrical Eng. Assigned: Rome Air Development Center

PARTICIPANT LABORATORY ASSIGNMENT

C. PARTICIPANT LABORATORY ASSIGNMENT (Page 1)

1989 USAF/UES SUMMER FACULTY RESEARCH PROGRAM

AERO PROPULSION LABORATORY (WRDC/APL)
(Wright-Patterson Air Force Base)

1. Mingking Chyu
2. Jerry Clark
3. Wayne Eckerle
4. Frank Gerner
5. Thomas Lalk
6. Baruch Lieber
7. Larry Roe
8. William Schulz
9. Richard Tankin
10. Robert Wheasler

ARMAMENT LABORATORY (ATL)
(Eglin Air Force Base)

1. Peter Armandarez
2. Joseph Brown
3. Roger Bunting
4. Satish Chandra
5. David Cicci
6. George Coleman
7. Boghos Sivazlian
8. Steven Trogdon
9. Asad Yousuf

HARRY G. ARMSTRONG AEROSPACE MEDICAL RESEARCH LABORATORY (AAMRL)
(Wright-Patterson AFB)

1. Ernest Hallford
2. Carl Ingling
3. Charles Kincaid
4. Thomas Lockwood
5. Lewis Lutton
6. Ethel Matin
7. Randy Pollack
8. Michael Stanisic
9. Joseph Szucs
10. Chi-Ming Tang
11. Ebo Tei
12. Bonnie Walker

ARNOLD ENGINEERING DEVELOPMENT CENTER (AEDC)
(Arnold Air Force Base)

1. Brian Beecken
2. Lee Britt
3. Brian Circelli
4. Stephen Cobb
5. John Francis
6. Orlando Hankins
7. Lang-Wah Lee
8. Chun Fu Su
9. Richard Tipping
10. D. Mitchell Wilkes

ASTRONAUTICS LABORATORY (AL)
Edwards Air Force Base)

1. John Kenney
2. M. Inga Kenney
3. Lynn Kirms
4. Mark Kirms
5. Faysal Kolkailah
6. Bipin Pai
7. Vittal Rao
8. Richard Robertson
9. Larry Swanson
10. Roger Thompson
11. Ji Wang
12. Phillip Wapner

AVIONICS LABORATORY (WRDC/AL)
(Wright-Patterson Air Force Base)

1. David Choate
2. R. H. Cofer
3. Larry Crum
4. Mohammad Karim
5. Dar-Biau Liu
6. James Noyes
7. Robert Shock

C. PARTICIPANT LABORATORY ASSIGNMENT (Page 2)

ELECTRONIC SYSTEMS DIVISION (ESD)
(Hanscom Air Force Base)

1. Beryl Barber
2. Ajit Choudhury
3. S. Natarajan

ENGINEERING AND SERVICES CENTER (ESC)
(Tyndall Air Force Base)

1. Jon Anderson
2. William Bannister
3. Emerson Besch
4. Anthony Carlisle
5. Derald Chriss
6. Avery Demond
7. Kirk Hatfield
8. Kim Hayes
9. Deborah Ross
10. Teresa Taylor
11. George Veyera

FLIGHT DYNAMICS LABORATORY (WRDC/FDL)
(Wright-Patterson Air Force Base)

1. Larry Byrd
2. Kenneth Cornelius
3. Dennis Farrell
4. Augustus Morris
5. Arnold Polak
6. Nisar Shaikh
7. William Wolfe
8. Juin Yu
9. Lawrence Zavodney

FRANK J. SEILER RESEARCH LABORATORY (FJSRL)
(USAF Academy)

1. R. Granger
2. L. Hillman
3. John Lanning
4. John Sanders
5. Clay Sharts
6. Timothy Troutt
7. Hung Vu

GEOPHYSICS LABORATORY (AFGL)
(Hanscom Air Force Base)

1. Pradhip Bakshi
2. Chi Chen
3. P. Das
4. Alan Kafka
5. Charles Lishawa
6. Amy Miller
7. Thomas Miller
8. Henry Nebel
9. Hugh Nutley
10. Craig Rasmussen
11. Robert Willis
12. John Wills

HUMAN RESOURCES LABORATORY (HRL)
(Brooks, Williams, and Wright-Patterson Air Force Bases)

1. Christopher Bell
2. Kevin Bennett
3. Kathryn Cochran
4. Deborah Mitta
5. Miles Simpson
6. William Smith
7. Stanley Stephensen
8. P. Tomporowski
9. David Woehr
10. Michael Wolfe
11. Yehoshua Zeevi
12. Robert Zerwekh

C. PARTICIPANT LABORATORY ASSIGNMENT (Page 3)

MATERIALS LABORATORY (ML)
(Wright-Patterson Air Force Base)

1. Karren Brito
2. Donald Chung
3. Kenneth Currie
4. Peter Henrisken
5. Joseph Newkirk
6. Harvey Paige
7. Michael Resch
8. James Sherwood
9. Michael Sydor

OCCUPATIONAL AND ENVIRONMENTAL HEALTH LABORATORY (OEHL)
(Brooks Air Force Base)

1. Barbara Alvin
2. Stewart Maurer
3. Edmund Shearer
4. Gregory Zagursky

ROME AIR DEVELOPMENT CENTER (RADC)
(Griffiss Air Force Base)

1. Charles Alajajian
2. Ian Grosse
3. John Hadjilogiou
4. Henry Helmken
5. Stuart Hirshfield
6. Michael Klein
7. William Kuriger
8. Jay Lee
9. Robert O'Connell
10. Sally Sedelow
11. Khaja Subhani
12. Donald Ucci
13. William Wallace
14. James Wolper
15. Henry Zmuda

SCHOOL OF AEROSPACE MEDICINE (SAM)
(Brooks Air Force Base)

1. Thomas Abraham
2. Robert Blystone
3. Carolyn Caudle-Alexander
4. James Chambers
5. Mark Cornwall
6. Vito DelVecchio
7. Patrick Hannon
8. Cynthia Hardy
9. Jeffrey Himm
10. Gwendolyn Howze
11. Tze San Lee
12. Harold Longbotham
13. Rex Moyer
14. Raymond Quock
15. Paul Scheie
16. Ronald Seaman
17. Ram Tripathi

WEAPONS LABORATORY (WL)
(Kirtland Air Force Base)

1. Thomas Dwyer
2. William Filippone
3. William Grissom
4. Harry Hogan
5. Duc Nguyen
6. Duane Sanders
7. Hugh Siekfen
8. John Silvestro

WILFORD HALL MEDICAL CENTER (WHMC)
(Lackland Air Force Base)

1. Walter Drost-Hansen

RESEARCH REPORTS

RESEARCH REPORTS

1989 SUMMER FACULTY RESEARCH PROGRAM

Technical Report Number	Title	Professor
Volume I		
Armament Laboratory		
1	Reactive Compositions Using Light Metals and Metal Alloys	Dr. Peter Armendarez
2	Maneuvering Hard Target Penetrators	Dr. Joseph Brown
3	A Study of Ionic Polymer Membranes for Application as Capacitor Electrolytes and Preliminary Investigations on Photo-Activated Stripline Switches	Dr. Roger Bunting
4	Multisensor Seeker for Medium Range Air-to-Air Missiles	Dr. Satish Chandra
5	Extended Kalman Filter Tuning and Alternative Techniques	Dr. David Cicci
6	Statistical Analysis of Blast Loading in Concrete	Dr. George Coleman
7	A Methodology for Evaluating the Effectiveness of Smart Submunition Systems	Dr. Boghos Sivazlian
8	Shock Wave Initiated Detonation of an Explosive	Dr. Steven Trogdon
9	Distributed Filter Architecture Implementation with VLSI and Expert Systems	Dr. Asad Yousuf
Arnold Engineering Development Center		
10	Response of Infrared Detectors to Pulsed Radiation	Dr. Brian Beecken
11	An Analysis of Focal Plane Irradiance Effects on IR Detectors	Dr. Lee Britt
12	Code Development for Design of a High Temperature Hypersonic Facility Mixer	Dr. Brian Circelli

Arnold Engineering Development Center (continued)

13	Laser-Induced Fluorescence of Iodine and Sodium for Application in Resonant Doppler Velocimetry of Hypersonic Flows	Dr. Stephen Cobb
14	Thermal Analysis of Bodies Subjected to Aerodynamic Heating	Dr. John Francis
15	Diagnostics for Determination of Arc Plasma Parameters of the AEDC HEAT H1 Arc Heater	Dr. Orlando Hankins
16	The Design of Jet Mixers for an Arc Heater: An Experimental Approach	Dr. Lang-Wah Lee
17	Laser Induced Fluorescence (LIF) of Nitric Oxide (NO)	Dr. Chun Fu Su
18	Spectroscopic Monitoring of Exhaust Gases	Dr. Richard Tipping
19	Distributed and Parallel Image and Signal Processing	Dr. D. Wilkes

Astronautics Laboratory

20	Magnetic Perturbations of the Structural Characteristics, Photophysical Properties and Photochemical Behavior of Cryogenic Noble Gas-Alkali Metal Matrices	Dr. John W. Kenney
21	I_{sp} Enhancement Via Adsorption/ Absorption of Small Energetic Molecules on Solid Propellants	Dr. M. Inga Kenney
22	Studies Toward the Synthesis of Pentanitrobishomocubane	Dr. Lynn M. Kirms
23	The Preparation of Poly(imide Siloxane) Polymers: Oxygen Resistant Space Polymers	Prof. Mark Kirms
24	Numerical Presentation of Stress Analysis, Design and Fracture Mechanics for Composite Materials and Structures	Dr. Faysal Kolkailah
25	Fracture Behavior of a Composite Solid Rocket Propellant	Dr. Bipin Pai
26	Robust Control of a L Experimental Grid Using Reduced Order Models	Dr. Vittal Rao

Astronautics Laboratory (continued)

27	A Neural Network Approach to the Adaptive Control of Large Space Structures	Dr. Richard Robertson
28	Cryogenic Heat Pipes	Dr. Larry Swanson
29	Design and Development of a Flexible Multi-Body Dynamics Experiment	Dr. Roger Thompson
30	Synthesis of Active Space Structure Vibration Control Systems for an Astrex Test Article	Dr. Ji Wang
31	Dynamic Mechanical Response of Carbon/ Carbon Composites by Vibrating Reed Measurements	Dr. Phillip Wapner

Electronics Systems Division

32	Carrier Free Radar	Dr. Beryl Barber
33	Detection Performance for Over Resolved Targets with Varying Energy Level in Cells	Dr. Ajit Choudhury
34	Analysis of Testability Concepts and its Application to RSIP	Dr. S. Natarajan

Engineering and Services Center

35	Proposed Innovative Semi-Hard Aircraft Shelter	Dr. Jon Anderson
36	JP-8 Ignitability	Dr. William Bannister
37	Effect of Jet Aircraft Noise on Domestic Goats	Dr. Emerson Besch
38	An Algorithmic System for Subjective Comparisons	Dr. Anthony Carlisle
39	The Study of Alkali-Enhanced Cements and Concretes	Dr. Derald Chriss
40	Prediction of the Capillary Pressure-Saturation Relationships for Aquifiers Contaminated with Jet Fuels	Dr. Avery Demond
41	Contaminant Flux Reduction Through In Situ Solubility Modification	Dr. Kirk Hatfield

Engineering and Services Center (continued)

42	An FT-IR Spectroscopic Investigation of Surfactant Adsorption at the Mineral-Water Interface	Dr. Kim Hayes
43	Biodegradation of Jet Fuel JP-8	Dr. Deborah Ross
44	Further Development of the AFESC Centrifuge Facility	Dr. Teresa Taylor
45	Static and Dynamic Behavior of Compacted Unsaturated Sands	Dr. George Veyera

Volume II
Frank J. Seiler Research Laboratory

46	The Vibration of Thin Leading Edges	Dr. Robert Granger
47	Second Harmonic Generation in Optical Fibers	Dr. Lloyd Hillman
48	Evaluation of Cold Fusion in Molten Salt Systems	Dr. John Lanning
49	High Charge Density Batteries Employing Ionic Liquid Electrolytes	Dr. John Sanders
50	A Convenient Preparation of Nitronium Triflate and its Use for Nitration	Dr. Clay Sharts
51	An Investigation of Dynamic Stall Vortex Characteristics	Dr. Timothy Troutt
52	Modeling of a Structure-Actuator System with Structure-Borne Reaction-Mass Actuators and Optimal Design of Passive Vibration Absorbers	Dr. Hung Vu

Geophysics Laboratory

53	Impulse Approximation Formalism for Atom Molecule Collisions: Exact Theory and Limitations	Dr. Pradip Bakshi
54	A Statistical Analysis of the Geomagnetic Indices, 1932-1989	Dr. Chi Chen
55	Cumulus Parameterization in Numerical Prediction Models: Proposal for a New Parcel-Dynamical Approach	Dr. Phanindramohan Das

Geophysics Laboratory (continued)

56	Estimating Characteristics of Chemical Explosions in New England and Eastern Kazakhstan Using Local and Regional Seismic Data	Dr. Alan Kafka
57	A Study of the Water Vapor Cation-Neutral Reactions	Dr. Randal Lishawa
58	Acidities of Iron Hydride and Various Transition-Metal Compounds; Reactions of Iron and Iron Carbonyl Anions	Dr. Amy Miller
59	Acidities of Iron Hydride and Various Transition-Metal Compounds; Reactions of Iron and Iron Carbonyl Anions (Same Report as Dr. Amy Miller)	Dr. Thomas Miller
60	CO2(4.3μm) Vibrational Temperatures and Limb Radiances Under Sunlit Conditions in the 50-120 KM Altitude Range	Dr. Henry Nebel
61	Estimating Solar Flare Proton Fluences From 1850 with Tritium Data	Dr. Hugh Nutley
62	Electric Fields in the Middle-and Low-Latitude Ionosphere and Plasmasphere	Dr. Craig Rasmussen
63	Review and Assessment of Carbon Dioxide Pressure Broadening Data	Dr. Robert Willis
64	Non-Uniform Clouds	Dr. John Wills

Rome Air Development Center

65	Design Considerations in the Implementation of ACT Programmable Transversal Filters	Dr. Charles Alajajian
66	Automating Finite Element Reliability Assessment of Microelectronic Components	Dr. Ian Grosse
67	Design for Testability: From Components to Systems	Dr. John Hadjilogiou
68	Development of a High Resolution Research Facility	Dr. Henry Helmken
69	Iterative V&V: A Model for Verification and Validation in the Rapid Prototyping Life Cycle	Dr. Stuart Hirshfield

Rome Air Development Center (continued)

70	Capable Neural Networks for Applications in Data Analysis (1988 Participant)	Dr. Oleg Jakubowicz
71	A Study of Interacting Tunneling Units with Possible Application to High Temperature Superconductors	Dr. Michael Klein
72	Design of a Practical Binary Phase-Only Optical Correlator	Dr. William Kuriger
73	A Computer for Temporal Frequency Spectrum of Vegetation Clutter Return	Dr. Jay Lee
74	Material Effects in Photoconductive Frozen Wave Generators	Dr. Robert O'Connell
75	Parallel Processing for Associative Semantic Space Analysis	Dr. Sally Sedelow
76	Characterization of an Optical Switch	Dr. Khaja Subhani
77	Study of a Communication Receiver for Spread Spectrum Signals	Dr. Donald Ucci
78	Tactical Command and Control: A Group Problem Solving and Decision Making Process	Dr. William Wallace
79	Neural Networks for Invariant Pattern Recognition: A Survey of the State of the Art	Dr. James Wolper
80	Optical Beamforming for Phased Array Antennas	Dr. Henry Zmuda

Weapons Laboratory

81	An Experimental Protocol for Line-of-Sight Slewing, Optical Alignment and AFT Body Station Keeping Control Emulation	Dr. Thomas Dwyer
82	Linking the Twodant S_N Code and the MCNP Monte Carlo Code	Dr. William Filippone
83	Simulation of a Spray Reactor for Generating Excited Oxygen	Dr. William Grissom
84	Modeling the Response of Pressurized Composite Cylinders to Laser Damage	Dr. Harry Hogan

Weapons Laboratory (continued)

85	Parallel and Vector Processing for Nonlinear Finite Element Analysis ** To be published at Weapons Lab as Technical Memorandum **	Dr. Duc Nguyen
86	Scattering of Elastic Waves in a Random Inhomogeneous Soil Media	Dr. Duane Sanders
87	A Possible New Source of Negative Hydrogen Ions	Dr. Hugh Siefken
88	The Effect of a Maverick Missile on a Test Antenna at Spacings Less than $2D^2/\lambda$	Dr. John Silvestro

Volume III
(Wright Research Development Center)
Aero Propulsion Laboratory

89	Preliminary Report on Measurements of Turbulent Transport in a Rib Roughened Channel	Dr. Mingking Chyu
90	Experimental Study of Electronic Excitation of Xenon by Electron Impact	Dr. Jerry Clark
91	No Report Submitted	Dr. Wayne Eckerle
92	Flow Limitations in Micro Heat Pipes	Dr. Frank Gerner
93	Conceptual Design of an In-House Facility for Endothermic Fuels Research (Report is not publishable at this time)	Dr. Thomas Lalk
94	Large-Scale Motion and Coherent Structures in Axisymmetric Swirling Flow of a Dump Combustor	Dr. Baruch Lieber
95	Stability Modification and Flowfield Evaluation of a Ramjet Combustor Model	Dr. Larry Roe
96	Oxidative Thermal Degradation Studies of a Surrogate JP-8 with a Modified Thermal Precipitation Apparatus	Dr. William Schulz
97	Measurements of Droplet Velocity and Size Distributions in Sprays	Dr. Richard Tankin
98	Aircraft Engine Compressor and Fan Rework Practices	Dr. Robert Wheasler

Avionics Laboratory

99	A Theoretical Resolution of Multiple Frequencies	Dr. David Choate
100	Ladar Target Detection and Recognition	Dr. R. H. Cofer
101	Toolbox for Image Processing using Distributed Computing	Dr. Larry Crum
102	Analytical Model of a Unique E-O Beam Scanner	Dr. Mohammad Karim
103	Dynamic Task Scheduling for the "ADA Distributed System Evaluation Testbed (ADSET)"	Dr. Dar-Biau Liu
104	Ada Compiler Efficiency Evaluation	Dr. James Noyes
105	Towards a Course-Grained Test Suite for VHDL Validation	Dr. Robert Shock

Flight Dynamics Laboratory

106	Parametric Study of Combined Boiling and Partial Dryout in Liquid Metal Heat Pipe Wicks	Dr. Larry Byrd
107	3-D Analysis of Laser Measurements of Vortex Bursting on Chined Forebody Fighter Configuration	Dr. Kenneth Cornelius
108	Robust Design Using Internal Model Control	Dr. Dennis Farrell
109	Neural Networks and their Role in Visual Object Recognition	Dr. Augustus Morris
110	A Study of Surface Roughness Effects in Hypersonic Flow	Dr. Arnold Polak
111	Life Prediction of Aircraft Transparencies by Accelerated Crazing Tests	Dr. Nisar Shaikh
112	Strain Distribution in Composite Coupons in Tension	Dr. William Wolfe
113	Characteristics of an Osmotically Driven Thermal Transfer Cycle	Dr. Juin Yu
114	The Influence of Viscoelastically Damped Members on the Dynamic Response of Flexible Elastic Structures	Dr. Lawrence Zavodney

Materials Laboratory

115	No Report Submitted	Dr. Karren Brito
116	The in-situ Laser Deposition of Superconducting Thin Film	Dr. Donald Chung
117	An Intelligent Neural Model for Recognition of Input/Output Patterns for a Molecular Beam Epitaxy Process	Dr. Kenneth Currie
118	Scanning Tunneling Microscopy and Ballistic-Electron-Emission Spectroscopy	Dr. Peter Henriksen
119	Evaluation of CR-SI Alloys for Aerospace Structural Applications	Dr. Joseph Newkirk
120	Molecular Modeling and Computational Chemistry: Studies of Additives for Fluids and Lubricants	Dr. Harvey Paige
121	Improvement in the Detection of Microcrack Initiation and Growth During Fatigue Cycling by Surface Acoustic Wave Scattering	Dr. Michael Resch
122	Investigation of the Thermomechanical Response of a Titanium Aluminide Metal Matrix Composite Using a Viscoplastic Constitutive Theory	Dr. James Sherwood
123	Photoreflectance of AlGaAs/GaAs Interfaces	Dr. Michael Sydor

Volume IV
Human Systems Division Laboratories
Harry G. Armstrong Aerospace Medical Research Laboratory

124	Perceived Time to Contact as a Function of Event Structure During Self Motion	Dr. Ernest Hallford
125	The Effect of Luminance on the Perceived Saturation of Lights	Dr. Carl Ingling
126	Comparison of Microsaint and Colored Petri Nets as Modeling Techniques	Dr. Charles Kincaid
127	Degradation of the Renal Peritubular Basement Membrane in Relation to Toxic Nephropathy of Fuels of Military Interest	Dr. Thomas Lockwood

Harry G. Armstrong Medical Research Laboratory (continued)

128	Heart Rate and Other Cardiovascular Parameters as Measures of Mental Effort	Dr. Lewis Lutton
129	Breakdown of Total Information Processing Time into During-Display and Post-Display Components for Serial and Spatially Distributed Visual Presentations	Dr. Ethel Matin
130	An Investigation Into Techniques for Landmark Identification on 3-D Images of Human Subjects (Not publishable at this time)	Dr. Randy Pollack
131	Kinematic Mappings Between the EXOS Handmaster Exoskeleton[1] and the Utah/MIT Dexterous Robot Hand	Dr. Michael Stanisic
132	Harness Belt Task	Dr. Joseph Szucs
133	Articulated Total Body (ATB) View Program with Harness-Belt Implementation	Dr. Chi-Ming Tang
134	Insights into Human Factors in Aviation with Emphasis on Non-Canonical Flow Fields	Dr. Ebo Tei
135	Effects of Data Error on Problem-Solving Heuristics	Dr. Bonnie Walker

Human Resources Laboratory

136	Software Development to Support Data Collection and Analysis of Cognitive Task Analysis Studies	Dr. Christopher Bell
137	Computer-based Training for Complex, Dynamic Tasks	Dr. Kevin Bennett
138	Working Memory and Cognitive Structure	Dr. Kathryn Cochran
139	Investigation of Color Appearance within Low Light Levels (1988 Participant)	Dr. Douglas Mandra
140	Fisheye Representation of Information: IMIS User Interface	Dr. Deborah Mitta
141	The Validation of the Occupational Learning Difficulty (OLD) Index as a Predictor of Retrainee Performance	Dr. Miles Simpson

Human Resources Laboratory

142	Assessment of Intelligent Tutoring Systems	Dr. William Smith
143	The Role of the Instructor in Computer Based Training (CBT)	Dr. Stanley Stephenson
144	Evaluation of Air-Intercept Performance: Observer Reliability Issues	Dr. Phillip Tomporowski
145	Career Progression in Air Force Enlisted Personnel: An Examination of Two Alternate Criterion Measures	Dr. David Woehr
146	Development of the "City of Quality (Coq)" Group Decision Support System	Dr. Michael Wolfe
147	Variable Resolution Imagery for Flight Simulators	Dr. Yehoshua Zeevi
148	Neurocomputing the Student Model in an Intelligent Tutoring System	Dr. Robert Zerwekh

Occupational and Environmental Health Laboratory

149	Statistical Analyses of Data Pertaining to Ground Water Contamination and Laboratory Quality Control	Dr. Barbara Alvin
150	Design of an Automated Radiofrequency Radiation Measurement System (ARRMS)	Dr. Stewart Maurer
151	Construction and Use of an Identification Manual for Identifying Fibrous Material by Scanning Electron Microscopy with Attached X-Ray Analyzer	Dr. Edmund Shearer
152	Biological Analysis of Three Ponds at Peterson AFB, Colorado Springs, CO	Dr. Gregory Zagursky

School of Aerospace Medicine

153	Convergence Properties of the Occurrence/Exposure Rate	Mr. Thomas Abraham
154	Transmission Electron Microscopy of Mouse Macrophase RAW 264.7 Cells treated with Lipopolysaccharide, 3-Amino Tryosine, and RFR	Dr. Robert Blystone
155	Effects of Microwave Radiation on Cultured Cells	Dr. Carolyn Caudle-Alexander

School of Aerospace Medicine (continued)

156	The Effects of Three Reputed Carboxyesterase Inhibitors Upon Rat Serum Esterase Activity Using Paranitrophenyl and Naphthyl Esters as Substrates	Dr. James Chambers
157	Anti-G Suit Inflation Influence on Lower Extremity Muscle Performance during Sustained +G_z Acceleration	Dr. Mark Cornwall
158	PCR Analysis and in situ Detection of Ureaplasma urealyticum and Mycoplasma hominis	Dr. Vito DelVecchio
159	The Influence of Broad Spectrum Illumination on Circadian Neuroendocrine Responses and Performance	Dr. Patrick Hannon
160	The relationship between locus of control, performance on cognitive tasks, and affective states after the consumption of antihistamines in hi- and low-workload conditions among aircrew personnel	Dr. Cynthia Ford Hardy
161	Aspects of the Diffusion of Inert Gases in Biological Systems	Dr. Jeffrey Himm
162	Studies of Interactions Between Microwaves, Melanin and Melanocytes	Dr. Gwendolyn Howze
163	Two-Phase Regression Model with Application	Dr. Tze-San Lee
164	System and Signal Analysis of VEP Data and Joystick Error Analysis	Dr. Harold Longbotham
165	Higher Plant Hormones Effect Upon Chlamydomonas Phototaxis	Dr. Rex Moyer
166	Influence of Radio Frequency Radiation on Psychotropic Drug Effects	Dr. Raymond Quock
167	Porous Glass as Bed Material in a Pressure Swing Adsorption Unit Used for Air Purification	Dr. Paul Scheie
168	Models for RFR Biological Effects	Dr. Ronald Seaman

School of Aerospace Medicine (continued)

169	An Investigation of Dioxin Half-Life Heterogeneity in Humans Based on Two Measurements per Subject	Dr. Ram Tripathi

Wilford Hall Medical Center

170	Temperature Effects on Erythrocyte Sedimentation Rates in Whole Blood and on Erythrocyte and Platelet Volumes	Dr. Walter Drost-Hansen

1988 USAF-UES SUMMER FACULTY RESEARCH PROGRAM/GRADUATE STUDENT RESEARCH PROGRAM

Sponsored by the

AIR FORCE OF SCIENTIFIC RESEARCH

Conducted by the

UNIVERSAL ENERGY SYSTEMS, INC.

FINAL REPORT

PRELIMINARY REPORT ON MEASUREMENTS OF TURBULENT TRANSPORT IN A RIB ROUGHENED CHANNEL

Prepared by:	Mingking K. Chyu
Academic Rank:	Assistant Professor
	Department of Mechanical Engineering Carnegie Mellon University Pittsburgh, PA 15213
Research Location:	Wright Research and Development Center, POTC, Dayton Ohio
USAF Researcher:	Dr. Richard B. Rivir

Date:	September 30, 1989
Contract Number:	F49620-88-R-0053

PRELIMINARY REPORT ON MEASUREMENTS OF TURBULENT TRANSPORT IN A RIB ROUGHENED CHANNEL

M. K. Chyu
Dept. of Mechanical Engineering
Carnegie Mellon University
Pittsburgh, PA 15213

R. B. Rivir
POTC
Wright Research Development Center
WPAFB, OH 45433

ABSTRACT

The primary focus of this study is to investigate both momentum and heat transfer in a channel with two of its bounding walls roughed by transverse ribs. Transverse ribs generally arranged in a periodic fashion exist in the internal cooling passage of a turbine blade or vane. To study the momentum transfer, it uses hot-wire anemometry for the measurements of flow and turbulence distribution over an complete period. The heat transfer study utilizes the thin liquid crystal method operated in a transient mode. Detailed local heat transfer coefficient is inferred according to the color response of the liquid crystal. Fabrication of the test rig has been completed, and measurements are currently under way. In addition to description of the experimental system, this report contains a literature review of rib surface heat transfer and results of a preliminary study using analogous mass transfer. The latter has provided the on-going study with valuable background information and basis for future verification and comparison.

Acknowledgements

The first author (MKC) of this report is grateful to Air Force Systems Command, Air Force Office of Scientific Research, Universal Energy System and AFWAL/POTC for the appointment of Summer Faculty Research Fellowship.

In addition, he expresses his special appreciation to Dr. Richard B. Rivir at AFWAL/POTC for his collaboration in this project and personal friendship. Thanks to Mr. Jerry Reed for his assistance in fabrication of test apparatus.

I. INTRODUCTION

In advanced gas turbine airfoil designs, serpentine-pass internal cooling channels are often used to alleviate the effects of thermal loading on blade or vane exteriors [1]. To further enhance the heat transfer in a cooling channel, transverse ribs, often termed turbulence promoters, are installed on the channel surface. A surface-mounted roughness rib penetrates the viscous sublayer to promote turbulent transport which, in turn, increases the heat transfer from the surface as compared to its smooth counterpart. This increase in heat transfer is accompanied by a rise in frictional loss. If the heat transfer increase per unit of friction increase is of concern, an "efficiency index," sometimes defined simply as the ratio of Stanton number to friction factor (St/f), is used to characterize the overall performance of a roughened surface. Geometric parameters including the ratio of rib height-to-channel hydraulic diameter (e/D_h), ratio of pitch to height (p/e), rib angle-of-attack (θ), and the relative arrangement of ribs on different walls are often have pronounced effects on both the heat transfer and friction factor. In modern turbines with serpentine passage cooling, the passage aspect ratio, which varies considerably from the leading edge through the mid-chord and to the trailing edge, is also an important parameter.

II. OBJECTIVES OF RESEARCH EFFORTS

The primary objective of this study is to gain an insight of the transport phenomena in a duct with two of its bounding walls roughened by transverse ribs. The entire study is comprised of two different types of experimental research, one deals with momentum transfer and the other concerning heat transfer. For momentum transfer, emphasis is placed on investigating the characteristics of secondary flow and turbulence. Information in this regard is little available, especially for the cases with inclined ribs. The momentum study will be followed by a detailed local heat transfer measurement using the same test rig and flow conditions. Results obtained from these two approaches provide further understanding in the fundamental aspects of flow and heat transfer with ribbed surface. In addition, it will benefit future designs of internal cooling passage.

III. BRIEF LITERATURE REVIEW

Most of studies on transverse ribs are directed toward investigating the relationship between average heat transfer and friction loss for various channel geometries. An earlier study by Webb et al. [2], with $10 \leq p/e \leq 40$ and $\theta = 90^\circ$ in a circular pipe, has suggested that the heat transfer coefficient attains a maximum value when $10 < p/e < 15$. Several investigators have suggested that ribs with an oblique angle-of-attack, rather than 90°, will yield a higher heat transfer coefficient and/or a higher efficiency index. Metzger et al. [3] using a paint-melting technique studied the effects of rib angle and length in a triangular duct which simulates the first cooling passage near the leading edge of a blade. For $Re \leq 2 \times 10^4$ and $p/e = 10$, their results show that ribs with 60° orientation produces the highest heat transfer among three rib angles tested, (i.e. $\theta = 30^\circ$, 60° and 90°). Similar observation for flow in a rectangular channel are also reported in another study by Metzger et al. [4]. They have concluded that the heat transfer enhancement with inclined ribs is mainly caused by the streamwise growth of a rib-induced, cross-channel secondary flow, rather than from a direct effect of the flow-to-rib incidence angle. Han et al. [5,6] reported the rib angle effects on rectangular and square ducts with several values of e/D_h and p/e. Data obtained from these studies are also consistent with those reported by Metzger et al. [3,4]; surfaces roughened with 60° ribs yield the highest heat transfer coefficient, but frictional loss is also the greatest. In addition, the maximum efficiency index occurs at $\theta \approx 45^\circ$. For $3 \times 10^4 \leq Re \leq 5 \times 10^4$, heat transfer with $\theta = 60^\circ$ is about 5 to 10% higher than that of $\theta = 90^\circ$; however, the accompanied increase in friction factor is about 35%. The difference of heat transfer between $\theta = 60^\circ$ and 90° decreases with an increase in Reynolds number. Similar results have also been reported for circular pipes by Gee and Webb [7].

Surface heat transfer near a rib turbulator is determined by the nature of flow field in the region. Flow past a rib roughness includes the phenomena of boundary layer separation, followed by separated shear layer reattachment and boundary layer re-development. For repeated ribs with 90° orientation, flow in the near wall region is primarily determined by the value of p/e. The shear layer reattachment on the surface between two neighboring ribs only occurs when $p/e \geq 6.6$, according to a earlier study by Mantle [8]. However, other studies have reported higher values of p/e, approximately equal to 10, required for the existence of reattachment [9,10]. The distance between the reattachment location and the rib downstream-facing wall is termed the reattachment length, X_r. For $p/e \approx 10$, X_r/e is approximately 3 to 5 [8-11].

In the region near reattachment, the heat transfer coefficient reaches a local maximum. This is the primary reason for the heat transfer augmentation for p/e ≈ 10.

For cases with small values of p/e, the separated shear layer reattaches at the front wall of the downstream rib, and the space between ribs is filled completely with a recirculating bubble. The magnitude of heat transfer coefficient is expected to be low, and it generally increases along the streamwise direction. However, a local maximum heat transfer coefficient near the mid-pitch, similar to that caused by the reattachment effect, has been reported for a p/e value as low as 7 [11,12]. Moreover, in the same studies for p/e = 5, a sharp rise of heat transfer coefficient is noted to exist immediately ahead of a square rib. A peculiar flow pattern including strong corner vortices and intermittent unsteady bursts near the region is speculated [12]. The bursts can be a very effective means for energy transport between the near wall region and the mainstream. These observations infer that the enhancement of heat transfer with p/e < 10 can be very significant, contradictory to previous speculation.

IV. EXPERIMENTAL APPARATUS AND MEASUREMENT

Experiments are carried out in a specially designed wind tunnel made of plexiglass. It measures approximately 6 m in total length with a square cross section of 152 mm each side. The wind tunnel is operated in suction mode by installing a centrifugal blower downstream of the test section and driven by a one horsepower AC motor. The air enters the belmouth opening of the rig and passes through a honeycomb flow straightener before reaching the test section. Flow rate passing through the tunnel is varied by adjusting the size of four bleeding holes immediately ahead of the blower.

In the test section, there are 6 periods of square, transverse ribs located both top and bottom walls. The side walls are smooth without ribs. The rib made of aluminum has a height of 25.4 mm which is equal to one-sixth of the duct height. Note that the rib length varies depending on the degree of rib inclination. The values of p/e ratio are 5 and 10, and $\theta = 45^{\circ}$ and 90°.

The measurement of flow and turbulence uses hot-wire anemometry. Most detailed data are taken in the fourth period where the periodic nature is considered to be prevailing in both momentum and energy transport. A traversing device driven by a

stepper-motor carries the hot-wire probe scanning the entire period in all three coordinates. For the measurement of local heat transfer coefficient, it uses thin liquid crystal coating sprayed on the surface of interest, and the heat transfer coefficients are inferred based on the color reflected from the coating. This is a very fast and relatively inexpensive technique, and has many favorable aspects compared to conventional heat transfer methods. A significant advantage of this method, especially for heat convection involved flow separation and recirculation as existed in the present ribbed surface, is that appropriate thermal boundary conditions are naturally imposed on the coating surface.

Currently, fabrication of the test rig has just completed and under further testing. The rest of the report discusses some important findings from a recent experiment using a mass transfer analogous method. Results from this mass transfer experiment have provided background information and design criteria for the primary tasks with hot-wire anemometry and liquid crystal.

V. ANALOGOUS MASS TRANSFER RESULTS

The particular mass transfer technique used is the naphthalene sublimation technique. By invoking an analogy between heat and mass transfer, the mass transfer results can be transformed into their heat transfer counterparts [13]. In fact, mass transfer experiments are often more effective and accurate for obtaining detailed local transfer information that the corresponding heat transfer techniques. Direct heat transfer experiments for a local study can be inaccurate because of difficulties associated with thermal insulation of small sections of the surface and with measurements of the local heat flux and surface temperature. To measure the local mass transfer coefficient, the change of naphthalene thickness at a specific location needs to be determined. This is accomplished by using an automated, micro-computer control naphthalene surface measurement system. Details of the measurement system and operating procedures have been discussed earlier by Goldstein et al. [14].

There are four test cases in this study for both p/e = 5 and 10, each with θ = 60° and 90°. The same Reynolds number, based on bulk mean velocity and hydraulic diameter, is about 4×10^4. Figure 1 shows a schematic of the rib surface and coordinate system designated. Note that the nature of the flow in this study is primarily the type of flow over an external surface, rather than flow in a confined

channel. To achieve the periodic condition, the test section contains ten periods preceding the actual measurement domain. The area-averaged mass transfer results for ribbed surface are tabulated in Table 1, listing the average Stanton number, $\overline{St}$, and the ratio $\overline{St}/\overline{St_o}$, where $\overline{St_o}$ is the average mass transfer from a smooth surface without rib. The latter is a normalized index representing the mass transfer enhancement caused by the presence of the ribs. The highest $\overline{St}$ (and $\overline{St}/\overline{St_o}$) exists for p/e = 5 and θ = 90°, and the lowest is for p/e = 10 and θ = 90°.

For θ = 90°, values of $\overline{St}/\overline{St_o}$ for p/e = 5 is approximately 27% higher than that of p/e = 10 (2.70 vs. 2.12). Several earlier studies using different experiment systems from the present one have found contradicting results. Han et al. [5], using a rectangular duct with e/D_h = 0.056, has reported that heat transfer Stanton number for p/e = 10 is always higher than that of p/e = 5. However, the difference appears to be diminishing as the Reynolds number increases, nearly 30% for Re = 4×10^3 and less than 10% for Re = 1.5×10^4. The Reynolds number in the present study, 4×10^4, exceeds the test range of Re used by Han et al. [5]. Berger et al. [11] use the electrochemical mass transfer technique to investigate the rib effects on the mass transfer in a circular pipe. Such a mass transfer system has very high Schmidt number, typically of the order of 10^3. Their results indicate that, for Re $\leq 3 \times 10^4$, the magnitudes of $\overline{St}/\overline{St_o}$ between p/e = 5 and 10 are almost equal, approximately 2.5 for p/e = 5 and 2.6 for p/e = 10. An earlier study by Kattche and Mackewicz [15], using the naphthalene sublimation technique similar to the present one, has reported a higher $\overline{St}/\overline{St_o}$ for p/e = 7 than p/e = 8.5, by approximately 25%.

The factors possibly causing difference in the aforementioned results include the testing conditions, the Prandtl/Schmidt number dependency, and the experimental set-up. The last one can be crucial to the result accuracy. A typical heat transfer experiment uses discretely located thermocouple(s) to measure the surface temperature. In some cases, it uses only one thermocouple located near mid-pitch and adopts its reading as the mean temperature over the entire pitch. Heat transfer coefficient is then calculated by a given surface heat flux and the measured temperature. Therefore, it is arguable whether the heat transfer coefficient obtained this way is an accurate representative of the period-averaged value. Such a concern is especially justifiable when the distribution of the local transfer coefficient is highly non-uniform, which indeed is the case as to be shown later.

A change of rib angle-of-attack, θ, from 90° to 60° produces opposite effects on the mass transfer for p/e = 5 and 10. The value of $\overline{St}/\overline{St}_o$ increases approximately 21% (2.56 vs. 2.12) for p/e = 10 and decreases slightly, about 4% (2.70 vs. 2.59), for p/e = 5. This indicates that θ may have insignificant effects on the heat/mass transfer for a ribbed surface with small p/e ratios. However, no relevant studies for p/e < 10 has been found in the literature. Han et al. [6] recently have studied the angle effects on the heat transfer for p/e = 10 in a square channel, and their results show that the heat transfer coefficient for θ = 60° is always higher than 90°. The difference decreases with the Reynolds number, nearly 75% for Re = 10^4 and approximately 15% for Re = 5 x 10^4. The present 21% increase of $\overline{St}/\overline{St}_o$ at Re = 4 x 10^4 shows a very good agreement with the corresponding result reported by Han et al. [6].

Figures. 2 to 5 display the contour plots of $St/\overline{St}$ to describe the relative distribution of mass transfer coefficient within the entire pitch. Features disclosed in these figures also provide explanation for the average results shown in Table 1. Each case displays a very non-uniform distribution, as it possesses several local maxima and minima. For θ = 90°, the present results are in good agreement with those reported in several previous studies [11,12]. For p/e = 5 (Fig. 2), St increases almost linearly with X/e. It starts with a relatively low value immediately behind the upstream rib and reaches a peak value of nearly four times that of the smooth case just in front of the downstream rib (1.6 times of $\overline{St}$). For p/e = 10 (Fig. 3), the maximum St caused by the reattachment effect locates approximately two rib-height downstream, i.e. $X_r/e \approx 2$. Its magnitude is about 2.5 times larger than that of the smooth case. Downstream of this maximum, St decreases with X, then rises sharply at approximately 1.5 rib-height ahead of the downstream rib.

The rib inclination affects the distribution as well as the magnitude of the local mass transfer coefficient significantly. Particularly in Fig. 5 that the very non-uniform distribution of $St/\overline{St}$ further attests to the flow complexity for p/e = 10 with θ = 60°. For θ = 90°, the distributions for both p/e ratios are quite symmetric relative to the duct center line. Mass transfer in regions near the channel side walls is slightly higher than that in the middle. One distinct feature noted for all cases studied is that the mass transfer close to the front corner of the downstream rib is always very high. This is somewhat contradicting to the notion of heat transfer just ahead of a two-dimensional obstacle. As flow approaches the obstacle, the adverse pressure gradient induces boundary layer separation which, in turn, forms a vortex recirculating in the

front corner. The relatively stagnant flow associated with this recirculation generally implies low mass transfer coefficients prevailing in the region. However, evidence has shown that, even with a generally two-dimensional rib geometry, the flow nature in the corner vortex is by no means a "dead air." Instead, the vortex rotates intensely in helical fashion across the span and bursts periodically into the mainstream [12,16]. Such flow characteristics involving three-dimensionality and unsteadiness produce higher turbulent mixing in general, thus enhance convective transport. For p/e = 5, a different and alternative explanation is that the high turbulence level associated with the free shear layer are imposed on the intense unsteady vortex structure by reattachment that is located at approximately the same location.

The details of local mass transfer with 60° rib inclination can be understood by examining the flow pattern in the near wall region. Fig. 6 displays two sketches of wall streak lines visualized by using the graphite-oil mixture method, for $\theta = 60°$ at p/e = 5 and 10, respectively. The transparent (bright) portion represents region with higher flow velocity, hence higher convection transport, than the opaque (dark) part. At the upstream-most corner, the transparent and the opaque portions are clearly segregated by a dividing streak line which obliques from the rib axis at an approximately 20° angle. This oblique angle appears to be independent of p/e ratio and is a function of θ only. It is clear that the inclined rib diverts the fluid away from the upstream-most corner, gaining a spanwise component, and towards the downstream-most corner. Near the upstream-most corner, by continuity, the excessive diversion must be accompanied by a replenishment of less naphthalene enriched air (equivalent to cooler air in heat transfer) from the mainstream. Accordingly, the mass transfer in this region is higher. On the other hand, the opposite effect exists in the mid-section and towards downstream-most corner as the diverted flow imparts more naphthalene enriched air into the region. For p/e = 5, this appears to be the primary cause for the lower mass transfer compared to the corresponding case without rib inclination. For p/e =10, such an effect prevails only in the region not too far behind the upstream rib, approximately X/e < 3. As the diverted flow moves toward the downstream-most corner, it becomes unstable and a wavy motion has been observed during the flow visualization test. Several transparent spots existing near the mid-pitch shown in Fig. 6 (b) are the result of this phenomenon. This flow instability is deemed to be largely responsible for the increase in heat or mass transfer from a surface mounted with inclined ribs and having a large p/e ratio.

CONCLUSIONS AND RECOMMENDATIONS

An experimental investigation of momentum and heat transfer with rib-roughened surface are presently being pursued. The effects of rib inclination and rib pitch-to height ratio on the fundamental transport phenomena are the primary concern. A survey of the literature reveals that virtually no information is available concerning the secondary flow and turbulence in a ribbed channel, particularly for inclined ribs. The heat transfer measurement uses the newly-developed liquid crystal thermal visualization operated in a transient mode. Such a technique has been considered to be very effective for a heat transfer study with strong flow separation. As an auxiliary study, a mass transfer experiment using the naphthalene sublimation technique has revealed important background information and local transfer coefficient. According to the mass transfer results, it is speculated that the inclined-ribs induced secondary flow diverts the heated boundary layer fluid leaving the upstream-end region and replaces it with relatively cool fluid from the core flow. A high local heat transfer should exist in this region. Nevertheless, the rib inclination has opposite effects on the overall area-averaged heat transfer between p/e = 5 and 10. The value of St with θ = 60° is approximately 21% higher than with θ = 90° for p/e = 10; however, it is 4% lower for p/e = 5. The case with p/e = 5 and θ = 90° has the highest overall heat transfer in the present study, and its St is approximately 27% higher than that of p/e = 10, θ = 90°. This is in sharp contrast to the results from several previous studies concerning heat transfer enhancement with surfaces roughened by transverse ribs; the generally accepted notion is that surfaces with p/e = 10 is more favorable than those with p/e = 5. The sharp rise of mass transfer just ahead of a rib is speculated to be caused by vortex helical motion and periodic boundary layer bursting in the region. The conventional concept of steady, two-dimensional, "dead air" type of flow recirculation generally applied to the ribbed surfaces with short p/e ratios may be inappropriate. It is hoped that the results obtained from the ongoing research can provide viable evidence to either confirm or challenge these speculations.

REFERENCES

1. Metzger, D.E., "Development in Air Cooling of Gas Turbine Vanes and Blades," ASME Paper 83-GT-160, 1983.

2. Webb, R.L., Eckert, E.R.G. and Goldstein, R.J., "Heat Transfer and Friction in Tubes with Repeated-Rib Roughness," Int. J. Heat Mass Transfer, Vol. 14, 1971, pp. 601-617.

3. Metzger, D.E., Vedula, R.P. and Breen, D.D., "The Effect of Rib Angle and Length on Convection Heat Transfer in Rib-Roughened Triangular Ducts," Proc. ASME-JSME Thermal Engineering Joint Conference, Vol. 3, 1987, pp. 327-333.

4. Metzger, D.E., Chyu, M.K. and B:nker, R.S.,"The Contribution of On-Rib Heat Transfer Coefficients to Total Heat Transfer from Rib-Roughened Surfaces," Proc. of Second International Symposium on Transport Phenomena, Dynamics, and Design of Rotating Machinery, Vol. 2, pp. 324-336, March, 1988,

5. Han J.C., Glickman, L.R. and Rohsenow, W.M., "An Investigation of Heat Transfer and Friction for Rib-Roughened Surfaces," Int. J. Heat Mass Transfer, Vol. 21, 1978, pp. 1143-1156.

6. Han J.C., Park, J.S. and Lei, C.K., "Heat Transfer Enhancement in Channels with Turbulence Promoters," ASME Paper 84-WA/HT-72, 1984.

7. Gee D.L. and Webb R.L.,"Forced Convection Heat Transfer in Helically Rib-Roughened Tubes," Int. J. Heat Mass Transfer, Vol. 23, 1980, pp. 1127-1136,

8. Mantle, P.L., "A New Type of Roughened Heat Transfer Surface Selected by Flow Visualization Technique, " Proc. 3rd. Int. Heat Transfer Conf., Chicago, Vol. 1, 1966, pp. 45-55.

9. Klein, D.E., Miles, J.B. and Bull, S.R., "Pressure Drop Measurements and Flow Visualization Surrounding Roughness Elements," J. Energy, Vol. 18, No. 1, 1979, pp. 53-63.

10. Aytekin, A. and Berger, F.P., "Turbulent Flow in Rectangular Ducts with Low Aspect Ratios Having One Rough Wall," Nuclear Energy, Vol. 18, 1979, PP. 53-63.

11. Berger, F.P., Lau, K.F. and Lau, F.L., "Local Mass/Heat Transfer Distribution on Surfaces Roughened with Small Square Ribs," Int. J. Heat Mass Transfer, Vol. 22, 1979, pp. 1465-1656.

12. Williams, F. and Watts, J., "The Development of Rough Surfaces with Improved Heat Transfer Performance and a Study of the Mechanisms Involved," Proc. 4th Int. Heat Transfer Conf., Vasailles, Vol. 4, paper FC 5.5, 1970.

13. Eckert, E.R.G., "Analogies tc Heat Transfer Processes," Measurements in Heat Transfer, ed. by Eckert, E.R.G. and Goldstein, R.J., Hemisphere Publishing, New York, 1976.

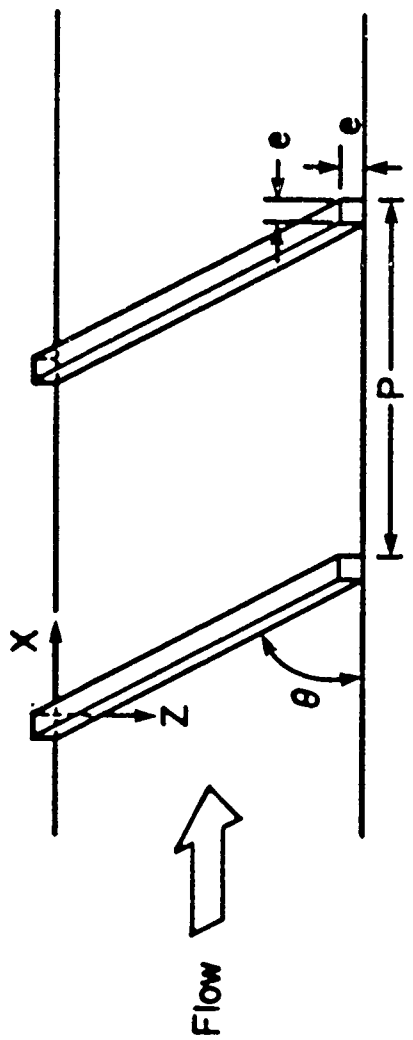
14. Goldstein, R.J., Chyu, M.K. and Hain, R.C., "Measurement of Local Mass Transfer on a Surface in the Region of the Base of a Protruding Cylinder with a Computer-Controlled Data Acquisition System," Int. J. Heat Mass Transfer, 1985.

15. Kattchee, N. and Mackewicz, W.V., "Effects of Boundary Layer Turbulence Promotors on the Local Film Coefficients of ML-1 Fuel Elements," Nuclear Sci. & Eng., Vol. 16, 1963, pp. 31-38.

16. Jeans, A.H. and Johnston, J.P., "The Effects of Streamwise Concave Curvature on Turbulent Boundary Layer Structure," Report MD-40, Dept. of Mech. Eng., Stanford University, 1982.

P/e	θ	$\overline{St} \times 10^3$	$\overline{St}/\overline{St}_o$
5	90	5.96	2.70
10	90	4.45	2.12
5	60	5.73	2.59
10	60	5.37	2.56

Table 1 Average Mass Transfer Results



P/e = 5, 10
θ = 90°, 60°

Fig. 1 Transverse Ribs

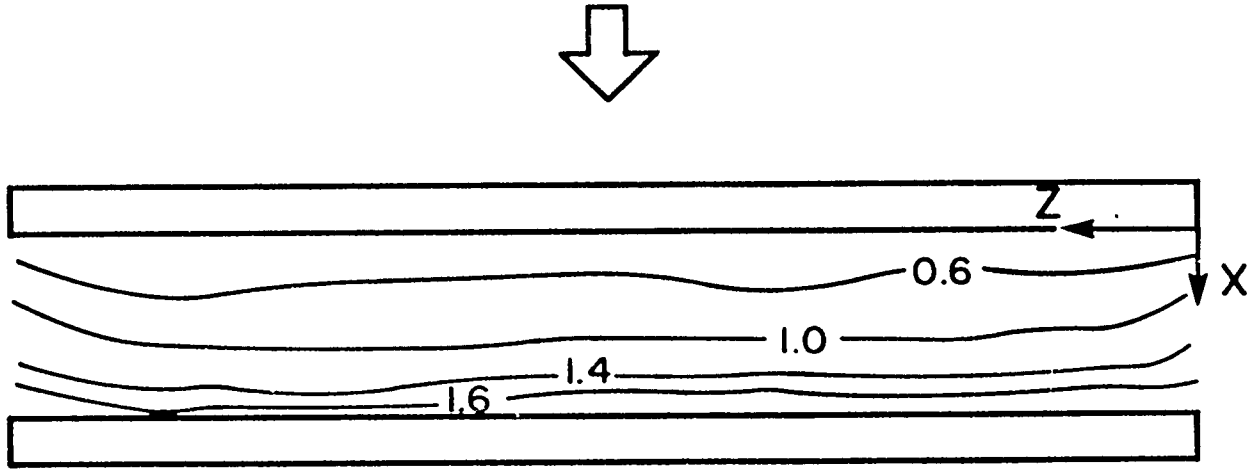


Fig. 2 Contours of $St/\overline{St}$, P/e = 5, $\theta = 90^{o}$

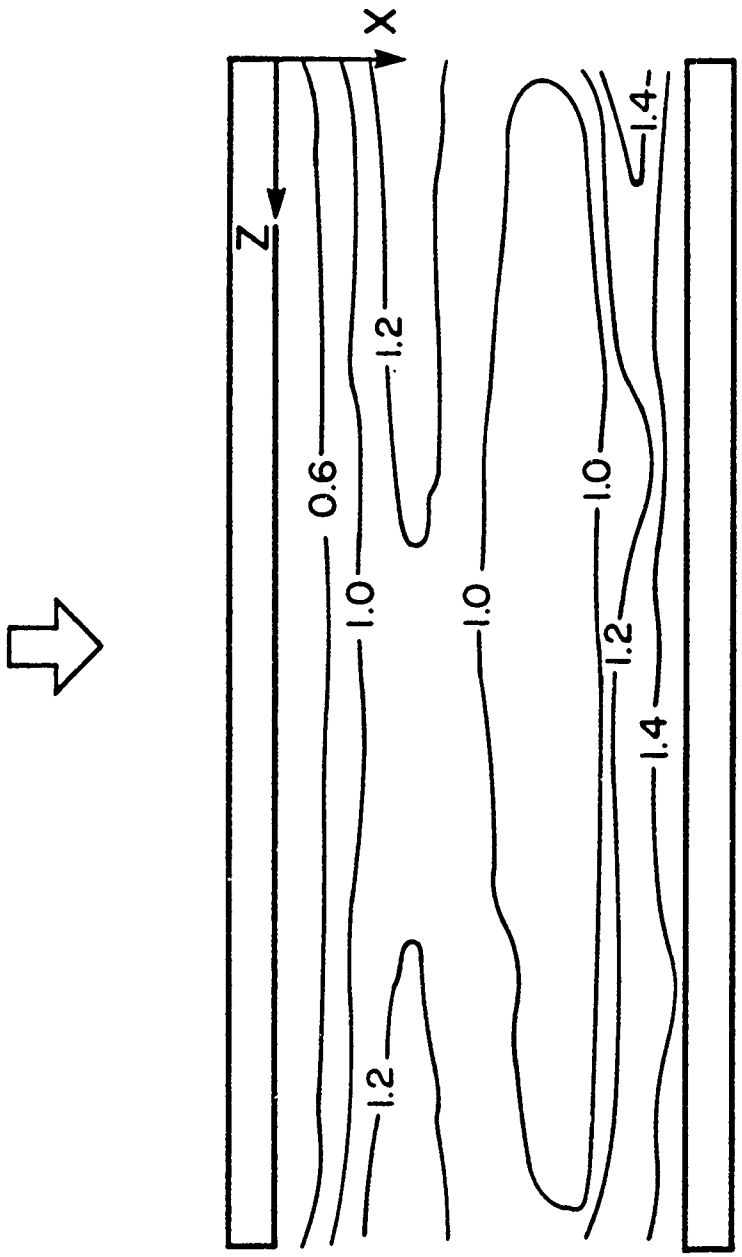


Fig. 3 Contours of $St/\overline{St}$, P/e = 10, $\theta = 90^{o}$

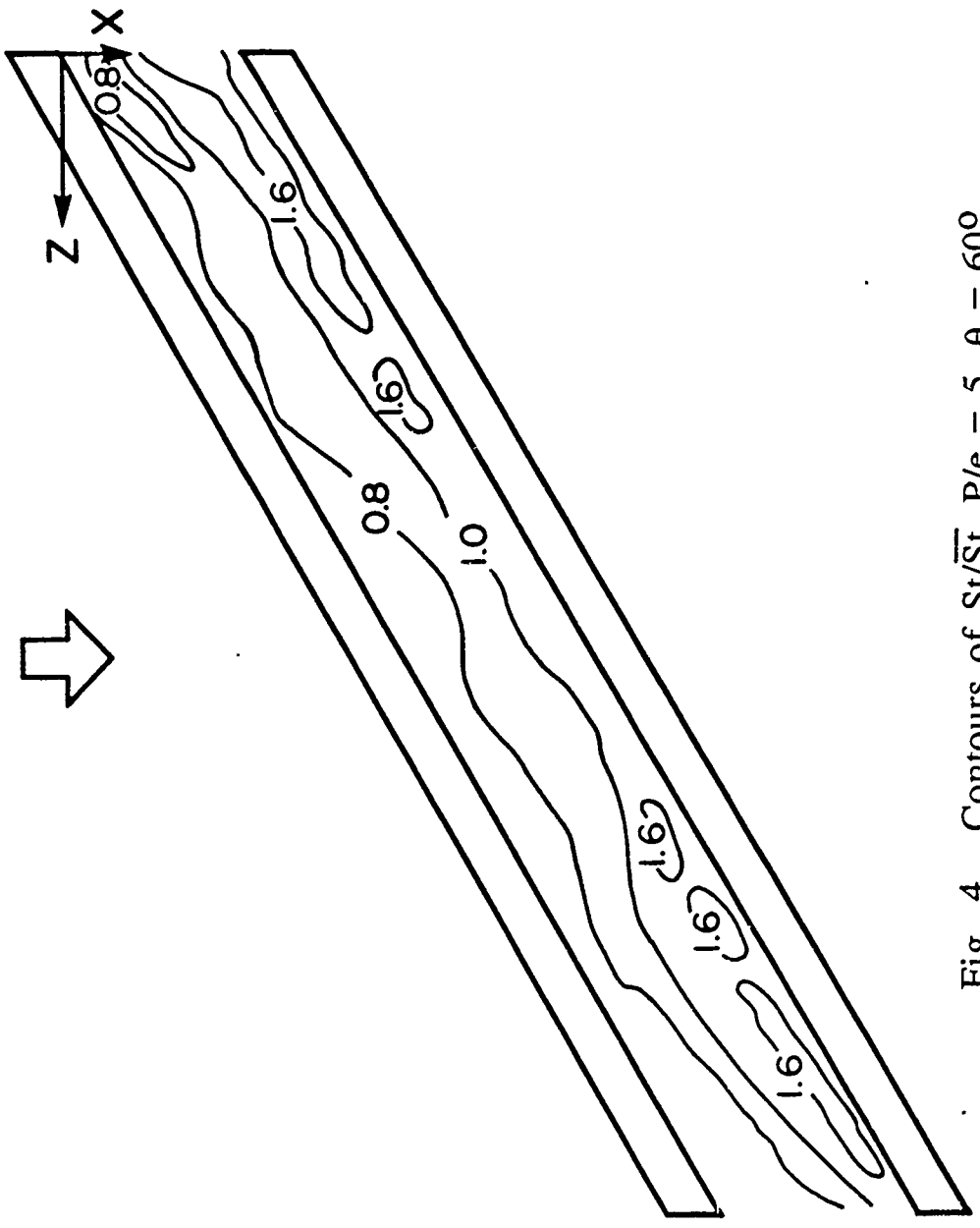


Fig. 4 Contours of $St/\overline{St}$, P/e = 5, $\theta = 60^{o}$

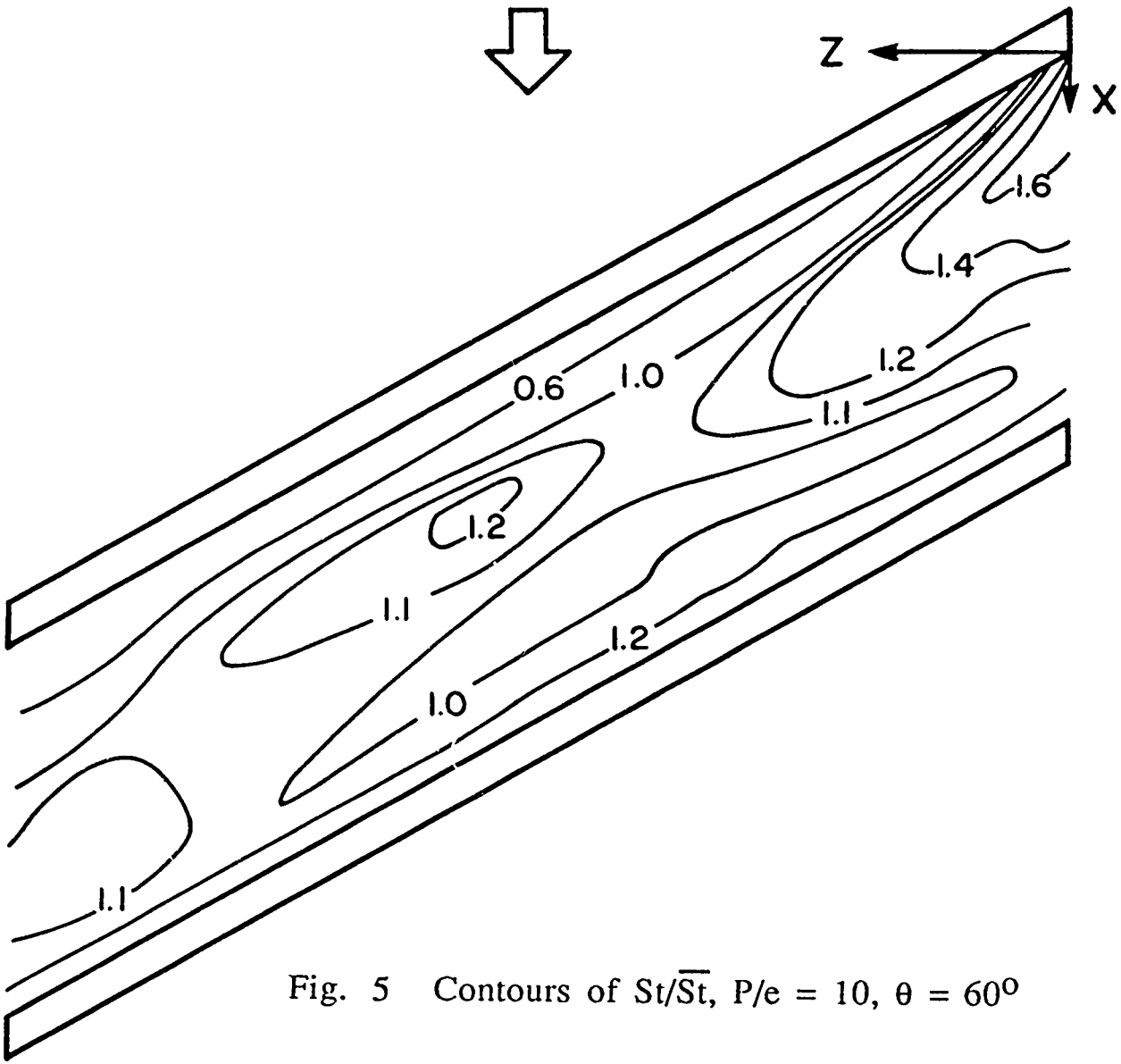
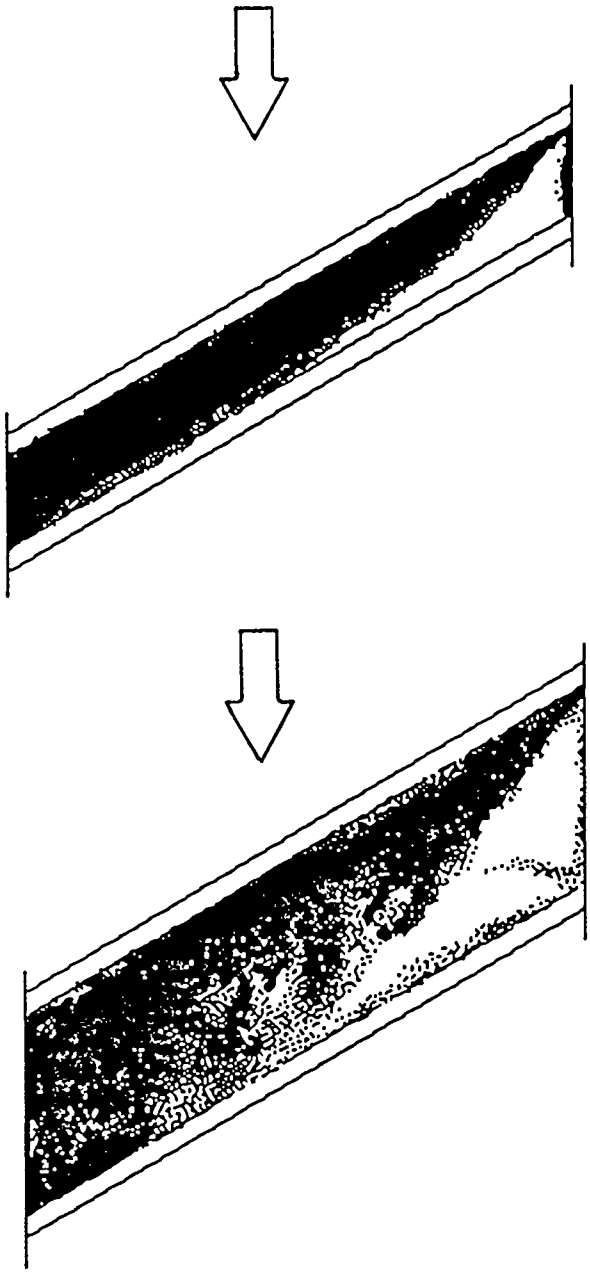


Fig. 5 Contours of $St/\overline{St}$, P/e = 10, $\theta = 60^{o}$



(a). p/e =5

(b). p/e =10

Fig. 6 Near-Wall Flow Patterns for $\theta = 60^{o}$

1989 USAF-UES SUMMER FACULTY RESEARCH PROGRAM

Sponsored by the

AIR FORCE OFFICE OF SCIENTIFIC RESEARCH

Conducted by the

Universal Energy Systems, Inc.

Final Report

Experimental Study of Electronic Excitation of Xenon by Electron Impact

Prepared by:	Jerry D. Clark, Ph.D.
Academic rank:	Assistant Professor
Department and University:	Physics Department Wright State University
Research Location:	Aero Propulsion Laboratory Wright Patterson Air Force Base Dayton Oh
USAF Researcher :	Charles DeJoseph, Ph.D.

Date: Aug 22, 1989

Contract No: F49620-88-C-0053

Experimental Study of Electronic Excitation of Xenon by Electron Impact

by

Jerry Clark

ABSTRACT

The novel application of fourier spectroscopy has been applied to acquire optical excitation functions for the 5d levels of atomic xenon. These electron impact excitation functions were measured from the onset to 150 eV. Cross sections for 5d[3/2]1, 5d[3/2]2, 5d[5/2]2, 5d[5/2]3, 5d[1/2]0, and 5d[1/2]1 levels are reported. Transitions from these levels include the 3.5 μm, 3.27 μm, 2.65 μm, 2.03 μm, and 1.73 μm lines all of which are strong laser transitions. The pressure dependence of the optical cross sections was analyzed yielding collision excitation transfer rates for two of the 5d levels.

Acknowledgement

The author would like to express his gratitude to the Air Force and Universal Energy Systems for the administration and sponsorship of the valuable program. The helpfulness and friendliness of the personnel at UES and Aero Propulsion Laboratory make this summer a real pleasure.

The rewarding research experience I had this summer is in no small part due to the collaboration with Charles DeJoseph. Bob Knight who was always willing to help also deserves a mention. A special thanks to Dr. Alan Garscadden for the opportunity to work within his group.

I. INTRODUCTION

Xenon the largest of the stable rare gases is an important constituent in many laser systems due the high relative energy content in the excited states and their high reactivity. Several lines in neutral xenon lase in the 1 to 5 micron region with very large gains. Many of these also fall within transmission windows of the atmosphere. Recent reports[1-3] have identified an argon xenon mixture at high pressure as a potent high energy laser. Yet Lawton[3] in a modeling study of the kinetic processes responsible for this laser noted a lack of fundamental data for kinetic processes such as dissociative recombination rates with exit channels, collisional mixing between states in the upper and lower laser levels, and electron impact cross sections for direct excitation. In the past few years many efforts[4-6] have attempted to address these short comings but in general have been limited to excited states above the lasing levels or to the lower laser levels. Very little work has been published concerning the upper laser levels the 5d levels. This work addressed the need for basic data on electron excitation processes.

II. RESEARCH OBJECTIVES

The goal of this project was to measure the optical excitation functions for the 5d levels in neutral xenon. The optical excitation function or optical cross section is obtained by exciting a sample of gas with a flux of electrons of defined energy and measuring the radiance from the excitation region. Consider an electron beam of cross sectional area A and current I the photon flux from the interaction region of length Δx is given by:

$$F_{ij} = N \, \Delta x \, Q_{ij} \, I/e$$

Here F_{ij} is the photon flux from transition i to j and Q_{ij} is the

optical cross section. N is the gas density and e is the charge on the electron. The radiance from the transition which can be measured by a calibrated spectrophotometer is given by:

$$R_{ij} = F_{ij} \frac{hc}{\lambda} \frac{1}{4\pi \Sigma} \frac{1}{\Delta\lambda}$$

Here Σ is the surface area of the emitting region and $\Delta\lambda$ is the doppler broadened linewidth given by:

$$\Delta\lambda = \left[8kT \ln(2)/mc^2 \right]^{1/2}$$

Therefore by measuring the gas pressure, the electron current, and the transition radiance the optical cross section for that level may be determined. The following is a discussion of the summers effort to perform this measurement.

III. EXPERIMENT

The apparatus used in these studies involves three basic components: (1) an evacuated collision chamber, (2) an electron gun to provide a flux of electrons into the field free collision region, (3) the necessary electronics to detect and record the radiation emitted from the excited atoms. The details of the apparatus were reported[7] in last summers report and for space considerations will not be repeated here.

Briefly the experimental system consisted of a fourier spectrometer, Bomem DA3 system, which collected the emissions from an interaction region at ninety degrees to an electron beam. The electron gun was built in house and provided a uniform beam 1 cm in diameter with beam currents from 0.2 to 1.0 milliamps during data collection. The sample gas, research grade xenon, flooded the chamber containing the electron gun and interaction region. The sample gas pressure was

measured with a MKS Baratron connected directly to the chamber. The emissions were collected through a four inch sapphire window and detected using a Cincinnati Electronics InSb detector with an IR grade quartz cold filter.

The pressure and current were monitored during spectra collection using an HP computer. The output consisted of the average current and pressure and respective standard deviations. An additional error of 0.05 mtorr or 1/2 LSB of the MKS readout was added to the standard deviation of the pressure. The statistical standard deviations in pressure and current were always less than 5 percent.

CALIBRATION

The calibration of the emission spectra in terms of electron impact cross sections was based on the benchmark cross sections of the 728 nm. line of helium made by Van Zyl *et al*[8]. The radiance of the helium line was measured using a silicon detector and quartz beam splitter at 50 volts electron energy and 4.0 mtorr of helium. The radiance from two xenon lines, 10074 cm^{-1} and 10201 cm^{-1} were made under similar conditions, 50 volts and 4.0 mtorr. After determining the relative response function of the spectrometer the cross sections for the xenon lines were determined with respect to the benchmark cross of helium. The cross sections for the 10074 cm^{-1} and 10201 cm^{-1} were used as transfer standards for lines obtained in the 2500 cm^{-1} to 11000 cm^{-1} region using the InSb detector.

The instrument response functions were obtained by viewing radiant sources of known temperature. The IRF for the spectrometer with the silicon detector and quartz beam splitter was obtained by viewing a NBS traceable tungsten ribbon standard lamp. The shape of the IRF was then determined from the comparison of the observed emission from the

standard lamp to that of a theoretical blackbody. The temperature was determined by fitting the tabulated radiance of the lamp to the shape of a blackbody in the range of 0.6 to 1.0 microns. The IRF for the InSb detector and CaF beam splitter was determined in a similar manner with the spectral range from 2500 cm^{-1} to 6500 cm^{-1} determined using a 1000 K Infrared Industries blackbody. The spectral range of 6500 cm^{-1} to 11000 cm^{-1} was determined using the standard lamp with a temperature determined from the fit to the tabulated radiance between 0.9 and 1.7 microns.

IV RESULTS

The apparent optical cross sections for xenon transition which lie in the spectral region of 1 to 4 microns were sought in this study. This report will limit itself to the presentation and discussion of the results on the 5d levels. Table 1 provides a tabulation of the 5d levels and identifies transitions which were observed. For those transitions identified, the apparent optical cross section has been obtained as a function of electron energy and as function of pressure at 50 eV electron energy. The excitation functions were obtained at pressures of 1, 2, 3 and 4 mtorr of xenon from threshold to 150 eV. The excitation functions obtained at 4 mtorr are shown in figures 1-4. The excitation functions show two distinct shapes. The 5d[3/2]1 state has a broad excitation function which peaks at approximately 80 eV, while the other states all have rather sharp excitation functions peaking at approximately 15 eV. The shapes of the excitation function are reasonably consistent with relative excitation functions reported by Borozdin *et al*[9]. However Borozdin did not see the resonant structure in the 5d[3/2]1 transitions at about 20 eV. This is possibly due to lower electron energy resolution in his work. The excitation functions at

other pressures were similar but had some pressure dependencies. A shift in the excitation function toward lower electron energy with increasing pressure was also observed. Similar effects have been reported previously by Walker[10] and make the determination of thresholds from this data unreliable.

All of the 5d levels show some pressure dependence, see figures 5 and 6. The pressure dependence was evaluated at 50 volts, where the excitation functions are fairly flat, from approximately 0.5 mtorr to 13 mtorr. Two of the levels have significant and predictable pressure dependencies and are the resonance states 5d[3/2]1 and 5d[1/2]1. The other states have a small but systematic dependence which have yet to be identified with typical pressure dependant processes such as cascading, beam divergence or atomic processes such as collisional transfer or recombination. A pressure variation of twenty percent occurs between 0.5 and 5 mtorr and only at the higher electron energies. The pressure variation appears constrained to electron energies above 30 eV with the peak in the excitation function showing no pressure dependence, see figure 4b. The reason for this strange behavior is unclear at this time.

Two of the 5d levels the 5d[3/2]1 and the 5d[1/2]1 are connected to the ground state and have pressure effects dependent on the trapping of their resonance radiation. To further discuss this a framework must be developed relating the measured optical cross sections to apparent level cross sections and the probability of imprisonment of the resonance radiation. Let Q_{ij} be the optical cross section then the apparent level cross section is $Q_i = Q_{ij} / \beta_{ij}$ where β_{ij} is the branching ratio of the observed transition. The apparent cross section can be expressed as[11] :

$$Q_i = \frac{Q_i^e + J + \sum_x k_{xi} N \tau_x Q_x}{1 - (1 - g)\,\beta_{io} + \sum_i k_{ij} N \tau_i}$$

where Q_i^e is the cross section for direct electron impact, J the cross section for cascading from higher levels, g the fraction of resonance photons which can escape from the collision chamber without being absorbed, β_{io} the branching ratio to the ground state, τ the lifetimes of the levels and k the rate constant for collisional excitation transfer. The parameter g is pressure dependant and was first calculated for doppler broadened transitions by Holstein[12]. We have used the functional form of Holstein and incorporated the 30 % increase suggested by Phelps[13].

$$g = 1.12/(\alpha_o l \sqrt{\pi \log(\alpha_o l)})$$

Here l is the effective length of the interaction region (approximately half the distance to the nearest wall) and α_o is the absorption coefficient at the center of the line and given by:

$$\alpha_o = \frac{\lambda^3 G_i}{8 \pi^{3/2} G_o} N A_{io} \left(\frac{M}{2 k T} \right)$$

Where λ is the wavelength of the resonance line, G_i and G_o are the statistical weights of the upper and lower level, M is the mass of the gas atoms, k is the Boltzmann's constant, and T is the gas temperature.

The 5d[3/2]1 level is a resonance state from which three transitions 3771 cm^{-1}, 4934 cm^{-1} and 5770 cm^{-1} can be observed. The pressure dependencies of this level were analyzed using the above equation. The transition probability of the resonance transition was determined from the lifetime ($1.4 \cdot 10^{-9}$ sec.) measured by Matthias *et al*[14]. and the branching ratios determined from the ratio of the measured excitation functions. The level cross section plus cascade determined from the fit is $3.62 \cdot 10^{-17}$ cm^2 at 50 eV which is a little over a factor

of two smaller than the level cross section determined by Filipovic *et al*[15] in an electron loss scattering experiment. The collisional transfer rate obtained from the fit is $1.81 \cdot 10^{-11}$ $cm^{-3}s^{-1}$ which is consistent in magnitude with collisional transfer rates for the 6p levels seen by Bowering *et al*[4].

The 5d[1/2]1 level is also a resonance level although weakly coupled to the ground state. The 2717 cm^{-1} transition is the only transition from the level we can observe but represents the majority of the branching probability. This transition was analyzed as above using the theoretical transition probabilities and branching ratios of Aymar *et al*[16]. The level cross section determined by the fit is $3.72 \pm 0.7 \cdot 10^{-18}$ cm^2. This level was not resolved in the work of Filipovic.

The other levels whose transitions were observed are not resonant to the ground state. These levels 5d[1/2]0, 5d[3/2]2, 5d[5/2]2, 5d[5/2]3, and 5d[7/2]3 all have similar shaped excitation functions. The apparent level cross sections for these level have been calculated for comparison with the results of Filipovic. The branching ratios have been determined experimentally if all transitions were observed otherwise from the theory of Aymar. The results are displayed for several electron energies in Table 1.

V. RECOMMENDATIONS

The optical excitation functions for many of the transitions from the 5d levels in the IR region have been measured this summer. More importantly the principle of using the fourier spectrometer to acquire excitation functions for multiple lines under identical experimental conditions has been demonstrated. Although much has been accomplished this summer several areas should be mentioned for further study.

The pressure variations for many of the lines are perplexing.

Careful study of this variation possibly as a function of excitation energy may lead insight into this variation. Interestingly the pressure variation of the resonance levels behaves normally with the ability to extract information about collisional excitation transfer. Further study in this area may lead to extraction of collisional excitation transfer rates for many of the levels.

Finally we have demonstrated a powerful technique for extracting excitation functions which can be extended in several ways. First the extension to the visible will allow many lines to be measured which the 5d cascade into allowing detailed evaluation of direct electron impact cross sections. Second the technique could be applied to other gases such as krypton which has many transitions in the IR or to gas mixtures were other atomic processes affecting the levels may be observed. Finally analysis of transitions from other atomic levels, many of which were observed this summer, should be continued.

References

1. F.V. Bunkin *et al*, "High-Power laser of 270-liter active volume utilizing infrared transitions in Xenon", Sov. J. Quantum Electronics 16, 576-577, April 1986.

2. N.G. Basov *et al*, "Possibility of construction of a pulse-periodic large- volume electron beam-controlled laser utilizing infrared transitions in Xenon atom and characterized by a specific output of 0.5-1 W/cm^3, Sov. J. Quantum Electronics, 16, p. 1008-1009, Aug. 1986.

3. S.A. Lawton, J.B. Richards, L.A. Newman, L. Specht, and T.A. Detemple, "The high-pressure neutral infrared xenon laser", J. Appl. Phys., 50, 3888-3898, 1979.

4. N. Bowering, M.R. Bruce and J.W. Keto, "Collisional deactivation of two-photon laser excited xenon $5p^5 6p$. I. State to state reaction rates", J. Chem. Phys., 84, 709-714, 1986

5. N. Bowering, M.R. Bruce and J.W. Keto,"Collisional deactivation of two-photon laser excited xenon $5p^5 6p$. II. Lifetimes and total quench rates.", J. Chem. Phys., 84, 715-726, 1986

6. Gen Inoue, J.K. Ku, and D. W. Setser, "Laser induced fluorescence study of Xe($5p^5 6p$,$5p^5 6p'$,$5p^5 7p$, and $5p^5 6d$) states in Ne and Ar: Radiative lifetimes and collisional deactivation rate constants.", J. Chem. Phys., 81, 5760-5774, 1984.

7. J.D. Clark, "Experimental Study of Electronic Excitation of Xenon by Electron Impact", Final Report 1988 UES Summer Faculty Program.

8. B.Van Zyl,G.H. Dunn, G. Chamberlain, and D.W. Heddle,"Benchmark cross sections for electron-impact excitation of $n\ ^1S$ levels of He", Physical Rev A, 22, pp1916-1929,1980.

9. V.S. Borozdin and Yu. M. Smirnov, "Excitation of Xe infrared lines by low-energy electrons", Opt. Spectrosc. 46, pp 634-636,1979.

10. Keith G. Walker, "Electronic Excitation of Atomic Xenon by Electron Impact", Final Report 1983 USAF-SCEEE Summer Faculty Research Program.

11. A.F.J. van Raan and J van Eck, "The influence of collisional transfer of excitation energy in helium on the electron-impact excitation of the $4\ ^3D$ level",J.Phys.B.,7,pp.2003-2020,1974.

12. T. Holstein,"Imprisonment of Resonance Radiation in Gases. II",Physical Rev.,83,pp1159-1168,1951.

13. A.V. Phelps,"Effect of the Imprisionment of Resonance Radiation on Excitation Experiments",Physical Rev.,110,pp1362-1368,1958.

14. E. Matthias, R.A. Rosenberg,E.D. Poliakoff,M.G.White,S.T.Lee, and

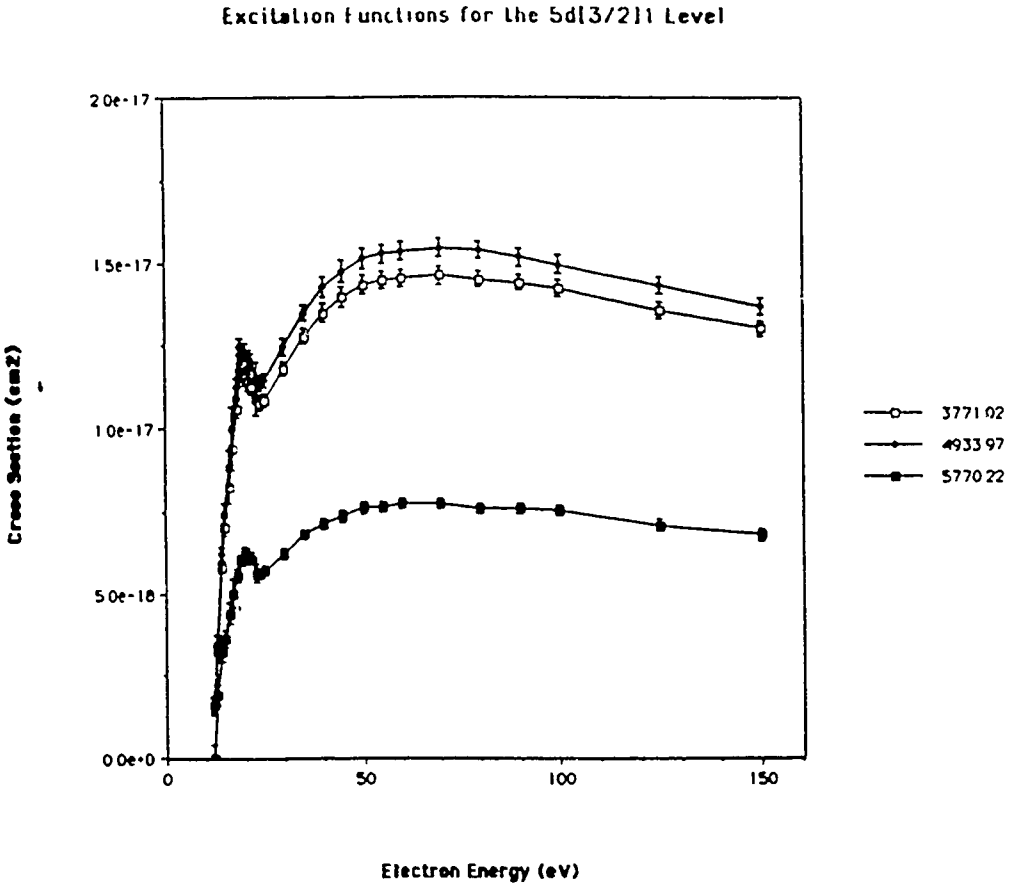
D.A. Shirley,"TimeResolved VUV Spectroscopy Using Synchrotron Radiation: Fluorescent Lifetimes of Atomic Kr and Xe*",Chem. Phys.Letters,52,pp.239-244,1977.

15. D. Filipovic *et al*, "Electron-impact excitation of xenon at incident energies between 15 and 80 eV", Physical Rev. A , 37, p. 356-364, 1988.

16. M. Aymar and M. Coulombe,"Theoretical Transition Probabilities and Lifetimes in Kr I and Xe I Spectra",Atomic Data and Nuclear Data Tables,21,pp537-566,1978.

TABLE 1

LEVEL TRANSITION cm^{-1}	Optical or Level Cross Sections (10^{-18} cm^2) This work					Filipovic etal			
	15eV	20eV	30eV	50eV	80eV	15eV	20eV	30eV	80eV
5d[3/2]1				36.2		29.0	37.0	88.8	73.5
5d[3/2]1-6p[1/2]1 3771	7.04±.26	11.54±.22	11.81±.21	14.37±.27	14.52±.24				
5d[3/2]1-6p[3/2]1 4933	7.44±.29	12.32±.25	12.48±.25	15.15±.29	15.40±.27				
5d[3/2]1-6p[5/2]2 5770	3.65±.25	6.26±.17	6.22±.14	7.61±.16	7.57±.15				
5d[1/2]1				3.72					
5d[1/2]1-6p[1/2]1 2717	3.01±.17	1.90±.08	1.43±.05	1.31±.05	1.25±.05				
5d[1/2]0	5.41±.24	2.62±.1	1.65±.06	1.58±.06	1.54±.06				
5d[1/2]0-6p[1/2]1 2502	5.41±.24	2.62±.1	1.65±.06	1.58±.06	1.54±.06				
5d[3/2]2	18.56	8.42	4.67	4.00	3.74				
5d[3/2]2-6p[1/2]1 3053	15.55±.55	7.06±.16	3.91±.09	3.35±.08	3.13±.07				
5d[5/2]2	11.37	5.83	3.84	3.41	3.33	10.7	5.92	3.29	
5d[5/2]2-6p[5/2]2 3805	5.56±.22	2.85±.08	1.88±.05	1.67±.05	1.63±.05				
5d[5/2]2-6p[3/2]1 2969	5.00±.20	2.50±.08	1.64±.05	1.49±.05	1.44±.05				
5d[7/2]3	15.79	9.30	6.91	6.21	5.77	15.5	10.2	9.42	
5d[7/2]3-6p[5/2]2 2850	13.88±.48	8.17±.17	6.07±.12	5.46±.11	5.07±.10				
5d[5/2]3	6.49	5.47	5.14	5.00	4.74	4.62	4.34	7.66	
5d[5/2]3-6p[3/2]2 3217	3.89±.17	3.35±.09	3.20±.07	3.10±.07	2.90±.06				
5d[5/2]3-6p[5/2]3 4027	1.76±.13	1.50±.07	1.37±.05	1.31±.05	1.26±.05				
5d[5/2]3-6p[5/2]2 4310	0.84±.13	0.62±.07	0.57±.05	0.59±.05	0.58±.05				


Excitation Functions for the 5d[3/2]1 Level
Cross Section (cm2)
20e-17
15e-17
10e-17
50e-18
00e+0
0
50
100
150
Electron Energy (eV)
377102
493397
577022

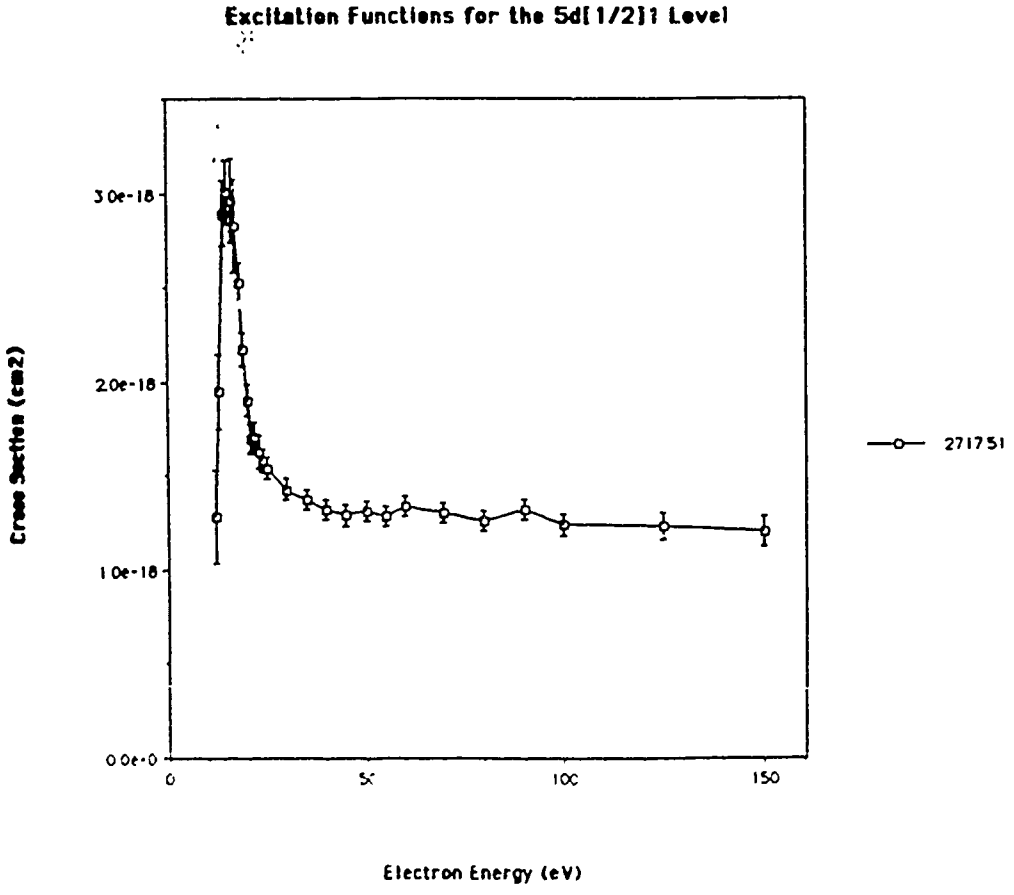
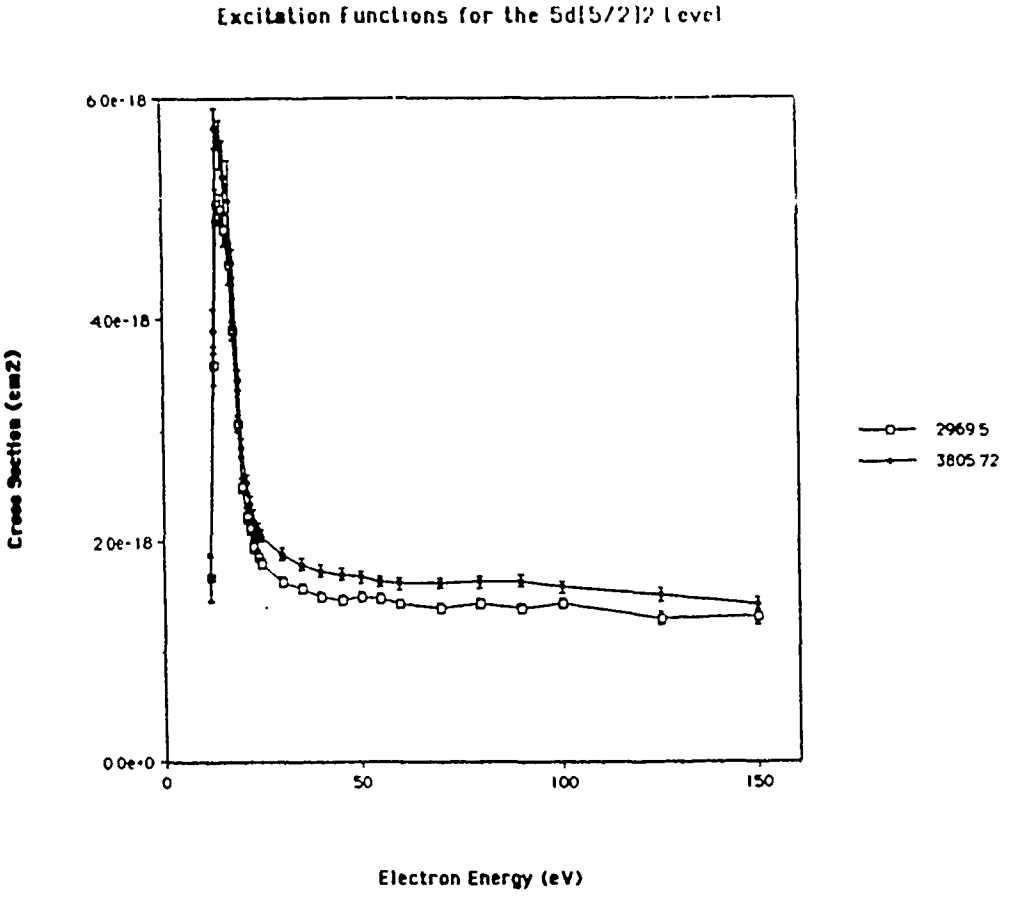

Excitation Functions for the 5d[1/2]1 Level
Cross Section (cm2)
30e-18
20e-18
10e-18
00e+0
0
50
100
150
Electron Energy (eV)
271751

Figure 1


Excitation Functions for the 5d[5/2]2 Level
60e-18
40e-18
20e-18
00e+0
Cross Section (cm2)
0
50
100
150
Electron Energy (eV)
29695
380572

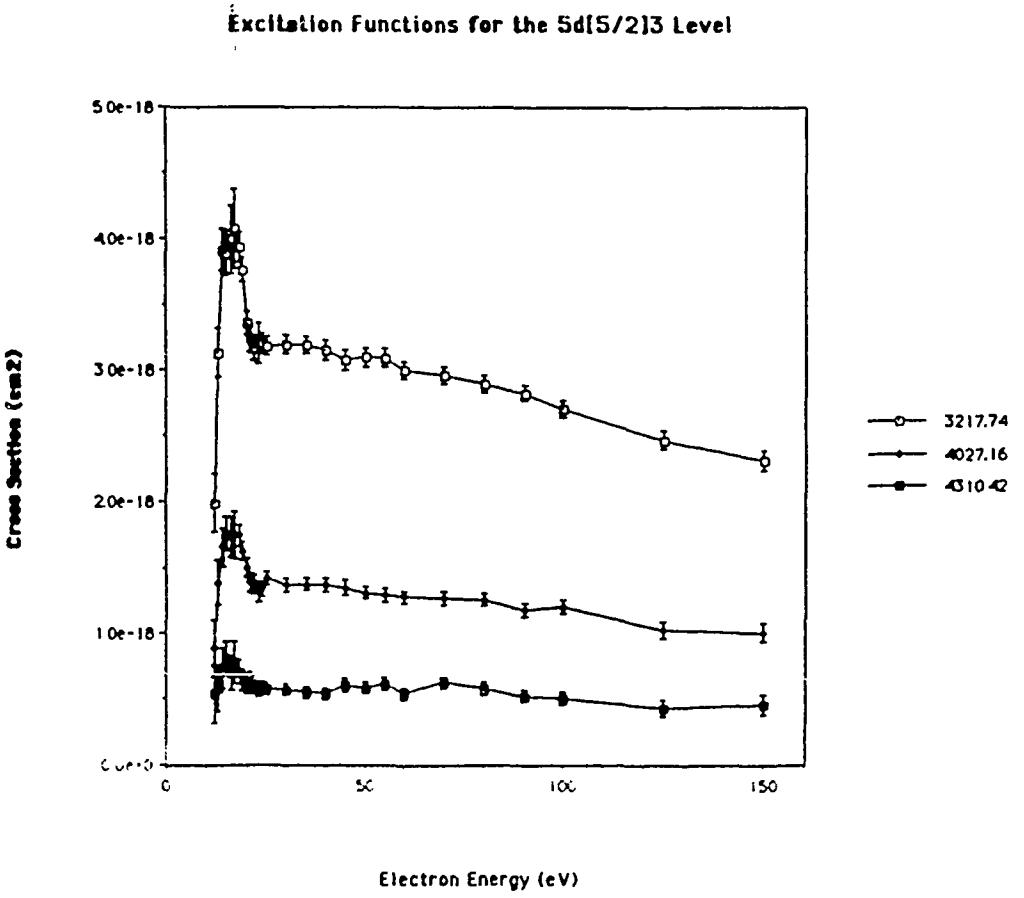
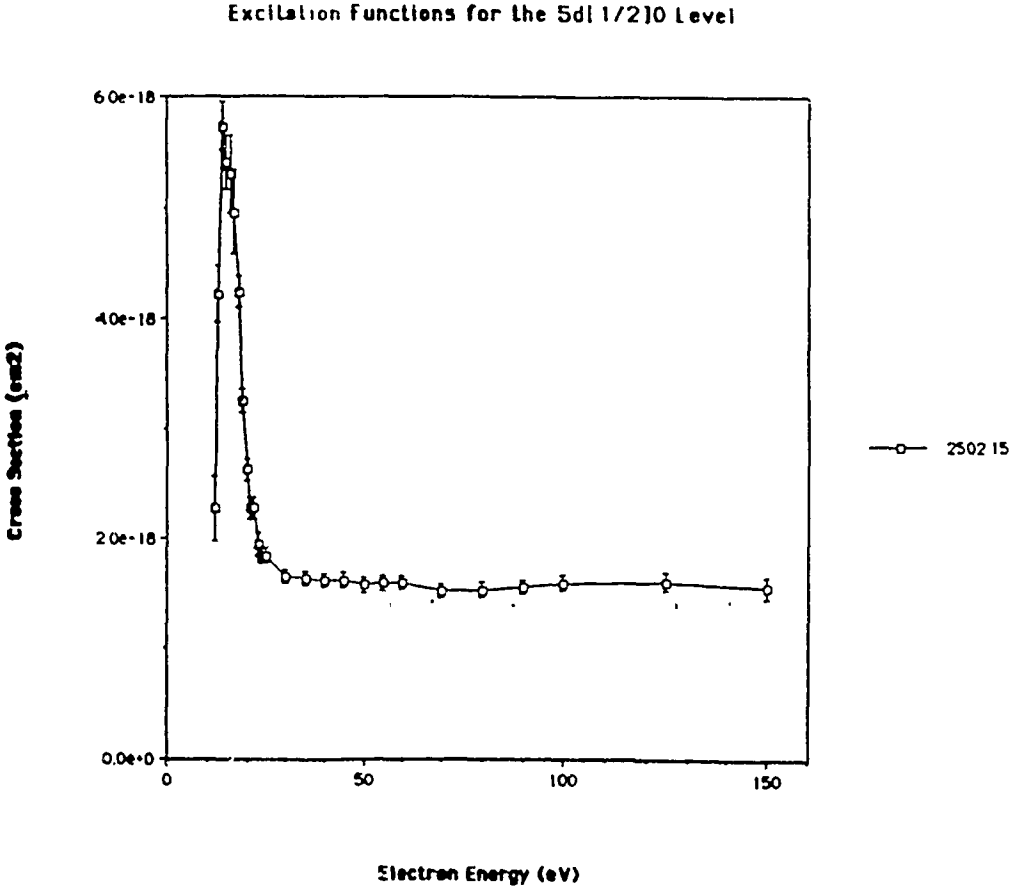

Excitation Functions for the 5d[5/2]3 Level
50e-18
40e-18
30e-18
20e-18
10e-18
0
50
100
150
Cross Section (cm2)
Electron Energy (eV)
3217.74
4027.16
4310.42

Figure 2


Excitation Functions for the 5d[1/2]0 Level
6.0e-18
4.0e-18
2.0e-18
0.0e+0
Cross Section (cm2)
0
50
100
150
Electron Energy (eV)
2502 15

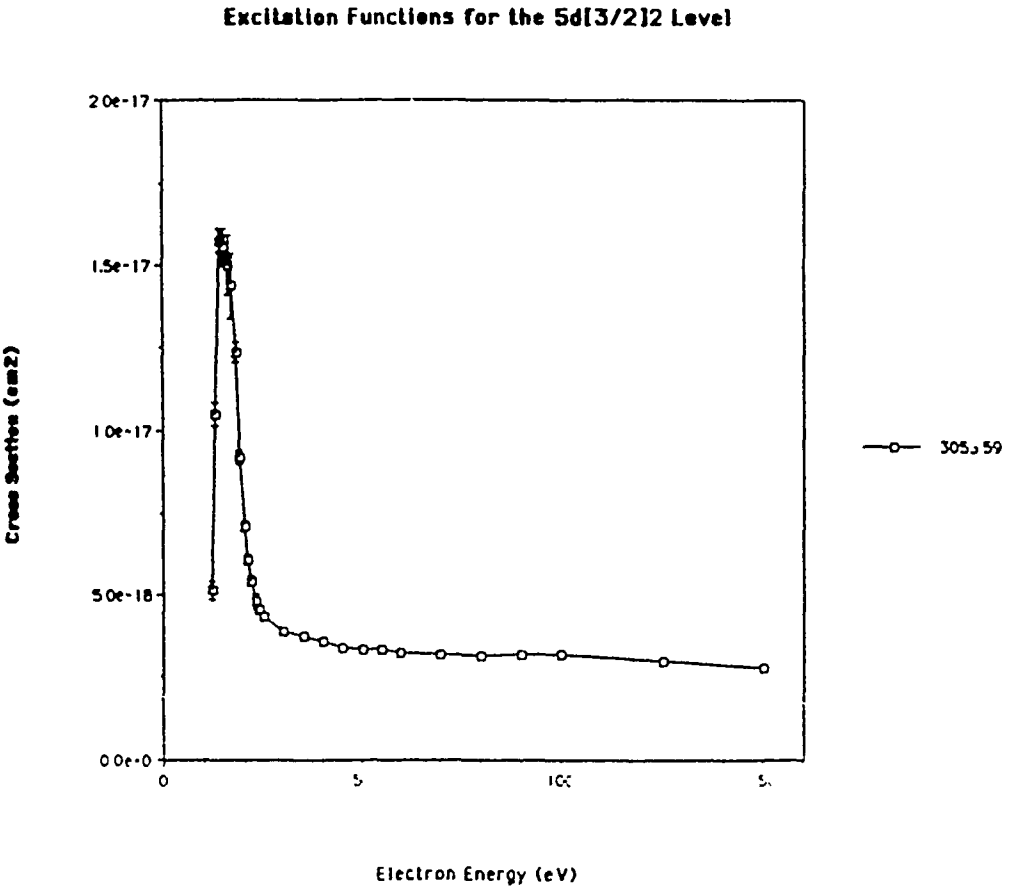
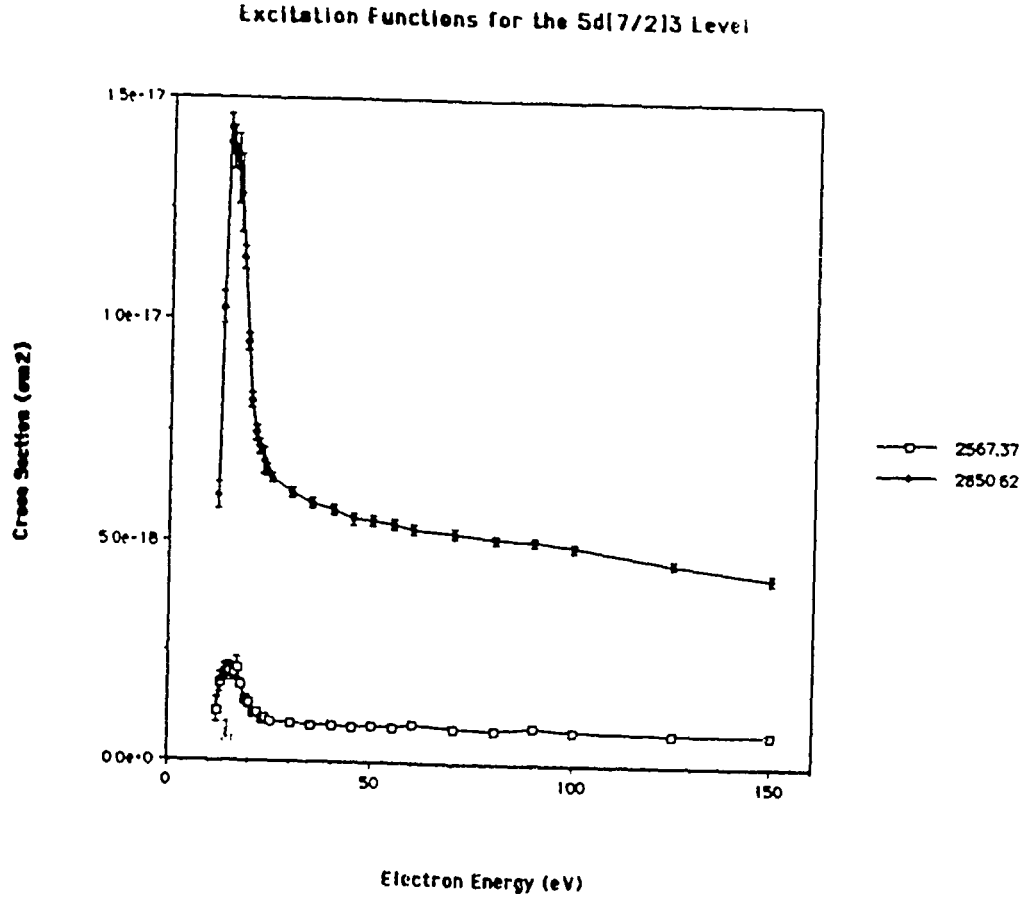

Excitation Functions for the 5d[3/2]2 Level
2.0e-17
1.5e-17
1.0e-17
5.0e-18
0.0e+0
Cross Section (cm2)
0
Electron Energy (eV)
305.59

Figure 3



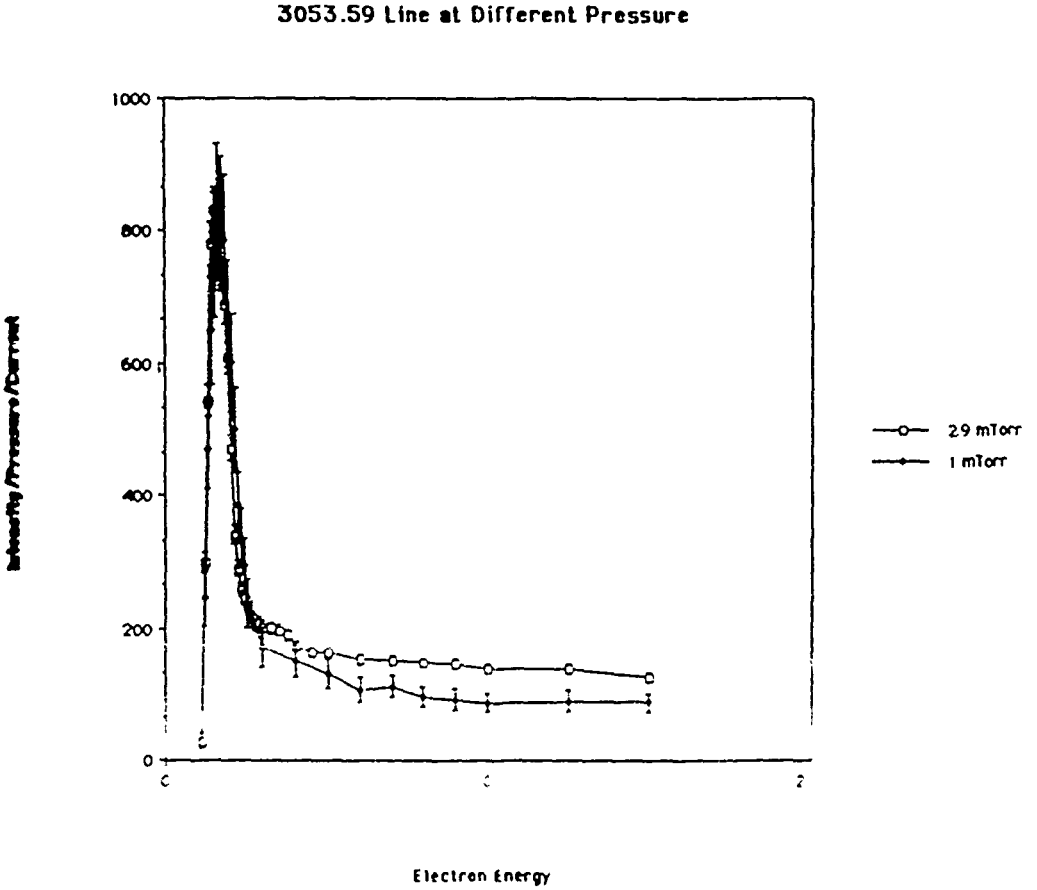
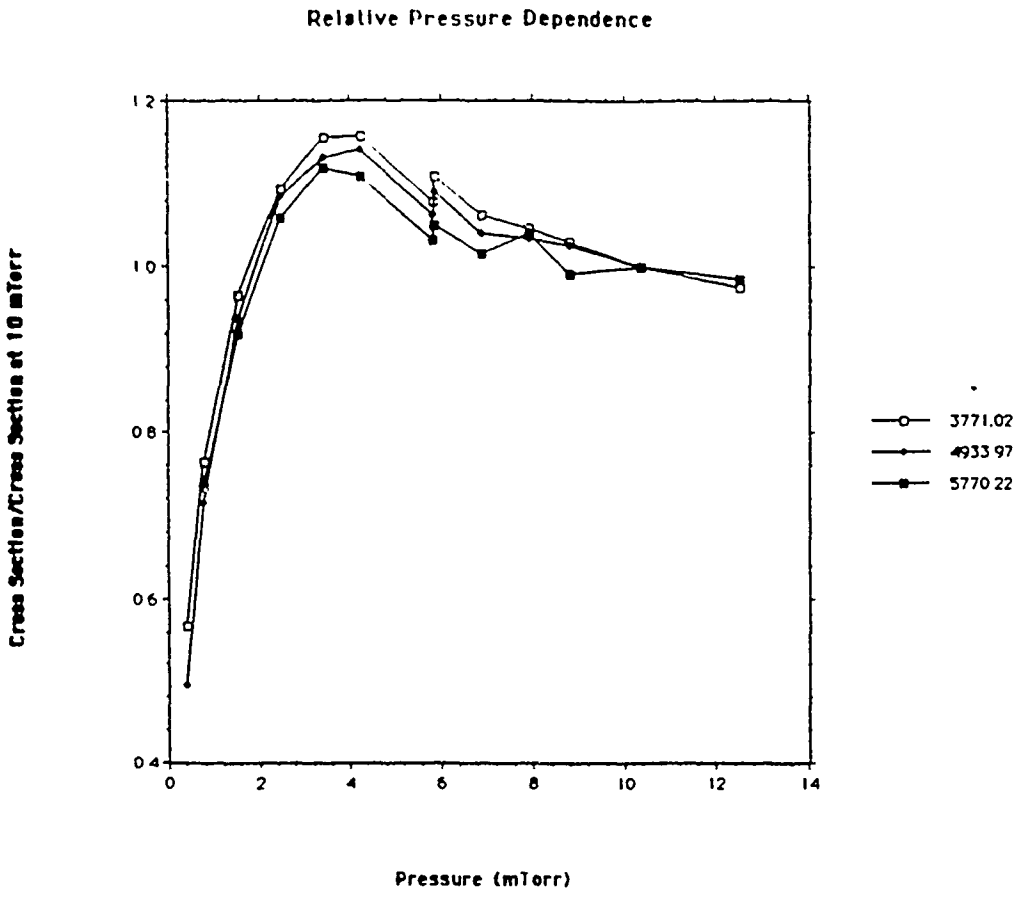


Figure 4
90-18


Relative Pressure Dependence
Cross Section/Cross Section at 10 mTorr
1.2
1.0
0.8
0.6
0.4
0
2
4
6
8
10
12
14
Pressure (mTorr)
3771.02
4933.97
5770.22

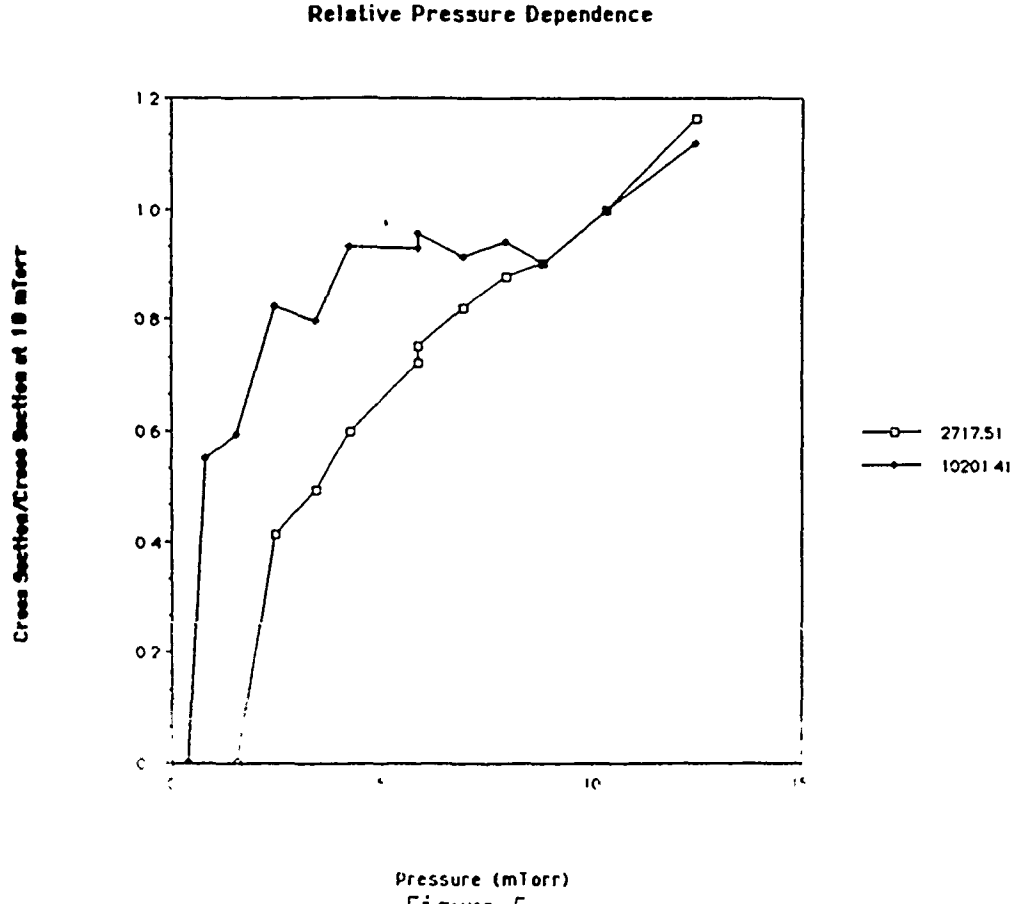
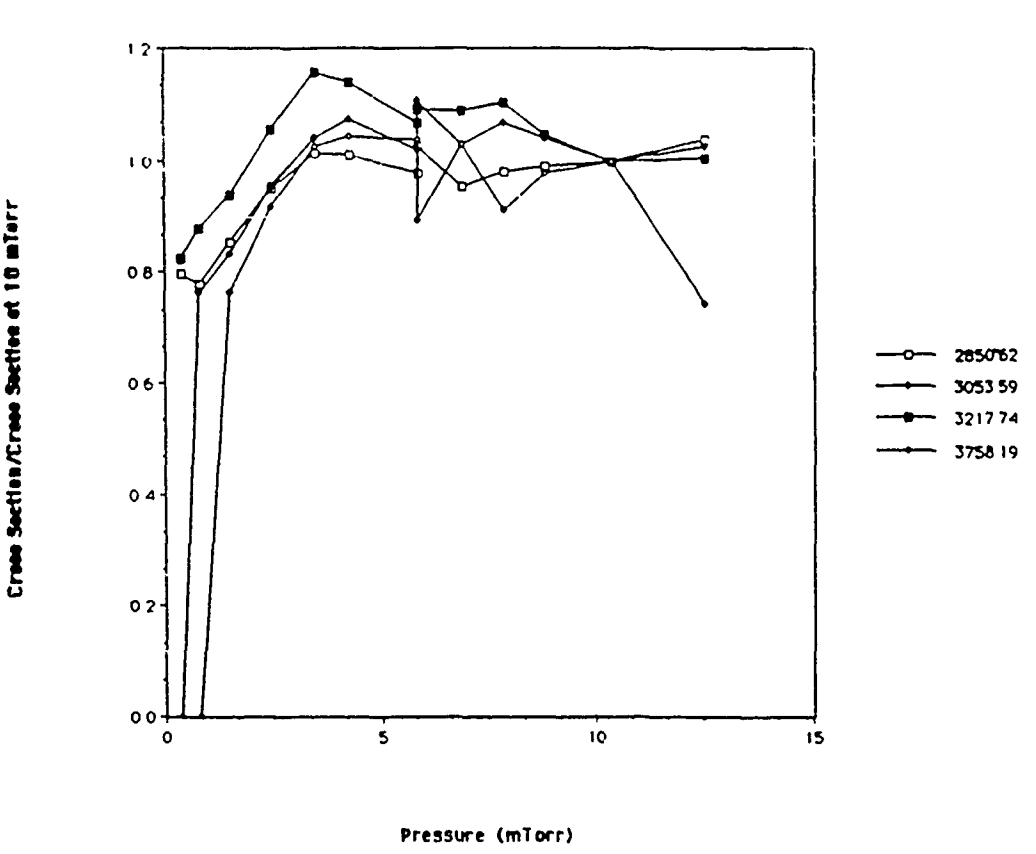

Relative Pressure Dependence
Cross Section/Cross Section at 10 mTorr
1.2
1.0
0.8
0.6
0.4
0.2
0
10
Pressure (mTorr)
2717.51
10201.41

Figure 5


Relative Pressure Dependence
Cross Section/Cross Section at 10 mTorr
1.2
1.0
0.8
0.6
0.4
0.2
0.0
0
5
10
15
Pressure (mTorr)
2850762
3053 59
3217 74
3758 19

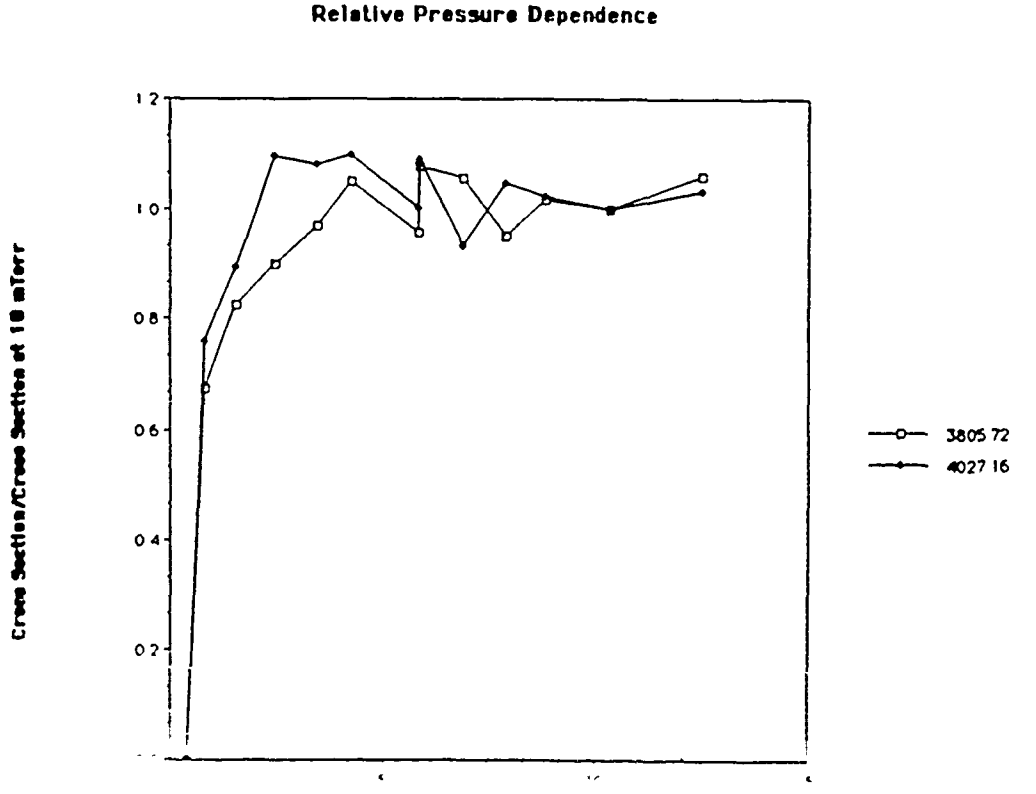

Relative Pressure Dependence
Cross Section/Cross Section at 10 mTorr
1.2
1.0
0.8
0.6
0.4
0.2
Pressure (mTorr)
3805 72
4027 16

Figure 6

Dr. Wayne Eckerle

No Report Submitted

(Report # 91)

1989 USAF-UES SUMMER FACULTY RESEARCH PROGRAM

GRADUATE STUDENT RESEARCH PROGRAM

Sponsored by the

AIR FORCE OFFICE OF SCIENTIFIC RESEARCH

Conducted by the

Universal Energy System, Inc.

FINAL REPORT

FLOW LIMITATIONS IN MICRO HEAT PIPES

Prepared by:	Frank M. Gerner, Ph.D. Jon P. Longtin, Graduate Student
Academic Rank:	Assistant Professor
Department and University:	Department of Mechanical and Industrial Engineering University of Cincinnati
Research Location:	Aero Propulsion and Power Laboratory Wright Research and Development Center Wright-Patterson AFB, OH 45433
USAF Researcher:	Won S. Chang
Date:	8 Sept., 1989
Contract No:	F49620-88-C-0053

FLOW LIMITATIONS IN MICRO HEAT PIPES

F.M. Gerner and J.P. Longtin

ABSTRACT

This paper examines the basic physics governing operation of micro heat pipes. It also explores the operating limits which will determine the maximum heat transfer capability of these devices. These devices, which utilize latent energy to transport thermal energy at very uniform temperatures, will be extremely useful for dissipating the large heat fluxes expected in the next generation of computers.

A simple analytic model is shown to predict the operating limit for 1 mm hydraulic diameter devices. This model is then used to show the expected effectiveness for 100 μm hydraulic diameter devices currently being built. Not only is the expected heat flux large, 10 - 15 W / cm^2, the temperature drop should be very small, of order $0.01^o C$.

Acknowledgements

I wish to thank the Air Force Systems Command and the Air Force Office of Scientific Research for sponsorship of this project. I also wish to thank Universal Energy systems for managing this project.

The work performed for the Aero Propulsion Laboratory at WRDC was extremely rewarding. I especially wish to thank the following members of the Thermal Laboratory for their help: Dr. Won Chang, Dr. Jerry Beam, Dr. Tom Mahefky, Mike Morgan and Don Reinmuller.

I. INTRODUCTION:

Currently, one of the major limitations to electronic chip miniaturization is the resulting high heat fluxes and temperatures. Therefore, new technologies must be developed to cool electronic components.

The Thermal Laboratory, which is part of the Aero Propulsion Laboratory at Wright Research and Development Center, is particularly interested in the thermal control of electronics on-board spacecraft. In particular, it is desirable to decrease the thermal resistance right at the chip level. One of the most efficient ways to accomplish this is to micromachine cooling structures directly into the silicon. One of these devices, the micro heat pipe, is being investigated.

My research interests include: electronics cooling, condensation heat transfer, interfacial transport and two-phase flows. The unique aspect that I bring to this project is that, in addition to my expertise in fluid mechanics and heat transfer, I have at my disposal, at the University of Cincinnati, the photolithography and wet-chemical etching facilities required to fabricate these devices.

II. OBJECTIVES OF THE RESEARCH EFFORT:

Presently, there is no research which has been published demonstrating the utility of using micro heat pipes embedded in silicon to cool electronic chips. There have been some experimental data reported for larger metal-water heat pipes. These devices, however, behave more like conventional thermosyphons, in that gravity is important in their operation. Also these devices were not embedded in silicon, so that their fabrication procedure is totally different.

The major objective of this summer's research was to assess the feasibility of using micro heat pipes to cool electronic chips. The approach taken was to develop a model to predict the maximum heat transport which micro heat pipes can handle and their thermal resistance. It was found that micro heat pipes can handle heat loads in the range 10-15 W/cm^2 with extremely small thermal resistances, temperature drops of order 0.01^oC occur inside these devices.

In addition to the work being done at Wright-Patterson AFB, some preliminary fabrication is taking place at the University of Cincinnati. It has been demonstrated that an array of micro heat pipes can be etched into silicon. Work is also proceeding on the anodic bonding which will be required to close the micro heat pipes.

III. BACKGROUND:

An important trend in computer technology is the miniaturization of electronic components. This miniaturization is necessary in order to increase the efficiency and capacity of computers. As the chip density increases, however, it becomes increasingly more difficult to dissipate the heat which is generated. Currently, heat fluxes on the order of 10 W/cm^2 occur on the chip level. Also uniform

temperatures are often desired. In order to manage these extremely high heat loads, without large temperature increases, new cooling technologies which utilize forced-convective liquid flow and phase change must be developed. One novel two-phase flow device which has been proposed (Cotter, 1984) for this purpose is the micro heat pipe. The small size of these devices, lengths of the order of 1 cm and diameters of between 10 and 500 μm, allow them to be used on the chip level. The evaporator end can be embedded in the silicon and the device used as a very efficient fin, due to the high effective thermal conductivity which results from utilizing the latent heat of the working fluid. Another option is to etch the micro heat pipes into the silicon and use them as very efficient thermal spreaders.

A micro heat pipe differs from a conventional heat pipe in that it is much smaller. Also it does not contain a wick, but rather uses capillary pressure, due to sharp edges, to return the condensate to the evaporator. A typical example with a triangular cross-section is shown in Fig. 1. The evaporator section contains less liquid, has a smaller radius of curvature at the vapor-liquid interface and a lower liquid pressure.

$$P_v - P_l = \sigma / R \tag{1}$$

There is more liquid condensate at the condenser, and hence there is a larger radius of curvature at the vapor-liquid interface and a higher liquid pressure. This pressure gradient in the liquid is what drives the liquid flow and returns the condensate to the evaporator.

Conversely, the small radius of curvature in the evaporator, and large radius of curvature in the condenser create a pressure gradient in the vapor which drives the vapor flow from the evaporator to the condenser.

As for many conventional heat pipes the aspect ratio is very high

$$L / D >> 1 \tag{2}$$

In order for this device to function properly the capillary pressure must be much larger than gravity forces. This requires that $\rho_l g R L / \sigma$ be of order 1 or less. If $\rho_l g R L / \sigma << 1$, then capillary action dominates gravity and orientation of the heat pipe in unimportant. Now the requirement that $\rho_l g R L / \sigma$ be of order 1 or less is a necessary, but not sufficient, condition for a micro heat pipe. It is possible for a "large" thermosyphon, or wickless heat pipe, to operate with the assistance of capillarity. For a "large" heat pipe, with a sharp-edged cross-section, the device may not be operating at anywhere near its maximum capacity, but it can function in the capillary-assisted mode at low heat inputs. Of course in space any size sharp-edged cross-section can be used for a capillary-assisted heat pipe. Even in terrestrial applications, grooves are etched in conventional heat pipes to utilize capillary action.

What distinguishes micro heat pipes are their small hydraulic diameters. A small capillary radius is needed to ensure enough "pumping power" to return the condensate to the evaporator. Since the film thickness is related to the capillary radius, a thin film is desired. The idea behind the micro heat pipe is that a diameter several orders-of-magnitude larger than the capillary radius is unnecessary.

According to Cotter (1984) and Babin et al. (1989), a micro heat pipe has a capillary radius as large or larger than the hydraulic radius, or

$$\frac{r_c}{r_h} \geq 1 \tag{3}$$

It is perhaps, preferable to say that the hydraulic radius of a micro heat pipe is comparable in magnitude to the capillary radius. As before, it is still necessary for $\rho_l g R L / \sigma$ to be of order 1 or less, but by also having a small hydraulic diameter it allows micro heat pipes to be used in very small places.

Currently, micro heat pipes are being constructed at the University of Cincinnati. The basic design, which is shown in Fig. 1, is to form an array of micro heat pipes in silicon and use them as a very efficient thermal spreader. The procedure is to use photolithography and wet-chemical etching to create triangular grooves of width 100 μm (the depth is comparable, since the etch angle is 54.7 degrees) and space them 100 μm apart. Anodic bonding of a sheet of pyrex will be used to close the devices. They will then be filled and sealed. Although each device may not transport a tremendous amount of energy, the dense packing allows very high heat fluxes.

Before fabrication and detailed numerical modeling was attempted, however, some simple scaling analysis was performed. The major results of this study, which are reported here, were the determination of the basic flow patterns and heat transfer occurring in the micro heat pipe. In particular, it is very important to know how high of an energy flux a micro heat pipe can transport, before the basic flow pattern is disturbed and further energy transport is obstructed.

IV. OPERATING LIMITS:

The operating limits for micro heat pipes should be controlled by either a capillary limit or an interfacial instability. Both of these analyses have been performed. This analysis will be presented at the **Ninth International Heat Transfer Conference** in Israel, in August of 1990. Therefore, only the results will be presented here.

From a scaling analysis, it was determined that micro heat pipes will reach their maximum heat load due to a capillary limitation when

$$Q_{max} = \frac{3\pi}{2048} \frac{\sigma h_{vl} D^3}{\nu_v L} \tag{4}$$

For micro heat pipes of length of 1 cm or greater, gravity is the predominant stability mechanism and the maximum heat load predicted by an interfacial instability is

$$Q_{max} = \rho_v h_{vl} (\pi D^2 / 4) \left(\frac{\rho_l}{\rho_v} \frac{g D}{16}\right)^{1/2} \tag{5}$$

From comparing their ratio

$$\frac{3\sigma}{128 \mu_v L} \left(\frac{\rho_v}{\rho_l} \frac{D}{g}\right)^{1/2} \tag{6}$$

it can be determined which is the controlling mechanism. If this is less than one, the capillary limit will control. If greater than one, interfacial instability will be the operating limit.

If the hydraulic diameter is very large, the interfacial instability will determine the operating limit. This is what is known as flooding in conventional two-phase closed thermosyphons. If the tube is very long the capillary limitation will occur first. There is also, however, a large range where the tube is long enough for the interface to be gravity stabilized, but short enough so that an interfacial instability will limit the maximum power input.

To date there has been no experimental data reported for "true" micro heat pipes. Babin et al. (1989) , however, have reported data on a small , 1 mm by 1 mm

cross-section length 57 mm, metal-water heat pipe. Estimating the capillary radius as half the hydraulic diameter implies (at $50^{\circ}C$)

$$\rho_l g R L / \sigma \sim 4 \tag{7}$$

This implies that gravity is very significant in these devices. In fact, as they experimentally verified by tilting the device, their heat pipe is essentially a capillary-assisted thermosyphon.

Nonetheless, it is useful to compare the model with their experimental data. Their tube is long enough to be capillary dominated. In other words, Expression (6) is less than one. Therefore, the capillary limit should prevail and the maximum heat flux is given by Equation (4).

This expression is compared with Babin et al.'s experimental data for a silver-water heat pipe in Fig. 2. Since the ratio, Equation (6), is not much less than one, the limit predicted by an interfacial instability, Equation (5), is also plotted. The reason why both are shown is that scaling predictions are not expected to be exceedingly accurate. It is seen that the interfacial instability overpredicts the operating limit as compared to the experimental data. This is consistent with the expectation that the capillary limit controls the operating limit.

It is also seen that the experimental data lie consistently above the capillary prediction. This is not really a problem, since this prediction is based solely on a scaling analysis. In fact, for such a simple prediction, the agreement is quite good. The major reason for the discrepancy is probably due to underpredicting the maximum capillary pressure. As mentioned previously, the film in the evaporator is likely to be much smaller than the hydraulic diameter. Therefore, the mean radius

of curvature is smaller, the maximum capillary pressure is larger and the maximum heat transport is larger.

In order to attempt a simple procedure to improve this prediction, a correction factor is introduced

$$Q_{\max} = C \frac{3\pi}{2048} \frac{\sigma h_{vl} D^3}{\nu_v L} \tag{8}$$

Figure 2 is then used to determine this correction factor, by averaging the ratios of the experimental data over the capillary prediction, and is found to be 2.38. The correlation then becomes

$$Q_{\max} = 0.01 \frac{\sigma h_{vl} D^3}{\nu_v L} \tag{9}$$

This correlation is then compared with Babin et al's (1989) experimental data for a copper-water heat pipe in Fig. 3. It is seen that the agreement is excellent. Although it is suggested that Equation (9) be used to predict the maximum heat transport for micro heat pipes which are long enough so that Equation (6) is less than one, it should be kept in mind that it has been verified for only one size heat pipe with only one working fluid. New experiments should either confirm or refute this statement. Currently, 100μm micro heat pipes are being built at the University of Cincinnati, which will serve this purpose.

Silicon Heat Pipes

The micro heat pipes being built at the University of Cincinnati are etched directly into silicon and will be filled with water. This arrangement is very close to that which will be used to electronic chips. In order to demonstrate their

effectiveness, before fabrication and testing, some simple calculations were performed.

These new heat pipes are true micro heat pipes; they have a hydraulic diameter of $100\mu m$ (with a triangular cross section) and a length of 1 in (2.54 cm). For these devices, in the operating range of $30^{o}C$ to $70^{o}C$ the ratio given by Equation (6) is less than 1 and the capillary limit prevails. Using Equation (9), the maximum heat transport is estimated and is shown in Table 1. It is seen that for water, heat transport on the order of 1 mW can be expected per device. Of course, 127 of these devices per inch will be used; so that, assuming that all of the energy is transferred through the end of the evaporator, the heat fluxes given in Table 1 will occur. So that up to $15\ W / cm^2$ can be dissipated.

The real advantage to using micro heat pipes; however, is that the temperature gradients are very low, therefore the temperature within the device is very uniform. Comparing the thermal resistance of pure silicon

$$R_{sil} = \frac{L}{k_{sil}\,(\pi D^2 / 4)} \tag{10}$$

with that for the micro heat pipe

$$R_{HP} = \frac{1}{\pi D\, L\, h} \tag{11}$$

with

$$h = k_{wat} / \delta = 4\, k_{wat} / D \tag{12}$$

or

$$R_{HP} = \frac{1}{4\,\pi\, k_{wat}\, L} \tag{13}$$

yields

$$\frac{R_{HP}}{R_{sil}} = \frac{1}{16}\frac{k_{sil}}{k_{wat}}\left(\frac{D}{L}\right)^2 \tag{14}$$

For these micro heat pipes, at an operating temperature of $50^{o}C$, this ratio is about 10^{-4}.

This decrease of the thermal resistance is what makes micro heat pipes so effective. Expressing this in terms of temperature drop

$$\Delta T_{HP} = \frac{Q}{4\pi k_{wat} L} \tag{15}$$

and

$$\Delta T_{sil} = \frac{Q L}{k_{sil}\frac{\pi}{4}D^2} \tag{16}$$

It is expected for the 100 μm hydraulic diameter micro heat pipe that the temperature drop will be less than $0.01^{o}C$, whereas obtaining this flux in silicon would require a temperature drop of about $26^{o}C$. For the 1 mm hydraulic diameter heat pipe, a temperature drop of about $1^{o}C$ is expected, which is in agreement with Babin et al's (1989) experimental results before dryout begins. Obtaining the same flux in silicon would require about a $25^{o}C$ temperature drop.

Flow Regimes

The last thing that needs to be accomplished is to justify the assumptions used in the models presented in this paper. The primary ones being that both the liquid and vapor flows are laminar and incompressible. Of course since the vapor flow is incompressible, the sonic limit is not a problem. Table 2 shows estimates of the

various parameters for both 1 mm and 100 μm hydraulic diameter micro heat pipes containing water at $50^{o}C$. As can be seen, the Reynolds numbers are extremely low. Both the liquid and vapor flows are certainly laminar. Also from the small Mach number it is seen that the flows are incompressible.

Summary

In this paper, the basic physics governing operation of a micro heat pipe are investigated. In order for the capillary action in the sharp-edged corners to effectively return the condensate to the evaporator, it is necessary for the capillary force to overcome gravitational forces. If $\rho_l \, g \, R \, L \, / \, \sigma$ is less than 1, this will be true regardless of orientation. The other unique feature of micro heat pipes is that their hydraulic radius is very small; it is of the same order as the capillary radius. It is also shown that the flow in both the liquid and the vapor is laminar incompressible flow.

Very simple scaling arguments are used to develop an analytic expression for the maximum heat input when the capillary limit is reached. This limit was found to be the operating limit for most micro heat pipes; whereas a Kelvin-Helmholtz instability controls flooding in large diameter tubes which behave more like conventional two-phase closed thermosyphons. Comparison with other researcher's experimental data validate this model.

The last thing which is accomplished is to predict the heat transfer capability for $100 \mu m$ hydraulic diameter micro heat pipes, which are being constructed. It is estimated that these devices will each transfer about 1 mW of energy, which yields a net flux of 10 - 15 W / cm^2. The remarkable thing about these devices, however, is that due to their small thermal resistance, about 10^{-4} times that of pure silicon, temperature drops of order $0.01^{o}C$ can be expected.

V. RECOMMENDATIONS:

The work reported here demonstrates that, due to their ability to dissipate fairly large heat fluxes and their extremely low thermal resistances, micro heat pipes show great promise as devices to cool electronic chips.

It is recommended that a one-dimensional or control-volume model be developed to predict both steady state and transient operating characteristics of these devices. In addition to predicting temperatures and heat fluxes, the model should predict dryout and indicate the proper fill quantity for micro heat pipes.

It is also recommended that fabrication of micro heat pipes be completed. The major obstacle which needs to be surmounted is the proper way to fill these devices. After this is accomplished, the devices need to be instrumented and tested.

In short, further development of micro heat pipes is definitely warranted. Funding from the Mini-Grant Program will be sought so that fabrication and testing of micro heat pipes can proceed.

References

Babin, B.R., Peterson, G.P., and Wu, D., 1989, "Analysis and Testing of a Micro Heat Pipe During Steady-State Operation," to be presented at the ASME National Heat Transfer Conference, Philadelphia, PA.

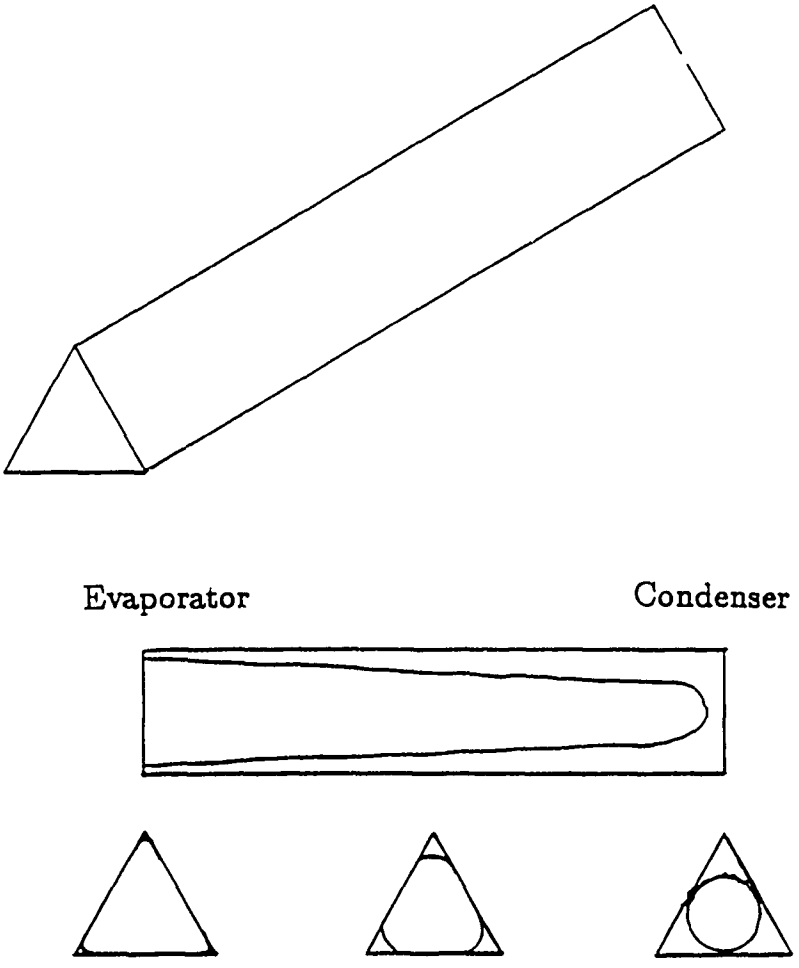
Chi, S.W., 1976, Heat Pipe Theory and Practice, McGraw-Hill, New York.

Cotter, T.P., 1984, "Principles and Prospects of the Micro Heat Pipes," Proceedings 5th International Heat Pipe Conference, Tsukuba, Japan, pp. 328-335.

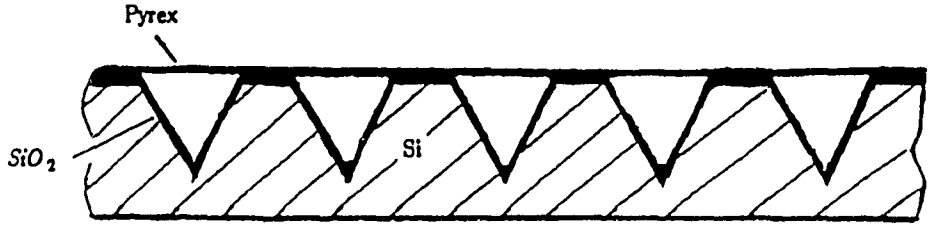
Gerner, F.M. and Tien, C.L., 1988, "Axisymmetric Interfacial Condensation Model," presented at The 25th National Heat Transfer Conference, Houston, Texas.

Reed, J.G., and Tien, C.L., 1987, "Modeling of the Two-Phase Closed Thermosyphon," J. Heat Transfer, Vol. 109, pp. 722-730.

Tien, C.L., Chung, K.S., and Liu, C.P., 1979, "Flooding in Two-Phase Countercurrent Flows," EPRI NP-1283.



(a) Basic Physics



(b) Arrayed in Silicon

Fig. 1 Micro Heat Pipe

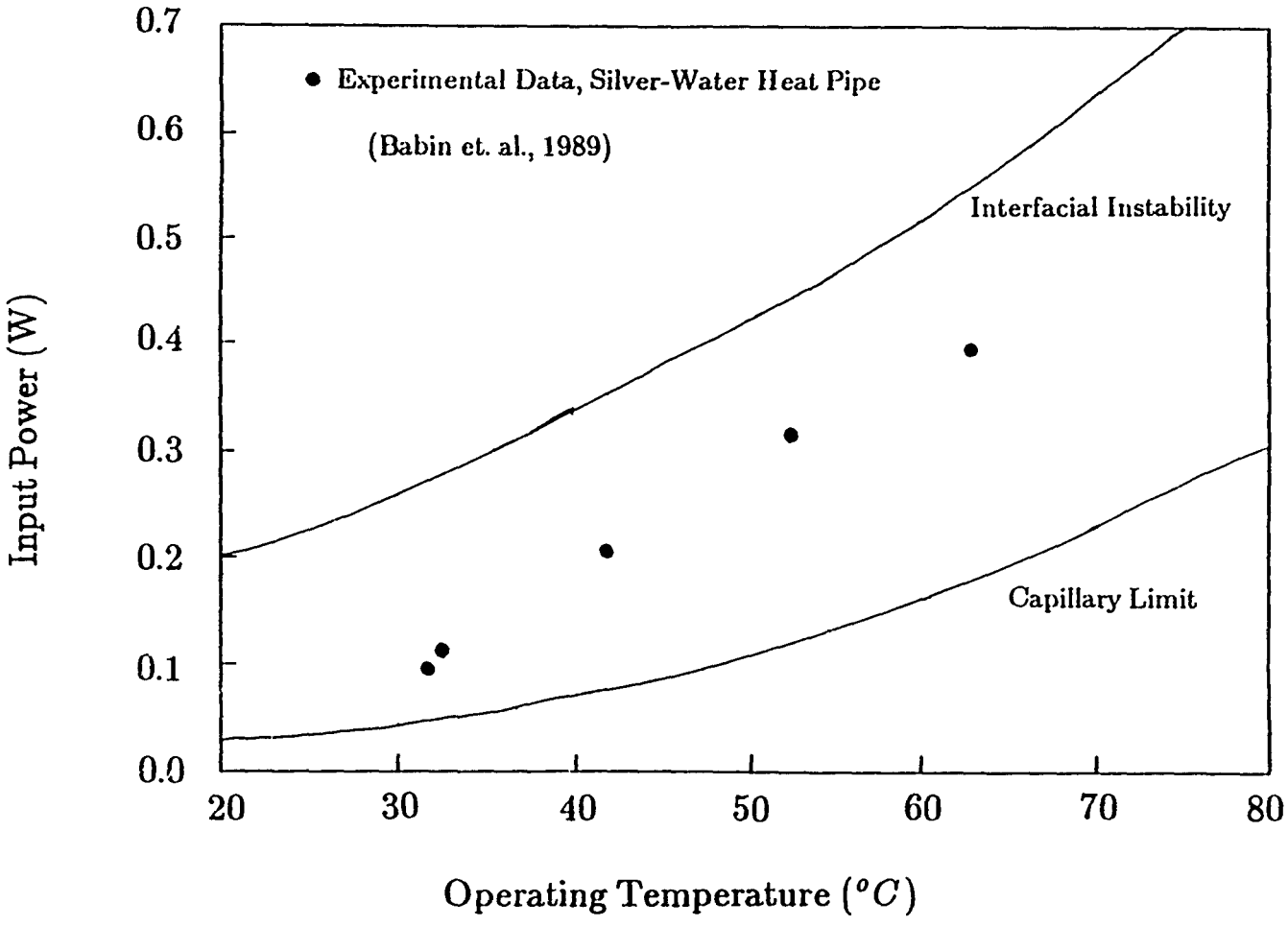


Fig. 2 Maximum heat transport as a function of operating temperature

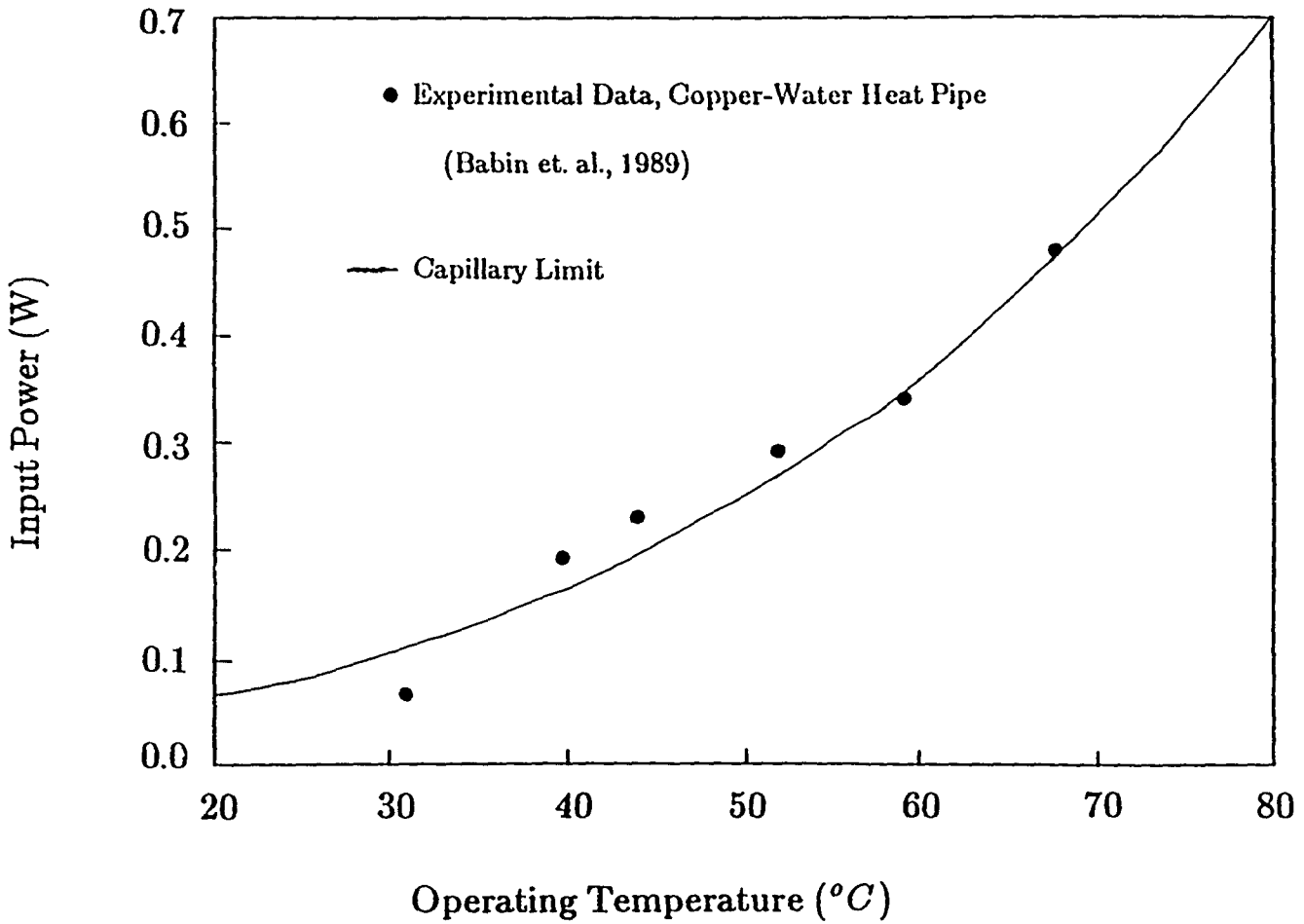


Fig. 3 Maximum heat transport as a function of operating temperature

Table 1 - Maximum heat transport and net heat flux for micro heat pipes with hydraulic diameter of 100 μm and length of 2.54 cm, filled with water.

Operating Temperature $T\,[^{\circ}C]$	Maximum Heat Transport	
	Q [mW]	q'' $[W / cm^2]$
30	0.25	3.09
40	0.38	4.86
50	0.58	7.33
60	0.83	10.61
70	1.18	15.04

Table 2 - Parameters for micro heat pipes filled with water operating at $50^{\circ}C$.

	$D_h = 100\ \mu m$	D = 1 mm
Q [W]	$6.0X10^{-4}$	$3.0X10^{-1}$
$m_l = m_v$ [Kg/s]	$2.5X10^{-10}$	$1.3X10^{-7}$
U_l [m/s]	$4.3X10^{-5}$	$2.2X10^{-4}$
U_v [m/s]	1.6	7.7
Re_l	$5.9X10^{-3}$	$2.9X10^{-1}$
Re_v	$6.4X10^{-1}$	$3.2X10^{1}$
Ma_v	$3.5X10^{-3}$	$2.0X10^{-2}$

Final Report

Prof. Thomas Lalk

Not Publishable At This Time

(REPORT # 93)

1989 USAF-UES SUMMER FACULTY RESEARCH PROGRAM

GRADUATE STUDENT RESEARCH PROGRAM

Sponsored by the

AIR FORCE OFFICE OF SCIENTIFIC RESEARCH

Conducted by the

Universal Energy Systems, Inc.

FINAL REPORT

Large-Scale Motion and Coherent Structures in Axisymmetric Swirling Flow of a Dump Combustor

Prepared by:	Baruch B. Lieber, Ph.D.
Academic Rank:	Assistant Professor
Department and University:	Mechanical and Aerospace Engineering State University of New York at Buffalo
Research Location:	WRDC/POPT Wright-Patterson AFB, Ohio 45433
USAF Researcher:	Abdollah S. Nejad, Ph.D.

Date:	28 August 1989
Contract No:	F49620-88-C-0053

Large-Scale Motion and Coherent Structures in Axisymmetric Swirling flow of a Dump Combustor

by

Baruch B. Lieber, Ph.D.

ABSTRACT

The flowfield in an axisymmetric dump combustor is investigated under isothermal conditions with a two component laser Doppler velocimeter. The combustor can accomodate different coaxial swirlers with a swirl number ranging from zero to 0.5. The raw data is collected and stored permanently on digital magnetic tapes. Subsequently, the data are subjected tc extensive off-line analysis in both the time domain and spectral domain. The analysis includes phase conditioning, ensemble averaging, spectral transformations and matched filtering. the purpose of the analysis is (a) to reveal the nature of the various flow disturbance phenomena and; (b) to decompose flow disturbances into the different physical categories such as large-scale organized motion, coherent structures and incoherent turbulence. The decomposition of experimental data into these categories is valuable as it provides the necessary input information to computational schemes which try to predict flow behavior and performance of such combustors.

ACKNOWLEDGEMENTS

I wish to thank the Air Force Systems Command and the Air Force Office of Scientific Research for sponsorship of this research. Also, the administrative support of Universal Energy Systems is gratefully acknowledged

My research effort at WRDC/POPT was both enriching and rewarding, working with Dr. A.S. Nejad was truly an inspiring experience. His encouragement and support provided an enjoyable working atmosphere. The help of Dr. S.A. Ahmed and Mr. Ken G. Schwartzkopf was invaluable in overcoming many technical problems. Special thanks are due to Mr. Brian L. Peffley and Mr. Marti E. Marcum from the Computer Technology branch for their tremendous help in leading me through the maze of the local computer network. The assistance of Dr. D.C. Rabe from WRDC/POTX in providing me with access to computer-graphic peripherals in his laboratory is greatly appreciated. Last but not least I wish to thank Mr. John T. Hojnacki, the branch chief, for the opportunity to conduct this research project and his support.

I. INTRODUCTION:

Dump combustors with a coaxial swirler are of considerable interest in integral rocket/ramjet applications. The full potential of such combustors, however, is yet unknown due to the fact that insufficient experimental data are available. Furthermore, current numerical prediction schemes lack the ability to describe such complex flowfields.

The experimental branch of WRDC/POPT has undertaken an experimental study of a model combustor which includes a coaxial swirler and a dump in an effort to produce reliable experimental data. These data will assist in the development of computational schemes which can be verified against the experimental data and predict performance of similar combustors. The initial phase of the study was conducted on an experimental apparatus under isothermal conditions. The subsequent phase will deal with chemically reacting flow. A thorough understanding of the isothermal flow is of great value in constructing computational methods and is necessary to the understanding of the chemical kinetics and evaluation of chemical reaction.

My research interest have been in the area of unsteady undeveloped ("young") flows. Such flows maintain complex physical phenomena which cannot be modeled by using customary turbulence closure models. My work in unsteady flows both experimental and analytical has resulted in the development and application of new techniques for analyzing and describing flow disturbance phenomena in unsteady flows.

II. OBJECTIVES OF THE RESEARCH EFFORT:

Currently there are no turbulence prediction models which can faithfully describe a complex flowfield such as swirling flow through an axisymmetric dump combustor. Furthermore, the development of predicting models is severly impeded by the lack of a comprehensive database against which such models can be verified and validated. This project deals with an experimental model study of the flowfield in an axisymmetric dump combustor which includes a coaxial swirler upstream of the dump plane. Velocity measurements are obtained with a laser Doppler

velocimeter (LDV) for both isothermal and reacting flows. The objective of the research is to develop analysis methods which will decompose the various flow disturbance phenomena and describe them based on the physical principles which govern such phenomena. Disturbances which are induced by fluid motion may include large-scale motion, various coherent structures and fine-grain turbulence. The analysis includes conventional statistics and time domain methods, spectral transformation and conditional sampling. Initially, analytical methods are developed and applied to existing experimental data of isothermal flow through the combustor which includes a swirler of swirl number 0.3. The application of the developed methods to the existing data provide verification and applicability tests. Subsequently, the developed methods will be applied rigorously to different flow configurations commencing with isothermal flow through the combustor for zero swirl case and continuing with more complex cases by adding non-zero swirler and chemical reaction.

III. BACKGROUND AND APPROACH:

The interest in complex flowfields that do not subscribe to the simple cases of either laminar or fully developed turbulent is inspired primarily by practical applications. Such is the case, for example, for an axisymmetric dump combustor or swirling flow for ramjet/turbojet applications. Even if one considers only the isothermal case, these complex flowfields do not lend themselves to turbulence modeling by the use of customary closure models (i.e., mixing length or k-ε). The flow regimes may include an induced vortex - either forced or free, vortex shedding, puff formation, coherent structures, separation-reattachment regions and flow reversal. Such complex characteristics severely impeded the development of a comprehensive data base for practical applications due to the lack of instrumentation capable of measuring such flows. During the last two decades, however, the mapping process of complex flowfields materialized with the development of optical measuring techniques such as laser Doppler velocimetry (LDV). Albeit, such measurements are obtained in an Eulerian framework and the data do

not readily reveal the spatial nature of flow disturbance phenomena. Lagrangian methods, on the other hand, which can provide two or even three dimensional view of the flow domain are limited to a qualitative description only. Nonetheless, they provide insight to the physics of the processes and can help in the interpretation of Eulerian-obtained quantitative data.

As the database on practical flowfields expanded so did the database for well controlled laboratory experiments. The expanding knowledge prompt considerable interest in "coherent structures" which have been identified in a variety of flowfields. Such structures, play an undeniable role in "young" undeveloped flows and even in well-controlled simple experiments they are considered a major mechanism in the production of the turbulent energy. The aim of such studies is to analyze the data, based on the physical phenomena, in order to provide new information to alleviate the closure problem of turbulence modeling theory. Thus, promoting new more realistic models which can describe practical flowfields (e.g., large-eddy simulations). Nonetheless, such models rely on experimental data as input and must be validated against accurate fluid dynamic measurements which include elaborate data processing methods.

For almost a century fluid dynamicists have attempted to describe turbulence by decomposing dependent flowfield variables into deterministic and random components with varying degrees of success (Reynolds 1895). The commonly used decomposition, which has been developed primarily for fully developed turbulent flows, assumes a steady mean and random fluctuations which are defined as the departure of the instantaneous variable from the mean (i.e., Reynolds averaging). During the past two decades, however, considerable effort has been devoted to the study of large scale organized motion which have been observed in turbulent flows many years before (Townsend 1956). The efforts to incorporate such coherent motion in turbulence modeling theory led to a modified decomposition scheme of flow variables for the analysis of fluid motion. The modified decomposition, often referred to as the "triple decomposition", suggests to separate flow variables into a steady mean value, a coherent contribution and random variations

(Hussain and Reynolds 1970, Liu 1981). However, it must be recognized that the closure problem of turbulence modeling theory manifested in the "apparent" or Reynolds stress tensor, which arises from the mathematical manipulation of the Navier-Stokes equations using Reynolds averaging, is further complicated by the use of triple decomposition.

The study of coherent structures in the past two decades accumulated sufficient information to establish the existence and diversity of such behavior. However, most of the studies resulted in a rather qualitative description of coherent motion. The interest in coherent structures that was initiated by observations made in free shear flows prompt the search for organized structures in bounded flows. While free shear flows give rise to large energetic structures which separate turbulent from non turbulent zones, observations made in so-called fully developed turbulent fields that are bounded are difficult because the structures may wax and vane and any residual organized motion will maintain only a small portion of the turbulent energy. More recently, investigators have been examining flows which are "younger", closer to their origin, and such flows which carry an important practical value contain structures which are more organized and more energetic then those present in fully developed turbulent flows. A comprehensive discussion on coherent structures in turbulent flows is given in review articles by Cantwell (1981), Hussain (1986) and Fiedler (1988).

Phase conditioning, or conditional sampling, has been implemented by many researchers as a method to extract information on organized motion (e.g., the near field of free jets, boundary layers or wakes, see for example Blackwalder 1978, Antonia 1981). The central issue in these studies is to devise a proper (independent) trigger or pattern recognition schemes. Given a proper phase conditioning criterion, organized behavior is lumped into an ensemble average which can than be employed in the search for characteristic eddies.

To describe the various transition characteristics one may assume that any flow variable may be decomposed to three parts in the following manner

$$y(\vec{x},t) = Y(\vec{x}) + \tilde{y}(\vec{x},t) + y'(\vec{x},t) \qquad 0 \leq t \leq T \qquad (1)$$

where: Y is the underlying mean flow.

$\tilde{y}$ is some large-scale periodic behavior.

y' represent the pseudo stochastic variations, and these are assumed to be uncorrelated with the two previous variables.

T is the time window of observation.

The decomposition described by equation (1) is a time domain representation of a flow variable, however, it is convenient to transform it into the spectral domain. Also, one may assume a quasi periodic behavior for the organized motion. That is, each realization may contain an oscillatory contribution which may vary from one observation to another. The quasi periodic assumption is evidentially justified in practical applications where initial/boundary conditions may experience variations in consecutive realizations. Nonetheless, organized phenomena as viewed from the frequency domain reoccur at a narrow frequency band, although, it may experience "large" magnitude and phase variations in independent observations. Magnitude and phase variations are considered large in this context when conditional averaging in the time domain will smear large-scale organized structures characteristics.

If one removes the underlying mean of a flow variable, the remainder represents a nonstationary stochastic process $\{y_n(\vec{x},t)\}$ with zero mean where each sample function is given by

$$y_n(\vec{x},t) = \tilde{y}_n(\vec{x},t) + y_n'(\vec{x},t) \qquad 0 \leq t \leq T \qquad (2)$$

Where $y_n'(\vec{x},t)$ is a sample function from a stationary stochastic process and $\tilde{y}_n$ is some "quasi periodic" function.

The quantity of interest is the one sided power spectral density (PSD) function, $G(\vec{x},f)$. It is obtained via the square magnitude of the finite Fourier transform of the temporal variations for the newly

obtained sample functions over the time interval [0,T]. Expanding the spectrum of the sample functions to the constitutive parts and taking the square magnitude results in:

$$G_y(\vec{x},f) = 2 \lim_{T\to\infty} \frac{1}{T} \varepsilon[|\tilde{F}_n(\vec{x},f,T)|^2 + |F'_n(\vec{x},f,T)|^2 +$$

$$2|\tilde{F}_n(\vec{x},f,T)||F'_n(\vec{x},f,T)|\cos\{\theta'_n(\vec{x},f,T) - \tilde{\theta}_n(\vec{x},f,T)\}] \qquad (3)$$

Here G_y is the one sided power spectral density function, $\varepsilon[\ ]$ is the expected value operation over the ensemble index n in question and F if the Fourier transform of the sample functions. Note that in general the PSD of the sum of two sets of functions depends on the power spectrum of the individual sets as well as cross-spectral quantities and phase relationship over the entire frequency argument.

When two processes are said to be uncorrelated or incoherent for a frequency interval of interest, the coherence function assumes the value zero for all frequencies, f, within that frequency band. In other words, incoherence will require that the magnitude of the cross-spectral density function be zero within the appropriate frequency interval. If one assumes that $\tilde{y}_n$ and y'_n are uncorrelated, or incoherent, then the last term in equation 3 be zero for all f within the band of interest. This will be true only if the the sample pairs under consideration compose an orthogonal set of functions. For such a set the power spectral density function is given by:

$$G_y(\vec{x},f) = G_{\tilde{y}}(\vec{x},f) + G_{y'}(\vec{x},f) \qquad (4)$$

and the argument relation is:

$$\theta'_n(\vec{x},f,T) - \tilde{\theta}_n(\vec{x},f,T) = \pi/2 + m\pi \qquad m = 1,2,3... \qquad (5)$$

In general the PSD function of $\{y'_n\}$ is non zero over a wide (possible infinite) range of frequencies while an organized contribution, $\{\tilde{y}_n\}$, usually occurs within a narrow frequency band, $[f_1, f_2]$, which will dictate the frequency interval of interest. In practice one may estimate the power spectrum of the combined sample functions, $\{y_n\}$, whereas the power spectrum of the constituents is unknown. In fact, obtaining the PSD function of the data is the first most important step to identify whether large-scale structures are present in the data or not. Also, the spatial variations of organized structures will modify the spikes (magnitude and possibly frequency) of the power spectrum at different locations in the flow. Consequently, the PSD function must be evaluated at many spatial locations in the flowfield. Nonetheless, if orthogonality prevails we may proceed to device matched filtering methods to decompose the given functions. It should be noted that to decompose the sample functions to their constituents and preserve the phase relationship of the decomposed parts, $y_n(t)$ needs to be passed through a pair of filters that perform an orthogonal decomposition. Also, such filters should have a linear minimum phase response to permit preservation of phase relationship with respect to a fixed origin. For a discussion on matched filters see Lieber et al 1989.

IV. RESULTS:

The experimental apparatus at WRDC/POPT was undergoing extensive structural modifications and upgrading during the summer of 1989. This included the flow facility itself to enable the accommodation of chemically reacting flow. The data aquisition system was upgraded as well to include a VMS based VAX computer. Consequently, to avoid any delay in the development of analysis tools we employed data from earlier experiments on this apparatus that were recorded on digital magnetic tapes. Velocity data were obtained with a two component LDV. The coordinate system that was used to denote the various velocity

components, and the schematic of the dump combustor are shown in Figure 1 (the origin is at the dump plane). The swirler used in the experiment

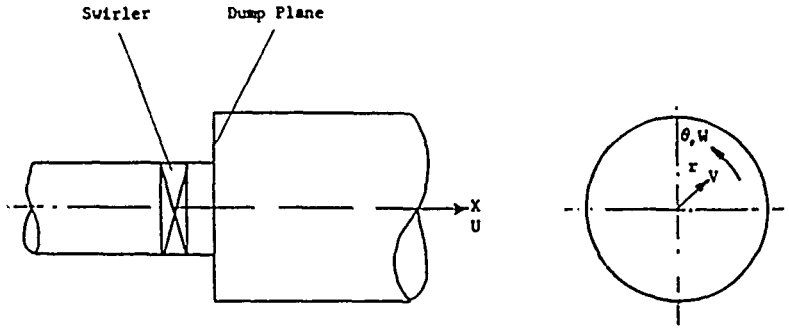


Figure 1. Schematic of the Dump Combustor

is a constant angle axial flow type with a swirler number of 0.3 and twelve circular arc inlet guide vanes (Buckley et al 1983). The inlet section pipe has a diameter of 101.6 mm and is 2850 mm long. The dump pipe diameter is 152.4 mm and the swirler was located 50.8 mm upstream of the dump plane. The inlet centerline velocity was maintained at 19.2 m/s which corresponds to a Reynolds number of 125000 based on upstream pipe diameter. Further details on the experimental methods can be found in Favaloro et al 1989. The radial development of the average axial velocity component, at different axial locations downstream of the dump plane, is shown in Figure 2. The radial development of the average radial velocity component, at different axial locations downstream of the dump plane, is shown in Figure 3. These profiles have been compared to the results published by Nejad et al, 1989, to verify the validity of the recorded data.

The laser Doppler velocimeter is a unique instrument which registers velocity data only at discrete instances in time as a result of a singular event. That is, a data point is generated only when a light scattering particle in the flowfield (seed particle) is crossing the light beams intersection point (probe volume). The seed particles arrive to the probe volume in random time intervals which depend on the concentration of particles in the flow. If one constructs a time series from the collection of data points which were generated by the particles, the resulting series is known as an unequally-spaced time

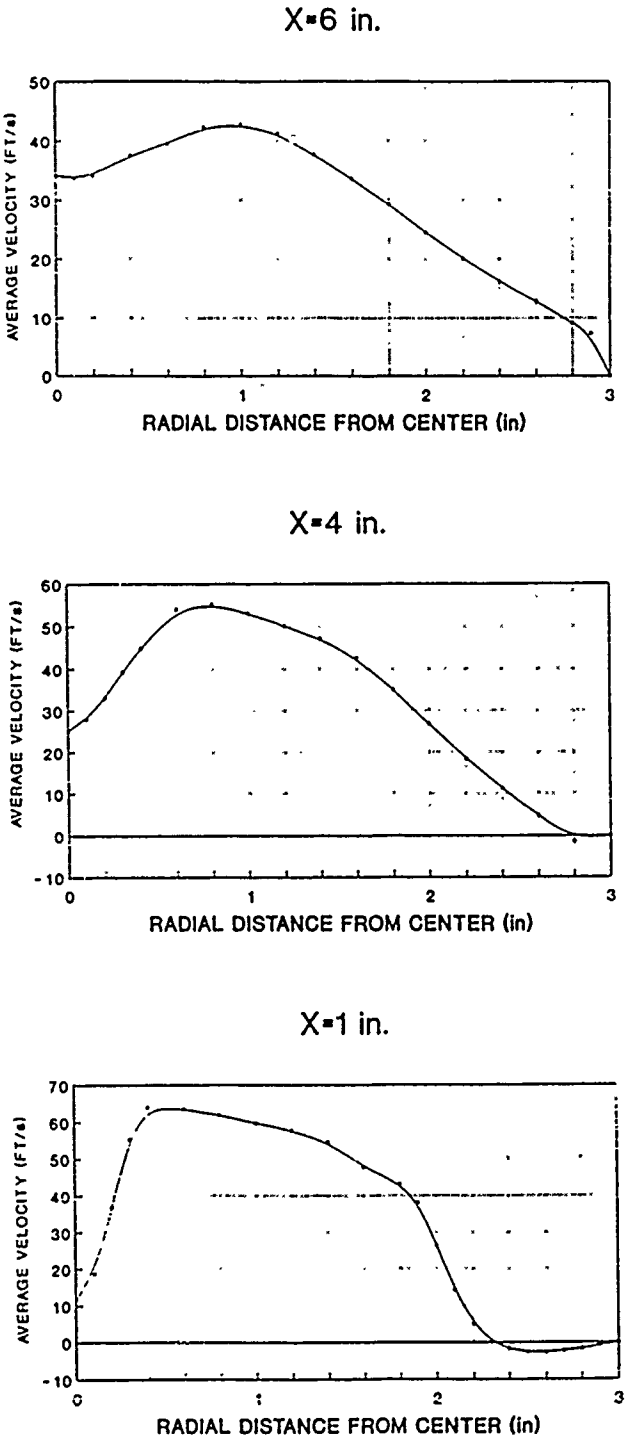


Figure 2. Average axial velocity at different axial positions downstream of the dump plane.

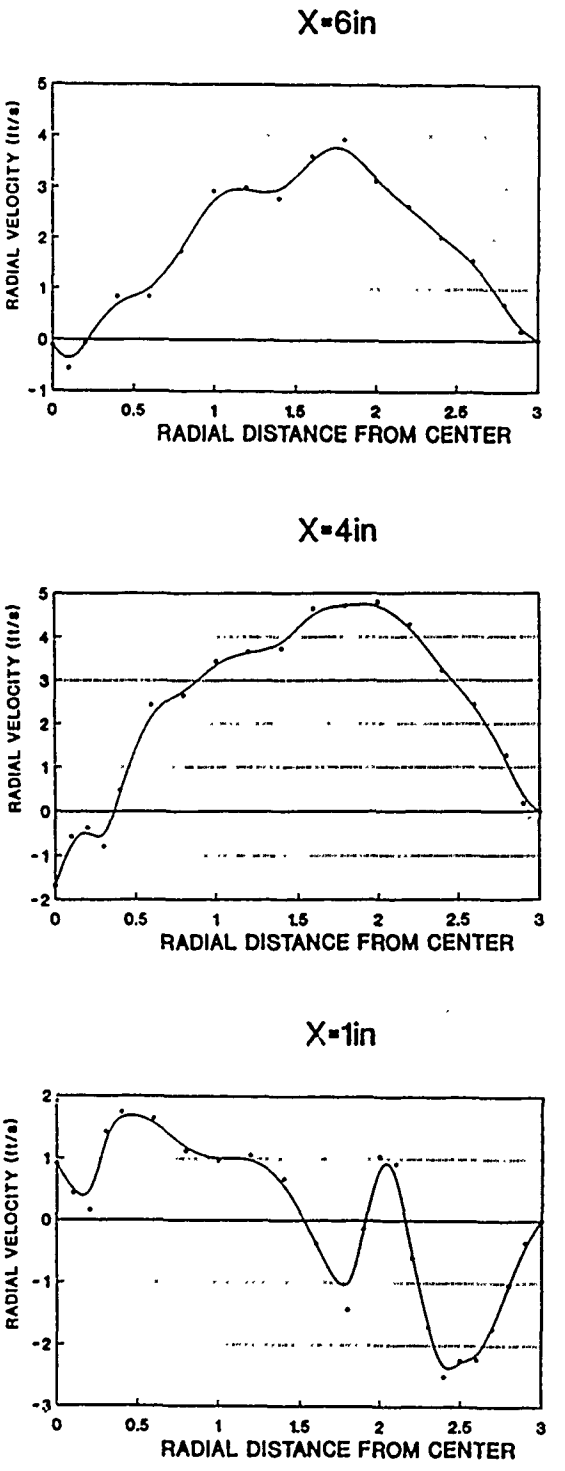


Figure 3. Average radial velocity at different axial positions downstream of the dump plane.

series (see Fig. 4). There are currently methods available which enable one to obtain a power spectral density (PSD) estimate of an unequally-spaced time series, however, these methods involve transformations which are extremely cumbersome. Furthermore, the obtained PSD estimates are

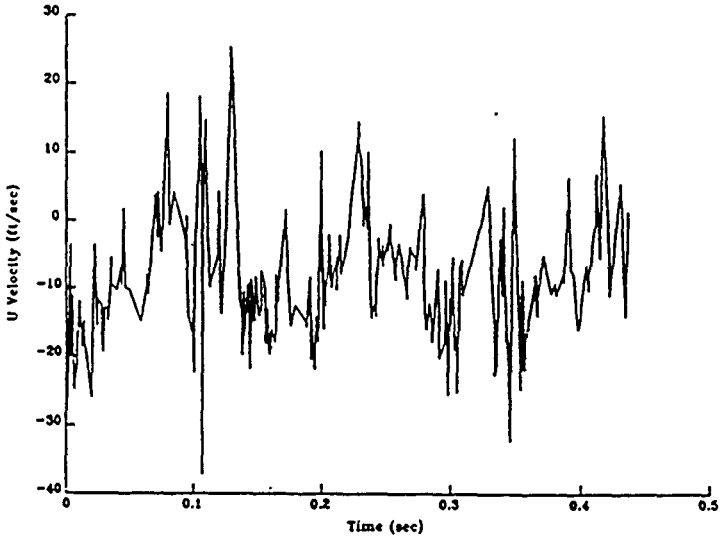


Figure 4. Time series of instantaneous velocity at X = 1.0 in., R = 2.6 in.

limited to serve as an end result only. This is of course undesirable as it blocks the path for further analysis of the data which is based on the spectral estimates. Therefore, it is desirable to convert the unequally-spaced time series into an equally-spaced time series before further analysis. In doing so one has to take care not to produce extraneous information which is not actually present in the original time series. The program that was developed for equally-spacing the data includes three conversion alternatives. The first is that of linear interpolation between the existing points. The second alternative is a common technique known as sample-and-hold which is implemented usually on the hardware of the LDV system itself. In both options one is restricted to an equally-spaced sampling rate which is at the most one half of the average sampling rate of the unequally-spaced time series. The third option is a quasi-equally-spaced slotted-time window data search technique which is similar to the "slotted autocorrelation method". In this technique one chooses an arbitrary

sampling rate (Usually about 1/10 of the average sampling rate of the unequally-spaced data) and searches for data points which lie within a prescribed small time window around a desired reference time. The disadvantages of this option are (a) a large portion of the original data is lost which makes the spectral resolution very low, and (b) if no data point exists within a prescribed time window around any reference time, the equally-spaced series will contain a hole at such point which is not so unusual. However, if the LDV's average data rate is very high (at least ten times higher than the highest frequency of interest) implementation of this method is desirable since it imposes the fewest assumptions on the experimental data.

In this study the velocity data was equally-spaced using linear interpolation. The results of the the spectral behavior of the axial and radial velocities at 1.0 inch downstream of the dump plane are shown in Figure 5. This is a three dimensional representation which shows the spectral behavior of the velocity as a function of radial position ranging from the centerline of the pipe to the outer wall. One can clearly observe the high magnitude of velocity fluctuations at the low frequencies in the vicinity of the centerline (i.e., in the central recirculation zone). Although not shown in the figure, the spectra at this radial zone drops sharply at higher frequencies. The spectral behavior in the neighborhood of R = 0.5 in. is quite different. It is forming a valley void of spikes and is characterized by spectral broadening of velocity fluctuations. In the region of $1.8 < R < 3.0$ velocity disturbances exhibit spectral spikes which can be attributed to shed vortices which are generated in the shear layer. Although generated in the shear layer these vortices influence the flowfield in the vicinity of the wall including the peripheral recirculation zone. The only major difference between the radial and axial spectra occurs near the wall in the neighborhood of R = 3.0. Due to the large amplitude of the axial velocity relative to the radial one, it maintains spectral spikes in the vicinity of the wall. The radial component, on the other hand, due to low amplitude and geometrical constraints cannot maintain such spikes near the wall. Figure 6 is one sample of the power spectrum in the peripheral recirculation zone for the axial velocity and in the

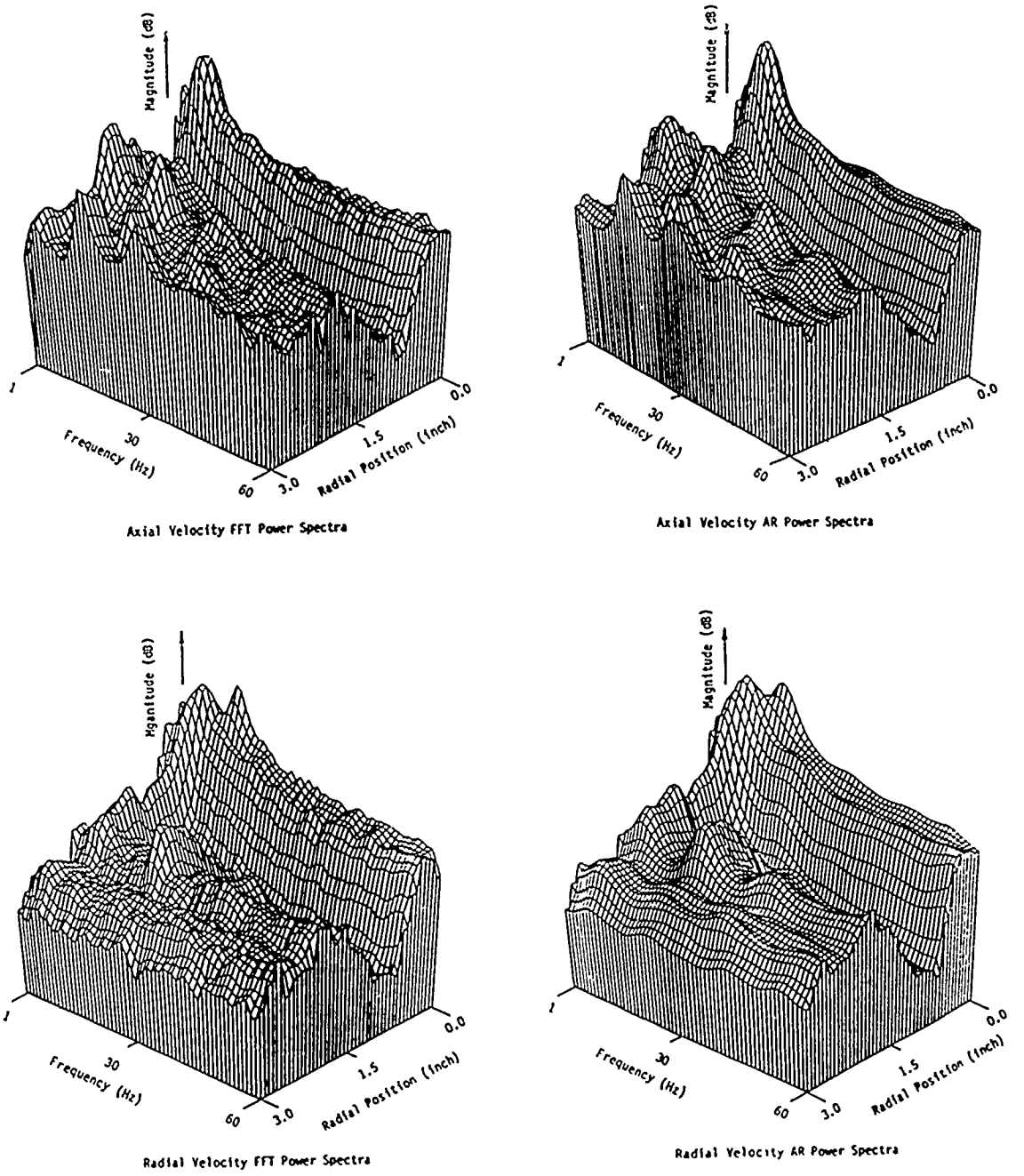


Figure 5. Radial variation of the power spectra for axial and radial velocity disturbances at the axial location 1.0 in. downstream of the dump plane.

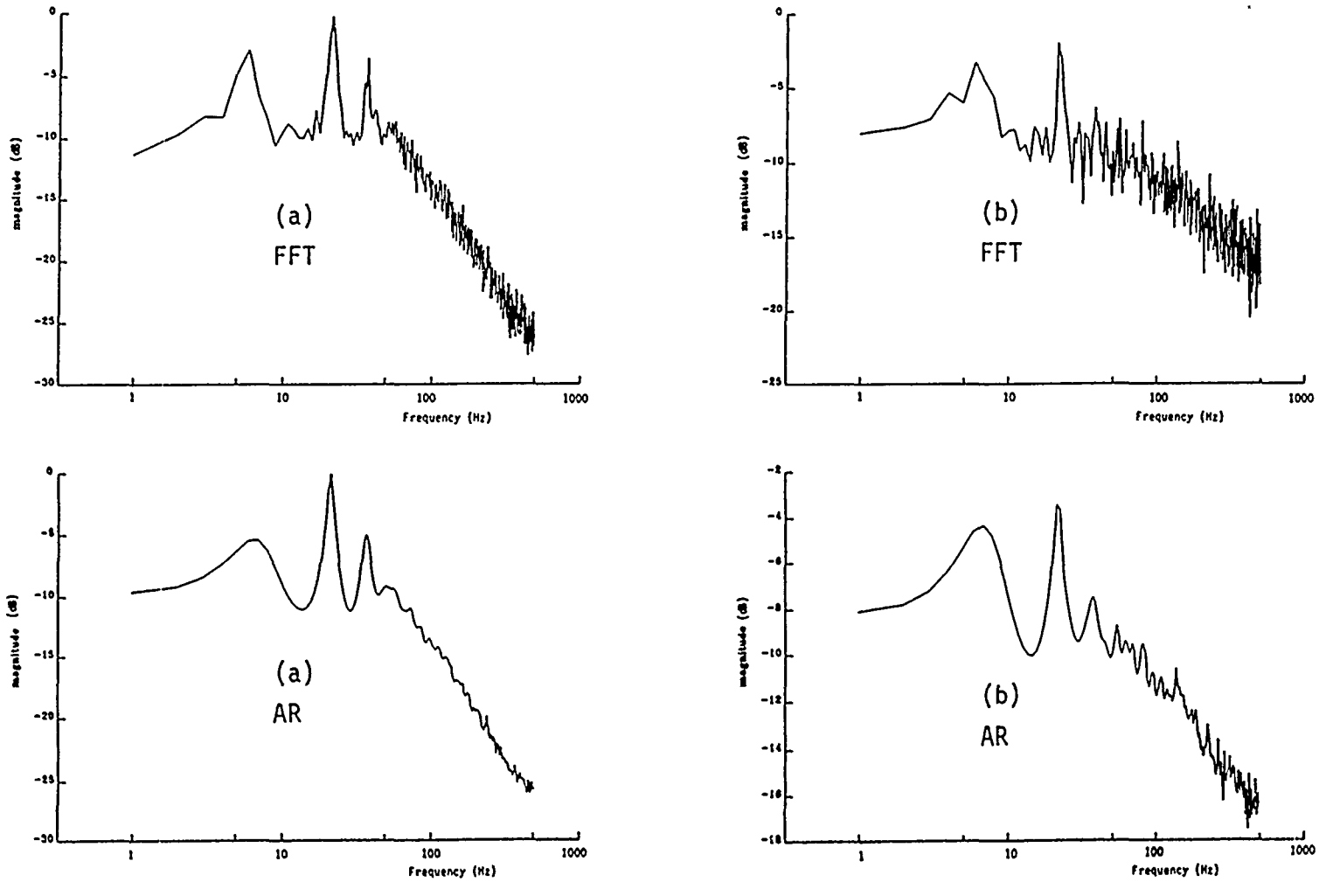


Figure 6. Power spectra of velocity disturbances at the axial location X = 1.0 in. (a) axial velocity, R = 2.6 in. (b) radial velocity, R = 2.0 in.

shear layer for the radial velocity. The power spectral density estimates were obtained using both fast Fourier transformation (FFT) and autoregressive modeling (AR). The potential advantage of AR modeling over FFT obtained spectra are discussed by Lieber and Giddens 1989. One can clearly observe the presence of organized structures which are manifested as sharp spikes of the spectrum at frequencies of approximately 6, 21 and 31 Hz. Following the evaluation of the spectral response for the velocity disturbances the data are ready for executing decomposition.

V. RECOMMENDATIONS:

The analysis of LDV data from the experimental apparatus at WRDC/POPT, thus far, included conventional statistics which were limited to average velocity quantities and turbulence intensity. Due to recent modifications and upgrading the opportunity for more elaborate analysis of LDV data has been materialized. Within the limited scope of a summer research effort (10 weeks) we developed analysis tools to enable the evaluation of the spectra for flow disturbances. These spectra demonstrate the existence of intense large-scale structures in the flowfield which demand further exploration. Naturally, this is only a first step which has to be proceeded by more complex analysis to determine, for example, the portion of the turbulent energy which is maintained by these structures. This can also serve as a database for comparison with chemically reacting flow. The addition of chemical reaction will most likely change the turbulent energy budget due to density gradients of combustion products and radicals. An equivalent approach to combustion data can elucidate the differences between isothermal and chemically reacting flow. Finally, the undertaking of such a research effort is well within the capability of the author of this report at his laboratory in collaboration with WRDC/POPT.

REFERENCES

1. Antonia, R.A., "Conditional Sampling in Turbulence Measurements", Ann. Rev. Fluid Mech., Vol. 13, 1981, pp. 131-156.
2. Backley P.L., Craig R.R., Davis D.L., Schwartzkopf K.G., "The design and combustion performance of practical swirlers for integral rockets/ramjets", AIAA Journal Vol. 21, No. 5, 1983, pp. 733
3. Blackwelder, R.F., "Pattern Recognition of Coherent Eddies", Proc. Dynamic Flow Conf. 1978, Baltimore, MD, Sept. 1978, pp. 173-190.
4. Cantwell, B.J., "Organized Motion in Turbulent Flow", Ann. Rev. Fluid Mech., Vol. 13, 1981, pp. 457-515.
5. Favaloro S.C., Nejad A.S., Ahmed S., Miller T., "An experimental and computational investigation of isothermal swirling flow in an axisymmetric dump combustor", AIAA Paper No. 89-0620, 1989.
6. Fiedler, H.E., "Coherent Structures in Turbulent Flows", Prog. Aerospace Sci., Vol. 25, 1988, pp. 231-269
7. Hussain, A.K.M.F. and Reynolds, W.C., "The Mechanics of an Organized Wave in Turbulent Shear Flow", J. Fluid Mech., Vol. 41, 1970, pp. 241-258.
8. Hussain, A.K.M.F., "Coherent Structures and Turbulence", J. Fluid Mech., Vol. 173, 1986, pp. 303-356.
9. Lieber, B.B. and Giddens, D.P., "Autoregressive Spectral Estimation in Transitional Pulsatile Flow", Exp. in Fluids, 1989, in press.
10. Lieber, B.B., Giddens D.P., Kitney R.I., Talhami, H., "On the Discrimination Between Band-Limited Coherent and Apparent Stresses in Transitional Pulsatile Flow", J. Biomech. Eng., Vol. 111, 1989, pp. 42.
11. Liu, J.T.C., "Interactions Between Large-scale Coherent Structures and Fine-grained Turbulence in Free Shear Flows", in: Transition and Turbulence, Academic Press Inc., 1981 (editor: Meyer, R.E.).
12. Nejad A.S., Vanka S.P., Favaloro S.C., Samimy M., Langfeld C., "Application of Laser Velocimetry for Characterization of Confined

Swirling Flow", J. Eng. for Gas Turbines and Power, Vol. 111, 1989, pp. 36.

13. Reynolds, O., "On the Dynamical Theory of Incompressible Viscous Fluids and the Determination of the Criterion", Phil. Trans. R. Soc. London, A 186, 1895, pp. 123-164.

14. Townsend, A.A., "The Structure of Turbulent Shear Flow", Cambridge University Press, 1956.

1989 USAF-UES SUMMER FACULTY RESEARCH PROGRAM/

GRADUATE STUDENT RESEARCH PROGRAM

Sponsored by the

AIR FORCE OFFICE OF SCIENTIFIC RESEARCH

Conducted by the

Universal Energy Systems, Inc.

FINAL REPORT

STABILITY MODIFICATION AND FLOWFIELD EVALUATION OF A RAMJET COMBUSTOR MODEL

Prepared by: Larry A. Roe, Ph.D.

Academic Rank: Assistant Professor

Department and University: Mechanical Engineering Department, Virginia Polytechnic Institute and State University

Research Location: WRDC/POPT
Wright-Patterson AFB, OH 45433

USAF Researcher: Abdollah S. Nejad

Date: 22 Sept 89

Contract No: F49620-88-C-0053

STABILITY MODIFICATION AND FLOWFIELD EVALUATION OF A RAMJET COMBUSTOR MODEL

by

Larry A. Roe

ABSTRACT

The attainment of acceptably stable operating conditions in a research combustor is documented. This dump combustor, simulating many of the important physical processes occurring in operational ramjet engines, was operated at a pressure of one atmosphere and ambient inlet temperature. Initial operation was highly unstable. Modifications to the air supply system, fuel injection characteristics, and supply duct acoustics were successful in attaining stable combustion. The acquisition of velocity data proceeded, utilizing a laser Doppler anemometry system with titanium dioxide seeding. A change in the seeding material is indicated to increase the data rates.

Acknowledgments

I would like to express appreciation to all those in the Advanced Propulsion Division who contributed to making my stay both personally enjoyable and technically satisfying, and to the Air Force Systems Command, Air Force Office of Scientific Research, for providing sponsorship. Special thanks go to Abdi Nejad, whose drive and technical expertise kept the program always heading in the right direction, and Charles Smith and Jeff Bryant, whose mechanical and operational skills made them indispensable elements of the research team.

I. INTRODUCTION

An ambitious program had been initiated at WRDC to investigate reacting flows in channels with sudden expansions. The objectives of this experimental program were twofold; first, to investigate, understand, and document the effects of heat release on the characteristics of a dump combustor flowfield; second, to provide a benchmark set of experimental data to aid the development of numerical codes. Baseline LDA results had been previously obtained for nonreacting flows (1). A two-component, frequency-shifted, backscatter LDA system was used to obtain detailed mean velocity and turbulence data in a plexiglass model. A chemical seeder produced micron-size titanium dioxide seed; data rates in the nonreacting flows were on the order of 5000/sec. Large samples were collected to calculate mean velocities, RMS fluctuations, and Reynolds stress.

To expand this investigation into the regime of reacting flows, a water-cooled, stainless steel combustor of the same dimensions as the plastic model was designed. Construction of this system was in progress, and a need arose for a researcher with experience in the application of laser anemometry to separated, reacting flows. This was the area of my PhD dissertation, and my application for the SFRP was accordingly accepted. My experimental and operational capability with research combustion systems was also required for this assignment.

II. OBJECTIVES OF THE RESEARCH EFFORT

The initial goal of the summer program was to apply a two-component laser doppler anemometer to a reacting flowfield in a dump combustor, including full characterization of the operational aspects of the

instrumentation system. An existing LDA system was deemed to be appropriate for this task; the combustion system was under construction at WRDC when I arrived. The long-term goal of the overall research effort is to acquire baseline-quality data in this combustor geometry and analyze the results for the influence of reaction and swirl on mean velocity, separation, turbulence parameters, and pressure distributions. It was recognized from the outset that expeditious completion of the required experimental hardware and fast resolution of any operational and instrumentation difficulties which might arise would be necessary if a significant extent of the long-term goal were to be completed during my summer study. As the term progressed, the effort began to focus heavily on the attainment of acceptable operational stability of the combustor through modifications to the original system configuration.

III. PROGRAM DEFINITION

To help define the direction of the overall research effort for both the summer term and the several months following, a brief literature review of relevant topics was conducted. As considerable expertise already was available at WRDC/POPT in the areas of laser anemometry and fluid mechanics, the review was directed toward the effects of reaction on flows with swirl and/or sudden expansions.

Some limited data were available in geometries which were felt to be applicable to this program. Parameters of interest include the mean flowfield, especially the extents of the corner recirculation zone (CRZ) and central toroidal recirculation zone (CTRZ), the axial pressure distribution, and turbulence characteristics. Experiments conducted in rectangular ducts with backward-facing steps, axisymmetric sudden expan-

sions, swirling free jets, and ducted flows with swirl give some indication of the type of results which may be observed in the case of swirling flow in a duct with a sudden expansion.

Corner recirculation zone effects

Pitz and Daily (2) investigated reacting flow behind a step in a duct with a 2:1 area ratio. The presence of reaction (equivalence ratio = 0.57) reduced the length of the CRZ by 20 to 30 percent. Turbulence parameters were not a prime interest and were not heavily discussed; the limited data which was plotted indicated no large effect on TKE.

El Banhawy et al. (3) looked at reacting flows behind a step and observed a CRZ extending about three step heights, which is less than half the usually observed value in nonreacting flow and 30 to 40 percent lower than the reacting flows of Pitz and Daily (2). Equivalence ratio ranged from 0.77 to 0.95 and the expansion area ratios were 2.0 and 4.0.

Stevenson et al (4) reviewed relevant results to that time and tested in an axisymmetric expansion. It was found that the reaction shortened the CRZ by about 15 percent, increased the maximum backflow velocity, and increased the axial TKE on the centerline but reduced it elsewhere. Equivalence ratio was 0.28. It was noted that prior investigators had found a large influence of axial pressure gradient on CRZ length in nonreacting flows, indicating that this parameter needs to be monitored closely to separate any possible direct reaction effects on the CRZ from influences consistent with perturbed pressure gradients.

Smith and Giel (5) evaluated a ducted coannular burner operating on hydrogen. The central air velocity was 335 ft/sec, and the hydrogen flow in the annulus was 3 ft/sec. The annular area was screened, and the velocity was so low that the flow exhibited a CRZ pattern. Equivalence ratio was 0.14. Th diameter ratio was approximately 2.5:1. The reaction caused a significant change in the axial pressure distribution, with a lower gradient in the reacting case. The CRZ was nearly twice as long in the reacting case, although previous research was quoted showing no change in CRZ when the diameter ratio was 10:1. The maximum TKE showed little change with reaction, although the peak value occurred farther downstream in the reacting case.

Central toroidal recirculation zone effects

Fujii et al. (6) studied swirling flows exhausting into free air from a combustor with a relatively large centerbody. Swirl numbers ranged from 0.69 to 1.50; the reacting cases were stoichiometric. When compared to nonreacting flows, the reaction was found to shorten the CTRZ by about 25 percent, lengthen the distance from the burner exit plane to the point of maximum axial backflow velocity, and increase the TKE slightly. The reaction also decreased the measured swirl number for a fixed geometry swirler by about 60 percent.

Gouldin et al. (7) investigated a ducted, coannular burner with several swirl configurations. The equivalence ratio was 0.84 based on the inner duct only, 0.23 overall. For coswirling cases (same direction both flows), the swirl numbers were 0.50 for the central, premixed flow and 0.56 for the annular air flow. The reaction was found to create a CTRZ under conditions where one did not exist in nonreacting flow. This was

not expected based on pressure gradient arguments and was attributed to vortex breakdown, with the argument that the flow expansion associated with the reaction can cause an adverse pressure gradient along the duct centerline and consequent flow reversal. Turbulence parameters were not heavily discussed; a presentation of the results shows some increase in axial TKE near the burner exit. The flowfield was described as very sensitive to inlet conditions and equivalence ratio.

Combined swirl and expansion results

F. K. Owen and associated researchers conducted a series of tests (typical references are 8 and 9) on a ducted combustor with a centerbody, swirl vanes, and a sudden expansion. Unlike the studies reviewed above, the combustion was non-premixed, with either a gaseous or liquid fuel injected through the centerbody. Swirl numbers from 0.0 to 0.6 were utilized, equivalence ratio was typically 0.9, and the inlet air was generally preheated to 750K. The major thrust of these investigations was the influence of swirl, and nonreacting data were not usually presented.

Baker et al. (10) studied a coaxial burner exhausting into a larger chamber. Only the outer (annular air) flow was swirled, the central fuel flow was not. Swirl numbers were 0.0 and 0.52 and the equivalence ratio was approximately 1.0. In the nonreacting case, the swirler created a CTRZ and decreased the extent of the CRZ. Similar results were obtained in reacting flow. A comparison of reacting to nonreacting results shows the hot flow to exhibit a 30 percent larger CRZ in both swirling and nonswirling cases, and a CTRZ approximately twice as long for the swirling case.

The program was thus defined as a quantification of the effects of combustion (with or without swirl) on the flowfield in a ramjet combustor as modeled by an axisymmetric sudden expansion.

IV. COMBUSTOR OPERATIONAL DEVELOPMENT

For the reacting studies, a water-cooled, stainless steel combustor model was constructed. This device (Figure 1) has the same characteristic dimensions as the nonreacting model and uses a high-quality quartz window for optical access to the flowfield. Before progressing into the acquisition of LDA data for reacting cases, it was necessary to establish stable operational conditions for this combustor. Variable parameters included fuel composition, diffusion or premixed operation, fuel injection geometry, equivalence ratio, exhauster operational conditions, and acoustic configuration. Stability was identified by pressure spectra obtained under various operating conditions, using a pair of piezoelectric transducers mounted in the duct upstream of the dump, and a Nicolet 660A dual-channel FFT analyzer. Desirable characteristics included a low operating temperature, low pressure fluctuations, a nonpredominance of specific frequencies, and a minimum very-low-frequency component (11). The aforementioned parameters were adjusted to produce the desired results.

The baseline configuration operated on ethylene and closely resembled the low-temp model, with the addition of four fuel injection ports in the combustor sidewall upstream of the dump. This was expected to produce a flame which was largely diffusional in nature, allowing operation over a wide range of equivalence ratios. However, light-off was accom-

panied by a large detonation, and the combustor operated in an unstable mode, as evidenced by very-low-frequency fluctuations and frequent flashback. The flashback was apparently occurring in the lower velocity regions of the flowfield near the wall, and was eliminated by a fuel change to propane, which has a lower turbulent flame speed and longer quenching distance. Nonetheless, the combustor operation was generally unstable.

Figure 2 shows the coherent output power spectrum for diffusion operation of this baseline geometry with propane. (Coherent output power indicates the output power of one channel that is linearly related to the other. It is a good indication of the output power due to system response.) Note the predominance of distinct peaks in the spectra and the extreme low-frequency content. The total rms pressure level for this case was 0.296 psi in the duct interior; the equivalent value for nonreacting flow was 0.0228 psi.

Numerous modifications to this configuration were implemented. Operation was converted to a premixed mode, with the fuel being introduced through four injector tubes located 11 ft upstream of the dump. Each 0.125 inch diameter tube entered the duct radially, had a fuel orifice of 0.065 inch diameter located in the side, and allowed for injection at various radial distances from the duct centerline. Since the orifices were choked under the operational fuel flow conditions, it was believed that fuel-feed-coupled instabilities would be minimized. To reduce airflow-coupled instabilities, isolate the reaction region from the large resonant contribution of the settling chamber, and provide some acoustic tuning capability, a 2.00 inch diameter orifice was installed in the

4.00 inch diameter feed duct. The first location selected for this orifice was immediately upstream of the fuel injection tubes. The tubes could then be positioned so that injection occurred in the recirculation region downstream of the orifice expansion, in the high shear regions of the orifice flowfield, or in the high-speed core region near the orifice (and duct) centerline. This geometry was tested over a range of injector radial positions and equivalence ratios.

Figure 3 shows the effect of the orifice alone, with injection maintained at the original location near the dump plane. Examination of this power spectrum shows that, although the pressure fluctuations are still dominated by narrow bandwidth signals, the total levels have been reduced by an order of magnitude. Spectral data were not obtained for the case of upstream injection without the orifice plate, as combustion could not be maintained below an equivalence ratio of approximately 0.8, apparently due to large-scale coupled oscillations between the reaction region and the upstream settling chamber.

Considerable improvement was observed when both the upstream injection location (premixed operation) and the orifice were utilized. With this promising development, investigations were conducted on the effects of equivalence ratio and radial position of the injection ports. Figure 4 shows the influence of injector position for a fixed phi of 0.70. The best operation was attained with the fuel ports near the centerline. This is believed to be due to injection into the high velocity region immediately downstream of the orifice plate, coupled with maximum injector tube penetration into the flowfield and associated turbulent mixing enhancement.

The effect of equivalence ratio is seen in Figure 5. At the higher fuel flows, the coherent output power varies directly with fuel flow, as would be expected from thermoacoustic efficiency arguments. Below a phi of about 0.60, however, the power increases as the thermodynamic energy release decreases. This was accompanied by sensibly unstable operation and a shift of the spectrum to low frequency dominant peaks.

As a result of these trends, the operating condition for further studies was defined as premixed combustion, with an equivalence ratio of 0.65, and fuel injection near the upstream duct centerline. The coherent power spectrum for this condition is seen in Figure 6. Compared to the initial operating point of Figure 2, it can be seen that the spectrum is broadened, shifted to higher frequencies, and the coherent output power is lower by two orders of magnitude. The internal total rms pressure level is 0.065 psi, indicating a decrease in combustion-induced pressure fluctuations to 15 percent of that obtained from the original configuration.

V. FLOWFIELD STUDIES

The LDA system was disassembled, realigned, and used to acquire preliminary data under nonreacting conditions. Comparison of these data to prior results from a plexiglass cold rig showed good agreement for the mean velocities, but higher turbulence levels for the new rig.

Spatially sparse LDA data were obtained with the combustor operating at the optimum condition identified through earlier stability testing. Data rates averaged approximately 100 Hz, which produces reasonable mean

velocity data but questionable turbulence statistics. Three days were then devoted to modifying the optics to a forward scatter configuration, but the data rates were not improved sufficiently to warrant the increased operational difficulties associated with this geometry. A return to backscatter operation was accomplished, but data rates are still low near the optical access windows. A change of seeding material from the current titanium dioxide to zirconia is indicated based on the generally relevant results of Witze (12), and an investigation has been initiated to determine the best method to seed with this material.

VI. RECOMMENDATIONS

As the acquisition of benchmark-quality LDA data requires higher data rates than those obtained with the existing system, it is recommended that the development of an improved seeder be initiated. Zirconia is indicated as a premier candidate for the seed material, but the means to introduce sufficient quantities of this material into the air stream is not immediately identifiable. Options include a large-capacity fluidized bed system, with associated bulk material handling problems, and an in-situ generation of particles via chemical reaction, with the unwanted production of acidic by-products. Both techniques should be studied and considered for implementation.

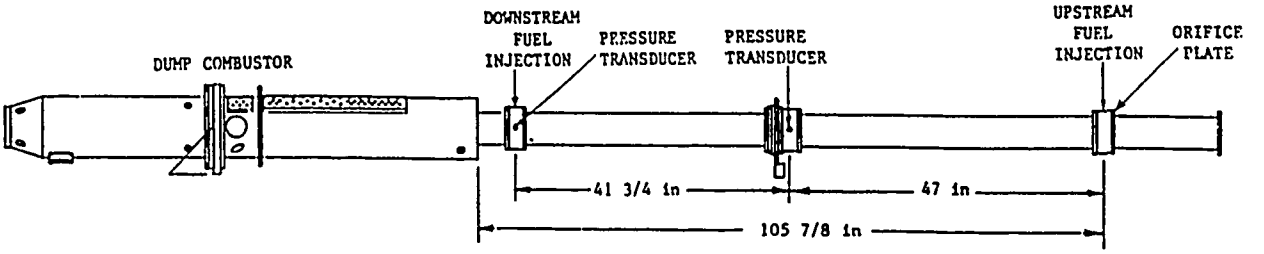


Fig. 1. Schematic of Combustor System

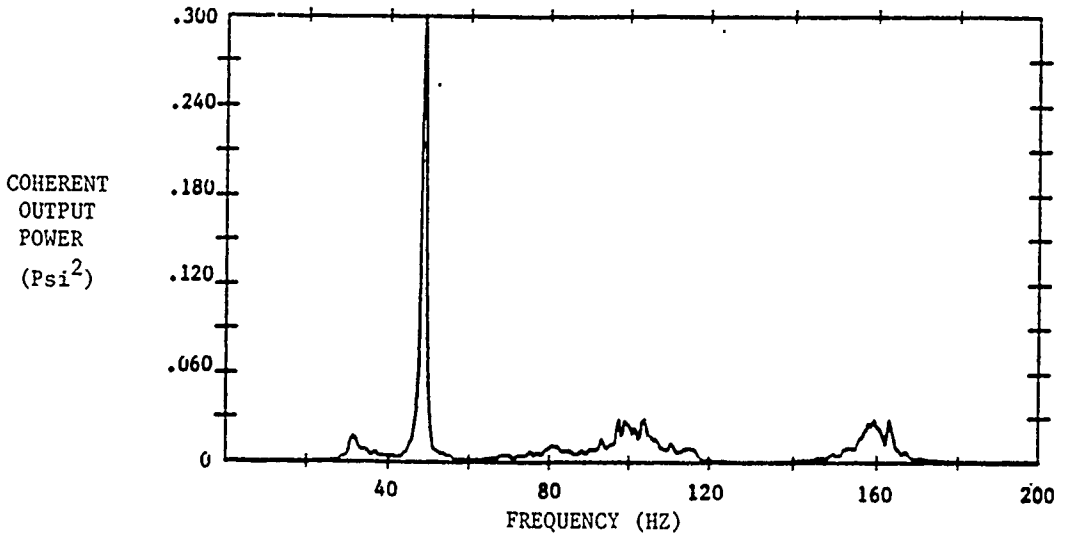


Fig. 2. Coherent Output Spectrum for Downstream Fuel Injection With No Orifice Plate

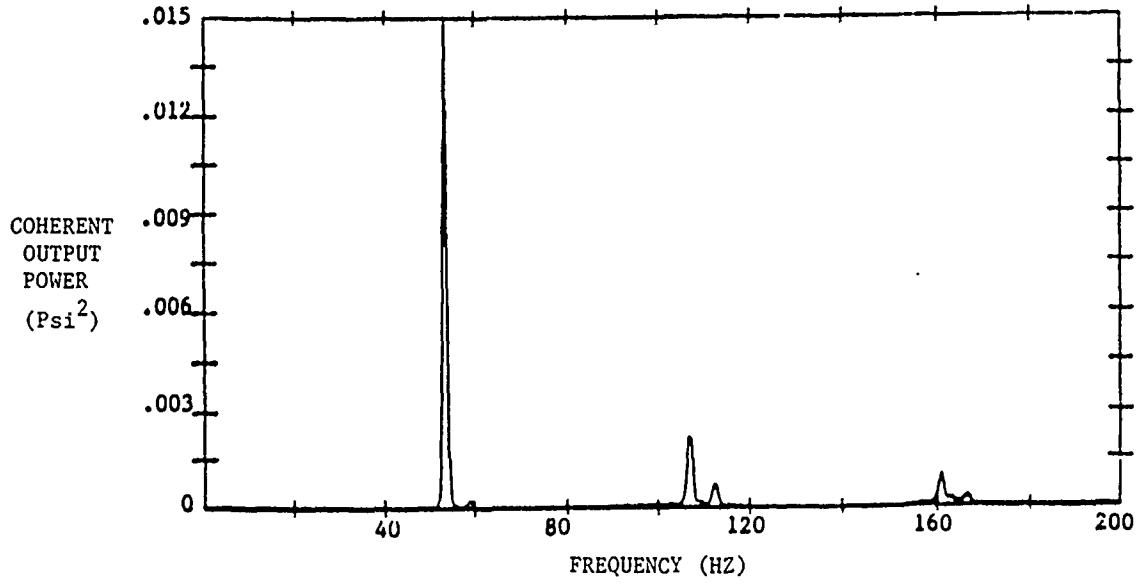


Fig. 3. Coherent Output Power Spectrum for Downstream Fuel Injection With Orifice Plate

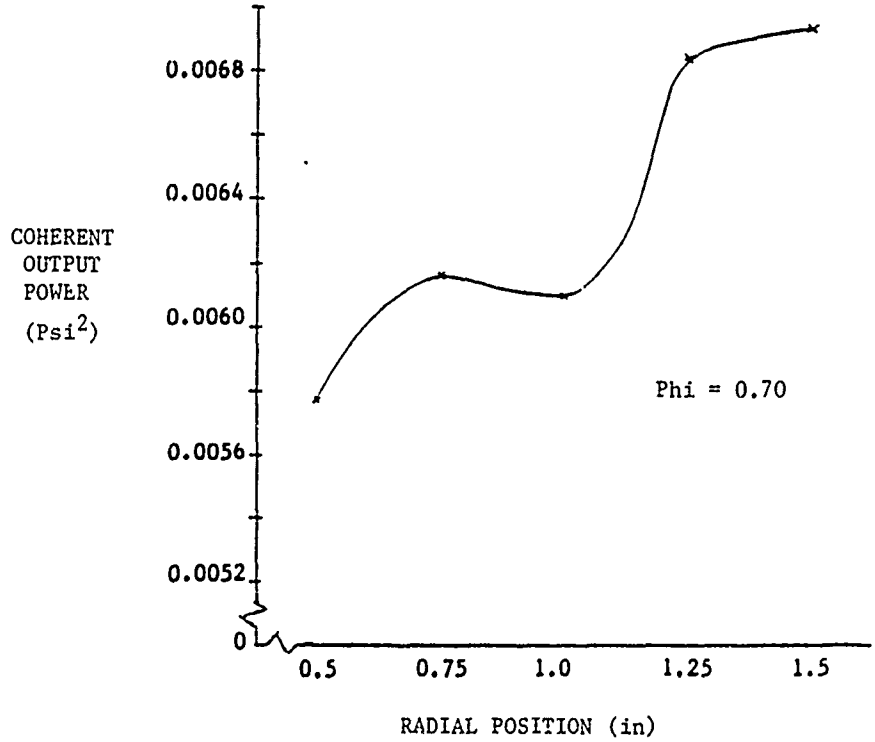


Fig. 4. Coherent Output Power Dependence on Injector Position

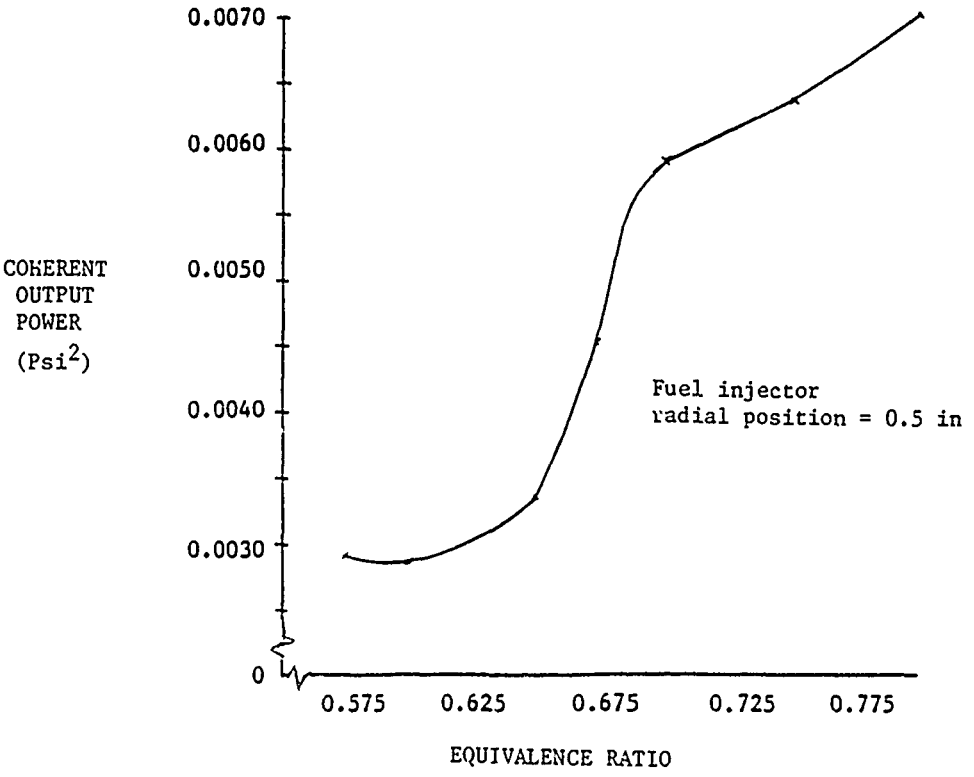


Fig. 5. Coherent Output Power Dependence on Equivalence Ratio

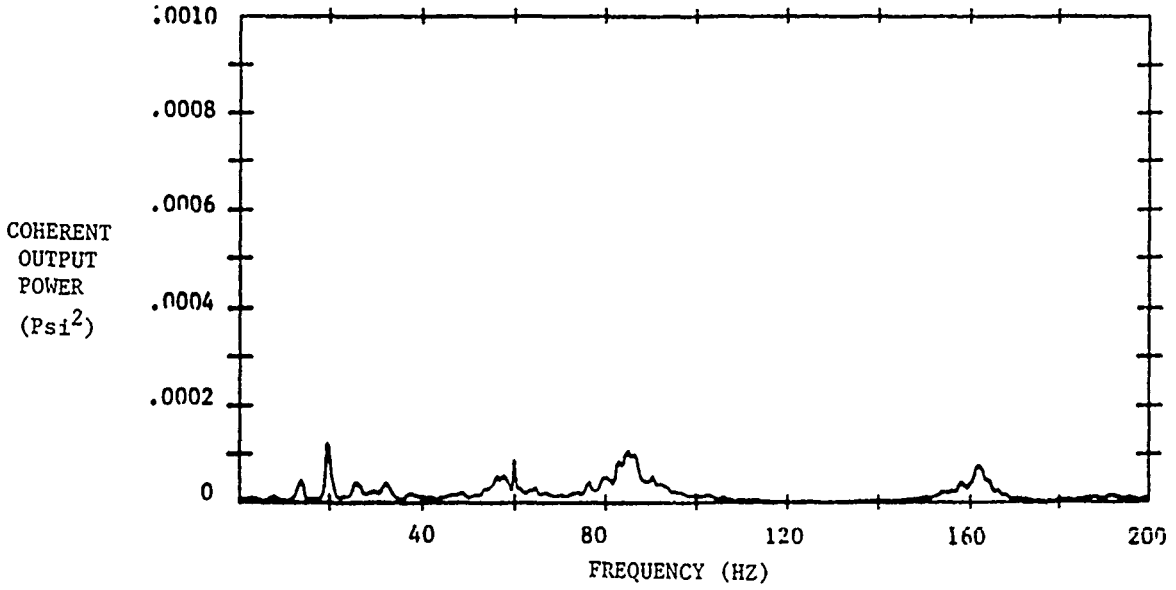


Fig. 6. Coherent Output Power Spectrum for Optimum Upstream Injection Position and Orifice Plate

REFERENCES

1. Favaloro, S. C., Nejad, A. S., Ahmed, S. A., Miller, T. J., and Vanka, S. P., "An Experimental and Computational Investigation of Isothermal Swirling Flow in an Axisymmetric Dump Combustor," AIAA 89-0620, 1989.

2. Pitz, R. W., and J. W. Daily, "Combustion in a Turbulent Mixing Layer Formed at a Rearward-Facing Step," AIAA Journal, vol. 21, no. 11, pp. 1565-1570, 1983.

3. El Banhawy, Y., S. Sivasegaram, and J. H. Whitelaw, "Premixed, Turbulent Combustion of a Sudden-Expansion Flow," Combustion and Flame, vol. 50, pp. 153-165, 1983.

4. Stevenson, W. H., H. D. Thompson, and R. D. Gould, "Laser Velocimeter Measurements and Analysis in Turbulent Flows With Combustion," AFWAL-TR-82-2076, part II, 1983.

5. Smith, G. D., and T. V. Giel, "An Experimental Investigation of Reactive, Turbulent, Recirculating Jet Mixing," AEDC-TR-79-79, 1980.

6. Fujii, S., K. Eguchi, and M. Gomi, "Swirling Jets with and without Combustion," AIAA Journal, vol. 19, no. 11, pp. 1438-1442, 1981.

7. Gouldin, F. C., J. S. Depsky, and S-L. Lee, "Velocity Field Characteristics of a Swirling Flow Combustor," AIAA Journal, vol. 23, no. 1, pp. 95-102, 1985.

8. Owen, F. K., L. J. Spadaccini, and C. T. Bowman, "Pollutant Formation and Energy Release in Confined Turbulent Diffusion Flames," 16th Symposium on Combustion, The Combustion Institute, pp. 105-117, 1977.

9. Owen, F. K., L. J. Spadaccini, J. B. Kennedy, and C. T. Bowman, "Effects of Inlet Air Swirl and Fuel Volatility on the Structure of Confined Spray Flames," 17th Symposium on Combustion, The Combustion Institute, pp. 467-473, 1978.

10. Baker, R. J., P. Hutchinson, E. E. Khalil, and J. H. Whitelaw, "Measurements of Three Velocity Components in a Model Furnace With and Without Combustion," 15th Symposium on Combustion, The Combustion Institute, pp. 553-559, 1974.

11. Reardon, F. H., "An Examination of Some Possible Mechanisms of Combustion Instability in Liquid-Fuel Ramjets," AFWAL F33615-81-C-2078, 1986.

12. Witze, P. O., "Application of LDV to Spark-Ignition Engines," Flow Lines, TSI Incorporated, pp. 3-9, Summer 1989.

1989 USAF-UES SUMMER FACULTY RESEARCH PROGRAM/

GRADUATE STUDENT SUMMER SUPPORT PROGRAM

Sponsored by the

AIR FORCE OFFICE OF SCIENTIFIC RESEARCH

Conducted by the

UNIVERSAL ENERGY SYSTEMS. INC.

FINAL REPORT

Oxidative Thermal Degradation Studies of a Surrogate JP-8 with a Modified Thermal Precipitation Apparatus

Prepared by:	William D. Schulz
Academic Rank:	Professor of Chemistry
Department and	Department of Chemistry
University:	Eastern Kentucky University
Research Location:	Aero Propulsion Laboratory
	WRDC/POSF
	Wright-Patterson AFB, OH 45433
USAF Research:	Dr. W. M. Roquemore
Date:	September 26, 1989
Contract No.:	F49620-88-C-0053

OXIDATIVE THERMAL DEGRADATION STUDIES OF A SURROGATE JP-8 WITH A MODIFIED THERMAL PRECIPITATION APPARATUS

By William D. Schulz

ABSTRACT

A 12 component surrogate JP-8 fuel was developed and used in thermal oxidation studies with a modified thermal precipitation test apparatus. The apparatus features a fused quartz capillary tube for controlled feed of air or gas mixture. It is operated at atmospheric pressure and is inexpensive, convenient and completely inert. The surrogate JP-8, stressed in the test apparatus provides a means to study the effects of thermal stress on different classes of fuel component compounds simultaneously. The surrogate and method are particularly suited to comparative studies of antioxidant and other additive efficiencies.

ACKNOWLEDGMENTS

I would like to thank the Air Force Systems Command and the Air Force Office of Scientific Research for sponsorship of my research. The staff at the Aero Propulsion Laboratory, Wright-Patterson AFB, WRDC/POSF, provided an efficient and cooperative atmosphere for research.

Special thanks to Dr. W. M. Roquemore, Mr. Ed Pitzer and Mrs. Ellen Stewart for friendship, help and being great people to work with.

Thanks to Steve Anderson, Dr. Ron Butler and Lt. Jeff Moler for the same reasons. Charles Martel is especially appreciated for sharing his knowledge of the research subject at the time of his retirement. Finally, Universal Energy System, Incorporated deserves appreciation for the helpful and efficient administration of their program.

I. INTRODUCTION

Fuel stability to storage and thermal oxidation and subsequent gum and solids deposits has probably been of concern since the invention of internal combustion engines. The importance of fuel stability, particularly thermal stability, has increased greatly with the increasing need to use the fuel as a heat exchange fluid in modern aircraft. Literature reviews [1-3] contains hundreds of references, yet Reddy [4] in a February 1989 paper states: "Although considerable effort has been devoted to understanding and solving the fuel degradation problems, knowledge of the detailed chemistry is lacking." Reddy also cites a considerable amount of work for which results "are unclear and at times contradictory."

The complexity of jet fuels and of the degradation mechanisms, the nature of deposition process and the large number of degradation products implicated in deposit formation combine to make such studies difficult. Specification tests for jet fuels, such as the JFTOT test and the thermal precipitation test (appendix B,(MIL-T-38219) produce subjective measures of fuel stability but do not provide reproducible, rapid, inexpensive or readily quantifiable methods for kinetic or mechanistic chemical studies of fuel degradation. Even measurement of gum formation are varied on different investigations. For these

reasons, we felt that a small scale, modified thermal precipitation test would be of value for thermal degradation studies.

Because of the complexity of JP-8 and the interest in JP-8 stability we felt that a surrogate JP-8 would provide a good test of a modified thermal precipitation apparatus, reproducibility of stressed fuel measurements and a starting point for the study of effects of antioxidants, other additives, temperature, oxygen availability and other variables on fuel degradation.

My research interests in high resolution gas chromatography-mass spectrometry of pyrolysis products, fuels, air particulates and previous experience with fuel surrogates contributed to my assignment in this program and collaboration with WRDC/POSF.

II. OBJECTIVES OF THE RESEARCH EFFORT

The small scale thermal precipitation test as described by Maj. Roylance [5] has promise for thermal oxidative fuel stability studies, but presents heat control problems. In addition, one liter of fuel is required, oxygenation of test fuels is regulated only by the rate of magnetic stirring and fuel degradation is measured by filter color comparison to ASTM D 2276, appendix A-3 standards.

A goal of this research was to devise an oxidative thermal stress apparatus that would rapidly attain

reproducible fuel temperatures between 100 and 250 deg C, use a minimum of fuel, have inert surfaces and a regulable oxygen supply. We chose standard taper glassware so that the fuel volume could be varied from 100mL to one liter. A Claissen adaptor with a Friedrich condenser is fitted to the flask. The adaptor is also fitted with a standard thermometer adaptor and a "Viton" thermometer seal. A thermometer is inserted through the seal to near the bottom of the flask. A gas purge/sparge inlet (5 M length of 0.53 uM polymide coated, deactivated fused quartz capillary tubing is run through the Viton seal alongside the thermometer. The capillary is connected to a regulated supply of desired sparge gas. The gas delivery system can be regulated for flow rates of five to over twenty mL/minute. Samples can conveniently be withdrawn from this apparatus at any time.

Oil bath heating proved not sufficiently stable over 150 degrees C to be worth the danger of hot oil. Standard heating mantles and Variacs were then used as heat sources. These attain high temperatures quickly but do not readily produce specific temperatures. Since temperature control devices are readily available but not obtainable within the time frame of the research, we simply continued experiments using full power to the heating mantle and achieving a measure of temperature stability with a quasi equilibrium of heating and condensation.

To test the apparatus and investigate the effect of several variables on thermal stability of fuels, we chose to mix a surrogate fuel that approximates the chemical class composition and properties of authentic JP-8 samples, but has a simple composition so that degradation product separation and identification are feasible. The surrogate (JP-8S) contains less stable species represented by Cyclooctane (strained ring cycloalkane), tetralin ("napthenic") and 1-methylnapthlene (substituted napthalene). Other compounds were characteristic (O-xylene and butyl benzene as aromatics, C-10, 12, 14 and 16 normal alkanes) and we did not include expensive components that do not have unique properties.

After the surrogate fuel and test apparatus design the goal of the research is method development for thermal stress tests. We felt that containing oxidation products in the test flask and simply removing all volatile fuel components would be a simple method of gum and particles quantitation. To ensure that additional thermal stress was not introduced, we tried to remove fuel at reduced pressure with a "Rotovap" system. For real JP-8 fuel, this failed, even at a pressure of 10^{-4} torr and a temperature of 105 degrees C. Small amounts could not be removed from the gum in a reasonable time. Lower pressures or higher temperatures are not reasonable, so we chose to employ filtration with "Anotec" 0.2 uM inorganic membrane filters. These filters are new and have high promise for such applications.

The oxidative thermal stress of fuels was monitored by gas chromatography-mass spectroscopy (GC-MS) by a Hewlett-Packard 5890 GC-5970 "MSD" with on-column, high resolution capillary column chromatography.

The combination of all glass apparatus, surrogate fuel and analytical method provide means to observe the effects of such variables as oxygen supply, unstable components, dopant antioxidants, and other additives. As much experimentation as possible would be done after establishing materials and methods.

III. SURROGATE FUEL COMPOSITION

The composition of the 12 component surrogate JP-8 (JP-8S) is attached as table 1. The fuel consists of 5.0 weight percent each of isooctane, methyl cyclohexane, cyclooctane, m-xylene, butylbenzene, 1,2,4,5 -tetramethylbenzene, tetralin and 1-methylnapthalene with 15.0% n-decane, 20.0% -dodecane, 15.0% n-tetradecane and 10.0% n-hexadecane. These fuel components present no chromatographic interference. The aromatic/aliphatic ratio is 22/78 by weight. The JP-8S could be criticized as containing high concentrations of the components at the 5.0% level, but they represent many minor fuel constitituents of their respective types. Observation of thermal oxidation products is simplified by the reduced number of components at higher concentrations. JP-8S components were Aldrich Chemical Company (Milwaukee, WI) 99+%

grade. No component had detectable levels (10 ppm) of contaminant by GC-MS. Some components (cyclooctane, tetralin and 1-methylnapthalene) were chosen because of known instability and because of experience with a surrogate JP-4, supplied by Dr. G. S. Samuelsen, (UC-Irvine) for a different purpose. Some typical components of JP-8 were excluded on a basis of cost and purity. The surrogate fuel is a fairly good model of JP-8, as shown by the comparison in attached table II. Major differences are flash point and freezing point.

IV. MODIFIED THERMAL PRECIPITATION TEST

The modified thermal precipitation apparatus described in the "Objectives" section of this report was operated in a qualitative manner for several fuels. Stress tests were conducted with full heating power, and changes observed with time. This method gives reproducible results for a given fuel but does not give comparable results for different fuels because of different volatiles loss. This fact led us to conduct several exploratory, qualitative experiments. Observations are as follows. Quasi equilibrium temp. of 160 deg. C is attained in 20 min for 250 mL JP-8S or JP-8 in a 500 mL r.b. flask. After this, temperature rise is slow. Temperature of 205 deg. C is attained in 3.0 hrs; 212 deg. C in 8 hours.

Color formation: with N_2 sparge of JP-8S or JP-8, no color in 12 hrs heating time, to a temperature of 214 deg. C. Under an air sparge fuel yellows in 1.0 hrs. (180 deg. C), red-brown in 3.5 hrs (205 deg. C). Microdrops of immiscible phase appear in samples after 4.0 hours. Color does not change greatly but samples show more second phase with continued heating.

Particulate formation: No particulates observed in JP-8S Flasks even after 6.0 hrs heating if agitation by sparge air is maintained. If agitation is stopped for 30 min or more, heavy deposits will form on surfaces and particularly at the phase interface in under an hour. Color was not observed to be related to particulate load. Particles form on added zinc or copper metal surfaces under conditions that otherwise don't produce particles. An antioxidant, 2,6-di-tert butyl-4-methylphenol ("BHT" or Dupont A.O.#29) suppresses particle formation but not color. A coal derived JP-8X gives particle formation in 1.8 hrs (180 deg. C), compared WPAFB tank #7 JP-8 in 4.0 hrs. (204 deg. C).

Unstable species (cyclooctane, tetralin) oxidize rapidly but are not found to effect the oxidation of stable n-hydrocarbons or promote decomposition rate. Addition of 0.05% benzoyl peroxide also did not promote decomposition. Restressing the distillate of a stressed fuel seemed to produce gum at about the same rate as did the original fuel.

V. THERMAL OXIDATION OF SURROGATE JP-8

Surrogate JP-8 was stressed as previously described. Samples were withdrawn at regular time intervals for filtration and/or GC-MS analysis. A series of samples was subjected to UV-Vis and IR analysis. No useful information was gained from either. IR had increases in the broad O-H and C=O peaks and UV had no usable maxima. For GC-MS analysis 20uL fuel was diluted to 1.5mL with Freon 113 or acetone. Chromatography was on-column injection; 50M x 0.25 uM x 0.25uM HP-5 column. Temperature program was 40 deg for 4 min, 5 deg/min to 250 deg then 20 deg/min to 300 deg and held for 5.5 minutes. The Mass Spectrometer (70eV., E.I.) was scanned 35-400 Daltons (1.2H_2). J.T. Baker 1.0 gram silica gel solid phase extraction (SPE) cartridges were used to isolute and concentrate oxidation products. The scheme, in general, was: condition cartridge with pentane, add 2.0mL Fuel; wash with pentane (8mL); elute with 1.0mL acetone, then 1.0mL methanol. Oxidation products are completely separated from fuel and good mass spectra obtained.

Samples (10.0mL) of stressed fuel were filtered with syringe pressure on 25uM dia. 0.2uM pore "Anotec" filters. For gum, the syringe and filter were washed with two 5.0mL portions hexane. For particulates, 10mL methanol was added to 10.0mL sample, filtered and the syringe and filter washed

with two 5.0mL portions Methanol. Filters were dried under vacuum, 100 deg. C.,5 torr; overnight. Reproducibility is good. Three samples stressed JP-8S had 0.8, 0.6 and 0.6 mg.gum/10mL fuel. Particulates (MeOH) were 0.2, 0.1 and 0.2 mg/10mL fuel.

Figures Ia and b are chromatograms of fresh and stressed JP-8S. The low concentrations of oxidation products do not produce usable mass spectra. Figure II is a chromatogram of SPE extract of stressed JP-8S. The predominant oxidized species are nearly predictable from the relative stabilities of fuel components.

The most striking experiment with JP-8S was a stress comparison of the straight fuel and with 1.0% added BHT. No particulates are apparent in the BHT added sample after 9 hrs (220deg.C) while heavy deposits form in the control. (control; 34.8mg gum/10mL, 5.8 mg particulate/10mL; BHT added; 0.1 mg gum, 0.0 mg particulate/10mL) Space limitations preclude inclusion of a great deal of data gathered during this study. The results largely concur with Hazlett[6] and Reddy[4] and will be made available to WRDC/POSF.

VI. RECOMMENDATIONS

a. The all glass thermal stress apparatus is simple, inexpensive and effective. The value of the device for degradation studies of many kinds would greatly increase

with the addition of a moderately priced temperature monitor/control. These are available at $600-$800. Use of a control should produce reliable kinetic data and excellent reproducibility for gum and particle production. Constant temperature and integration of chromatograms from the SPE extracts can provide an excellent measure of gum formation potentials of fuels. The advantages of the all glass apparatus are low cost, inertness, rapid temperature attainment and control of gas or oxygen feed. Disadvantages are loss of volatile compounds and test times of several hours. These are not severe limitations for purposes such as testing relative efficiencies of additives. The need for a JFTOT is eliminated and products that would be lost by thermal precipitation are retained to indicate the degree of oxidation.

The major recommendation then is that this system be utilized for the study of effects of individual fuel additives, especially antioxidants. Hindered phenols and the amine in JFA-5 chromatograph well and the JP-8S affords a means of following oxidation rate. The 1-mercapto-2-phenyl-2-amino alkyls found so effective by Bol'shakov[7] should be investigated. Data from experiments could be used toward a U.S.A.F. formulation of a fuel additive package rather than reliance on proprietary commercial formulations. We will propose to begin such work under the Mini-Grant program.

REFERENCES

(1) Goetzinger, J. W., Thompson, C. J. and Brinkman, D. W., "A Review of Storage Stability Characteristics of Hydrocarbon Fuels 1952-1982," DOE/BETC/IC-83-3, October, 1983.

(2) Brinkman, D. W., Bowden, J. N. and Giles, H. N., (Lube Oil and Finished Fuel Storage Stability: An Annotated Review" DOE/BETC/RI-79-13, February, 1980.

(3) Hazlett, R. N., Ed., "CRC Literature Survey on the Thermal Oxidation Stability of Jet Fuel," CRC Report No. 589, April, 1979.

(4) Reddy, K. T., and Cernansky, N. P., J. Propulsion. Vol 5, No. 1, pp. 6-13, Jan-Feb 1989.

(5) Roylance, T. F., WRDC/POSF report, March 13, 1989 (in house, to Charles L. Delaney) March, 1989.

(6) Hazlett, R. N., Hall, J. M. and Matson, M., Ind. Eng. Chem, Prod. Res. Dev. Vol. 16, No. 2, pp 171-177 (1977)

(7) Bol'shakov, G. F., "The Physico-Chemical Principles of the Formation of Deposits in Jet-Fuels", FTD-MT-24-416-74 Translation, April 1974.

Table I: SURROGATE JP-8 COMPOSITION

Peak#	Ret.Time*	COMPOUND	Wt.%	D(g/cc)	bp.(C)
1	9.07	isooctane	5.0	.690	98
2	10.27	methylcyclohexane	5.0	.770	101
3	15.98	m-xylene	5.0	.868	138
4	18.40	cyclooctane	5.0	.834	151(740)
5	21.71	decane	15.0	.730	174
6	23.38	butylbenzene	5.0	.860	183
7	25.58	1,2,4.5-tetramethylbenzene	5.0	.838	197
8	27.06	tetralin	5.0	.973	207
9	28.74	dodecane	20.0	.749	215
10	31.87	1-methylnapthalene	5.0	1.001	240
11	34.74	tetradecane	15.0	.763	252
12	40.01	hexadecane	10.0	.773	287

*WSFUEL M GC Conditions

Table II: COMPARISON OF SURROGATE AND AUTHENTIC JP-8 FUELS

	TEST	SURROGATE JP-8	JP-8 WPAFB TANK S-15
D1319	Aromatics, Vol %	22.0	22.0
D1319	Olefins, Vol %	0.0	2.7
D2887	Distillation Initial Boiling Pt. Deg C	92	124
D2887	Distillation 10% recovered, Deg C	135	160
D2887	Distillation 20% recovered, Deg C	169	173
D2887	Distillation 50% recovered, Deg C	205	212
D2887	Distillation 90% recovered, Deg C	255	259
D2887	Distillation End Point, Deg C	286	296
D1298	Density, kg/l	0.800	0.811
D93	Flash Point, Deg C	26	59
D2386	Freezing Point, Deg C	-14	-54
D445	Viscosity @ -20 Deg C, cs	3.9	3.9
D3338	Net heat of Combustion, MJ/kg	43.1	43.1
D3343	Hydrogen Content, Wt %	13.7	13.6

Figure Ia and Ib:Comparison of Fresh and Stressed Surrogate JP-8

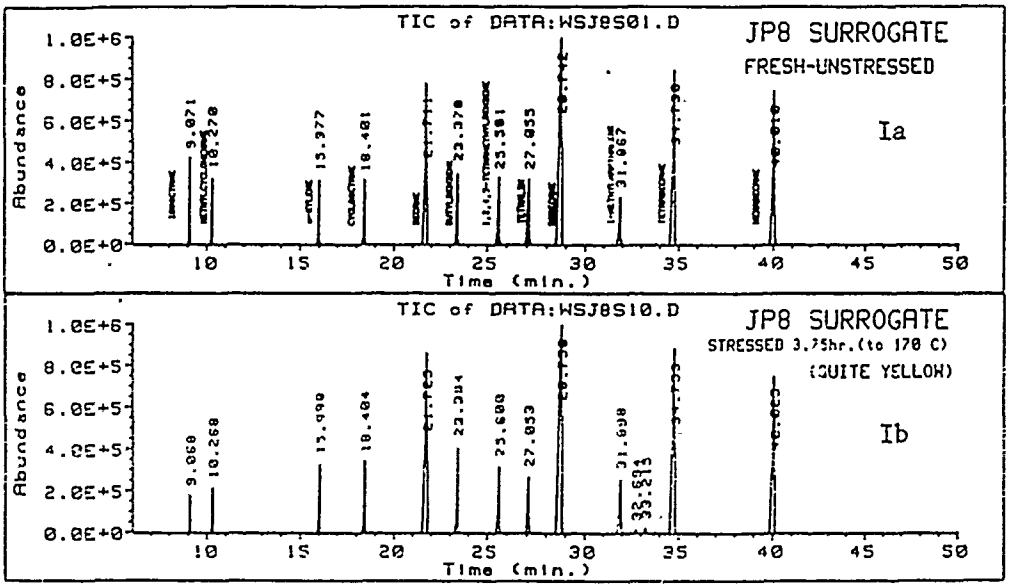
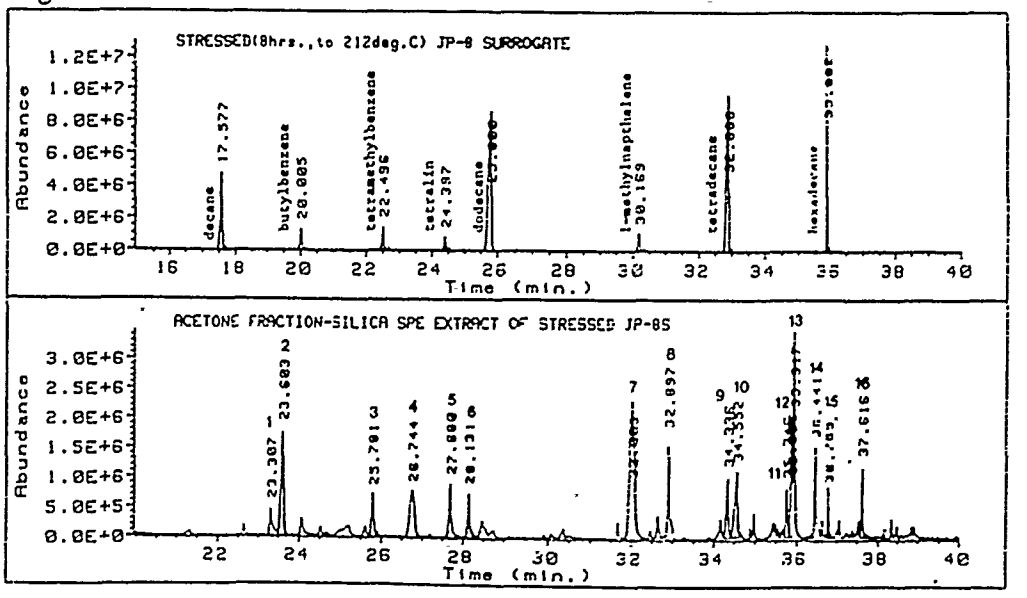


Figure II:Stressed JP-8S and Extracted Oxidation Products



OXIDATION PRODUCT TENATIVE PEAK IDENTIFICATION:

Peak#	Compound	Peak#	Compound	Peak#	Compound
1	3-methylbenzylalcohol	7	2,4,5-trimethylbenzylalcohol	13	hydroxymethylnapthalene
2	cyclooctanol	8	2-dodecanol	14	trimethylbenzoylester?
3	2-decanol	9	5-hexyldihydro-2-furanone	15	e dodecylketone?
4	aliphatic aldehyde'	10	2,4,5-trimethylbenzoic acid	16	1-hexadecanol
5	trimethylbenzylalcohol	11	furanone derivative		
6	furanone derivative	12	dimethyl-dimethanolbenzene		

1989 USAF - UES SUMMER FACULTY RESEARCH PROGRAM

GRADUATE STUDENT RESEARCH PROGRAM

Sponsored by the

AIR FORCE OFFICE OF SCIENTIFIC RESEARCH

Conducted by the

Universal Energy Systems, Inc.

FINAL REPORT

MEASUREMENTS OF DROPLET VELOCITY AND SIZE DISTRIBUTIONS IN SPRAYS

Prepared by:	Richard S. Tankin
Academic Rank:	Professor
Department and University:	Mechanical Engineering Department Northwestern University
Research Location:	WRDC/POSF Wright Patterson Air Force Base Dayton, Ohio 454336563
USAF Researcher:	W.M. Roquemore
Date:	25 August 1989
Contract No:	F49620-85-C-0053

MEASUREMENTS OF DROPLET VELOCITY AND SIZE DISTRIBUTIONS IN SPRAYS

by

Richard S. Tankin

Abstract

A phase doppler instrument was used to measure droplet sizes and two components of velocity in a water spray. Vertical traverses and horizontal traverses were made across the spray near the sheet break-up region. More than 400,000 samples were taken in each traverse. The results show that the spray is axially symmetric, which is important for the planned theoretical analysis. The tangential velocity component is small - as expected.

Acknowledgements

I wish to thank WRDC/POSF at Wright Patterson Air Force Base and the Air Force Office of Scientific Research for the sponsorship of this research. I also want to thank Universal Energy Systems for their efficient handling of all administrative aspects of the program.

This summer's research was beneficial to me and hopefully will lead to joint research activities with Wright Patterson. Having worked before with Dr. W. M. Roquemore and Dr. T. Jackson, it was no surprise to find them very cooperative and encouraging. The experimental work could not have been accomplished without the expertise and experience of Dr. G. Switzer. The ease and readiness with which Jeff Stutrud handled complex computer problems was invaluable. I found the staff at Wright Patterson to be friendly, stimulating, and helpful.

I. INTRODUCTION

Gas turbines in nearly all cases utilize liquid fuels. These fuels must be delivered as small droplets to the combustion zone if efficient combustion is to occur. The process by which these small drops are formed is called atomization. The method of achieving atomization is varied and not a topic for consideration in this study. In this study the droplet distributions from a hollow cone pressure atomizer are examined. The liquid spray discharges from the nozzle as a liquid sheet which breaks up downstream to form droplets.The liquid sheet for this type of nozzle has three components of velocity - axial, radial, and tangential. Pictures of the spray from this nozzle are shown in Figure 1. The light source for these photographs was a pulsed laser (pulse duration is about 10 μsec). These pictures were taken at different axial positions - 2.5mm intervals.

It is important to determine the spray characteristic if one hopes to correlate different sets of experimental data, compute numerical simulations, determine droplet trajectories, etc. In the past, these characteristics were limited to drop size distribution, patternation, cone angle, dispersion, and penetration. For example various techniques have been used to determine the drop size distribution - photographic, optical, collection devices, etc. Each of these techniques have very limited capabilities. The Malvern technique obtains a size distribution that is integrated over the optical path length. To determine radial distribution requires the use of Abel inversion. Dense sprays, or asymmetry can complicate this technique.Two situations have recently arisen - a vast improvement in instrumentation and a new approach for predicting droplet distributions.

Ia. INSTRUMENTATION

Recently a highly sophisticated instrument has been developed by Aerometrics which is capable of optically measuring the sizes and two velocity components of droplets. This method utilizes light scattering techniques, and consists of a transmitter, receiver, signal processor, computer an laser light source. The transmitter has a beam expander which reduces the size of the measuring point - which in our case is about 1 x $10^{-4}cm^2$. Thus excellent spatial resolution is achieved. Since the detectors in the receiver unit are photomultipliers (three), the

response time of this instrument is very short. Signals from individual drops can be processed and the data transferred to computer memory in 20 μsec. For the operator, an important aspect of this system is the software program associated with the signal processor. As data are being collected and stored by the computer, they are presented in bar graph form for the operator to observe. After a selected number of droplets are collected, a listing of pertinent data - such as attempts, validations, corrected count, probe area, etc. - are displayed. The bar graphs consist of particle size counts, and velocity distributions. A typical example of such a display is shown in Figure 2.

Ib. THEORY

The concept of information entropy was developed by Claude Shannon (1948), and Jaynes (1957) later extended this concept into the well-known method of maximum entropy formalism. This formalism can be applied to problems involving probability, i.e., where insufficient information is available to obtain exact solutions. We have applied the maximum entropy formalism to liquid sprays in which we predicted the droplet size and velocity distributions. Since the application to this problem has been adequately discussed by several researchers - Kelly (1976), Sellens and Brzustowski (1985, 1986), Sellens (1989), and Li and Tankin (1987, 1988, 1989), it will not be necessary to develop the background material once again (for details, see Li 1989). The data collected in this study will be examined using the maximum entropy principle. There has only been two papers in which comparisons between theory and measurements exist. In one, Li and Tankin (1988) used data that were obtained from holographic and photographic methods. Thus these results were limited to size distributions. The other paper is by Sellens (1989) in which he use a phase doppler instrument to obtain the data. However in this study there are some inconsistencies and the experiments are questionable (see Li and Tankin, 1989). Thus it was necessary to carefully obtain correct data with which to compare the theory. That is the purpose of this study.

II. OBJECTIVES OF THE RESEARCH EFFORT:

Currently, there are no precise measurements of radially integrated droplet size and droplet velocity distributions for sprays. My goal was to obtain such measurements and to present them as a three-dimensional matrix - one axis being

the droplet diameter, and the other two being the droplet velocities. From such a three-dimensional matrix of the data, one can then obtain a variety of other representations - droplet size distribution; velocity distributions for different diameter particles; total number of droplets; flow rates; average velocity as a function of drop size; three dimensional plot of velocity, diameter and joint probability distribution, etc. These measurements should be made as close to the sheet break-up region as possible.

My task this summer was to make these radially-integrated spray measurements using a phase doppler particle analyzer and to obtain the data in a three-dimensional matrix form. Then my task was to extract from this matrix the various probability distribution functions, average droplet velocity as a function of droplet diameter, flow rate, etc.
This experimental data is important because it can be used to verify recent theoretical predictions. One problem in collecting such data is the requirement that samples be sufficiently large for the statistical quantities to be significant. In our case we collected nearly 200,000 samples per run. Four such runs were completed.

III. RESULTS

We measured the radial droplet population 10 mm downstream from the nozzle exit (about 5mm beyond the sheet break-up). This iradial population was obtained from measurements at 0.5mm increments over a radial distance of 20mm - the width of the spray. From these radial measurements, we determined the axial symmetry of the spray. This is important because if axial symmetry exists a radial traverse over only half the spray diameter is required. Two such traverses were made over the complete spray diameter - both horizontally and vertically. Two velocity components and droplet diameter are measured simultaneously. Thus, in the horizontal traverse, axial and tangential velocity components were measured; in the vertical traverse, axial and radial velocity components were measured. Figures 3 and 4 show these results. Not only do the velocity measurements indicate the spray is axially symmetric but this is also evident when examining the root mean square values. Figures 5 and 6 show similar results for a horizontal traverse. In Figure 7 is a plot containing a comparison of the mean axial velocities from a horizontal traverse and a vertical traverse. Axial symmetry exists. It should

be added that between each of these traverses it was necessary to shut down the spray, refill the reservoir, and reset the flow rate. Thus there may be some variations in reestablishing the flow.

Figure 8 is a schematic plot of the three-dimensional matrix which is stored in the computer. Each axis is divided into 50 increments; thus there are a total of 125,000 elements. In computational terminology each matrix element is called a bin. In order to plot three- dimensionally, the velocity, diameter and joint probability distribution function, the three-dimensional matrix must be compressed to a two-dimensional matrix. This is shown schematically in Figure 9, where the shaded bins are summed to form a two-dimensional matrix as seen in Figure 10. From such a configuration the velocity, diameter and joint probability can be plotted.To obtain a plot of the diameter and the probability distribution function, one sums all the bins at a particular diameter. This is shown schematically in Figure 11., where the shaded bins are summed for that particular diameter.

This is conceptually what needs to be done. However before we carry out these operations, we must construct the integrated three-dimensional matrix from a set of 21 radial measurements consisting of 21 three-dimensional matrices. Corresponding with each radial measurement is a radial ring (annular region). The count in each bin (for a particular ring) must be multiplied by an appropiate constant - (ring area/probe area) x (corrected count/run time).This must be done for each radial measurement, and then all corresponding bins from the 21 rings are added together to from a integrated three-dimensional matrix.

IV RECOMMENDATIONS

The necessary data have been collected and stored on floppy disks. Aerometrics will supply us with the software to read these data and calculate the probe area for those runs in which this information is lacking. Then the integrated three-dimensional matrix will be formed. The following items are needed:

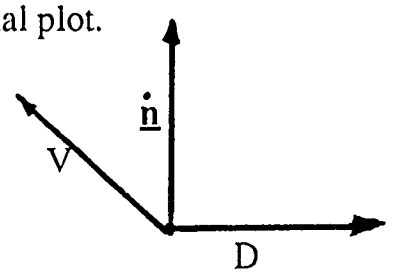
1. Sum the counts in all bins ; this will yield $\dot{n}$.

$$\Sigma \Sigma \dot{n}_{ij} = \dot{n}$$

2. Sum all counts in all bins of the same diameter and multiply by corresponding volume ($\pi D^3/6$); then sum over all diameters. This yields the flow rate.

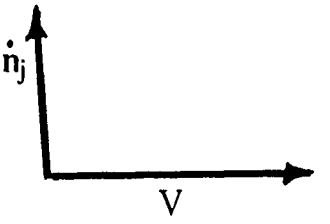
$$\Sigma\,\Sigma\,\dot{n}_{ij}\,(\pi D_j^3)/6$$

3. Normalize the matrix; divide the count in each bin by $\dot{n}$ ($\Sigma\Sigma\dot{n}_{ij}$) and represent the data in a three-dimensional plot.



where $\underline{\dot{n}}$ is $\dot{n}_{ij}/\dot{n}$.

4. Use the normalized matrix in item 3 above to plot the axial velocity (velocity 2) for representative diameters (say, 16.25 mm, 30.3 mm, 43.5 mm, and 57.0 mm).



where $\dot{n}_j$ is normalized with regard to column j; that is ($\dot{n}_{ij}/\Sigma\dot{n}_i$).

5. Plot $\Sigma\dot{n}_{ij}/\dot{n}$ versus diameter Dj.

6. Plot Vav and rms versus diameter - Dj.

$$(Vav)j = \Sigma V_i\dot{n}_{ij}/\Sigma\dot{n}_i$$

7. Use <u>corrected count</u> to obtain a plot of $\dot{n}_j$ versus diameter Dj.This data are given in a histogram for each radial position (see Figure 1). These must be converted in integrated values using probe area, time of run, etc. A flow rate based on corrected count is computed as follows:

$$\Sigma\,\dot{n}_j\Pi(D_j)^3/6$$

8. Normalize the data in item 6 by dividing each <u>corrected count</u> by $\Sigma\dot{n}_j$ and plot against Dj.

V. RECOMMENDATIONS:

Once the experimental data are in the correct form, the theory will be applied. In this portion of the study, the source terms in the theory have to be evaluated. For the case where the conservation of mass only is invoked, **n** is needed to determine the size distribution.

At Wright Patterson Air Force Base, the experimental setup has been moved into the room containing the combustion tunnel and realigned. Similar measurements will be performed on a combusting flow. Once these data are collected, analysis can begin on the source terms for such a flow. In this flow there will be heat, mass, and momentum transfer - much different from the cold flow experiments conducted this summer.

VI. REFERENCES:

1. Shannon, C. E., "A Mathematical Theory of Communication ", The Bell System Technical Journal, 27, 1948, p.379.

2. Jaynes, E.T., "Information Theory and Statistical Mechanics", Physical Review, 106, 1957, p. 620.

3. Kelly, A. J., "Electrostatic Metallic Spray Theory", J. of Applied Physics, 47, 1976, p. 5264.

4. Sellens, R. W. and Brzustowski, T. A., "A Prediction of Drop Size Distribution in a Spray from First Principle", Atomization and Spray, 1, 1985, p. 89.

5. Sellens, R. W. and Brzustowski, T. A., "A Simplified Prediction of Droplet Velocity Distributions in a Spray", Combustion and Flame, 65, 1986, p. 273.

6. Li, X. and Tankin, R.S., "Droplet Size Distribution:A Derivation of a Nukiyama-Tanasawa Type Distribution Function", Combustion Science and Flame, 56, 1987, p. 65.

7. Li, X. and Tankin, R.S., "Derivation of Droplet Size Distribution in Sprays Using Information Theory", Combustion Science and Flame, 60, 1988, p. 345.

8. Li, X. and Tankin, R.S., "On Prediction of Droplet Size and Velocity Distributions in Sprays Through Maximum Entropy Formalism", submitted for publication, 1989.

10 Li, X., PhD Thesis, Department of Mechanical Engineering, Northwestern University, June, 1989.

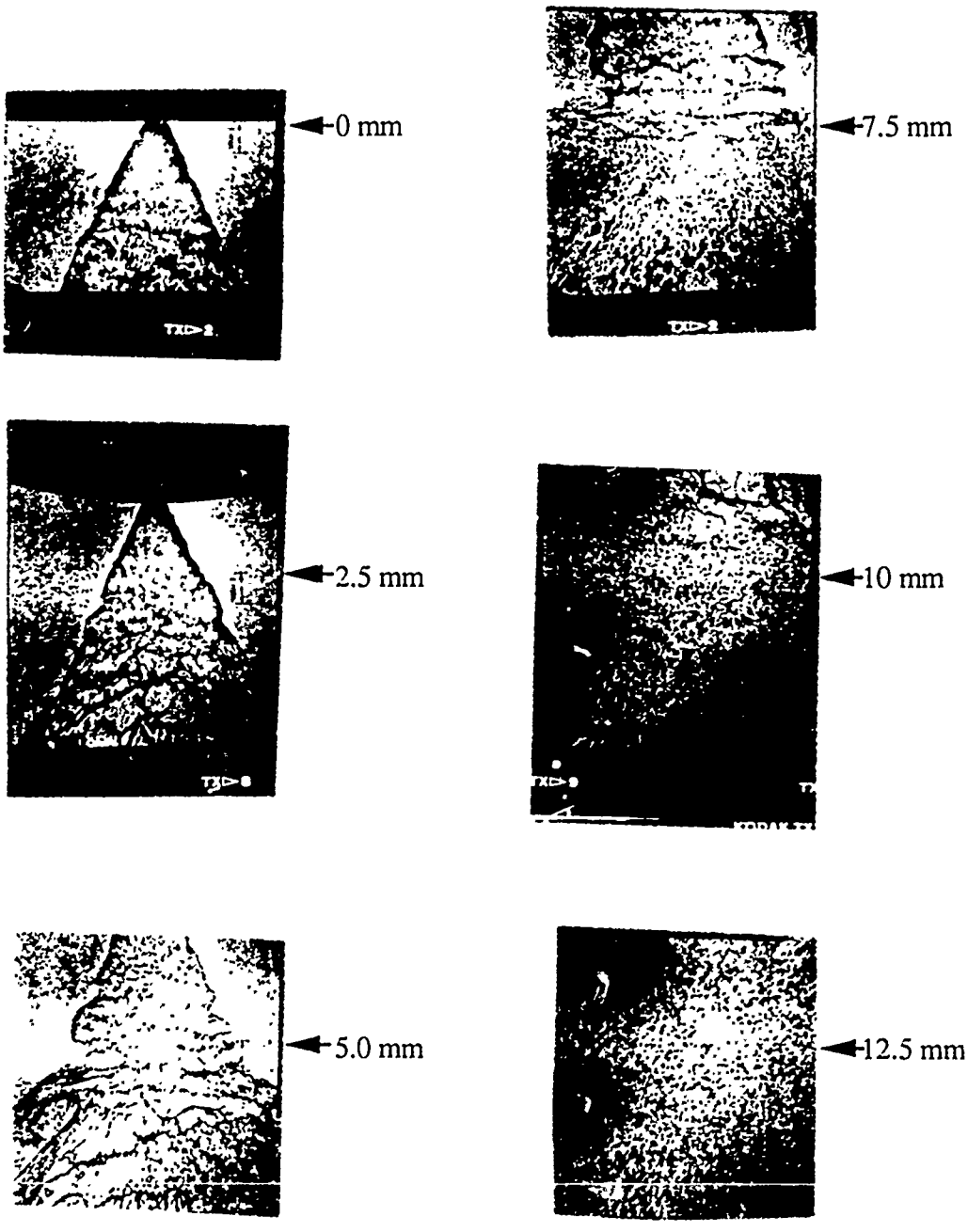


Figure 1. Photographs of the spray.

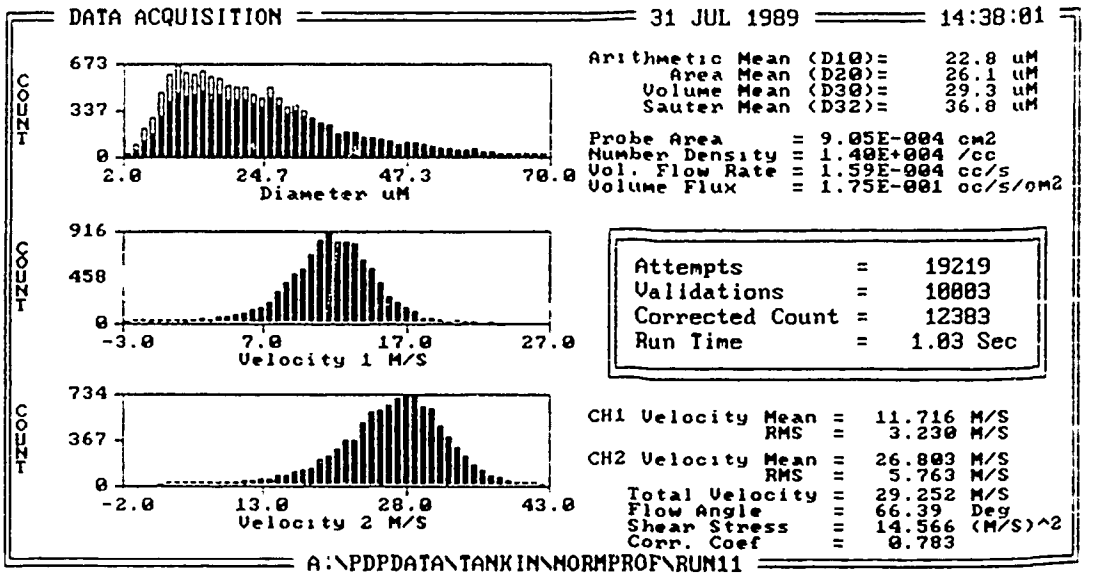


Figure 2. Histograms and data shown on computer monitor.

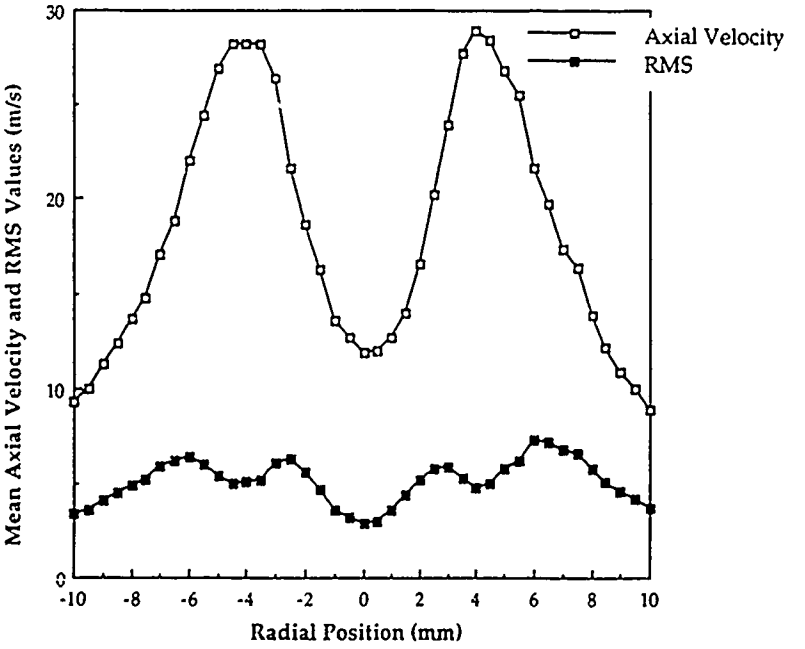


Figure 3. Plot of mean axial velocities and rms values obtained from vertical traverse.

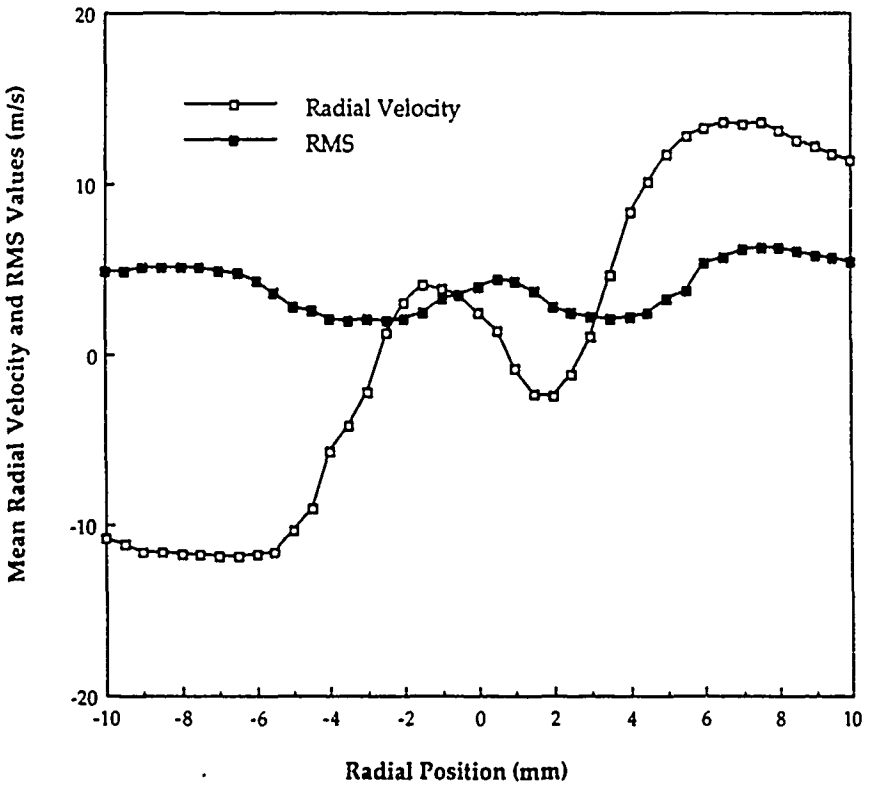


Figure 4. Plot of mean radial velocities and rms values obtained from a vertical traverse.

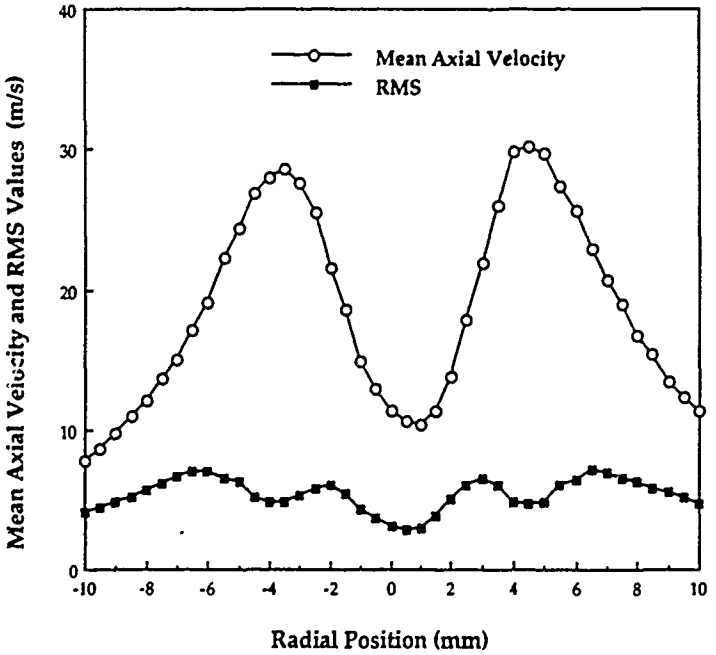


Figure 5. Plot of mean axial velocities and rms values obtained from a horizontal traverse.

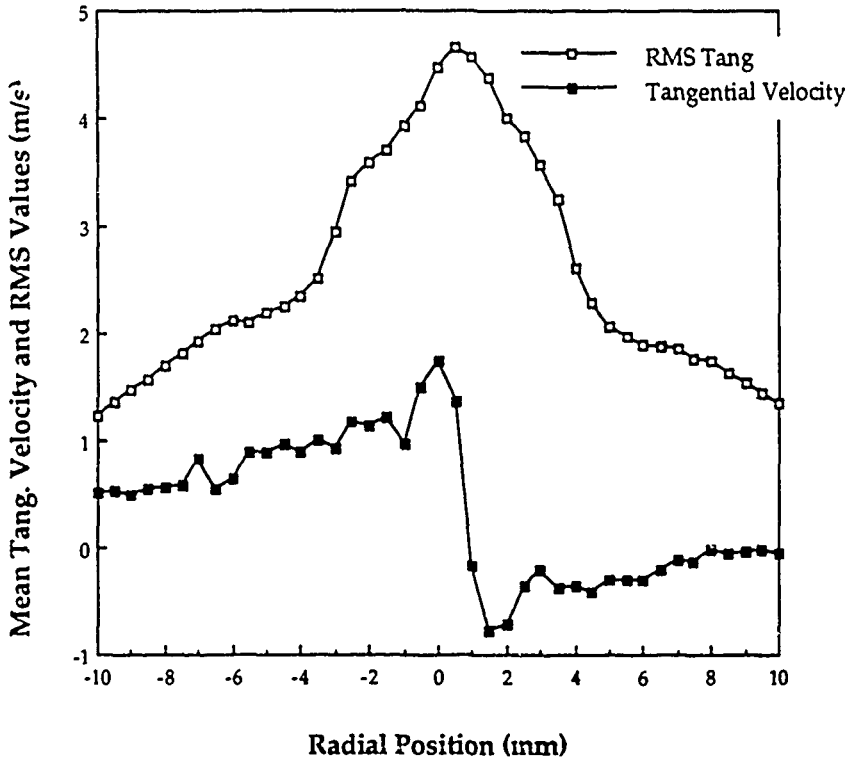


Figure 6. Plot of mean tangential velocities and rms values obtained from vertical traverse

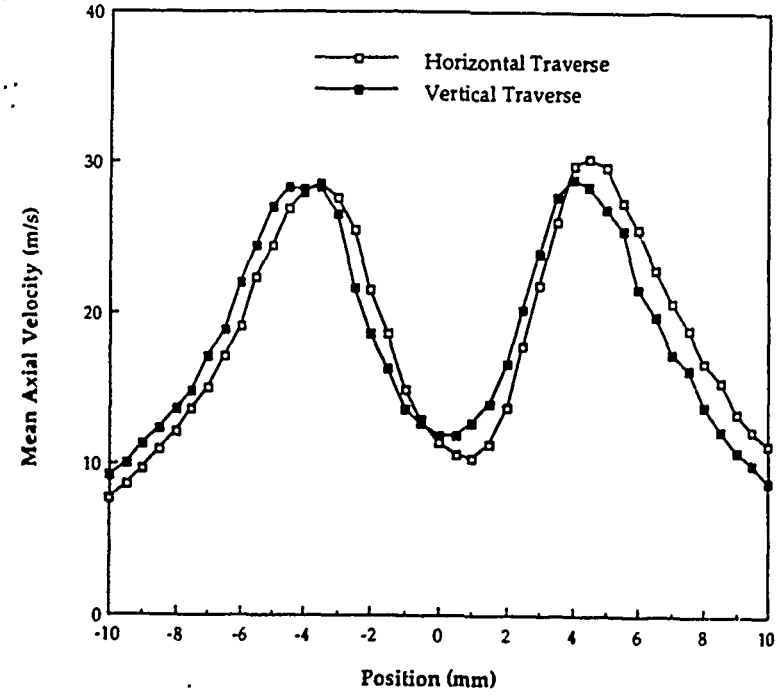


Figure 7. Plot comparing mean axial velocities obtained from vertical and horizontal traverses

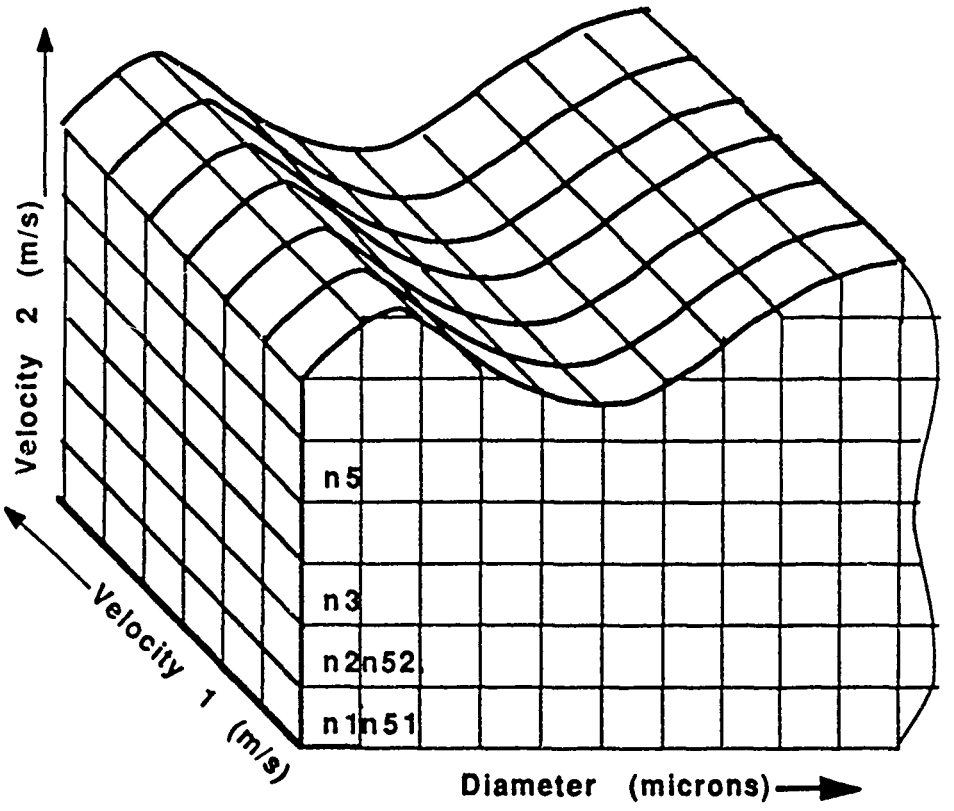


Figure 8. Schematic plot of three-dimensional matrix

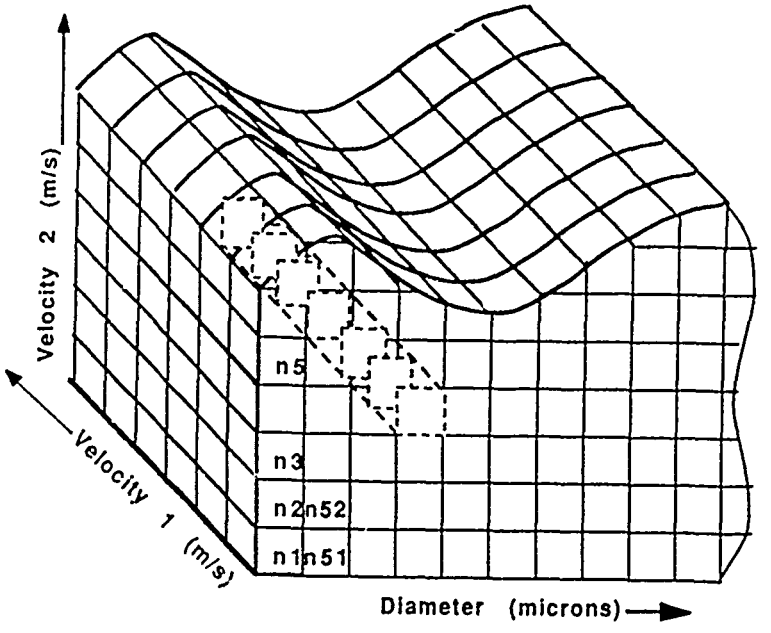


Figure 9. Schematic drawing of the summation process.

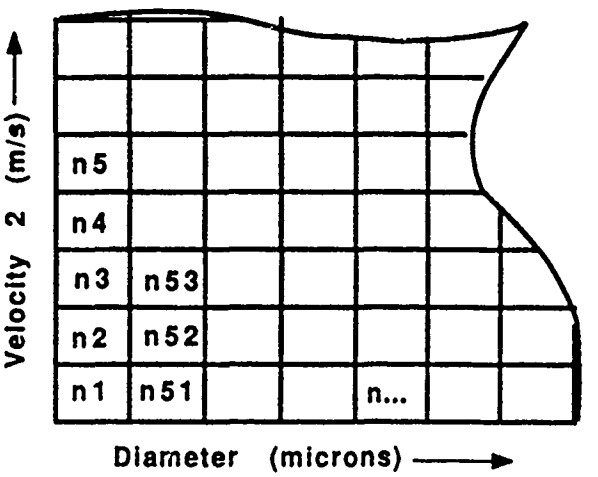


Figure 10. Two-dimensional matrix obtained after summation.

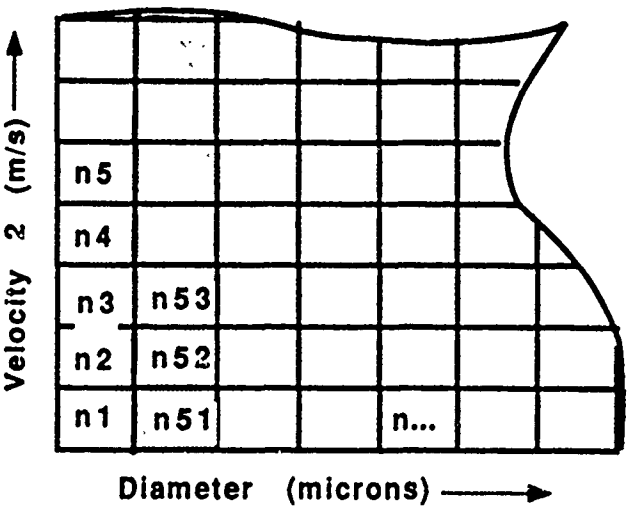


Figure 11. Schematic drawing of the summation process.

1989 USAF-UES SUMMER FACULTY RESEARCH PROGRAM/

GRADUATE STUDENT RESEARCH PROGRAM

Sponsored by the

AIR FORCE OFFICE OF SCIENTIFIC RESEARCH

Conducted by the

Universal Energy Systems, Inc.

FINAL REPORT

AIRCRAFT ENGINE COMPRESSOR AND FAN REWORK PRACTICES

Prepared by:	Robert A. Wheasler
Academic Rank:	Professor, Aeronautical and Mechanical Engineering
Department and	Mechanical Engineering
University:	University of Wyoming
Research Location:	WRDC/POTX, Wright-Patterson AFB, OH 45433
USAF Researcher:	Dr. Doug Rabe
Date:	22 September 1989
Contract No:	F49620-85-C-0013

AIRCRAFT ENGINE COMPRESSOR AND FAN REWORK PRACTICES

by

Robert A. Wheasler

ABSTRACT

An evaluation of Compressor and Fan blades and vane blending as practiced by the Air Force, Navy and some airline companies.

Overhaul Technical Manuals prescribing blade and vane rework limits and practices established by the Air Force, Navy and engine manufacture together with blade and vane engineering design specification drawings were evaluated, providing an incite into where losses may be expected to occur in compressor and fans during in-service use.

Examples of the losses to be anticipated in engine performance (specific fuel consumption, exhaust gas temperature) resulting from acceptable rework practices are presented.

ACKNOWLEDGEMENTS

I wish to thank the Air Force Systems Command and the Air Force Office of Scientific Research for the sponsorship of this project. It is through this type of sponsorship that enables studies to be performed which sheds some light on problem areas which may not otherwise receive attention. Also, to UES for their excellent management of the program. Dr. Doug Rabe and Dr. Chuck Elrod WRDC/POTX deserve my special thanks for their continued interest and guidance in a project of this nature.

Without the cooperation and the efforts of many personnel in the Air Force, Navy, and commercial airlines this study could not have been made possible. I wish to particularly recognize the following for their support and contributions:

Mr. Ed Jenkins, Oklahoma City Air Logistics Center

Captain Roger Gamache and Mr. David Crawley,
San Antonio Air Logistics Center

Mr. C.M. Sheldon, Manager, Propulsion Engineering,
Transworld Airlines

Mr. R.J. Walker, Senior Manager, Power Plant Engineering,
American Airlines

Mr. Gary Burrie, Naval Aviation Depot, NAS, Long Island, CA

Mr. Brian Peterson, Naval Aviation Depot, NAS, Alameda, CO

Mr. Jim Crouch, ASD/YZE, WPAFB, OH

I INTRODUCTION:

Although the basic principles of the gas turbine engine are understood, its operation seems over-simplified to some. The problems involved in developing a high-performance engine include applications of nearly every engineering discipline. The development of the gas turbine engine to its present stage is a result of the vast amount of research that has taken place during the past fifty years, as was the case in the development of the propeller-reciprocating engine. The demands for a high-performance engine have resulted in a highly sophisticated design which can only be successful through utilization of all the latest technologies.

It was recognized early by the Air Force that the high-performance engines being developed were continuing to be ever more difficult and expensive to maintain. Soon terms and phrases, such as reliability, maintainability, and affordability, became standard vocabulary throughout the Air Force. A great deal of emphasis is continuing to find ways in which all services can contribute to the reliability and maintainability of all weapons systems. The maintainability of engines is only a small part of this effort.

Contribution to the understanding of those factors which influence reliability and maintainability of aircraft engines lies fundamentally in an in-depth understanding of all components that make-up the complete engine. This includes an in-depth understanding of such sciences as aerodynamics, thermodynamics, materials, heat transfer, combustion, vibration, control mechanisms, hydraulics, and pneumatics. It is only through a continued effort to understand the scientific principles involved in the design of aircraft engines that these factors which impact reliability and maintainability can be injected into the philosophy of design.

One of the purposes of the present effort is to gain a better understanding of one of the engine components that has a strong influence on the operation of an engine; i.e., the compressor. In addition to those engineers whose primary function is to design and develop the high-performance engines for the Air Force, there are many whose responsibilities are to assist in the maintainability and reliability of the engines that have been fielded.

There are many problems that arise in the maintainability of engines and they must be confronted by the propulsion engineers in the engine depots, which demands that the problems be resolved as quickly as possible. The time constraints on resolution of these problems demand decisions oftentimes based on inadequate background and data. One area of concern that is often voiced by depot propulsion engineers is the question of the magnitude of degradation through normal field usage, how the degradation of one component affects the operation and degradation of other components, and the composite of these influences on the performance reliability and maintainability of these engines.

The importance of the compressor in the performance of an engine is well recognized. Compressor design and technology has attained a high degree of sophistication compared to the early engines, yet there continues to be a need for an increased understanding of the mechanisms of fluid flow through rotating machinery. These factors must be continually investigated if information is to become available which will have a serious impact on influencing the philosophy of compressor design. Propulsion engineers also recognize that in order to understand the operation of a gas turbine engine, the characteristics of each component must be understood. The basis for successful design of the gas turbine engine lies in the understanding of the characteristics of the individual components. It is only through an accurate determination of the operating line that the performance of engines can be predicted, which is an absolute necessity in the determination of the aircraft performance. Consequently, the understanding of the operation of the compressor is of primary importance to the propulsion design engineer, although this is not always appreciated.

In order to provide information on the question of how the degradation of a compressor from its original design condition (resulting from normal usage) affects other engine parameters, an effort has been underway to determine what information is available to assist an engineer in decision-making. At this point in time, it appears that no major effort has been made to quantitatively determine the magnitude of these losses, where they occur, and the mechanisms that contribute to these losses. The information gained so far has

indicated that the majority of the efforts to assess these losses have been based on theoretical analysis of flow mechanisms and test data accumulated on one-, two-, or three-stage "test rigs".

In addition, engine manufacturers have provided propulsion engineers in the field with information to assist them in evaluating and predicting losses in engines through data termed as Performance Influence Coefficients. Since knowledge of how these parameters and coefficients have been developed has not been made available for this study, it is assumed that these data are a result of a combination of regular testing, theoretical analysis, and the best engineering judgment available. The present and previous investigations have, therefore, not revealed any major effort to measure quantitatively the aforementioned losses. Therefore, there appears to be insufficient information on which to assess degradation in engine performance with a degree of reliability that would contribute to the decision-making processes confronting those involved in improving the reliability, maintainability, and affordability of engines.

The Compressor Research Facility (CRF), that has been developed in the Wright Research and Development Center (WRDC), has the sophistication and capability to acquire the information needed to explain losses in compressors. The thirst for technology in all fields of aircraft and engine performance demands careful programming of the utilization of research facilities available to the Air Force. The CRF has proved to be a great asset in contributing to compressor technology, but it will continue to have many demands on its use. Consequently, priorities for its use must be carefully evaluated prior to any commitment for the development of a proposed test. Although the determination of losses occurring in compressors is of considerable importance, it is recognized that the degree of importance must be weighed against other priorities essential to the Air Force. Since budgetary constraints are the major influencing factors in establishing such priorities, it is only prudent to determine from an economical standpoint whether any test will justify the necessary expenditure of funds. One must recognize that it is difficult to determine the comparative monetary value of improving

design through an in-depth understanding of compressor operation, relative to conforming to the present engine management philosophy.

A portion of this philosophy has been influenced by the necessity of reworking blades and vanes, which presently is considered to be a cost-effective approach in engine overhaul. Herein lies an important factor that must be carefully weighed; that is, to what extent the knowledge exists to adequately assess the cost factor in the current rework methods with their accompanying designated acceptable limits of rework. The question still remains as to the degree of knowledge available to assess the influence of the apparent degradation on other parameters of engine performance, such as thrust, SFC, and turbine-inlet temperatures.

One must recognize that the most important question to emphasize is <u>not</u> the comparison of whether to rework (blend) compressor blades and vanes, but to develop quantitative information which will enable the determination of the change in compressor component variations from the original nominal design characteristics. These variations occur as a result of normal field use of engines during their life cycle. Consequently, these changes will influence other engine component characteristics--which impact life cycle costs (LCC) of the engines in the Air Force inventory.

It has been recommended that the Compressor Research Facility initiate a detailed test program in order to evaluate the effects of deviations of compressor design parameters from their original design philosophy on the resulting performance (compressor map), and the consequential impact on other engine parameters that lead to reduced life cycle costs (LCC) of engine ownership.

II OBJECTIVES OF THE RESEARCH EFFORT:

One of the primary objectives of this effort is to acquire information on losses in compressors and fans experienced by the Air Force, the Navy, and commercial airlines and to evaluate their practices for restoring the aircraft engines under their responsibility to acceptable operating conditions. The Air Force, Navy, Marines, and commercial airlines do extensive rework of compressor and fan blades and vanes; consequently, one facet of the study was to determine the magnitude of compressor blade and rework effort in the depots and to gain an insight as to the established acceptable limits on blending of blades and vanes.

III APPROACH TO THE PROJECT:

A survey of the literature pertinent to the study was found to be limited; consequently, information was requested from engine overhaul depots of the Air Force, Navy, and commercial airlines. In addition, visits were made to the following:

Naval Aviation Depot, Naval Air Station, North Island, CA.

Naval Aviation Depot, Naval Air Station, Alameda, CA.

Oklahoma Air Logistics Center, Tinker AFB, OK.

TransWorld Airlines & Maintenance Center, Kansas City, MO.

American Airlines & Maintenance Center, Tulsa, OK.

Compressor and fan blade and vane overhaul "Wor Package's" found in the appropriate Air Force, Navy, and airline publications were obtained for analysis.

Technical Publications germain to the effort was analyzed for the following engines:

Air Force Technical Orders (T.O.s)

TF-30	TF-41	TF-110
TF-33	F-100	J-57
TF-33	TF-101	J-79
TF-34	TF-103	T-56
TF-39	TF-108	

NAVAIR Technical Publications

TF-34	J-79
F-404	T-56

Airline Technical Publications

JT8D	JT-9D	CF6
Series	Series	Series

Shop specification drawings for each blade and vane stage were obtained for the J-79, TF-30-P-9, TF-33-P-7, TF-39, F-100 and T-56 engines. These specification drawings were scrutinized for manufacturer's tolerances, with particular regard to the tolerances for chord, span, blade/vane thickness, and leading and trailing edge contours, in order to gain an insight into the variations in blades/vanes that could occur between average new parts in the fleet, and to acquire information which would assess the percentages of deviations from the nominal new part dimensions as a result of accepted rework practices.

Then, considering the magnitude of compressor design variations through blade/vane rework, the anticipated losses in compressor component efficiencies and the corresponding impact these efficiency decreases would have on other engine parameters, particularly the thrust specific fuel consumption (TSFC) and the turbine-inlet temperature (TIT), would be assessed. Additional attempts were made to evaluate, in part, these influences on range, payload, and fuel costs for representative aircraft in the Air Force fleet.

IV ANALYSIS AND DISCUSSION:

In reviewing the blend limits for several engines (see list in III-APPROACH TO PROJECT), the results indicate considerable deviation of blade and vane design characteristics from the original specifications. This data was obtained from detailed examination of blade and vane drawing specifications for the following engines, TF-33-P-7, TF-30-P-9, J-79-15/17, T-56, F-100, and T.O. inspection limits and procedures for these engines, as well as for numerous other engines used by the Navy, Marines and airlines. The reported values for deviation of design characteristics from original specifications are comprised of two parts: (1) those attributable to allowable tolerances during manufacture, and (2) deviations allowed through blending. In review of the tolerances allowable during manufacture, it was found that, in general, there were similar tolerances by the three engine manufacturers, Pratt and Whitney, General Electric, and Allison Division of General Motors. It was interesting to note that the allowable tolerances in the chords of all stages from the roots to the tips had approximately the same percentages of chord, that is 2.4 percent variation in chord, regardless of the stage. The tolerances allowed in blade thickness during manufacture varied between 5 and 13 percent.

Blade and vane rework (blending) practices fall into several ategories; namely, (a) leading edge-trailing edge long blends and scallops, (b) tip clearances, tip leading and trailing edge blends, and (c) removal of nicks, scratches, pits.

Similarities in blending limits were found for all manufacturers and users. That is, allowable blending limits and regions indicating the type of blend that can be accomplished are specified in overhaul technical documents for each engine. These documents include inspection and rework procedures noting those areas where blending is not allowed - primarily to maintain structural integrity of the blades/vanes. Since all the engine specifications analyzed express their blend zones and limits in a similar format, figures 1 and 2 have been included as examples of information that is typically found in these technical documents.

It was not the intent of this study to compare blade limits for each of the engines examined, but to gather some incite into the magnitudes of allowable blending rework required to restore compressors and fans back into service.

It was found that the leading and trailing edge blend limits ranged from 0.020 inches to 0.156 inches for the lower-half of a blade span, and from 0.030 inches to 0.375 inches for the upper-half of a blade span. The larger values, of course, were found on fan blades. As would be expected, the blend limits are, in part, dictated by the chord size of the blades. Consequently, calculations were performed to determine the percentages of chord removal allowed through blending for each stage and each engine. It was found that the allowable percentage of chord removable for the lower-half root of the span ranged from 4.8 percent to 10.8 percent with an overall average of 8.7 percent for all engines. The upper-half (tip) of the span ranged from 5.49 percent to 18.45 percent with an overall average of 12.4 percent for all engines.

It should be noted that the number of blended blades per stage is also limited as specified in the overhaul manuals. It was noted that considerable blade/vane rework is allowed at or near the tips with a variety of blend types to be found. In general, the criteria being minimum tip chord and span length. The blade tip-case (or seal) clearance allowable ranged from 0.030 inches 0.090 inches. This was found to be of particular interest since compressor and fan design practices dictate careful attention to the reduction of tip losses. In addition, numerous proposals have been submitted to the Air Force, Navy, and the airlines for incorporation of new technologies advertised to reduce tip losses and, hence, considerable reduction in specific fuel consumption (SFC) and exhaust gas temperature (EGT). An illustration of the impact that tip clearance and chord reduction have on SFC and EGT will be presented later.

A few comments on depot compressor and fan rework practices are in order. Nearly all blends are accomplished by hand grinding. As a result, the quality of the blend is personnel experience dependent. This was noted after examining a variety of reworked blades and vanes in the depots with particular attention to the leading and trailing

edges. As a consequence, the blade contour (airfoil profile) is not maintained through blending. The location of the maximum airfoil thickness is altered as well as the pressure distribution over both the concave and convex surfaces.

One company, known as the Airfoil Management Company, has developed a technique and process that advertises the capability to recontour blades having in-service chord changes and that meet the consumer's (Airlines) overhaul manual specifications. Airfoil Management Company brochures indicate that numerous airlines have utilized their services. One of the airlines contacted during the study stated they do contract some of their blades out for recontouring, although there are differing opinions within the organization regarding the economical value of the effort. This continues to be an area which requires additional testing study and evaluation to assist in management decisions.

The airlines contacted, contract-out blades and vanes that cannot be repaired through standard blending practices and or those that exceed limits and require extensive rework. This rework entails the removal (cutting) of the unserviceable portion of the blade, then welding on of a new section using an electron beam (EB), and then recontouring. It has been reported that the Marine Aviation Depot at the Marine Air Station, Cherry Point, NC is developing this type of capability.

In order to appreciate the magnitude of the engine overhaul operations at the various depots, one should realize the Air Force manages some 45,000 engines of various types which is approximately twenty-eight times more than the largest airline - United Airlines.

Some examples are being presented in order to develop an appreciation for some of the influences that blade and vane rework practices have on reduction in component efficiencies and their corresponding impact on engine and aircraft performance and costs. These illustrations are based upon the reports described above which were developed by Pratt and Whitney, and General Electric for their special-purpose studies.

The first illustrations consider the effect of blade/vane rework on the TF-33-P-7 engine and the C-141 aircraft performance. The

following calculations are based upon four assumptions:

(1) The average chord reduction (from nominal design) for all stages is considered to be 10 percent--this corresponds to an average of 0.159 inch per blade (5/32 = 0.1563 inch).

(2) The blade/vane clearances average 0.030 inch, which is equivalent to the manufacturing tolerance.

(3) 25 percent of each stage have been reworked (blended).

(4) Pits, dents, leading/trailing edge contour rework, and airfoil thickness deviations are not included.

It should be emphasized that these assumptions present a conservative picture of losses that can occur as a result of seal/tip clearances and other accepted blade/vane rework procedures. Scrutinizing all blade and vane specification drawings for the TF-33-P-7, the average blade and vane chord was equal to 1.596 inches. Note that 3/32-inch blending on the leading and trailing edges would be equivalent to 11.75 percent reduction in chord, which is well within allowable limits for any engine.

Based upon the data and methods available to evaluate compressor efficiency losses described above, and with the assumptions listed, the calculations indicated a 2.658 percent decrease in compressor efficiency when using the more conservative approach available. Using the calculated value of 2.658, 0.5944 percent TSFC increase per 1 percent decrease in compressor efficiency, and 6.097 million gallons used per year for each 1 percent increase in TSFC equates to 9.633 million gallons of fuel used per year for the C-141 fleet. Other calculations show that the 2.658 percent loss in compressor efficiency is equivalent to 69.36 nautical-mile range loss at constant gross weight per aircraft, or 1540 pound loss in payload at constant range. In addition, an increase in turbine inlet temperature of 26 degrees Fahrenheit could be expected.

Assuming only ten percent of the aircraft in the fleet have blade blending to the extent assumed in the conservative value used in this example, the additional annual fuel cost would be 963,000 dollars (using one dollar per gallon of fuel).

However, when making comparisons of fuel cost as a result of blade and vane rework cost savings, it should be borne in mind that

the C-141 engines return to the depot maintenance shops about once every seven years (Engine Depot actuarial data). Consequently, the increased fuel cost to be used for rework cost comparisons should be 6,741,000 dollars. Since blade/vane rework cost savings data for those TF-33 engines used in the C-141 fleet were not readily available, no comparison was included in this report.

The above discussion was directed to the C-141 fleet, but one should not lose sight of the fact that there are other TF-33 series engines installed in Air Force aircraft; namely, B-52-H (768 versus 1100 C-141 installed engines), E-3A, KC-135-B, and EC-135.

Calculations for the J-79-15/17 (F/RF-4 aircraft) were performed in the same manner as illustrated by the TF-33-P-7 (C-141-A/B) example, with a decrease in component efficiency of 2.76 percent and an increase in specific fuel consumption (SFC) of 1.544 percent; or using the second method as discussed above, the decrease in component efficiency is 3.03 percent, with a corresponding increase in specific fuel consumption (SFC) of 1.8023 percent.

For the 3,390 installed engines in the F/RF-4 aircraft fleet (1988 data), the total annual fuel used is 607.69 million gallons, or 179,260 gallons per engine. If the fuel consumption were improved by 1.54 percent, the annual fuel savings for an engine would be 2,760.6 gallons, equivalent to 21,229 gallons per engine shop visit. Note that the cost of reworked blades and vanes per a shop visit reported from a previous study is 26,755.78 dollars per engine, and the additional cost in fuel due to the allowable blade rework practices is calculated as 21,229 dollars (based on one dollar per gallon fuel cost). Also, as in the TF-33 example, the anticipated average increase in turbine-inlet temperature for the J-79 engine is 28 degrees Fahrenheit.

Although the illustrations were not precise and include many assumptions, the magnitude of the blade/vane rework effort in the Air Force and its potential impact on engine performance and life-cycle-cost (LCC) should be evaluated carefully with the best information obtainable. Certainly the information/data presently available leaves a great deal to be desired.

V CONCLUSIONS:

Previous studies by the Compressor Research Facility (CRF) showed that the magnitude of blade and vane rework effort by the Air Force saves millions of dollars by restoring damaged or eroded blades and vanes to serviceable condition consistent with the existing limits of repair vis-a-vis the purchase of new blades and vanes.

However, using the very limited data available by which to assess the losses in engine performance as a result of compressor and fan degradation, preliminary calculations indicate that these losses contribute to significant loss in engine performance with the attendant increase in fuel costs and engine "hot-section distress".

The present effort compliments previous studies evaluating potential losses in compressors and fans resulting from in-service use by extending past knowledge, through the addition of the knowledge and experiences acquired by the Navy and airlines, as well as analyzing data for nearly every engine in the Air Force inventory.

Thorough understanding of the mechanisms and magnitude of all losses experienced by compressors and fans and their influence on compressor performance is limited and additional studies should be made with supporting test data.

VI RECOMMENDATIONS:

1. As a continuation of the present study, it is recommended that a request be made to Pratt and Whitney, General Electric and Allison Division for information on their analysis, experience, and test data for assessing losses in compressors and fans - including the determination of their published "influence coefficients".

2. It is recommended that a comprehensive test plan be developed by the Compressor Research Facility (CRF) which will evaluate the parameters necessary to determine the magnitudes of losses in compressors through in-service use.

SELECTED REFERENCES

Reports:

Birkler, J. L., and Nelson, J. R., "Aircraft Turbine Engine Monitoring Experience: An Overview and Lessons Learned from Selected Case Studies," Rand Report No. R-2440-AF, 1980.

Bolick, R. P., and Mancini, J.M., "Northwest JT8D Evaluation of Sermetel 'W' Coated Stators." Pratt and Whitney Aircraft Group, 1978.

Gieleghem, R. A., "CF-6 High Pressure Compressor Performance Management." General Electric Gas Turbine Division, March, 1987.

Kelley, S. E., "Resume of Engineering evaluation of Manufacturing's 'Cut and Burnish' Process for Sermetel 'W', PWA 110-2 Coated Stators and Effect on Engine TSFC." Pratt and Whitney Internal Correspondence: Kelley, S.E., to Acker, W. L., 20 December 1977.

Kimball, J. C., "Effect of Sermetel 'W' Coating of J73P Production Engine Compressor Stators." Pratt and Whitney Internal Correspondence, Kimball, J. C., to McMahon, M. P., 23 July 1976.

Mullan, D., "TF-39 Performance Analysis," Aircraft Engine Group, General Electric, Lynn, MA/Cincinnati, OH, May, 1987.

Ross, E. (Capt. USAF), "The Silver Streak Effort," Demonstration of Jet Engine Performance Improvements by Smoothing Compressor Airfoil Surfaces. Oklahoma City Air Logistics Center, 1979.

"Sermetel 'W' for Surface Repair of Compressor Vane and Shroud Assemblies - J57/J75/TF-33 Engines." Pratt and Whitney Report to Commander, OC-AMA, Tinker AFB, OK, 25 July 1973.

Stiles, R. J., "Roughness Effects in Axial Flow Compressors - An Empirical Model." Note: Source of publication of report by Captain R. J. Stiles, USAF, date, unknown.

Syphers, G. N., "Results of P/L 13225 Sermetel 'W' Stator Coatings, JT3D-3B and JT3D-7." Pratt and Whitney Internal Correspondence, Syphers, G. N., to Yenker, C. E., 14 February 1977.

Urban, L. A., "Gas Path Analysis of Commercial Aircraft Engines." Pratt and Whitney (Presented at 11th AIDS Symposium DFVLR AIDS Study Group, Cologne, Germany, 22-24 September 1981).

Volponi, A. J., "Gas Path Analysis - An Approach to Engine Diagnostics." Pratt and Whitney ESP. 8222 (Presented to 35th Symposium, Mechanical Failures Prevention Group, Gaithersburg, MD, 20-22 April 1982).

Werner, F. T., "Sermetel 'W' coated J-57 Compressor." Headquarters SAC, Engineering report No. P-185, 30 July 1981.

"A Feasibility Study on Improving the Thrust Specific Fuel Consumption for the TF-33-P-7, 7A Engines," (A Technical Planning Estimate). Pratt and Whitney Aircraft Group (GPD), 1980.

"C-5 Propulsion System Study," Final Engineering Report for the period 21 September 1987 - 31 March 1988; Defense Logistics Support, General Atomics, Project: F4 1608-86-D-A113-3A276, May, 1988.

"Test Results of a Redesigned Low-Pressure--Intermediate Pressure Compressor." Detroit Diesel Allison (Division of General Motors Corporation), Date unknown.

Briefing:

"TF-33 Fuel Consumption Improvement Feasibility." United Technologies, Pratt and Whitney (GPD), 1982 (?).

Papers:

Urban, L. A., "Parameter Selection for Multiple Fault Diagnostics of Gas Turbine Engines," ASME Paper No. 74-GT-62, 1974.

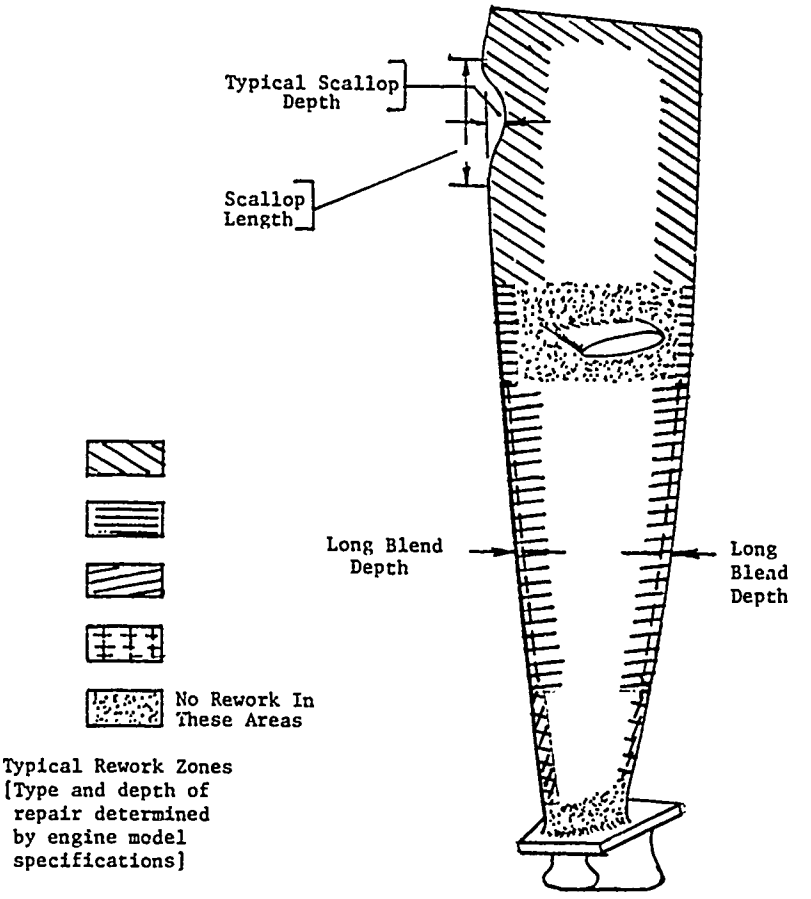
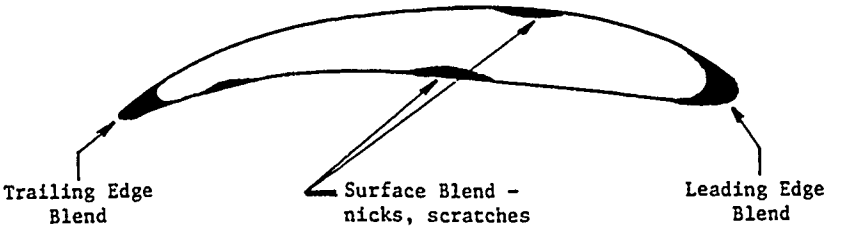


Figure 1. Typical Format Indicating Allowable Blending Zones



Examples of Typical Allowable Airfoil Blends



Examples of Typical Allowable Tip Blends

Figure 2. Examples of Typical Airfoil and Tip Blending

1989 USAF-UES SUMMER FACULTY RESEARCH PROGRAM

GRADUATE STUDENT SUMMER SUPPORT PROGRAM

Sponsored by the

AIR FORCE OFFICE OF SCIENTIFIC RESEARCH

Conducted by the

Universal Energy Systems, Inc.

FINAL REPORT

A THEORETICAL RESOLULTION OF MULTIPLE FREQUENCIES

Prepared by:	Dr. David B. Choate and Diana Major
Academic Rank:	Assistant Professor
Department and University:	Science Division, Transylvania University
Research Location:	Air Force Avionics Laboratory, Electronic Support Measure Group, WPAFB, Ohio
USAF Researcher:	Dr. James Tsui
Date:	August 15, 1989
Contract No.	F49620-88-C-0053

A THEORETICAL RESOLUTION OF MULTIPLE FREQUENCIES

by

David Choate

ABSTRACT

An algorithm is developed to pair multiple frequencies with their residues modulo IFM receiver bandwidths. If these residues are distinct within each receiver and the number of these receivers exceeds the number of frequencies, then this pairing is perfect; that is to say, spurious frequencies can never arise. These conditions are shown to be the best possible. A suggestion is made on how to control noise.

ACKNOWLEDGEMENTS

I would like to thank the Air Force Wright Aeronautical Laboratories and the Air Force Office of Scientific Research for sponsoring this program. I also wish to thank Universl Energy Systems, Inc. for their competent assistance regarding administrative matters.

The Electronics Support Measure Group associated with the Avionics Laboratory at WPAFB, Dayton, Ohio provided me with excellent working conditions as well as ready access to computing facilities. In particular, I would like to thank Dr. James Tsui who provided me with encouragement, support and guidance throughout the work on the project. In addition, I was able to benefit from the insight and assistance of Dr. William McCormick, a former summer research fellow associated with this group. And I owe a very large debt to my research assistant, Diana Major, for her careful programming.

I. INTRODUCTION:

In signal processing the 2π-ambiguity problem in frequency estimation is associated with the Chinese Remainder Theorem of number theory. I may have been assigned to the Avionics Laboratory because I am a number theorist and have worked before with signal processing. Diana Major was chosen to do the computer work.

II. OBJECTIVES OF THE RESEARCH EFFORT

The preliminary goals associated with this project included the study of various numerical schemes for the estimation of parameters related to radar signals. During the course of this research the goal became that of a theoretical resolution of a 2π-ambiguity problem in multiple frequencies. (Just as the Chinese Remainder Theorem is a theoretical resolution of a 2π-ambiguity problem of a single frequency.) Once this was made, the objective then became that of using it to control noise.

III. A GENERALIZATION OF THE CHINESE REMAINDER THEOREM

Let a and b be integers. Then a <u>divides</u> b, written $a|b$, if there exists an integer c such that $ac = b$. By (a,b) we mean the greatest common divisor of a and b and by $[a,b]$ the least common multiple of a and b.

Lemma 1 (i) if $a|b$ and $a|c$, then $a|b \pm c$.

(ii) if $a|b$, then $a|db$ for any integer d.

Proof. Clear.

Theorem 1. The system $x = c_1 \bmod F_1$
$x = c_2 \bmod F_2$
. . .
$x = c_I \bmod F_I$

is solvable if and only if $(F_i, F_j) \mid c_i - c_j$ for each i and j.

If there is a solution, then it is unique modulo $[F_1, F_2, \ldots, F_I]$.

Proof: ($\rightarrow$) $c_i + K_iF_i = x = c_j + K_jF_j$ implies $c_i - c_j = K_jF_j - K_iF_i$. Since $(F_i, F_j) \mid F_j$ and $(F_i, F_j) \mid F_i$, $((f_i, F_j) \mid c_i - c_j$ by Lemma 1.

"$\leftarrow$ " (We enclose this arrow in quotes because, although the theorem is true as stated, we choose to prove it only for a special choice of F_i's because it is these which are used by Diana Major to write the FORTRAN program "genchin.f".)

Set $F_1 = p_2p_3 \cdots p_I$
$F_2 = p_1p_3 \cdots p_I$
. . .
$F_I = p_1p_2 \cdots p_{I-1}$

,where all the p's are pairwise prime; i.e. $(p_i, p_j) = 1$ whenever $i = j$.

Since $x = c_1 \bmod F_1$, $x = c_1 \bmod p_2$
$x = c_1 \bmod p_3$
$x = c_1 \bmod p_4$
. . .
$x = c_1 \bmod p_I$

Since $x = c_2 \bmod F_2$, $x = c_2 \bmod p_1$
$x = c_2 \bmod p_3$
$x = c_2 \bmod p_4$
. . .
$x = c_2 \bmod p_I$

Since $x = c_I \bmod F_I$, $x = c_I \bmod p_1$
$x = c_I \bmod p_2$
$x = c_I \bmod p_3$
. . .
$x = c_I \bmod p_{I-1}$

(B)

Consider first the case when I is even.

We form a new system by selecting one congruence from each

system in (B), namely,

$$\left.\begin{array}{l} x = c_1 \bmod p_I \\ x = c_2 \bmod p_{I-1} \\ \quad \cdots \\ x = c_I \bmod p_1 \end{array}\right\} \quad (C)$$

Observe that it is possible to construct the system (C) of congruences $x = c_j \bmod p_j$, $j + i = I + 1$ and $i \neq j$. For if $i = j = (I+1)/2$, then $I + 1$ would be even which is not the case.

Since the p's of (C) are distinct, they are pairwise prime by definition; so the congruence has a unique solution, say s, modulo $p_1p_2 \ldots p_I = [F_1, F_2, \ldots, F_I]$ by the Chinese Remainder Theorem. We claim that s is the solution to every other congruence in (B), $x = c_j \bmod p_i$, as well. We know that s is a solution to $x = c_{(I+1-i)} \bmod p_i$, $i = 1, 2, \ldots, I$, because these congruences are taken from (C). We also know that $p_i \mid (F_{(I+1-i)}, F_j)$ since the subscripts of p and c can never be the same. But $(F_{(I+1-i)}, F_j) \mid c_j - c_{(I+1-i)}$ by assumption. So $p_i \mid c_j - c_{(I+1-i)}$, or $s = c_{(I+1-i)} = c_j \bmod p_i$ for $i \neq j$. It is now clear that s is a unique solution modulo $[F_1, F_2, \ldots, F_I]$ to system (B).

If I is odd, then we replace the congruences $x = c_j \bmod F_i$ in system (C) when $j = (I+1)/2$ and $j = (I+3)/2$. We use instead the congruences $x = c_{(I+1)/2} \bmod p_{(I-1)/2}$ and $x = c_{(I+3)/2} \bmod p_{(I+1)/2}$. With this adjustment the argument is similar.

IV. SPURIOUS FREQUENCIES

In [2] incorrect or spurious frequencies are said to repeat at random before the method of exhaustion is used to resolve the 2n-

ambiguity problem arising in spectral estimation of multiple frequencies. The discussion below, based on Theorem1, indicates that they may not.

As in [2] we denote the noise protection by q, the number of frequencies by M, the number of receivers by I and their bandwidths are chosen to be $F_i = (4q+1)p_i$, $1 \leq i \leq I$, when the p's are pairwise prime. The unambiguous bandwidth B_u, given by $F_1F_2 \ldots F_I/(4q+1)^{I-1}$, is computed in [1]. As in [2] we observe that $(F_i,F_j) = 4q + 1$ for $i \neq j$, but we also note that a system of congruences of a true frequency there is guaranteed a solution which is unique modulo $[F_1, F_2, \ldots, F_I]/(4q+1)^{I-1} = B_u$, the unambiguous bandwidth.

In the M x I matrix of congruences displayed in ,2.

$$\left.\begin{array}{l} x = c_{1i} \pmod{F_i} \qquad i = 1, \ldots, I \\ x = c_{2i} \pmod{F_i} \\ \quad \cdots \\ x = c_{Mi} \pmod{F_i} \end{array}\right\} \quad (K)$$

we observe that $M^I - M$ <u>spurious systems</u> can be chosen. (A spurious system is defined to be a system of congruences made up of one congruence taken from each column of (K) whose unique solution modulo B_u, if it exists, is not a true frequency.)

Let

$$\left.\begin{array}{l} X = \alpha_1 \bmod F_1 \\ x = \alpha_2 \bmod F_2 \\ \quad \cdots \\ X = \alpha_I \bmod F_I \end{array}\right\} \quad (Q)$$

be a typical spurious system, where each $x = \alpha_i \bmod F_i$ is taken from the ith column of (K).

This system (Q) has a unique solution modulo B_u if and only if $(F_i, F_j) = 4q + 1 \mid \alpha_i - \alpha_j$ by Theorem 1. But since (F_i, F_j) is fixed, this condition will be met if and only if

$4q + 1 \mid \alpha_1 - \alpha_j$, $2 \leq j \leq I$, by Lemma 1 (i). So a spurious solution is protected by the matrix (K) only if $4q + 1$ divides $I - 1$ random numbers*, each taken from a set of M numbers.

The probability that $4q + 1$ will divide a random integer is $1/(4q+1)$. The probablity that $4q + 1$ will divide an element in a set of two random integers is $1/(4q + 1) + 1/(4q + 1) - 1/(4q +1)^2 = 1 - (1 - 1/(4q+1))^2$. In general the probability that $4q + 1$ will divide an element in a set of M random integers is $1 - (1 - 1/(4q+1))^M$.

The probability that $4q + 1$ will divide a number in $I - 1$ sets of M elements is $\left[1 - (1 - 1/(4q+1)^M\right]^{I-1}$. Note that this value increases with M and decreases as I or q increases. It represents that probability that a system choosen at random from (K) (one congruence from each column) has a solution.

But the probability of selecting a spurious system at random is only $(M^I - M)/M^I$ since there are M true solutions. (It is easy to show that no frequency is a solution to more than one system if the columns of (K) are distinct; that is to say, if tne receivers distinguish the frequencies.)

So we conclude that if M frequencies are distinguished by I receivers, then the probability that the matrix (K) will protect a spurious frequency is $\left[1 - (1 - 1/(4q+1)^M\right]^{I-1} \cdot ((M^I - M)/M^I)$.

---

* Regard them as $I - 1$ random directed distrances from a fixed point α_1.

For example, if 2 frequencies which require a noise protection of 1, are distinquished by 3 receivers, then the probability that a spurious frequency will exist is

$$[1 - (1 - 1/5)^2]^2 ((2^3 - 2)/2^3) = .0972$$

which is large enough to cause some insecurity if not alarm. So it is important (especially when q is only 1) to eliminate spurious frequencies. We will succeed in doing this with the help of a principle from discrete mathemantics.

V. THE PIGEON HOLE PRINCIPLE

In the sequel we will find a use for the following lemmas.

Lemma 2. (Euclid's first theorem) If $a|c$ and $b|c$ and $(a,b) = 1$, then $ab|c$.

Lemma 3. Let $\{p_1, p_2, \ldots, p_I\}$ be a set of integers, all greater than 1,which are pairwise prime. Define

$$F_1 = p_2p_3 \cdots p_I$$
$$F_2 = p_1p_3 \cdots p_I$$
$$\cdots$$
$$F_I = p_1p_2 \cdots p_{I-1}.$$

Then (i) $(F_1, F_2, \ldots, F_I) = p_1p_2 \cdots p_I$

and (ii) set $d = (p_j, (F_j, F_i))$ and let q be a prime factor of d. Then $q|p_j$ and $q|(F_j, F_i)$. So q divides some p_t where $t \neq j$. So q is a common divisor of p_j and p_t. Thus $q \leq (p_j, p_t) = 1$. This implies $q = 1$. But q is prime, a contradiction. So d contains no prime factors, or $d = 1$.

The Pigeon Hole Principle: If more than n pigeons are stuffed into n holes, then one hole contains more than one shrieking pigeon.

Note: In the sequel F_i, $1 \leq i \leq I$, will be as in Lemma 3.

Theorem 2. Suppose we have I receivers with unambiguous bandwidtns F_i which distinguish M noise free frequencies. Then the frequencies can be determined provided $I > M$.

Proof. Choose I integers $p_1, p_2, \ldots, p_I$ which are greater than 1 and pairwise prime such that $p_1 p_2 \ldots p_I \geq B$, the desired bandwidth. Write

$$\left.\begin{array}{llll} x = a_{11} \bmod F_1 & x = a_{12} \bmod F_2 & \ldots & x = a_{1I} \bmod F_I \\ x = a_{21} \bmod F_1 & x = a_{22} \bmod F_2 & \ldots & x = a_{2I} \bmod F_I \\ \ldots & \ldots & \ldots & \ldots \\ x = a_{M1} \bmod F_1 & x = a_{M2} \bmod F_2 & \ldots & x = a_{MI} \bmod F_I \end{array}\right\} (1)$$

where each row represents a true signal.

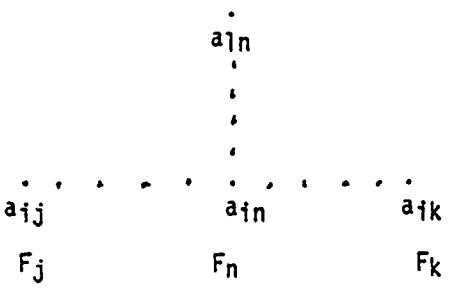
Since the receivers distinquish the signals, the constants are distinct up to columns; i.e. $a_{ij} = a_{kj}$ implies $i \neq k$. We now show a spurious frequency cannot exist under these conditions.

Any spurious frequency is a solution to a spurious system consistimg of one congruence taken from each column. Since $I > M$, at least two congruences, say $x = a_{ij} \bmod \bmod F_j$ and $x = a_{ik} \bmod F_k$, $j \neq k$, must be taken from the same row by the pigeon hole principle. Moreover, since the system is spurious, not every congruence in it lies on the same row i. Call one such congruence $x = a_{1n} \bmod F_n$ where $i \neq 1$ and j, k and n are distinct. (For Figure 1 we have assumed without loss of generality that $j < n < k$ and that $i > 1$.)

By Theorem 1 $(F_j, F_n) \mid a_{ij} - a_{1n}$ and $(F_j, F_n) \mid a_{ij} - a_{in}$. So $(F_j, F_n) \mid a_{in} - a_{in}$ by Lemma 1 (i). Similarlty $(F_k, F_n) \mid a_{1n} - a_{in}$. So $p_j \mid a_{1n} - a_{in}$ since $k \neq j \neq n$. Now $(p_j, (F_j, F_n)) = 1$ by Lemma 3 (ii). So $F_n = p_j \cdot (F_j, F_n) \mid a_{1n} - a_{in}$ by Lemma 2. Thus

$F_n \mid |a_{1n} - a_{in}|$. But $|a_{1n} - a_{in}| < F_n$; so $|a_{1n} - a_{in}| = 0$, or $a_{1n} = a_{in}$ contrary to assumption.

Finally we observe that the M true frequencies are unique up to $[F_1, F_2, \ldots, F_I] = p_1 p_2 \ldots p_I \geq B$, the desired bandwidth, by Lemma 3(i).



(Fig. 1)

Remark 1. If M = 1 and I = 2, then $F_1 = p_2$ and $F_2 = p_1$; so $(F_1, F_2) = 1$. And certainly

$$x = a_{11} \bmod F_1 \text{ and } x = a_{12} \bmod F_2$$

is solvable since $(F_1, F_2) = 1 \mid a_{11} - a_{12}$. And clearly the columns of this M x I = 1 x 2 matrix are distinct since they contain only one element. In other words, the theoretical solution given in Theorem 2 for multiple frequencies has as a special case the classical theoretical solution for the single frequency case which makes use of the Chinese Remainder Theorem in which (F_1, F_2) is required to be one.

Remark 2. Theorem 2 allows us to write an algorithm which pairs frequencies with their residues. See the program "mult_sig.f" with subroutine "following the misty trail" written by Diana (the Huntress) Major.

If four IFM receivers with bandwidths F_1 = 3.5.7, F_2 = 2.5.7., F_3 = 2.3.5 measure three noise free signals whose residues (remainders) are recorded in the matrix below,

F_1	F_2	F_3	F_4
(5)	[43]	[29]	(20)
[8]	(40)	36	30
15	50	(26)	[23]

then the remainders can be immediately paired with their proper frequencies by imposing the condition in Theorem 1. (It is, by the way, easy to show that this trail is unique.) So our first "blue" frequency f_1 is the unique solution modulo 210 to the system

$$\begin{aligned} x &= 5 \bmod 105 \\ x &= 40 \bmod 70 \\ x &= 26 \bmod 42 \\ x &= 20 \bmod 30 \end{aligned}$$

or $f_1 = 110$.

Another is the "red" frequency f_2 which is the unique solution modulo 210 to the system

$$\begin{aligned} x &= 8 \bmod 105 \\ x &= 43 \bmod 70 \\ x &= 29 \bmod 42 \\ x &= 23 \bmod 30 \end{aligned}$$

or $f_2 = 113$.

Similarly, $f_3 = 120$.

VI. A SHARP INEQUALITY

The condition $I > M$ imposed on the matrix (1) in Theorem 2, which permits our frequencies to be determined, is the best possible; that is to say, this inequality is sharp. As the next examples show, matrices for which $I \leq M$ may or may not protect a spurious solution.

Example 2. If $I = M$ coose the p's so that $\min \{p_1, p_2, \ldots, p_I\} \geq I$. Then the matrix

$$\begin{bmatrix} 0 & 0 & \cdots & 0 \\ 1 & 1 & \cdots & 1 \\ \cdot & \cdot & & \cdot \\ \cdot & \cdot & & \cdot \\ I-1 & I-1 & \cdots & I-1 \end{bmatrix}_{I \times I}$$

,whose columns are distinct, cannot protect a spurious frequency divides any element in the set $\{0, 1, 2, \ldots, I-1\}$. Therefore the condition of Theorem 1 can never be satisfied except by "row systems".

Example 3. We now show that there is a 5 x 5 matrix which can protect a spurious solution.

Consider the five primes $p_1 = 2 < p_2 < p_3 < p_4 < p_5$. Let F_i, $i = 1, \ldots, 5$, be as defined in Lemma 3 if $I = 5$. Now let

$c_1 = F_1/p_5$, $c_2 = F_1/p_5 + F_1/p_2$, $c_3 = F_1/p_5 + F_1/p_3$,

$c_4 = F_1/p_5 + F_1/p_4$, $c_5 = 0$.

We first observe that all the c's are nonnegative. It is also clear that $c_i < F_i$. For example, since $p_4 < p_5$, $p_4 + p_5 < 2p_5 = p_1p_5$. And so $p_2p_3p_4 + p_2p_3p_5 < p_1p_2p_3p_5$. Thus $c_4 = F_1/p_5 + F_1/p_4 < F_4$.

In general it is true that $0 \leq c_i < F_i$, $i = 1, \ldots, 5$. And so the c_i's are candidates for residues modulo F_i.

We now determine that $(F_i, F_j) \mid (c_i - c_j)$ for $1 \leq i < j \leq 5$. First observe that $(F_1, F_2) = p_3p_4p_5 \mid -p_3p_4p_5 =$ $-F_1/p_2 = F_1/p_5 - (F_1/p_5 + F_1/p_2) = c_1 - c_2$. Similarly $(F_1, F_i) \mid (c_1 - c_j)$, $j = 3, 4$.

Also $(F_1, F_5) = F_1/p_5 \mid F_1/p_5 = c_1 = c_1 - c_5$. And so $(F_1, F_j) \mid (c_1 - c_j)$ for $j = 2, 3, 4\ 5$.

In addition $2 = p_1 \mid (p_3 - p_2)$ since $p_3 - p_2$ is even.

An so $p_1p_4p_5 | p_3p_4p_5 - p_2p_4p_5$. Therefore

$(F_2, F_3) | (F_1/p_2 - F_1/p_3) = (F_1/p_5 + F_1/p_2) - (F_1/p_5 + F_1/p_3) = c_2 - c_3$. Similarly $(F_i, F_j) | c_i - c_j$ for $2 \leq i < j \leq 4$.

Also since $2 = p_1 | (p_2 + p_5)$, we know

$p_1p_3p_4 | (p_2p_3p_4 + p_3p_4p_5)$, or $(F_2, F_5) | (F_1/p_5 + F_1/p_2)$

$= c_2 = c_2 - c_5$. Similarly $(F_i, F_5) | (c_i - c_5)$ for $i = 3, 4$.

Also observe that the c's are distinct. For example, if $c_2 = c_3$, then $p_3p_4p_5 = F_1/p_2 = F_1/p_3 = p_2p_4p_5$, or $p_3 = p_2$ which is not the case.

So we conclude that the 5 x 5 matrix,

$$\begin{bmatrix} c_1 & c_1 & \cdots & c_1 \\ c_2 & c_2 & \cdots & c_2 \\ \cdot & \cdot & & \cdot \\ \cdot & \cdot & & \cdot \\ c_5 & c_5 & \cdots & c_5 \end{bmatrix}$$

whose columns are distinct, protects a spurious solution along the left diagonal.

This example inspires the following proposition whose proof would now be pretentious.

Proposition. Consider the I primes $p_1 = 2 < p_2 < p_3 \quad \cdots < p_I$. Let F_i, $1 \leq i \leq I$, be defined as in Lemma 3. Set

$c_1 = F_1/p_I$, $c_2 = F_1/p_I + F_1/p_2$, $c_3 = F_1/p_I = F_1/p_3$, ... ,

$c_{I-1} = F_1/p_I + F_1/p_{I-1}$, $c_I = 0$.

Then the I x I matrix

$$\begin{bmatrix} c_1 & c_1 & \cdots & c_1 \\ c_2 & c_2 & \cdots & c_2 \\ \cdot & \cdot & & \cdot \\ \cdot & \cdot & & \cdot \\ c_I & c_I & \cdots & c_I \end{bmatrix}$$

has distinct columns and protects a spurious solution along the left diagonal.

Since square matrices of the types presented in Example 2 and the Proposition can sit comfortably inside a matrix for which $I<M$, solutions cannot be excluded for certain from (1) unless $I > M$, But, of course, they do not necessarily exist.

VII. Coffeehouse Mathematics

!. No man cometh unto the Father except by me [3].

Not only is the condition $I > M$ the best possible for the F_i's selected as in Lemma 3, there is also some evidence that these are the only bandwidths (up to a constant) which permit the frequencies to be determined. This is certainly the case when $M = 2$ and $I = 3$.

Before establishing this let us first recall that $[a,b] = ab/(a,b)$; e.g., if $a = 6$ and $b = 15$, then $30 = 90/3$. This will help us to prove

Theorem 3. If $M = 2$ and $I = 3$ and there are no spurious solutions, then $F_1 = up_2p_3$, $F_2 = up_1p_3$ and $F_3 = up_1p_2$ where the p's are three numbers which are pairwise prime and $u = (F_1, F_2, F_3)$.

Proof: We assume first that $(F_1, F_2, F_3) = 1$. We now show that $[(F_1, F_2), (F_2, F_3)] \leq F_2$. Set $d_1 = (F_1, F_2)$ and $d_2 = (F_2, F_3)$. Then $d_1 | F_2$ and $d_2 | F_2$. So F_2 is a common multiple of d_1 and d_2.

So $F_2 \geq [d_1, d_2]$.

Also we have

$[(F_1, F_2), (F_2, F_3)] = (F_1, F_2).(F_2, F_3)/((F_1, F_2), (F_2, F_3))$

$= (F_1, F_2).(F_2, F_3)/(F_1, F_2, F_3) = (F_1,F_2).(F_2, F_3)$.

So $1 \leq (F_1, F_2).(F_2, F_3) = [(F_1, F_2), (F_2, F_3)] \leq F_2$. (i)

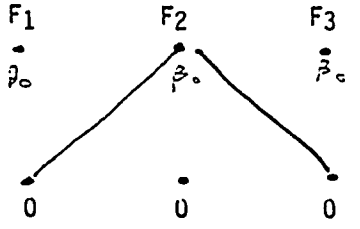
Similarly $1 \leq (F_1, F_2).(F_1, F_3) = [(F_1, F_2), (F_1, F_3)] \leq F_1$ (ii)

and $1 \leq (F_2, F_3).(F_1, F_3) = [(F_2, F_3), (F_1, F_3)] \leq F_3$ (iii)

Suppose the right hand inequality of one of these three strings is strictly less than. Without loss of generality suppose $1 \leq [(F_1, F_2), (F_2, F_3)] < F_2$. Now $[(F_1, F_2), (F_2, F_3)]$ is a candidate for a nonzero residue modulo F_2. Set

$\beta_o = [(F_1, F_2), (F_2, F_3)]$.

Then the system



protects a spurious solution indicated by the red line since

$(F_1, F_2) \mid -[(F_1, F_2), (F_2, F_3)] = 0 - \beta_o$

and $(F_2, F_3) \mid [(F_1, F_2), (F_2, F_3)] = \beta_o - 0$.

So we conclude that

$$F_1 = (F_1, F_2)\,(F_1, F_3)$$
$$F_2 = (F_1, F_2)\,(F_2, F_3)$$
$$F_3 = (F_2, F_3).\,F_1, F_3)$$

Set $p_1 = (F_2, F_3)$, $p_2 = (F_1, F_3)$ and $p_3 = (F_1, F_2)$. As we have seen above, $(p_i, p_j) = 1$ for $i \neq j$.

Now let $(F_1, F_2, F_3) = u$. The $(F_1', F_2', F_3') = 1$ where $F_1' = F_1/u$, $F_2' = F_2/u$ and $F_3' = F_3/u$. A spurious system over F_1, F_2, F_3 is also one over F_1', F_2', F_3'. And by the above argument $F_1' = p_2' p_3'$, $F_2' = p_1' p_3'$ and $F_3' = p_1' p_2'$ for some pairwise prime set $\{p_1', p_2', p_3'\}$.

Therefore $F_1 = up_2' p_3'$, $F_2 = up_1' p_3'$ and $F_3 = up_1' p_2'$.

2. At most one black sheep is a square pen [4].

In view of the fact that a spurious frequency cannot be the solution to a system having two congruences fromthe same row we conclude that the matrix (1) can protect at most I! spurious solutions when I = M. There is some evidence that this bound is unreasonably high, that in fact a square matrix can protect at most one spurious frequency. This is certainly the case when I = M = 3. To demonstrate this we will find it convenient to relabel the constants in matrix (1) as

α_1 β_1 γ_1

α_2 β_2 δ_2

α_3 β_3 δ_3

The 6 = 3! possible spurious solutions are represented below in Figure 1, 2, and 3

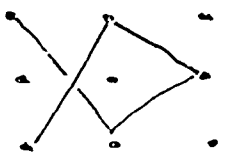


Fig 1

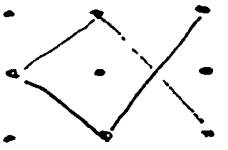


Fig 2

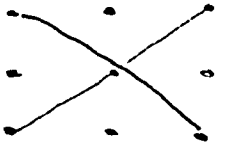
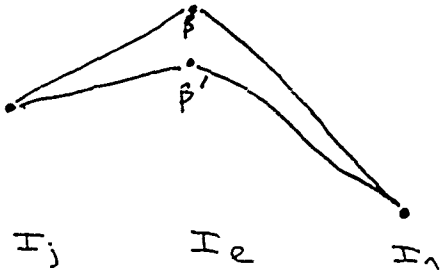


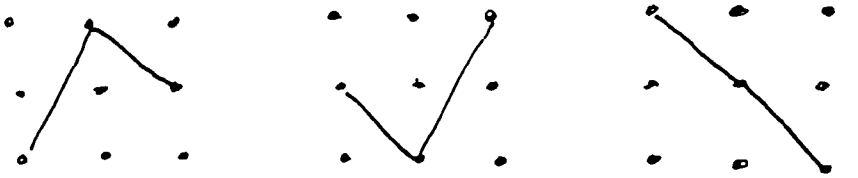
Fig 3

But in any matrix if a point is connected to two points, then these two points cannot themselves be connected to a third diffferent from the first. For consider



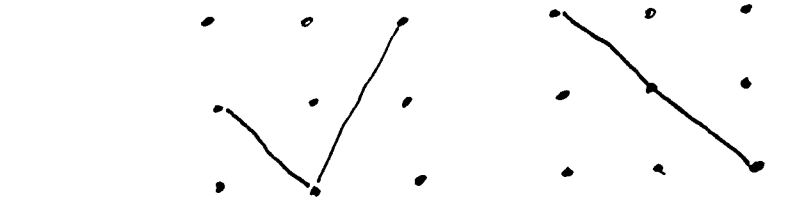
Then we have $(F_j, F_1) \nmid \beta - \beta'$ and $(F_1, F_m) \nmid \beta - \beta'$ since row points are automatically connected. So $F_1 \mid\mid \beta - \beta' \mid < F_1$, a contradiction.

In view of this the 6 possible spurious solutions in Figures 1, 2, and 3 cannot coexist in pairs as shown. In Figure 1, for example, α_3 is connected to β_1 and β_3 which are themselves connected to γ_2. Without loss of generality we now need only consider the red systems:



(a) (b) (c)

Now observe that the systems (a) and (b) cannot coexist. If so, then α_3 is connected to β_1 and β_3 which are themselves connected to γ_1. Without loss of generality we may now consider only



(b) (c)

But (b) and (c) cannot coexist either. If so, then α_2 is connected to β_2 and β_3 which are themselves connected to γ_3. So a 3 x 3 can protect at most one spurious frequency.

RECOMMENDATIONS

(a) Single frequency with noise

Take M = 1 and I = 3. Then we have bandwidths $F_1 = p_2p_3$, $F_2 = p_1p_3$ and $F_3 = p_1p_2$, where p_1, p_2 and p_3 are pairwise prime. Let α_C, β_C and γ_C be the computed values of a single frequency's residues modulo F_1, F_2 and F_3. If α_T, β_T and γ_T are the true values of this frequency's residues, then we know

$$\begin{aligned} x &= \alpha_T \bmod F_1 \\ x &= \beta_T \bmod F_2 \\ x &= \gamma_T \bmod F_3 \end{aligned} \qquad (3)$$

and that

$$\begin{aligned} &(F_1, F_2) \mid \alpha_T - \beta_T \\ &(F_1, F_3) \mid \alpha_T - \gamma_T \\ &(F_2, F_3) \mid \beta_T - \gamma_T \end{aligned} \qquad (4)$$

by Theorem 1.

The three conditions on the true residues given in (4) would have gone unnoticed by us had we simply used the Chinese Remainder Theorem since $(F_i, F_j) = 1$, $1 \leq i < j \leq 3$, in this case. But they could very well show us how to correct the perturbations on the residues α_T, β_T and γ_T caused by noise.

At first there seems to be insufficient information to determine the frequency. Suppose that it so happens that

$$(F_1, F_2) \mid ((\alpha_C - \beta_C)) + 1 \qquad \text{(i)}$$
$$(F_2, F_3) \mid ((\beta_C - \gamma_C) - 1) \qquad \text{(ii)}$$
and $$(F_1, F_3) \mid (\alpha_C - \gamma_C) \qquad \text{(iii)}.$$

By (i) $\alpha_T = \alpha_C + 1$ and $\beta_T = \beta_C$
or $\beta_T = \beta_C - 1$ and $\alpha_T = \alpha_C$
and not both.

By (ii) $\beta_T = \beta_C - 1$ and $\gamma_C = \gamma_T$
or $\gamma_T = \gamma_C + 1$ and $\beta_T = \beta_C$
and not both.

So $\alpha_T = \alpha_C + 1$, $\beta_T = \beta_C$, $\gamma_T = \gamma_C + 1$ or $\alpha_T = \alpha_C$, $\beta_T = \beta_C - 1$, $\gamma_T = \gamma_C$.

Substituting these values in (3) we conclude that the frequency is precisely one of at most two values. And if these values are indeed distinct, the distance between them is often huge because of a "butterfly effect" that results from a small perturbation of the residues. The trick is to roll with this punch, that is, to choose the p's initially so that all possible false values are flung outside a desired bandwidth. This can be done when q = 1. But time did not permit the investigation of larger q's.

But there is another way to proceed without scrutinizing the p's so jealously. Theorem 3 suggests that the F's in Theorem 2 can share a constant multiple. This is in fact the case when this constant is pairwise prime to the p's. So it can bechosen to be 4q+1 since we, of course, select the p's as well. With 4q+1 as a common factor of each F we can now mimic the argument in [1] to get a similar result but with much less precision. But recall we know that the frequency is precisely one of at most two values. This combination of ambiguity and vagueness will permit us to determine the precise frequency <u>if the error is large enough</u> - the error, of course, caused by the butterfly effect.

The argument above permits a simple geometric analogy. If we know a point x is either the point y or z, and we know x is within a given circle of diameter D;then we can determinex precisely if the distance between y and z is greater than D.*

~~* This is a variation of the pigeon~~ hole principle.

But to what end? Why this neurotic need for precision when the procedure described in [2] is sufficient to avoid catastrophic error?

(b) Multiple frequencies with noise

It is because in the multiple frequency case we are haunted by the fact that a solution, which we have carefully found with sufficient precision, could very well be spurious. (See section IV.) Of course to avoid spurious solutions we can always change the F's to (4q+1 times) those used in Lemma 3.* But in mimicing the argument used in [2] for these new F's we lose precision and sometimes this loss is catastropic. To recover it we can repeatedly apply the method described above in section VIII (a) to correct the residues of multiple frequencies. This procedure would give the precise values of true frequencies even when noise is present.But in order for it to be carried out the false solutions mentioned in section VIII (a) would have to avoid more and more circles. And, of course, whether or not they accommodate us is a matter of chance.

Any future research should use this approach to generalize our mult_sig.f program to control noise.

* in order to distinguish the column elements when noise is present we would require that $|a_{mi} - a_{ni}| > 2q$.

REFERENCES

1. McCormick, William S., Tsui, James B. Y. and Bakke, Vernon L., "A noise insensitive solution to a simultaneous congruence problem in real time spectral estimation", IEEE (to appear)

2. McCormick, William S., "Resolution of a 2π ambiguity problem in multiple frequency spectral estimation", Signal Processing (to appear)

3. John 14:6

4. Orwell, George, Animal Farm.

1989 USAF-UES SUMMER FACULTY RESEARCH PROGRAM

Sponsored by the

AIR FORCE OFFICE OF SCIENTIFIC RESEARCH

Conducted by the

Universal Energy Systems, Inc.

FINAL REPORT

LADAR TARGET DETECTION AND RECOGNITION

Prepared by:	Dr. R. H. Cofer
Academic Rank:	Associate Professor
Department and University:	Electrical Engineering Florida Institute of Technology
Research Location:	WRDC/AARA Wright Patterson AFB Area B, Bldg. 23 Dayton, OH 45433-6543
USAF Researcher:	Jim Leonard
Date:	18 Aug 89
Contract No:	F49620-88-C-0053

LADAR Target Detection and Recognition

by
Dr. R. H. Cofer

ABSTRACT

LADAR has served as the focal point for this Summer Research Program into performance improvement of model matching forms of automatic target detection and recognition. The key result obtained is a theoretically encompassing strategy of probabilistic evidence accumulation based upon optimal use of readily available 3-D target and sensing phenomenology modeling. Utilities of the strategy lie in such areas as: fusion of spatial data within and across sensors, indexing or final evidence accumulation within the ongoing AF SAR Expert System test bed development, detection and recognition at extreme ranges where optimal performance is critical, and in developing upper performance bounds for specific ATR problem domains.

Significant results were also achieved at a more physical level, as well. A detailed breakdown of the above theory in terms suitable for the LADAR problem is given. A mini-SAR Expert System computer environment has been developed on the SUN work station in advance support of continuing Research Initiation Program research and ultimate integration of code into the AF SAR Expert System work bed. Quantities of LADAR data has been rehosted to this new environment to improve accessibility. Finally initial exploratory concepts have been formulated to improve overall executability of the concepts advanced.

Acknowledgements

I wish to thank the Air Force Systems Command and the Air Force Office of Scientific Research for sponsorship of this research. Universal Energy Systems must be mentioned for their smooth and timely administration of this program.

My experience was particularly rewarding and enriching because of the cutting edge research environment provided by the Target Recognition Technology Branch of the Air Force Avionics Laboratory under sensitive leadership of Mr Paul Johnson. The richness of this environment was much more a function of the assembled expertise than of the material environment. Mr Jim Leonard, my USAF research colleague, has a unexcelled intuitive understanding of advanced probability theory. He was constantly ready at all times in all matters, large and small, to insure the maximum progress possible. Dr. Zelnio, the cognizant group manager, exhibits a very rare blend of management skill underscored with considerable facilitating wit and humor. Furthermore his 'right on' technical vision will do much to mature Automatic Target Recognition technologies to serve as a very significant future AF force multiplier. Mr Dan Kinser, worked tirelessly to develop the best possible portable software environment for my continued research activities throughout the remainder of the academic year. He also improved my UNIX skills immeasurably and with graceful patience. Mr Kevin Willey was most helpful in explaining features of the SAR Expert System. Mr Bill Foley spent many lunchs describing intricacies of FLIR modeling. Mr Vince Velten, Mr Marty Justice, Mr Lloyd Clark, Dr John Spicer, Mr Mike Bryant and Mrs Mary Jarratt all provided helpful information as well.

I INTRODUCTION

All branches of the military have requirements for rapid reliable battlefield tactical target detection and recognition capability. Characteristics of these targets are that they are generally vehicular, sometimes seen through partial obscuration, and may be camouflaged.

CO_2 LASER Radar (LADAR) perhaps has the highest potential for rapid reliable battlefield tactical target detection and recognition. It is multi functional, supplying absolute or modulo range to target, reflectance of target, and target Doppler. It is often operated in pixel registration with FLIR to detect target thermal emissions.

LADAR Automatic Target Recognition (ATR) algorithms have to date been ad hoc, although the Target Recognition Technology Branch of the Avionics Laboratory has been developing a more general AI model based/hypothesis reasoning approach called SAR Expert System. The SAR Expert System is proving useful against synthetic Aperture Radar but has not yet been extended to the realm of LADAR ATR. The purpose of this summer research program has therefore been directed toward that aim.

My long standing research interests support hypothesis reasoning approaches to automated vision, based upon first principle considerations. Prior to this Summer Research Program, I had developed precursor hypothesis testing approaches for the detection of extended targets in Synthetic Aperture Radar. This allowed a speedy transition into investigation of evidence gathering for LADAR and FLIR ATR along the advanced model matching/hypothesis reasoning paradigm.

II OBJECTIVES OF THIS RESEARCH EFFORT

The initial and final objectives of this research effort were determined to be:

A INITIAL Advance the state of art in LADAR target detection and recognition technology by development of new and pertinent algorithms.

FINAL Advance the state of art in evidence accumulation within the SAR expert System paradigm with emphasis upon LADAR forms of imagery while avoiding duplication of ongoing AF research.

B INITIAL & FINAL Checkout of SAR Expert System Test bed flexibility to receive new alternate sensor and problem types.

C INITIAL Speed and consolidate LADAR target detection and recognition research by transfer to the AF SAR Expert System Test bed.

FINAL Pending stabilization and documentation of the AF SAR Expert System, develop a mini-SAR Expert System computer environment on the Sun Work station suitable for continuing independent research and easy integration of results into the SAR Expert System at a later date.

D INITIAL & FINAL Make independent third party recommendations for improvements and modifications to the SAR Expert System test bed to enhance its overall reliability, flexibility, friendliness, and or power.

Variation between initial and final objectives were a matter of tuning during the effort as discussed in the following section.

Sections III through V document the successful completion of each of the above goals. The stage is now properly set for actual development of a high performance LADAR target detection and recognition capability during the ensuing follow on Research Initiation Program Phase. Superior LADAR ATR performance may be expected at the conclusion of this next phase of research, especially at the critically longer ranges.

III OVERALL RESEARCH APPROACH TAKEN

Because the Target Recognition Technology Branch of WRDC is conducting and managing considerable ongoing research activities in the area of model matching approaches to ATR, the initial thirty percent of this Summer Research Program has been utilized to become acquainted with these ongoing efforts. The goal was to come up to speed, avoid duplication of effort, and provide new results in needed areas.

The key efforts to become acquainted with were the SAR Expert System projects. This was accomplished by review of all existing technical documentation and related papers, holding extended technical discussions with key contractors and AF laboratory engineers, attending SAR Expert System related meetings, and exercising the user interface of the preliminary delivered system itself. Two key facts emerged to all concerned. First the system, not yet near final delivery, was not yet stable enough nor documented well enough to support immediate heavy direct use by an independent researcher for some time. This fact resulted in modification of Objective C, as detailed above, to set up an alternate interim research computer environment on the same

machine and operating environment. The second and more important fact that emerged was that there was considerable room for detailed theoretical investigation of better or more optimal means of evidence accumulation. Grasping the opportunity, it was agreed (with further reasoning as documented below) to modify Objective A as shown above.

The second set of efforts to become acquainted with was that of LADAR specific ATR efforts. The first of these was a prior Summer Faculty effort showing how to segment LADAR range imagery via use of concurrent Doppler, if the targets were moving. This review showed that the existing body of LADAR imagery would need to be rehosted to the Sun work station environment to meet Objective C above. The other efforts to become acquainted with were larger, nearly completed contractual efforts to develop practical ATR LADAR techniques. Again existing technical documents were reviewed, contractor technical personnel gave briefings at WRDC and their own facility and a physical inspection of representative sensors themselves followed. These reviews showed that quite a body of reasonably efficient (in terms of performance accuracy and execution speed) ad hoc LADAR ATR algorithms had already been developed for reasonably near range conditions. This provided additional impetus to modify Objective A to the provision of a more general formulation for LADAR ATR which could more generally integrate into the index-hypothesis interactions of the SAR Expert System concept.

With the final objective structure now firmly in place, it became time to set up approaches toward their solution. The satisfaction of Objective A was deemed to be largely an individual effort based upon a breakdown of probabilities required by Bayesian decision processes. The very successful

results of this effort, largely documented below in Section IV, was favorably briefed within the Target Recognition Technology Branch. Two Target Recognition teams will be incorporating several of the concepts advanced into their own immediate research activities against FLIR and LADAR imageries.

Satisfaction of Objective B was completed rather easily, since unfortunately the final code of the SAR Expert System project will not be delivered or documented for some time. This, of course, forced modification of Objective C as discussed above. The development of an alternate mini-SAR Expert System capability on the Sun Work station with incorporation of LADAR imageries was carried out with the help of laboratory personnel and is discussed in more detail in Section V below.

This report constitutes final satisfaction of Objective D via the theory of Section IV and the recommendations of Section VI. Other directly related activities were the holding of informal discussions, semi-formal briefings, demonstration of a high performance minisupercomputer well suited for hosting of future SAR Expert Systems, setting up of toy but highly informative "problems" illustrating the theory, and discussing relevancies for new in house research.

IV THEORETICAL DEVELOPMENT

The following is an account of the theoretical development accomplished this Summer Research Period. It is the theoretical account of probability space breakdown in support of Bayesian ATR. Not all development could be included here. Further breakdown in support of the LADAR/FLIR ATR problem,

examples, and a table showning the potential error range in assuming independence have been documented elsewhere.

IV.1 PROBABILITY SPACES, THE HOLDERS OF EVIDENCE IN ATR PROBLEMS

Let $(S,\mathcal{E},P)$ be a probability space where

S is some countable set of points (hereafter equivalently called the sample or outcome set or space in accordance with common practice),

$\mathcal{E}$ is the set of all subsets of S (each subset is hereafter called an event. Also $\mathcal{E}$ is called the event space),and

P is a real valued function $P:\mathcal{E}\rightarrow E_1$ (hereafter written as $P(e|S)$, $e\in\mathcal{E}$, and termed the probability of e conditioned on S, or simply p(e) when no confusion will arise)

such that

Axiom 1 $P(a)\geq 0$ for every $a\in\mathcal{E}$,

Axiom 2 $P(S)=1$,

Axiom 3 If $a_1,a_2,a_3,\cdots$ are mutually exclusive (i.e. $a_i\cap a_j=0$, $i\neq j$) events, then

$$P(\cup a_i)=\sum P(a_i)$$

It can be somewhat surprising that these three axioms are all that is needed to generate all of the properties that a probability function can have. The entirety of probability theory is thus simply the study of the logical consequences of these three axioms. This in turn has profound consequences for the entire ATR arena which therefore rests in totality on a slender tripod of three simple axioms.

IV.2 RANDOM VECTORS OR, IN ATR PARLANCE, FEATURES

Let $(S,\mathcal{E},P)$ be a probability space. An n-dimensional vector X is a vector valued function $X:S\rightarrow E_n$. Then $(E_n,\mathcal{E}_n,P_X)$ is a new probability space induced by the random vector, or feature, X, when

> E_n is the range space of X (hereafter called the sample space of the random vector X),
>
> $\mathcal{E}_n$ is the set of all subsets on E_n (each such subset is called an event on E_n. Also $\mathcal{E}_n$ is called the event space of the random vector X),
>
> P_X is a real valued function $P_X:\mathcal{E}_n\rightarrow E_1$ (hereafter written as $P_X(e|E_n)$, $e\in\mathcal{E}_n$, and termed the probability of e conditioned on E_n, or simply written as $P_X(e)$ or even P(e) when noconfusion will arise) such that
>
> $$P_X(e)=P(s \text{ such that } X(s)\in e|S), \quad \text{for} \quad \text{every } e\in\mathcal{E}_n.$$

The proof that $(E_n,\mathcal{E}_n,P_X)$ is a probability space follows from the definition of probability spaces.

From fundamental considerations the probability of any random

vector, or feature, is given as

$$P_X(x|E_n) = \sum_{s\in S_X} P(s|S), \quad \text{where } S_X = \{s\in\mathcal{L}\,|\,X(s)=x\}.$$

IV.3 EVIDENCE COMBINATION OF RANDOM VECTORS, OR OF FEATURES

Let $(S,\mathcal{L},P)$ induce the probability spaces $(E_n,\mathcal{L}_n,P_X)$, $(E_m,\mathcal{L}_m,P_Y)$ individually for the random vectors or features, X and Y. What is their combined store of evidence? It is defined as the new probability space $(E_{mn},\mathcal{L}_{mn},P_{XY})$ where

$$E_{nm} = E_n \times E_m,$$

$$\mathcal{L}_{nm} = \text{event space of } E_{nm}, \text{ and}$$

$$P_{XY}:\mathcal{L}_{nm}\longrightarrow E_1 \text{ where}$$

$$P_{XY}(x,y|E_{nm}) = P(s \text{ such that } X(s)=x \text{ and } Y(s)=y\,|\,S),$$
$$\text{for every } x\in E_m \text{ and every } y\in E_n.$$

In the new evidence accrual space $(E_{mn},\mathcal{L}_{mn},P_{XY})$, the case that the original random vector or feature X takes the value x is the event $\{xxy\,|\,x\in E_m, \text{all } y\in E_n\}\in\mathcal{L}_{mn}$, and is defined as $x\in\mathcal{L}_{mn}$. The case that the original random vector or feature Y takes the value y is the event $\{xxy\,|\,\text{all } x\in E_m, y\in E_n\}\in\mathcal{L}_{mn}$, and is defined as $y\in\mathcal{L}_{mn}$. The event (x,y) is defined as the singleton set $\{xxy\,|\,x\in E_m, y\in E_n\}\in\mathcal{L}_{mn}$, and is the combined evidence of the fact that the random vectors X and Y simultaneously take on values x and y respectively. When the values x and y can not coexist, the event (x,y) is quite reasonably the null set.

Thus two random vectors X and Y have at all times the joint probability P_{XY} in the probability space $(E_{nm}, \mathcal{E}_{nm}, P_{XY})$ of

$$P_{XY}(x,y \mid E_{nm}) = \sum_{s \in S_{XY}} P(s \mid S), \quad \text{where } S_{XY} = \{s \in \mathcal{E} \mid X(s)=x, Y(s)=y\}.$$

IV.4 INDEPENDENCE IN EVIDENCE ACCRUAL

The random vectors X and Y are defined throughout statistics as independent iff

$$P_{XY}(x,y \mid E_{nm}) = P_X(x \mid E_n) \cdot P_Y(y \mid E_m)$$

for all $x \in E_m$ and all $y \in E_m$, otherwise they are dependent. As a corollary, no combination of events existing in the sample space itself can be independent.

This simplifies to

$$P_{XY}(x,y \mid E_{nm}) = \sum_{s \in S_X} \sum_{t \in S_Y} P(s \mid S) \cdot P(t \mid S)$$

where $S_X = \{s \in \mathcal{E} \mid X(s)=x\}$ and $S_Y = \{t \in \mathcal{E} \mid Y(t)=y\}$,
and for all x and all y

Remembering the general definition of joint probability from above, we have in this case of independence the relation

$$\sum_{u \in S_{XY}} P(u \mid S) = \sum_{s \in S_X} \sum_{t \in S_Y} P(s \mid S) \cdot P(t \mid S), \text{ for all values of X and Y}$$

which is a *very curious* result indeed. Conceivably the relations between the sets S_{XY}, S_X and S_Y could be quite

complex but yet the probabilities defined on these sets must *always* obey a very simple multiplicative relationship. This so stretches one's credulity that he is forced to wonder just what lies underneath the surface of probabilistic independence to cause such a remarkable result. What I've found is surprisingly simple, matches one vague intuition of what's going on in nature, but is not discussed in any statistics text I've ever seen.

What I can see is that if two or more random vectors are independent, the underlying experiment sample space S is an inferred composite from other yet more basic underlying sample spaces. Assume that one has two totally distinct and separated experiments on sample spaces Q and R with both ongoing at the same time. Assuming he wishes to refer to them jointly as a single experiment on a sample space S, how is he to do it? The answer is to array the elements of Q into one sub space and R into a different and distinct sub space of S. Thus the mutually exclusive nature of the elements of the the new composite sample space S is maintained even though S is referring to two constituent underlying experiments which are decidedly not mutually exclusive. The question then arises as to what probabilities to assign to the elements of S? The historical answer as given above: the product of the probabilities of the two points in Q and R that made up the corresponding point in S[1]. Thus a much more pleasing mathematical definition of probabilistic independence than the relatively uninformative answer above is:

---

[1] Thus foreordaining the logarithmic form of information in information theory

Two different collections of events, whether you want to call them random variables or not, are defined as independent of each other only if they are each full projections onto different non overlapping sub spaces of a composite sample space. The above equation of independence follows automatically. Any and all other cases will certainly (well, almost certainly) result in non independence.

IV.5 POTENTIAL NON INDEPENDENCE OF EVIDENCE ACCRUAL

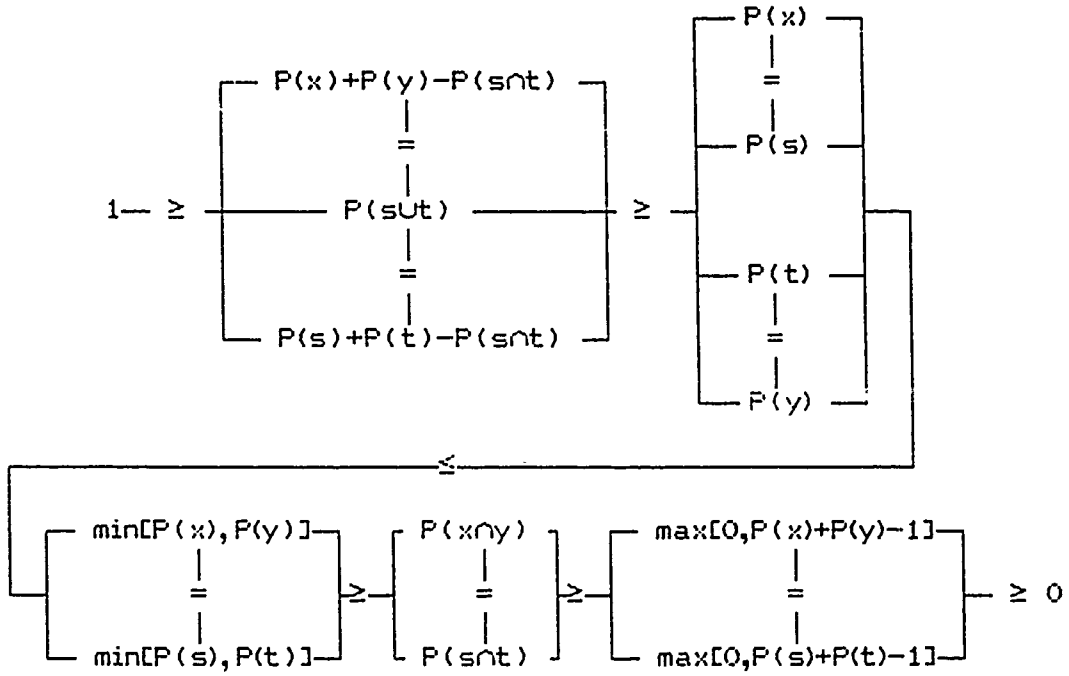
A little thought here will provide much revelation. Independence refers to different slices through S perpendicular to sub spaces of S. Logically; therefore, non independence refers to all other cases such as incompleted projective slices and or slices not perpendicular to sub spaces of S. In yet other words, non independence is the viclation of the orthogonality principal of evidence accrual by probability spaces.

Probabilistic independent projections are formed by nested integrals or sums — one per axis with fixed limits each. Probabilistic dependent projections are again formed by nested integrals or sums, again with one per axis. This time the limits of one or more of the outer integrals is dependent upon inner integrals — which force great analytic difficulties which are best avoided when possible. We presently discuss cases where analytic solutions can be found.

IV.6 POSSIBLE ERRORS INDUCED BY ASSUMPTIONS OF INDEPENDENCE

DURING EVIDENCE ACCRUAL

How far wrong can one go if he assumes independence of random vectors during evidence accrual when in fact they may be dependent. That is, mathematically, what is the relation of an arbitrary general space integral to its arbitrary perpendicular projection on different sub spaces? If one random variable X has the value x, then the probability P(x) is P(s|S) where s is the event {s|X(s)=x}. If the other random variable Y has the value y, then the probability P(y) is P(t|S) where t is the event {t|Y(t)=y}. This interpretation leads to the following inequality structure



Extracting the least upper bound and greatest lower bound on P(x,y), we have

$$\min[P(x),P(y)] \geq P(x \cap y) \geq \max[0,P(x)+P(y)-1]$$

which holds whether X and Y are independent or not. The ratio

$$\aleph = \frac{P(x)\cdot P(y)}{P(x,y)}$$

gives the multiplicative factor by which the evidence accrual can be in error due to an assumption of independence. This ratio is bounded as

$$\frac{P(x)\cdot P(y)}{\max[0,P(x)+P(y)-1]} \geq \aleph \geq \frac{P(x)\cdot P(y)}{\min[P(x),P(y)]}$$

and numerically evaluated in the following figure. Note that X and Y are independent always for the special cases

$$P(x)=0, \text{ any } P(y)$$

$$\text{any } P(x), P(y)=0$$

$$P(x)=1, P(y)=1$$

as $\aleph$ takes the value 1 in these cases. Also note that the matrix of results has a row-column replacement symmetry.

As a typical example, if P(x)=0.5 and P(y)=0.8, then one sees result: $0.5 \leq \aleph \leq 1.33$. This is the range of potential evidence accrual errors during the combination of the fact that x and y were seen with marginal probabilities of P(x)=0.5 and P(y)=0.8 <u>assuming</u> <u>independence</u>. That is, the probabilistic evidence combination, assuming independence, can never be lower than 1/2 the correct answer and never higher than 1.33 times the correct answer.

Such knowledge of error possibilities can often be heuristically used in an AI sense to decide whether it is

worth going after the more costly general calculation of P(x,y) under the assumption of dependence. For example, a simple inspection of the final Bayesian decision could show that the possible error introduced would not affect the ATR result, If the Bayesian likelihood ratio value under an assumption of X, Y independence is Z and the Bayesian threshold is T, then if both Z/δ_{max} and z/δ_{min} are jointly $\geq$ or $\leq$ T, then the assumption of independence of X and Y can cause no decision error.

Obviously there must be an error at times between assuming and not assuming independence. What is surprising is that the error range can be found to be well within bounds based upon trivially easy data to obtain. I believe that there are other simple data which can provide better bounds yet and thus will be of use in those cases where the above bound analysis is too loose. This thread will be picked up at the initiation of the next effort. Results are anticipated that will further reduce all unnecessary calculation while upholding the maximum of decision accuracy.

V DEVELOPMENT OF MINI SAR EXPERT SYSTEM ENVIRONMENT

The SAR Expert System paradigm is the current conceptual culmination of the collective expertise of highly experience Target Recognition Technology Branch engineers. As such, it lies at the heart of ongoing and future research activities sponsored by the lab. Initially, it was thought that the results of this Summer Research Program should be directly embedded into the current code of the SAR Expert System. However; the SAR Expert System is so cutting edge that the code has not had a chance to stabilize or be documented. Upon much consultation with lab personnel, it was decided to

set up an alternate but more controllable environment. This mini-SAR Expert System environment should echo important concepts of the SAR Expert System to in turn allow easy later integration of results.

Supporting goals were set up. The system was to be UNIX based, reside on the popular Sun work station, be coded in C, be user friendly with SAR Expert System like mouse/window user interfacing, allow use of the standard CVL image format, and include a library of ported LADAR images.

The laboratory generously made 50% availability of Dan Kinser to carry out the body of the effort with myself serving in the role of an advisor/team member. Much effort by both were expended in insuring an understanding of the SunTool, SunWindow, SunCore programming environment for managing the mouse, windowing, and 3-D rendering environments. Then starting from an existing piece of imaging code, a highly user friendly environment was developed to :

Access images by scene or sensor

Zoom and pan any selected image by mouse selected values

Manipulate with great flexibility the color rendition of the image

Manually segment the scene for further detailed analysis

Store and retrieve prior scene segmentations

Display segmented data in 3-D form, with adjustable lighting and surface shadings (to be fully completed subsequent to this final report submission)

Perhaps the most important point of this software is that it is designed to be extremely researcher friendly and extendable. The existing code is in line documented with examples of how to manipulate all features of the user interface. The image file interface is developed on the standard and powerful CVL format so as to allow input of new data from other sources and as partial products of prior processing. The researcher can now easily add new problem specific code in a standard language, against a standard scientific operating system, and on a well know and popular work station. These latter three factors will be particularly important when it comes time to migrate to the SAR Expert System itself.

A copy of the mini-SAR Expert System is being carried by to Florida Institute of Technology for continued research during the academic year. It is expected the the Target Recognition Lab and myself will forward updated versions periodically.

VI CONCLUSIONS AND RECOMMENDATIONS

A very general framework has been developed for breaking down the probability generation problem in Bayesian ATR. Using this framework, one can introduce new state variables of nature to allow increased use of the mathematical regularities of conditional independence and conditional mutual exclusiveness. As a result, it was seen how to develop conditional independence between LADAR and FLIR registered imagery, find independent target features for the SAR Expert System, handle forms of obscuration and rigorously incorporate sensor, sensor platform, atmospheric, and target modeling into the probabilistic calculation.

It is recommended that this promising research be continued along both theoretical and practical lines via the Research Initiation Program and other means. Theoretically, further effort should be expended in basic research on probabilistic characterization of background; maximum likelihood selection of state variable values; and execution speedup through use of sufficient statistics, sub domain selection, and numeric approximations. Practically speaking, further effort should be expended in developing upper ATR performance bounds for ad hoc techniques; developing probabilistic indexing and final evidence accumulation code for the SAR Expert System test bed; developing probabilistic sensing models for the LADAR and FLIR target environments and testing them against sensor noises backed out from real data; implementing LADAR/FLIR probabilistic data fusion along the lines advanced; and developing pure Bayesian ATR techniques for the critical longer ranges. Some thought should also be paid to transfer to a minisupercomputer as host test bed hardware for model matching/hypothesis reasoning. It can, for example, speed 3-D target modeling by one to two orders of magnitude.

1989 AFOSR SUMMER FACULTY RESEARCH PROGRAM

GRADUATE STUDENT RESEARCH PROGRAM

Toolbox for Image Processing using
Distributed Computing

Sponsored by the

AIR FORCE OFFICE OF SCIENTIFIC RESEARCH

Conducted by the

Universal Energy Systems, Inc.

FINAL REPORT

Prepared by:	Larry A. Crum, Ph.D.	Michael A. Costarella
Academic Rank:	Professor	Graduate Student
Department:	Computer Science & Engineering	Computer Science & Engineering
University:	Wright State University	Wright State University

Research Location: Wright Avionics Lavoratory
Wright-Patterson AFB
Dayton, Ohio

USAF Researcher: Louis Tamburino, Ph.D.

Date: 11 Nov 89

Contract No: F9620-88-C-0053

Toolbox for Image Processing using Distributed Computing

Prof. Larry Crum and Graduate Student Michael Costarella

Abstract

Introduction

Present learning algorithms are highly computation intensive. Requirements for computer time severly limits practical application. Whereas computers can be expected to significantly improve in speed, speed increases alone cannot provide the orders of magnitude increases needed. Highly parallel computation will be necessary to render learning as a practical reality in systems. Transputers provide the most reasonable environment to study and develop new high speed alternatives.

The summer program provided an opportunity to be introduced to transputer networks and physical options for their usage, programming in OCCAM II and in higher level languages which have translators to OCCAM II, tools which are becoming available to develop and implement transputer algorithms, and some perspective on present applications of transputers. A variety of well-known image processing algorithms was viewed in terms of effective implementation on transputers. Initial work on a set of tools for Image processing was begun.

Focus

The focus of our research is to consider aspects of data distribution throughout various topologies of transputer networks. Hopefully methods suitable for use in the implementation of a collection of "parallel" image processing algorithms can be developed. These will be combined with a number of other software subsystems to create an adaptive vision system built on transputer technology.

Research commenced with familiarization with transputer architecture and programming environments. An appropriate data structure for image representation was investigated. The image processing algorithms complementation, convolution, filtering, and histogram measurement and modification were reviewed in terms of abilities to implement using the data structure.

Acknowledgements

The summer research was performed under the direction of Dr. Louis Tamburino of the Wright Avionics Laboratory at Wright Patterson Air Force Base and in collaboration with Dr. Mateen Rizki of Wright State University Department of Computer Science & Engineering. Both were very supportive and helpful in introducing the researchers to new aspects of the research area. Dr. Tamburino's direction included technical stimulus and focus, plus helpful liaison with Wright Patterson Air Force Base personnel. His constant help was critical to the project. Dr. Rizki has been working with the laboratory since participating in the summer program last year. His complementary work served as a guide and base for some of this work.

Universal Energy Systems deserves special thanks for being continually supportive and graciously tolerant!

Toolbox For Image Processing (TIP)

The OCCAM Toolbox For Image Processing (TIP) is a specification for a group of executable programs which perform a variety of well-known Image Processing operations on a Network of Transputers. This library is being designed to enhance the capabilities of the host operating system kernel. By using the TIP, a programmer may apply the computing power of a transputer network at an operating systems level interface.

A primary concern is utilization of the parallel processing capabilities of a transputer network. This requires the TIP specification to consider a number of "popular" network configurations while deciding upon the optimal configuration for a particular image processing operator.

The TIP promotes a transparent view of the underlying OCCAM computing environment. The programmer views the TIP as an additional group of host operating system services. Processes which issue calls to TIP may be made to poll for their results, but it is not mandatory. This feature depends upon the power of the process synchronization primitives provided by the host operating system.

The TIP is designed to be independent of any characteristics of the host operating system. This is accomplished by the use of the OCCAM 2 programming language as a basis for portability. Guidelines for optimal network configurations for each operation are provided as a result of this research project. The functionality of the TIP should be highly portable. Currently, Sun-Unix 3.x, Sun-VMS, and PCDOS 3.x all support interfaces. Both the Sun-Unix 3.x and the PCDOS 3.x interfaces are being explored.

Toolbox for Image Processing (TIP)

1 Introduction

2 System Architecture

2.1 Hardware Architecture

2.1.1 Host System

2.1.2 Pipeline Network

2.2 Software Architecture

2.2.1 TIP Monitor

2.2.1.1 Input Server (input_server)

2.2.1.2 Output Server (output_server)

2.2.2 Root Transputer Interface

2.2.2.1 Input Process (inputter)

2.2.2.2 Element Processes (element_proc)

2.2.2.3 Output Process (outputter)

2.2.3 Pipeline Transputers

3 TIP Shell Program

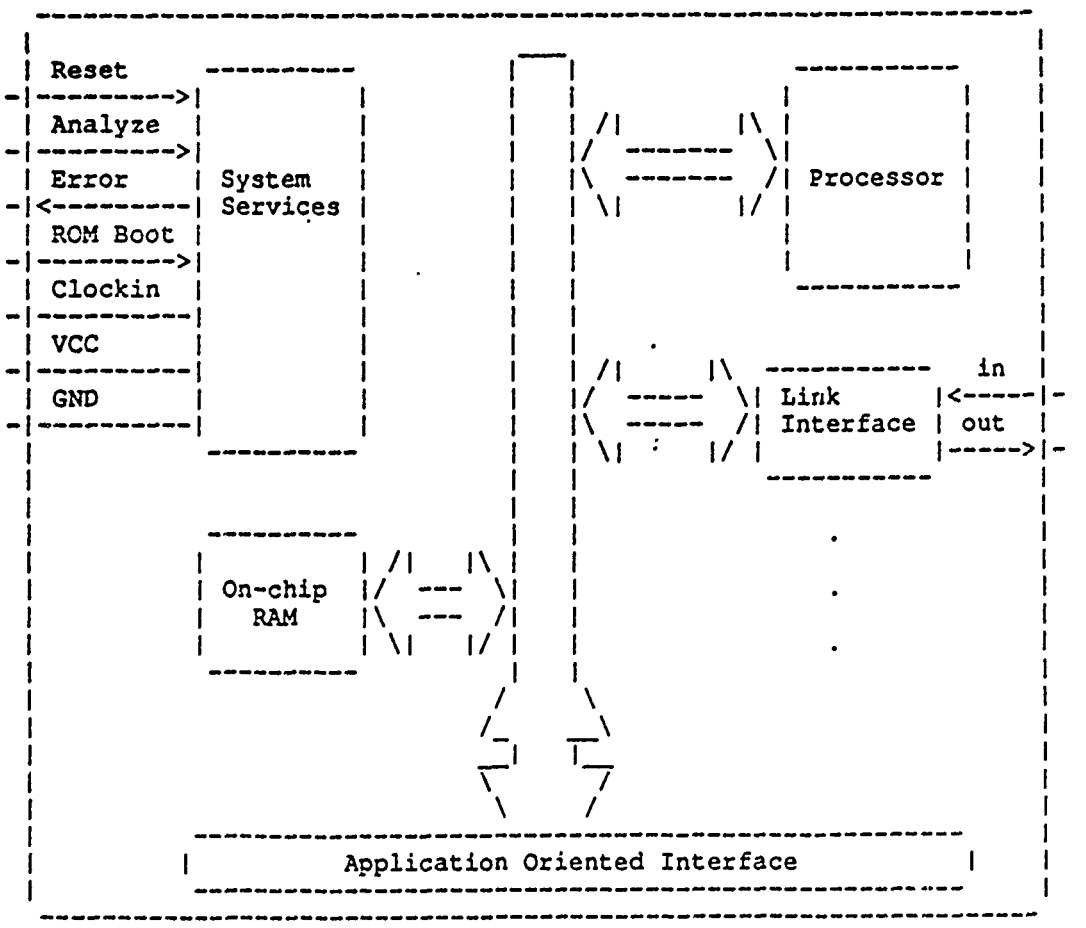
4 Bibliography

1. Introduction to Transputer Architecture

1.0. Introduction to Transputers

1.1.0. Hardware Description

A transputer is a group of VLSI components integrated onto a single chip. It consists of a RISC microprocessor, local RAM, 4 input channels, 4 output channels, and one clock pulse channel, as well as some circuitry which allows a transputer to be designated a special purpose (i.e. tailored to interface with a disk or graphics terminal). Information is transmitted from one transputer to another via a physical link or wire from an output channel of one transputer to the input channel of another. Thus, transputers may be utilized as a single processing system or as building blocks for large parallel processing systems. A diagram of the transputer architecture is shown below.



1.2.0 System Services

1.2.0.1 Reset

By setting the Reset bit, one of two things may happen :

1) If the ROM Boot bit is on, then the next instruction to be executed is located at the top two bytes of the transputer's local memory.

2) If the ROM boot bit is off, then the transputer attempts to load a bootstrap program from the first data link that indicates incoming program data. The first byte contains the number of bytes in the program that follows. The transputer then receives each byte of the incoming bootstrap program and places it in memory, starting at location MemStart.

1.2.0.2 ROM Boot

If this bit is set, then upon Reset, control is transferred to the instruction located at the top two bytes of the transputer's local memory. These two bytes contain a jump instruction which transfers control backward in ROM, which contains micro-code to reinitialize the transputer.

1.2.0.3 Processor (CPU)

The architecture of the transputer's cpu is based on the presence of fast on-chip memory For this reason, the cpu contains only a small number of registers. Only six of these registers are used for the execution of a sequential process.

The six registers are:

workspace pointer - points to a memory location where local variables are stored.
instruction pointer - points to the next instruction to be executed.
operand register - used in the formation of instruction operands.
general purpose - registers A B & C form an evaluation stack.

1.2.0.4 Applications Oriented Interface

It is very common for a network designer to dedicate certain transputers to administrative or system oriented functions. For example console I/O, printing, modem, etc. For this purpose, a transputer may be equipped with a specialized interface designed to control a specific peripheral, or perhaps families of peripherals. This specialized device is known an application oriented interface and when installed usually indicates that the transputer is dedicated as a controller unit for a particular peripheral device. For example, transputers are often dedicated to secondary storage mediums, and graphics displays. The software driver is implemented as a OCCAM process.

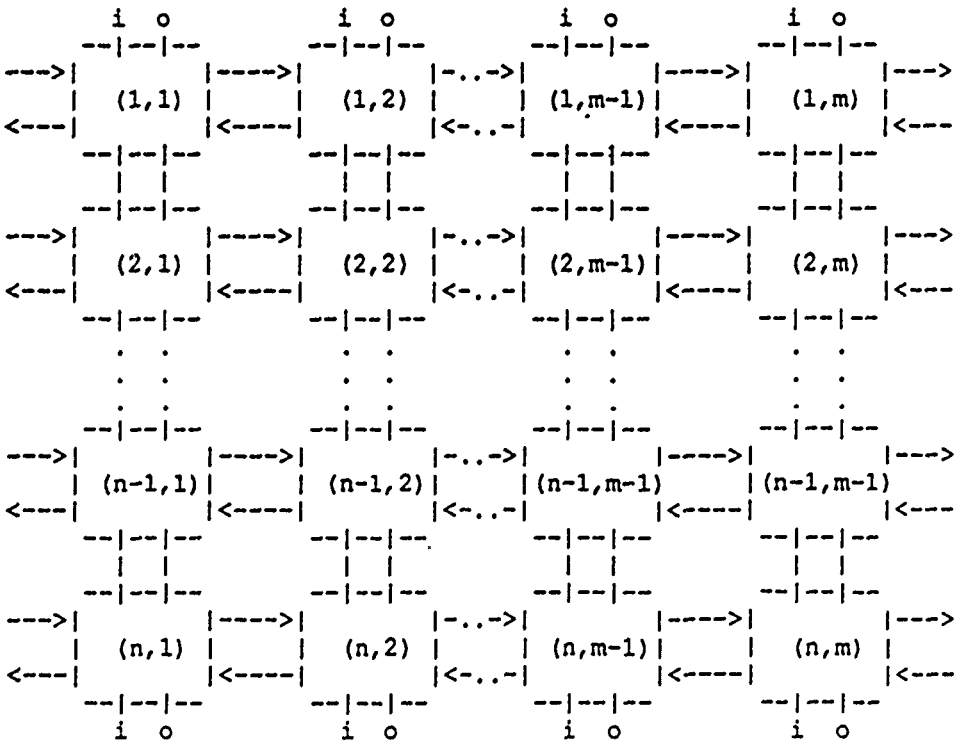
1.3.0 Transputer Networks

1.3.1. Topologies

There is a multitude of possible transputer topologies. In fact, transputers with programmable data links may be tailored to suit the needs of a particular application.

1.3.1.1. Grid

The transputer network depicted below is an example of an n x m grid topology.

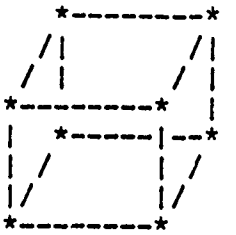


Note that each node has four bidirectional point-to-point data links.

This topology is among the most terse and comprehensible. It is dynamic, in that it the dimension variables m and n may be as low as 1 and as high as economical issues allow.

1.3.1.2. Hypercube

The links of a transputer network may be configured to form the vertices of a three dimensional cube. This topology is referred to as a hypercube. The logical view of a hypercube is shown in the diagram below.



It should be brought to light that each of the vertices of the cube represent a bi-directional data link. This is true of most hypercube topologies, but not mandatory. Also note that each node of the hypercube requires three sets of point-to-point data links. A fourth set may be used to provide direct access to a host I/O data bus.

Tool Box for Image Processing (TIP) is a specification for a group of software primitives capable of performing a number of well- known image processing operations upon a Multiple-Instruction, Multiple Data (MIMD) distributed processing network. This specification is designed to enhance the capabilities of the UNIX operating system, via the services of a group of daemon processes collectively known as the TIP server. By using this server, a programmer may apply the computing power of a distributed network (i.e. transputer, Sun NFS, etc) at an application level interface. TIP is designed to perform a variety of graphics operations in a parallel environment. Application programs which use the TIP may be constructed with little knowledge of the underlying architecture of the physical, and possibly heterogeneous, distributed system. Additionally, the TIP will provide a structured and standard method for image I/O. This will be accomplished by a the processing of the TIP server and a group of C header files and functions which work together to maintain flat files of images and operators in a variety of formats.

The TIP allows a program executing on the host to transparently request the services of a MIMD distributed computing network. The application programmer may conceptualize the TIP as an additional library of functions or operating system services. In actuality, the TIP is a group of server processes which facilitate a gateway to the underlying network. This paradigm between a host computing system and a slave network is depicted in Figure 1, entitled "TIP Architecture".

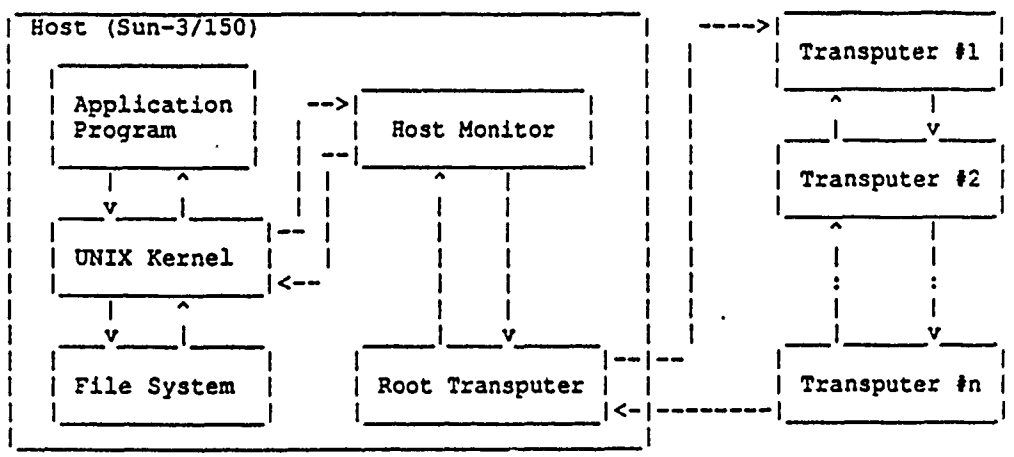


Figure 1 TIP Architecture

Figure 1 depicts Transputers as building blocks of the serving network. This decision was based on the low cost and dynamic expansion capabilities of Transputer technology as compared to super-computer technology. Although, certain configuration procedures may be performed to optimize TIP's performance, from one network to another, the functionality of the TIP should remain a reasonably portable software development tool. Currently, INMOS has implemented interfaces for the IBM PC & Compatible, and the Sun Workstation families of computers.

During the design phase of TIP, both the Sun Workstation 3.x and IBM PC & Compatible interfaces were researched. This effort revealed that the IBM PC version provided an interactive software support tool known as the Transputer Development System (TDS). The TDS is a complex, "function-key" based program which executes partly on the host and partly on the Root Transputer. An alternate approach at Transputer software development is to use standard UNIX facilities and construct code for the distributed OCCAM environment remotely from the host. The TDS is not fully supported by the Sun development environment. Transputer News reveals that professional software developers are beginning to use derivatives of the C Programming language designed specifically for use in the OCCAM environment. These languages include OCCAM-like programming constructs designed to facilitate

control over a MIMD computing system. use in distributed applications. These software development systems allow the programmer to utilize development tools provided by the host operating system. Thus, the TDS was not considered an acceptable means of software development. In fact, this decision is what prompted the initiative to construct the TIP specification.

INMOS does provide a library of batch-oriented support tools for both the Sun and IBM versions. These tools will allow the TIP to be developed independent of the TDS, via the software editing facilities of the host's operating system. INMOS also provides portable tools that allow OCCAM 2 processes to input and output from host operating system data streams. For this reason, these tools should most likely be used to implement the protocol between the host and the network.

The original goal of the TIP specification was to support three types of primitives, each corresponding to a category of image processing operations. These three categories are : Point Processing (PP), Group Processing (GP) and Frame Processing (FP). Based on time and hardware limitations throughout the research program, This goal was reduced to an implementation of the Frame Processing (FP) primitive. Before discussing how this primitive operates, it is convenient to discuss the some data structures associated with image representation and packaging.

2 System Architecture

A generalized system architecture of TIP was shown in Figure 2.1 and discussed in brief detail in section 1. This section discusses, more thoroughly, the specification proposed for the TIP system architecture.

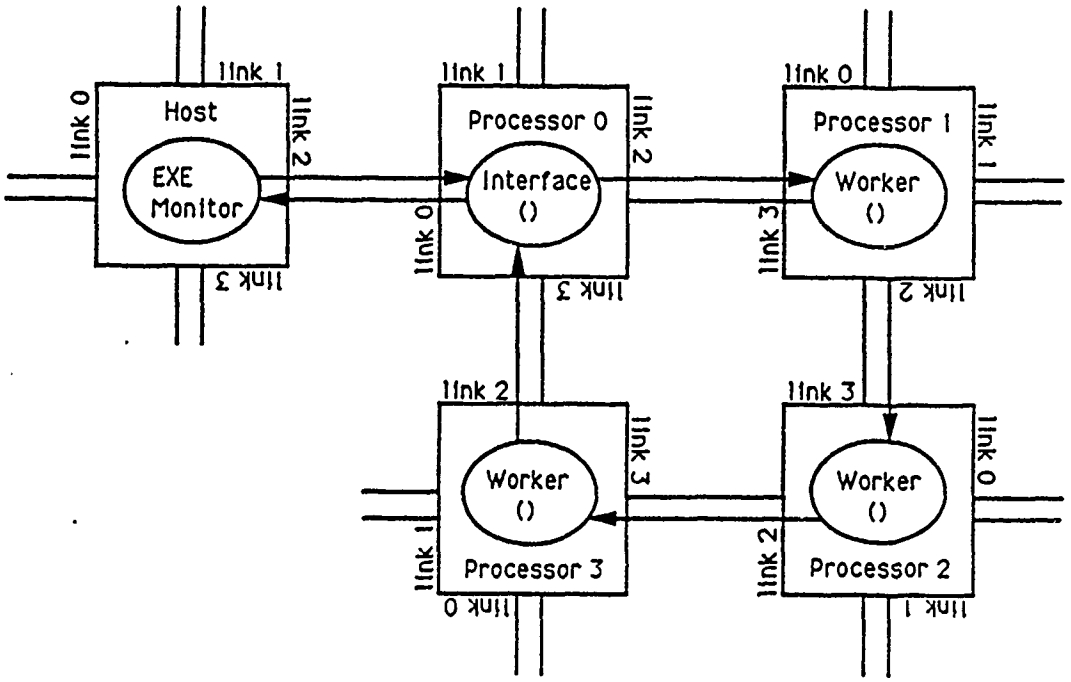


Figure 2.1 Pipeline Network Architecture

2.1 Hardware Architecture

The use of TIP requires the cooperation of two distinct computing environments; a Sun 3/50 host server and 1 or more networks of INMOS Transputers.

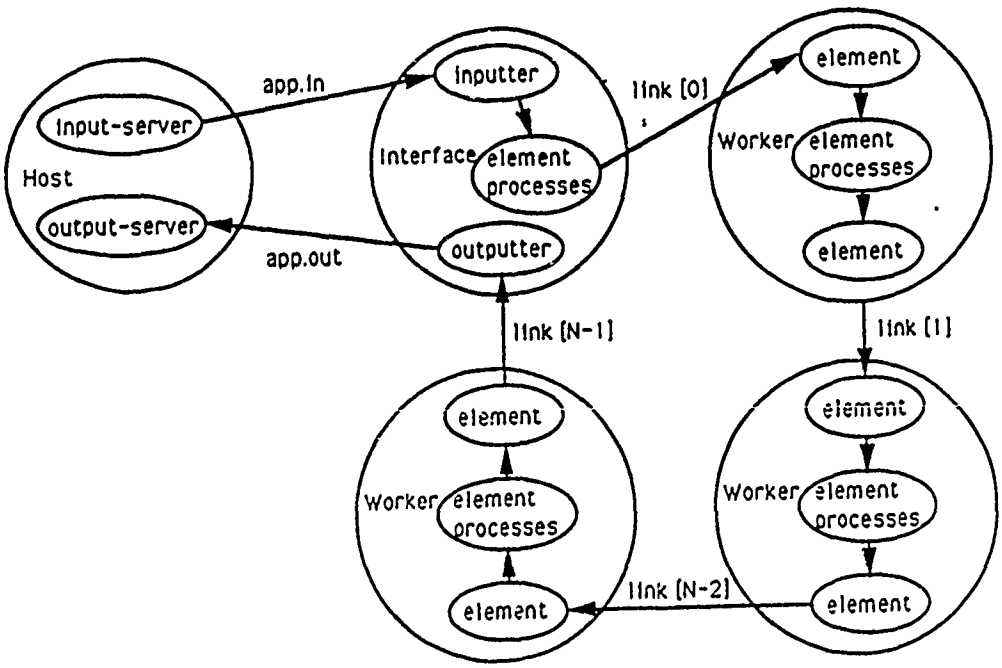
2.1.1 Host System

The Sun workstation performs the function of an I/O server. It provides a UNIX operating system interface into the OCCAM network. Connected directly to the SUN, is a transputer interface device known as a "host" transputer. This device is implemented as an expansion board and directly connects to a 32-bit data bus located on the motherboard. An entry should be installed in the device table, /dev/devtab, informing UNIX of its existence. This may be accomplished through the use of the makdev() utility program. Each bidirectional communications link installed on the host transputer enables an additional Pipeline network to be installed. Figure 2.1 shows a host serving a single Pipeline Network. Note that three additional "pipelines" could have been added.

2.1.2 Pipeline Network

Each Pipeline network consists of 1 or more groups of transputers, cooperating in an assembly line fashion. Figure 2.1 displays a four node pipeline. This network consists of Processors 0 thru 3. Processor zero is known as the "root" transputer. It serves as a gateway to and from the rest of the pipeline. The root transputer employs three of its four communication links. All other nodes only require two to be a member of a "pipe."

2.2 Software Architecture



2.2.1 TIP Monitor

At the host server, two processes collectively compose the TIP Server (Monitor), input_server() and output_server(). In actuality these processes execute as UNIX daemons. Process input_server() provides a buffered, unidirectional data communications link from the host and the root transputer. Process output_server() provides a buffered link from the root transputer to host computer.

2.2.1.1 Input Server (input_server)

The input server process receives packets containing an input and template image. It then subdivides the input image into subimages whose dimensions are equivalent to those of the template image. Each of these subimages are then piped to a particular element process to be operated on by a convolution algorithm.

2.2.1.2 Output Server (output_server)

The second portion of the TIP server is a daemon process known as output_server. This process receives data from the app.out data channel. The type of data returned from the pipeline is an output image whose dimensions are identical to the input image received by process input_server().

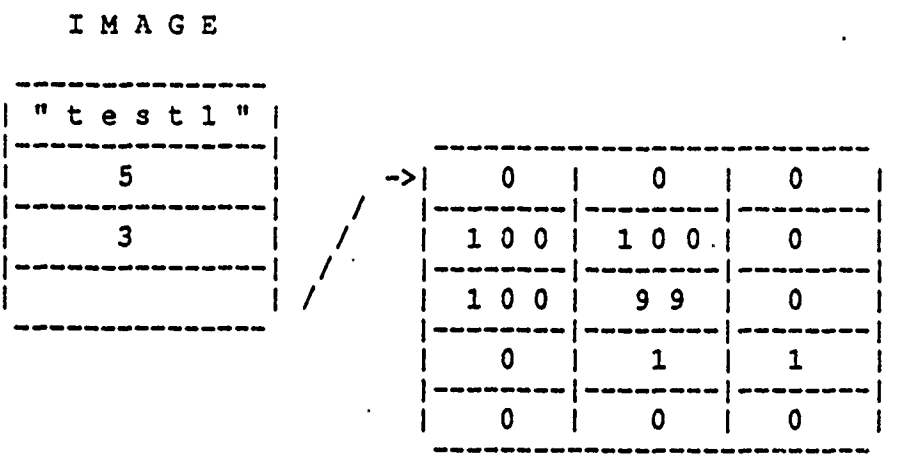
3. The TIP Shell Program

The Toolbox for Image Processing provides a basic user interface program which executes on the platform of the host. It is written in the C programming language and should be a portable fool for basic maintenance of IMAGE-related data structures.

3.1 Image Data Structure

The IMAGE Data Structure is used to represent a dynamic image instance. It contains overhead data which contains the number of rows and columns, a data pointer to the actual PIXEL grid. Since TIP is at such an early development stage, a symbolic name field is also attached to each IMAGE. The name field is intended for debugging purposes.

Example: 5 x 3 IMAGE named "test1."



3.1.1 Image_Vector Data Structure

An IMAGE_VECTOR is a data structure used to store a dynamic array of IMAGE data structures. It contains the length, name, and pointer to the actual dynamically allocated array of images.

Bibliography

Bieleman, Hans. Between Transputers: The Communication Manager. Micro Cornucopiua, #38, Nov-Dec 1987.

Cooper, R.E.M. A Microprogrammed occam Interpreter for the HLH Orion. John Wiley & Sons, Ltd, 1988.

Fay, D.Q.M. Experiences Using INMOS PROTO-OCCAM. SIGPLAN Notices, V19 #9, September, 1984.

Fisher, A. J. A Multi-processor Implementation of occam. London: John Wiley & Sons, Ltd, 1986.

Fisher, A. J. A Multi-processor Implementation of occam. London: John Wiley Sons, Ltd, 1986.

Homewood, Mark. The IMS T800 Transputer. IEEE Micro, 1987.

Kerridge, Jon M. Three Solutions for a Robot Arm Controller Using Pascal-Plus, occam and Edison London: John Wiley & Sons, Ltd, 1984.

Kerridge, Jon M. Communicating Parallel Processes. London: John Wiley & Sons, Ltd. 1986

Parasoft Corp. An Introduction to Parallel Programming and Transputers. Kingston, M.A., MicroWay, Inc.

Pountain, Dick A tutorial introduction to OCCAM programming.

Roelofs, Bernt. The Transputer: A Microprocessor Designed For Parallel Processing. Micro Cornucopia, #38, Nov-Dec, 1987.

Taylor, Richard. Concurrent Programming in Occam.

Vaughan, Jonathan Transputer application to speech recognition. London: Butterworth & Co, 1987

Walker, Paul. The Transputer: A building block for parallel processing. Byte Magazine, May, 1985.

Wayman, Russell. OCCAM 2: an overview from a software engineering perspective. London: Butterworth & Co. Ltd., October, 1987.

1989 USAF-UES SUMMER FACULTY RESEARCH PROGRAM

Sponsored by the

AIR FORCE OFFICE OF SCIENTIFIC RESEARCH

Conducted by the

Universal Energy Systems, Inc.

FINAL REPORT

ANALYTICAL MODEL OF A UNIQUE E-O BEAM SCANNER

Prepared by:	Mohammad A. Karim
Academic Rank:	Associate Professor
Department and	Department of Electrical Engineering &
	The Center for Electro-Optics
University:	The University of Dayton
Research Location:	WRDC/ELOT
	Wright-Patterson AFB; Dayton; Ohio
USAF Researcher:	Joseph E. Brandelik
Date:	25 September 1989
Contract Number:	F49620-88-C-0053

ANALYTICAL MODEL OF A UNIQUE E-O BEAM SCANNER

by

Mohammad A. Karim

ABSTRACT

This report summarizes the research performed during the USAF-UES Summer Faculty Research Program. The work consisted of developing an analytical model for characterizing the beam-steering characteristics of a unique electro-optic (E-O) beam scanner. The beam scanner in question consists of a combination of an echelle grating and a nonlinear refracting material sandwiched in between two transparent electric plates. Two particular schemes for introducing electric field were explored. The current quantitative results along with those expected to be generated through a follow-up mini-grant study would be able to dictate the design characteristics of the most optimum nonlinear refracting material based optical beam scanning system.

ACKNOWLEDGEMENTS

I wish to thank the Air Force Systems Command and the Air Force Office of Scientific Research for sponsorship of this research. I would also like to thank the Universal Energy Systems, Inc., for providing administrative support of this program.

The support and encouragement of many people made my research experience both rewarding and enjoyable. I would especially like to thank Joseph E. Brandelik, Richard Lane and Capt. John D. Hoeft of WRDC/ELOT, Wright Patterson AFB, for the valuable technical assistances and for providing me with a comfortable working environment.

I. INTRODUCTION

Electro-optic beam deflection concept (Karim, 1990) is of growing importance in modern warfare scenario. The effect of electric field on the direction of light propagation can be best utilized to avoid the mechanical inertia that otherwise plagues the electromechanical steering devices. The constraints of a space-borne system, however, rules out the possibility of using simple electro-optic Pockels (linear) and Kerr (nonlinear) effects for beam steering primarily because of their high voltage requirements.

The WRDC/ELOT Division of the Wright-Patterson AFB is currently interested in designing a reliable low-voltage E-O beam steering device. The time response of this to-be-designed device is expected to be relatively small. An interesting concept that is being currently explored at WRDC/ELOT involves the use of a combination of echelle grating and a nonlinear refracting material which in turn is placed in between a pair of transparent electrodes. As a first attempt, one may design and test the suitability of this device for only a single wavelength of light. The problems associated with the broadband beam steering devices are definitely more cumbersome and, therefore, the corresponding design involves more difficult engineering decisions.

One of my current research interests at the University of Dayton has been directed towards exploring the various possibilities of designing and characterizing optical beam transforming systems. The long range goal of the research includes designing optical systems to either transform, shift, or modify an input beam of

light. Some of my recent works were geared towards designing high-efficiency binary filter based optical systems for transforming a Gaussian laser beam into a uniform-intensity laser beam (Karim et. al., 1985), designing systems for the measurement of a micron-sized Gaussian beam radius (Karim, 1985; Karim et. al., 1987a), designing low-loss refracting systems for transforming a uniform-intensity annular laser beam into an equivalent uniform-intensity circular beam (Karim. et. al., 1987b) and designing refracting systems for converting a Gaussian laser beam into a uniform-intensity output beam (Jahan and Karim, 1989). In addition, I had also developed analytical as well as software tools for verifying Liquid Crystal based beam agility devices for the AFWAL/AARI-2 during my 1988 SFRP work. These experiences have served as motivation for the current SFRP work that also consists of both analysis and design of beam deflecting system whose functional characteristics are controlled, in real-time, by means of either voltage or field.

II. OBJECTIVES OF THE RESEARCH EFFORT

There has been an ever growing interest in achieving rapid large-angle pointing and scanning of large-diameter diffraction-limited laser radar beams. To date, available technology has failed to deliver the perfect beam steering system that meets the required specifications. In the past, experimenters had developed a variety of beam deflection schemes employing mechanical, acoustical, and electro-optic methods. However, to date, development of a real-time optical phased array antenna (Brookner, 1985) has

not materialized fully, due in great part to the lack of sufficiently small, electrically tunable, optical phase shifters. My assignment as a Summer Research Fellow was to perform basic research into the theory and characterizations of a unique E-O beam scanner system, shown in Fig. 1, that consists of a combination of an echelle grating and a nonlinear refracting material which along with a linear refracting material is sandwiched in between two transparent electric plates.

The objectives of this research is three-fold: (a) to develop model for describing the performance of the aforementioned E-O beam scanner; (b) to develop theory to identify which of the two possible means of employing electric field is more desirable; and (c) to develop software tools for studying the performance of the scanning device primarily for a single wavelength.

III. MODEL DEVELOPMENT

(a) BLAZED AND FLAT PHASED GRATING ARRAY

Grating configuration that can be used to design an optical beam scanner can be either flat or blazed. In the former configuration, the active element provides a constant phase while that in the latter the phase of the active element varies linearly across the element. The far-field diffraction pattern of such optical systems are calculated by determining (1) the intensity distribution which results from the interference of multiple plane waves arriving at an angle; and (2) far-field intensity distribution of

a single slit (which is the intensity which results when light intensity is transmitted through one active element only). The intensity distribution are then multiplied (Jenkins and White, 1976) to obtain the far-field diffraction pattern of the system in question.

For a flat grating array having N active elements each with a constant phase delay of $\Delta\phi$, the far-field diffraction pattern (as a function of angle θ) is obtained as:

$$I = A_o^2 \frac{\sin^2\left(\frac{\pi b}{\lambda}\sin\theta\right)}{\left(\frac{\pi b}{\lambda}\sin\theta\right)^2} \frac{\sin^2\left[\frac{N}{2}\left\{\frac{2\pi}{\lambda}d\sin\theta + \Delta\phi\right\}\right]}{\sin^2\left[\frac{1}{2}\left\{\frac{2\pi}{\lambda}d\sin\theta + \Delta\phi\right\}\right]} \qquad (1)$$

where d is the width of each element, $b \leq d$ is the width of the active part of each element, λ is the wavelength, and A_o is a constant. Similarly, one can also calculate the far-field diffraction pattern of a blazed grating array. For simplicity, the blazed grating array element may be assumed to have a phase that varies "linearly" with distance. Then the intensity distribution is given by

$$I = A_o^2 \frac{\sin^2\left[\frac{\pi b}{\lambda}\sin\theta + \frac{\Delta\phi}{2}\right]}{\left[\frac{\pi b}{\lambda}\sin\theta + \frac{\Delta\phi}{2}\right]^2} \frac{\sin^2\left[N\left\{\frac{\pi d}{\lambda}\sin\theta + \frac{\Delta\phi}{2}\right\}\right]}{\sin^2\left[\frac{1}{2}\left\{\frac{2\pi d}{\lambda}\sin\theta + \frac{\Delta\phi}{2}\right\}\right]} \qquad (2)$$

It may be noted that the E-O beam scanner in question is not strictly blazed since the associated phase delay distribution varies not exactly linearly with distance. However, as a first approximation we shall use Eq. (2) for our purposes.

(b) LIGHT PATH IN INHOMOGENEOUS MEDIUM

Consider an optical medium whose refractive index n is variable along only x-direction and it is constant along both y and z. In such a scenario, L(x,y,z) satisfying the eikonal equation

$$\left|\vec{\nabla} L(x,y,z)\right|^2 = n^2 \tag{3}$$

can be safely assumed to be separable so that it can be given as

$$L(x,y,z) = f(x) + g(y) + h(z) \tag{4}$$

where f(x), g(y) and h(z) are functions solely of x, y , and z respectively. Eq. (4) can be used to rewrite Eq. (3) as

$$\{[f'(x)]^2 - [n(x)]^2\} + [g'(y)]^2 + [h'(z)]^2 = 0 \tag{5}$$

Accordingly, Eq. (4) can be rewritten as

$$L(x,y,z) = \pm \int_c^x [(n(x))^2 - (a^2 + b^2)]^{1/2} dx \pm ay \pm bz \tag{6}$$

where a, b, and c are constants. The values of a and b are determined by the boundary conditions pertaining to launching position and angle.

Consider the optical system shown in Fig. 2 where the launching point is $(0,0,C_o)$. Further consider that the launched ray is making an angle of θ_o and ϕ_o with respect to x-axis and y-axis respectively. Thus, the projection of the launched ray to y-z plane is a straight line since n is a variable only along the x-axis. Accordingly, a rigorous mathematical manipulation of Eq. (6) yields a set of two equations that interrelates x, y, and z

coordinates which in turn can be used to describe the corresponding light path in inhomogeneous medium. These two equations are (Lizuka, 1985):

$$y = \int_0^x \frac{n_0 \sin\theta_0 \cos\phi_0}{\sqrt{[n(x)]^2 - n_0^2 \sin^2\theta_0}}\, dx \tag{7}$$

$$Z - C_0 = \int_0^x \frac{n_0 \sin\theta_0}{\sqrt{[n(x)]^2 - n_0^2 \sin^2\theta_0}}\, dx \tag{8}$$

where n_0 is the refractive index at the launching point. It must be pointed out that for the case of a refractive index in which n(x) is a monotonically decreasing function, there is every chance that the light ray may undergo a "total" internal reflection at $x = x_0$ where $n(x_0) = n_0 \sin\theta_0$. In a medium with n(x) always larger than n_0, no total internal reflection may take place regardless of the distribution of refractive index.

(c) OPTICAL PATH LENGTH OF THE E-O SCANNER

There are two means of subjecting the E-O scanner to electric field. In one case (referred to as Case I), the voltage is applied between the two transparent parallel plates that sandwiches the combination of echelle grating and a nonlinear refracting material. In the other case (referred to as Case II), one of the electric plates is etched along a zig-zag surface parallel to the echelle grating. In the former, therefore, n(x) is constant and the corresponding phase delay arises only from the variation in

the thickness of the nonlinear material. In the latter case, however, n(x) is a variable and the corresponding phase delay is caused by both (a) the variation in thickness of the nonlinear material; and (b) the variation in electric field across each of the active elements.

The refractive index n_4 of the nonlinear refracting medium is given by

$$n_4(x) = n_a + n_b[V/t(x)] + n_c[V/t(x)]^2 \tag{9}$$

where $n_a = 1.5$, $n_b = 10^{-3}$ or higher; $n_c = 10^{-5}$ or higher, V is the applied voltage; and t(x) is the thickness of the nonlinear material in question such that

$$t(x) = \begin{cases} t_2 + t_3 + t_{41} + t_{42} + t_{43}, & \text{Case I} \\ t_2 + t_3 + t_{41} + t_{42}[1 - (x/d)], & \text{Case II} \end{cases} \tag{10}$$

Once the optical path difference has been determined, one can then determine the corresponding optical phase difference by multiplying the path difference with $2\pi/\lambda$.

It is important to realize that evaluation of path difference corresponding to a propagating ray in the nonlinear refracting medium is very tricky and very difficult. To accomplish this, in the short course of SFRP program, one may determine the set of (x,y) coordinates by numerically solving both Eqs. (7) and (8). The curve between the neighboring sets of (x,y) coordinates is approximated by directing a straight line through them. The

length of this hypothetical straight line element is next multiplied by the average of the refractive indices measured at those two points. Such similar products from all of the neighboring elements are finally added to yield the corresponding path difference encountered at each of the active elements (containing the nonlinear refracting material).

IV. SIMULATION

A computer program was written to simulate the design of the E-O beam scanner introduced in the last section. Figs. 3(a) and 3(b) show the far-field diffraction patterns obtained using -0.4V and -1.75V respectively with a scanning system corresponding to case I for the normal incidence. The peak intensity value is found to be distinctly associated with a particular deflected angle. However, Figs. 4(a) and 4(b) show that for the same input voltage of -0.4 V, for example, there can be two peaks - one at 45° and the other at 60°. This confirms the fact that the total input power is shared by these two output peaks. Similar observation holds true also for case II, as shown by Figs. 5(a) and 5(b). Figs. 6(a) and 6(b) show the plot of intensity di.tribution as a function of applied voltage for both case I and case II at 85°, for example. Note the number of peaks is reduced but at the cost of severe power loss. Another such case is seen in Fig. 7 for the case of 15° deflection. Figs. 8(a) and 8(b) show the far-field diffractions for cases I and II respectively for the applied voltage of 0.25 V. The plots make us aware of the fact that the input power may be distributed quite randomly at many different

angles in both of the systems. But this again is not always the case. For example, with 0.75 V, there is only one peak at 33° for the system of case I while there are only two peaks at 37° and 87° for the system of case II. Figs. 10(a) and 10(b) show that it is possible to obtain a larger deflection using the system of case II when 2V, for example, is applied across its terminals.

V. DISCUSSION AND RECOMMENDATIONS

Preliminary calculations made during the current work is indicative of the fact that it is possible to deflect a beam with very little voltage. Interestingly, even negative voltages can be used for deflection of input beam. However, there appears to be a loss of power in the process.

Before the design characteristics of the E-O beam scanner system is finally specified, a few more aspects need to be considered and investigated in the follow-up research. They are:

(i) The model still does not account for the fact that there exists a region of field interactions in between the neighboring active elements.

(ii) The ratio b/d is different for different (a) angles, when applied voltage is a constant; and (b) voltages, when deflection angle is a constant.

(iii) Within the length of each active element, the phase delay is neither a constant nor linearly distributed. In fact the phase delay varies non-linearly with distance.

(iv) The analytical model and the simulation considered in this research only accounts for normal incidence. The model must be updated to accommodate non-incident light beams.

(v) The model has been used to study the behavior of only monochromatic light beams. An extension of it should be able to study the broadband scanning characteristics of the device.

(vi) The simulation only considered a particular set of values for n_a, n_b, and n_c.

(vii) Realistic transmission characteristics of the available electrodes like that of indium tin oxide need to be identified for proper evaluation of the system efficiencies.

V. REFERENCES

Brookner, E., "Phased-array radars", Sci. Am., February 1985, p. 94.

Jenkins, F. A., and White, H. E., Fundamentals of Optics (4th Ed), New York, NY. McGraw Hill Book Co., 1976.

Jahan, S. R., and Karim, M. A., "Refracting systems for Gaussian-to-uniform beam transformations", Opt. Laser Technol., Vol. 21, 1989, p. 27.

Karim, M. A., Electro-Optical Devices and Systems, Boston, Massachusetts, PWS-KENT Pub. Co., January 1990.

Karim, M. A., Hanafi, A. M., Hussain, F., Mustafa, S., Samberid,

Z., and Zain, N. M., "Realization of a uniform circular source using a two-dimensional binary filter", Opt. Lett., Vol. 10, 1985, p. 470.

Karim, M. A., "Measurement of Gaussian beam diameter using Ronchi rulings", Elect. Lett., Vol. 21, 1985, p. 427.

Karim, M. A., Awwal, A. A. S., Nasiruddin, A. M., Basit, A., Vedak, D. S., Smith, C. C., and Miller, G. D., "Gaussian laser-beam-diameter measurement using sinusoidal and triangular rulings", Opt. Lett., Vol. 12, 1987, p. 93.

Karim, M. A., Cherri, A. K., Awwal, A. A. S., and Basit, A., "Refracting system for annular laser beam transformation", Appl. Opt., Vol. 26, 1987, p. 2446.

Lizuka, K., Engineering Optics, Springer-Verlag, Berlin, Germany, 1985.

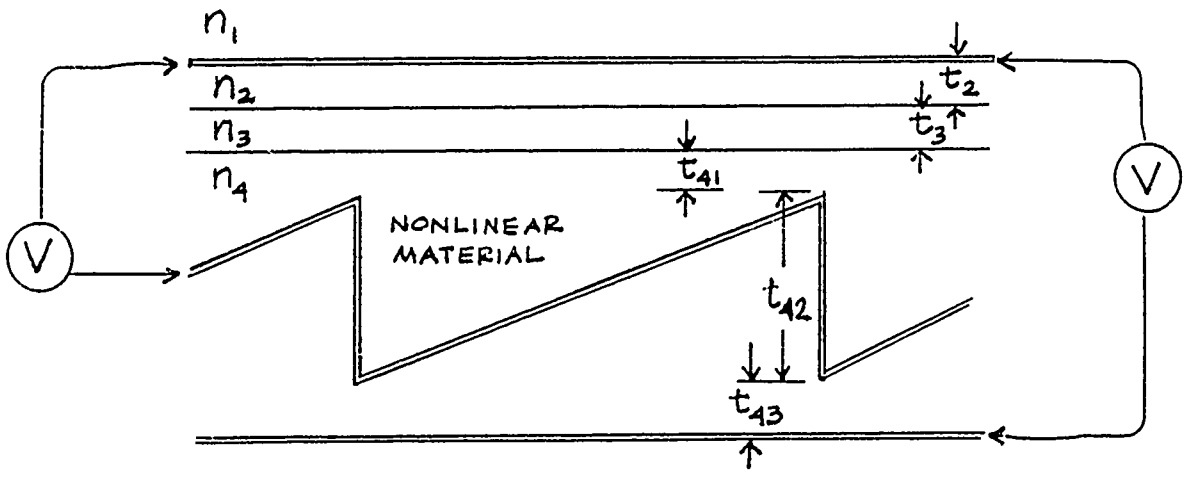


Fig. 1. The E-O beam scanner.

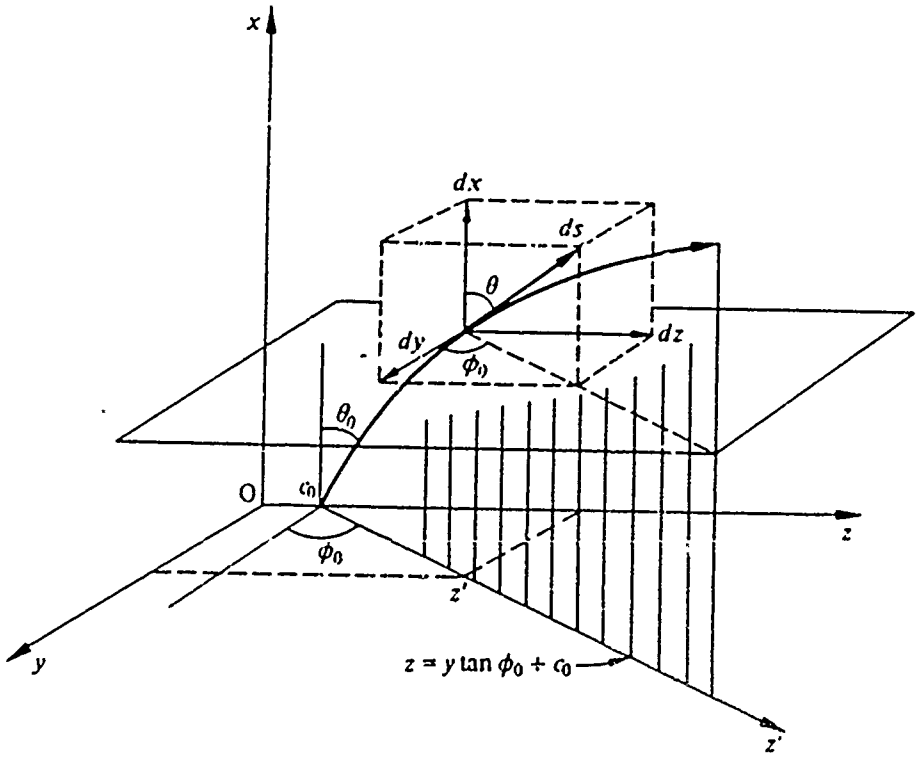


Fig. 2. The geometry of a ray in a inhomogeneous medium.

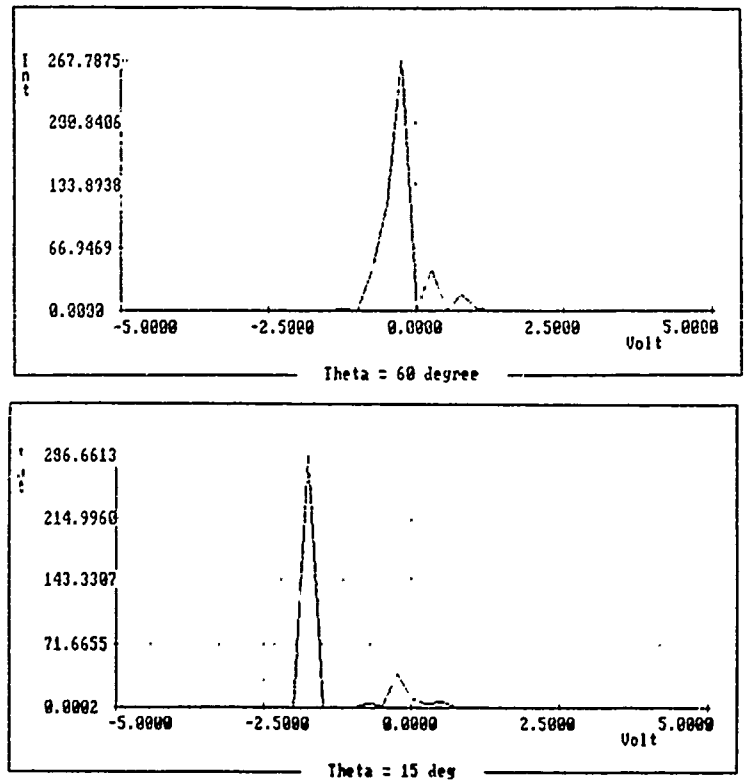


Fig. 3. Intensity distribution at 60° and 15° for case I.

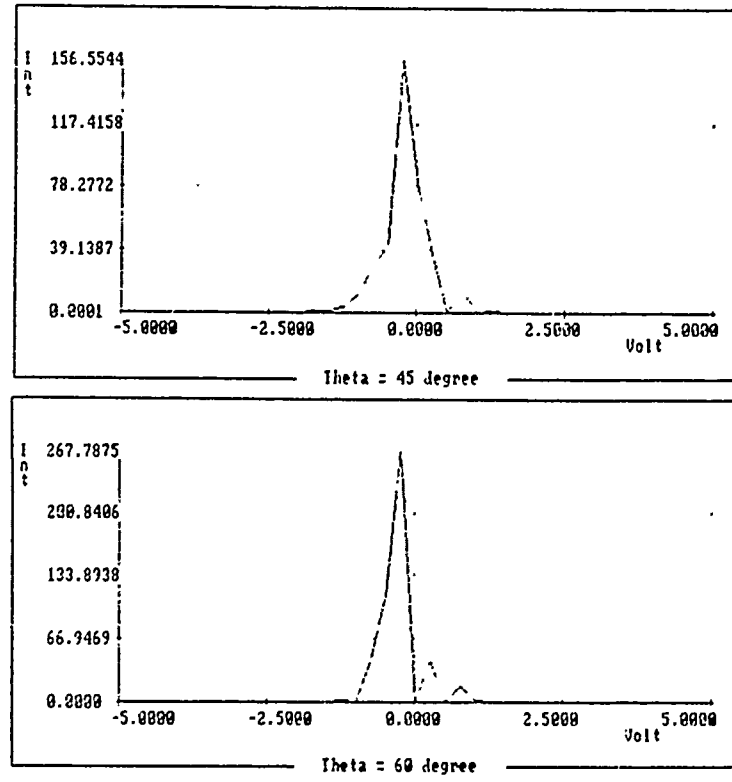


Fig. 4. Intensity distribution at 45° and 60° using -0.4V.

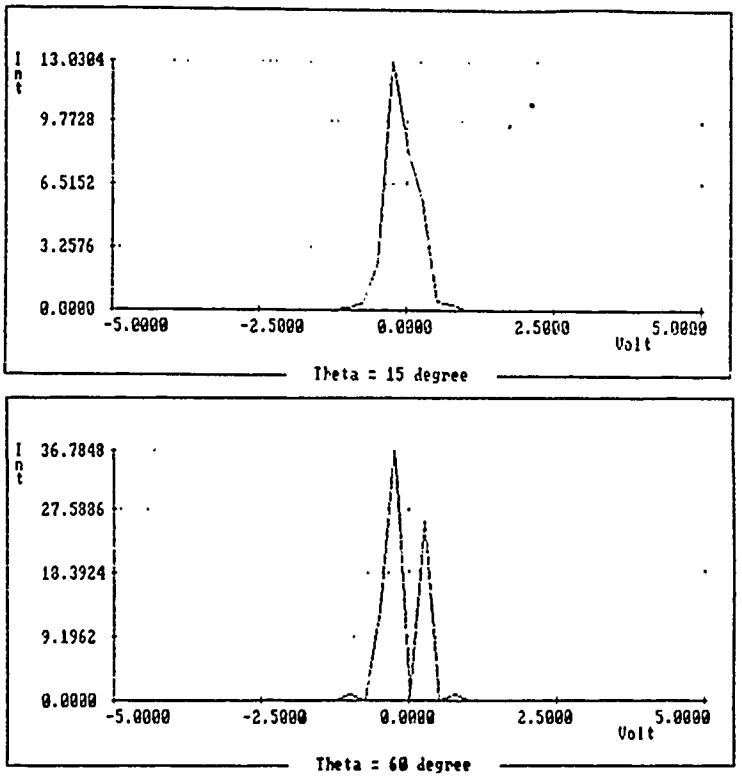


Fig. 5. Intensity distribution for case II at 15° and 60°.

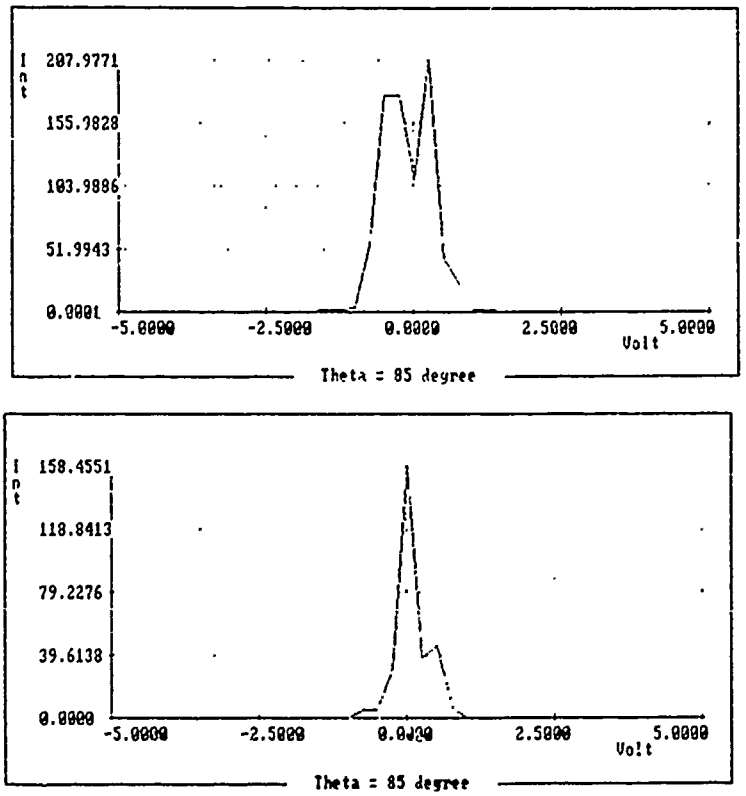


Fig. 6. Intensity distribution at 85° for both cases.

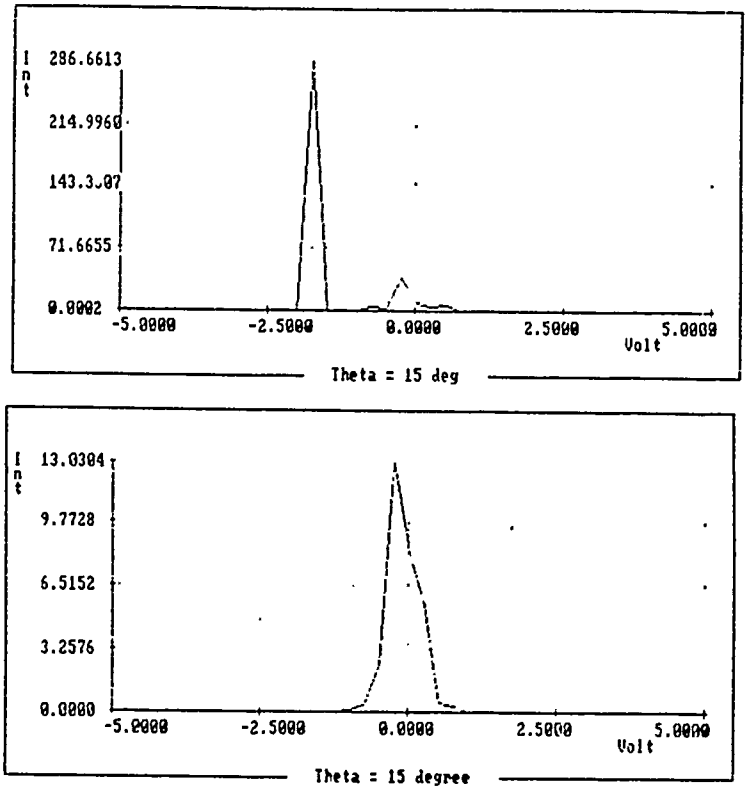


Fig. 7. Intensity distribution at 15° for both cases.

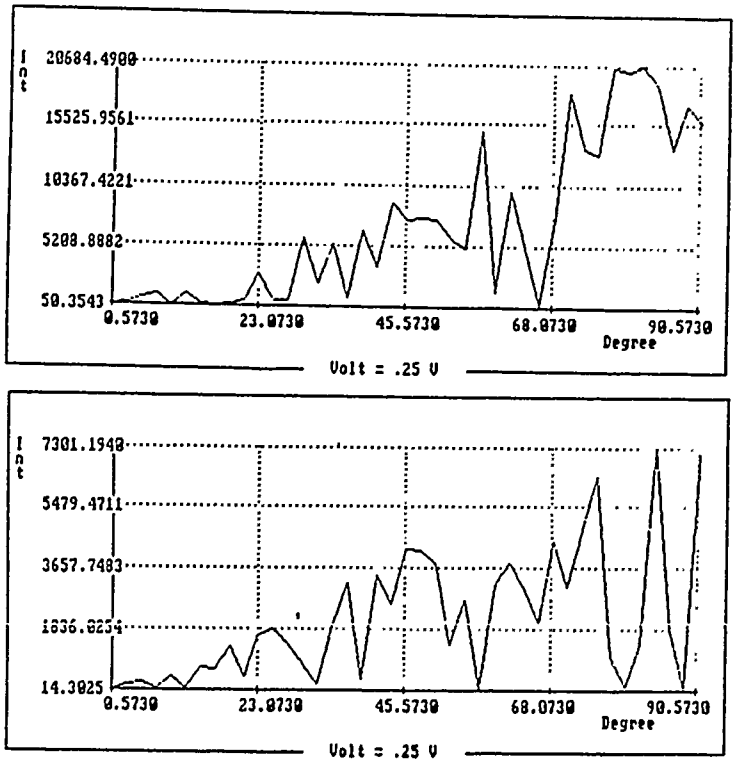


Fig. 8. Intensity distribution with 0.25V for both cases.

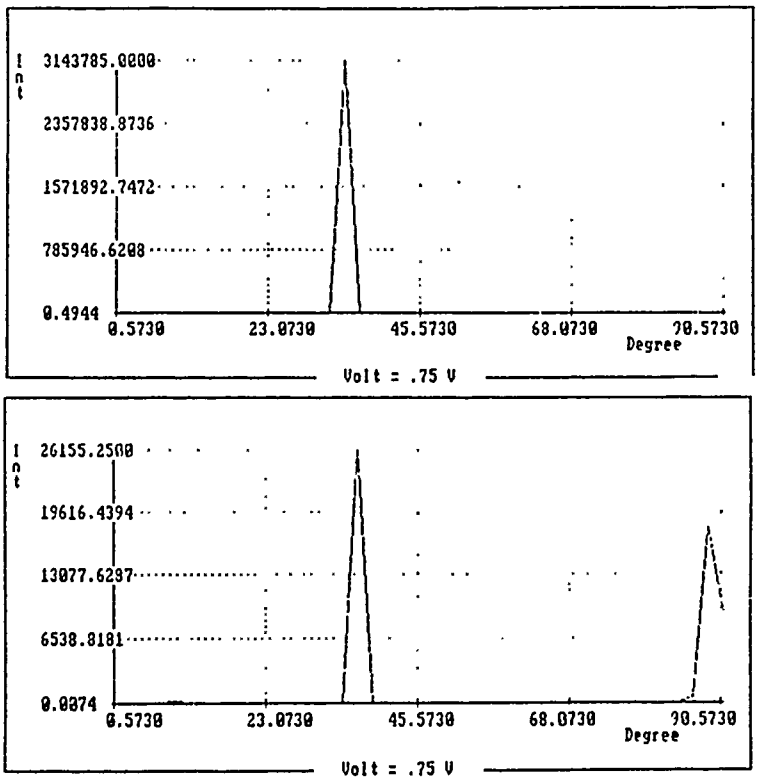


Fig. 9. Intensity distribution with 0.75V for both cases.

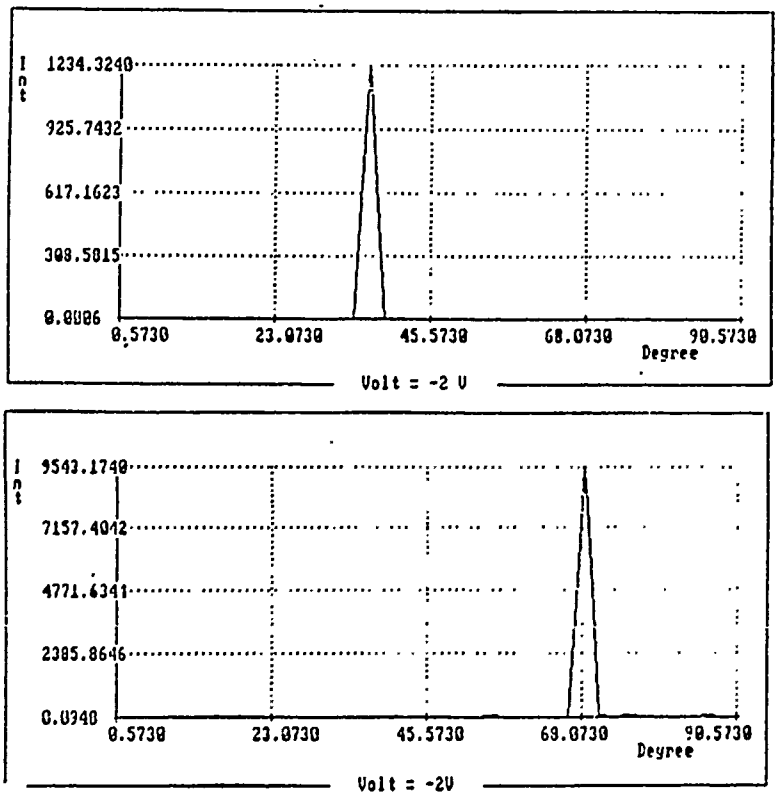


Fig. 10. Intensity distribution with -2V for both cases.

1989 USAF-UES SUMMER FACULTY RESEARCH PROGRAM

SPONSORED BY THE
AIR FORCE OFFICE OF SCIENTIFIC RESEARCH

CONDUCTED BY THE
UNIVERSAL ENERGY SYSTEMS, INC.

FINAL REPORT

DYNAMIC TASK SCHEDULING FOR THE "ADA DISTRIBUTED SYSTEM EVALUATION TESTBED (ADSET)"

Prepared by : Dar-Biau Liu

Academic Rank : Professor

Department and University : Department of Computer Science and Engineering
California State University, Long Beach.

Research Location : Avionics Laboratory,
Wright Research and Development Center
WPAFB, OH. 45433

USAF Researcher : Capt. Marc J. Pitarys

Date : August 15, 1989

Contract No. : F49620-88-C-0053

DYNAMIC TASK SCHEDULING FOR THE "ADA DISTRIBUTED SYSTEM EVALUATION TESTBED (ADSET)"

BY

Dar-Biau Liu

ABSTRACT

The ADSET (Ada Distributed System Evaluation Testbed) has the capability to support an Advanced Multi-Purpose Support Environment (AMPSE). The AMPSE's simulation software will be written in Ada. It provides a real-time simulation support environment for testing and evaluation of Embedded Computer System (ECS) Operational Flight Programs (OFPs). The simulation software is hosted on multiple distributed processors connected with SMARTNet (Shared Memory Architecture Network). Two dynamic task scheduling algorithms on ADSET system are proposed.

Acknowlegements

I would like to thank the Air Force Systems Command and the Air Force Office Of Scientific Research for sponsorship of this research, and the Universal Energy Systems for their help to me in all administrative aspects of this program. Special thanks should go to Capt. Marc J. Pitarys who provided me with support, encouragements, and a truely enjoyable working atmosphere.

I. INTRODUCTION:

The Advanced Multi-Purpose Support Environment (AMPSE) is a generic, modular, and extendable system, designed to improve the overall supportability of weapon system software by reducing the costs and increasing the capability and flexibility of the real-time support environment. It uses a modular building block approach in its design to allow for system modifications and enhancements. It provides a real-time simulation support environment for testing and evaluation of selected Embedded Computer System (ECS) Operational Flight Programs (OFPs). The support environment communicates with the OFPs via a dedicated ECS interface computer and the high speed real-time simulation network called SMARTNet (Shared Memory Achitecture Real-Time Network).

The simulation software hosted on multiple distributed processors provides the real-time simulation of the aircraft in an operational environment (including the aircraft's aerodynamics, avionic senors, weapon systems and targets). Simulation models are addressed as separate software modules that can be plugged into the simulation and easily moved among the simulation computers as requirements dictate. The AMPSE provides for future enhancements which would allow ECS models to be swapped with the actual aircraft ECS's or LRUs (Line Replaceable Units) executing their actual OFPs.

The AMPSE provides the capability for multiple configurations ranging from a single LRU with several models to a complete set of LRUs with only the aerodynamics and external environment models.

The AMPSE is comprised of the following functional segments:-

1). Modular Flight Console (MFC)

2). Embedded Computer Systems (ECSs) -- LRUs and their interfaces

3). Simulation Models

4). Networks -- Data Switch, Ethernet, SMARTNet

5). System Support -- it consists of

   a). Simulation Initiation

   b). Simulation Interface

   c). Simulation Distributed Executive

   d). The Shared Memory Data Display/Recording

   e). The Mission Scenario Generator (MSG)

   f). The Simulation Monitor and Controller.

The AMPSE operates in three modes :-

1). Configuration : In this mode, the operator will define the configuration of the simulation. This includes the MRU (Module Replaceable Unit) and LRU configurations and specific test case requirements to be satisfied during the initialization and execution modes.

2). Initialization : In this mode, operator will set up the simulation based on testing requirements set by the configuration mode and available hardware. It will run the diagonstic routines, initialize the hardware, and load and initialize the proper software.

3). Execution : It will provide a realistic real-time test environment for the OFPs under tesc. From this mode, the operator will perform real-time testing; interact directly with the real-time simulation, monitor simulation data and execution, and control the simulation testing.

In this report we will emphasis on simulation models, networks, system support and their relationships. Especially, we will conduct a feasibility study on the possibilty of building a dynamic task scheduling algorithm for the distributed simulation computers connected with the slot-ring topology using the SMARTNet.

II. RESEARCH OBJECTIVES.

The AMPSE's simulation consists of a set of software models that must be executed at a specified rates in order to provide a dynamic, realistic, simulated environment. Each model contains the algorithm (equations) and /or data required to simulate a specific function of overall environment.

There are two kinds of models under consideration:- the physics/environment models and the avionics models. The first kind of models are designed to simulate the host aircraft, outside world, and the actual physics of the weapon system. The second kind of models are actually duplicating the LRUs executing their respective OFPs. The avionics models are written in such a way to allow the software to be directly replaced with the actual ECS or LRUs they are simulating.

The AMPSE uses a RS-232 Data Switch, Ethernet, and SMARTNet for network communication within the system, see figure 1. The Data Switch provides manual operation and direct terminal to computer connection capabilities. It allows users to work at any terminal and connect to any of the simulation computers. Ethernet with DECnet protocol provides the non-real time network file transfers between the various simulation computers during the initialization and configuration modes.

The SMARTNet is a specially designed network replicated shared memory developed to support real-time multiprocessor simulation applications. It is the real-time network used in the AMPSE. It solves a combination of communication network problems frequently encontered in real-time simulations using distributed processors, such as :-

1). The software overload to implement network protocols consume too much of the processor throughput.

2). Poor network error recovery in real-time.

3). Software developers must be constantly aware of the network throughputs, and the timing of communications between processors.

4). Physically, the processors cannot be located too far apart.

With SMARTNet, each computer on the network has its own local copy of shared memory. The shared memory is continuously updated over a high speed slot-ring network, see Figure 2. There is no software overhead to pass simulation data between various computers in the network, because all the network protocol is implemented in the SMARTNet hardware. The protocol is transparent to the computer. This frees up computer processing power for

model execution and other real-time tasks. Since any computer on the network can have access to the data in the shared memory, any computer can read or write to this shared data and thus communicate with other computers on the network.

The system support function mainly includes the Simulation Interface, Simulation Initialization, Simulation Distributed Executive and other subfunctions. The Simulation Interface subfunction is the primary interface to the overall simulation. It is a menu-driven interface with on-line help. From this interface , the user is able to initiate execution of most of the AMPSE software.

The Simulation Initialization is an on-line configuration manager. It allows the user to set up the initial simulation model distribution across the various simulation computers. It uses the shared memory to communicate the configuration to the executive (local scheduler) of each simulation computer. It is a menu-driven spreadsheet program which can be run from any simulation computer on the network. The configuration sheets of each simulation is stored in a data file for later references.

Simulation Distributed Executives play a major role in the system support segment. Each simulation computer has its own executive routines (local scheduler) to schedule and executive the models configurated to that computer. The local scheduler will schedule the models based on the data placed on the shared memory by the simulation initialization and interface, and begin to execute the scheduled models when an interrupt is received. Interrupts are generated at a rate of 50 Hertz, and therefore the models are executed at a maximum rate of 50 Hertz.

As the current system sets up, all the simulation computers are homogeneous. They are all running at the same speed. There is a SMARTNet node inside each simulation computer. And each node in SMARTNet has its own FIFO queue of interrupts to execute the scheduled models. The execution time of each model is known to the local scheduler when it arrived (the execution time for each model is fixed at the configuration time and transmited to the local scheduler through the SMARTNet). In the SMARTNet, there is only one FIFO queue to collect data changes. And the time periods for updating data changes of the shared memory is different from the interrupt rates for execution at each simulation computer.

The current system support segment is working in FORTRAN under the MicroVaxes connected with Ethernet and SMARTNet. There is almost no task scheduling mechanism in its distributed executive. If there is one we can consider it only as static, at most. The models assigned to the simulation computer for execution were predetermined at the configuration time, therefore the processing power of the simulation computers are not fully utilized. In this regards, we first conducted a feasibility study on building a dynamic task scheduling algorithm for the distributed system when all simulation computers are homogeneous and connected with Ethernet and SMARTNet. And then we continued to study the possibility of building a dynamic one on a heterogeneous system.

III. MAIN RESULTS AND APPROACHES.

Real-time processing usually involves time-critical (as well as non-real time critical) activities. The time-critical activities may be periodic or aperiodic. Both periodic and aperiodic activities can be triggered by events(/or interrupts) generated by some equipment, or by other activities. Aperiodic activities (e.g., recovery processing) may have to execute at any random time and may require that the system perform fast reconfiguration (in the event of faults). A real-time distributed executive should be designed to support time-critical activities to guarantee that any of these activities never run before the event which requires its execution occur, and that the activity terminates within a fixed time interval. In this respect, the real-time distributed executive has to implement an effective processor allocation and activity scheduling policies. It has to provide the user with scheduling policies that, combined with the IPC (Inter Processor Communication) mechanisms, allow one to overcome such problems as the priority inversion problem, and the problem of system stability under transient overload as mentioned in Goodenough,J.B. and Lui Sha [4, 8] and in Falcone,M.,Panzieri,S., et al. [3]; It has to provide the user with resources allocation mechanisms that can support the asynchronous transfer of the CPU control among activities; It also has to provide such timing information as time-out exceptions, deadlines, and duration at which periodic activities can occur. By all means, it requires an efficient dynamic task scheduling algorithm in the real-time distributed executive.

We will first focus on the distributed system with all simulation computers N_1, N_2, ... , N_n are homogeneous and connected with SMARTNet. Assume that each simulation computer has a local task scheduler which will schedule the local tasks submitted by the local users for execution either locally on that computer or remotely on another computer. Each computer periodically sends an update message to each of the computers in the network.

Assume that an update message containing task loads and status informations on computer N_i is sent at each instant $m\tau$ for m=1,2,.....

Let $T_m = (m\tau, (m+1)\tau)$ be the m-th update period, where τ is the update period length, and $M_i(m)$ be the message to be sent at instant $m\tau$ on computer N_i, which includes the following observables and estimates of the load parameters stored at the SMARTNet node of the simulation computer N_i :-

$Q_i(m)$ = the number of tasks queued at computer N_i at $m\tau$.

$\hat{Q}(m)$ = the average queue length at instant $m\tau$ during previous update period T_{m-1}.

We will then establish a dynamic task scheduling algorithm using the probability of tasks being served with respect to the length of queue of interrupts at each simulation computer; similar to the one established by Hsu Huang,C.Y. and Liu, Jane W.S. in [5]. It consists of the following steps:-

STEP1. Determine whether a task is to be executed locally or remotely as following :

If $Q_i(m) - \hat{Q}(m) < k$, (one reasonable choice is k=2)
then the task is executed locally at N_i and the algorithm terminates, otherwise go to next step.

STEP2. Determine the probability $P_{ij}(m)$ for sending a task to a remote computer N_j as following :

Let $P_{ij}(0) = 1/N$ for $j = 1,2,\ldots,n$.

and $L_{ij}(m) = Q_i(m) - Q_j(m)$ for $j = 1,2,\ldots,n$.

$$L_i(m) = \sum_{j=1}^{n} L_{ij}(m)$$

$$P_{ij}(m) = L_{ij}(m) / L_i(m).$$

STEP3. Dispatching an incoming task according to the ascending order of the probabilities $P_{ij}(m)$, $j = 1,2,\ldots,n$, calculated in STEP2.

STEP4. Adjusting the probabilities for remote hosts :

Each time when the selected remote computer N_r , received a local task from N_i , records the number of local tasks, $R_{ir}(m)$, sent to remote computer N_r . If $R_{ir}(m)$ is greater than a predetermined number $\sigma > 0$, then the probability for selecting the computer N_r is decreased by a predefined amount $\epsilon > 0$. i.e.,

$$P_{ir}(m) = P_{ir}(m) - \epsilon ,$$

and $$P_{ij}(m) = P_{ij}(m) + \epsilon/(N-1) , \quad j = 1,2,\ldots,r-1,r+1,\ldots,n.$$

A second algorithm, which is similar to the one developed by Biyabani, S. R., Stankovic, John A., and Ramamritham, K. in [1, 9, 10, 12], although it was designed for a distributed operating system (DOS) over a heterogeneous system of computers [11], seems to be work in our current setting except the network topology which we replace it with is slot-ring and connected by SMARTNet. The following assumptions will be made regarding the application tasks :-

-- Tasks arrive dynamically and independently

-- At run-time, there is no a priori knowledge of which tasks will arrive and when they will arrive

-- There are no precedence constraints on the tasks

-- All tasks are aperiodic

-- A task is ready to execute as soon as it arrives in the system.

-- Each task has the following characteristics which are known at the time of arrival :-

* An arrival time : the time at which the task is invoked.

* A worst-case computation time : the maximum time needed for it to complete execution.

* A criticalness : one of the q possible levels of importance of the task.

* A deadline : the time by which the task has to complete execution.

We will outline the system architecture as follows :- The system consists of n simulation computers connected with slot-ring topology and SMARTNet. Each computer could contain more than one processor, but for simpilicity, we will assume that each computer in the system contains only one processor. There is a SMARTNet node and a local scheduler in each processor. Besides, there is also a global scheduler for the whole system, certainly there is a SMARTNet node in the processor where the global scheduler resides. There is a data structure, STT (System Task Table) in each SMARTNet node. Each entry in STT contain fields of Computer-ID, Task Arrival-Time, Latest-Start-Time, Criticalness, Deadline, and Computation-Time. The task's Latest-Start-Time, which was computed when the task was guarenteed (see [1]), is the latest time in which the task can start executing and still meet its deadline. The entries in STT can be reordered, be removed, or be inserted by the respective local scheduler and is updated through SMARTNet at each of the simulation computers.

The local scheduler is activated upon the arrival of a new task at the computer, or in response to the bidding which is initiated by the global scheduler. The local scheduler determines if a new task can be inserted into the current STT such that all previous tasks in the STT as well as the new task meet their deadlines. If so, we say that the new task is guaranteed, the latest start time is then computed and put into the corresponding entry in the STT. If the new task can not be guaranteed locally, or can only be acomodated at the expenses of some previously guaranteed tasks, then the rejected tasks are handed over to the global scheduler.

activity scheduling policies. This requires an efficient Dynamic Task Scheduling Algorithm in the Distributed Executive.

Although two dynamic task scheduling algorithms has been proposed in this report, no simulation has been done because of time shortage. It still requires a lot of research in this area. We can improve the second algorithm by introducing some experimental parameters such as Weight Guarantee Ratio (WGR) and the Balance Factor (BF) as indicated in Biyabani and Stankovic [1]. There should be some benchmark results in a later day.

Some problems will be encountered in the implementation of Ada code for the ADSET to support real-time processing due to the nature of Ada programming language such as Scheduling, Interrupt Handling, Fault Tolerance, Efficency of Memory Management, Timing, and problems dealt with Distributed Targets. But we can build an Real-Time system support tailored to specific application requirements so as to incorporate those real-time features which are not available (or not very efficient) in the standard Ada.

As a final remark, I would like to recommand that the system architecture be restructured as outlined in Figure 3 in order to make the entire distributed system more dynamic and flexible. All the ESCs which contain LRUs will be connected by SMARTNet and Ethernet and form a subnet S1. All the Simulation Computers which contains Simulation Modules form a subnet S2 connected by SMARTNet and Ethernet. All the computers which contain the Cockpit, VAPS, and Paragon form a subnet S3 connected by SMARTNet and Ethernet. And then S1, S2, and S3 will be connected by SMARTNet to SimMAC, DATA SWITCH through Gateways G1, G2, and G3 respectively. A distributed operating system should be built for the heterogeneous case.

V. REFERENCES.

1. Biyabani, S.R., Stankovic, J.A. and Ramamritham, K., "The Integration of Deadline and Criticalness in Hard Real-Time Scheduling", IEEE, Proceedings of Conference on Real-Time processing and its Applications, 1988.

2. Cheriton, D.R., "The V Distributed System", ACM Communications, Vol.31. No.3, March, 1988.

3. Falcone, M., Panzieri, F., et al., "Issues in the Design of a Real-Time Executive for On-Board Applications", Sixth IEEE Workshop on Real-Time Operating Systems and Software, SEI, Pittsburgh, PA., May, 1989.

4. Goodenough, J.B., Sha,Lui, "The Priority Ceiling Protocol: A Method for Minimizing the Blocking of High Priority Ada Tasks", Ada Letters, Special Edition, International Workshop on Real-Time Ada Issues, Fall, 1988.

5. Hsu Huang, C.Y., and Liu, Jane, W.S., "Dynamic Load Balanced Algorithms in Distributed Systems", IEEE Proceedings, The 6th International Conference on Distributed Computer Systems, May, 1986.

6. Liu, C.L., and Layland, J.W., "Scheduling Algorithms for Multiprogramming in a Hard Real-Time Environment", ACM Journal, Vol. 20, No.1, Januray, 1973.

7. Liu, D.B., "Dynamic Task Scheduling With Resources Requirements in Hard Real-Time Distributed Computer Systems", Proceedings, Second International Symposiums on Computers, December, 1986.

8. Locke, C.D., Sha, L., et al., "Priority Inversion and its Control : An Experimental Investigation", Ada Letters, Special Edition, International Workshop on Real-Time Ada Issues, Fall, 1988.

9. Ramamritham, K., and Stankovic, J.A., "Dynamic Task Scheduling in Hard Real-Time Systems", IEEE Software, Vol. 1, July, 1984.

10. Sha, L., Lehoczky, J.P., and Rajkumar, R., "Task scheduling in Distributed Real-Time Systems", IEEE, Proceedinds, Industrial Electronics Conference, 1987.

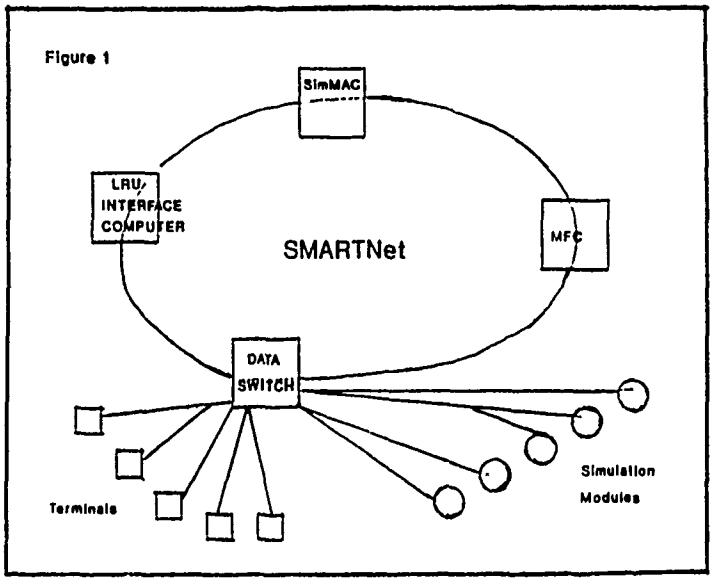
11. Stankovic, J.A., and Ramamritham, K., "The Spring Kernal : A New Paradigm for Real-Time Operating System", Sixth IEEE Workshop on Real-Time Operating Systems and Software, SEI, Pittsburgh, PA., May, 1989.

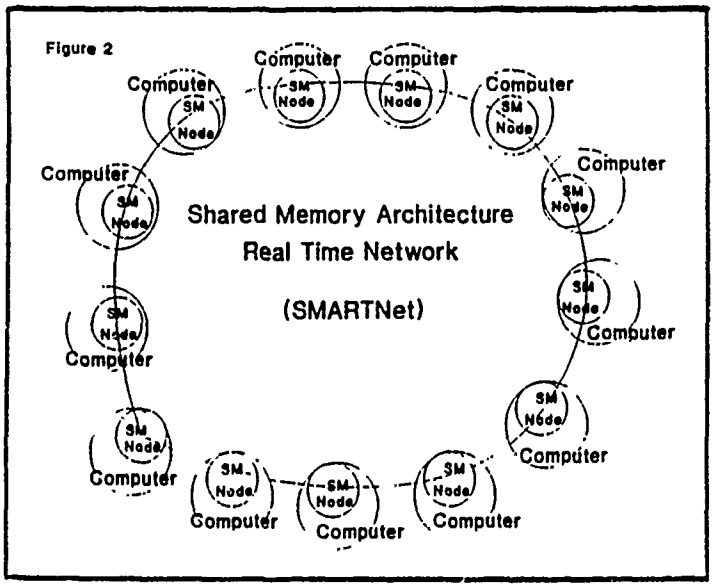
12. Stankovic, J.A., Ramamritham, K., and Cheng, S., "Evaluation of a Bidding Algorithm for Hard Real-Time Distributed Systems", IEEE Transactions on Computers, Vol. C-34, No.12, December, 1985.

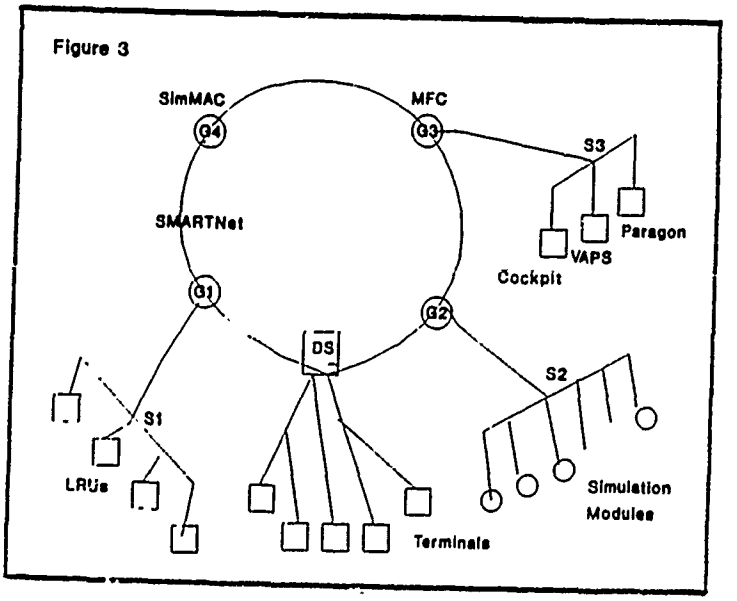
13. Zhao, W., and Ramamritham, K., "Simple and Integrated Heuristic Algorithms for Scheduling Tasks with Time and Resources Constraints", Journal of Systems and Software, 1987.

14. Zhao,W., Ramamritham, K., and Stankovic, J.A., "Scheduling Tasks With Resources Requirements in Hard Real-Time Systems", IEEE Transactions on Software Engineering, May, 1987.

15. Zhao, W., Ramamritham, K., and Stankovic, J.A., "Preemptive Scheduling Under Time and Resources Constraints", IEEE Transactions on Computers, Vol.C-36, No.8, August, 1987.


Figure 1
SimMAC
LRU/
INTERFACE
COMPUTER
SMARTNet
MFC
DATA
SWITCH
Terminals
Simulation
Modules


Figure 2
Computer
SM
Node
Shared Memory Architecture
Real Time Network
(SMARTNet)


Figure 3
SimMAC
MFC
G4
G3
S3
SMARTNet
Paragon
VAPS
Cockpit
G1
G2
DS
S2
S1
LRUs
Simulation
Modules
Terminals

1989 USAF-UES SUMMER FACULTY RESEARCH PROGRAM

Sponsored by the

AIR FORCE OFFICE OF SCIENTIFIC RESEARCH

Conducted by the

Universal Energy Systems, Inc.

FINAL REPORT

Ada Compiler Efficiency Evaluation

Prepared by:	James L. Noyes, Ph.D.
Academic Rank:	Associate Professor
Department and	Mathematics and Computer Science Department
University:	Wittenberg University
Research Location:	USAF WRDC/AAAF-3 Wright-Patterson AFB Dayton, OH 45433
USAF Researcher:	Capt. Marc Pitarys

Date:	25 Aug 89
Contract No:	F49620-88-C-0053

Ada Compiler Efficiency Evaluation

by

James L. Noyes

ABSTRACT

Due to the complexity of the Ada Programming Language, it is not only important to validate the Ada compilers, but it is also necessary to compare their relative efficiencies. The ACEC (Ada Compiler Evaluation Capability) system was developed by the Boeing Military Airplanes Company for the Ada Joint Program Office (AJPO) to help determine these relative efficiencies. One of the key programs in this system is called Median, which may be used to evaluate the relative efficiency of Ada application code (compilation and execution) time and memory storage. Median is based upon a Median Polish technique for examining and summarizing tabular data. The rows of this table correspond to benchmark test problems and the columns correspond to Ada compiler systems to be evaluated. The table entries can be (1) execution times, (2) compilation times, or (3) memory used by each benchmark application program. Due to the importance of this evaluation process, the Median technique needs to be investigated. Because of the large number of benchmark programs available, a methodology is also needed to aid the ACEC user in choosing the appropriate benchmark programs to test the required Ada language features. Once this is done, Median can be better used to help in selecting an Ada compiler system.

Acknowledgments

I wish to thank the Air Force Systems Command and the Air Force Office of Scientific Research for sponsorship of this research. In particular, Capt. Marc J. Pitarys WRDC/AAAF-3, was instrumental in the selection of this research project and was extremely supportive throughout this research period.

Universal Energy Systems must be mentioned for their concern and help to me in all administrative and directional aspects of this program. Mr. Dan Danishek and Ms. Lou Henrich are two of the most organized administrators with whom I have ever worked.

I. INTRODUCTION:

The Wright Research and Development Center (WRDC) awarded a contract to the Boeing Military Airplanes Company (BMAC) to develop the Ada Compiler Evaluation Capability (ACEC) for the AJPO. The ACEC was managed by the Avionics Logistics Branch, WRDC/AAAF of the Avionics Laboratory. Of particular concern is the effective use of the ACEC program.

A key program in the ACEC system is called Median, which may be used to estimate the relative efficiency of code generated by the Ada compiler systems in terms of code execution time, compilation time and memory used. Median is based upon a Median Polish technique for examining and summarizing table data. The rows of this table correspond to benchmark test problems and the columns correspond to Ada compiler systems to be evaluated. Due to the importance of the evaluation process, the Median technique needs to be investigated and a methodology is also needed to aid the ACEC user in selecting the appropriate benchmark programs to test the required Ada language features and in selecting an Ada compiler system based upon the Median results.

While my research interests are primarily in the area of artificial intelligence, I have also worked in the creation and evaluation of mathematical software. This particular problem was of interest because it involves three different disciplines: computer science, mathematics and statistics.

II. OBJECTIVES OF THE RESEARCH EFFORT:

The primary objective was to design a system that assists users in interpreting the results using the ACEC program. This involved the following:

1. Location and review applicable ACEC documentation and related reference material.

2. Review the output from sample ACEC test runs.

3. Examination of the ACEC Median methodology and determine if the Median program correctly processes the Ada compiler performance data.

4. Development of heuristics, rules and other methods for interpreting compiler performance results produced by the Median program. The focus was on factors most relevant to avionics applications (e.g., time-sensitive and memory-sensitive limitations).

5. Design and development of a prototype system that assists in selecting an Ada compiler.

A more detailed version of the research is presented in [Noye89].

III. THE MEDIAN POLISH METHODOLOGY

The Median Polish methodology used by BMAC is described in [Vell81] (also see [Tuke77] and [Tiet86]). It is a method used in what Tukey calls Exploratory Data Analysis (EDA) [Tuke77]. EDA

involves a preliminary look at a set of data and is usually followed by a more detailed data analysis using standard statistical techniques [Tiet86]. The Median Polish technique is presented by Velleman in [Vell81] as a methodology to fit an Additive Model to table data based upon row and column effects. The model is given as:

$$fit_{i,j} = \text{common} + \text{row effect}_i + \text{column effect}_j$$

with

$$\text{residual}_{i,j} = \text{data}_{i,j} - fit_{i,j}.$$

Here the notation in [Vell81] is used. The Median Polish algorithm arbitrarily starts by determining and subtracting each of the row medians from all of the observations in the corresponding rows. These could be called row median$_i$. The median of all of these row medians is found, subtracted from each row median and is saved as a common factor called common. This is called a row sweep or half-step. Next, the algorithm determines and subtracts each of the column medians from all of the observations in the corresponding columns. These could be called col median$_j$. The median of all of these column medians is found, subtracted from each column median and added to the current value of common. This is called a column sweep or half-step. A full-step is when this pair of sweeps is done.

The idea is for these full-steps to be repeated as often as necessary so that the resulting data values, called the residual$_{i,j}$, are sufficiently small. Velleman in [Vell81] states (but does not prove) the following:

> "Of course, not every residual will be made smaller [during each sweep]. Some may grow substantially. But overall, most residuals will be brought closer to zero by performing additional sweeps."

As more steps are repeated the row and column medians are accumulated, respectively as row effect$_i$ and column effect$_j$. When this entire process is complete (two full-steps are recommended for most situations), fit$_{i,j}$ should be "close" to data$_{i,j}$. Velleman also states that (the underlining is mine):

> "In addition, users must choose whether to remove medians from rows or columns first. For some data, the final fit and residuals will differ when these two starts are compared. Although it is quite rare for the gross structure of the fitted models to differ in important ways, the availability of machine-computed median polish makes it practical to find both versions and compare them."

The Boeing Median program is based upon a Product Model. In [Read88] they give this model in terms of time (or memory space). Here it is written as:

```
Time(Problem,System) = Problem_Factor(Problem)*
                       System_Factor(System)*
                       Residual(Problem,System).
```

That is, they assume that these two independent factors can be found. The main factor of interest is the system factor because this is used to help make relative comparisons among various Ada compilers. In Median, the first system identified is arbitrarily used as a baseline (with its systems factor normalized to 1.0) so that faster systems will always have values less than 1.0 while slower systems will have factors greater than 1.0.

What the Boeing Product Model guarantees is that if one were to begin with the data generated by

$$Time(Problem_i, System_j) = P_i * S_j \text{ for } i=1,2,\ldots,m;\ j=1,2,\ldots,n.$$

where P_i is a positive constant representing a specified time required to solve $Problem_i$ and S_j is a positive constant representing a specified time used by the code generated by the compiler $System_j$ then the Median Polish algorithm will yield

$System_Factor(System_1) = 1$, and

$System_Factor(System_j) = S_j/S_1$ for $j=2,3,\ldots,n$.

$Problem_Factor(Problem_k)/Problem_Factor(Problem_l) = P_k/P_l$ for any two problems k and l.

and

$$Residual(Problem_i, System_j) = 1 \text{ for } i=1,2,\ldots,m;\ j=1,2,\ldots n.$$

Note that this method <u>cannot</u> return the absolute factors, only the <u>relative</u> ones. Hence for exact data, this is like a vector <u>outer product</u> representation of the form: $ps^T = T$. To convert this into an Additive Model, natural logarithms are used. That is, the Median program essentially uses:

$$\begin{aligned} Ln\{\ Time(Problem,System)\ \} = {} & Ln\{\ Problem_Factor(Problem)\ \} + \\ & Ln\{\ System_Factor(System)\ \} + \\ & Ln\{\ Residual(Problem,System)\ \} \end{aligned}$$

which is of the form:

$$\begin{aligned} data_{i,j} &= row\ effect_i + col\ effect_j + residual_{i,j} \\ &= fit_{i,j} + residual_{i,j} \end{aligned}$$

where the common factor mentioned earlier is included by Boeing in the row and column effects of their Product Model formulation.

The Boeing Median program always uses 10 full-steps and always starts with a row sweep. As stated by Velleman, it was found that starting with a column sweep can produce different results and system rankings. To help evaluate the Median program's methodology, I wrote the Med program and some other data manipulation utilities to evaluate the Median Polish process.

It should be noted that other methods have also been used to estimate the relative performance of computer systems on a suite of benchmark problems. Boeing noted this in [Read88]. Both the arithmetic and geometric means for each system have been used as illustrated in [Flem86]. These other methods can produce different rankings than those produced by Median. They also are simpler to use, but do not allow for the problem rankings as does the Boeing method.

IV. EXAMINING THE MEDIAN POLISH METHODOLOGY

In order to examine the Median Polish methodology itself, an interactive Med program was written. The code is implemented in VAX Pascal. This strategy simplifies the process required to execute the Boeing Median program [User88]. The features of Med are given in [Noye89].

In Appendix I of [Trep88] the Boeing Median program was used to analyze execution time results for 1076 problems against five systems using row-column iterations. Their results are shown in

the first column of Table 1. The interpretation of these results alone would indicate that the HARRIS_800 and AIMS_88 Ada Systems were slower than the TELESOFT and APOLLO Ada Systems while the DEC_VAX Ada System was faster. Having a single measure to be used in this way is very desirable [Flem86].

The second column of Table 1 may be obtained from the first by normalizing with respect to the fastest indicated system and ordering these from fastest to slowest. This was done in order to aid in comparing systems and to relate the Boeing Median results with the Med results shown later in Table 2.

	System 1 Normalized		Normalized to Fastest	
System 1.	TELESOFT	1.00	DEC_VAX	1.00
System 2.	HARRIS_800	1.07	TELESOFT	1.10
System 3.	DEC_VAX	0.90	APOLLO	1.10
System 4.	AIMS_88	1.24	HARRIS_800	1.17
System 5.	APOLLO	1.00	AIMS_88	1.34

Boeing Median Test Results (Using 1076 Problems)

Table 1

Of all 1076 problems, only 99 of them were executed by all systems! This was less than 10% of the total, hence more than just these numbers should be used when comparing systems. The Med program was run with the same data (taken from [Trep88]) on these 99 problems, first using row-column iterations and then using column-row iterations. These results are shown in Table 2 in terms of the fastest system chosen.

Row-Column Steps			Column-Row Steps		
DEC_VAX	1.00	fastest	TELESOFT	1.00	fastest
TELESOFT	1.09	9% slower	DEC_VAX	1.02	2% slower
APOLLO	1.09	9% slower	APOLLO	1.14	14% slower
HARRIS_800	1.19	19% slower	HARRIS_800	1.52	52% slower
AIMS_88	1.55	55% slower	AIMS_88	1.62	62% slower

Med Test Results (Using 99 Problems)

Table 2

Note that the Med results for the row-column iterations are shown in the first column of Table 2 and are rather close to those of Median, considering that less than 10% of the 1076 problems could be used. The Med program was run again with everything else being the same, except that the iterations began with column sweeps using column-row iterations. The results are shown in the second column. Notice this resulted in a position interchange, between the first and second system as well as significant differences in the relative speeds. Other cases were run that also produced different rankings using row-column iterations vs. column-row iterations. These differences do not always occur and may not be significant when more data is used, but it is impossible to tell this ahead of time.

Overall, the Boeing Median Polish Methodology works correctly under the given product model assumptions. However, despite the intuitive appeal, it is not clear that a resource expenditure is adequately modeled as a product relationship. Of course, other types of models could require a significant change in the solution algorithm.

One way to check the sensitivity of the results is to take the Boeing timing data, add a normally distributed error with a mean of zero and a given sigma error and see how this error is propagated into the final system and problem factors. It is especially important not to violate what might be termed the Heisenberg Principle of Software Evaluation: "The software measurement process should not affect the quantity being measured."

One of the most significant aspects of the ACEC process is related to the selection of appropriate test problems and the interpretation of the ACEC results. This is addressed in the next section.

V. TEST PROBLEM SELECTION AND INTERPRETATION

As previously mentioned, there are 1076 test problems in the ACEC benchmark suite. Each of these appears to be well-commented in a standard way and includes references to sections in the Ada Language Reference Manual (LRM) that correspond to the constructs to be tested.

Before examining the selection and interpretation of the test problem results, it is necessary to state the importance of well-written benchmark problems. In [User88] Boeing states that:

> "A problem intended to test one feature may actually test another."

The reason for knowing what features are being tested, is that if one or two features are present in many problems it will have the effect of implicitly weighting the data and therefore biasing the final system factors.

The statistical model used by Boeing assumes that the measured test problem times are independent [Read88]. They state that,

> "The statistical model assumes that measured test problem times are independent. Based upon the construction of the test suite, this is not completely true, although it should be a good approximation."

This statement is not completely clear. If they mean that the execution of a previous problem did not affect the measured execution time of a subsequent problem (as the first sentence indicates), then I agree that this should be the case. If they mean that the problem times are independent because the application code is different, then I disagree. The benchmark problems taken all together are not really very independent. In some cases (such as two different Ada compilers run on the same computer) the systems will not be independent at all. In other cases (such as two different problems using many of the same Ada language features) the problems will be highly correlated. The effect of this type of implicit weighting will have to be judged on a case-by-case basis, once the features are known.

Problem Selection for Median:

There are two approaches to problem selection: (1) pick problems that contain Ada language features that are important to a given

class of applications, (2) pick a representative mix of problems from a given class of applications without regard to the features included. Both approaches are common, but the second requires less knowledge on the part of a user. In the following, it will be assumed that a sufficient number of benchmark programs already exist that test what is required and that the corresponding benchmark data is available in a benchmark file. See Figure 1.

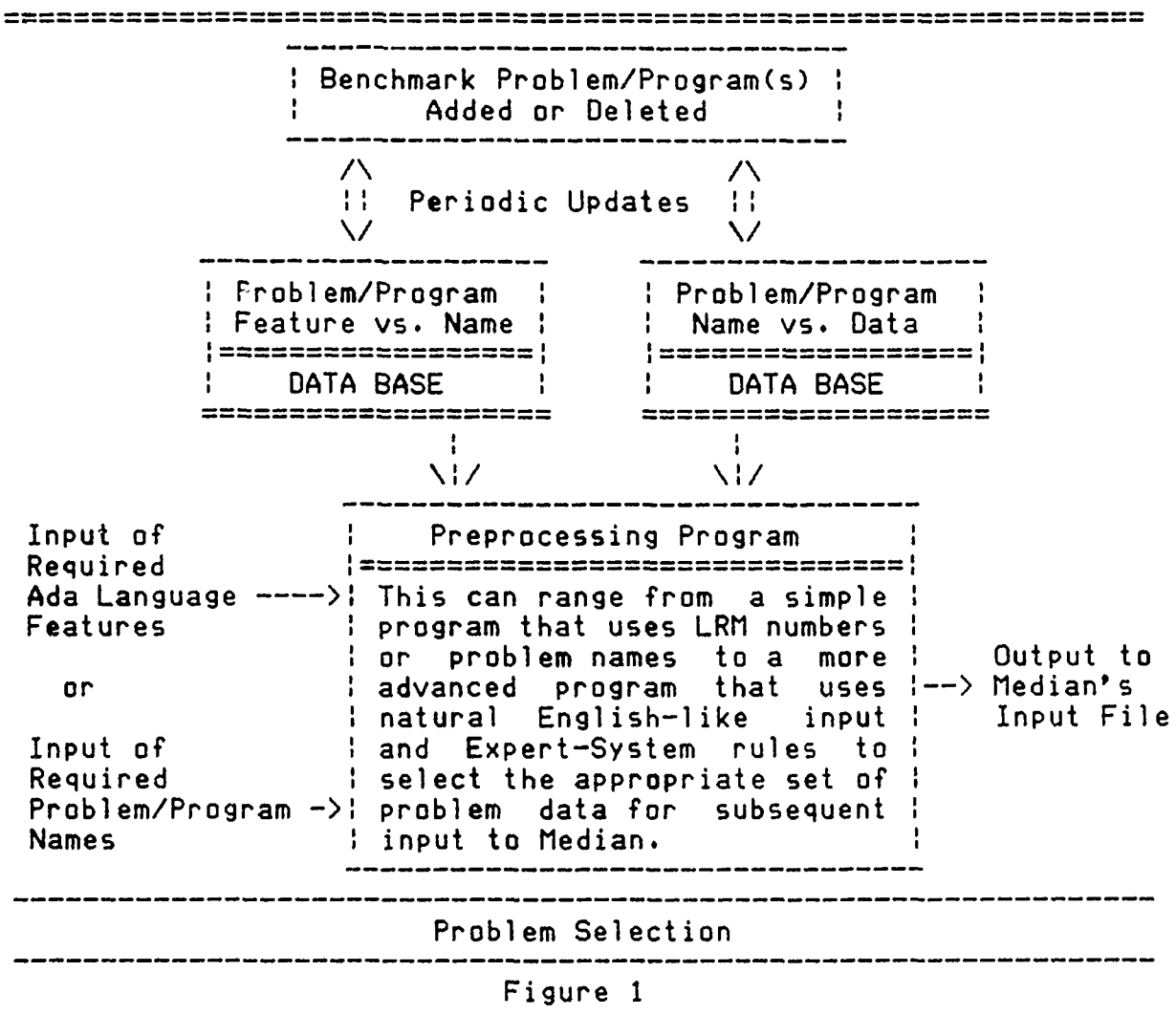


Figure 1

If the first approach is followed, it should be recognized that a typical benchmark program will contain a subset of these features

since it is virtually impossible to construct a benchmark program that evaluates just one feature by itself. Note also that two problems using the exactly the same features will not normally produce the same compiled code since these features are typically combined in different ways in the source code. The resulting programs will also have different test data and produce different results. It is very difficult without examining the compiled code to identify exactly what there is about a given feature combination that causes more or less resources to be used.

If it is desired to select a subset of the benchmark data that corresponds to a required set of Ada language features, then the process is relatively easy since this information is already documented by Boeing as the "Feature Cross References" in Appendix V of [Vers88]. The information from this appendix could be placed in a data base and automatically searched. If found, the associated benchmark data can be copied from the standard benchmark file to the file to be processed by the Boeing Median program. (Note also that the source code for each benchmark program contains a list of documented "LRM Features.") Using Expert System notation one is using the following rule:

If {Feature$_k$ is required}
then {Select Problem$_a$ & Problem$_b$ & ...}, for k=1,...,l.

If the second approach is followed, the process is even easier since the benchmark problems can be directly identified by name. The data copying process is the same. Here, of course, one should be sure to choose a representative mix in terms of the expected frequency of use (or importance) of the programs.

A preprocessing program could be used to implement both approaches. However, for the reasons stated earlier, the user should be aware of exactly what Ada language features are being evaluated and how often they appear. That is, one should use the equivalent of the following rule to show this to the user:

> If {Problem$_1$ & Problem$_2$ & ... & Problem$_n$ have been selected}
> then {Feature$_r$(O$_r$) & Feature$_s$(O$_s$) & ... are being evaluated}.

For example,

> If {SEARCH & SIEVE & PUZZLE & ACKER1 have been selected}
> then { Numeric_Literals(4) & String_Literals(2) &
> Type_Declarations(1) & ... & Function_Subprograms(3)
> are being evaluated}.

Here the quantity within parenthesis indicates how often the corresponding feature appears in this problem set. An alternate way to display this information is by a Problem vs. Feature Table. An example is shown here:

Feature / Problem	Num Lit	Str Lit	Type Decl	...	Func Subp	Total
SEARCH	*	*			*	20
SIEVE	*		*			12
PUZZLE	*	*			*	23
ACKER1	*				*	11
Total	4	2	1		3	56

Interpretation of Median's Results:

The worst possible use of Median will occur when someone makes a Median run, looks only at the "bottom line" called SYSTEM FACTORS and uses these to rank the Ada compilers. Unfortunately, this is what I expect most of the users to do because it is so easy. In addition to (a) system factors, Boeing provides output of (b)

problem factors, (c) residuals, (d) mean and standard deviation of the logarithms of the residuals, (e) histogram printer-plots, (f) Kolmogorov-Smirnov statistics and (g) other measures of fit. The problem is that unless the user has a statistical background or has been appropriately trained (which most have not), he or she won't know what to do with the rest of the information. The problem factors may be the exception. The users must at least have some sort of quantitative measure of confidence on each of the system factors or else they will think that these factors are "perfectly correct." I have already shown examples where this is not the case.

In normal types of least-squares fitting, for both linear and nonlinear functions, it is possible to compute expressions for the variances and covariances of the fitted parameters as a function of the variances of the data. Something like that is needed here. Ideally each systems factor S_i (and perhaps each problem factor P_i) would be output with an estimate of its standard deviation. These "sigma" values could be used to compute confidence intervals. If these intervals were all distinct, then it would be likely that the output Ada compiler rankings were correct. If some of these intervals overlapped, then all of the associated compiler systems would be ranked in the same class or subsequent Median runs would be made in order to make a better distinction among them.

VI. RECOMMENDATIONS:

The following recommendations for the improvement of the ACEC system are grouped into three categories in order to facilitate software implementation:

Preprocessing:

1. A method could be developed to allow the user to easily identify specific Ada language features, which in turn is used to select benchmark data for use in the compiler system evaluation.

2. A method could be developed to allow the user to easily identify problem names used to select a subset of the benchmark data, for use in the compiler evaluation process.

3. Once the test problem data has been selected, the user should be able to determine which features are included as well as information about where or how often the feature appears.

Median Processing:

1. Both row-column and column-row iterations should be performed (starting with both an initial column sweep and an initial row sweep) before any system rankings are quoted. If any two systems are "sufficiently close" in ranking, then they should be considered as having the same rank. It is especially necessary for the user to check the residuals and other output in these cases and perhaps try alternate methods [Flem86].

2. Boeing should provide a stronger theoretical justification for their Median methodology because of the existence of alternate (and simpler) methods for estimating system performance.

3. Boeing should clearly document how the Median results are to be interpreted. This includes the factors, residuals and the Kolmogorov-Smirnov statistics. This could be done with a small Analysis Guide. Ideally this could be supplemented with a 2-4 hour training course on the use of ACEC and Median.

4. Alternate models should be investigated for this type of problem to determine if a better "fit" could be obtained.

5. The Median program should also output the maximum row and column medians after each iteration in order for the user to have more assurance in the final results. Testing these values and terminating the steps when they are both small, instead of always using ten steps should also reduce processing time in many cases.

6. A sensitivity analysis should be performed on the data in order to see how perturbations in the data cause perturbations in the final system and problem factors.

7. The Median program could be modified to perform an absolute and relative error check on the computational difference between each observation and the product of the corresponding system factor, problem factor and residual in order to test for possible roundoff error. Double precision computations would insure a reduced roundoff error.

8. Consideration could be given to modifying the Median program to provide an option of rearranging the output according to increasing system factors and problem factors.

Postprocessing:

1. In many types of statistical parameter estimation problems, a confidence estimate is also provided with each parameter. Numerical confidence estimates should at least be provided for all system factors, even if they are pessimistic (large). A single number should be presented with each factor output so the ACEC user can easily tell which factors are the most reliable.

2. If single confidence estimates cannot be provided, then one could employ the geometric and even arithmetic means as shown by Fleming [Flem86]. These normalized results can also be used to provide auxiliary rankings. Heuristic rules, based upon empirical data, could be used to express this confidence. (For example, if Median ranked a particular system as the fastest and the same held for both the arithmetic and geometric means, then the user could have a high confidence in this result.)

3. Confidence estimates could also be provided for all problem factors. A single number presented with each problem factor output would aid in assessing the resources used by each problem.

4. The residuals that are currently plotted and displayed in histograms, together with the other statistics (and confidence factors) should be used by Median or a postprocessing program to automatically inform the user if Median should be rerun with a modified data set.

This entire process can be made interactive so that a user could continue to refine the processing in these three stages until satisfied. Note that this requires more effort by the user and therefore the entire process should not be made interactive unless there are enough ACEC users to make this cost-effective.

REFERENCES

AdaL83 Reference Manual for the Ada Programming Language, ANSI/MIL-STD-1815A-1983, Springer-Verlag, New York, NY, 1983. (Called the LRM - Language Reference Manual.)

Cody80 William J. Cody, Jr. and W. Waite, Software Manual for the Elementary Functions, Prentice-Hall, Englewood-Cliffs, NJ, 1980.

Flem86 Philip J. Fleming and J. Wallace, "How Not to Lie with Statistics: The Correct Way to Summarize Benchmark Results," CACM, Vol. 29, No. 3, Mar 1986, pp. 218-221.

Noye89 James L. Noyes, ACEC Compiler Efficiency Evaluation, White Paper, WRDC/AAAF-3, Contract No. F49620-88-C-0053, August, 1989.

Pres86 William Press, et.al., Numerical Recipes, Cambridge University Press, New York, NY, 1986.

Read88 Ada ACEC TOR Reader's Guide, D500-11790-2, BMA, 10 Jun 1988.

Tiet86 Gary L. Tietjen, A Topical Dictionary of Statistics, Chapman and Hall, New York, NY, 1986.

Trep88 Ada ACEC Software Test Report, D500-11504-1, BMA, 27 May 1988.

Tuke77 John W. Tukey, Exploratory Data Analysis, Addison-Wesley, Reading, MA, 1977.

User88 Ada ACEC TOR User's Guide, D500-11790-1, BMA, 10 Jun 1988.

Vell81 Paul Velleman and D. Hoaglin, Applications, Basics, and Computing of Exploratory Data Analysis, Duxbery Press, Boston, MA, 1981.

Vers88 Ada ACEC Version Description Document, D500-11790-3, BMA, 29 Mar 1988.

1989 USAF-UES SUMMER FACULTY RESEARCH PROGRAM

GRADUATE STUDENT RESEARCH PROGRAM

Sponsored by the

AIR FORCE OFFICE OF SCIENTIFIC RESEARCH

Conducted by the

Universal Energy Systems, Inc.

FINAL REPORT

TOWARDS A COURSE-GRAINED TEST SUITE FOR VHDL VALIDATION

Prepared by:	Robert C. Shock, Ph.D.
Academic Rank:	Associate Professor
Department and	Computer Engineering
University:	Wright State University
Research Location:	WRDC/ELED WPAFB OH 45433-6543
USAF Researcher:	Dr. John Hines
Date:	30 Aug 89
Contract No:	F49620-88-C-0053

Towards a Course-Grained Test Suite for VHDL Validation

by

Robert C. Shock

ABSTRACT

One of the paramount issues facing the electronic community is how it should respond to the various implementations (compilers) of the newly developed standardized language VHDL. The properties of uniformity and portability of source code must be ensured else chaos, duplication and soaring cost will follow. It is suggested that a course-grained approach of testing these compilers be enacted. This report also describes the development and implementation of a tool set that allows the programmer to control individually the letter style, the type style and the shape style of source code.

Acknowledge

I wish to thank the Air Force Systems Command and Air Force Office of Scientific Research for sponsorship of this research. I thank Universal Energy Systems for their concern and assistance to me in the administrative aspects of this program.

I thank in alphabetical order these people who enriched by knowledge and assisted me in my work:

Darrel Barker
Ben Carrol
Luis Concha
Jack Ebel
Stuart Labovitz, CAPT
Karen Serafino, CAPT
Gerald Tromley, 2ND LT

I sincerely thank Dr. Hines for introducing me to VHDL and for his encouragement in this area. I thank him for allowing me to take a short course in VHDL.

I. INTRODUCTION:

The Very High Speed Integrated Circuits (VHSIC) Program Office of the Department of Defense recognized in 1981 the need for a standard hardware description language in the microelectronics community. A standard language became a reality in 1987. The standardization process of the IEEE gave birth to the reference manual IEEE Std-1076-1987 that specifies the VHSIC Hardware Description Language (VHDL). VHDL is a modern comprehensive, flexible language that extols the software engineering principles of abstraction and hierarchical organization. It is independent of both technology and process, it supports various design methodologies (top-down, bottom-up, library-based), and it allows behavioral descriptions to range from the unit digital system level to the atomic component gate level. VHDL's complexity and infancy spawn standard, predicted problems that normally trail new complex languages such as Ada.

These problems filter to three areas: tools, users, and language. A severe shortage of support tools exists for VHDL. These tools include the compilers, the library-systems, the load-linkers, simulators, optimizers, and performance evaluation programs (benchmarks). Secondly, the vast majority of 'must' users of VHDL still remain unexposed to the language. No consensus has been reached on what constitutes a 'good' VHDL program. No user defined language constructs have been fashioned to curb errors or to facilitate reuse. The third category focuses on two aspects of the VHDL language, language maintenance and validation. Language maintenance must detect, isolate and correct the unknown, buried ambiguities that arise relative to the syntax, semantics, and implementation of VHDL. Lastly, but perhaps the most important, is the necessity to test whether a VHDL implementation conforms to the language definition specified in IEEE Std 1076 1987. If the validation process receives only minimal attention, the two most salient features of uniformity and portability will be lost. The absence of these features will drive astronautically the cost for the government to interact with the

microelectric community. There exists no formal validation process to test whether a VHDL implementation conforms to the language specified in IEEE Std 10761987. I would like to continue working on the process of validating VHDL compilers.

A compiler, being a software product, should be subjected to the standard procedures of testing a software product. The source code should be evaluated by function tests, performance tests, stress tests, and structure tests. Stress testing analyzes the boundaries of the software product embedded in its systems environment, while structure testing analyzes the internal processing units and data path structures. Both function tests and performance tests focus on the external specifications of the product. Performance testing centers on response times to various loads, while function testing compares the actual outcome of the operational aspects of the product to the expected outcome.

The granularity of a test is one of the standard features used to classify test programs. The fine-grained tests measure individual, isolated features of the the product. The Ada validation process relies almost exclusively on this method of testing. The process proceeds consecutively through the chapters of the Ada manual starting with the first chapter. A fine-grained test is applied to each implementation/syntax feature in each paragraph of each chapter. Course-grained testing validates the combination of many features. These tests can be either synthetic or derived from actual application code. Very little course-grained testing occurs in the Ada validation process.

II. OBJECTIVES OF THE RESEARCH EFFORT:

The term source code refers to a software product written in a specific programming language such as VHDL, Ada, Fortran, and etc. The logical structure of a source code is a sequence of lexical elements of the language. The list of lexical elements typically include reserved words, non-reserved words, string literals, numeric literals, and

comment literals. The different characterizations of the lexical elements either implicitly or explicitly define the style of the source code. Letter style defines the case of a letter. The letter styles of a lexical element of the word VhdL_leXicoN are lower case (vhdl_lexicon), upper case (VHDL_LEXICON), mix case (Vhdl_Lexicon) and unchanged case (VhdL_leXicoN). Type style defines the type set of a letter on paper, and typically consists of numerous variations of the standard type set of roman, bold, and italics. Shape style defines the features of source code that change when it is displayed on different devices. Different devices operate on different column widths. The standard terminal displays an 80 column width, a line printer 132 column width, and a laser writer various widths depending on parameters such as point size, margin widths, type size, etc. The shape features expound the management of the "wrap around" of text lines that extends beyond the column width. Which lexical elements should be separated in a wrap around, how should the wrap around be accomplished relative to preserving previous indentation, should the wrap around have a unique identifying mark? The shape style answers these and other such questions.

One focal point of activity was the development and implementation of a tool set that manipulates VHDL source code. The objective of the tool set is to provide the programmer with a mechanism to standardize all the objects of each lexical element category of each of the three styles. This style uniformity of the objects enchances the readability of source code. The usage of the tool set saves time for the programmer. Individual style preference does not effect others in sharing and reusing code. The programmer concentrates only on the contents of code as it is scrolled to a screen of a terminal, workstation, etc. There is no need to hunt for the scroll key or to strain to read an ill shaped separated lexical element. The laser writer tool saves time in addition to saving eye strain on the clarity of print when compared to a line printer. The operation of a line printer entails stopping the printer, advancing the paper, aligning the top of form, walking around it, tearing the paper, tearing off the banner page, and walking

back around to put the line printer on line. The use of the laser writer requires only the retrieval of the paper from a tray. In summary the fine-grained, isolated control of these styles enhances readability of source code, individualizes programming style, and saves the programmer's time.

There are three main goals that interact with each other.

1. To learn the VHDL programming language and its impact on future design of digital systems relative to the government electronic community. What problems does VHDL pose for the government?

2. To develop a tool set that customizes VHDL source code style to an individual programmer's work style. The customized features include isolated control of letter style, of type style, of shape style, and of scrolling code to the screen while preserving its shape.

3. To interact directly with personnel to understand their projects, to learn from them, and to help them.

It is clear to me that the most urgent and important task in the electronic government community is to ensure the uniformity and portability of the present VHDL compilers and of those in the immediate future. There is no formal mechanism that accomplishes this task of ensuring uniformity and portability. These features are necessary to prevent the government from becoming totally dependent on one vendor and being unable to share and reuse VHDL application code developed on different compilers.

III.

Several approaches were taken to learn VHDL. I attended a short course that taught VHDL to beginners, consulted the manual, and read application code written by others. I also wrote code. The details of the lexical element structure of VHDL was realized through the development of the tool set designed specifically for VHDL code. The reading of journal articles and textbooks provided a clearer understanding of the past, present, and future states of VHDL.

One fellow worker introduced me to a comprehensive tool that synthesis Ada and VHDL simultaneously and interactively. Although this tool resides in an infant state, it addresses the ultimate problem of optimizing in one environment the hardware expressed in VHDL and the software expressed in Ada. Future developments will allow a design team to analysis the immediate impact that will occur when one alters the specific components of either the hardware expressed in VHDL or the software expressed in Ada. Such tools further the necessity of ensuring uniformity and portability of VHDL. The task of providing means for embarking on the process of validating VHDL compilers is indeed most urgent.

Considerable time was spent on the development and implementation of the VHDL tool set. The tool set provides the customization of textual code features of VHDL code to an individual's style of programming. These tools allow one to control the letter style, the type style (postscript-laser writer), the shape style, and the scrolling of code to the screen while preserving the shape of the code. *In summary the fine-grained, isolated control of these three styles enhances readability of source code, individualizes programming style, and saves the programmer's time.* One tool that summarizes the frequencies of each atomic lexical component of source code remains in the incompleted stage. The missing segment is the design and implementation of an easy access method for the users.

The work environment displayed the many complexities facing the laboratory worker each day. I was astounded at the number of software products each worker had to know and use in addition to having detailed knowledge of so many projects that were in progress. I experienced how the productivity of professional people was effected by the degree of uniformity and portability of software products.

IV. RECOMMENDATIONS:

Because the tool set is currently being used there will be feedback that either detects errors or suggests enhancements. There has been one feedback at the time of this writing. When the VHDL compiler creates a list file with embeddeds syntax error messages in the source code, the list file does not conform to the VHDL language specifications. The upfront assumption of the laser writer type set tool is that the input be compilable. The slight code adjustment of transforming an error message to a comment line extends the range of the laser writer tool. It is hoped that standard maintenance of debugging, enhancements, and of porting of the tool set can be realized. Also the structural tool that counts the frequencies of atomic components of source code awaits completion.

The most important, urgent recommendation is that a mechanism be established to assist in the process of validating VHDL compilers. The validation process should be conducted by an agent who has no direct or indirect ties either now or in the past with the industrial community that makes, distributes, or sells VHDL compilers. Total separation avoids the obvious charge of conflict of interest.

It is clear to me that the government does not plan to finance the entire management and control of licensing VHDL compilers for several reasons. The IEEE Computer Society not the government owns the rights of the VHDL reference manual. The Ada validation process consumes a rather large financial budget that continues to grow because additional testing is needed. The crucial question is how does the government maximize its investment in validating VHDL compilers? It is suggested that the course-grain approach not the fine-grain approach dominate the validation effort. The immediate future will experience the integration of several hundred thousand or a million transistors on a chip (wafer). It is the integration not the individual component construction that presents the greatest challenge for designers. Programs will be complex in both their logic processing and their size. Course-grained testing examines the

combination of and integration of components. A serendipity is that a well constructed course-grained test may later serve as a performance test.

REFERENCES

[1] R. E. Fairley
Software Engineering Concepts
McGraw-Hill, New York 1985

[2] IEEE Standard VHDL Language Reference Manual IEEE Std 1076-1987
The Institute of Electrical and Electronics Engineers, Inc
345 East 47th Street, New York, NY 10017 USA

[3] R. Lipsett, C. Schafer, C. Ussery
VHDL: Hardware Description and Design
Kluwer Academic Publishers, Boston 1989

[4] Software User's Manual for the Enhanced Automated VHDL/Microcode
Compiler Synthesis and Design System
JRS Research Laboratories
1036 W. Taft Avenue, Orange, CA 926665-4121

[5] R. Waxman
"Hardware Design Languages for Computer Design & Test"
IEEE Computer Society Vol 19 Apr 1986 p90-97.

[6] N. E. Weiderman
Ada Adoption Handbook: Compiler Evaluation and Selection Ver. 1.0
Technical Report, CMU/DEI-89-TR-13 ESD-TR-889-21
Software Engineering Institute

1989 USAF-UES SUMMER FACULTY RESEARCH PROGRAM

Sponsored by the

AIR FORCE OFFICE OF SCIENTIFIC RESEARCH

Conducted by the

Universal Energy Systems, Inc.

FINAL REPORT

PARAMETRIC STUDY OF COMBINED BOILING AND PARTIAL DRYOUT IN LIQUID METAL HEAT PIPE WICKS

Prepared by:	*Larry W. Byrd*
Academic Rank:	*Assistant Professor*
Department:	*Engineering*
University:	*Arkansas State University*
Research Location:	*WRDC/FDL*
	Structures Division/Structural Integrity
	Branch
	Loads & Criteria Group
USAF Researcher:	*Christopher L. Clay*
Date:	*August 11, 1989*
Contract No:	*F49620-88-C-0053*

PARAMETRIC STUDY OF COMBINED BOILING AND PARTIAL DRYOUT IN LIQUID METAL HEAT PIPE WICKS

by

Larry W. Byrd

ABSTRACT

Boiling heat transfer in a wick with partial dryout was modeled. The vapor flowrate consists of molecules evaporated from the liquid/vapor interface plus those in bubbles formed at the base of the wick and convected to the interface. The evaporation rate was estimated as that due to conduction to the interface. The equivalent thermal conductivity was calculated from wick, liquid and vapor properties. Darcy's law was used to relate mass flowrate to pressure drop in both the two phase and vapor filled regions of the heat pipe. In the two phase region, a linear relation between the liquid saturation in the pores and the relative permeability was used.

The effect of the interface location depended on the core temperature. Above approximately 1000° K the heat flux varied as the inverse of the thickness of the wetted portion of the wick. At lower temperature the heat flux was greatly reduced due to the relatively large pressure drop in the vapor filled portion of the wick. Decreasing the liquid saturation down to approximately 10% caused an almost linear decrease in the heat flux. Below this saturation the heat flux began to increase in a non-linear fashion.

ACKNOWLEDGMENTS

I wish to thank the Air Force Systems Command and the Air Force Office of Scientific Research for sponsorship for this research. Universal Energy Systems provided orientation to the Summer Faculty Research program. Mr. Christopher Clay, Ms. Estelle Anselmo and Dr. Don Paul of FIBEB, and Dr. Kevin Hallinan of the University of Dayton provided assistance and insight to the problem. I found my stay at Wright Patterson AFB to be quite pleasant and rewarding.

I. INTRODUCTION:

The Structural Division of the Flight Dynamics Laboratory has been investigating the use of heat pipes to provide cooling for air craft leading edges and surfaces under laser attack. At high heat transfer rates two phase flow exists in the heat pipe wick. A better understanding of the relation between the heat flux and the different two phase regimes is needed.

Interest in heat transfer and thermodynamics contributed to my assignment to the Loads and Criteria Group of the Structural Integrity Branch. The present modeling represents an extension of work done in the summer of 1988. Previous work includes a study of transient thermal stresses in gun tubes, freezing flow in pipes and direct-contact, two phase heat transfer between immiscible liquids.

II. OBJECTIVES OF THE RESEARCH EFFORT:

The objectives of my summer research program were to extend the theoretical modeling of two phase phenomena in a heat pipe wick.

III MATHEMATICAL FORMULATION

Wick dryout in heat pipes can be modeled as occurring in any of three different modes as shown in figures 1a-1c. In (1a) the evaporation from the upper surface of the liquid occurs faster than it can be replaced with little bubble formation at the wall. The liquid vapor interface recedes into the wick until it reaches the wall with complete dryout. In (1b) the mechanism is the same except there is also some nucleate boiling. In (1c) there is a trapped vapor layer at the wall similar to film boiling. This paper will model the situation in (1a) and (1b) with partial wick dryout. The geometry is shown in more detail in Figure 2. At steady state, P_B the pressure in a vapor bubble forming at the wall can be approximated as: [1]

$$P_B \simeq P_c + \Delta P_m^{\ell} + \Delta P_v^{v} + 2\left(\sigma_w / r_n - \sigma_i / r_p\right) \qquad (1)$$

where: P_c = pressure in the vapor core above the wall (N/m^2)

ΔP_m = pressure drop in the 2 phase region of the wick (N/m^2)

ΔP_v = pressure drop in the vapor region of the wick (N/m^2)

σ_w = surface tension at the wall temperature (N/m)

σ_i = surface tension at the interface temperature (N/m)

r_n = minimum nucleation radius for vapor bubbles at the wall (m)

r_p = mean wick pore radius (m)

The "l" superscript indicates the property values are evaluated at the mean liquid temperature, $\bar{T}_l$ which is

$$\bar{T}_l = (T_w + T_i)/2$$

The mass flowrate per unit area $\dot{m}_v/A$ through the vapor filled portion of the wick can be written in terms of ΔP_v using Darcy's law:

$$\frac{\dot{m}_v}{A} = \frac{\rho_v^v K_o \Delta P_v}{\mu_v^v (\delta - z_i)} \qquad (2)$$

ρ_v^v = vapor density (kg/m^3)

K_o = wick permeability (m^2)

μ_v^v = vapor dynamic viscosity (Ns/m^2)

$\bar{T}_v$ = mean vapor temperature (^oK) = $(T_i + T_c)/2$

The "V" superscript indicates the property values are evaluated at the mean vapor temperature. In the two phase region of the wick the vapor and liquid flows can be written in terms of the relative permeabilities of the liquid and vapor.

$$\dot{m}_v/A = \frac{\rho_v^l K_v \Delta P_m}{\mu_v^l z_i} \qquad (3)$$

$$\dot{m}_l/A = \frac{\rho_l^l K_l \Delta P_m}{\mu_l^l z_i} \qquad (4)$$

Several equations have been suggested for K_v & K_l in terms of the single phase permeability and the liquid saturation S, of the pores. (S is equal to the volume of liquid in the pore divided by the total wetted pore volume). Bau and Torrance [2]

and Singh [3] have used a linear relation which was also used in this paper.

$$K_\ell = s K_0 \tag{5}$$

$$K_v = (1-s) K_0 \tag{6}$$

It was assumed that the rate of evaporation at the interface equals that due to heat conduction through a uniform material of thickness z_i. The thermal conductivity is calculated assuming randomly dispersed vapor bubbles in randomly dispersed pores in a continuous material as suggested by Dunn & Reay [4]

$$\frac{\dot{m}_\ell}{A} = \frac{k_e^\ell}{h_{fg}^\ell}\left(\frac{\partial T}{\partial z}\right)_{z_i} \simeq \frac{k_e^\ell (T_w - T_i)}{h_{fg}^\ell z_i} \tag{7}$$

This assumption is more suitable for liquid metal heat pipes due to the large thermal conductivity of the liquid. The effective thermal conductivity can be written as:

$$k_e = k_s \left[\frac{2 + k_{\ell v}^\ell / k_s^\ell - 2\varepsilon\left(1 - k_{\ell v}^\ell / k_s^\ell\right)}{2 + k_{\ell v}^\ell / k_s^\ell - \varepsilon\left(1 - k_{\ell v}^\ell / k_s^\ell\right)} \right] \tag{8}$$

$$k_{\ell v}^\ell \simeq k_\ell^\ell \left(\frac{2s}{3-s}\right) \tag{9}$$

k_s^ℓ = thermal conductivity of wick material (W/m$^\circ$K) at $\overline{\overline{T}}_\ell$

$k_{\ell v}^\ell$ = effective thermal conductivity of the liquid/vapor mixture evaluated at $\overline{\overline{T}}_\ell$

k_ℓ^ℓ = liquid thermal conductivity (W/m$^\circ$K) at $\overline{\overline{T}}_\ell$

ε = wick porosity (pore volume divided by total wick volume)

The total vapor flow is equal to the mass evaporated at the interface plus the vapor flow due to bubbles convected to the interface.

$$\dot{m}_v = \dot{m}_l + \dot{m}_b \qquad (10)$$

A heat and mass balance then gives the heat flux, $\dot{q}$ as:

$$\dot{q} = \dot{Q}/A \cong \frac{\dot{m}_v}{A} h_{fg}^{\ell}$$

It was also assumed the vapor remains saturated as it expands from the interface pressure to the core pressure. As shown on the T-s diagram in Figure 3 there are any number of possible alternative processes. An isentropic path from 1 to 2s would mean some condensation of the vapor in the upper portion of the wick. An isothermal path 1 to 2T would result in a superheated state. This could result in equation (11) underpredicting the heat flux by 20-25% if the vapor ΔT is $100^{o}K$ following the saturation line.

The additional equations necessary to arrive at a solvable set come from empirical equations giving the liquid and vapor properties as a function of temperature. The equations were combined to arrive at one equation with T_i as the unknown.

$$P_B - P_c - \frac{k_e^l (T_w - T_i)}{h_{fg}^l \, s \, K_o}\left[R_l^l + R_v^v\left(\frac{\delta}{z_i} - 1\right)\left(s + R_*^l (1-s)\right)\right] - 2\left(\frac{\sigma_w}{r_n} - \frac{\sigma_i}{r_p}\right) = 0 \quad (12)$$

$$T_w = T_i + \underbrace{\frac{K_o \Delta P_v}{R_v^v\left(\frac{\delta}{z_i} - 1\right)}}_{f(\bar{T}_v)} \underbrace{\left(\frac{h_{fg}^l}{k_l^l}\right)\left(\frac{s}{s + R_*^l (1-s)}\right)}_{f(\bar{T}_l)} \quad (13)$$

$$R_v^v = \left(\frac{\mu_v^v}{\rho_v^v}\right) \quad ; \quad R_l^l = \left(\frac{\mu_l^l}{\rho_l^l}\right) \quad ; \quad R_*^l = \frac{\left(\mu_l^l / \mu_v^l\right)}{\left(\rho_l^l / \rho_v^l\right)} \quad (14)$$

$$P(T) = \frac{101781\left(10^{(6.67176 - 5520/T)}\right)}{T^{(.61344)}} \quad (15)$$

$$\sigma(T) = .27057 - 9.1(10^{-5})T \quad (16)$$

$$h_{fg}(T) = 5245.7 - 1.13286T \quad (17)$$

$$\rho_l(T) = 996.324 - .217625T \quad (18)$$

$$\mu_l^l(T) = \left(10^{(-1.09127 + 382/(40+T))}\right)/1000 \quad (19)$$

$$\rho_v(T) = e^{\left(\sum_{j=0}^{5} X_j T^j\right)} \quad (20)$$

$$\mu_v(T) = \sum_{j=0}^{5} X_{1j} T^j \quad (21)$$

$$k_l = 102.3 - .04146T \quad (22)$$

$$k_s = 34.175 + .025T \quad \text{(Nickel wick)} \quad (23)$$

Since the liquid and vapor properties are evaluated at average temperatures an iteration procedure must be used even when evaluating eq. (13) for a given value of T_i. A regula falsi iteration was used to solve for T_i for given values of S and δ/r_i.

Some comments on the nature of this model should be made before looking at the results. It is a parametric model because values of the two parameters S, δ/r_i, are simply assumed for a variety of core temperatures and the heat flux calculated. It cannot predict which of these states may occur for a given heat pipe. The state in the vapor core in this paper is assumed to be saturated vapor at the specified temperature. In an actual heat pipe the state also depends on the condenser geometry and heat transfer characteristics. This model cannot predict changes in S or δ/r_i at different locations in a heat pipe. It looks at a variation in states perpindicular to the wall independently of the changes that occur parallel to the wall. It is descriptive of the behavior at the center of circular disk fed with liquid at its perimeter.

It should be possible, however, to combine this with equations describing heat, mass and momentum fluxes parallel to the wall for an infinitesmal control volume. This can be integrated over the heat pipe wick and matched with models of the vapor core and condenser to describe steady state heat pipe behavior and states at any point in the wick. Including

transient terms in the equations would allow time varying behavior to be modeled.

IV. RESULTS AND DISCUSSION:

Figure 4 gives the heat flux as a function of the core temperature with $\delta/r_i = 1, 10$ for S=1. For $\delta/r_i = 1$ the wick has not started to dry out but there is incipient boiling at the wall. There is a steady decrease in the heat flux as the temperature increases due to the decrease in surface tension and latent heat of vaporization. For $\delta/r_i = 10$ a different behavior is seen. If the pressure drop in the wick was negligible the heat flux for $\delta/r_i = 10$ should be approximately ten times the value for $\delta/r_i = 1$ because it is assumed that heat is conducted through the wetted portion of the wick. This is shown by the dashed line. For temperatures greater than 1173° K (900°C) where the vapor flowrate is low and the density high we see close agreement with the conduction dominated, negligible pressure drop case. Below 900°C the heat flux drops below the dashed line due to the increasing importance of the pressure drop in the vapor filled portion of the wick.

Figure 5 shows the heat flux as a function of δ/r_i with $S = 1, .1$ for $T_c = 1073$, and 1273°K. At 873°K there is initially a drop in the heat flux but it begins to increase in an almost linear fashion for $\delta/r_i \geq 2$. At higher temperatures the heat flux increases monotonically with δ/r_i. One area where this could

be important is determining the proper amount of working fluid for the heat pipe. At the higher temperatures performance is immediately improved by the interface receding into the wick. At $873^{o}K$ the performance is worse if the heat pipe is slightly under charged. Decreasing the liquid saturation S resulted in a decrease in the heat flux. This is because the effective conductivity of the wetted portion of the wick decreases due to the presence of the low conductivity vapor. In systems where the presence of vapor increases convection we would expect the opposite result.

Figure 6 gives the heat flux as a function of S with For S between .1 and 1 the heat flux increases in an almost linear fashion as S increases. As S decreases below approximately .1 the heat flux begins to increase because the mass of vapor being convected to the interface as bubbles is becoming comparable to the mass evaporated at the interface. However, the conceptual model may fail at low values of S. It has been suggested that the vapor will preferentially fill the larger pores. Thus vapor channels may form creating localized hot spots.

Figure 7 gives the outside wall temperature T_o if the wall thickness is 1 mm and Haynes 188 alloy is used. It is obvious that this temperature by itself is inadequate to determine how far a wick has dried out. Even if the core temperature is known a small error in the temperature measurement could result in a

large error in the estimate of dryout. It also does not give an indication of the presence of vapor in the wetted portion of the wick.

V. RECOMMENDATIONS

It is recommended that an experimental flow visualization program be initiated. New methods of instrumenting heat pipes should be developed to determine the liquid vapor interface during high heat flux operation. Statistical thermodynamics has been used to predict evaporation rates from a surface assuming ideal gas behavior and neglecting surface tension. A better model is needed for heat pipe applications. This could be obtained from experimental and theoretical study of evaporation from a single capillary tube.

NOMENCLATURE

English Symbols:

A - *area* (m^2)

h_{fg} - *latent heat of vaporization* (J/kg)

k - *thermal conductivity* ($w/m^{\circ}K$)

K_o - *wick permeability* (m^2)

$\dot{m}$ - *mass flowrate* (kg/s)

P - *pressure* (N/m^2)

$\dot{q}$ - *heat flux* (W/m^2)

r - *radius* (m)

R - *ratio* (μ/ρ)

R_* - R_l/R_v

S - *liquid saturation (vol. liquid/pore volume) in the wetted portion of the wick*

T - *temperature* ($^{\circ}K$)

X_j - j^{th} *constant in NASA curve fit for vapor density*

X_{1j} - j^{th} *constant in NASA curve fit for vapor viscosity*

z_i - *distance from the heat pipe wall to the liquid/vapor interface* (m)

Greek Symbols:

δ - *wick thickness* (m)

ΔP_m - *pressure drop in the z direction in the wetted portion of the wick.*

ΔP_v - *pressure drop in the z direction in the vapor filled portion of the wick*

ρ - *density* (kg/m^3)

ϵ - *wick porosity (volume of voids/total wick volume)*

μ - *dynamic viscosity* (Ns/m^2)

σ - *surface tension (N/m)*

Subscripts

b - bubble

c - core

i - liquid/vapor interface

l - liquid

n - nucleution site

o - outside

p - pore

s - solid

w - wall

Superscripts

l - evaluated at average liquid temperature

v - evaluated at average vapor temperature

References:

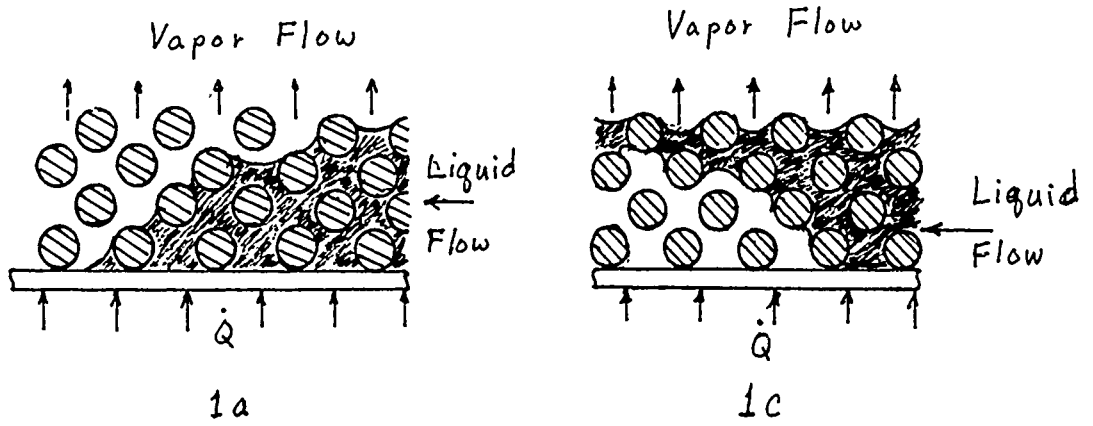
1. *Byrd, L.W., Heat Flux Prediction for Nucleate Boiling in Liquid Metal Heat Pipes*
   USAF-UES Summer Faculty Research Program
   Final Report Aug 1988 Contract No: F49620-87-R-0004

2. *Bau, H.H. and Torrance, K.E., "Boiling in Low-Permeability Porous Materials" Int. J. Heat, Mass Transfer, Vol 25, No 1, pp 45-55, 1982*

3. *Singh, B.S. and Shaubach, R.M., "Boiling and Two Phase Flow in the Capillary Porous Structure of a Heat Pipe" Multiphase Transport in Porous Media - FED Vol 60/HTD-Vol 91 published by ASME*

4. *Dunn, P.D. and Reay, D.A., Heat Pipes 3rd ed, Pergamon Press Inc., 1982 p 100*

5. *Dullien, F.A.L., Porous Media, Fluid Transport and Pore Structure, Academic Press, Inc. 1979*



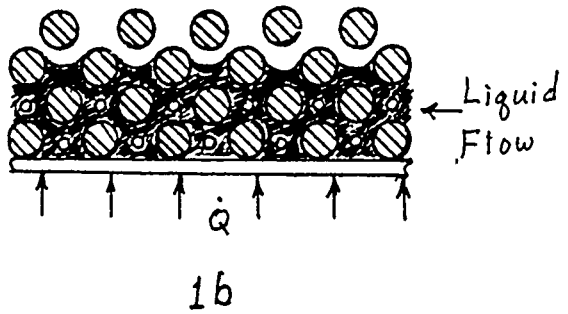


Figure 1. Wick Dry Out Modes

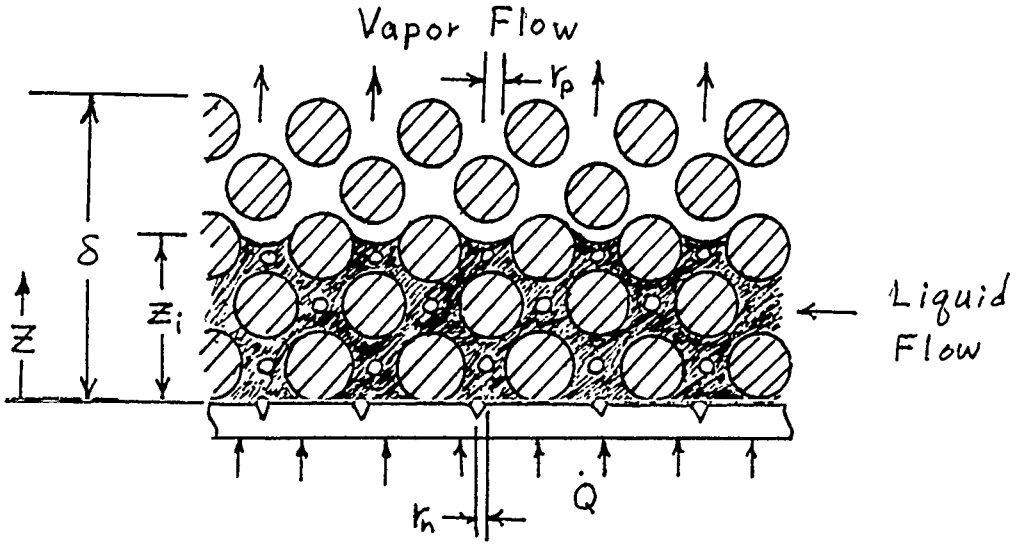


Figure 2. Wick Detail.

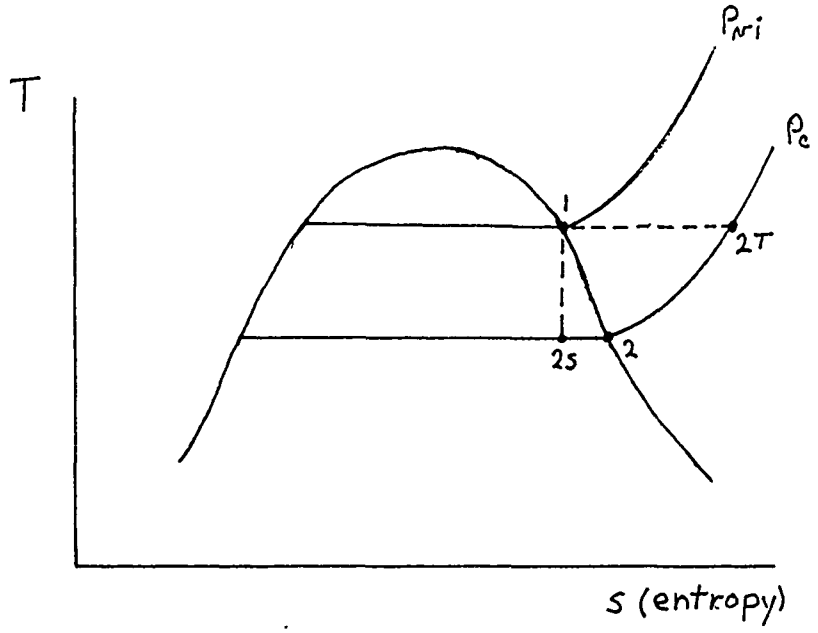


Figure 3. T-s Diagram

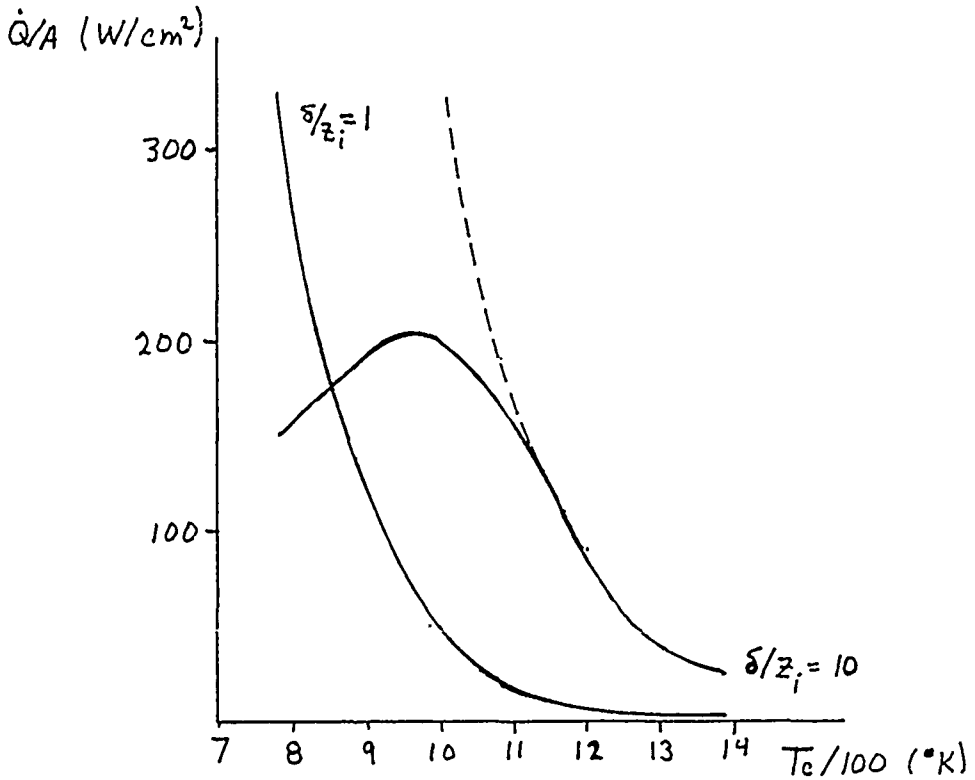


Figure 4. Heat Flux as a Function of Core Temperature

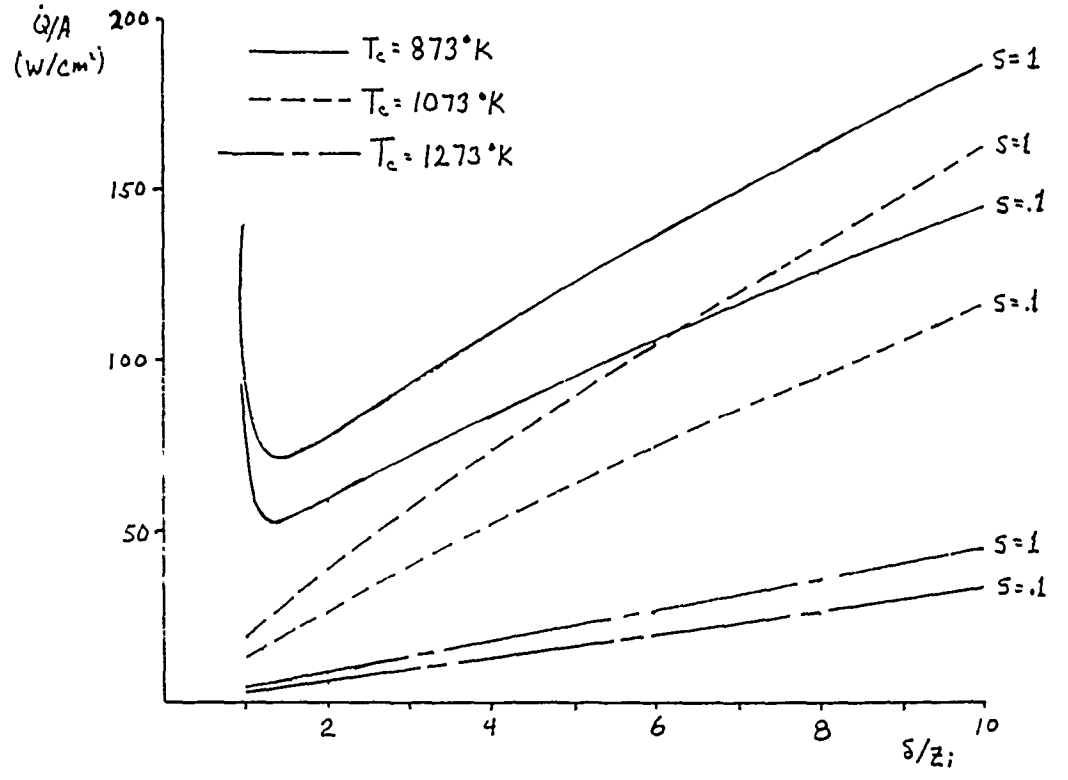


Figure 5. Heat Flux as a Function of δ/z_i

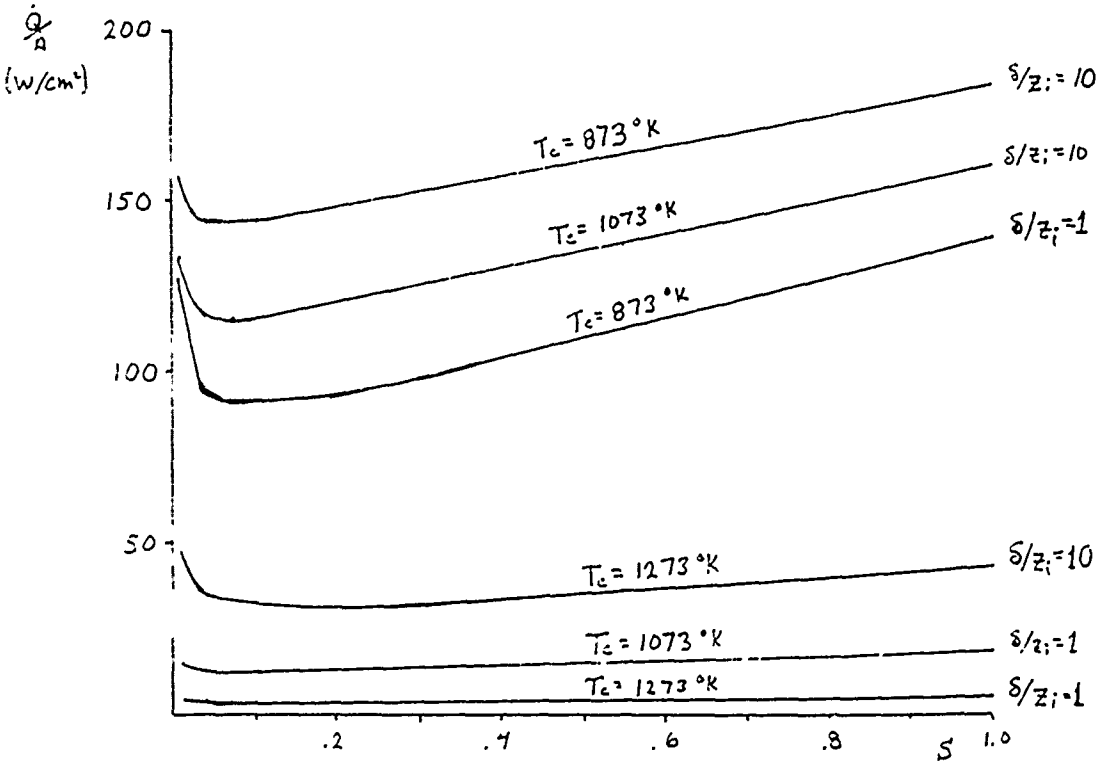


Figure 6. Heat Flux as a Function of Saturation

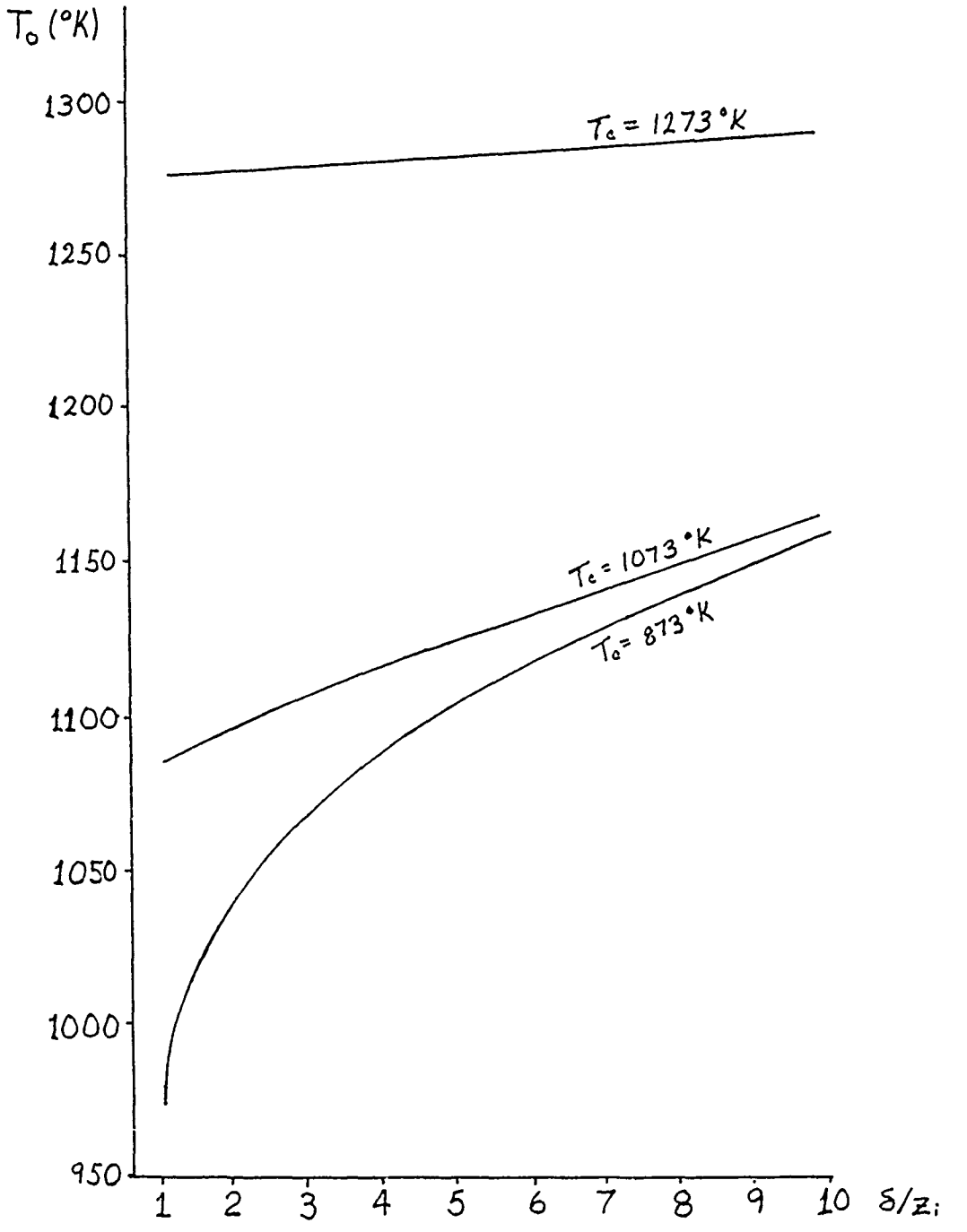


Figure 7. Outside Wall Temperature as a Function of δ/z_i

1989 USAF-UES SUMMER FACULTY RESEARCH PROGRAM

GRADUATE STUDENT RESEARCH PROGRAM

Sponsored by the

AIR FORCE OFFICE OF SCIENTIFIC RESEARCH

Conducted by the

Universal Energy Systems, Inc.

FINAL REPORT

3-D ANALYSIS OF LASER MEASUREMENTS OF VORTEX BURSTING ON CHINED FOREBODY FIGHTER CONFIGURATION

Prepared by:	Kenneth C. Cornelius, Ph.D.
Academic Rank:	Asst. Professor
Department and University:	Mechanical and Materials Engineering Wright State University
Research Location:	Flight Dynamics Laboratory, Aeromechanics Div. Wright-Patterson AFB, OH
USAF Research:	Russ Osborne
Date:	28 September 1989
Contract No:	F 49620-88-C-0053

3-D Analysis of Laser Measurements of Vortex Bursting on a Chined Forebody Fighter Configuration

by

Kenneth C. Cornelius

ABSTRACT

Future air combat will require aircraft maneuver performance that will exceed the capability of present day fighters. At high angle of attack in the post stall region, the aerodynamic control surfaces such as the vertical tail and rudder becomes engulfed in the separated flow field of the wing, and lose their ability to impart the yawing moment and side force required for active control of the vehicle. The key technology that is needed is the extension of aerodynamic control in the post stall regime of the flight envelope. The most promising approach for enhanced dynamic control of the aircraft is the use of properly placed blowing pneumatic jets in the nose of the forebody which eliminates the bistable nature of the asymmetrical development of the vortical separations. The main body of this report examines the physics of vortex breakdown to shed some light on possible blowing schemes that would have the greatest impact on this problem. From experimental 3-D velocimeter data of a vortex burst condition, a criteria for vortex breakdown has been formulated in terms of the local vortex flow variables which delineates between the onset of vortex burst and spiral instability. The Rosby parameter set which governs stability can be influenced by a jet which maximizes entrainment and imparts axial momentum to the outer helical streamlines.

ACKNOWLEDGEMENTS

The author would like to thank the Air Force Systems Command, the Air Force Office of Scietific Research for providing him with the oppurtunity to spend an enlightening summer at the Flight Dynamics Laboratory, Wright Paterson Air Force Base, Ohio. The author would like to acknowledge the helpful discussions and encouragement with Group Leader, Russ Osborne. Also I am indebted to Bob Guyton, Larry Rogers and Scott Lemay from the Aerodynamics Group for their support and encouragement throughout this project.

I. INTRODUCTION

The separated three dimensional flow structure on the upper side of highly swept delta wing planforms as well as flow separation around the pheriphery of the symmetric forebody nose at high angles of attack are extremely complex. At high angles of attack the leeward flow field is dominated by an organized vortical flow structure emanating from the shear layer of the separated 3-D flow from the wing leading edge and forebody. The vorticity shed from the leading edge and separated forebody rolls up in an organized fashion to produce separate vortex flows. The flowfield of modern fighters is further complicated by the use of low aspect ratio strakes, ie. leading edge extensions (LEX) in front of the main wing, which allows highly manueverability fighters such as the F-16 and F/A-18, to increase the stability range of their operational envelope. The vortices generated from the LEX interact with the main wing flow to enhance lift, and provide aerodynamic stability throughout an expanded operational flight regime. However the extension of the flight envelope to higher angles of attack and the increase of the stall/spin resistence is limited by the onset of vortex breakdown from either of the individual vortex formations and their interactions with the control sufaces. This is a striking phemonena due to the nature of the abrupt changes in the vortex flow physics which results in the turbulent dissipation of energy and the dramatic increase in the boundary of the axial vorticity. Recently, in Ref.(1,2) it has been demonstrated that decoupling of the LEX vortex flow from the

wing vortex delays the vortex breakdown and significantly increases the maximum lift. The decoupling was achieved by physically moving the LEX planform above the wing plane which prevented the strong interaction and the eventual merging of the LEX vortex with the wing vortex. The LEX vortex traversed a trajectory closer to the root of the main wing which provided boundary layer control and delayed bursting of the vortex to higher angle of attack. Roll agility in modern fighters often is limited by the onset of lateral-directional instability which is governed by the bistable vortex separation around the periphery of the aircraft nose. By blowing tangentially to the forebody surface on the leeward side of the vortex in the nose region, various investigators Refs.(3,4,5) have demonstrated significant control and aerodynamic enhancement of maneuverability. Both yaw and side force control at high angle of attack can be enhanced by controlling the forebody vortex separation position and strength around the pheriphery of the nose. Recent experiments from Ref.(6) show that spanwise blowing in the direction of the wing vortex coordinates can influence the vortex breakdown position and extend the range of maximum lift. Future designs of fighter aircraft, Ref.(7,8) have incorporated a chined forebody which is contoured and merged with the wing planform both for structural reasons, and to circumvent the bistable nature of the vortex separations of the rounded forebody. However, the strong vortex interactions at high angle of attack, especially when the aircraft is yawed, leads to destabilizing moments. The ultimate goal is

to control the vortex interactions to achieve greater stability derivatives in the higher angle of attack regime by a symmetric set of blowing ports with minimum penalty of bleed air from the compressed stages of the engine. The research I have been associated with in the past has involved the (LDV) Laser Doppler Velocimeter measurements in complex flows including vortex flows for the specific purpose of providing insight into the physics of such flows and providing a data base for advanced computational methods.

II. OBJECTIVES OF THE RESEARCH EFFORT

The goal of this report was to identify parameters which relate to the physics of vortex breakdown, and recommend various forebody blowing schemes to enhance the favorable interaction in terms of the aerodynamic moments and side forces of the aircraft at high angle of attack. The difficult question is what configuration ie. axisymmetric jet , two dimensional jet, or variation of jet exit boundary conditions including pulsed jet or jet with circulation, will enhance or amplify the favorable jet/vortical interaction with the local aerodynamic surfaces? To answer in part this question the author has designed two nozzle geometries to be investigated on the high angle of attack X-29 model to be tested in the near future. This test will explore the enhanced entrainment effects of each nozzle configuration and the impact on controlling the forebody vortical separations for the desired goal of producing the maximum yawing moment and side force with minimum air bleed from the compressor stage of the engine. The secondary task reported herein was to analyze the

experimental data from a generic chined- forebody fighter configuration obtained previously by the author and his associates at LASC-Georgia utilizing a three dimensional Laser Velocimeter. This data consists of the mean (U,V,W) velocity components as well as turbulence measurements at various x/c locations along the fighter wing at two separate angles of attack. This fighter configuration has a chined forebody with a wing sweep of 56 degrees and is therefore considered a blended wing-body configuration. Both the forebody and wing have sharp leading edges which is conducive to a three dimensional separation leading to a strong vortex flow at high angles of attack. For this configuration the forebody vortex turns abrubtly and merges with the separated wing flow vorticity. The vortex flow about the chined forebody and wing geometry leads to favorable aerodynamic characteristics until the resulting flow approaches the breakdown condition which can be categorized as vortex bursting. This data contains a case in which vortex bursting occurs at an angle of attack of 21. degrees with a domain of reverse flow which is characteristic of the "bubble" type breakdown at an axial location of x/c=.59. At an angle of attack of 10 degrees of the model relative to the free stream there is no reverse flow in the vortex domain but a significant increase in the core size typical of the spiral mode of instability. These two cases represent the two distinct forms of instability as observed by a host of other investigators for the symmetric vortex flow problem in a tube. The corresponding stability analysis can be found in Refs.(9,10,11,12). However, there

has been insufficient data for the non-symmetric wing vortex flow problem to correlate the relationship or differences, relative to the case with axisymmetric boundary conditions. This data will provide a better understanding of the physics of the wing leading edge vortex flow as it approaches the breakdown position. The axisymmetric or bubble type breakdown is characterized by the sudden increasing of the diameter of vortex core and the formation of an internal stagnation point along the core axis with a recirculating flow region with enhanced turbulent mixing downstream. The effects of the vortex burst leads to unstable aerodynamics of the vehicle and is responsible for an adverse or nose up pitching moment and in some cases wing rock and buffeting. Another detrimental feature during high angle of attack maneuvers is the unsteady vortex wake flow interaction with the vertical stabilizer causing large transient loads on the control surface which may lead to premature failure of the load bearing structure due to fatigue. It becomes imperative that to achieve higher angle of attack maneuverability for fighter aircraft that this phenomena of separated-induced vortex flows and the bursting process be better understood so that a rational scheme of control such as a blowing jet underneath the vortex flow could be implemented . The onset of the vortex burst is a combination of a stability problem and the triggering of a conjugate state very similar to the hydraulic jump phenomena . A critical threshold is reached where large growth rates of axisymmetric or non-symmetric disturbances become evident from flow visualization of the vortex flow. This problem has been

studied extensively in the past for axisymmetric flows utilizing stability calculations as well as solving the full Navier Stokes equations numerically. The Navier Stokes studies have calculated the bubble type breakdown, but only recently demonstrated the spiral mode instability in certain flows. An excellent review article is provided by Hall and Leibovich in Refs.(13,14) where they discuss different spatial regimes during breakdown. The governing dimensionless parameters for the stability problem are the Rosby and Reynolds number, where the length scale is the radius of the core axial vorticity ,the rotation rate is defined from the axial vorticity, and the velocity scale is the centerline axial velocity. As pointed out in Ref.(15) there is no universal parameter that predicts or collapses the data for the vortex instability problem that encompasses different boundary conditions such as vortex flow inside a tube or those generated by the shear layer over a delta wing even though these flows show similarity in the breakdown process.

III. LDV VELOCITY DATA ANALYSIS FOR CRITICAL PARAMETERS

The LDV velocity data is presented in the form of contour plots of various quantities such as the mean vorticity ,axial, and crossflow velocity components as well as the turbulence kinetic energy. Various parameters were integrated in the core vorticity domain to formulate a Rosby number criteria which shows that there is a critical threshold or condition which demonstrates the onset of the breakdown and instability of the vortex flow. However there appears that there is another parameter besides the Rosby number which triggers the

alternate conjugate state which leads to the axisymmetric "bubble" breakdown. This data agrees in principle with Benjamin's theory and hypothesis that vortex bursting is synamonous with two conjugate states where the approaching vortex flow is supercritical and after bursting subcritical. The group velocity of finite amplitude waves travels upstream in the subcritical conjugate state which perpetuates the breakdown. This alternate state is similar in physics to the hydraulic jump in open channel flow and represents a more violent form of dissipating energy. A secondary parameter is defined which supports Benjamins theory that the integrated flow force in the finite domain of the axial vorticity must be a minimum of the solution set. This concept was proved theoretically by Benjamin by invoking the calculus of variations and is crucial in his argument and development of the subcritical state. The second parameter is defined the ratio of the integrated (axial /crossflow) kinetic energy flux in the finite domain defined by the boundary of the axial vorticity. When this parameter approaches one, then the transition from super to subcritical is imminent which implies the "bubble" type breakdown. If the analogy is made to the hydraulic jump this criteria represents the minimum specific energy of the bounded vortex flow. The Rosby parameter set can be utilized in computational codes to decipher a location along the chord when the physics of the vortex flow will change dramatically and this will have to be modelled acccordingly to take into account the formation of the "bubble and or spiral" instability and the impact on the resulting

turbulent flow downstream . These flow-field measurements obtained from a non-intrusive measurement of the velocity field in the vortex burst region provide a valuable data base for the validation of advanced computational methods.

a. LDV Measurements

For the LDV measurements the generic fighter model was rotated about the tunnel centerline to achieve an angle of attack range up to 21 degrees. Three-dimensional velocity measurements were acquired using LASC-Georgia Co. 3-D LV system. The (U,V) data was acquired in the conventional manner with a 18 watt argon-ion laser providing blue and green coherent light scource. Another 18 watt argon-ion laser configured with an internal prism provided the purple coherent light scource and was mounted at 45 degrees to the free stream to measure the combination of (U,W) components of velocity. The two sets of collection optics operated in the back-scatter mode. The bragg cells operated in the 40-48 MZ range which shifted one of each beam pair and the difference frequency was achieved electronically. A 3-D positioning table allowed traversing in the X,Y,Z coordinate directions with a resolution of .0025 cm. Figure (1) shows a planform view of the laser orientation and traverse table. Since, the laser Doppler data was configured electronically to be coincident in time, all of the Reynold's stresses were measured and the $\overline{W}$ component was extracted instantaneously from the second set of measurements utilizing the geometry of the beams. Each enseble average represents 1000 data points in a spatial volume of .005 in. radius by .025 in. length , which was

dictated by the focussing and collection optics. The seeding particles for the LDV were oil droplets of 1.0 micron diameter were introduced in the wind tunnel through a compressed air line downstream of the model for the purpose of providing scattering cross-sections throughout the flow field and the free stream of the closed return tunnel. A table was constructed for the (y,z) coordinates at any desired axial station and this information was used for automatic traversing of the three dimensional traverse table. The (y,z) plane where data was obtained was configured to be normal to the axis of the model. The (U,V,W) measured velocities were in the wind tunnel coordinate axis. The data was acquired with the vertical tails removed at various x/c chordwise positions to assess the development of the streamwise vorticity .

IV. DATA ANALYSIS

The coordinate system which has relevance to previous theoretical and experimental research in terms of vortex bursting is the coordinate axis along the vortex core. Hence the (U,V,W) velocity components were rotated by the Euler angles (alpha, psi) relative to the orthoganal coordinate system of the wind tunnel axis to coincide with the trajectory of the core-vorticity at each axial station along the chord. The trajectory of the core was obtained by software which allowed integration of the vorticity domain to determine the average positions (y,z) of the vortex core. A least square curve fit through these points in the (x) direction was used to determine the respective Euler angles. The data presented below is transformed to the orthoganal coordinate system along

the vorticity-core. The significant differences between the axisymmetric vortex studies and wing generated vortices is the boundary conditions. Below the wing vortex there is an opposite sence vorticity region from the 3-D boundary layer commonly referred to the secondary vorticity which has the effect of amplifying the cicumferential velocity component near the surface . Additionly the circulation increases downstream as the shed vorticity from the wing merges into the outer circumpherence of the vortex core.

a. Crossflow Velocity Vectors and Axial Vorticity

The (V,W) velocities are shown in Figure (2) where the length of the vector represents the magnitude of the crossflow component. A well organized structure and large swirl component is apparent for the 20 degree angle of attack case before breakdown of the vortex at x/c=.59. The local axial vorticity was determined by the use of Stokes theorem ie. the circulation around four adjacent grid points and divided by the elemental area dy*dz. The nemerical value was assigned at the center of each grid and normalized by the free stream velocity and root chord of the wing. Figure (3) shows the axial vorticity contour at x/c=0.59. The chined forebody vortex turns abruptly at the wing juncture and merges with the main wing vortex, where two distinct elongated vortical cores are visible at x/c=0.13. For the model oriented at 21 degrees angle of attack the vortex bursting and the onset of axial flow reversal occurs at an x/c=0.59 location . The vorticity is convected to a larger physical domain by the turbulence energy producing eddies which is characteristic of the

breakdown process. The values were normalized by the respective calculations of the initial area. The circulation in the half plane was determined by integrating the vorticity throughout the measurement domain. The positive circulation decreases downstream of the burst vortex location for the high angle of attack case since a stronger turbulent mixing between the interfaces of positive and negative regions of vorticity near the wing surface decreases the integrated time average value of this quantity. The high angle of attack case shows that the slope of this of the first moment of vorticity which is proportional to the vertical momentum flux and therefore related to the local lift, is reduced near the trailing edge of the wing which has a direct impact on the adverse pitching moment of the aircraft.

b. Axial Velocity Contours

Figure (4) shows the axial velocity contours at the onset of reverse flow. The breakdown is initiated at x/c=.59 where the axial velocity contours show a distinct region of reverse flow and considerable region of decellerated flow. Thereafter the recirculating flow region, defined by the time mean streamline encompassed in the interior region of the zero velocity contour, grows to a maximum width at x/c=.87. This width is 20% greater than the corresponding vortical diameter before the onset of the burst. The reverse flow region then reattatches in the near wake region at x/c=1.2.

c. Turbulent Kinetic Energy Contours

Turbulent kinetic energy contours have shown t he maximum turbulence levels coincided with the center core region of

vorticity which is consistent with Ludweig's stability analysis. This theory predicted a region at the core center which was always unstable to symmetric disturbances due to the local velocity gradients in this region. Although this instability may contribute to the formation of the conjugate state it has limited utility in predicting the onset of the burst location as defined by the stagnation point along the axial flow. The region of turbulent flow grows in a manner which reflects the intensity of the breakdown process after bursting, with turbulent kinetic energy levels on the order of 40%. The increased area of the turbulent flow beyond the burst location at x/c=.59 reflects the large scale convection process of the energy contaning eddies and the dissipation of mean flow energy.

V. ROSBY CRITERIA

A Rosby number was defined as the centerline axial velocity divided by the average rotation rate times an equivalent radius. The radius and mean rotation rate were obtained from the integrated area, and vorticity respectively in the region bounded by the axial vorticity . The Rosby number is defined as

$$Ru = \frac{u_e}{\sqrt{r}\,r} \qquad 1.$$

In all cases this number approached a value of 0.52 at the onset of either bursting or spiral breakdown. The calculated Rosby number is consistent with the average trend of the data presented in Ref.(16) for wing tip vortices, but was not consistent with the limited tabulated data for leading edge

vortices which showed a factor of two greater in the Rosby parameter for breakdown. This difference was based on the limited measurements of leading edge vortices that have been published and, in that regard, may be somewhat speculative. The fact that this data agrees with the symmetric vortex studies is considered to be significant, since most of theoretical framework for vortex stability has evolved from initial symmetric boundary conditions. As discussed in the introduction the second parameter which delineates the form of the instability is defined the ratio of the integrated (axial /crossflow) kinetic energy flux in the finite domain defined by the boundary of the axial vorticity. A necessary condition for a conjugate state as proposed by Benjamin is that the integrated flow force be a minimum in the solution set which implies a minimum in the local specific energy. The following analysis leads to a parameter similar to the Rosby number but uniquely different depending on the integral shape factors of the axial and crossflow velocities. From vector calculus the following formulation is valid.

$$\nabla H + \rho \nabla(\vec{U}\cdot\vec{U}) - \tfrac{1}{2}\rho\nabla q^2 + \nabla \tau^t = 0 \qquad 2.$$

Integrating this equation to the finite boundary dictated by the presence of axial vorticity the following results,

$$\oint H\, dA + \tfrac{1}{2}\rho \oint \left[U^2 - (V^2+W^2)\right] dA + \oint \overline{u_i u_i}\, dA = 0 \qquad 3.$$

For this quantity to be a minimum,ie once a vortex flow has been established so that a deficit in total head is formed, and neglecting the turbulent shear stress, the action of a axial adverse pressure gradient will alter the axial and

crossflow momentum terms, leaving the total head integral unchanged. A minimum occurs when the axial and crossflow integrals are equal. The constraint proposed by Benjamin can be specified in terms of the minimum specific energy as given by the following parameter.

$$Re = \frac{\int U^2 \, dA}{\int (V^2 + W^2) \, dA} \qquad 4.$$

When this parameter approaches one, then the transition from super to subcritical is imminent which implies the "bubble" type breakdown. The 10 degree angle of attack case was significantly above this threshold and no reverse flow was evident, even though a significant increase of the core radius was apparent indicating the spiral instability. Benjamin's theory has received criticism because momentum must be conserved for both the initial and conjugate states, which can only be true if one includes the Reynolds stress term in the unsteady momentum balance. The production of axial turbulence is sufficient to provide for the mean momentum balance for the unsteady conjugate state. Benjamin's suceeding arguments concerning the group velocity for the conjugate state was derived from a small pertubation analysis. This theory, analigous to the hydraulic jump transition of states, has provided a condition or threshold which is consistent with the experimental data. Unfortunately, this criteria has been overlooked by previous investigators, since Benjamin proposed a critical parameter based on the group velocity ratio which was derived from stability analysis.

V1. RECOMMENDATIONS

Experimental data from a 3-D Laser Velocimeter has been analyzed for a chined forebody fighter configuration for two separate angles of attack. These data sets embody the physics of vortex instability which limits the lateral and directional control as well as the maximum lift of fighter aircraft. The velocity vectors were rotated along the vortex axis coordinates to examine the relevant parameters for vortex instability. Two Rosby numbers were defined from integrated parameters of the vortex flow which delineate between the spiral and bubble form of breakdown.

1. Ru=0.52 and Re$>$1.0 then the growth of the spiral instability leads to a gradual dissemination of the vortex.

2. Ru=0.52 and Re=1.0 then the bubble form of breakdown is imminent which can be categorized as a more violent dissipation of mean flow energy and large increase of the turbulent wake.

The Rosby parameter based on the energy raio is a critical parameter for the onset of the bubble breakdown which was indirectly formulated from Benjamin's theory of conjugate states. This form of breakdown has a direct analogy to the hydraulic jump phenomena in open channel flow. Although the wing vortex analyzed in this paper is inherently a more complex flow than the specific case formulated by Benjamin, the main thesis of his argument is generally applicable for vortex flows undergoing the "bubble" transition. The ramifications of controlling the vortex instability are

apparent from these results. A pneumatic jet placed upstream of the vortex breakdown location will have the following favorable chacteristics in terms of altering the Rosby number.

a.The jet growth rate will indirectly impart a less adverse pressure gradient on the vortex flow by virtue of changing the resulting external potential flow in this region.

b.The turbulent entrainment of the jet will impart axial momentum to the outer pheriphery of the helical flow of the vortex relative to the crossflow component, hence increasing the local Rosby number.

c.Recommendations for follow up research

Implement wind tunnel experimental study of chined forebody at high angle of attack by incorporating various blowing jet schemes adjacent to the apex of the forebody. The particular focus of this research effort will examine various jet exit boundary conditions which will enhance the jet entrainment characteristics. A systematic study utili.ing state of the art experimental techniques such as the LDV and six component force balance will explore the physics of jet/vortical interactions and their impact on the local Rosby number.

REFERENCES

1 Erickson G E and Rogers L W Schreiner J A Lee, D.G , "Subsonic and Transonic Vortex Aerodynamics of a Generic Forebody Strake-Cropped Delta Wing Fighter" AIAA-88-2505, AIAA 6th Applied Aerodynamics Conference, June 1988

2 Erickson, G E., Rogers, L W Schreiner, J.A , Lee, D G , "Further Studies of the Subsonic and Transonic Vortex Aerodynamics of a Close-Coupled Forebody-Slender Wing Fighter" AIAA-81-4369, AIAA Atmospheric Flight Mechanics Conference, Aug 1988

3 Skow, A M Titiriga, A , Moore W A "Forebody/Wing Vortex Interactions and Their Influence on Departure and Spin Resistance", Agard CP-247 High Angle of Attack Aerodynamics, Oct 1978

4 Skow, A.M , Peake, D.J , "Control of the Forebody Vortex Orientation by Asymmetric air Injection", Agard CP-262-15 May 1979

5 Peake, D.J , Owen, F K , and Johnson, D A , "Control of Forebody Vortex Orientation to Alleviate Side Forces", AIAA-80-0183 Jan 1980

6 Visser, K.D Ivanoki, K P Nelson,R C and Ng,T T "Control of Leading Edge Vortex Breakdown by Blowing", AIAA-88-0604 AIAA 26th Aerospace Sciences Meeting, Jan. 1988

7 Hall, R M., and Del Frate, J H , "Interaction Between Forebody and Wing Vortices a Water Tunnel Study", AFWAL TM-88-232 Jan. 1988

8 Erickson, G.E , and Brandon, J M , "On the Nonlinear Aerodynamic and Stability Characteristics of a Generic Chine-Forebody Slender Wing Fighter Configuration", NASA TM 89447 June 1987

9 Squire, H B "Analysis of the Vortex Breakdown Phenomena", Aero Dept Rep Vol.102 Imperial College, London, 1960

10 Ludwig,H , "Vortex Breakdown" DLR FB 70-40, Sept. 1970

11 Benjamin, T B "Theory of Vortex Breakdown Phenomenon", Journal of Fluid Mechanics 14 1962

12 Benjamin, T B "Some developments In the Theory of Vortex Breakdown" Journal of Fluid Mechanics 28, 1967

13 Hall, M.G "Vortex Breakdown" Ann Rev Fluid Mechanics Vol 4,1972

14 Leibovich, S "The Structure of Vortex Breakdown" Ann Rev Fluid Mechanics 10,1978

15 Singh, S N , and Mahney, J L "On Vortex Breakdown and Instability" AFWAL-TR-81-3021 Mar 1981

16 Spall, R E Gatski T B Grosch, C E "A Criteria For Vortex Breakdown" Phys Fluids 30, Nov 1987

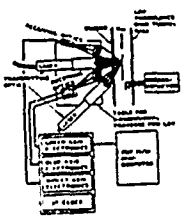


Figure 1 Fineform View of LDV System

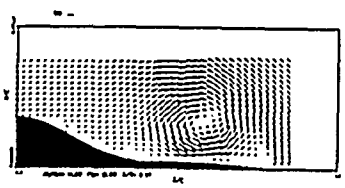


Figure 2 Rotated V-W Vectors Along the Core Trajectory at Alpha=21

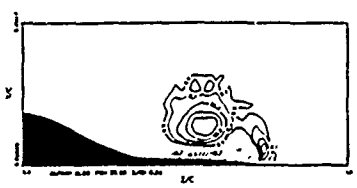


Figure 3 Vorticity Contours Along the Core at Alpha=21 Degrees

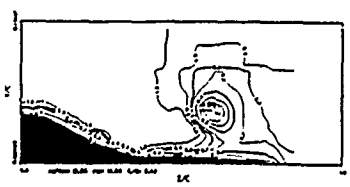


Figure 4 Axial Velocity Contours Along Vortex Axis at Alpha=21

1989 USAF-UES SUMMER FACULTY RESEARCH PROGRAM/

GRADUATE STUDENT RESEARCH PROGRAM

Sponsored by the

AIR FORCE OFFICE OF SCIENTIFIC RESEARCH

Conducted by the

Universal Energy Systems, Inc.

FINAL REPORT

ROBUST DESIGN USING INTERNAL MODEL CONTROL

Prepared by:	Dennis W. Farrell, MSEE, P.E.
Academic Rank:	Associate Professor
Department and	Electrical Engineering Technology
University:	University of Cincinnati
Research Location:	Flight Dynamics Laboratory WRDC/FIGL Wright-Patterson AFB Dayton OH 45433-6553
USAF Researcher:	Duane P. Rubertus
Date:	15 Sep 89
Contract No:	F49620-88-C-0053

ROBUST DESIGN USING INTERNAL MODEL CONTROL

by

Dennis W. Farrell

ABSTRACT

A two step controller design procedure is derived for MISO plants to achieve robust performance and robust stability. Internal model control (IMC) structure is used to control stable (includes poles at the origin), minimum phase (MP) and nonminimun phase (NMP) plants. The IMC structure, if used to control unstable plants (poles in open RHP), would be unstable, i.e., plant output increases without bound for a plant/model input disturbance. However, the derived IMC structure parametrization can be used directly to find a robust controller for a classic feedback structure that is stable. The unstable plants can be MP or NMP. Plant uncertainty in this paper is bounded by a disk shaped region, an approximation that encircles a complex mathematical described region with exact gain, phase, and parametric bounds. The disk shaped uncertainty bound is a compromise to have an analytic/numerical design procedure, for easier CAD implementation, at the expense of tighter performance and stability bounds that require graphical design procedures. The design procedures presented would apply to aircraft control and could be expanded to MIMO plants, two-degree-of-freedom controllers, and adaptive control.

ACKNOWLEDGMENTS

I would like to thank the Air Force Systems Command, Air Force Office of Scientific Research for sponsoring the USAF Summer Faculty Research Program (SFRP) and Universal Energy Systems for organizing and administering the program.

I wish to thank Mr Duane P. Rubertus of the Flight Dynamics Laboratory, Wright-Patterson AFB OH for being my SFRP Effort Focal Point and for giving me the freedom to enhance my research interests and capabilities in automatic controls. I want to thank the Control Techniques Group, especially Mark Mears for the personal effort and patience in helping me through this research period, and Peggy Cassidy for typing the final report.

Finally, I want to thank my wife, Donna, and children for their patience and understanding during my absence the past ten weeks.

I. INTRODUCTION:

No matter what design technique is used, or whether using a classical or modern control approach, controllers are designed based on information about the dynamic behavior of the system to be controlled. The model (information) of the system can be in the form of differential equations or state equations, which reflect only approximate parameters, order, and structure of the system. The accuracy of the model varies and is only an approximation, never perfect. Furthermore, the system being modeled could be nonlinear and/or time variant, qualities which are rarely captured in models. It is important that the controller be robust, that is, be insensitive to model uncertainty.

The Control Techniques Group of the Flight Dynamics Laboratory, Wright-Patterson AFB, is particularly concerned about robustness of aircraft controllers because the model of the aircraft changes with speed, altitude, angle of attack, etc., during normal flight. Also, the Air Force is interested in Failure Detection and Identification (FDI) and Reconfiguration Strategies in the event of component failure, such as a failed servo actuator resulting in a fixed control surface, or battle damage resulting in the loss of control surface effectiveness. Failure in flight can lead to drastic changes in the dynamic behavior of the aircraft, falling outside the designed robustness range of the controller and requiring a more sophisticated control schemes, such as adaptive control.

My research interests have been in the area of application of a variety of control techniques resulting in robustness, i.e., controller design for performance and stability which is insensitive to model uncertainty. At Wright-Patterson AFB my research has been concentrated in Internal Model Control (IMC), since work has not been done in this area in the Flight Techniques Group to my knowledge, although other robust design techniques such as Quantitative Feedback Theory (QFT) has been used extensively. Also, IMC was chosen because it could be the basis for adaptive control research in the future, an alternative to the now widely used adaptive control scheme of gain scheduling.

II. OBJECTIVES OF THE RESEARCH EFFORT:

The research topic area stated in my SFRP application was "Design Procedures for Robust Aerodynamic and Propulsion (vectored thrust) Control." A requirement before starting the SFRP was to submit preliminary research goals and objectives. Mine centered around the following: studying dynamics of atmospheric flight and automatic control of aircraft; familiarizing myself with the Aquila Remotely Piloted Vehicle (RPV), which uses vectored thrust; and, investigate computer software available for simulation, analysis, and design of aircraft controllers (linear and nonlinear).

I modified my preliminary goals and objectives to concentrate on the control aspects more than specific plants being controlled after spending a couple of weeks in the Control Techniques Group. I realized that evaluation of aerodynamic and vectored thrust controllers, that were designed, would require a dynamic flight simulator based on the nonlinear aircraft equations. This flight simulator is not presently available in the Control Techniques Group. The following will attempt to explain why this is needed, followed by my 1989 SFRP goals.

The computer software package available in the Control Techniques Group for simulation, analysis, and design was MATRIXX, which only handles linear systems. Robust controller design would then be based on linearized aircraft equations of motion specified as a function of flight condition, e.g., Mach 0.9 speed and 20,000 feet altitude. For any other flight condition the aircraft model would not be correct. A limitation to robust design using these linearized equations is that varying a parameter(s) too much to check robust performance and stability ranges, could result in exceeding the valid linearized range about the specified flight condition.

Aircraft with vectored thrust engines allow the pilot to maintain precise control during slow speed, low altitude flight conditions, even when the plane is moving so slowly that its wings are stalled (sufficient lift to sustain flight stops). However, a sophisticated on-board computer system

is necessary to assist the pilot in keeping the plane stable during violent combat maneuvers made possible by vectored thrust. Linearized aircraft equations at a specific flight condition is surely inadequate here.

Considering the short time period of SFRP, my research goals were limited to one control structure to control different kinds of plants, such as stable, unstable, minimum phase (MP), and nonminimum phase (NMP) plants, types of plants found in aerodynamic and vectored thrust controlled aircraft. This will lay the ground work for the future when a dynamic flight simulator is available. My 1989 SFRP research goals were as follows:

(1) Research Internal Model Control (IMC) structure and model uncertainty for robust performance and stability.

(2) Establish a design procedure for IMC with stable plants.

(3) Establish a design procedure for IMC with unstable plants.

(4) Use above design procedures on a variety of plants (stable, unstable, MP and NMP).

(5) Verify the above designs with computer simulations demonstrating robust performance and stability.

The above design procedures should lend themselves to computer-aided design (CAD) implementation in the future. The design procedure should work for any plant or process, e.g., aerodynamic controlled aircraft, vectored thrust controlled aircraft, machine tools, distillation columns, etc. The design procedure is limited to MISO, but could be expanded to MIMO in the future much like QFT was expanded.

III. INTERNAL MODEL CONTROL AND MODEL UNCERTAINTY:

The control structure known as Internal Model Control (IMC) is shown in Figure 1 below for MISO, stable, unstable, minimum phase, and nonminimum phase processes. The controller plays the role of a feedforward con-

troller, but with the advantage of being able to cancel the influence of unmeasured disturbances. Design procedures for such a control structure have been derived for nominal performance, robust stability, and robust performance in the presents of model uncertainty.

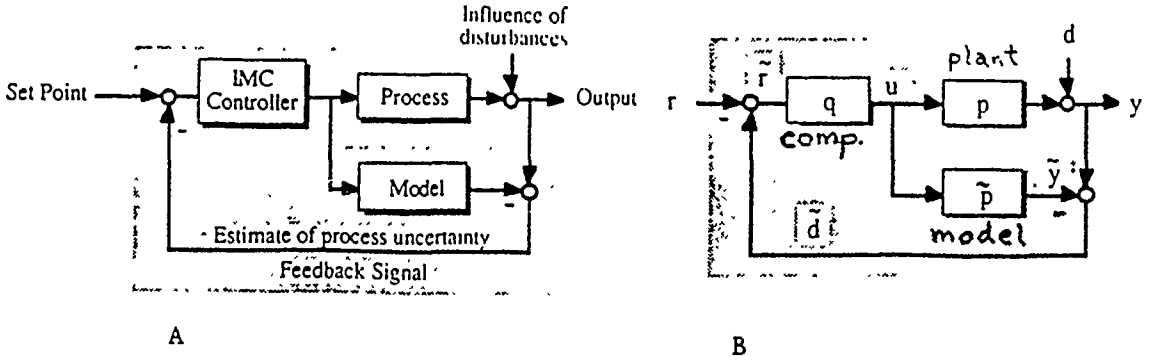


Figure 1. Internal Model Control

Model uncertainty can be described in many different ways. We will assume the dynamic behavior of a plant is described by a family of linear time invariant models defined in the frequency domain. The transfer function at a particular frequency ω is not confined to a point, but can lie in a region $\pi(\omega)$ on the Nyquist plane. Figure 2 below shows a $\pi(\omega)$ region for exact gain, phase and parametric bounds, that has a complex mathematical description and require graphical design procedures. Figure 2 also shows a disk shaped region used to approximate this $\pi(\omega)$ region with more or less conservatism, that will be used throughout this paper because it allows an analytic/numerical design procedure.

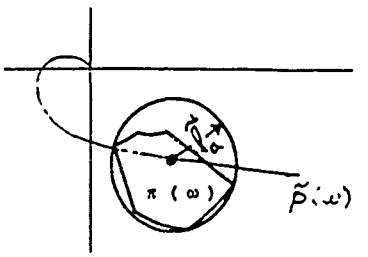


Figure 2. Uncertainty Region

A family of plants, p, is described by the disk with radius l_a (additive uncertainty) and $\tilde{p}$ is the nominal plant or the model defining the center

of all the disk shaped regions. Algebraically the family of plants described by the disk is

$$|p(j\omega)-\bar{p}(j\omega)|\leq\bar{l}_a(\omega) \tag{1}$$

and satisfies

$$p(j\omega)=\bar{p}(j\omega)+l_a(j\omega),\ \text{with}\ |l_a(j\omega)|\leq\bar{l}_a(\omega) \tag{2}$$

The family of plants can also be represented by

$$[|p(j\omega)-\bar{p}(j\omega)|/\bar{p}(j\omega)]\leq l_m(\omega) \tag{3}$$

and satisfies

$$p(j\omega)=\bar{p}(j\omega)(1+l_m(j\omega)),\ \text{with}\ |l_m(j\omega)|\leq\bar{l}_m(\omega) \tag{4}$$

and is referred to as a multiplicative uncertainty.

A typical plot of $\bar{l}_m(\omega)$ is shown in Figure 3 below and shows that our models tend to describe well the steady-state and low-frequency behavior of processes, but become inaccurate for high-frequency inputs.

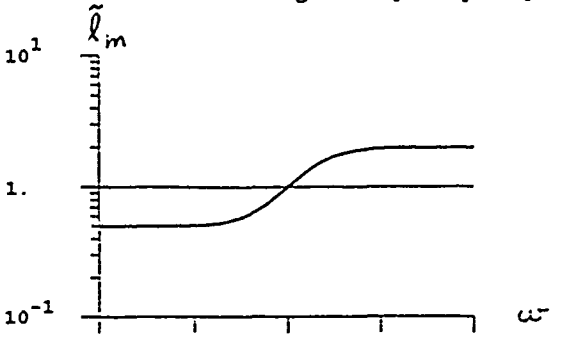


Figure 3. Typical Multiplicative Uncertainty $\bar{l}_m$

IV. INTERNAL MODEL CONTROL DESIGN OVERVIEW

Using the IMC structure in Figure 1B above the sensitivity Function, ϵ, and the complementary sensitivity function, η, are defined below as

$$\epsilon = y/d = 1 - \bar{p}q \tag{5}$$

$$\eta = y/r = \bar{p}q \tag{6}$$

$$\epsilon(s)+\eta(s)=1 \tag{7}$$

To have good setpoint tracking and disturbance rejection requires $\epsilon\approx 0$ and $\eta\approx 1$. The compensator, $\bar{q}$, is an H_2 - optimal controller designed without regard to robustness which minimizes the ISE for a particular input, and

will usually be an improper transfer function. The complete compensator, q, is then

$$q=\bar{q}f \tag{8}$$

where f is a low-pass filter needed to make q proper and to detune the controller, to provide the rolloff necessary for robustness and milder action of the manipulated variable, i.e., if the model is not perfect (the usual case), then the feedback signal includes the effect of this model error and could lead to possible stability problems at higher frequencies. For a typical plot of $|\bar{\epsilon}|$ and $|\bar{\eta}|$ shown in Figure 4 below, with compensator $\bar{q}$ before adding filter, f, some observations can be made.

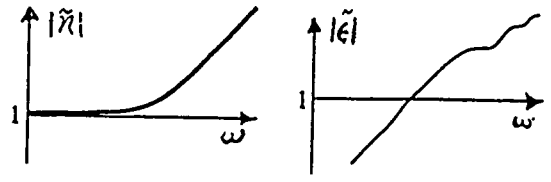


Figure 4. Sensitivity $|\bar{\epsilon}|$ and complementary sensitivity $|\bar{\eta}|$ with optimal controller $\bar{q}$

From the plot of $|\bar{\eta}|$, low frequency (sluggish) inputs, high performance is paid for with poor robustness, i.e., $|\bar{\eta}|>1$ for higher frequencies can result in stability problems. From the plot of $|\bar{\epsilon}|$, higher frequency (fast) inputs tend to be amplified and performance can be quite bad. The rolloff frequency of the low-pass filter, f, should be determined such that an optimal compromise between performance and robustness is reached. Increasing the filter time constant, λ, to detune the controller sacrifices performance (ϵ increases) for robustness (η decreases). From equation (7), if ϵ is increased, then η has to decrease and visa versa.

V. REQUIRED INFORMATION IMC DESIGN PROCEDURE:

For the design of an Internal Model Control controller the following essentials in table 1 have to be specified.

TABLE 1. REQUIRED INFORMATION - STABLE AND UNSTABLE PLANTS

1. Process model $\tilde{p}$
2. Type of inputs (setpoint and disturbances) v affecting the process output - e.g., step, ramp, etc.
3. Performance specifications:
   (a) Closed - loop system type (1 or 2)
   (b) Frequency dependent performance weight, W. The maximum allowable peak height 1/W of the sensitivity function ϵ (typically $0.3<W<0.9$).
4. Uncertainty Information $\tilde{l}_m(\omega)$. Family of plants described by

$$|[p(j\omega)-\tilde{p}(j\omega)]/\tilde{p}(j\omega)]| \leq \tilde{l}_m(\omega)$$

The most basic objective of an IMC controller is to keep the error between the plant output y and the reference r small when the overall system is affected by external signal r and d. The H_∞ - optimal controller for robust performance minimizes the worst ISE which can result from a set of inputs or equivalently it minimize the peak of ϵ weighted by W. To relax performance would require decreasing W.
In the next section after the design procedure, an example will be given which should clarify table 1.

VI. IMC DESIGN PROCEDURE FOR STABLE PLANTS:

A. After obtaining the required information of table 1, previous section, the following design procedure can be followed:

TABLE 2. DESIGN PROCEDURE - STABLE PLANTS

STEP 1: Nominal Performance

The H_2 - optimal controller $\tilde{q}$ is determined for a specified input v

$$\tilde{q}=(\tilde{p}_M v_M)^{-1}\{\tilde{p}_A^{-1} v_M\}_* \qquad (9)$$

STEP 2: Robust Stability and Performance

a. The controller $\tilde{q}$ is augmented by the IMC filter f, $q = \tilde{q}f$.

Type 1 Input: $f=(\lambda s+1)^{-n}$ and Type 2 Input: $f=(n\lambda s+1)(\lambda s+1)^{-n}$ (10)

Here n is selected large enough for q to be proper.

b. Robust Stability:

Check if $|\eta\tilde{l}_m|<1$ for $\omega=0$ (11)

This is necessary and sufficient for a filter time constant $\lambda>0$ to exit for which the system is robustly stable.

c. Robust Performance: Increase λ just enough to meet the condition

$$|\eta\tilde{l}_m|+|\epsilon W|<1 \text{ for all } \omega \quad (12)$$

Nomenclature:

$\tilde{l}_m$	bound on the multiplicative uncertainty
MP	minimum phase
NMP	nonminimum phase
$\tilde{p}_A$	all pass with the NMP elements of $\tilde{p}(s)$
$\tilde{p}_M$	MP factors of $\tilde{p}(s)$
v_M	MP factors of $v(s)$
W	performance weight
ϵ	sensitivity function
η	complementary sensitivity function
$\{\cdot\}_*$	operator denotes that after partial fractionexpansion all terms involving the poles of $\tilde{p}_A^{-1}$ are omitted

For robustness $\tilde{q}$ has to be augmented by a low-pass filter, f, whose parameters are chosen such that an optimal compromise between performance and robustness is reached. Also, f is chosen such that the closed-loop system retains its asymptotic tracking properties. Thus for asymptotically constant inputs (Type 1) and asymptotically ramp-like inputs (Type 2), equation (10) for f meets all requirements.
The H_2 - optimal controller $\tilde{q}$, equation (9), was derived by Frank, 1974 (reference 6). Robust stability equation (11) is generally attributed to Doyle & Stein, 1981 (reference 4). The robust performance condition follows as a special case from the MIMO Structured Singular Value Analysis proposed by Doyle, 1984, 1985 (reference 2 and 3).

B. EXAMPLE 1. First Order Lag with Uncertain Deadtime (NMP plant)

Required information:

1. $\tilde{p}= (s+1)^{-1}e^{-s\theta}$
2. Step input
3. Performance
   (a) Type 1, no offset for steps
   (b) Let W=0.4. Then maximum peak of $\epsilon=W^{-1}=2.5$

4. Uncertainty information

(deadime ± uncertainty)$=(\theta\pm\tilde{\delta})=(1\pm0.3)$ seconds

$$\tilde{l}_m=|(p-\tilde{p})/\tilde{p}|$$

where $p=(s+1)^{-1}e^{-s(\theta+\delta)}$ and $\tilde{p}=(s+1)^{-1}e^{-s\theta}$

divide numerator and denominator by $\tilde{p}$ and let $s=j\omega$

$$\tilde{l}_m(j\omega)=|e^{-j\omega\tilde{\delta}}-1|$$

A plot of this equation is shown in Figure 5 below and it is easily seen that

$$\tilde{l}_m(\omega)=2 \quad \omega\delta\geq\pi$$

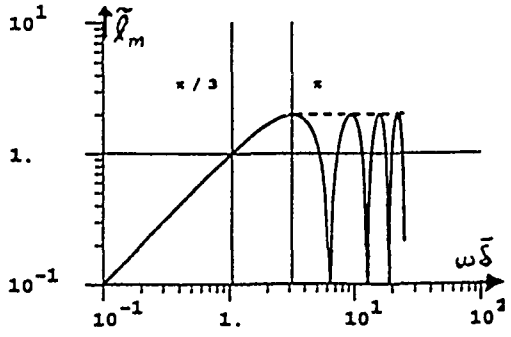


Figure 5. Multiplicative Uncertainty $\tilde{l}_m$ versus $\omega\delta$

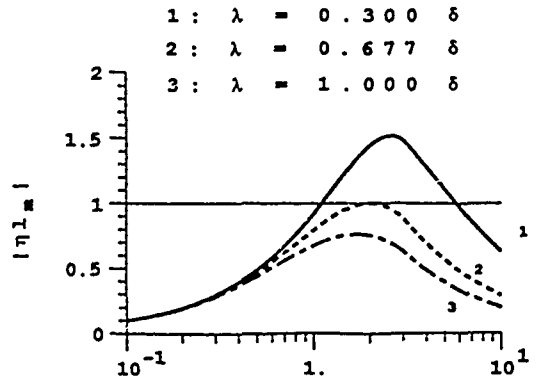


Figure 6. Robust Stability Bound $(|\tilde{\eta}\tilde{l}_m|$ versus $\omega\delta$

Design procedure:

STEP 1: Nominal Performance from equation (9)

$$\tilde{q}=(\tilde{p}_M v_M)^{-1}(\tilde{p}_A^{-1}v_M)_*$$

$$\tilde{q}=(s+1)s(1\cdot s^{-1})_*$$

$$\tilde{q}=s+1$$

STEP 2: Robust Stability and Performance

a. Using equation (10) for type 1, n=1 for q proper

$$f=(\lambda s+1)^{-1}$$

using equation (8)

$$q=\tilde{q}f=(s+1)(\lambda s+1)^{-1}$$

b. Robust stability using equation (11)

$$|\eta\tilde{l}_m|=|\tilde{p}\tilde{q}f\tilde{l}_m|=|e^{-s}f\tilde{l}_m|=|f\tilde{l}_m|<1$$

is plotted in Figure 6 above and implies that $\lambda=0.67\tilde{\delta}=0.2$ for robust stability.

c. Robust performance using equation (12)

$$|\eta\tilde{l}_m|+|\epsilon W|=|f\tilde{l}_m|+|(1-e^{-jw}f)0.4|<1$$

is plotted in Figure 7 below and implies that λ=0.65 for robust performance. Therefore, the IMC controller $q=(s+1)(0.65s+1)^{-1}$.

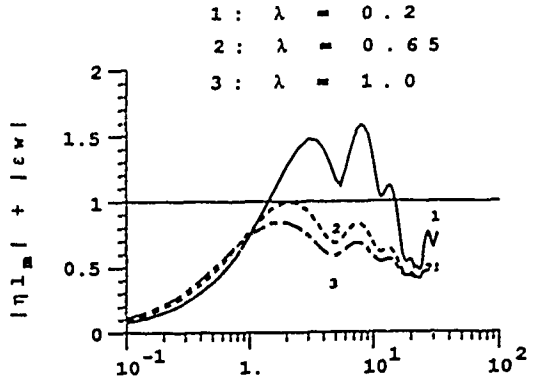


Figure 7. Robust Performance Bound

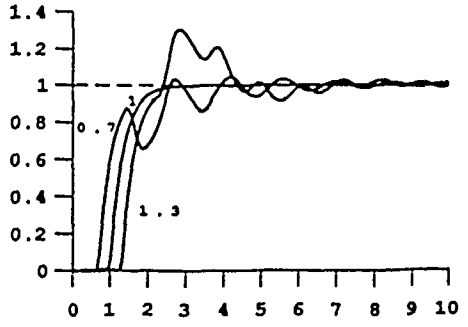


Figure 8. System Step Response

Closed-loop responses with λ=0.65 chosen for robust performance is shown in Figure 8 above for $(\theta\pm\delta)=(1\pm0.3)$ seconds delay.

C. EXAMPLE 2. Position Servo with Pole at Origin (MP plant)

Required information:

1. $\tilde{p}=0.787[s(s+4.6)]^{-1}$
2. Step input
3. Type 1
4. $K=0.787+\delta_1$ where $\delta_1=+0.787,-0.3935$
   $\alpha=4.6+\delta_2$ $\delta_2=\pm2.3$

Design procedure:

STEP 1: For MP plant equation (9) yields $\tilde{q}=\tilde{p}^{-1}$

$\tilde{q}=(0.787)^{-1}s(s+4.6)$

STEP 2a. Using equation (10) for a type 1, n=2 for q proper

$f-(\lambda s+1)^{-2}$ Using equation (8)

$q=\tilde{q}f=(0.787)^{-1}(\lambda s+1)^{-2}s(s+4.6)$

b and c. Using IMC structure with above compensator q, no positive K or α combination between zero and infinity, can make system unstable. Therefore, pick filter time constant λ for performance desired, but not too small to exceed the bandwidth because of noise.

Figure 9 below shows the step response for various λ's where uncertainty δ_1=+0.787 and δ_2=-2.3 is used, i.e., process $\tilde{p}$ parameters are K=1.574 and α=2.3.

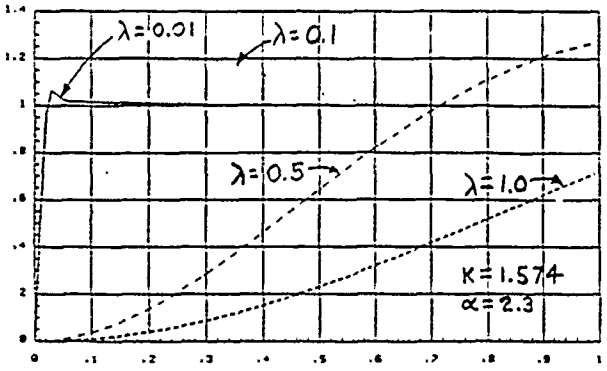


Figure 9. System Step Response for Various Filter Time Constants λ

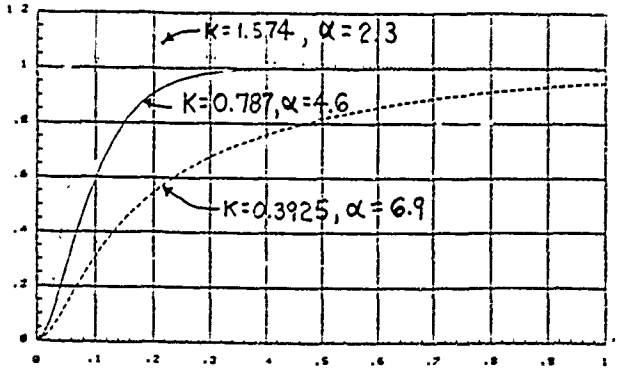


Figure 10. System Step Response λ=0.05

Figure 10 shows step response robustness over extreme range of uncertainties δ_1 and δ_2 for the design with λ=0.1.

VII. IMC DESIGN PROCEDURE FOR UNSTABLE PLANTS:

A. The required information for unstable design is the same as that for stable systems, TABLE 1: process model, input type, performance specification and uncertainty information.

TABLE 3. DESIGN PROCEDURE - UNSTABLE PLANTS

STEP 1: Nominal Performance

The H_2 - optimal controller $\tilde{q}$ is determined for a specified input v

$$\tilde{q}=b_p(p_M b_v v_m)^{-1}\{(b_p p_A)^{-1} b_v v_M\}_* \qquad (13)$$

If all the unstable plant/input poles are at the origin, use Table 2 design procedure.

STEP 2: Robust Stability and Performance

a. The controller $\tilde{q}$ is augmented by the IMC filter f, $q=\tilde{q}f$.

$$f(s) = \frac{1}{(\lambda s+1)^n}\sum_{j=1}^{k}(\lambda\pi_j+1)^n \prod_{\substack{i=1\\ i\neq j}}^{k}\frac{s-\pi_i}{\pi_j-\pi_i} \qquad (14)$$

where $\pi_1,\ldots,\pi_k$ are the unstable plant/input poles. Here n is selected large enough for q to be proper.

b. Robust Stability:

$$\text{Check if } |\eta \tilde{l}_m| < 1 \text{ for } w \neq 0 \tag{11}$$

This is necessary and sufficient for a filter time constant $\lambda > 0$ to exist for which the system is robustly stable.

c. Robust Performance: Increase λ just enough to meet this condition

$$|\eta \tilde{l}_m| + |\epsilon W| < 1 \text{ for all } \omega \tag{12}$$

but keep $\lambda < (\pi+\delta)^{-1}$ where π is stable pole with uncertainty δ. If $\lambda^{-1} < \pi$, undesirable performance and robustness properties occur.

Nomenclature (In addition to TABLE 2 Nomenclature):

b_p all pass with the open RHP poles of $\tilde{p}(s)$

b_v all pass with the open RHP poles of $v(s)$

RHP right hand plane

For unstable systems (plant/input poles in open RHP) we have to abandon the IMC structure. The stability of both p and q is required for internal stability of an IMC structure. In Figure 11 below, IMC structure A is equal to B, which is equal to C. Even for unstable systems we can still use the IMC parametrization for the design of the feedback controller c, because IMC parametrization offers two advantages:

(1) The controller which yields good closed-loop behavior is greatly simplified - any IMC controller q automatically yields a feedback controller c for which the closed-loop system is stable.

(2) Closed-loop stability is preserved in the presence of constrains and controller nonlinearities.

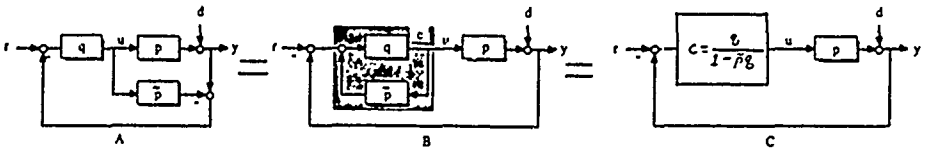


Figure 11. Alternate Representation of the IMC structure

Controller parametrization was proposed by Zames and Francis, 1983 (reference 18) to find q such that the feedback controller $c=q(1-pq)^{-1}$ is internally stable. The IMC filter f to satisfy pole-zero excess, internal stability and asymptotic tracking of inputs requirements translate to $f(s)=1$ at $s=\pi_1,\ldots,\pi_k$ (k distinct poles in the closed RHP). Solving these equations is reported by Golub and VanLoan, 1983 (reference 10).

B. EXAMPLE 3 Inverted Pendulum (MP with pole in open RHP)

Required information:

1. $\tilde{p}=-1.188s(s^3+s^2-11.65s-11.65)^{-1}$

   $=-1.188s[(s+3.4132)(s-3.4132)(s+1)]^{-1}$

2. Step input

3. Performance

   a. Type 1, no offset for steps

   b. Let W=0.4. Then maximum peak of $\epsilon=W^{-1}=2.5$

4. Uncertainty information

   Let uncertainty of unstable pole be 50%

   $s_{1,2,3}=\pm 3.4132\pm\delta,0$

   $=\pm 3,4132\pm 1.7066,0$

   $=\pm 5.1198,0$

   $\tilde{l}_m = |(p-\tilde{p})|\tilde{p}|$

   where $p=-1.188s[(s+5.1198)(s-5.1198)(s+1)]^{-1}$

   $\tilde{p}=-1.188s[(s+3.4132)(s-3.4132)(s+1)]^{-1}$

   $\tilde{l}_m(jw)=-14.56(s^2-26.2124)^{-1}$

Design procedure:

STEP 1: Nominal Performance from equation (13) normally, but $\tilde{q}=\tilde{p}^{-1}$ always for a MP plant whether open loop system stable or not.

$$\tilde{q}=-(s+3.4132)(s-3.4132)(s+1)(1.188s)^{-1}$$

STEP 2: Robust Stability and Performance

a. Using equation (14), n=3 for q proper

$$f(s)=(a_1s+a_0)(\lambda s+1)^{-3}$$

where $a_0=1$

$$a_1=(3.4132)^2\lambda^3+3(3.4132)\lambda^2+3\lambda$$

b. Robust stability using equation (11)

$$|\eta\tilde{l}_m|=|\tilde{p}\tilde{q}f\tilde{l}_m|=|f\tilde{l}_m|<1 \qquad \text{for } w=0$$

$$|[(a_1s+1)(\lambda s+1)^{-3}][14.56(s^2-26.2124)^{-1}]|<1$$

$0.555<1$ checks

c. Robust performance using equation (12)

$$|\eta\tilde{l}_m|+|\epsilon W|<1 \text{ all } \omega$$

is plotted in Figure 12 below and implies that $\lambda=0.37$. But, must keep $\lambda<(\pi+s)^{-1}=(3.4132+1.7066)^{-1}=0.195$. Let $\lambda=0.1$. Therefore, the feedback controller c is equal to

$$c=q(1-\tilde{p}q)^{-1} \qquad \text{where } q=\tilde{q}f$$

$c=-(0.414s^3+2.827s^2+5.826s+3.4132)(0.001188s^3+0.0397s^2)^{-1}$

and would be the controller for Figure 11C.

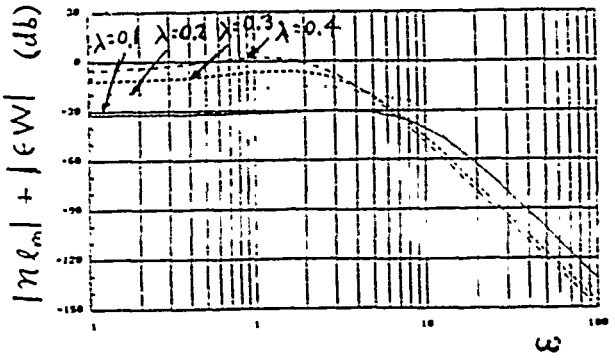


Figure 12. Robust Performance Bound

Figure 13 shows the pendulum position due to a unit step input. Robustness over extreme range of unstable pole location uncertainty of ±50% is shown for multiple step inputs.

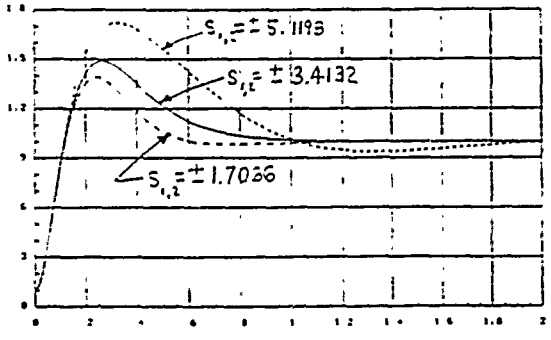


Figure 13. System Step Response

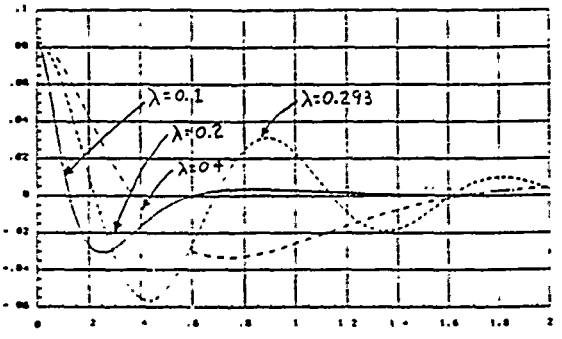


Figure 14. Pendulum Position for Initial Position of 0.0842 Meter

Figure 14 shows pendulum position due to an initial position of 0.0842 meters for varying λ. Note oscillatory response at $\lambda=(3.4132)^{-1}=0.293$. Figure 15 is a plot showing phase margin and gain margin as a function of λ. Note at $\lambda=(3.4132)^{-1}=0.293$ the dip in phase margin, which explains the oscillatory response seen in Figure 14. This is why the design procedure requires λ to be less than the reciprocal of the unstable pole plus uncertainty.

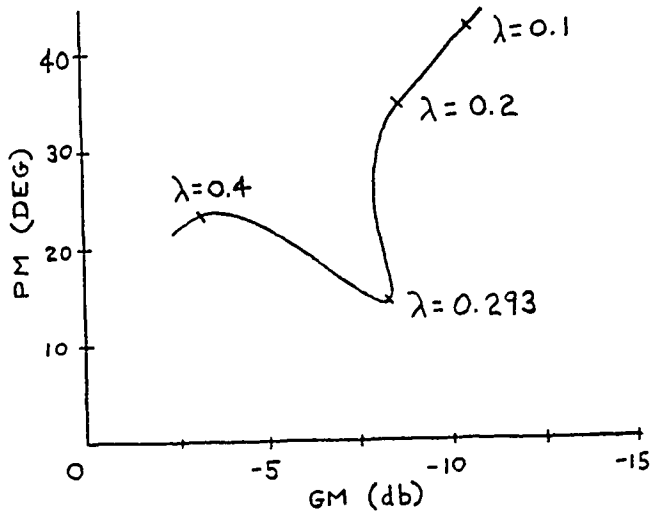


Figure 15. Phase Margin and Gain Margin as a Function of λ

VIII. RECOMMENDATIONS:

A. Although MATRIXX is a very powerful software package, it is limited to linear systems. What is needed for design, analysis and evaluation, is dynamic flight simulation capabilities using nonlinear equations in real time. This is presently not available in the Control Techniques Group.

B. Internal Model Control has been developed in this paper for MISO, stable, unstable, minimum phase and nonminimum phase plants. The controller in this paper was one-degree-of-freedom, but could easily be expanded to two-degree-of-freedom in the future to handle more than one type of input signal. The two step design procedures for MISO could be directly applicable to MIMO plants by breaking apart a MIMO plant into MISO plants, like is done with QFT. The two step design procedure could be implemented by a CAD package since the parameter uncertainty used lends itself to analytic/numerical design procedures, unlike QFT which requires graphical design procedures. The Internal Model Control could also be used as the basis for adaptive control using model referencing in the future.

C. A second design method for unstable plants that could be investigated in the future allows the use of the IMC structure. Pole placement using a state estimator is used to stabilize the plant and then wrapped around this is the standard IMC structure for stable plants. This then allows the use of standard IMC, two step, design procedure for stable plants.

REFERENCES

1. Blakelock, John H., Automatic Control of Aircraft and Missles. New York: John Wiley & Sons, Inc., 1965.

2. Doyle, J.C., Lecture Notes - ONR/Honeywell Workshop on Advances on Multivariable Control, 1984.

3. Doyle, J.C., "Structured Uncertainty in Control System Design," Proc. IEEE Conf. on Decision and Control, Ft. Lauderdale, FL, 1985.

4. Doyle, J. C. and G. Stein, "Multivariable Feedback Design: Concepts for a Classical/Modern Synthesis," IEEE Trans. Autom. Control, AC-26, p 4, 1981.

5. Etkin, Bernard, Dynamics of Atmospheric Flight, New York: John Wiley & Sons, Inc., 1972.

6. Frank, P.M., Entwurf von Regelkreisen mit vorgeschriebenem Verholten, Braun, Karlsruhe, 1974.

7. Garcia, C.E. and M. Morari, "Internal Model Control - 1. A Unifying Review and Some New Results," Ind. Eng. Chem. Process Des. & Dev., 21, pp 308-333, 1982.

8. Garcia, C.E. and M. Morari, "Internal Model Control-2. Design Procedure for Multivariable Systems," Ind. Eng. Chem. Process Des. & Dev., 24, pp 472-484, 1985.

9. Garcia, C.E. and M. Morari, "Internal Model Control-3. Multivariable Control Law computation and Tuning Guidelines," Ind. Eng. Chem. Process Des. & Dev., 24, pp 484-494, 1985.

10. Golub, G.H. and C.F. Van Loan, Matrix Computations, Baltimore, MD: John Hopkins University Press, 1983.

11. Houpis, Dr C.H., Quantitative Feedback Theory (QFT): Technique for Designing Multivariable Control Systems, AFWAL-TR-86-3107, AFWAL/FIGl, Wright-Patterson AFB, OH: National Technical Information Service, January 1987.

12. Kwakernaak, Huibert, and Raphael Sivan, Linear Optimal Control Systems, New York: John Wiley & Sons, Inc., 1972.

13. Laughlin, D.L., K.G. Jordan, and M. Morari, "Internal Model Control and Process Uncertainty: Mapping Uncertainty Regions for SISO Controller Design, "Int. J. Control, 44, pp 1675-1698, 1986.

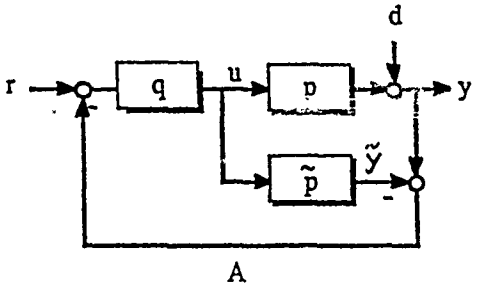
14. Morari, Manfred, and Evanghelos Zafiriou, Robust Process Control, Englewood Cliffs, New Jersey: Prentice Hall, 1989.

15. Phillips, Charles L., and Royce D. Harbor, Feedback Control Systems, Englewood Cliffs, New Jersey: Prentice Hall, 1988.

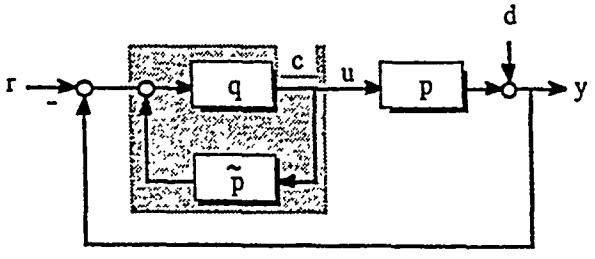
16. Sastry, Shankar, and Marc Bodson, Adaptive Control: Stability, Convergence, and Robustness, Englewood Cliffs, New Jersey: Prentice Hall, 1989.

17. Zames, G. "Feedback and Optimal Sensitivity: Model Reference Transformation, Multiplicative Seminorms and Approximate Inverses," IEEE Trans. Autom. Control, AC-26, pp 301-320, 1981.

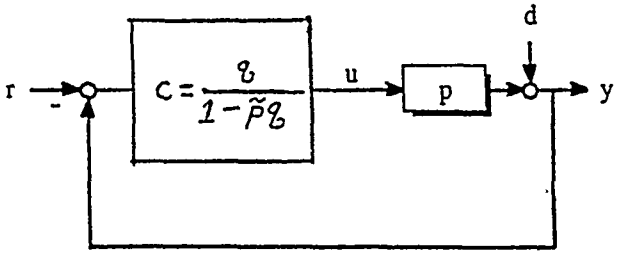
18. Zames, G. and B.A. Francis, "Feedback, Minimax Sensitivity and Optimal Robustness," IEEE Trans. Autom. Control, AC-28, p 585, 1983.



A



B



C

Figure 1. Alternate representations of the IMC structure.

1989 USAF-UES SUMMER FACULTY RESEARCH PROGRAM/

GRADUATE STUDENT RESEARCH PROGRAM

Sponsored by the

AIR FORCE OFFICE OF SCIENTIFIC RESEARCH

conducted by the

Universal Energy Systems, Inc.

FINAL REPORT

Neural Networks and their Role in Visual Object Recognition

Prepared by:	Augustus Morris, Jr., Ph.D. and Nancy Faulkner *
Academic Rank:	Assistant Professor *Graduate Student
Department and	Manufacturing Engineering
University:	Central State University
Research Location:	Flight Dynamics Laboratory, Special Projects,Group
USAF Researcher:	Mangal Chawla, Ph.D.
Date:	September 30, 1989
Contract No:	F49620-88-C-0053

Neural Networks and their Role in Visual Object Recognition

by

Augustus Morris, Jr., Ph.D.
and Nancy Faulkner

ABSTRACT

This work effort primarily explored the use of neural networks for object recognition. A compilation of institutions and companies doing work in this field was completed so that expert advice could be sought during the lab's development of neural network technology. Through the use of neural network development software, a preliminary network was designed to recognize simple geometrical shapes. Moments were used as features in the classification. Results were encouraging enough to pursue further development of this area.

ACKNOWLEDGEMENTS

I would like to show my appreciation to the entire staff of the Special Projects Group of the Flight Dynamics Lab. The guidance of Dr. Mangal Chawla was very helpful during this experience. Mr. David Perez and Capt. Samuel Hagins provided moral support and encouragement. This opportunity would not be possible without the sponsorship of the Air Force Office of Scientific Research and the administration of Universal Energy Systems.

I. INTRODUCTION

With the increasing power and availability of computers, more applications in image processing and object recognition are in the commercial market. More institutions are conducting research in this area as computer power becomes cheaper. Even with this explosion in activity, much is still in its infancy particularly in the area of object recognition. Research in object recognition is well over 30 years old, and many of the fundamental principles and theories came from this era.

However, the work during this era was limited by the lack of computer power of even ten short years ago. Now is the time to reinvestigate this area with the same vigor as it was in the 1950's and 1960's. Indeed this has been happening, and more new technologies are direct spin-offs from this effort.

Neural networks technology is one of those spin-off efforts of the object recognition research. Neural networks have been studied for as long as object recognition; however, the history of neural networks was more unstable than the history of object recognition.

The first efforts actually came from researchers in the learning psychology field (17). Hebb (6) proposed one of the first learning rules which could simulate learning behavior of interconnected neurons. It was the Perceptron model of

Rosenblatt which gave birth to neural networks research (16,21). There were many claims at that time that the Perceptron model would be capable of doing the same things as the human brain does. These exaggerations were brought to rest in the late 1960's by the report of Minsky and Papert (13). This report was so convincing that there was a large exodus from the neural network area to the artificial intelligence area. Further research in neural networks was nil until the late 1970's and early 1980's when researchers such as Hopfield revitalized the field (7,21). Today, research in this area is conducted at the fervor as it was in the late 1950's and 1960's.

It is because of this renewed effort that neural networks technology is being applied to the object recognition field. The purpose of this summer effort was to assess the progress in this area and to show feasibility of using neural networks technology for the object recognition needs of the Special Projects Group of the Flight Dynamics Lab.

My abilities primarily are in the modeling and analysis of the man-machine interface of man-machine systems. Since my position at Central State University, I have participated in research towards the development of a large robotic hand. During the summer of 1988 I worked for the same lab as under this present appointment to apply image processing methods to a scale model service robot. It is logical to pursue

neural networks technology as it applies to robot vision and object recognition.

II. OBJECTIVES

The objectives of this effort were aimed at the current capabilities of the neural network field. These objectives could be broken into the following areas:

1.) A survey of what is currently being published in the neural networks and object recognition.
2.) A list of institutions involved in neural network research and contacts
3.) A list of companies involved with neural networks along with their hardware and software products.
4.) A preliminary demonstration of using neural networks to identify simple shapes.

III. LITERATURE REVIEW

This is not meant to be a complete review of the literature; however, a basic idea of where the research is should be evident. A more extensive survey of the literature is planned under the Research Initiative Program.

Neural network applications are being investigated more by researchers in the computer vision area. Object recognition is one such application. One of the most challenging applications presently is the use of neural networks to handprinted Chinese character recognition (22). Most research; however, follow one of two pathways. Neurobiologists for many years have attempted to model the processing of the visual retina and cortex. Neural networks provide a convenient way of modeling. Work by Kolodzy (10) and Mueller et al. (14) are examples of this work.

The other approach to using neural networks in object recognition uses the network as a typical classifier. The features presented to the network are typical to standard methods of object recognition (2,4,18). This approach is taken mainly to give the entire system more robustness in the case of physical damage to the system.

Some novel applications of neural networks are being researched which may also have some influence on the biological modeling approach. Gevins (5) is using neural networks to analyze the electrical potentials of the human cortex of the brain, commonly known as the EEG. A fascinating approach by Dawes (3) attempts to map the architecture of actual interconnected neurons through transfer functions of the input and output.

IV. INSTITUTIONS INVOLVED IN RESEARCH

The number of institutions involved in neural network research has increased dramatically since the early 1980's. There are over 200 universities, institutions, and companies currently doing research in this area. Some are doing basic research while others are designing innovative neural network architectures. Commercial products are beginning to enter the marketplace. Appendix A contains a list of the many people working in this field (12).

V. COMPANIES AND THEIR HARDWARE AND SOFTWARE PRODUCTS

There are over 20 companies that have on the market software or hardware neural network products. There are basically three major categories of products (19). Some products are solely for educational purposes while others allow you to create applications. Commercial user products comprise the last category of neural networks products.

Generally, the educational products are strictly software, consist of a limited number of network paradigms, and are considerably lower in cost than the other products (15,19). The toolkit products, which allow the creation of applications, are generally more expensive. Several of these products require a hardware board in order to speed learning times (1,15). The toolkit products require a longer training time, but the rewards are greater flexibility. Most of the

products have minimum hardware requirements of an IBM compatible computer with 256K memory. A hard disk is highly recommended (15,19).

In Appendix B is a list of companies who sell commercial neural networks products. Included in this list are the name of the products and a current price list (14).

VI. NEURAL NETWORK DEMONSTRATION

The neural network method to be used was chosen after careful review of the current methods used. The backpropagation method was chosen because of its utility and popularity. This method was a natural extension of the delta rule used by the Perceptron model of Rosenblatt (11,13,16,21). However, the backpropagation method overcomes the fundamental problems of the Perceptron (8,11,21). In addition, the backpropagation method allows for multilayers and is a viable method for most network architectures. The system was constructed to distinguish circles from squares and also triangles from squares. All images were binary images.

Hardware and Software Requirements

A Tandy 4000 microcomputer with an 80386 microprocessor was used in the development of the neural network. The NeuralWorks Professional II software package by NeuralWare

Inc. was borrowed from Tractell Inc. for use in the development of the network.

The Tandy 4000 microcomputer was also used in the implementation. A standard black and white video camera was used to sense the objects while a digitizer board captured the image. The digitizer board was capable of four levels of grey with a resolution of 320 by 200 pixels. The software supporting the digitizer was in Basic language, therefore, Basic was also used in this implementation.

Design of the Neural Network

It has been known for a long time that an infinite set of moments can theoretically completely describe the shape of a two dimensional object (9,20). Realistically, only a limited number of moments can be used to describe the shape of an object. For this demonstration, the second through seventh moments including the cross moments were determined as features for each object. The total number of moments used in the feature vector was 23.

The number of processing elements (PE's) in the input layer of the neural network was 23. The hidden layer had the same number of PE's. Since only two objects were being recognized in the demonstration, the output layer consisted only of two PE's. The output of the input layer was linearly scaled to make full use of the output's linear range. The hidden layer used a sigmoidal output transfer function which

limited the output to the range of zero to one. The output layer allowed each PE to work in competition so that only one of the PE's gave an output of one. The other PE had an output of zero.

Each of the moments were made position invariant, and the entire input vector was normalized to a unit vector. Each layer used the backpropagation method to update the weights of the . Each layer was fully interconnected with the layer adjacent to it.

The training set consisted of computer generated circles, squares, and equilateral triangles. Each shape had ten different sizes to fully make use of the display size. The test objects were made from black poster board in five different sizes. The camera was approximately two feet from the objects when the tests were taking place.

Results from the Demonstration

The results from the demonstration were very preliminary; however, the feasibility of using neural networks in object recognition still appears viable. The results of classifying circles and squares were less than acceptable, with a classification probability of 60%. This was mainly due to the similarity of the moments of both circles and squares. However, for the recognition of equilateral triangles and squares, a much higher probability

of 80% was attained. Better results would certainly be possible with more development and training time.

VII. RECOMMENDATIONS

The results of the demonstration show that neural network technology provides an alternate approach to other methods used in the area of object recognition. With further experience and research, it is quite possible to have an object recognition system which could be of practical use with this technology. General recommendations include a current and complete survey of the literature along with intense training of the neural network methods. A comparison of the neural network method with traditional methods in object recognition would also be useful in the evaluation of methods. Neural network products with hardware boards would greatly decrease training time and free the computer to do other tasks, such as data acquisition. A digitizer board with higher resolution and more levels of gray along with an image processing package could produce images with less noise before classification.

These recommendations will be proposed for additional funding through the Research Initiation Program.

REFERENCES

1. Barrons, Janet J. and Obermeier, Klaus K., "Time to Get Fired Up", **Byte**, August 1989, pp.217

2. Chen, S.,"Neural Networks and Computational Vision," **IEEE Int. Con. on Neural Networks**, vol 4, 1987, pp IV-659 IV-666.

3. Dawes, R.L.,"Biomasscomp: A Procedure for Mapping the Architecture of a Living Neural Network into a Machine," **IEEE Int. Con. on Neural Networks**, vol 3, 1987, III-215 III-225.

4. Dodd, N.," Multi-layer Perceptron Inversion Applied to Image Neighborhood Operations," **IEEE Int. Con. on Neural Networks**, vol 4, 1987, pp IV-293 IV-299.

5. Gevins, A.S.,"How the Human Brain Thinks and Acts: Results of Latest research Using Neural Networks to Analyze Brain Signals," **IEEE Int. Con. on Neural Networks**, vol 4, 1987, pp IV-41 IV-47.

6. Hebb, D.O.,"**Organization of Behavior**," New York: Science Editions,1961.

7. Hopfield, J.J.,"Neural Networks and Physical Systems with Emergent Collective Computational Abilities," **Proc. of the National Academy of Sciences USA**, 1979, pp 2554-2558.

8. Hoskins, Josiah and Jones, William P., "Back-Propagation: A Generalized Delta Learning Rule", **Byte**, October 1987, pp. 155-162.

9. Hu, Ming-Kuei, "Visual Pattern Recognition by Moment Invariants", **IRE Transaction on Information Theory**, 1962, pp.179-187.

10. Kolodzy, P.J., "Multidimensional Machine Vision Using Neural Networks," **IEEE International Conference on Neural Networks**, Massachusetts Institute of Technology, Lincoln Laboratory, Lexington, Massachusetts, 1987, Vol 2, pp.II-747 II-758

11. McClelland, James L. and Rumelhart, David E. and et. al., **Parallel Distributed Processing: Explorations in the Microstructure of Cognition**. Vol.1 and 2, 1986.

12. Miller, Richard K., **Survey On Artificial Neural Systems**, Survey Report #11, Future Technology Surveys Inc.

13. Minsky, Marvin L. and Papert, Seymour A., **Perceptions**, 1988.

14. Mueller, P. et al.,"Neural Computation of Visual Images," **IEEE Int. Con. on Neural Networks**, vol 4, 1987, pp IV-75 IV-88.

15. "Neural Networks: Theory and Practice", **Byte**, August 1989.

16. Nilsson, Nils J., **Learning Machines**, McGraw-Hill Book Company.

17. Pitts, W., and W.W. McCulloch, "How We Know Universals," **Bulletin of Mathematical Biophysics**, 9:127-47,1947.

18. Reber, W.L., and J. Lyman, "An Artificial Neural System Design for Rotation and Scale Invariant Pattern Recognition," **IEEE Int. Con. on Neural Networks**, vol 4, 1987, pp IV-277 IV-283.

19. Schwartz, T.J.,"12-Product Wrap-up: Neural Networks," **AI EXPERT**, August 1988, pp 73-85.

20. Wahl, Friedrich M., **Digital Image Signal Processing**, Artech House Inc., 1987.,

21.Wasserman, Philip P., **Neural Computing: Theory and Practice**, Van Nostrand Reinhold, 1989.

22. Young, Yao, "A Neural Network Model of CAAM and its Application to Handprinted Chinese Character Recognition," **IEEE Int. Con. on Neural Networks**, Vol 3, 1987, pp III-309 III-316.

APPENDICES MAY BE OBTAINED

FROM THE AUTHOR OR

UES

1989 USAF-UES SUMMER FACULTY RESEARCH PROGRAM

Sponsored by the

AIR FORCE OFFICE OF SCIENTIFIC RESEARCH

Conducted by the

Universal Energy Systems, Inc.

FINAL REPORT

A Study of Surface Roughness Effects in Hypersonic Flow

PREPARED BY: ARNOLD POLAK

ACADEMIC RANK: Professor

DEPARTMENT and UNIVERSITY: Aerospace Engineering and
Engineering Mechanics
University of Cincinnati

RESEARCH LOCATION: Wright Research and Development Center
Flight Dynamics Laboratory
High Speed Aerodynamics (WRDC/FIMG)

USAF RESEARCHER: NORMAN E. SCAGGS

DATE: August 4, 1989

CONTRACT No: F49620-88-C-0053

A Study of Surface Roughness Effects in Hypersonic Flow

by

Arnold Polak

ABSTRACT

This report presents results from a theoretical study of surface roughness aerodynamic effects on hypersonic flow with strong viscous - inviscid interaction. Special interest is focused on the flow separation effects. The study centers around the numerical solution of the reduced Navier-Stokes equations. The algebraic eddy viscosity model is adopted for the turbulence closure and the roughness is represented by discrete arrays of uniformly distributed drag forces and heat source/sinks. The particular flow configuration studied is the hypersonic strong viscous - inviscid interaction induced by a compression ramp. The theoretical predictions are compared to the Flight Dynamics Laboratory Experimental data.

ACKNOWLEDGEMENT

I wish to acknowledge the opportunity and support by the Air Force Systems Command, the Air Force Office of Scientific Research, and the Universal Energy Systems, Inc.

My experience during the ten week tenure at the High Speed Aero Performance Branch of FDL was most rewarding, to a great measure because of the friendly atmosphere and the cooperation I have received from everyone. On the technical side I am indebted and extend special thanks to Mr Norman E. Scaggs for his keen interest and for the helpful discussions during the entire course of this study. Additional thanks are due to Dr Edmund G. Brown-Edwards for the spice of his wit that brightened many a moment, yet more importantly, for the generosity of his time which aided the efficient initiation of my project.

1. OBJECTIVES

The prediction of surface roughness effects on the aerodynamic characteristics of hypersonic vehicles is one of the challenging problem areas [1] which is yet to be performed with a reasonable accuracy. This effect becomes dominant when surface roughness appears in the vicinity of strong interaction regions. For example, because surface roughness will considerably increase the extent of flow separation regions, the effectiveness of control surfaces becomes a critical issue in the hypersonic design. An extensive literature survey disclosed that there is little information available, either theoretical or experimental, about separated flows influenced by surface roughness. A recently completed experimental project at the Flight Dynamics Laboratory is one such study wherein the surface roughness effects on hypersonic flow separation over a basic configuration at Mach 6 is investigated. The objective of the present effort is to complement the aforementioned experimental work by developing a numerical method for predicting separation characteristics over rough surfaces at hypersonic speeds.

The calculated surface pressure distributions, skin friction distributions, boundary layer profiles and the separation geometry are to be compared with the FDL experimental data.

2. ANALYTICAL APPROACH

2.1 INTRODUCTION

In a theoretical study the problem of hypersonic separated turbulent boundary layer must be formulated as a strong interaction flow with strong embedded shock waves. The approach taken in this study is that a reduced form of Navier-Stokes equations, when modified to include the effect of surface roughness, is an appropriate set of governing equations for the study of such a problem. This set of equations developed [2,3] for solving strong viscous - inviscid interaction flows is essentially a composite of interacting boundary - layer equations[4] (IBL) and the Euler equations. An important feature of the solution of reduced Navier-Stokes (RNS) equations is the repeated streamwise marching coupled with the global iteration on the pressure field. The global iteration reflects the requirements of a downstream boundary condition and thus the proper accounting for the upstream propagation of information in the subsonic flow regions. In the numerical differencing scheme this is accomplished by the use of Vigneron [5] type splitting of the axial pressure gradient term into a hyperbolic (for local $M > 1$, and elliptic (for local $M < 1$) components. This RNS set of equations has been previously applied to interacting separated flows with embedded shock waves at moderate supersonic Mach number [6]. For the present work the application is extended to hypersonic speeds.

The modification of this aforementioned RNS equations consists of implementing an appropriate roughness model into the analysis and enhancing the shock capturing capability of the code. A direct approach of considering the geometric details of each roughness element as an integral part of the body contour is not feasible. Instead the roughness elements, assumed

to be small relative to the boundary layer thickness, are represented by a discrete array of force and heat sink/sources. The distribution and magnitude of these forces and sink/sources is based on spacing, shape and size of the actual roughness element. This discrete element concept has been developed and utilized by other authors [7,8]. However, the magnitude of roughness drag and strength of the heat source in their work is based on low speed empirical data. We employed a simple algebraic eddy viscosity turbulence model. All shock waves, including the leading edge shock, are captured. To enhance the shock capturing capability of the code an explicit numerical damping term is introduced into the transverse momentum equation.

2.2 GOVERNING EQUATIONS

The governing equations are taken to be the RNS equations with the inclusion of an algebric eddy viscosity turbulence model and a roughness discrete element model. Uniformly distributed cylindrical roughness elements with square shaped cross-section are assumed. For two-dimensional compressible laminar and/or turbulent flow these equations, written in Cartesian coordinates and dimensionless conservation form are:

CONTINUITY

$$\frac{\partial}{\partial x}(B_x \rho u) + \frac{\partial}{\partial y}(B_y \rho v) = 0 \qquad (2.1)$$

X-MOMENTUM

$$\frac{\partial}{\partial x}(B_x \rho u^2) + \frac{\partial}{\partial y}(B_y \rho u v) + \frac{\partial}{\partial x}(B_x p)$$

$$- \frac{1}{Re} \frac{\partial}{\partial y}\left[B_y (\mu + \mu_t) \frac{\partial u}{\partial y}\right] = - \frac{1}{2} \rho u^2 C_D D(y) / (\ell_x \ell_z) \qquad (2.2)$$

Y-MOMENTUM

$$\frac{\partial}{\partial x}(B_x \rho u v) + \frac{\partial}{\partial y}(B_y \rho v^2) + \frac{\partial}{\partial y}(B_y p) = 0 \qquad (2.3)$$

ENERGY

$$\frac{\partial}{\partial x}(B_x \rho u H) + \frac{\partial}{\partial y}(B_y \rho v H) - \frac{1}{R_e P_r}\frac{\partial}{\partial y}\left[B_y \mu \frac{\partial H}{\partial y}\left(1 + \frac{\mu_t}{\mu}\frac{P_r}{P_{r_t}}\right)\right]$$
$$-\frac{(\gamma-1)M_\infty^2}{R_e}\left\{B_y u \frac{\partial}{\partial y}\left[\mu\left\{\left(1-\frac{1}{P_r}\right)+\frac{\mu_t}{\mu}\left(1-\frac{1}{P_{r_t}}\right)\right\}\frac{\partial u}{\partial y}\right]\right.$$
$$\left. + B_y \mu\left[\left(1-\frac{1}{P_r}\right)+\frac{\mu_t}{\mu}\left(1-\frac{1}{P_{r_t}}\right)\right]\left(\frac{\partial u}{\partial y}\right)^2\right\} = \frac{4\mu N_u}{R_e P_r}(T_w - T)/(l_x l_z). \qquad (2.4)$$

In addition the following auxiliary relations for air as a perfect gas are employed: $p = \rho T/(\gamma M_\infty^2)$, $H = T + \frac{\gamma-1}{2} M_\infty^2 (u^2+v^2)$, $\mu = T^\omega$ or Sutherland viscosity law. Here u and v are the x and y velocity components; ρ and p are density and pressure; T and H are temperature and total enthalpy; μ and μ_t are the coefficient of viscosity and eddy viscosity; R_e is the Reynolds number based on a characteristic length (=distance from the leading edge to the plate/ramp juncture); Pr and Pr_t are the laminar and turbulent Prandtl number; γ and M_∞ are the specific heat ratio and free stream Mach number. All the variables were nondimensionalized by their free stream values, except for pressure and total enthalpy which were nondimensionalized by $\rho_\infty u_\infty^2$ and $c_p T_\infty$, respectively.

In these equations the effect of roughness is included through the blockage parameters B_x and B_y and the source terms on the right hand side of the x-momentum and energy equations. In the present case for the uniformly distributed square shaped roughness $B_x = B_y = 1 - D^2/(l_x l_z)$, where D = width of the roughness element and l_x, l_z = spacing in x and z direction, respectively. For flow past smooth bodies, the right hand side in these equations is zero and $B_x = B_y = 1$. The same is true for the rough surface when $y > k_r$, where k_r is the roughness height. C_D and N_u are empirical values of the local drag coefficient and Nusselt number of the roughness element.

BOUNDARY CONDITIONS

At the body surface, $u = v = 0$ and $T = T_w$, or $\partial T/\partial y = 0$. The far field boundary conditions, $u \to 1, \rho \to 1$ and $H \to H_\infty$ at $y \to \infty$ are also used. It is noteworthy that even with adiabatic wall conditions and the simplying assumption $Pr = Pr_t = 1$, the solution to the energy equation is not trivial (and therefore neither is the obtaining of the value of the adiabatic wall temperature). Thus the energy equation must be solved simultaneously with the continuity and momentum equations. For our calculations, $Pr = 0.72$ and $Pr_t = 0.90$.

2.3 TURBULENCE AND ROUGHNESS MODEL

The turbulence closure in the governing equations is accomplished by the use of a simple algebraic turbulence model. Both the two layer Cebeci-Smith and the Baldwin-Lomax turbulence model were incorporated into the computer code. It is assumed that the effect of roughness on turbulence is sufficiently represented through the effect of the blockage parameters and source terms on the mean flow quantities.

To simulate the surface roughness effect on the boundary layer flow we adopt the discrete element method developed by Taylor et al [8]. Because this model utilizes low speed empirical data its application to the present problem must be approached with caution. It is desirable to recalibrate this model for high Mach number flows. Unfortunately our literature survey did not disclose the existence of the high speed experimental data needed for carrying out this task. To fill in this gap we opt to use a naive

approach. From Hoerner's [9] collection of data for a single cylinder we find the ratio of the drag coefficient at supersonic Mach number to its value at low speeds to be over 1.5. Therefore a value of $C_D = 0.9$ instead of 0.6 value, quoted in Reference 8 seems more appropriate.

2.4 SKIN FRICTION COEFFICIENT

The skin friction coefficient is calculated as the sum of that portion of the viscous drag due to the smooth part of the wall plus the contribution due to the drag force on the roughness elements.

$$C_f = \left[B_y \left(\bar{\mu} \frac{\partial \bar{u}}{\partial \bar{y}} \right)_w + \frac{1}{2} \frac{1}{\bar{x}_r \bar{z}_r} \int_0^{\bar{k}_r} \bar{\rho} \bar{u} |\bar{u}| C_D \bar{D} \, d\bar{y} \right] \Big/ \frac{1}{2} \bar{\rho}_\infty \bar{u}_\infty^2 \qquad (2.5)$$

The over bars denote dimensional quantities.

2.5 NUMERICAL METHOD

A finite difference scheme is used to obtain numerical solutions to the governing equations (2.1) - (2.4). The computational plane (ξ, η) is formed by using a simple shearing transformation, with $\xi = x$ and $\eta = y - y_b(x)$. The governing equations are discretized using a variable mesh size in the transverse direction with grid points clustered near the surface. Similarly, a more dense streamwise grid distribution is used in the neighborhood of the strong interaction region. Our calculations were performed with 140 X 75 grid points in the streamwise and transverse direction, respectively. Since the RNS equations are solved in a marching manner, a boundary layer differencing is employed. In the streamwise momentum and energy equations the η - derivatives are approximated by central difference expressions, with one exception; an upwind differencing of the transverse convective term is used to enhance the stability of the numerical scheme.

All the ξ - derivatives are approximated by a first order backward difference, except for the elliptic portion of the $\partial p/\partial \xi$ term which is discretized by a forward difference. The Vigneron type finite difference form is employed for this pressure gradient. It is written as:

$$\frac{\partial p}{\partial \xi} = \epsilon_i \frac{p_j - p_{j-1}}{\Delta \xi_i} + (1-\epsilon_i)\frac{p_{j+1} - p_j}{\Delta \xi_{j+1}} \quad ; \quad \epsilon = \min\left(1, \frac{\gamma M_\infty^2}{1+(\gamma-1)M_\infty^2}\right). \qquad (2.6)$$

Within the separated regions, the ξ - convective terms are upwinded. The continuity and the transverse momentum equations are centered at $j \pm 1/2$ respectively, and the two point trapezoidal rule is used. To enhance the shock capturing capability of the code we add an explicit damping term to the transverse momentum equation.

This term is $C\,|p_{j+1} - 2p_j + p_{j-1}|\,/\,(p_{j+1} + 2p_j + p_{j-1})$.

The value of the constant C in our calculations is $0.04 < C < 0.07$. Since $p_{j+1} - 2p_j + p_{j-1} \sim \frac{\partial^2 p}{\partial \eta^2}\Delta\eta^2$ the damping term does not affect formally the accuracy of the numerical scheme. The resulting algebraic equations, corresponding to continuity and momentum equations are solved simultaneously for u, v and ρ , whereas the energy equation is solved for H in an uncoupled form.

3. RESULTS AND DISCUSSION

The purpose of the present study was the development of a computer code for predicting aerodynamic characteristics, including boundary layer separation, in hypersonic flow over rough surfaces. The surface and free stream conditions were chosen to correspond to a set of parameters in a wind tunnel experimental research program at FDL.

The nominal values of these conditions are Mach 6, Reynolds number per foot equal to 10^7, total temperature 930°R; uniformly distributed rectangular surface roughness and cooled wall conditions. Two-dimensional flow of air past a flat plate followed by a wedge shaped ramp, with surface roughness starting at 1.2 inch. from the leading edge was tested.

Figures 1 and 2 present numerical results of such a flow past a plate/ramp configuration at $M_\infty = 6$, $R_e/ft = 1.16 \times 10^7$, $T_{t\infty} = 930°R$, $Tw/T_{t\infty} = 0.8$, with and without surface roughness. The surface roughness elements are 0.010 inch wide, 0.005 inch high, with 0.020 inch spacing. The ramp angle is 16 degrees. The surface pressure distribution over the smooth and rough surface is compared in Figure 1. The surface pressure signatures differ only slightly due to flow separation occurring over the rough surface. However, in Figure 2. we observe substantial increase in the total tangential surface stress caused by roughness. The considerable increase in this stress is due to the large increase in density and also increase in velocity near the ramp surface, as compared to the corresponding locations over the flat plate. Simultaneously, because of the decrease of the viscous stress component over the rough surface, a small separation bubble is formed. Comparison of these flow separation characteristics with experiments is not made because the FDL data are only available for ramp angles of 22 degrees and higher. Converged numerical solutions were produced up to only 20 degrees.

However, in Figures 3 and 4 we compare some of the calculated and measured profiles over the flat plate portion of the model, at locations ahead of the interaction region. The purpose of this comparison is to test the feasibility of the present roughness model, which was originally calibrated for low speed data[8].

Here the roughness width is 0.040 inch, and height is 0.020 inch. The predicted velocity profile, when compared to the smooth wall case (Figure 3) shows the correct trend. However, the momentum defect caused by roughness is not as strong as shown in the experiments. This points to the need for further improvements in the roughness model. A re-calibration of the roughness model with respect to the combined Reynolds number and Mach number effects should improve this comparison. The predicted total temperature profile (Figure 4) over the rough surface shows a very minute overshoot at about one third from the boundary layer edge. It is not as pronounced as in the experiments.

4. CONCLUSIONS AND RECOMMENDATIONS

The capability of the spatially marching reduced Navier-Stokes code with global pressure interation was extended to strongly interacting hypersonic flow over rough surfaces. Due to the presence of strong imbedded shock waves and additional disturbance caused by sinks/sources distributed near the surface, we were able to obtain converged solutions up to only 20 degrees ramp angles at Mach 6. The following suggestions are offered for further improvements of this code:

(1) Apply the Roe's method to the RNS code and/or include additional terms previously omitted in the transverse momentum equation. This should eliminate the need for artificial dissipation, requiring cumbersome numerical experimentation with the damping coefficient.

(2) Recalibrate the roughness model by including the combined effect of local Mach number and Reynolds number.

5. REFERENCES

1. Holden, M.S., "A Review of Aerothermal Problems Associated with Hypersonic Flight, " AIAA Paper 86-0267, January 1986.

2. Rubin, S.G., and Reddy, D.R., "Analysis of Global Pressure Relaxation for Flows with Strong Interaction and Separation," Computers and Fluids, Vol 11, 1983, pp. 281-306.

3. Khosla, P.K., and Lai, H.T., "Global PNS Solutions for Subsonic Strong Interaction Flow over a Cone-Cylinder-Boattail Configuration, "Computers and Fluids, Vol 11, 1983, pp. 325-339.

4. Davis, R.T, and Werle, M.J., "Numerical Methods for Interacting Boundary Layers," presented at the Heat Transfer and Fluid Mechanics Institute, University of California at Davis, 1976.

5. Vigneron, Y.C., Rakich, J.V., and Tannehill, T.C., "Calculation of Supersonic Viscous Flow over Delta Wings with Sharp Subsonic Leading Edges," AIAA Paper 78-1137, July 1978.

6. Khosla, P.K., Polak, A., and Liang, T., "A Global Pressure Relaxation for High Speed Laminar and Turbulent Separated Flow with and without Roughness," presented at the Data Exchange Meeting, David Taylor Research Center, Bethesda MD, 1988.

7. Finson, M.L., and Clark, A.S., "The Effect of Surface Roughness Character on Turbulent Reentry Heating," AIAA Paper 80-1559 July 1980.

8. Taylor, R.P., Coleman, H.W., and Hodge, B.K., "A Discrete Element Predictive Approach for Turbulent Flow over Rough Surfaces," Report TFD-84-1, Mississippi State University, 1984.

9. Hoerner, S.F., Fluid Dynamic Drag, published by the Author, 1965.

10. Disimile, P.J., and Scaggs, N.E., "An Investigation Into Wedge - Induced Turbulent Boundary Layer Separation on a Uniformly Roughened Surface at Mach 6.0," Paper presented at AIAA 7th Applied Aerodynamics Conference, Seattle, WA, 31 July - 2 August 89.

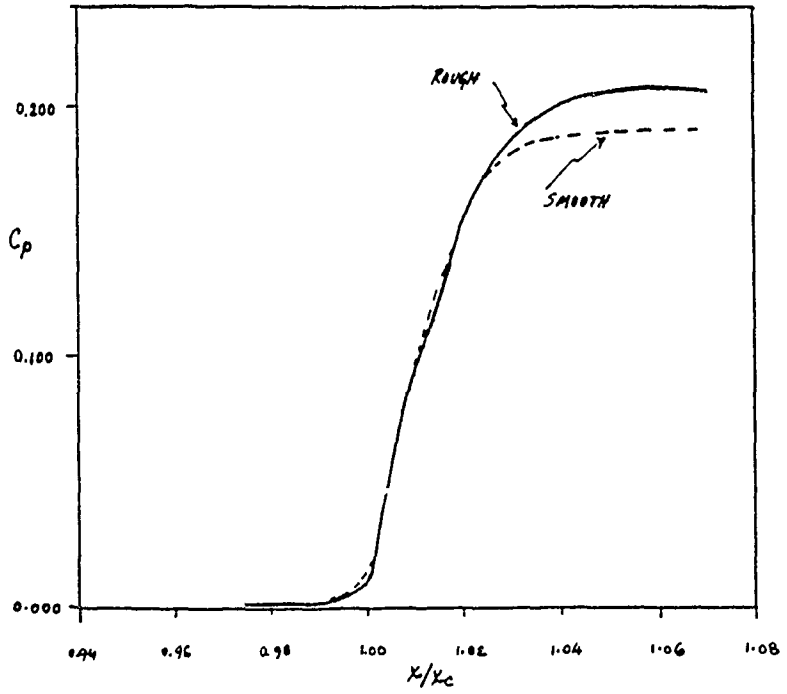


Figure 1. Wall Pressure Distribution

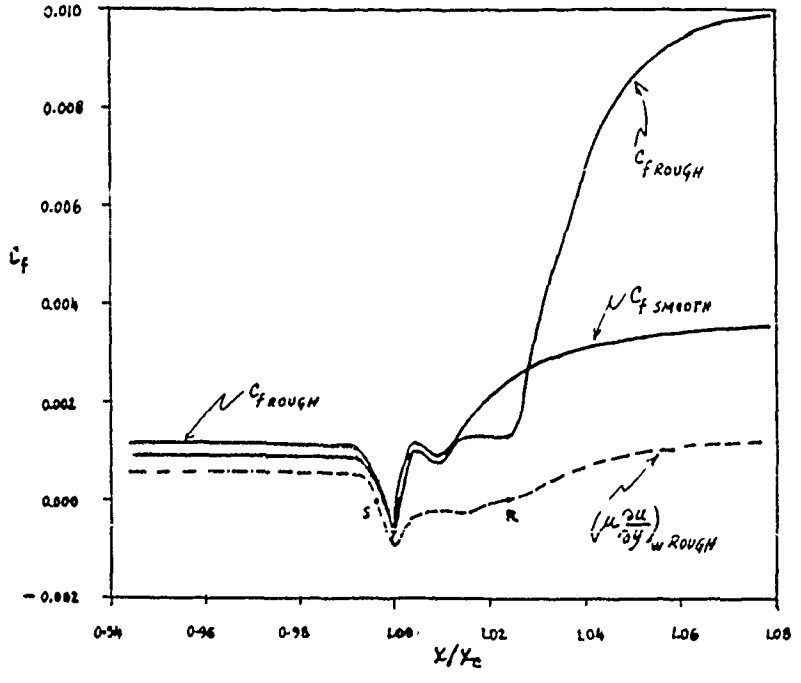


Figure 2. Wall Shear Stress Distribution

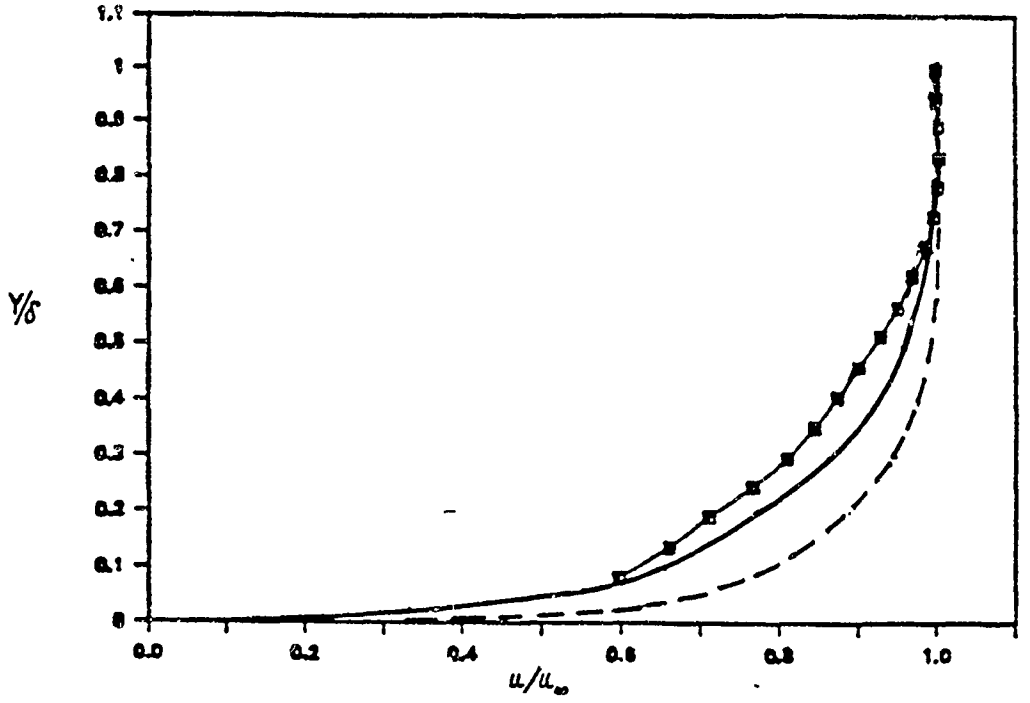


Figure 3. Velocity Profiles at $x = 13.83$ inch.

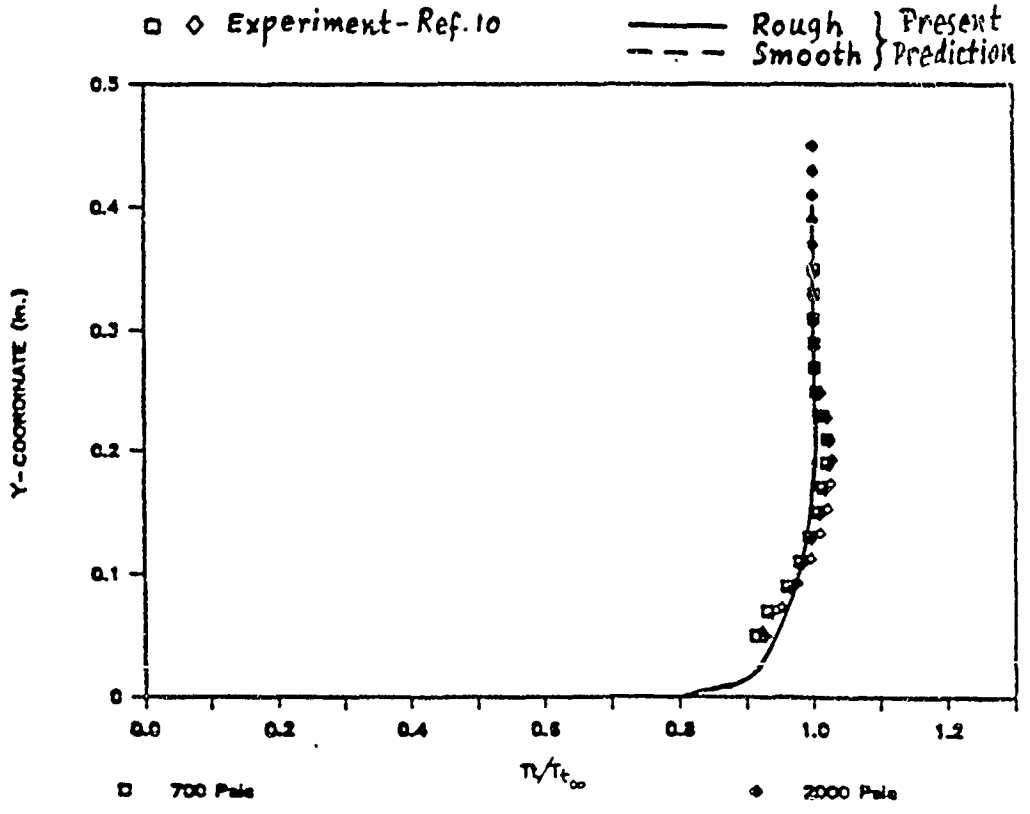


Figure 4. Total Temperature Profiles at $x = 9.52$ inch.

1989 USAF-UES SUMMER FACULTY RESEARCH PROGRAM

GRADUATE STUDENT RESEARCH PROGRAM

Sponsored by the

AIR FORCE OFFICE OF SCIENTIFIC RESEARCH

Conducted by the

Universal Energy Systems, Inc.

FINAL REPORT

LIFE PREDICTION OF AIRCRAFT TRANSPARENCIES BY ACCELERATED CRAZING TESTS

Prepared by:	Nisar Shaikh
Academic Rank:	Assistant Professor
University:	Department of Engineering Mechanics, University of Nebraska-Lincoln Research
Location:	Aircrew Enclosures Group, Vehicle Subsystems, Flight Dynamics Laboratory, WPAFB USAF
Researcher:	Robert McCarty
Date:	July 22, 1989
Contract Number:	F49620-88-C-0053

LIFE PREDICTION OF AIRCRAFT TRANSPARENCIES BY ACCELERATED CRAZING TESTS

by

NISAR SHAIKH

ABSTRACT

Reducing the cost-of-ownership of aircraft transparencies made of various plastics is a principle concern of the Vehicle Subsystems Division and efforts are being made to increase the service life of these components. A durability validation plan is being developed which will enable prediction of the service life of a transparency design based on tests of the material at the fabrication stage.

Failure modes that necessitate the rejection of the transparencies include scratches, cracks, crazing, coating deterioration and delaminations. The validation scheme will be based on a chosen failure mode, namely acrylic crazing in F-16 canopies. Once a successful scheme has been devised, additional schemes will be devised for other failure modes of various aircraft transparency systems.

The plan is divided into three segments: 1. Accelerated laboratory crazing tests; 2. Generation and analysis of field data; 3. Correlation of laboratory and field data and derivation of a validation procedure.

ACKNOWLEDGEMENTS

I wish to thank the Air Force Systems Command and the Air Force Office of Scientific Research for sponsorship of this research.

I owe acknowledgements to many individuals at the Flight Dynamics Laboratory, Wright Patterson AFB. Special thanks go to Robert McCarty and Mike Gran of the Aircrew Enclosures Group, Vehicle Subsystems Division for their efforts in making my research with them a productive and rewarding experience. Thanks are also due to Dr. A. H. Mayer and W. C. Buzzard for their interest in this project. I also want to express my appreciation for my graduate assistant, Kerry Christopher of the University of West Florida, for his contributions to my work.

LIFE PREDICTION OF TRANSPARENCIES by ACCELERATED CRAZING TESTS

INTRODUCTION

Great cost savings can be realized if the frequency of replacement of aircraft transparency systems can be reduced. At present, the acceptance of the parts from a vendor is based largely on their meeting the optical and other performance standards with little effective regard to the expected service life. A durability validation scheme is being developed by the Vehicle Subsystems Division that aims to predict the service life of transparencies from various manufacturers, representing different designs, materials and fabrication techniques. When incorporated, such schemes will allow the comparison of alternative transparency designs from different manufacturers based on their service life and thus help determine cost effectiveness. The technique will specify certain tests on coupons from trimmings or a randomly selected transparency from a batch of the production lot and predict durability based on this test data.

Failure modes that necessitate the removal of transparencies from service include scratches, cracks, coating deterioration, delamination and crazing. The details on various failure modes for the F-16 and F-111 are

tabulated and discussed elsewhere. Guided by this data, the accelerated life prediction plan concentrates on acrylic crazing, the most important failure mode for acrylic polycarbonate laminated transparency designs, as representative for development of the technique.

After the successful execution of the plan, a validation scheme will result which can be outlined in brief as follows: 1. Take the accelerated crazing data from the coupons from trimmings of several transparencies of a production batch; 2. Measure the residual stress nondestructively by ultrasound on the new transparency; 3. Consult a table or execute a software program using this data to determine the service life for acrylic crazing of the transparency for the Air Force base of choice. As time goes by, more field data will be generated and with the availability of convenient means of stress measurement more accurate and elaborate prediction schemes will be possible.

The plan is sound and the merits of the individual mechanisms need to be mentioned. It is recognized that crazing is one of the major costs of transparency replacement and therefore its study is important. It is also well established that stress is essential for the incipience of craze. Thus, the efforts in development of stress measurement methods for transparent material are necessary.

The transparency with higher residual stress will craze earlier. However, with the completion of the validity plan, more elaborate and specific predictions will be possible.

The first part of the summer tenure was spent in review of the earlier activities by various participants at the Air Crew Enclosure Group (FIVRB). Subsequently the plan was compiled with interaction of the engineer at FIVRB. The latter part of the summer was spent outlining the tasks for the execution of the plan. In an ambitious attempt, some tasks were begun in collaboration with the University of Dayton Research Institute but were not concluded due to the limited duration of the fellowship.

THE PLAN

The execution of the plan constitutes three task groups:

I. Laboratory tests for accelerated chemical crazing of coupons.

II. Statistical and engineering analysis of the field data obtained for transparencies removed from service.

III. Correlation of the above field data and laboratory test data.

I. LABORATORY TESTS FOR ACCELERATED CRAZING

The accelerated crazing test consists of loading a

specimen exposed to a solvent of known concentration and noting the time of appearance of the craze. The value of strain can be obtained from the strain gages mounted on the specimen. The stress at the location of craze incipience may be calculated from elasticity. A family of curves can be plotted for stress vs. crazing time for different test temperatures as well as the various solvents.

A. Background

Stress is essential to the induction of craze in plastics. Experiments on stressed specimens taken in dry air and those taken in contact with moisture have shown that the growth rate of craze is significantly accelerated by the presence of solvents - even distilled water [1]. The presence of an organic liquid is found to have a dramatic effect on the induction of craze in PMMA. The crazing strain is lowered by small molecules of liquid diffusing into the polymer and, hence, increasing the mobility of the micromolecular chains. In the field, exposure to various solvents has the undesirable effect of reducing the service life of the canopy. In laboratory tests the liquid is used advantageously to reduce the experiment time. Cantilever bending specimen tests are a simple and convenient means of characterizing a material's tendency to craze. However, for correlation with field data where the stresses present will be biaxial, it would be appropriate for the laboratory tests to also be biaxial. Ideally, the coupon should be cut from a

new transparency in the region where the crazing occurrence is of most concern or most predominant. The crazing at the surface depends solely on the local state of stress and the quality of the material. The polycarbonate substrate can be removed from the coupon for convenience of loading.

B. Biaxial Test

A rectangular plate can be fixed at one edge and free at the other three. Concentrated forces can be applied to the side opposite of the fixed edge to simulate a varying biaxial state of stress. Downward forces can be applied at the two free corners while an upward force can be induced by a support in the middle. By raising or lowering the position of the middle support, one of the principle stresses can be changed from tension to compression.

C. Tasks for the Laboratory Tests

A set of ten coupons should be cut from specified areas of a new optically rejected canopy from each of two vendors. Five of the coupons from each vendor should be tested by applying a 50% concentration of Isopropanol in water. The first set of tests should be run at room temperature. A second set at 90 degrees F should be considered. Blowing steady hot air and continuous monitoring of the specimen temperature may be adequate. A detailed plan for the accelerated tests is contained in Appendix I. The results of some preliminary accelerated tests are contained in

Appendix II.

D. Data Reduction

The maximum tensile stress vs. crazing time will be plotted in parametric form, with vendor and temperature as parameters. Various studies [3-6] have shown that the mathematical relationships describing crazing involve a logarithmic function of time. The data will be transformed to logarithmic coordinates or some other desired curvilinear system and plotted by using standard plotting software.

II. FIELD MEASUREMENTS AND ANALYSIS

The Aircrew Enclosures Group has collected data over the years on transparencies removed from service that exhibited various failure modes. A subset of data should be separated for the validation study and be used in the analysis.

A. Selection of the Variables

The selection of the field variables should be guided by the factors responsible for the craze formation. The initiation and growth of crazing is effected by a combination of factors such as temperature, stress, abrasion and exposure to chemicals. The surface stress is the essential element in forming the craze; it can always be expected to exist as residual stress resulting from

fabrication and as applied stress due to structural and thermal loading. The higher the temperature, the closer PMMA is to the glass transition temperature and, thus, the greater the chance for craze to form. A transparency is exposed to different solvents through cleaning fluids and rain which accelerates the growth of craze. The energy required to cause crazing of PMMA in alcohols is found to fall rapidly as the temperature is increased. The scratches and abrasions due to dust particles provide stress concentration areas for craze initiation.

The first objective should be to condense the variables where possible. For example, 'Rainfall' may be a subset of 'Base' (location) variable. The average daily temperature is also a characteristic of the base, however the variable 'Temperature' would have to be redefined to represent the real thermal condition which a transparency experiences. This should include effects due to solar and aerodynamic heating. It is also suggested that for the initial analysis, the crazing variable should be reduced to take only the values 1 and 0, where 1 denotes a level of craze that would result in the removal of a canopy from service and 0 represents no significant craze.

The proposed test variable categories and subcategories are:

1. Vendor: The vendor designation relates to the quality of

materials used and residual stresses that may be trapped due to their proprietary forming processes and the quality of fit into the frame.

2. Base: The base location relates to the type of environmental effects, such as proximity to a quarry, industrial regions or sea water and rainfall and local temperature. The mission typical to a base may be the cause of different levels of structural and thermal loadings.

3. Service Life: This would include the date of manufacture, date of installation, date of removal from service, and flight hours.

4. Degree of Crazing: The degree of crazing is denoted by an ordinal variable with the value 1 indicating the incipience of craze while 5 denotes the highest amount of craze. For present analysis this is compressed to only two values, 0 for a craze free transparency and 1 for the existence of the craze.

5. Surface Stress: Except in cases of severe loading, crazing is not an instantaneous phenomenon, but takes place over a long period of time showing the cumulative effect of the environment and temperature in the stressed region. The effect of environmental agents and heating is most concentrated on the surface and that is where crazing mostly occurs. Therefore the surface stresses are the most relevant of the stresses.

The stresses in a canopy are produced by several factors: i. Cabin pressure; ii. Dynamic loads through shocks and vibration of the airframe; iii. Tolerance of frame mountings; iv. Thermal stresses due to aerodynamic and solar heating; v. Residual stresses induced during the forming processes.

Unlike other stresses, the residual stresses exist throughout the life of the canopy, even while on the shelf prior to installation on the aircraft. The net stresses are

the combination of residual stresses and applied stresses. There is a need for the estimation and measurement of the relative magnitude and nature of the various stresses.

First and foremost is the absence of a nondestructive method to measure the stresses, which can be circumvented by use of the hole-drilling method in the case of residual stresses. Some consideration is needed to account for the stress relieved due to the formation of the craze. The strain energy released in the formation of craze in turn reduces the value of the stresses. More difficult is the question of relating the strain data to the stresses because of the different material properties of a locally crazed region. Some testing is needed to answer these questions. If an unaffected region can be found which is surrounded by a crazed zone then one can make comparative measurements and determine the stress relief or changes between the two regions. It would be appropriate to assume that the stress field does not change significantly within inches. Subsequent measurements can be confined to craze free areas.

One approach to making measurements in the crazed region would be to allow for the stress relaxation that occurs in the craze formation. In laboratory tests on cantilever specimens it was found that below a certain level of stress, crazing does not occur for an indefinite period of time or, conversely, a certain minimum stress is necessary for a

craze to form [2]. We can term this quantity a 'threshold stress'. The threshold stress can be measured and catalogued as properties of a batch of material, much like the elastic modulus is treated. Subsequently a threshold stress can be added to the measured value of the residual stress to estimate the value of the initial stress that existed in the material after installation. Only after proper measurements of residual and other applied stress can we ascertain the importance and significance of various stresses. One distinction for the residual stress is that it exists continuously, even when the aircraft is not in operation and, thus, has greater effect in craze initiation.

B. Field Data Collection and Organization

A great effort took place in collecting data over the years on removed transparencies. The data base has information on various aspects of transparency degradation and damage along with the flight hours and information on their Air Force base. Just prior to conducting these tests, transparencies in a suitable condition for stress measurements will be identified to provide coupons. The transparency data base will be updated to include this data.

The recommendation is to choose F-16 canopies of the type currently produced. Five canopies from each vendor and base will result in a total of twenty canopies to be studied. The two vendors chosen should be currently

qualified and the required number of their past canopies should exist in the warehouse. The Air Force bases should be chosen such that they have varied geographical locations, exhibiting different climates and environments. One of the difficult tasks of this plan is to find two bases that each have ten transparencies on which stress measurements can be made and the documentation exists for the relevant data. The remaining work will then involve determining the residual stresses.

C. Analysis and Modeling of Field Data

The field measurements lack the controlled setup of a laboratory and will likely exhibit larger deviation from a norm, requiring statistical considerations. In addition to the statistical analysis, an engineering analysis is also necessary to study the functional relationships of the various variables. Understanding the mechanism of crazing from the scientific literature and using guidance from the laboratory test results will contribute to the analysis. Appendix I reviews the craze criterion and develops the mathematics for later analysis.

The treatment of the field data will be guided by the analysis of the laboratory tests. The literature [1-3] on crazing shows a nonlinear relationship between time for incipience of crazing and stress. By logarithmic manipulation [4], the data can be cast in the linear form

which will be desirable for subsequent correlation with laboratory data. Statistical consideration will then be applied to determine the quality of the linear fit. Correlation of the lab and field data will establish a correspondence and this relationship will provide the validity of the accelerated life prediction scheme.

III. CORRELATION OF LAB AND FIELD TEST DATA

Correlation of the field and laboratory studies can be aimed to devise a scheme which can predict service life from the accelerated tests at the production stage. An anticipated approach would compare the slope of the lines of reduced field and laboratory data and predict service life from the ratio or some such factor. More can only be learned after some data is available both from laboratory and field tests.

RECOMMENDATIONS:

The task outlined above should be undertaken with the anticipation of some possible problems and shortcomings. The problems will have to be solved as they are encountered during the course of the tests. One of the critical elements in the plan is the availability of an adequate number of removed canopies representing the selected air force bases and vendors. This should be assured as soon as possible. Should there be difficulty in finding the number of canopies specified above, then we should know the maximum number and type of the canopies available and then modify the plan accordingly.

USAF-UES Summer Faculty Research Program participants, such as the author of this report, are provided the opportunity to apply for an AFOSR-Minigrant, which is also administered by UES, in the amount not to exceed $20,000. The execution of this plan could be conveniently carried out if the summer fellow succeeds in getting this grant.

REFERENCES

1. Hill, Bates, Lewis and Rees. The Fracture of Acrylic Polymers in Water. J. of Mat. Sc. 19 (1984) 1904-1916

2. Kerfalas and Argon. The Effect of Environmental Water on the Craze Growth Rate of Atactic Polystyrene. J. of Mat. Sc. 23 (1988) 253-258

3. Kinloch and Young. Fracture Behavior of Polymers. Applied Science Publishers, Ltd., London,1983.

4. Clayton, West and Bowman. Aircraft Transparency Test Methodology, University of Dayton Research Institute, AFWAL-TR-85-3125

5. Lee, Nkonge, Shaikh, Mayer and Gran, Management of Transparency Related Cost in Air Force Aircraft: A Pareto Approach. Conference on Aerospace Transparent Materials and Enclosures, WRDC-TR-89-4044

6. Oxborough and Bowden. A General Critical-Strain Criterion for Crazing in Amorphous Glassy Polymers. Phil. Mag . 28, 547 (1973)

7. Duckett, Smith, Sumner and Ward. Proceeding of Sixth International Conference on Deformation, Yield and Fracture of Polymers. April, 1985.

8. Sternstein and Ongchin, Ploym, Pre-prints, Amer. Chem. Soc., 19 (2), 1117, (1969)

9. Nicolais and DiBenedetto, J. of Appl. Poly. Sco., 15, 1585-1598, (1971).

10. Mayer, Private Communication, 1988.

APPENDIX I

CRAZE ANALYSIS

Experimental data indicate that the time for craze initiation depends linearly on the maximum principle stress [1]. Starting from the expression of nucleation growth by Nicolais and DiBenedetto [4], Dr. Mayer has derived the following equation for the time-to-craze in a uniaxially stressed specimen [5]:

$$\ln t = A - B\sigma \qquad (1)$$

where A and B are time-temperature-dependant constants, and σ is the stress. Experimental tests measuring time-to-craze on 'as cast acrylic' specimens are shown to verify these relations. The linear graph on semilog paper makes it convenient to analyze crazing in various materials for different temperatures and chemical environments. For validation studies, this offers a means of correlating field and laboratory data. Specifically, the slope and the intercepts of the line become the parameters of correlation.

The problem arises when we consider that the field test data will have a biaxial state of stress. To deal with biaxial data with the same ease as in the case of uniaxial stress, the following technique is proposed to transform the biaxial data to equivalent uniaxial data and carry out the correlation studies.

We use a modified version of Bowden and Oxborough [3] criterion:

$$e_c = C + D/K\theta \tag{2}$$

for the uniaxial state of stress $e_c = C$ and $\theta = (1-2\nu)e$ and, $K = E/3(1-2\nu)$

Substituting the above values and solving for e, we have

$$e = C/2 + \sqrt{(C/2)^2 + 3D/E} \tag{3}$$

and now substituting in Equation 1, we obtain the equation

$$\ln t = A - BE\left[C/2 + \sqrt{(C/2)^2 + 3D/E}\right] \tag{4}$$

The values of C and D from the biaxial stress data are yet to be determined.

Determination of Constants of Craze Criterion:

We employ again Equation 2 to evaluate these constants. This is facilitated by making the observation that the equation can be transformed to a linear form by taking the logarithm of both sides

$$\ln(e_c - C) = \ln(D/K) - \ln\theta \tag{5}$$

Recall that C and D are unknown. Rewrite the equation in the following form for clarity:

$$y = a - x \tag{6}$$

where $y = \ln(e_c - C)$, $a = \ln D/K$, $x = \ln \theta$

The equation is deceptively simple; recall that both C and D are unknown. An iterative numerical scheme will be employed. Starting with an initial value of C, a line of slope -1 will be fit to the data. The value of C that gives

the least squared error will be determined and the corresponding x-intercept will provide the value of D. (The asymptotic value of e_c, from the e_c vs. θ graph, will provide the initial value for C.)

Remarks:

The above analysis is of a general nature. We would like to briefly describe how this can be used for correlating laboratory and field data. From biaxial laboratory tests discussed elsewhere, one would construct an array of e_c and θ. These values will be used to calculate the values of C and D by employing Equation 6. From this, by use of Equation 4, we can evaluate A_ℓ and B_ℓ for laboratory data. Similarly, the biaxial field data will be used to evaluate A_f and B_f. The correlation will be between these field and laboratory variables. If this analysis turns out to be inadequate, having resolved to as few as two variables, A and B, we should consider introducing lesser restrictions on these variables and making them dependant on relevant parameters.

1989 USAF-UES SUMMER FACULTY RESEARCH PROGRAM/

GRADUATE STUDENT SUMMER SUPPORT PROGRAM

Sponsored by the

AIR FORCE OFFICE OF SCIENTIFIC RESEARCH

Conducted by the

Universal Energy Systems, Inc.

FINAL REPORT

STRAIN DISTRIBUTION IN COMPOSITE COUPONS IN TENSION

Prepared by:	William E. Wolfe, Ph.D. and Bryan Foos
Academic Rank:	Associate Professor, Graduate Student
Department and University:	Civil Engineering Department The Ohio State University
Research Location:	WRDC/FIBCA Wright Patterson AFB OH 45433
USAF Researcher:	Dr. R. S. Sandhu

Date:	30 Sep 89
Contract No:	F49620-88-C-0053

STRAIN DISTRIBUTION IN COMPOSITE COUPONS IN TENSION

by

William E. Wolfe

Bryan Foos

ABSTRACT

An accurate measurement of tensile strength of graphite/epoxy composites can be difficult due to non-uniformities in the stress field, particularly in the area where the load is applied. The typical design of a tensile test coupon includes a fiberglass tab which is gripped by the loading machine and bonded to the composite specimen. A finite element study of the effect of tab geometry on the distribution of stresses and strains in tensile coupons was performed. The results of the analysis indicate that the strains in the specimen near the tab line are related to the angle the tab makes with the axis of the coupon and to the ply orientation. It was observed that the strain state in the coupon is less uniform when the tab line perpendicular to the long axis of the coupon than when the tab line is inclined.

ACKNOWLEDGEMENTS

The author wishes to thank the Air Force Systems Command and the Air Force Office of Scientific Research for sponsorship of this research. Universal Energy Systems administered the project and was very helpful during my summer stay.

I want to thank the administration of the Flight Dynamics Laboratory, WRDC, for allowing me to participate in the Summer Faculty Research Program at their facility and while there to engage in many stimulating conversations with the laboratory staff. These conversations certainly contributed a great deal to my understanding of the behavior of composite structures.

I am particularly grateful to my program monitor, Dr. R. S. Sandhu, our branch chief, Mr. George Holderby, and the group leader Mr. Chuck Ramsey who have for three years provided me with the technical background and the work environment that have made these summers both educational and enjoyable. I hope the results of this work prove to be useful to them.

ACKNOWLEDGEMENTS

The author wishes to thank the Air Force Systems Command and the Air Force Office of Scientific Research for sponsorship of this research. Universal Energy Systems administered the project and was very helpful during my summer stay.

I want to thank the administration of the Flight Dynamics Laboratory, WRDC, for allowing me to participate in the Summer Graduate Student Research Program at their facility and by so doing have the opportunity to work with a very talented laboratory staff. The conversations we had contributed greatly to my understanding of the behavior of composite structures.

I am particularly grateful to my program monitor, Dr. R. S. Sandhu, and branch chief, Mr. G. R. Holderby, and group leader Mr. Chuck Ramsey who provided the technical background and work environment to make my summer both educational and enjoyable.

I. INTRODUCTION:

The material properties used in the design of structures are often obtained in the laboratory using procedures in which specimens having simple boundary conditions are subjected to known load or displacement conditions. One of the most widely used tests for measuring composite properties is the coupon tensile test. In this test, it is assumed that the simple specimen geometry assures that the longitudinal strains are uniform throughout the coupon. However, when the material properties of a graphite/epoxy composite are evaluated, the typical coupon consists of not only the composite specimen, but also end tabs that are gripped by the loading machine and through which the tensile load is applied, and an adhesive to bond the tabs to the specimen. The tabs are used to make the load transfer from the testing machine to the specimen more uniform, but the use of different materials causes mismatches in stiffness and Poisson's ratio at the tab line. This, in turn, results in nonuniformities in stresses and strains in the specimen. To minimize the effects of these nonuniformities on assessment of elastic properties, minimum coupon lengths are generally specified and the measurement of material strain is made well away from the tab line. Adjustments to the methods for making strength measurements cannot be accomplished as easily as those for elastic properties however. If the coupon fails near the tab line where the actual stress distribution is not known, precise strength determinations cannot be made. Therefore a tab design that minimizes the stress and strain nonuniformities would improve our

estimate of composite strength properties by increasing the reliability of critical laboratory test measurements.

II. OBJECTIVES OF THE RESEARCH EFFORT:

The primary objective of this summer research effort was to determine analytically whether or not modifications in the geometry of the tabs on graphite/epoxy tensile specimens could affect the distribution of strains in the tab region. To that end, finite element models of tensile specimens were constructed. In these models, the angle of the tab line was varied over a 50 degree range. Although the primary emphasis in this preliminary program was placed on analyzing unidirectional composites, the effect of ply orientation was studied using models of composite specimens having four different ply layups.

III. REVIEW OF LITERATURE:

The effects of end restraints on the uniformity of stresses in composite specimens loaded in tension has been studied by a number of investigators. A comprehensive review is presented by Sandhu and Sendeckyj (1985). Kural and Flaggs (1983) using a finite element approach that included modelling the grips, tabs and adhesive layers, analyzed the distribution of stresses in unidirectional graphite/epoxy tension coupons. Their work showed that tapering the tabs reduced the non-uniformities in the stress field near the tab line. Cunningham et.al. (1985) conducted a finite element study and performed laboratory experiments on unidirectional graphite/epoxy specimens of varying tab geometries.

They found that peak shear and normal stresses were related to tab length, taper and thickness. By increasing the length of the taper, non-uniformities in the stress field could be reduced. Observing that undesirable stress concentrations still exist in the tab area even for tapered tabs, Sun and Berreth (1988) have suggested using a new type of tab in which a fiberglass mesh is embedded in silicon rubber matrix. The strains measured by Sun and Berreth on specimens tested with the new tab material were found to be more uniform than those obtained with specimens bonded to the conventional fiberglass tabs. Sandhu and Sendeckyj discussed various experimental techniques for improving the uniformity of stresses in the tab region. Furthermore, they derived expressions that allow the designer to determine an optimum specimen design by varying the tab geometry. They also performed linear and non-linear finite element analyses on off-axis, unidirectional composite specimens and conducted an extensive program of experiments to support their theoretical work.

IV. TEST PROGRAM:

In an extension of the work reported by Sandhu and Sendeckyj, finite element analyses were made of tensile coupons having several different ply orientations and tab geometries. The modelled coupons were all eight ply graphite/epoxy composite specimens. The model accounted for the fiberglass tabs, the adhesive layer between the specimen and the tab and the steel grips. A schematic of a typical specimen is shown in Figure 1. The drawing given as Figure 1 shows a coupon with tapered tabs perpendicular to long axis of

the specimen. However, in the program described in this report, the angle of the tab line (refered to as λ in Sandhu and Sendeckyj) was not always square ended as shown in the figure, but was allowed to vary in five steps from 0 to 50 degrees (0,25,35,45,and 50). The ply layups studied were unidirectional, $\pm$ 45 degrees, 0/90 degrees and quasi-isotropic. Plan views of the meshes used in the study are presented in Figure 2. An elevation view of the finite element mesh representing the coupon and grips through the thickness is presented in Figure 3. Due to sample symmetry only one quarter of the specimen was modelled. The material properties used were the same as those reported by Kural and Flaggs.

V. DISCUSSION OF TEST RESULTS:

Calculation of the distribution of strains in composite specimens clearly indicates that the orientation of the tab affects the strain field the vicinity of the tab line. Figure 4 presents elevation views of the tab area of two coupons loaded in tension. Deformations are magnified by a factor of 1000 to make them visible. The first figure (4a) is a coupon with a square ended tab. The second figure (4b) is the deformed shape of a coupon with a tab angle of 50 degrees. In both cases, most of the deformation is in the tab and the adhesive layer, but there is a clear reduction in the amount of interlaminar deformation in the specimen with a tab angle of 50 degrees. The effect of the tab angle on strain at the tab line can also be seen in the plan views of the specimen. Figure 5 presents the deformed shape of a unidirectional

coupon in the area of the tab for the five tab angles studied. It is apparent from this figure that the in-plane strains are greater for the square ended tab than for the other geometries analyzed. In Figure 6, plots of longitudinal strain contours are presented for 50 degree tab angle coupons with a) unidirectional fibers, b) plies with fiber orientations of $(0/90)_{2S}$, c) plies with fiber orientations of $(\pm 45)_{2S}$, and d) the quasi-isotropic coupon. It can be seen from this figure that the strain gradient is greatest at or near the center of the specimen for all layups, but that the actual strain values are dependent upon the precise ply orientation at the tab line. The contour plot presented in Figure 7 for a specimen with square ended tabs shows that the largest gradients of strain are located not near the specimen midline, as was the case for the coupons shown in Figure 6, but at the free edge. A comparison of the peak values of strain as taken from the plots presented in Figures 6 and 7 shows that maximum values of strain difference decrease as the tab angle is increased. This result indicates that for strength testing, more reliable measurements should be expected when specimens with tab angles other than zero are used.

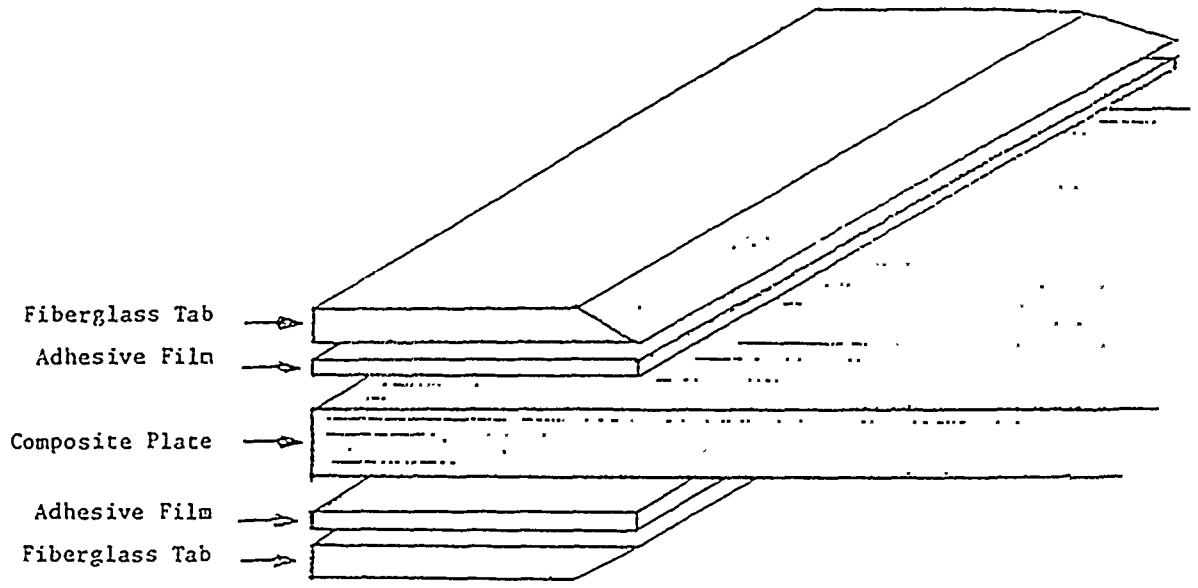
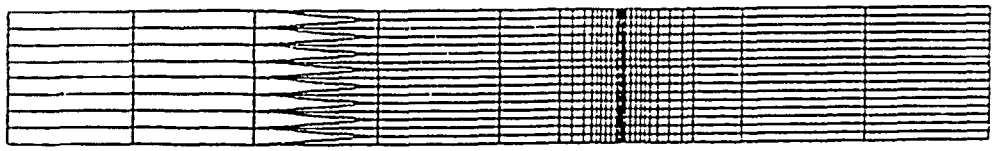
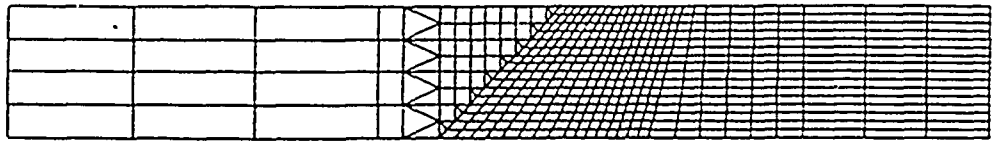


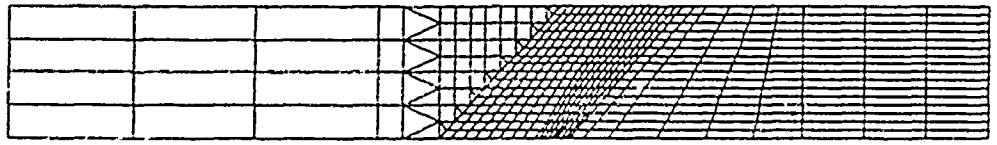
FIGURE 1. SCHEMATIC DIAGRAM OF A COMPOSITE TENSILE TEST SPECIMEN



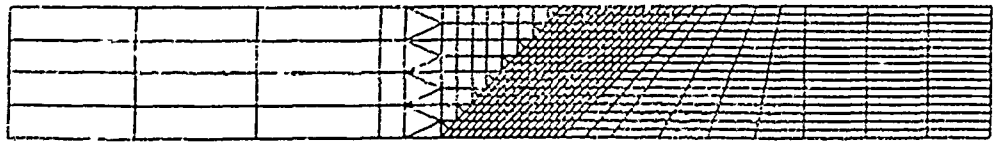
a) tab angle = 0 degrees



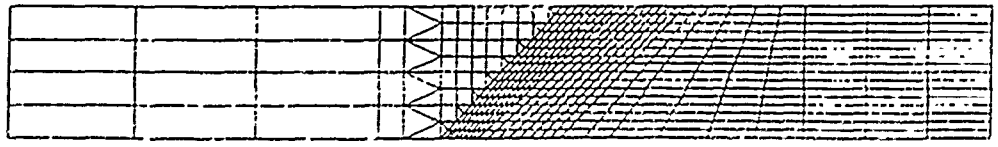
b) tab angle = 25 degrees



c) tab angle = 35 degrees



d) tab angle = 45 degrees



e) tab angle = 50 degrees

FIGURE 2. FINITE ELEMENT MODELS OF THE TENSION COUPONS FOR FIVE VALUES OF TAB ANGLE (PLAN VIEW)

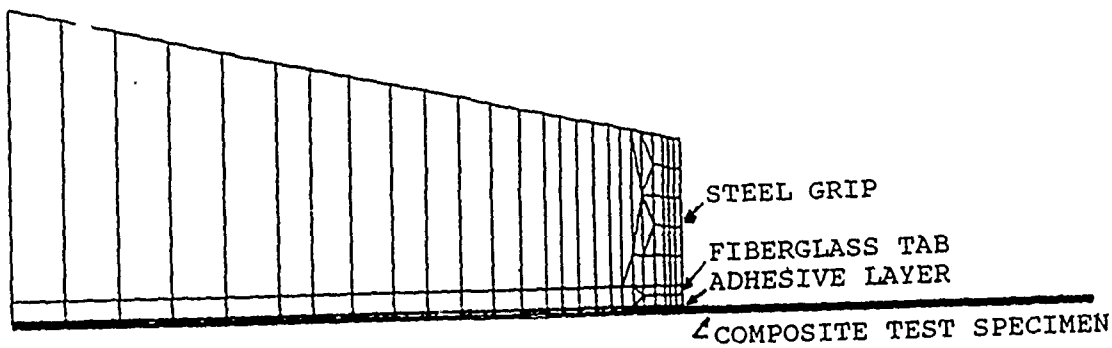
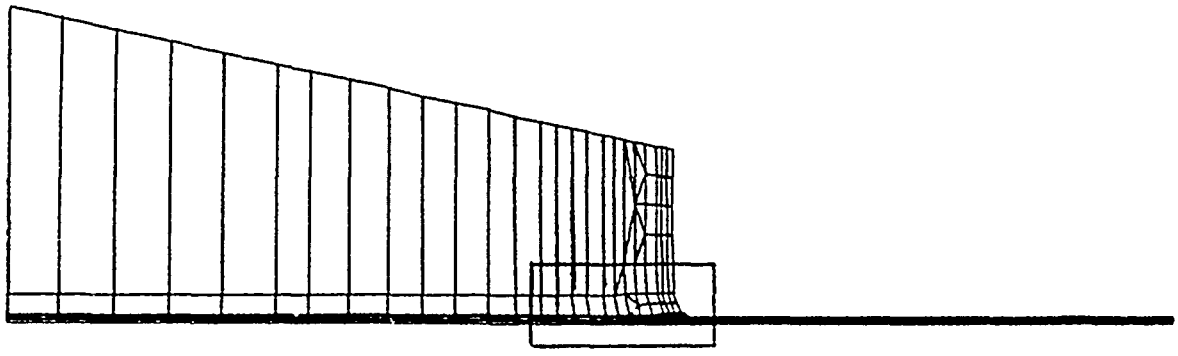


FIGURE 3. FINITE ELEMENT MODEL OF THE TENSION COUPONS
(ELEVATION VIEW)



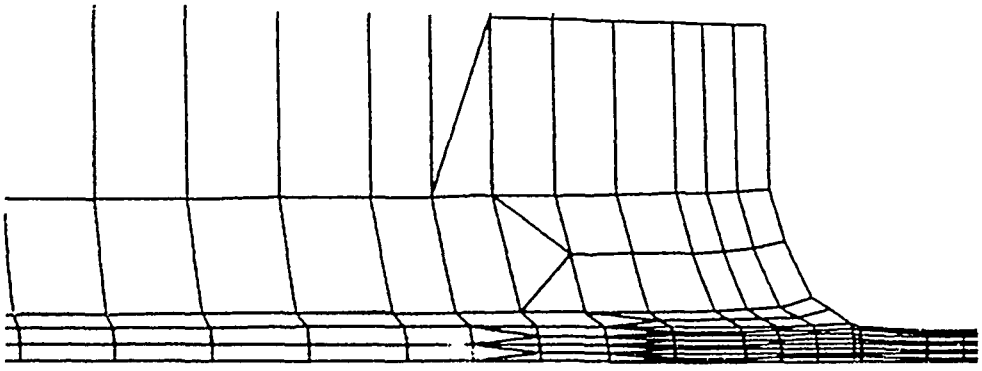


FIGURE 4a) DEFORMED SHAPE OF LOADED SPECIMEN (ELEVATION VIEW)
TAB ANGLE = 0 DEGREES

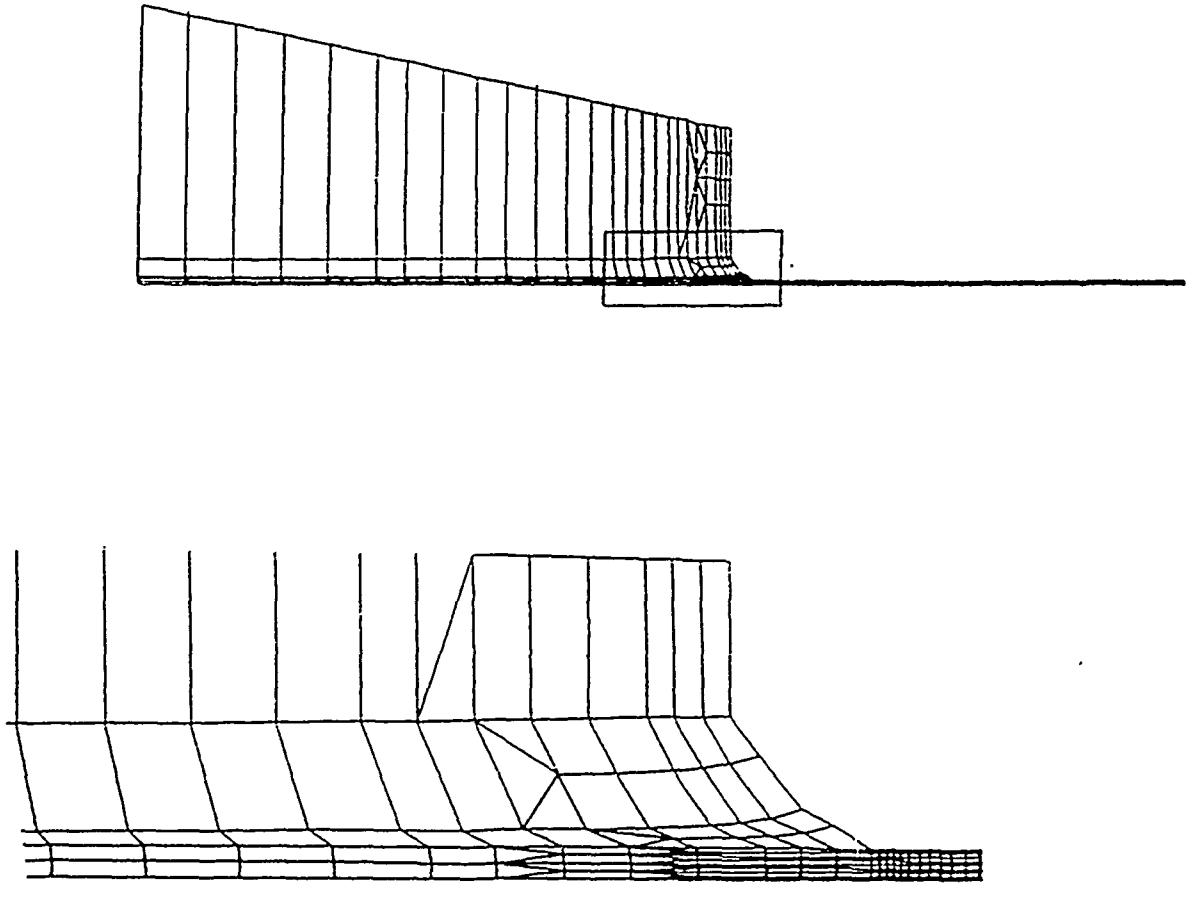
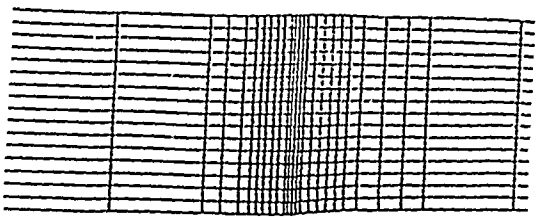
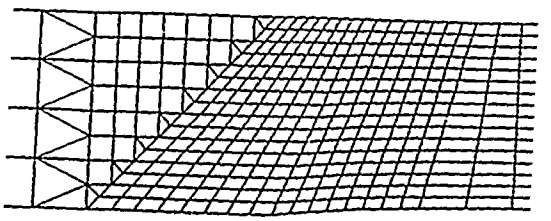


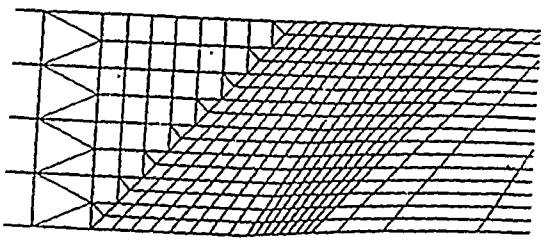
FIGURE 4b) DEFORMED SHAPE OF LOADED SPECIMEN (ELEVATION VIEW)
TAB ANGLE = 50 DEGREES



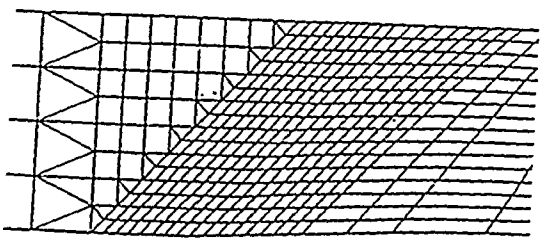
a) tab angle = 0 degrees



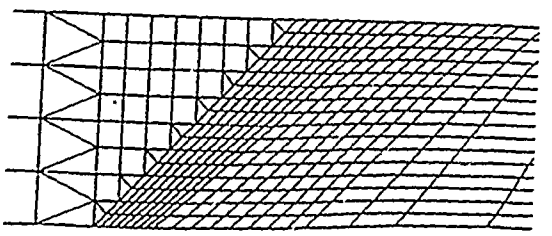
b) tab angle = 25 degrees



c) tab angle = 35 degrees



d) tab angle = 45 degrees



e) tab angle = 50 degrees

FIGURE 5. DEFORMED SHAPE OF LOADED SPECIMENS (PLAN VIEW)



a) Unidirectional



b) $(0/90)_{2s}$



c) $(\pm 45)_{2s}$



d) quasi-isotropic

FIGURE 6. STRAIN CONTOURS FOR COUPONS WITH TAB ANGLE = 50 DEGREES

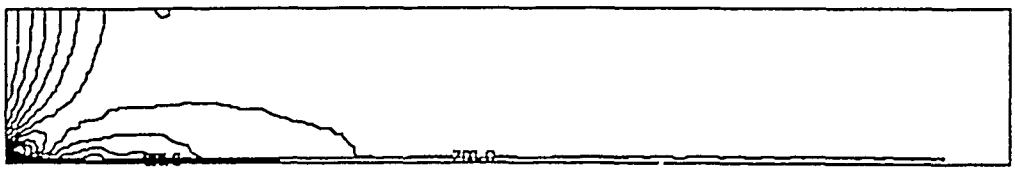


FIGURE 7. STRAIN CONTOURS FOR COUPON WITH TAB ANGLE = 0 DEGREES.

VI. RECOMMENDATIONS

The results of the finite element study presented in the above sections clearly show that the distribution of strains in graphite/epoxy tensile coupons, is dependent on the coupon geometry. In particular, the orientation of the tab line with respect to the plies may significantly affect measured strength results. To verify these analytical findings, an experimental program should be undertaken in which graphite/epoxy specimens having different ply orientations and tab angles are loaded in tension to failure. Since the quantity of primary interest is the distribution of strains in the coupon, especially in the tab area, techniques for measuring entire strain fields, such as photoelasticity, will have to be utilized.

REFERENCES

1. Sandhu, R.S. and G.P. Sendeckyj, "On Design of Off-Axis Specimens," Final Technical Report, AFWAL-TR-84-3098, Flight Dynamics Laboratory, Air Force Wright Aeronautical Laboratories, Wright Patterson AFB, Ohio, March, 1985.
2. Kural, M.H. and D.L. Flaggs, "A Finite Element Analysis of Composite Tension Specimens," Composites Technology Review, Vol. 5, No. 1., Spring, 1983, pp. 11-17.
3. Cunningham, M.E., S.V. Schoultz, and J.M.Toth, Jr.,"Effect of End-Tab Design on Tension Specimen Stress Concentrations," Recent Advances in Composites in the United States and Japan, ASTM STP 864, J.R. Vinson and M. Taya, Eds., American Society for Testing and Materials, Philadelphia, 1985, pp. 253-262.
4. Sun, C.T. and S.P. Berreth, "A New End Tab Design for Off-Axis Tension Test of Composite Materials," Journal of Composite Materials, Vol.22, August, 1988, pp.766-779.

1989 USAF-UES SUMMER FACULTY RESEARCH PROGRAM/

GRADUATE STUDENT RESEARCH PROGRAM

Sponsored by the

AIR FORCE OFFICE OF SCIENTIFIC RESEARCH

Conducted by the

Universal Energy Systems, Inc.

FINAL REPORT

CHARACTERISTICS OF AN OSMOTICALLY DRIVEN THERMAL TRANSFER CYCLE

Prepared by:	Juin S. Yu
Academic Rank:	Professor
Department and	Mechanical Engineering
University:	West Virginia Institute of Technology
Research Location:	WRDC/FIVE, WPAFB, Ohio 45433
USAF Researchers:	William L. Haskin and Won S. Chang
Date:	September 5, 1989
Contract No:	F49620–88–C–0053

CHARACTERISTICS OF AN OSMOTICALLY DRIVEN THERMAL TRANSFER CYCLE

by

Juin S. Yu

ABSTRACT

A thermal transfer cycle utilizing membrane osmotic transport of water against a pressure rise is investigated from the viewpoint of the operation of a conventional absorption heat pump using an aqueous solution as the working fluid. Physical sorption, similar or equivalent to condensation, of water vapor in the membrane material is considered to be an essential step in the overall process of water transport. The thermal nature of this step during which the heat of sorption similar in amount to the heat of condensation for water vapor must evolve at the evaporator temperature or lower disqualifies the system in performance as a heat pump. Simple flow relations for the aqueous sugar solution are derived under simplifying assumptions. A set of numerical calculations is given as an illustration to show that the inferred steps are well within the limits of thermodynamics.

ACKNOWLEDGEMENTS

This work was performed under the auspices of the Advanced Thermal Management Group of the Flight Dynamics Laboratory and the Nuclear/Thermal Technology Group of the Aero Propulsion Laboratory, WPAFB. I wish to express my gratitude to the Air Force Systems Command and the Air Force Office of Scientific Research for their financial sponsorship. The sincere help in various forms furnished by the Universal Energy Systems throughout the entire research period is greatly appreciated.

I am indebted to many who helped me make the summer experience possible. My principal debt is to Dr. A. H. Mayer of the Flight Dynamics Laboratory and to Drs. E. T. Mahefkey and J. E. Beam of the Aero Propulsion Laboratory, who candidly explained to me the significance of my summer assignment and frankly suggested various important matters of exposition. I wish to thank A. Basso and G. A. Kline for their constructive discussions and suggestions. I am indebted to W. L. Haskin and W. S. Chang, who have been collaborators, critics, as well as mentors during and after the performance period of this work. My thanks are due to J. E. Leland who provided all the information pertinent to the experimental setup and to D. L. Reinmuller who prepared, performed and documented the time–demanding experiments in an effort to verify the thermal nature of the membrane transport process.

I. INTRODUCTION:

A conventional absorption heat pump cycle uses a binary aqueous solution as the working fluid with the solvent water performing as the refrigerant. The aqueous solution can be either ionic or nonionic. A description of the working detail of this cycle is given in most textbooks dealing with refrigeration and air conditioning[1]. A scheme had been proposed to modify this cycle by making use of the thermodynamic phenomenon of osmotic flow of the solvent which takes place against an adverse pressure difference from the compartment of the pure water (the evaporator), across a semipermeable membrane which allows only water to permeate through, and into the compartment of the aqueous solution (the generator). The motivation behind the attempted modification was to remove the power input required for mechanically pumping the aqueous solution in the conventional cycle, an obviously desirable simplification from the viewpoint of system operation.

The Advanced Thermal Management Group of the Flight Dynamics Laboratory and the Nuclear/Thermal Technology Group of the Aero Propulsion Laboratory were interested in the exploration of this concept. An experimental unit dubbed as the osmotic heat pump has been fabricated by the Space and Communications Group of the Space Vehicles Division of Hughes Aircraft Company for the feasibility study of the attempted scheme[2].

Also of interest to these groups is the investigation, both theoretical and experimental, of the performance of gas–loaded heat pipes because of their potential application for temperature moderation in thermal control applications. Special attention is directed presently to the steady-state operating characteristics of a straight circular heat pipe uniformly filled with a circumferential wick.

By training and by practice, my research interests have been in the general area of study involving thermodynamic systems and heat and mass transfer processes of engineering relevance. Teaching thermodynamics has been my specialty for many years. I have regularly taught refrigeration and air conditioning both as a senior elective and as a

graduate course. For the last few years, my research work has been focused on the investigation of the dispersion process of matter in laterally bounded rectilinear flows. Most recently in collaboration with Dr. W. S. Chang a paper dealing with gas–loaded heat pipes, which has been submitted for publication, has received favorable comments from peer reviews[3]. It is believed that the suitability of my background to the specific task requirements contributed to my assignment as a participant in the 1989 USAF/UES summer research program.

II. OBJECTIVES OF THE RESEARCH EFFORT:

The use of osmosis to pump the refrigerant in a heat pump cycle is certainly an innovative idea in its own right. Whether such a cycle could operate to pump heat with a temperature lift, however, remains to be proved in thermodynamic principles. Hughes Aircraft has investigated experimentally a unit having such a combination[2], and it is definitely of significant interest to the Air Force to explore the idea from the viewpoint of its perceivable potential for possible space thermal management applications.

At the directive of Dr. A. H. Mayer, Assistant for Research and Technology of the Vehicle Subsystems Division at the Flight Dynamics Laboratory, my primary assignment to be completed within the ten–week summer research period was to find out if the osmotically driven thermal transfer cycle obtained by operating the Hughes' unit could be identified as a heat pump cycle. The objective of this effort is to try to come up with a conclusion, depending on the very nature of the eventual finding, whether future work should be pursued on the investigation of such a system for thermal management application in space. It was found that the operation of the osmotically driven unit fails to meet the thermodynamic prerequisites as a heat pump cycle because the water vapor issuing forth from the evaporator must release the heat of condensation by thermally

communicating with a heat sink at a lower temperature before it flows by osmotic transport across the membrane from the side of the solvent to the side of the solution.

Since the thermal transfer cycle of the osmotic unit turned out to be thermodynamically different from that of the operation of a heat pump, it was decided that no continued study was necessary because it failed to perform its intended function and that the study on the performance of gas–loaded heat pipes should be undertaken during the very short latter part of my summer program and to continue at my institution during the academic year with funding from the USAF/UES mini–grant program.

III. THE HUGHES' OSMOTIC THERMAL TRANSFER UNIT:

Figure 1 is a photographic description of the experimental osmotic thermal transfer unit assembled by Hughes Aircraft for performing process feasibility studies. The essential components of the unit are the generator, the condenser, the expansion valve, the evaporator and the membrane pumping module. Comparing with a standard absorption refrigeration cycle, the first four components remain unchanged both in nature and in function but here the membrane pumping module is made to take the place of the refrigerant absorber and the solution circulating pump. The space within the membrane module is divided into two distinctive, mutually exclusive compartments separated by cellulose triacetate membranes through which only permeation of pure water is possible. One of the compartments is connected to the generator by a standing concentric double-pipe structure for facilitating the circulation by natural convection, created by a density difference due to either a change in solute concentration or a change in temperature or both, of an aqueous sugar solution with a molality very close to being unity. The other compartment of the membrane module is spatially in open communication with the evaporator of the thermal transfer unit.

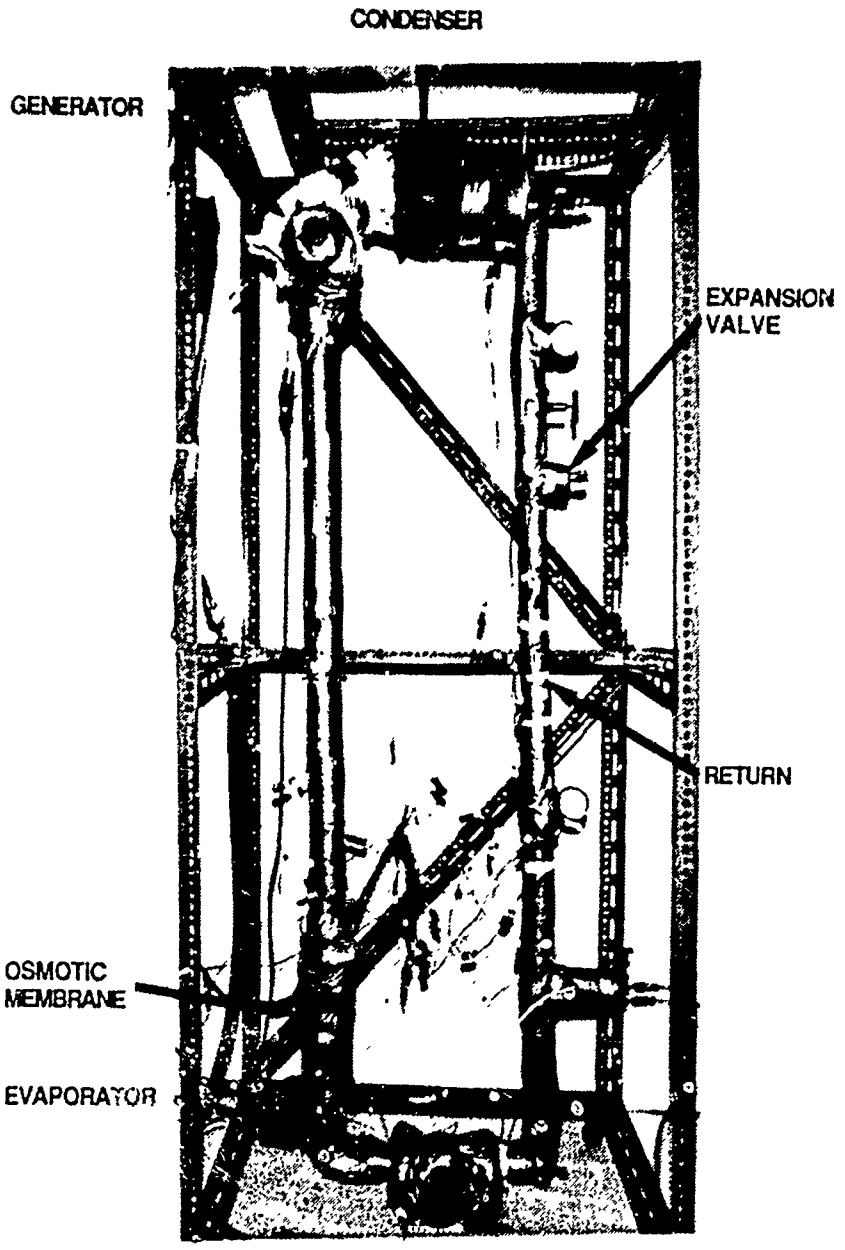


Figure 1. Physical setup of Hughes' experimental osmotic thermal transfer unit.

Water vapor boils off from the solution in the generator by receiving heat from a high temperature source. It then changes into liquid water in the condenser by heat transfer to the condenser cooling fluid. The condensate throttles across the expansion valve and a liquid-vapor mixture at a lower temperature is formed. In the evaporator the liquid water evaporates readily by heat absorption and the resulting vapor flows into the module where it is pumped by osmosis action across the cellulose triacetate membrane, mixed with the circulating flow of the solution and carried back into the generator, thus completing the mass transport cycle of the refrigerant water. The aqueous solution serving as only a refrigerant carrier is confined in circulating flow within the space formed by the generator, the standing double pipe, and the solution compartment of the membrane module. Transparent plexiglass windows are mounted on the walls of the generator and evaporator for observing the liquid levels which are visually estimated by using a linear scale.

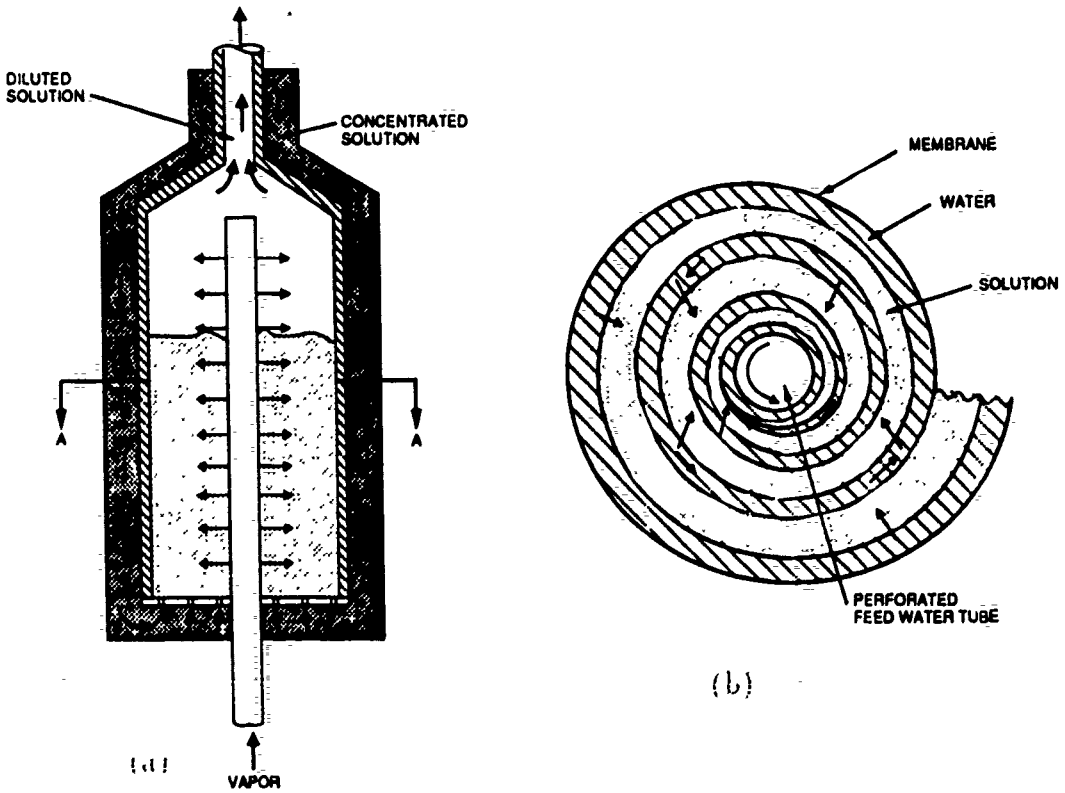


Figure 2. Schematic illustration of (a) osmotic membrane module and (b) spirally wrapped cellulose triacetate membranes.

A brief sketch of the membrane pumping module and the flow path of the aqueous sugar solution is given by Figure 2a and the geometrical arrangement of the cellulose triacetate membranes after having been wrapped around a perforated plastic tube, which is used to feed water vapor to the module, is shown in Figure 2b. Two separate sheets of the membrane, each doubled up with a sheet of plastic mesh which is probably considered as necessary for providing rigid support, are used in the wrapping structure and the top and bottom edges of these membrane sheets are joined together (see [2] for detail) so that the liquid solution can freely flow vertically upward through the membrane container while the water vapor fed via the perforated tube, appearing to be trapped within the space between neighboring sheets of membrane, can only somehow flow across the membranes by osmotic action.

Figure 3, which is reproduced from the Hughes' report[2], is a sketch of the experimental setup after the system is stripped off all external insulation. The sketch shows the locations of the thermocouples which are used to monitor the fluid temperatures. All thermocouples are of the type having self-adhesive backings and are tape mounted on the external surface of the metal walls except at points 7, 11, and 12 where the probes are made to directly sense the temperatures of the fluid. The generator and the evaporator are equipped with electric heaters for facilitating controlled heat input and polyglycol is used as the condenser cooling fluid of which the temperature at the inlet to the condenser is fixed by a constant temperature heat bath. The temperature of the latter can be adjusted and is fixed at a value to give the desired water vapor pressure in the condenser. The pressure gauges are of the Bourdon tube type giving both positive and vacuum readings, and Swagelok on-off service valves and fittings are used throughout the system. A fine metering valve for performing the throttling process, however, had to be employed in order to sustain a proper flow of the refrigerant into the evaporator[2].

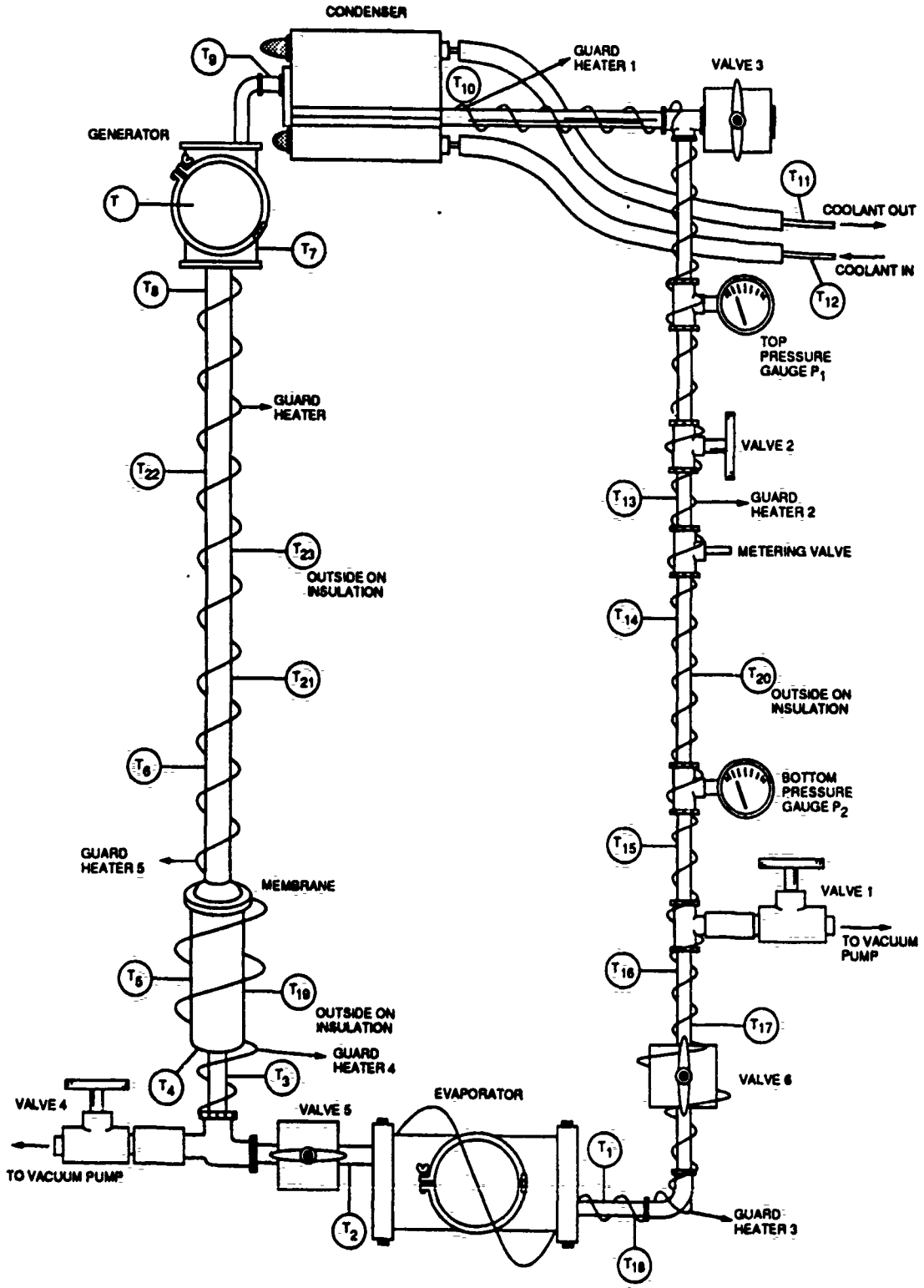


Figure 3. Diagram showing components of Hughes experimental thermal transfer system and locations of thermocouples.

IV. MEMBRANE TRANSPORT OF WATER VAPOR:

Since the components of the modified unit are the same as those of an absorption refrigeration cycle except the membrane pumping module, it is only necessary to find out the process characteristics of the latter in order to see if the performance of such a unit would qualify as a heat pump cycle. The transport of water across the membrane from the evaporator side, where water exists in the form of bulk vapor, to the solution side, where liquid water prevails, is believed to take place in the following steps: (1) physical adsorption of water vapor onto the membrane surface, (2) adsorbed water dissolves and diffuses in the membrane material to get transported to the other side, and (3) separation of dissolved water from the membrane to mix with the circulating aqueous solution. Adsorption of vapor on a surface is a spontaneous process and is therefore accompanied by a decrease in the free energy of the system. Since the process involves a loss of degrees of freedom (primarily normal to the surface) of the vapor, in passing from the free bulk vapor state to the adsorbed state confined on the surface, there is then also a decrease in entropy[4]. It therefore follows ($\Delta H=\Delta F+T\Delta S$ with $\Delta F<0$ and $\Delta S<0$) that heat is evolved in the transformation and, without exception, all physical adsorption processes must always be exothermic. The heat released ($-\Delta H$) is generally referred to as the heat of sorption.

Sorption of water vapor in organic polymers and colloidal fibers has been experimentally investigated by many workers[5,6,7]. Physical data showed that initially the heat of sorption either increases or decreases, depending on the nature of the forces involved, as the uptake of water goes up in the material. After sufficient water is sorbed, however, the heat of sorption becomes independent of the nature of the solid material but approaches close to the heat of condensation for water vapor[7]. This result suggests that, at high water uptake in the polymer, sorption is like condensation and, other than the difference in entropy, the behavior of the water adsorbed should resemble that of a liquid. This is true for all the polymer materials used in the experiments reported by these

authors, including cellulose triacetate in particular[7].

The cellulose triacetate polymer in the membrane module of the Hughes thermal transfer unit must be at a state of total imbibition in liquid water, perhaps with a significant degree of swelling, because the membrane which is permeable to water is physically in direct contact with the aqueous solution on one side. Rapid simultaneous heat and mass transfer takes place incessantly between the liquid–like water on the surface of the membrane material and the water vapor on the side of the evaporator. It appears inevitable that the vapor somewhat must be characterized by thermal equilibrium with the membrane at the interface before sorption can take place. The experimental observation indicated above suggests that the water vapor first cool to saturation and then condense upon the membrane by releasing the heat of condensation and the adsorbed water which is like a liquid in physical behavior is transported to mix with the aqueous solution. The process is spontaneous and the vapor is in thermal communication only with the aqueous solution via the membrane. Therefore, to accommodate the attendant heat transfer, such a process is possible if the membrane (and thus the solution) is at a temperature lower than that of the approaching vapor . This is born out by the simple fact that flow of water across the membrane has never been observed to take place under the condition that the system is in thermal equilibrium, i. e., when the aqueous solution, the membrane, and the water in the evaporator are at the same temperature. It is also demonstrated by Drolen, et al.[2] who noted from the results of their hot membrane experiments that "as the membrane temperature became closer to the evaporator temperature, the osmotic pumping started slowing down and eventually stopped".

In order to effect membrane pumping, the water in the evaporator must be continuously heated or maintained at an elevated temperature. Figure 4 shows a typical temperature–time tracing under the condition of a constant evaporator heat input of 40W and a generator input of zero. The entire system was blanketed with a layer (3/4" in thickness) of rubatex closed-cell insulation except the membrane module and the plexigalss

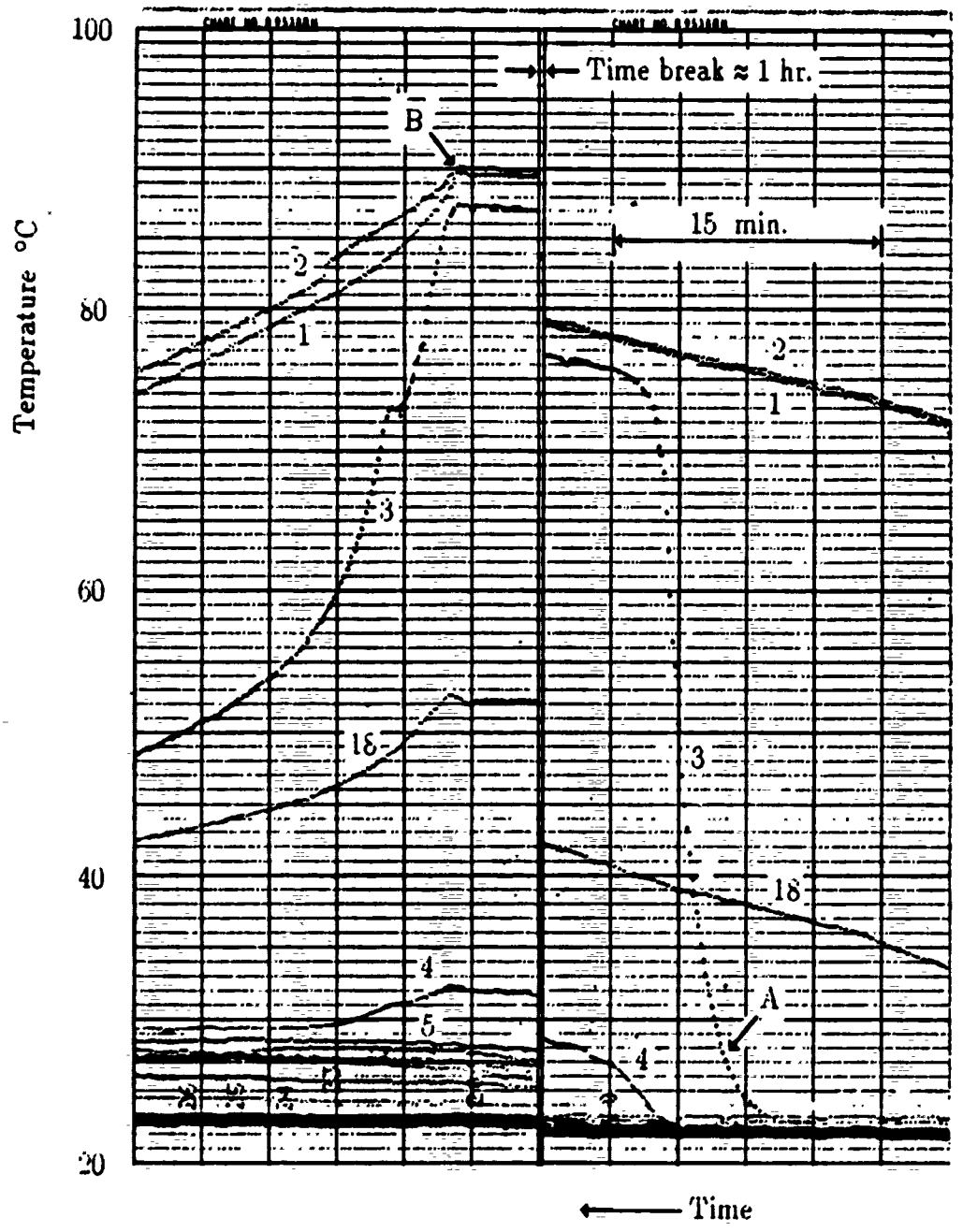


Figure 4. Typical thermocouple tracings obtained from membrane pumping tests, generator heat input=0, evaporator heat power=40 W, membrane module uninsulated. A: Pumping started by self-priming about 1 hr. after heater was turned on; B: Evaporator heat off, pumping stopped within minutes thereafter. Average pumping rate≈0.02 cc/sec. See Figure 3 for thermocouple locations.

viewports. Initially the system was in thermal equilibrium at a room temperature of about 23°C. The onset of membrane pumping, marked by the letter A in the graph, occurred at a time of about one full hour after the heater was turned on. The vapor in the membrane module must first be heated by the hot vapor in the evaporator by conduction through the initially cold stagnant vapor, essentially a vapor plug, inside the connecting tube in between. The long lead time required for priming appears to be the result of the very slow heat conduction through the stagnant vapor because of its small thermal conductivity[8]. As the vapor plug gets heated, free convection gradually sets in and the heat transfer process quickens in tempo because of direct mixing. Once primed, the temperature at the module vapor inlet (T_3) rises rather rapidly as a result of convective flow and correspondingly, the rate of water transport becomes nearly constant at about 0.02 cc/sec. The evaporator power was turned off at the time indicated by point B on the graph. It was noticed that pumping stopped within minutes thereafter and T_3 fell off at a much faster rate than T_1 and T_2, the latter being the evaporator temperatures at the inlet and outlet, respectively. There should be little or no vapor flow at all from the evaporator after its power has been turned off. It appears that the rapid fall of T_3 is due to the cooling effect rendered by the circulating aqueous solution (T_4, T_5).

It is of interest to note that, at constant evaporator heat input, the system temperatures never reached steady state conditions even after extended operation. A casual analysis of the evaporator temperature (T_2) showed that the massive evaporator wall and the large extent (judged from its small thermal diffusivity) of the attached rubatex insulation resembled the time response of the surface of a semi-infinite solid with the boundary condition of a constant surface heat flux[9]. Two separate runs, corresponding to cases of an insulated and an uninsulated membrane module, respectively, were performed under the condition of a fixed evaporator temperature of 81 °C and again a generator heat input zero. Using the the noninsulated case as a standard, the insulated test yielded a higher membrane temperature (T_4, T_5) and, correspondingly, a reduction of about 30% in

the water rate of transport has been observed. This seems to indicate that the membrane pumping rate is closely related to either the temperature or the enthalpy difference between the vapor bulk and the saturated vapor at the membrane temperature.

V. SOME ILLUSTRATIVE CALCULATIONS:

The mechanism assumed for membrane transport is deduced from the observations made in sorption studies of water vapor, that is, water sorbed in the membrane is liquid-like in character. To see that such a mechanism is well within the limitations set forth by the laws of thermodynamics, therefore lending some support for its justification, we proceed to make the following calculations.

The flow velocities of the circulating aqueous solution can be estimated by applying the steady state force balance equations to the two streams, one in the annular space where the strong (heavy) solution flows downward and the other in the center pipe where the weak (less heavy) solution flows upward, inside the coaxial standing double-pipe. These are

$$p_a + \rho_1 g l = p_b + f_1 \frac{\rho_1 V_1^2}{2} \frac{l}{D_1} \quad \text{for the upward pipe flow, and} \tag{1}$$

$$p_a + \rho_2 g l = p_b - f_2 \frac{\rho_2 V_2^2}{2} \frac{l}{D_2} \quad \text{for the downward annular flow,} \tag{2}$$

where ρ is to designate the density of the solution, f the friction factor, V the flow velocity, and D the hydraulic diameter; g=980 cm/s^2 is the gravitational acceleration, l is the total height of the solution column, and p_a and p_b are the static pressures at the top and the bottom of the column, respectively. The flows are laminar and thus

$$f = \frac{64}{Re} = \frac{64\mu}{\rho V D}, \tag{3}$$

where $Re=\rho VD/\mu$ is the Reynolds number with μ being the viscosity of the solution. Taking the difference of equations (1) and (2) by making use of equation (3) for the friction

factors to get

$$(\rho_2-\rho_1)g \simeq 32\mu\left(\frac{V_2}{D_2^2}+\frac{V_1}{D_1^2}\right), \tag{4}$$

where $\mu_1=\mu_2=\mu$ has been assumed. Conservation of mass gives

$$V_2 = (\rho_1 A_1 V_1 - m_w)/\rho_2 A_2 , \tag{5}$$

where m_w is the mass rate of water transport across the membrane into the pipe stream which is flowing upward, and A_1 and A_2 are the cross–sectional areas of the pipe and annular flows, respectively. Substituting V_2 from equation (5) into equation (4) to obtain

$$\frac{1}{32\mu}(\rho_2-\rho_1)+\frac{m_w}{\rho_2 A_2 D_2^2} = V_1\frac{1}{D_2^2}\left(\frac{\rho_1 A_1}{\rho_2 A_2}+\frac{D_2^2}{D_1^2}\right). \tag{6}$$

As a simplification, it is assumed that ρ_1 is not much different from ρ_2 so that the ratio ρ_1/ρ_2 can be replaced by unity in the brackets of equation (6). It is then obtained

$$V_1 = A_m\left[\frac{\rho_2 g}{32\mu}\left(1-\frac{\rho_1}{\rho_2}\right)+\frac{m_w}{\rho_2 A_2 D_2^2}\right]. \tag{7}$$

where

$$A_m = D_2^2/\left(\frac{A_1}{A_2}+\frac{D_2^2}{D_1^2}\right). \tag{8}$$

Variations in the solution density due to changes in temperature are not considered for the sake of simplicity. For illustration purposes, this work accounts for only the density change of the solution due to changes in solute concentration by assuming that the volume of the aqueous solution and that of pure water are additive upon mixing. Thus

$$A_1 V_1 = \frac{\rho_1 A_1 V_1 - m_w}{\rho_2} + \frac{m_w}{\rho_w}, \tag{9}$$

where ρ_w is the density of pure water. The first term on the rhs is the volume rate of flow of the solution in the annular region and the second term that of the pure water transported by the membrane. Combining equations (7) and (9), there yields

$$\left(1-\frac{\rho_1}{\rho_2}\right)\left[\frac{\rho_2 g}{32\mu}\left(1-\frac{\rho_1}{\rho_2}\right)+\frac{m_w}{\rho_2 A_2 D_2^2}\right] = \frac{A_m m_w}{A_1 \rho_w}\left(1-\frac{\rho_w}{\rho_2}\right), \tag{10}$$

which, with the use of experimentally measured mass rate of water transport through the membrane m_w, serves to determine the density ρ_1 of the solution in the center pipe. Then

the flow velocity V_1 is calculated from equation (7) and the mass flow rates of the streams are given by

$$m_1 = \rho_1 A_1 V_1 , \tag{11}$$

and

$$m_2 = m_1 - m_w . \tag{12}$$

It turned out that the second term, which contains m_w as a factor, in the square brackets of equations (7) and (10) is much smaller than the first term even with m_w set equal to the maximum experimental value of 0.091 g/s[2]. The corresponding equations obtained by ignoring this small term are

$$V_1 = \frac{A_m \rho_2 g}{32\mu}\left(1 - \frac{\rho_1}{\rho_2}\right), \tag{13}$$

and

$$\rho_1 = \rho_2\left[1 - \sqrt{\frac{m_w}{aA_1\rho_w}}\left(1 - \frac{\rho_1}{\rho_2}\right)\right], \tag{14}$$

where

$$a = \frac{\rho_2 g A_m}{32\mu}, \tag{15}$$

which, with A_m given by equation (8), has a dimension of velocity.

From the viewpoint of heat transfer, the membrane module works just like a condenser. Water vapor is cooled and condensate is formed on the membrane while the heat released is transferred into the aqueous sugar solution. For simplicity, it is here assumed that the solution reaches the temperature of the condensing vapor before mixing by osmotic flow takes place. An energy balance then gives

$$t_a = \frac{4.18 m_2 t_4 + m_w(1.87 t_3 + h_{fg})}{4.18 m_2 + 1.87 m_w}, \tag{16}$$

where t_a is the condensing temperature, h_{fg} is the enthalpy of condensation for water vapor, and t_3 and t_4 are the membrane inlet temperatures of the water vapor and the aqueous sugar solution, respectively (see Figure 3 for temperature labels).

The hydraulic diameters are D_1=1.26 cm, D_2=1.40 cm and the flow areas are A_1=1.24 cm^2, A_2=5.04 cm^2. The standing column has a length of $l \approx 5' = 1.5$ m.

For illustration, we use the temperature data of Run 1 at 3:00 p.m. of the Hughes report[2]: t_3=81.8°C, t_4=53.7°C, and a static pressure at the membrane on the solution

side, as given by Hughes data book, $p_b \approx 16$ psia+5'H_2O (column height) $\approx$ 18 psia=124 kPa. The strong aqueous sugar solution in the annular space has a nominal molality of unity. Its properties evaluated at 50°C ($\approx t_4$) are[10]: $\rho_2/\rho_w=1.13$, $\mu_2/\mu_w=3.19$ with ρ_w=0.988 g/cm^3 μ_w=0.547 centipoise and $h_{fg} \approx 2380$ J/g; thus ρ_2=1.11644 g/cm^3 and $\mu=\mu_2$=1.74 cp.

The simplified equations (13) and (14) are used and the calculated results are shown below, where p_a is the condensing pressure at t_a, for three different values of m_w.

m_w g/s	m_2 g/s	m_2/m_w	t_a °C	p_a kPa
0.020	3.39	170	57.12	7.42
0.055	5.63	102	59.36	19.34
0.091	7.16	77	61.05	20.91

The table shows that the condensing conditions of the water vapor are quite similar because of the large m_2/m_w ratios. The 1M aqueous sugar solution has a mole fraction of water x_w=0.9823. Using an average of t_a=332°K with p_a=19 kPa and a liquid water volume of v_f=0.019285 m^3/kgmole we find the system to have an availability

$$\Phi = -Rt_a \ln x_w = 49.3 \text{ kJ/kgmole of water.}$$

The work required for pumping liquid water is $v_f(p_b-p_a)$=2.025 kJ/kgmole which is more than an order of magnitude smaller than the availability Φ and therefore the process is thermodynamically possible. On the other hand, if water were to transport across the membrane by vapor compression, then the minimum work needed would be by compression along the saturation line. For this case, use T_a=332°K as before with h_a=2602 kJ/kg and s_a=7.9150 kJ/kg-°K, and for saturated vapor at p_b=124 kPa, one has T_b=379°K, h_b=2679 kJ/kg, and s_b=7.2706 kJ/kg; and the minimum work for vapor compression is equal to

$$h_b-h_a-\int_a^b T ds \approx h_b-h_a-0.5(T_a+T_b)(s_b-s_a)=300 \text{ kJ/kg}=5510 \text{ kJ/kgmole,}$$

where the path of integration is along the saturated vapor line. Since, at equilibrium, the free energy of the vapor is identical to that of the liquid, the system's availability remains the same as before. The above figure shows that the work required for vapor compression is

more than 100 times higher than what is thermodynamically available. It must therefore be concluded that for this case osmotic transport of water by vapor compression is not possible.

VI. RECOMMENDATIONS:

The use of the proposed membrane module in an absorption refrigeration system, where water is employed as the refrigerant, to take the place of the refrigerant absorber and the liquid circulation pump does provide water flow from the evaporator to the generator against a pressure rise. The thermal transfer cycle obtained from such a modification, however, no longer functions as that of a heat pump. This is because water vapor, initially in the free state, must first physically become attached to the membrane before transport can take place. Attachment of water vapor to the membrane material is by physical adsorption which is always accompanied by the release of heat from the vapor. At high moisture uptake by the membrane material, the sorption process is found to resemble that of condensation. Thus, unlike in a heat pump cycle where one might say that the heat from the evaporator is first lifted to and then released at a higher temperature, here nearly the same heat must be released from the refrigerant at a temperature equal to or lower than that of the evaporator before sorption can take place. It must be concluded that the system can not be made to perform as a heat pump.

REFERENCES

1. Stoecker, W. F., and J. W. Jones, Refrigeration and Air Conditioning, 2nd ed., McGraw–Hill, 1982.

2. Drolen, B. L., G. L. Fleischman, N. Sherman, R. R. Williams, and P. P. Wu, High Power Space Craft Thermal Management, Ch. 5, AFWAL–TR–88–2121, January, 1989.

3. Chang, W. S., and J. S. Yu, "A Note on the Gas Distribution in a Cylindrical Gas–Loaded Heat Pipe," ASME Journal of Heat Transfer, 1989, submitted after revision.

4. Brunauer, S., The Adsorption of Gases and Vapors, Clarendon Press, 1945.

5. Hedges, J. J., "The Absorption of Water by Colloidal Fibres," Transactions of the Faraday Society, vol. 22, 1926, pp. 178–193.

6. Bueche,F., "Diffusion of Water in Polymethyl Methacrylate," Journal of Polymer Science, vol. 14, 1954, pp. 414–416.

7. Day, A. G., "Water Sorption in Dielectrics, Evaluation of Some Thermodynamic Properties," Transactions of the Faraday Society, vol. 59, 1963, pp. 1218–1224.

8. Kreith, F., Principles of Heat Transfer, 3rd ed., Intext, New York, 1973.

9. Carslaw, H. S. and J. C. Jaeger, Conduction of Heat in Solids, Oxford University Press, 1959.

10. Weast, R. C., and M. J. Astle, eds., CRC Handbook of Chemistry and Physics, CRC Press, 63rd ed., 1982.

1989 USAF-UES SUMMER FACULTY RESEARCH PROGRAM

GRADUATE STUDENT RESEARCH PROGRAM

Sponsored by the

AIR FORCE OFFICE OF SCIENTIFIC RESEARCH

Conducted by the

Universal Energy Systems, Inc.

FINAL REPORT

The Influence of Viscoelastically Damped Members on the Dynamic Response of Flexible Elastic Structures

Prepared by:	Lawrence D. Zavodney, Ph.D.
Academic Rank:	Assistant Professor
Department and	Engineering Mechanics
University:	The Ohio State University
Research Location:	Wright Research and Development Center Flight Dynamics Laboratory Structures Division Structural Dynamics Branch Vibration Group (FIBGC) Wright-Patterson Air Force Base WPAFB, Ohio 45433-6553
USAF Researcher:	Robert Gordon
Date:	12 Sept 89
Contract No:	F49620-88-C-0053

The Influence of Viscoelastically Damped Members on the Dynamic Response of Flexible Elastic Structures

by

Lawrence D. Zavodney

ABSTRACT

The effect of replacing lightly damped elastic members of a flexible truss structure with highly damped viscoelastic members is investigated. Both Kelvin and Maxwell one-dimensional viscoelastic models are considered. 1DOF and 2DOF system models are developed and used to compare the effects of using the two viscoelastic models. Analytic solutions are obtained for the governing equations and characteristic frequency-response functions are plotted. The results show that the one-dimensional Kelvin model is adequate to predict the complete suppression of some modes when damping levels are sufficiently high, but the one-dimensional Maxwell model cannot predict the modal suppression. Higher order viscoelastic models are required. A nonlinear analysis that includes quadratic and cubic nonlinearity in the elastic modulus reveals that classical nonlinear resonances do not appear in the highly damped viscoelastic members.

ACKNOWLEDGMENTS

This work was sponsored by the Air Force Systems Command and the Air Force Office of Scientific Research. Universal Energy Systems administered the Summer Faculty Research Program.

This work would not have been possible without the help of the vibration group personnel in general, and Mr. Bob Gordon in particular. Bob Gordon is the manager of the 12-meter truss project; I appreciated the interaction that occurred between us and the other members of the vibration group. The Vibration Group is managed by Major Alan Janiszewski under Mr. Jerome Pearson, the Structural Dynamics Branch Chief.

I. INTRODUCTION

Structures to be placed into earth orbit will be lightweight and flexible. Hence, they will be susceptible to low-frequency vibration. Vibration typically is not a problem unless a resonance occurs (which is large-amplitude vibration), or unless pointing requirements are such that no vibration can be tolerated. Methods to suppress or minimize vibration fall into the general categories of passive or active control. Passive control may include frequency detuning (by structural modification), modal suppression (by adding stiffeners and braces), vibration absorbers (by attaching them to the structure), and increasing damping levels (by adding damping treatment). Active control usually consists of some kind of sensor (to detect vibration), an actuator (to provide a force or moment), and a "brain" to know when and how to activate the actuator. Active controllers usually regulate an energy source that drives the actuators; hence, there exists the possibility that if something goes wrong, an unstable condition might arise. The simplicity and robustness of the passive dampers makes them more appealing for permanent space structures.

The Flight Dynamics Branch has been investigating the dynamic response of a 12-meter truss. One of the objectives of the vibration tests was to investigate the influence of highly damped diagonals (incorporating viscoelastic material) on the dynamic response. The truss was tested with two types of diagonal members: Lexan members whose damping ratios were low, and viscoelastic members whose damping ratios were high. By performing the same tests on the same truss with two different diagonal members, the differences in the dynamic response would be attributed to the damping properties of the diagonals.

As a general rule, increased damping levels will always decrease the amplitude of vibration in externally (vs. parametrically) excited linear single-degree-of-freedom (SDOF) systems. By replacing the lightly damped diagonal members with highly damped members, it was expected that modal damping ratios would increase and that vibration levels would decrease. As it turned out, there was not a general distribution of increased damping levels; some modes had very little increase while some modes were

suppressed to the extent that they were no longer visible on the frequency-response plots.

II. OBJECTIVES OF THE RESEARCH EFFORT

The objectives during the 1989 SFRP were to investigate the nature of viscoelastic damping in the diagonals as it related to the truss. Often, viscoelastic material is softer and more plastic than conventional elastic materials; it may also creep, as the diagonals did when they were subjected to a static load. Noncreeping elastic materials are often modelled as a Kelvin body while creeping materials are often modelled as a Maxwell body. I proposed to develop several simple dynamic models that might correlate the observed behavior of the damped truss; moreover, the modelling would also include a Maxwell viscoelastic member to account for the observed creep behavior under a static load. Additionally, the role nonlinear stiffness (in the viscoelastic member) might play in the dynamic response would investigated.

III. DISCUSSION OF RESULTS

A. Single-Degree-Of-Freedom Model

A model consisting of a mass and two conventional Kelvin viscoelastic members was chosen; it is shown in Figure 1a. Since the highly damped replacement members creep under a static load, a Maxwell viscoelastic member was also included in the analysis; this is shown in Figure 1b. Both the Kelvin and Maxwell models are one-dimensional viscoelastic models. The SDOF model shown in Figure 1--containing an upper and lower member--was selected because the presence or absence of the replaceable lower member did not affect the stability of the equilibrium position. In the analysis that follows, the upper elastic member remains unchanged--it represents the original structure and is

modelled as a Kelvin body; the lower elastic member represents the member that was replaced. Although the term "viscoelastic" refers to materials that can store elastic strain energy and simultaneously dissipate strain energy through viscous damping terms, in this report it will be used to refer to the highly damped diagonal member (modelled as a Maxwell member) that replaced the lightly damped Lexan member. The equations of motion and solutions are given in Appendix A.

A direct comparison of the two models is shown in Figures 2a-2b. In these figures the elastic stiffness and damping coefficients of the lower member was the same. The effect of using the Maxwell model compared to the conventional Kelvin model caused an increase in the amplitude of the resonant response (from 329% for $\zeta = 0.001$ to 143% for $\zeta = 0.10$) accompanied by a 29% decrease in the resonant frequency. Hence, replacing a Kelvin model with a corresponding Maxwell model will, in general, lower the resonant frequency but increase the amplitude of response.

In practice, however, one would not normally replace a lightly-damped Kelvin member with a Maxwell member having equivalent elastic stiffness and damping ratio coefficients. Instead, one would replace a lightly damped Kelvin model with a highly damped Maxwell member. Typically, the more highly damped Maxwell members have a lower stiffness modulus compared to the Kelvin members.

All structural components have some frequency dependance; the engineering question is always "how much?" The viscoelastic member had a measured complex modulus that was moderately dependant upon the frequency; the damping ratios and stiffness were monotonic functions that changed gradually with the frequency. In this preliminary analysis the frequency dependance was neglected and constant values were used. The frequency dependance of the complex modulus could be included to improve the accuracy of the results, but would not affect the general trends observed.

A comparison of the frequency response of the system that has a lightly-damped Lexan member (Kelvin model with $k_K = 8100$ lb/in and damping ratio $\zeta_K = 0.02$) with a highly damped viscoelastic member (Maxwell model with $k_M = 6300$ lb/in) is shown in Figure 3. These numbers represent measured values for the members (the damping ratio of the viscoelastic

member is 1.2). From these results, we see that damping ratios greater than 0.8 are sufficient to suppress any resonance.

The results of varying just the damping ratios of the viscoelastic model while keeping all other parameters fixed are shown in Figures 4a-4b; Figure 4a shows results for a Maxwell stiffness k_M = 2000 lb/in and Figure 4b shows results for k_M = 8000 lb/in. In both figures, we see that increasing the damping levels causes a decrease in the resonant amplitude and, surprisingly, an increase in the resonant frequency. Another trend is that the softer the viscoelastic spring (Figure 4a), the larger the resonant amplitude. This can be explained as follows: as the member is deformed, strain energy is either stored or dissipated. If the real part of the complex modulus (elastic stiffness coefficient k) is large compared to the imaginary part of the complex modulus (damping ratio ς), then the element will dissipate more strain energy than it stores because the "damper" is more easily deformed. If the imaginary part is large compared to the real part, the element will store more strain energy than it dissipates because the "spring" is more easily deformed. Thus, the member with the smaller elastic stiffness stores more energy rather than dissipating it, and hence exhibits larger amplitudes of vibration.

B. Nonlinear Analysis

The influence of quadratic and cubic nonlinearity in the elastic element of the Kelvin and Maxwell members was considered. The analysis was performed using the Method of Multiple-Time Scales. A quadratic nonlinearity caused a softening type behavior that combined with the cubic nonlinearity (which can be either hard or soft) to produce an "effective" cubic nonlinearity. Hence, the Kelvin model was reduced to a standard Duffing oscillator with either a hardening or softening spring, depending upon the sign of the "effective" cubic coefficient. This sign depended upon the relative magnitude and sign of the cubic coefficient; if the cubic coefficient was positive and large enough, it would dominate the quadratic influence.

For the Maxwell model, a different problem was encountered. Since the Maxwell model was always associated with high damping levels, the ordering of the terms in the equations caused the nonlinear terms to appear at the second order--without the damping and excitation terms. If the damping was ordered with the nonlinear terms (implying small damping levels), the excitation would appear at the same level. This happens because one cannot have a hard resonant excitation (unless damping ratios are of order 1) nor a soft resonant excitation without damping. As a result, the first order solution was a linear damped oscillator excited near resonance; the nonlinearity was simply a perturbation to the linear damped response.

The conclusion was that nonlinear elastic stiffness in the highly-damped Maxwell model does not produce any of the classical nonlinear resonances. The reason for this is that the damping is of the order of the stiffness--not a small perturbation to the amplitude--which then interacts with the nonlinearity and excitation. Hence, the classical nonlinear solution does not apply to this problem. These results were sufficient to preclude a nonlinear analysis on the 2DOF system.

C. Two-Degree-Of-Freedom Model

A two-degree-of-freedom (2DOF) model was developed and analyzed to see if a behavior similar to experiments performed on the 12-meter truss--i.e., certain modes being suppressed--could be explained using a linear model. A 2DOF model can explain many of the behaviors of a multi-degree-of-freedom (MDOF) system and has the advantage that an analytic solution can be obtained without resorting to a symbolic manipulator or relying extensively upon computer simulation results. A 2DOF model can represent any two modes of the MDOF truss if they are sufficiently separated and uncoupled from other structural modes. The model used for this analysis is an extension of the SDOF model and is shown in Figure 1. In this model the center member is the replaceable element and is represented by the Kelvin and Maxwell models. The system with the viscoelastic member was

modelled as a three-degree-of-freedom (3DOF) system. The Complex Frequency Response Method was used to obtain frequency response solutions. The governing equations and solutions are given in Appendix B. A harmonic force is applied only to m_1 to excite the system.

The frequency response for the 2DOF system with a Kelvin member is shown in Figure 5. By increasing the damping ratio from $\zeta_K = 0.01$ to 0.10, we can completely suppress the second mode; there is negligible impact on the first mode. The reason one mode is severely affected while the other mode is not can be explained as follows. The first mode is characterized by both masses m_1 and m_2 moving in phase with each other; hence the relative motion between them is very small. However, for the second mode the two masses are moving 180° out of phase; in this case the relative motion between them is quite large. Therefore, a viscoelastic member between the two masses will be "idle" for the first mode but "active" for the second mode. Furthermore, if the damping in this member is significant, it will do little to the first mode, but it will quench the second mode.

Since the strain energy is related to the deformation of each member, the strain energy is an ideal candidate to gage damping effectiveness. There is very little strain energy stored in the undamped member for the first mode, but a significant amount is stored for the second mode. Hence, an energy-absorbing member placed between the two masses would significantly affect the second mode. This observation can be generalized as follows: to the degree that a lightly damped member stores strain energy for a particular mode, it will dissipate strain energy when replaced by a highly damped member. This is the premise of the Modal Strain Energy approximation used to estimate modal damping in structures being modified with viscoelastic damping materials.

If we examine the behavior of the 2DOF system with a Maxwell viscoelastic member, we discover that the results are not the same; examples of some frequency responses for the system are shown in Figure 6. For very small damping ratios, the second mode is absent from the displacement of mass m_1; in other words, m_1 is uncoupled from m_2 and behaves as a SDOF system. Since only m_1 is forced and ζ_M is very small,

the motion of m_2 does not affect m_1. As the viscoelastic damping ratio is increased from 0.2 to 1.2, we see two separated modes that have diminishing resonant amplitudes and increased modal damping. We do not see one mode suppressed as in the response of the Kelvin model. Note an interesting trend--increasing the damping ratio ζ_M causes the modal amplitudes of m_2 to decrease, but transfers the energy in m_1 from the first mode to the second mode.

A direct comparison of the two models using the same stiffness and damping coefficients is shown in Figure 7. This resonant response of m_2 occurs at a lower frequency in the Maxwell model compared to the Kelvin model and is accompanied by a very small damping ratio. This is quite obvious for the case of $\zeta_M = 0.02$. In the Maxwell model, an increase in the damping ratio tends to couple the modes, but only over a very narrow frequency range. Note also that the second mode is diminishing in the Kelvin model, but it is increasing in the Maxwell model. For $\zeta_M = 0.2$, the coupling of m_1 with m_2 has intensified. As ζ_K and ζ_M tend towards infinity we can expect the following: in the Kelvin model m_2 would be physically locked to m_1 resulting in essentially a SDOF system--in other words, no second mode; in the Maxwell model, there would be no strain energy dissipated in the viscoelastic member, hence we would actually lower modal damping ratios!

IV. CONCLUSIONS

1. The one-degree Maxwell viscoelastic model is too elementary to correlate the observed dynamic response of the 12-meter truss. It models the creep behavior of the individual member, but not the observed dynamic coupling between two modes when the member is incorporated into a structure.

2. The one-degree Kelvin model, which does not model the creep behavior of the individual member, is capable of modelling the observed dynamic

response of the 12-meter truss. The suppression of one of the modes in the model is consistent with laboratory experiments.

3. A nonlinear elastic stiffness in the highly damped viscoelastic member does not produce any of the nonlinear resonances associated with lightly damped weakly nonlinear systems.

4. Increasing the damping levels in selected members will not simply raise damping ratios in all modes. It will attenuate some modes, suppress others, and may channel energy into other modes, thus actually increasing the vibration levels in some modes.

5. To determine to what extent selected replacement members will have on the dynamic response of the damped system, a "modal strain participation factor" for each member in the undamped configuration should be determined. The percent of the strain energy in the member (compared to the whole structure) for a particular mode would give a good estimate. Then, a statistical average can be formed to determine which modes would be significantly affected if selected members were altered.

V. RECOMMENDATIONS

Higher order viscoelastic models should be developed to more accurately model the viscoelastically damped members. The higher-order models should include several elastic elements and several dissipation elements arranged in different configurations. A statistical analysis could determine each model's "best fit" to experimental data, from which a correlation coefficient would indicate the best model. With an improved model, simulation studies using the 2DOF model with a replaceable member would indicate what physical parameters in a damped member would yield optimal performance.

APPENDIX A

SDOF KELVIN MODEL

$$\ddot{x} + 2\zeta\omega_0(1 + \dot{\xi})x + \omega_0^2(1 + \nu)x = (F_0/m)\sin\Omega t \tag{1}$$

where $\zeta = \frac{c}{2\sqrt{km}}$, $\omega_0^2 = \frac{k}{m}$, $\xi_K = \frac{c_K}{c}$, $\nu_K = \frac{k_K}{k}$ (2)

Solution $$x_K(t) = \frac{(F_0/k)\sin(\Omega t - \phi_K)}{\sqrt{[1 + \nu_K - r^2]^2 + [2\zeta r(1+\xi_K)]^2}} \tag{3}$$

where $r = \Omega/\omega_0$ (4)

SDOF MAXWELL MODEL

$$\begin{cases} \ddot{x} + 2\zeta\omega_0\dot{x} + \omega_0^2(1+\nu_M)x - \omega_0^2\nu_M y = (F_0/m)\sin\Omega t \\ 2\zeta\xi_M\omega_0\dot{y} + \omega_0^2\nu_M y - \omega_0^2 x = 0 \end{cases} \tag{5}$$

where $\xi_M = c_M/c$, $\nu_M = k_M/k$ (6)

Solution $$x_M(t) = \frac{(F_0/k)\sin(\Omega t - \phi_M)}{\left\{\left[1-r^2 + \nu_M\left(\frac{\eta^2}{1+\eta^2}\right)\right]^2 + \left[2\zeta r\left(1 + \frac{\xi_M}{1+\eta^2}\right)\right]^2\right\}^{-1/2}} \tag{7}$$

where $\eta = \frac{2\zeta\xi_M r}{\nu_M}$ (8)

Plots

$$X_K = \left(\frac{F_0}{k}\right)\cdot\left\{\left[1-r^2 + \nu_K\right]^2 + \left[2\zeta r\left[1+\xi_K\right]\right]^2\right\}^{-1/2} \tag{9}$$

$$X_M = \left(\frac{F_0}{k}\right)\cdot\left\{\left[1-r^2 + \nu_M\left(\frac{\eta^2}{1+\eta^2}\right)\right]^2 + \left[2\zeta r\left(1 + \frac{\xi_M}{1+\eta^2}\right)\right]^2\right\}^{-1/2} \tag{10}$$

APPENDIX B

2DOF KELVIN MODEL

$$\begin{bmatrix} m_1 & 0 \\ 0 & m_2 \end{bmatrix} \begin{Bmatrix} \ddot{x}_1 \\ \ddot{x}_2 \end{Bmatrix} + \begin{bmatrix} c_1+c_K & -c_K \\ -c_K & c_2+c_K \end{bmatrix} \begin{Bmatrix} \dot{x}_1 \\ \dot{x}_2 \end{Bmatrix} + \begin{bmatrix} k_1+k_K & -k_K \\ -k_K & k_2+k_K \end{bmatrix} \begin{Bmatrix} x_1 \\ x_2 \end{Bmatrix} = \begin{Bmatrix} F_1 \\ F_2 \end{Bmatrix} \tag{11}$$

$$\text{Let } \omega_i^2 = k_i/m_i \ , \qquad \zeta_i = c_i/cc \ , \quad \text{for } i = 1,2$$

$$b = \omega_2/\omega_1 \ , \qquad cc = 2m_2\omega_1 \ , \quad \lambda = k_K/k_1 \ , \quad \zeta_K = c_K/cc \tag{12}$$

$$F_1 = F_0 \sin(\Omega t) \ , \quad F_2 = 0 \ , \qquad \mu = m_2/m_1 , \quad r = \Omega/\omega_1$$

$$\begin{bmatrix} 1 & 0 \\ 0 & \mu \end{bmatrix} \begin{Bmatrix} \ddot{x}_1 \\ \ddot{x}_2 \end{Bmatrix} + 2\mu\omega_1 \begin{bmatrix} \zeta_1+\zeta_K & -\zeta_K \\ -\zeta_K & \mu(\zeta_2+\zeta_K) \end{bmatrix} \begin{Bmatrix} \dot{x}_1 \\ \dot{x}_2 \end{Bmatrix} + \omega_1^2 \begin{bmatrix} 1+\lambda & -\lambda \\ -\lambda & \mu b^2+\lambda \end{bmatrix} \begin{Bmatrix} x_1 \\ x_2 \end{Bmatrix} = \begin{Bmatrix} (F_0/k) \sin\Omega \\ 0 \end{Bmatrix} \tag{13}$$

$$K_1 = 1 + \lambda - r^2 + 2i\mu r(\zeta_1+\zeta_K) - \frac{(\lambda + 2i\mu r\zeta_K)^2}{\mu(b^2-r^2) + \lambda + 2i\mu r(\zeta_2+\zeta_K)} \tag{14}$$

$$K_2 = \frac{\lambda + 2i\mu\zeta_K r}{K_1[\mu(b^2-r^2) + \lambda + 2i\mu r(\zeta_2+\zeta_K)]}$$

$$x_{K1}(t) = \frac{(F_0/k_1)}{|K_1|} \sin(\Omega t-\phi_{K1}) \ , \quad x_{K2}(t) = \frac{(F_0/k_1)}{|K_2|} \sin(\Omega t-\phi_{K2}) \tag{16}$$

2DOF MAXWELL MODEL

$$\begin{bmatrix} m_1 & 0 & 0 \\ 0 & m_2 & 0 \\ 0 & 0 & 0 \end{bmatrix} \begin{Bmatrix} \ddot{x}_1 \\ \ddot{x}_2 \\ \ddot{y} \end{Bmatrix} + \begin{bmatrix} c_1 & 0 & 0 \\ 0 & c_2 & 0 \\ 0 & -c_m & c_m \end{bmatrix} \begin{Bmatrix} \dot{x}_1 \\ \dot{x}_2 \\ \dot{y} \end{Bmatrix} + \begin{bmatrix} k_1+k_K & 0 & -k_M \\ 0 & k_2+k_M & -k_M \\ -k_K & 0 & k_M \end{bmatrix} \begin{Bmatrix} x_1 \\ x_2 \\ y \end{Bmatrix} = \begin{Bmatrix} F_1 \\ F_2 \\ 0 \end{Bmatrix} \tag{17}$$

$$M_1 = 1 + \lambda - r^2 + 2i\mu r\zeta_1 - \frac{\lambda^2[\mu(b^2-r^2) + \lambda + 2i\mu r\zeta_2]}{[\mu(b^2-r^2) + \lambda + 2i\mu r\zeta_2](\lambda+2i\mu r\zeta_M) - 2i\mu r\lambda\zeta_M} \tag{18}$$

$$M_2 = \frac{M_1}{\lambda^2}\left\{(\lambda+2i\mu r\zeta_M)[\mu(b^2-r^2) + \lambda + 2i\mu r\zeta_2] - 2i\mu r\lambda\zeta_M\right\} \tag{19}$$

$$x_{M1}(t) = \frac{(F_0/k_1)}{|M_1|} \sin(\Omega t-\phi_{M1}) \ , \quad x_{M2}(t) = \frac{(F_0/k_1)}{|M_2|} \sin(\Omega t-\phi_{M2}) \tag{20}$$

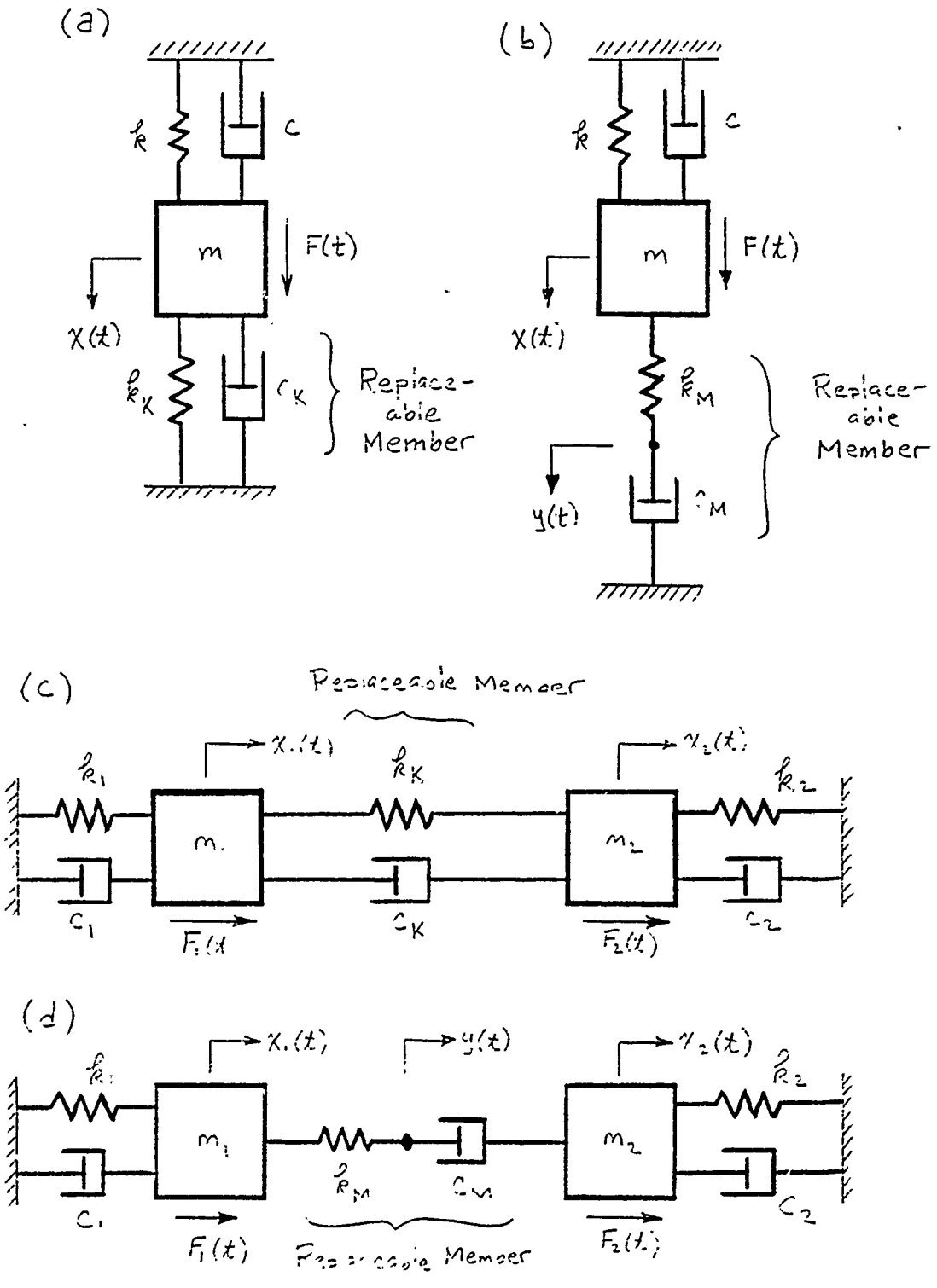


Figure 1. (a) SDOF system with a Kelvin viscoelastic member,
(b) SDOF system with a Maxwell viscoelastic member,
(c) 2DOF system with a Kelvin viscoelastic member,
(d) 2DOF system with a Maxwell viscoelastic member.

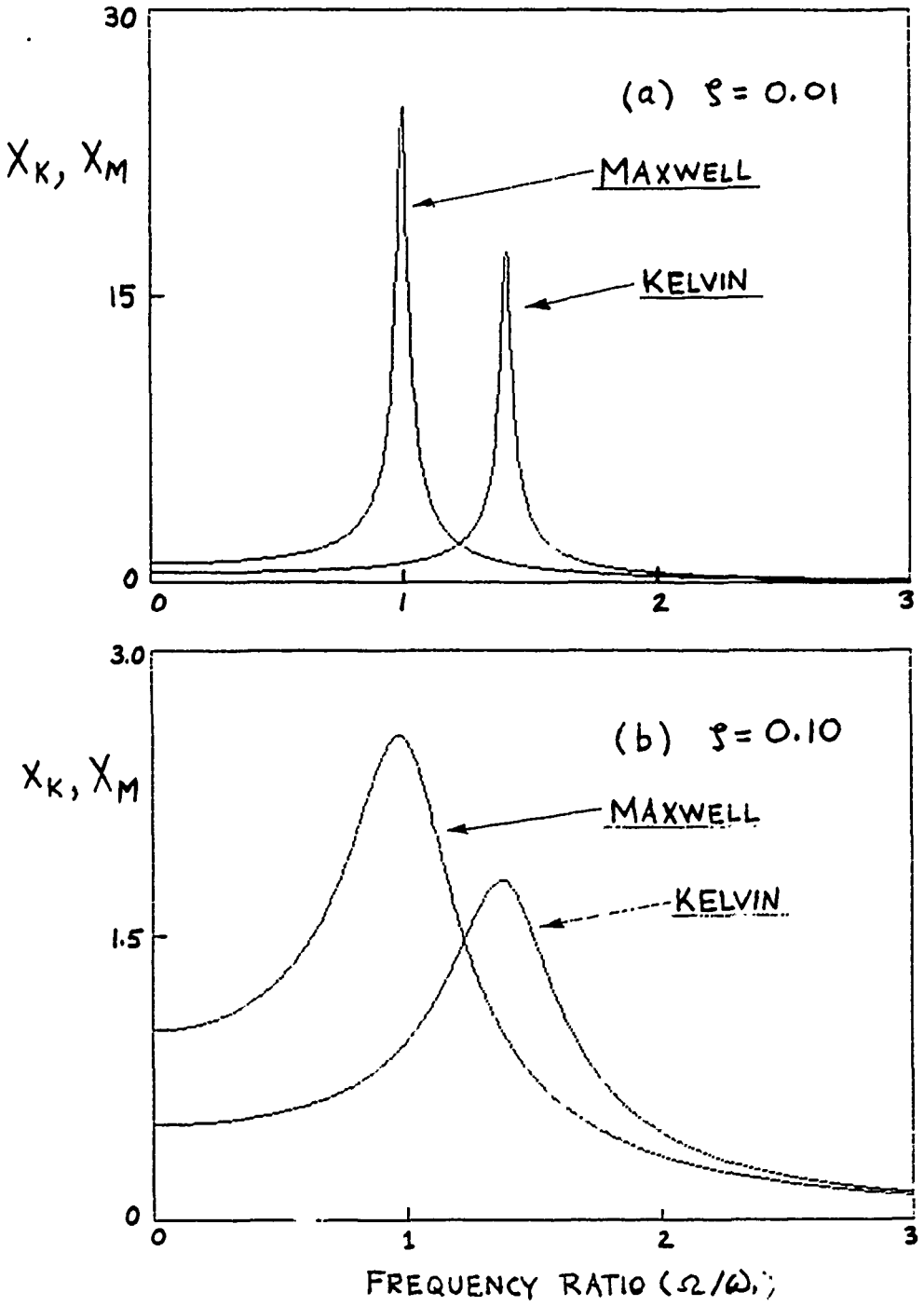


Figure 2. Comparison of the Kelvin and Maxwell viscoelastic models for identical elastic and damping coefficients; $\zeta = \zeta_K = \zeta_M$, $k = k_K = k_M = 10{,}000$ lb/in,.

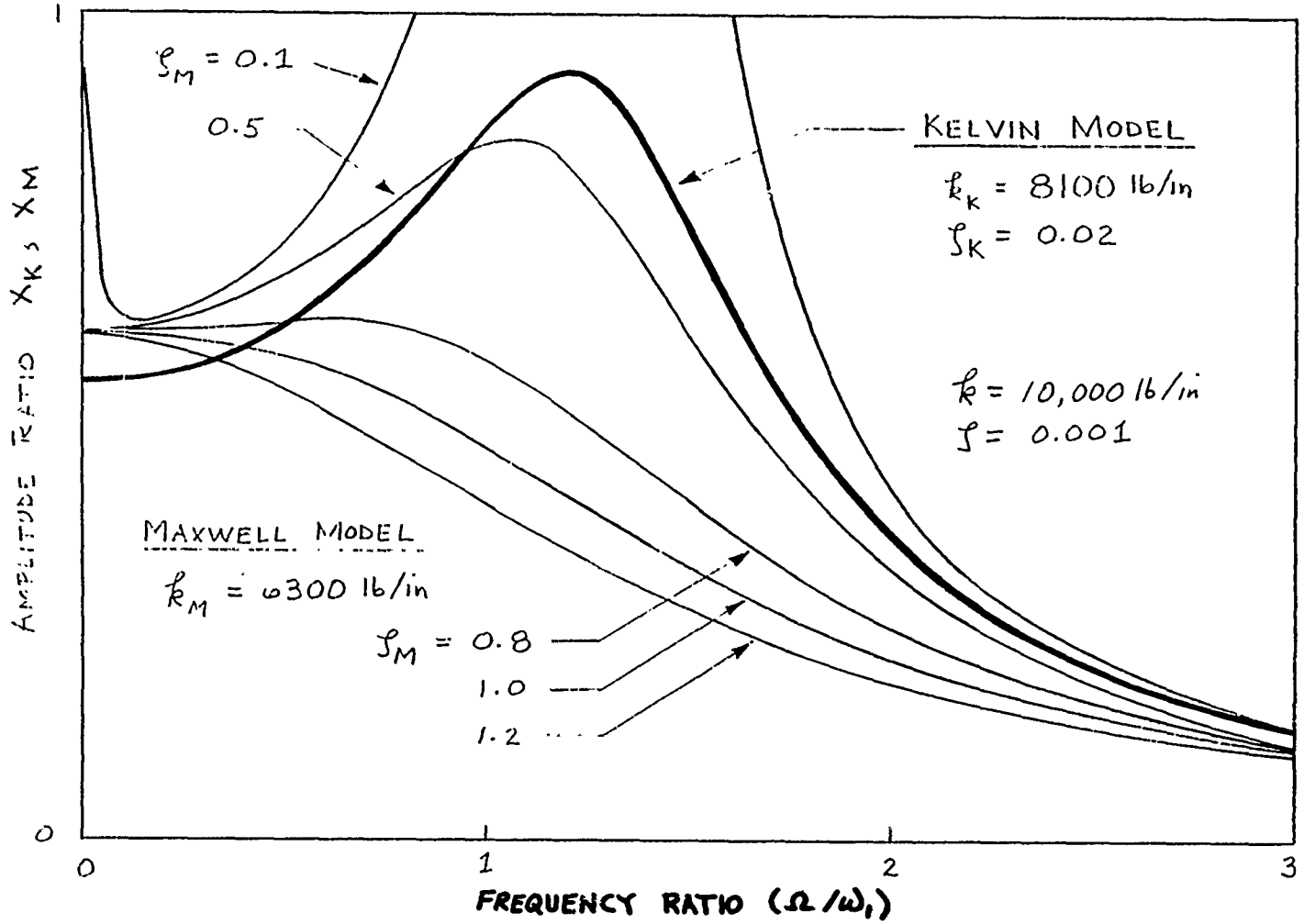


Figure 3. Effect of increasing the damping ratio of the Maxwell viscoelastic member from ζ = 0.1 to 1.2 compared to the Lexan member (Kelvin model).

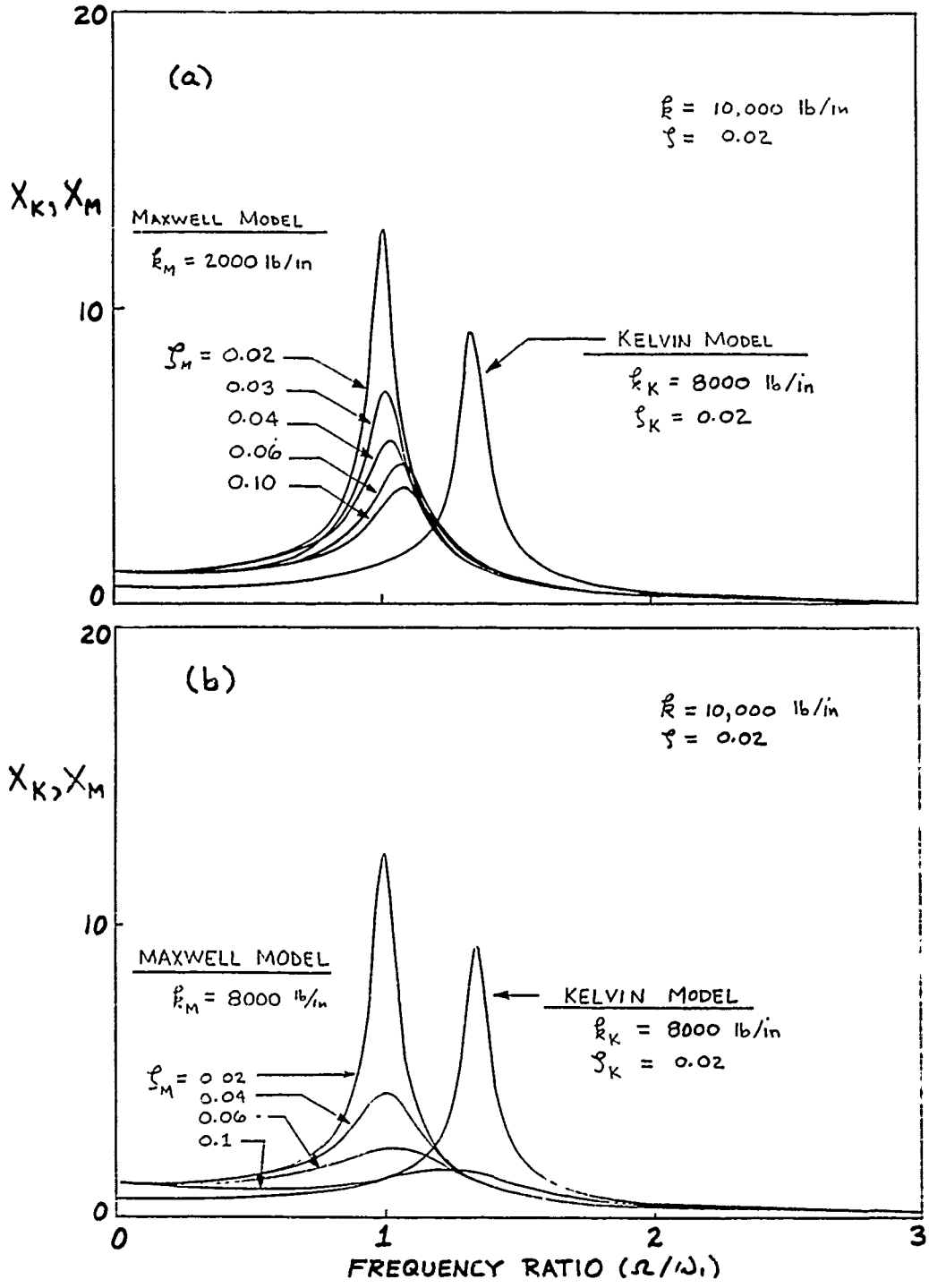


Figure 4. Frequency response for the SDOF system with the Kelvin and Maxwell members.

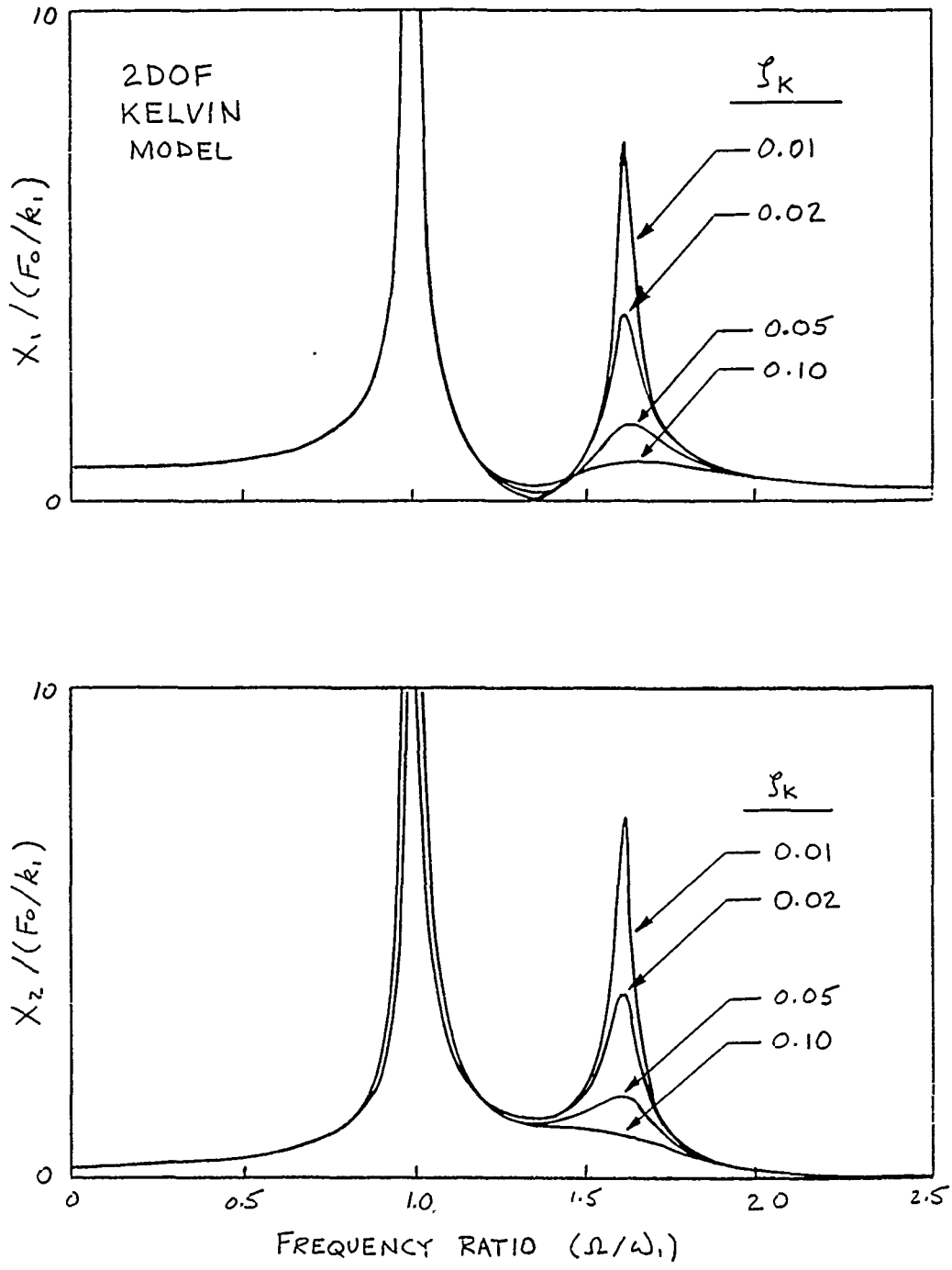


Figure 5. Frequency response of the 2DOF system with the Kelvin member for selected damping ratios ζ_K ; $\zeta_1 = \zeta_2 = 0.001$, $k_K = 8000$ lb/in, $k_1 = k_2 = 10{,}000$ lb/in.

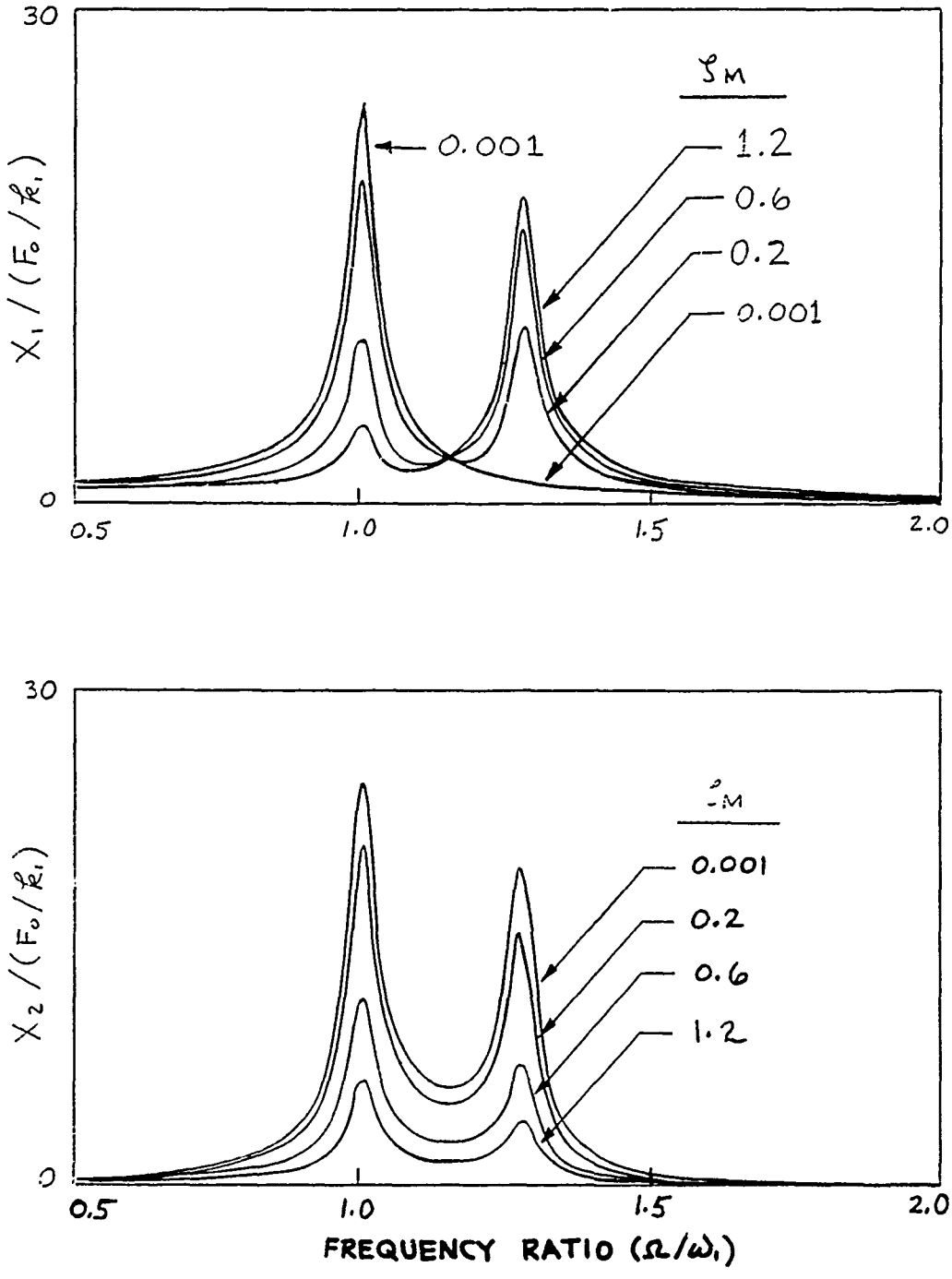


Figure 6. Frequency response of the 2DOF system with the Maxwell member for selected damping ratios ζ_M ; $\zeta_1 = \zeta_2 = 0.02$, $k_M = 6300$ lb/in, $k_1 = k_2 = 10{,}000$ lb/in.

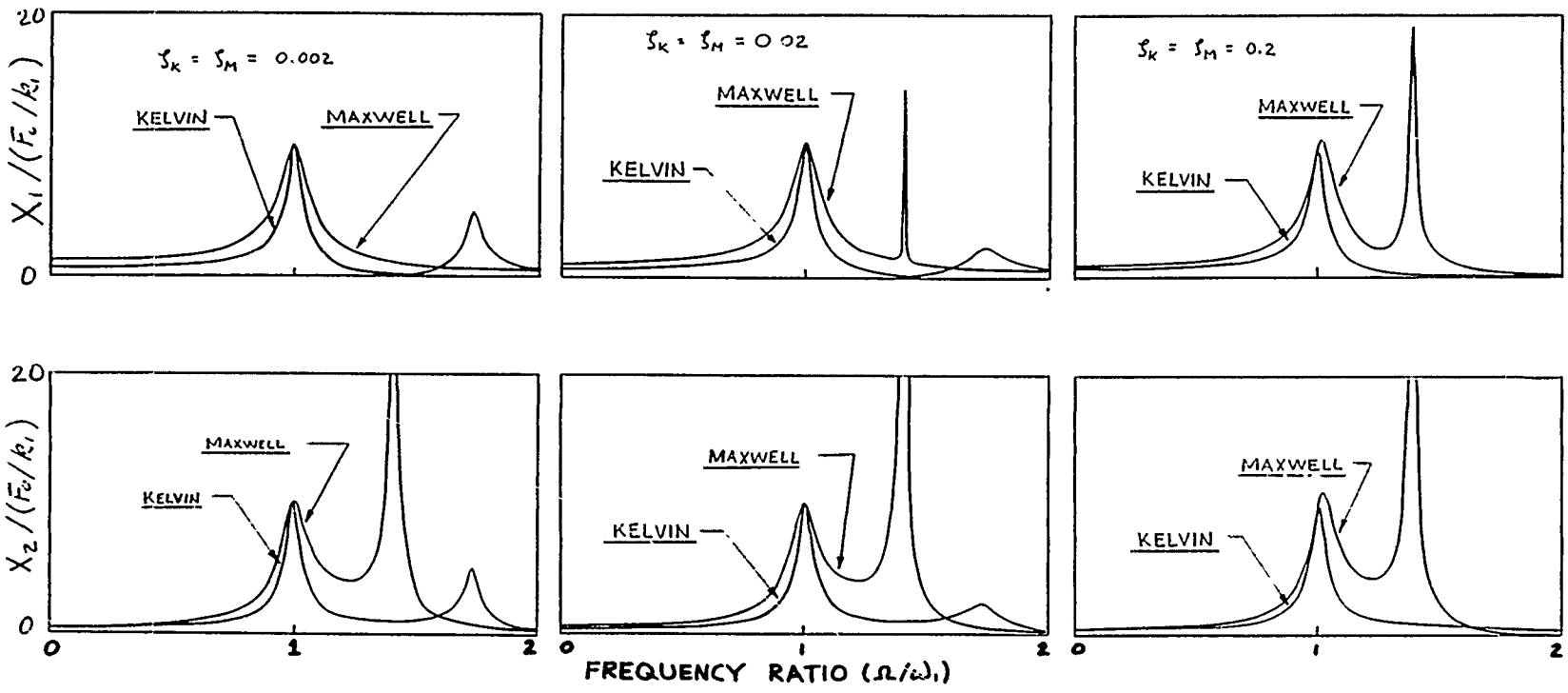


Figure 7. Comparison of the Kelvin and Maxwell viscoelastic models for the 2DOF system with identical elastic and damping coefficients; $k_1 = k_2 = k_K = k_M = 10{,}000$ lb/in, $\zeta_1 = \zeta_2 = \zeta_K = \zeta_M$.

Prof. Karren Brito

No Report Submitted

(Report # 115)

1989 USAF-UES SUMMER FACULTY RESEARCH PROGRAM

GRADUATE STUDENT RESEARCH PROGRAM

Sponsored by the

AIR FORCE OFFICE OF SCIENTIFIC RESEARCH

Conducted by the

Universal Energy Systems, Inc.

FINAL REPORT

The in-situ Laser Deposition of Superconducting Thin Film

Prepared by:	Donald D.W. Chung. Ph.D.
Academic Rank:	Associate Professor.
Department and	Materials Engineering
University:	San Jose State University
Research Location:	USAFWRDC/MLPO Wright - Patterson AFB, OH 45433
USAF Researcher:	Patrick M. Hemenger
Date:	28 Aug., 89
Contract No:	F49620-88-C-0053

The in-situ Laser Deposition of Superconducting Thin Film

by

Donald D.W. Chung

ABSTRACT

ArF excimer laser ablation of an $YBa_2Cu_3O_{7-x}$ pellet in 100 - 200 mTorr of O_2 ambient was used to deposit thin superconducting films onto $SrTiO_3$ and MgO substrates at 650 - 780 ^{o}C. The as-deposited 0.6 - 1 μm thick films at 730 - 780 ^{o}C substrate temperature were superconducting, without further high-temperature annealing. Cooled to ambient temperature in situ for 1.5 hours in flowing oxygen gas, the films showed complete diamagnetism and zero resistance up to 89 k with a critical current density of 5×10^{5} A/cm^{2} in zero magnetic field measured at 81 k. Low angle X-ray diffractive analysis showed that all the films were highly oriented with the C-axis perpendicular to their surface. Smooth surface morphology was observed in all films.

Acknowledgements

I wish to thank the Air Force Systems Command and the Air Force Office of Scientific Research for sponsorship of this research. Universal Energy Systems must be mentioned for their concern and help to me in all administrative and directional aspects of this program.

My experience was rewarding and enriching because of many different influences. Dr. Patrick Hemenger Provided me with support, encouragement, and a truly enjoyable working atmosphere. The help of Tim Peterson was invaluable overcoming many technical roadblocks. Dr. Iman Maartense's interest in every phase of this project truly served as source of stimulation. The encouragement and help of Dr. Terry Murray were deeply appreciated.

I. INTRODUCTION:

There has been considerable interest in preparing thin film of high critical temperature superconducting materials both for fundamental research and possible application in electronic devices. Such film preparation are being attempted by many film deposition techniques. Among them, one promising method has been by mean of laser ablation of a bulk target superconducting materials in vacuum or under the low oxygen pressure to deposit the film. Since the low temperature processing will be essential for making sophisticated electronic devices containing the superconducting films the laser deposition method for such film preparation are especially attractive in the potential for producing films with required heat treatment in oxygen at only modest temperature. Among the various types of laser processes short pulsed laser deposition has provided excellent epitaxial films with shallow resistance transition widths and high critical currents. Various researcher have obtained superconducting film without high temperature post-annealing using a background O_2 ambient in the Vacuum chamber.

The elimination of the post-annealing process is extremely important in terms of growing multiple layers of different materials for device applications. Recently the in situ processing of superconducting films at substrate temperature of 650 - 750 C has been reported by a variety of technique. The

electrical, magnetic and structural properties contributed to my assignment to the superconductor group; Materials Laboratory, MLPO division of the USAF.

II. OBJECTIVES OF THE RESEARCH EFFORT:

The thin film processes of high Tc superconducting $YBa_2Cu_3O_{7-x}$ compound can be divided into what require a high temperature annealing subsequent to deposition, and what require no further annealing, or low temperature annealing in Oxygen to achieve optimum superconductivity. Low temperature deposition techniques which do not require further annealing are, by far, the most promising technique for producing films for applications because of the reduced film/substrate interaction, and because a better film morphology is usually obtained. The pulsed laser deposition is one of the most successful method of achieving low temperature film in which it is capable of processing very smooth films with high transition temperature and critical current densities. However, further investigation are called for in this process in order for these to be a definitive evaluation of this technique with respect to applicability of the grown film properties as the practical device materials.

My assignment as a participant in the 1989 summer Faculty Research Program(SFRP) was to study and determine the process and the properties for depositing high quality high temperature

superconducting films and assess porcess parameters of laser deposition condition for optimum properties which would be required suitable for device structure application such as electronic detectors and sensor materials.

III.

High quality thin $YBa_2Cu_3O_{7-x}$ film has been produced by laser ablation technique. In many cases an amorphous film is deposited and a post annealing step upto 900 ^{o}C is necessary to form the crystalline superconducting phase. However, a good orientation of these films, a minimization of grain boundaries, and the prevention of inter diffusion are important points in order to achieve high critical current densities. All of the above is easier to abtain with an in situ growth process, as has recently been demonstrated by several research groups.

For our experiments, We used a ArF excimers laser with 193nm wavelength, 20 Hz, and 80 mJ per pulse. The laser beam was focused on a rotating, sintered $YBa_2Cu_3O_{7-x}$ pellet in a vacuum chamber. The target materials which was evaporated perpendiculary to the substrate surface was then deposited on the substrate at a distance of about 60mm. The substrate was heated up to 850 ^{o}C for cleaning and then cooled to the deposition temperature. Oxygen can be added both the deposition and

cooling processes. The chamber was evacuated by a turbo-molecular pump; the base pressure was less than 10^{-6} Torr. Single crystalline $SrTiO_3$ and MgO with < 100 > Orientation were used as substrate materials. The polished substrates were cleaned in an ultrasonic bath in trichloroethylene, acetone, methanol, and de-ionized water, in that order and heat treated at 850 °C for half an hour in situ before the deposition. The deposition was carried out about 30 minute with a typical deposition rate of 4 Å/sec, and the resulted film thicknesses ranged from .6Um to .9Um. Immediately after the deposition, pure O_2 was introduced into the deposition chamber. The films were then cooled down in flowing oxygen gas to ambient temperature in 1.5 hours.

X-ray diffraction analysis was performed with a slow scan diffractometer. The films were further examined by four-probe resistivity and A.C susceptibility measurements. For the measurments of resistivity, the films were patterned by a sputtering for bridges paths of 5mm length and 100Um width. Four silver contacts were evaporated onto the sample and bonded with gold wires.

To determine the desired film processes, we first investigated the film properties as a function of several deposition parameter such as the substrate temperature, oxygen pressure and target-substrate distance. The film properties were then evaluated by

introduction of oxygen jet into the laser, ablated plasma was found to be a key for in situ processing of superconducting thin film at 650 C. Further reductions in deposition temperature have been reported by the incorporation of an oxygen plasma. So far, epitaxial film growth of YBa_2Ca_{3-x} on $SrTiO_3$ has yielded films with the highest current densities, the sharpest resistance transitions, and in general, the best overall properties.

Superconducting thin film processes and control programs are particularly interested in space application for detectors and sensor devices in Materials Laboratory of MLPO of the USAF. A number of sensor devices have been demonstrated with high Tc superconducting thin films; namely, superconducting quantum interference devices(squids), tunnel junction, and a fast nonlinear switch for noise discrimination in digital circuits. Special attention is directed to the possbility of optical and infrared detection using these new materials.

My research interests have been in the area of application of a variety of thin film depositions techniques in the investigation of electrical, magnetic and structural properties as function of processing parameters. My work on the deposition of $YBa_2Cu_3O_{7-x}$ superconducting film by RF and DC magnetron sputtering in which the principle of deposition is complementary to the laser ablation deposition, which is in principle, the same physical vapor deposition, and characterization of the film in terms of

A.C magnetic susceptibility measurement and X-ray diffraction analysis. The in situ film growth behavior was depending sensitively on the substrate temperature and the oxygen pressure. Films deposited at a substrate temperature lower than 600 ^{o}C were semicrystalline and had to be annealed to 900 ^{o}C to form the desired crystal structure. At a substrate temperature higher than 650 C the film had grown in situ crystalline. For the epitaxial growth with the C axis perpendicular to the substrate plane, oxygen pressure between 100m Torr - 200m Torr and a substrate temperature between 730 and 780 ^{o}C were optimal. The X-ray diffraction pattern indeed showed a highly < 001 > oriented film grow expitaxially on both $SrTiO_3$ and MgO.

The quality of the C - axis orientation was also documented by observing the(001) peak from the x-ray diffraction pattern. It has been reported in the literature that the occupation of the oxygen sites in the lattice is strongly correlated with the c - axis parameter and the critical temperature. Films quenched after the deposition showed no superconductivity. For sample cooled slowly, no additional post-heattreatment step was necessary to obtain high quality superconductivity films. Although most of the films were exposed to the substrate temperature of above 750 ^{o}C. Little interdiffusion between the substrate and the film had taken place. For the majority of the in-situ film the resistivity behavior was metallic. We have observed critical transport current density values Jc above 10

b. The laser power and pulse rate during deposition must be controlled and optimized.

c. The experimental condition for low temperature deposition must be established for device application.

d. The oxygen content of the film after the deposition and cooling process must be monitored in junction with film property change.

e. The high dielectric constant and loss tangent of $SrTiO_3$ substrate would limit its practical utility, particularly in high-frequency microelectronic applications. Some other types of substrate such as NdGaO, LaGaO ,LaAlo which have good dielectric constants at high frequencies must be established for laser deposition condition.

f. Superconducting thin films of the TlBaCaCuO system must be made by laser ablation. In this case, a high-temperature anneal was used to produce high Tc materials. The high temperature annealed film usually produced a very rough and porous structure and are not suitable for further processing for electronic applications. The in-situ processing of the TlBaCaCuO film must be developed for the optimum surface condition as well as film properties.

A/cm^2 in above liquid-nitrogen temperature(81k).

In conclusion, we have succeeded in preparing epitaxial $YBa_2Cu_3O_{7-x}$ films with high critical current densities by laser ablation in an easily reproducible one step process. No additional oxygen plasma source was needed for the in situ crystalline growth. The laser beam itself had activated the necessary oxygen at every pulse. This was possible because of the high pulse energy.

IV. RECOMMENDATIONS:

The in-situ deposition of high critical temperature superconducting films ($YBa_2Cu_3O_{7-x}$) on SrTiO (100) substrate by an ArF excimer laser have been successfully accomplished without additional system modification. However, the evaluation of data showed a room for improvement in the future deposition condition by implementing the existing system modification in the following areas;

a. The accurate substrate(sample) temperature measurement must be established by installing a new substrate holder stage(including heating source) perhaps with a silver block which may be rotated during deposition. The film growth behavior must then be monitored with this new system modification.

REFERENCES

SINGH, R.K., et. al., In situ processing of epitaxial Y-Ba-Cu-O high Tc superconducting films on(100) SrTiO and(100) YS-ZrO Substrates at 500-650 C. Appl. Phys. Lett. 1989, Vol 54(22), PP. 2271-2273.

Bauerle, D., Lase-Induced formation and surface processing of high-Temperature Superconductors. Appl. Phys. A, 1989, Vol. 48, PP. 527-542.

Koren, G., A. Gupta, and R.J-Baseman, Role of atomic oxygen in the low-temperature growth of $YBa_2Cu_3O_{7-r}$ thin films by laser ablation deposition, Appl. Phys. Lett., 1989, Vol. 54(19), PP. 1920-1922.

Mogro-Campero, A., et, al., Epitaxial growth and critical current density of thin films of $YBa_2Cu_3O_{7-r}$ on $LaAlO_3$ Substrate, Appl. Phys. Lett., 1989, Vol. 54(26), PP. 2719-2721

Witanachchi, S., H.S. Kwok, X.W. Wang, and D.T.Shaw, Deposition of superconducting Y-Ba-Cu-O films at 400 °C without post annealing, Appl. Phys. Lett., 1988, Vol. 53, PP. 234-236

USAF-UES SUMMER FACULTY RESEARCH PROGRAM/

GRADUATE STUDENT RESEARCH PROGRAM

Sponsored by the

AIR FORCE OFFICE OF SCIENTIFIC RESEARCH

conducted by the

Universal Energy Systems, Inc.

FINAL REPORT

An Intelligent Neural Model for Recognition of Input/Output Patterns for a Molecular Beam Epitaxy Process

Prepared by:	Kenneth R. Currie, Ph.D., P.E.
Academic Rank:	Assistant Professor
Department and	Department of Industrial Engineering
University:	Tennessee Technological University
Research Location:	Materials Laboratory WRDC/CA-M Building 653 Wright-Patterson AFB, OH 45433
USAF Researcher:	Major Steven R. LeClair, Ph.D., P.E.

Date:	02 Aug 89
Contract No:	F49620-88-C-0053

An Intelligent Neural Model for Recognition of Input/Output Patterns for a Molecular Beam Epitaxy Process

by

Kenneth R. Currie

ABSTRACT

This paper discusses the problem of pattern recognition as applied to the rapid characterization of a Molecular Beam Epitaxy (MBE) process. The MBE process is a complex and difficult process to control, typically resulting in low production yields. The characterization of new materials may take months before the process can produce quality, repeatable results. This paper reviews the application of neural networks to recognize patterns within the input/output relationship of MBE process variables. The objective is the ability to self-improve process knowledge and thereby decrease the time necessary to find acceptable ranges for producing quality parts. Further research is suggested in order to incorporate the concepts of neural networks into a Qualitative Process Automation (QPA) philosophy that will make the MBE process both "self-directed" and "self-improving".

Acknowledgements

I would like to thank the Air Force Systems Command and the Air Force Office of Scientific Research for providing the financial support which has allowed me to initiate this research. I would also like to thank UES, Inc. for the administrative help which they provided throughout the summer.

I am particularly grateful to the people of the Materials Laboratory, who worked with me this summer. Major Steven LeClair provided invaluable guidance and motivation during the entire project for which I am very grateful. I would also like to acknowledge the interest shown by Dr. Melvin Ohmer and his helpful suggestions. Captain Oliver Patterson was also extremely helpful in acting as a liaison between myself and the personnel of WUD 50. Finally, I would like to express my deepest gratitude to the personnel of WUD 50 for enabling me to collect valuable information about the Molecular Beam Epitaxy process throughout the summer.

I. INTRODUCTION:

Molecular Beam Epitaxy (MBE) is a state of the art technique for growing thin film epitaxial layers for semiconductor devices in the microwave/digital and opto-electronic areas. Several optical and microwave devices have already found specific military applications. The MBE process is a very complex and unique process for growing epitaxial layers that conventional processes are unable to produce.

MBE utilizes advances in vacuum technology to create an implosion of a vaporous compound upon a rotating substrate at the molecular level. The result is a high degree of control of film thickness and surface morphology between layers. Another advantage of MBE is the capability of making surface and beam analyses, if not directly then indirectly, while the growth is in process. However, there are stumbling blocks to the widespread use of MBE as a production tool such as contamination and lack of precise process control, resulting in low yields. Typically, the empirical characterization of the process takes several months to produce a single, new material type that achieves the desired optical, electrical, and molecular properties.

The Materials Laboratory of the Wright Research Development Center at Wright-Patterson Air Force Base is interested in several facets of the MBE process. Research is being conducted in device type characteristics, computer modeling of the atomic interactions, control of process related variables, and an intelligent model to aid in the rapid characterization of operating parameters for new materials. The latter research area is the focus of this report.

My research interests are in the identification of trends or patterns in data that aid in the simplification of a complex task. Research into the classification of parts and machines in a

manufacturing setting (otherwise known as Group Technology) has shown the significance of pattern recognition to simplifying complex manufacturing tasks such as scheduling, process planning, and engineering design and/or retrieval. There are several techniques for pattern recognition including statistical, fuzzy clustering, and more recently using neural models. It is my interest in the advances of neural modeling that contributed to my selection by the Materials Laboratory for this assignment.

II. OBJECTIVES OF THE RESEARCH EFFORT:

As stated in the introduction the empirical characterization of the MBE process takes several months to produce a single, new material type that achieves the desired optical, electrical, and molecular properties. The interaction of several of the process variables along with a non-linear input/output relationship make this a non-trivial task.

My assignment as a participant in the 1989 Summer Faculty Research Program (SFRP) was to develop an intelligent neural model that would aid in the rapid characterization of the MBE process for new materials. Using a neural network software package called NNET (a trademark of AIWARE) a neural network model was constructed to identify patterns and trends of input/output relationships. The model was to determine a "recipe" of initial set points for operation of the MBE machine given a set of input parameters for growing a thin layer material(s), with the desired material characteristics. Historical process information was used as a knowledge base for training the network to associate input cues to a corresponding output pattern.

Historical data was thought to have existed that would aid in the characterization of the neural model, however the data available was too limited and to difficult to obtain within the ten week period. In the absence of sufficient historical data to model the MBE process,

the project objectives were changed to develop a proof of concept neural network utilizing simulated data assuming a variety of underlying causal input/output effects. The secondary objective was to define a plan for incorporation of the neural network output to improve control of the MBE process.

III. PATTERN RECOGNITION AND NEURAL NETWORKS:

The problem of pattern recognition as applied to the MBE process is one of recognizing trends and response surfaces of multivariate input data, and predicting an estimate of an output pattern of variables. In his book on adaptive pattern recognition, Pao [1] classifies the subject into two basic methods. The first method is to classify multivariate patterns as a member of a specific class of patterns. The second method is to estimate output attribute values given a particular mapping of an input pattern.

There are several approaches available for identifying class membership using statistical models for clustering and discriminant analysis [2, 3, 4]. There are also fuzzy clustering techniques when underlying assumptions about the population are unknown or vague [5,6]. More recently the use of neural networks for pattern discrimination has shown a great deal of promise without (the conventional) limiting assumptions [7,8,9]. The free form of neural nets is particularly helpful when dealing with numeric data as is the case in the MBE process. This class of network is also referred to as an auto-associative network and uses unsupervised learning. Unsupervised learning refers to the absence of a training set of patterns in order for the network to classify a new input pattern.

When using statistical models to predict input/output causal effects, distributional assumptions about the input values are critical to the success of the model. Neural networks are capable of establishing very complex mappings from the input space to the

output space such that the output space is linearly separated by hyperplanes. Distributional restrictions are not a problem in neural networks, and their ease of application is a definite advantage over applicable statistical methods. Two particular neural network architectures have provided a measure of success in identifying attribute estimates from a given input pattern; the backward propagation net [10] and the functional link net [11] (Figure 1(a) and 1(b) respectively). Both networks use a delta learning rule, however the back propagation network has a hidden layer thus requiring the use of the generalized delta rule. The functional link requires a functional enhancement of the inputs that helps to identify the proper dimension in which to map the inputs onto the output space. The back propagation allows the hidden layer to search over all combinations of the input nodes in which to find a satisfactory dimension in which to map the input space onto the output space. By apriori inserting a functional enhancement the time necessary to train the model is significantly reduced since the functional link net is not preoccupied with finding the appropriate dimensional structure.

IV. PROOF OF CONCEPT:

Due to a lack of any actual MBE process data a series of experiments was conducted using simulated data to test the feasibility of neural networks for pattern recognition. The neural network package used to facilitate these experiments was NNET 210 a trademark of AI WARE. The reason for selecting this particular software was the availability of both functional link and back propagation networks along with an unsupervised learning (clustering) algorithm.

The data used to test the various neural networks was simulated using the same variables used to model the MBE process. The range of input values was allowed to fluctuate

BACKWARD PROPAGATION NETWORK

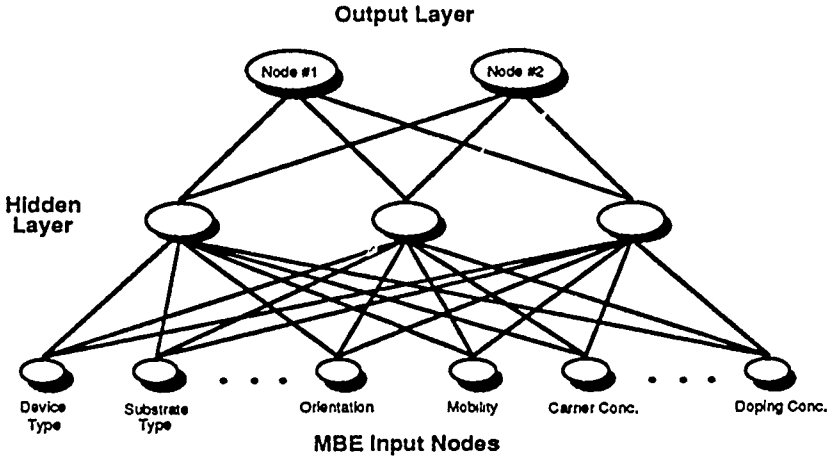


Figure 1(a). Backward Propagation Network

FUNCTIONAL LINK NETWORKS

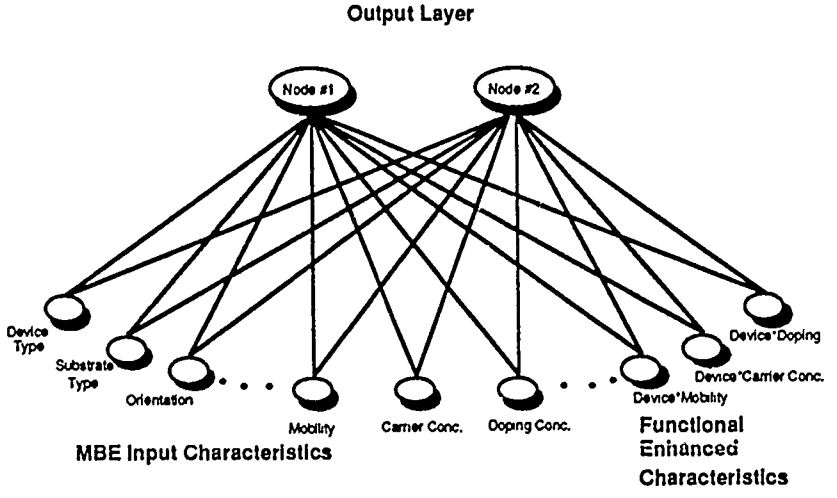


Figure 1(b). Functional Link Network

randomly between prescribed limits and a single output was calculated using one of the following functions to combine input variables:

1) Linear $f(x) = a * x_1 + b * x_2$

2) Polynomial $f(x) = a * x_1^2 + b * x_2^3 + c * x_3$

3) Discontinuous (Linear over half the range and Polynomial over the other half)

A typical network is shown in Figure 2 with the functional enhancements used to create a functional link network for the polynomial case. Several trials were made using various network architectures with some useful observations. It was found that the addition of a hidden layer increased the training time substantially without adding any apparent predictor value. That's not to say that a back propagation network is useless, simply that in the trials that we ran, given the circumstances the back propagation net merely inhibited training. Another valuable insight was the decomposition of the output pattern into a recursive set of networks with only a single output. The accuracy of prediction and the speed of training was significantly improved as opposed to a multivariate output pattern. The unsupervised learning network in NNET was very weak in terms of providing an easy and accurate means of clustering patterns of data. Table 1 is a summary of the key parameters of those networks which successfully trained and provided a reasonable prediction of the output variable.

The **linear** data set assumed all inputs to be linearly combined according to a prescribed equation to predict a single output value. Several enhancements were tested, and the network with the shortest training time and most accurate prediction of the output was a single layer network with no functional enhancements. To test the robustness of the NNET neural network a single variable that comprised approximately 5% of the variability in the output was omitted from the network . The network was still able to predict the output

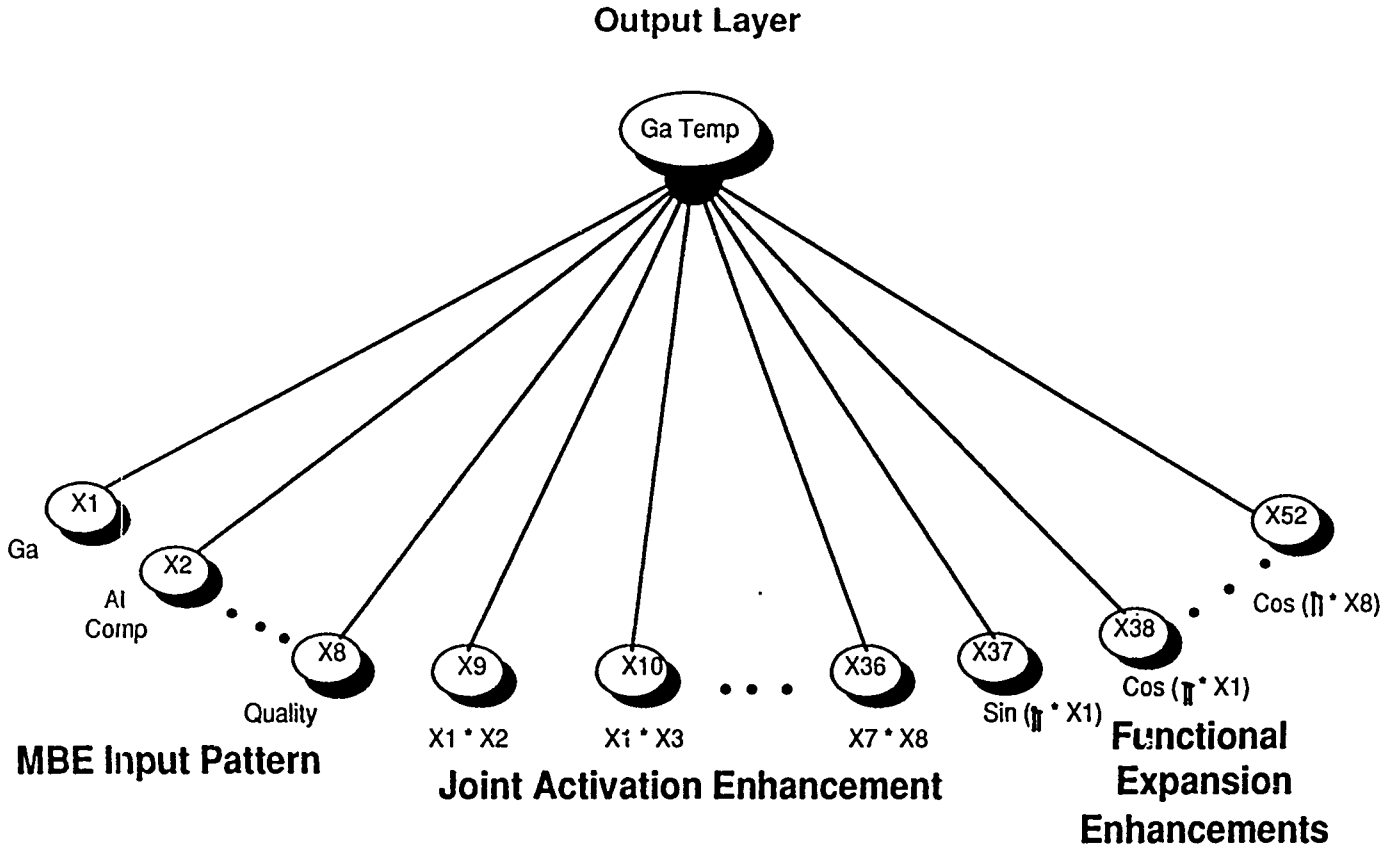


Figure 2. MBE Functional Link Network

TABLE 1. SUMMARY OF NEURAL NETWORK RESULTS

NETWORK CONFIGURATION				TRAINING			CONSULTING	
Input Function	Network Type	No. Input Nodes	No. Output Nodes	No. Patterns	No. Iterations	System Error	% Avg. Error	% Max. Error
Linear	Flat, No Enhan.	10	1	15	185	.00000328	1.01	2.56
Polynomial	JA(2),* FE(1)#	52	1	25	102	.00000097	0.57	1.02
Polynomial	X, X^2, X^3 Terms	24	1	25	549	.00001	0.30	0.53
Discontinuous	JA(2), FE(1)	52	1	20	230	.00000995	0.95	2.58

*

JA(2) denotes a joint activation enhancement of order 2 where the input terms are cross multiplied (i.e. x1*x2, x1*x3, ... , x7*x8)

#

FE(1) denotes a functional expansion of order 1 where each input is enhanced by the sine and cosine of pi times the variable (i.e. sin(*x1), cos(*x1), sin(*x2), cos(*x2), ..., sin(*x8), cos(*x8))

value to within an average of 1% error. When a pattern was tested that fell outside the range of output values within the training set, the error was only 0.325%.

The **polynomial** function was used to generate the simulated data included linear, quadratic, and cubic terms of the original input variables, but no interaction terms. More patterns were necessary to adequately predict the polynomial function. Two different functional enhancements were tried and both were extremely successful. It was observed that the more complex the pattern, the greater number of enhancements and training time is required to accurately predict the output.

The **discontinuous** data set was trained using the same type of functional enhancements as the polynomial , but required less training patterns to achieve similar prediction results. There appears to be an increase in the prediction error as values of the output variable approach the point of discontinuity, but only slightly.

V. "SELF-IMPROVING" MBE PROCESS CONTROL:

The Materials Laboratory at Wright-Patterson AFB has conducted highly successful research with "self-directed" process control of autoclave curing of composite materials. The technique used for "self-directed" control is a philosophy termed Qualitative Process Automation (QPA)[12]. QPA has resulted in time savings of over 70% in curing of composites. Central to the QPA philosophy is the creation of a knowledge base with process specific goals. In applying QPA to the MBE process the knowledge base is currently undefined. QPA requires that the knowledge about the process remain relatively static. If the process changes significantly causing changes in the rules and conditions by which goals are achieved and prevented then the knowledge base must be modified. By coupling QPA with neural networks, discovery of trends and patterns within the

processing information creates a "self-improving", "self-directed" control scheme for the MBE process. The neural network will encode the knowledge of the MBE process in the network by adjusting the weights to account for the strength of the relationship between input and output variables. As new materials are characterized or as the process parameters shift the network will be able to include the new processing information to create an improved knowledge base. In-situ "self-directed" control of the MBE process will still be carried out by QPA, however the knowledge base will be dynamically changing as new materials are characterized, and as ex-situ material properties confirm process trends and patterns.

The overall schematic of how QPA and a neural network interface will work together to self-direct and self-improve the MBE process is illustrated in Figure 3. The control is still left in the hands of the MBE operator, with suggestions from past runs and a predicted "recipe" from the neural network. The operator will input the processing knowledge about the specific run, and QPA will dynamically develop the knowledge bases to perform self-directed control.

Within the neural network interface, both types of pattern recognition methodologies, classifying pattern membership and attribute estimation, will be used in characterizing the MBE process as illustrated in Figures 4(a), (b), and (c). Figure 4(a) shows the input pattern as represented by a multivariate vector of features which are passed through a filter. The function of the filter will be to cluster or discriminate among a historical database of patterns those patterns similar to the input pattern. The resultant output of the filter is a class of patterns relatively similar to the new input pattern which is used to create a transparent mapping for pattern recognition and estimation of the feature attribute values (Figure 4(b)). By using a class of similar patterns as the training set the construction of the transparent mapping and the accuracy of the estimation of attribute values is significantly

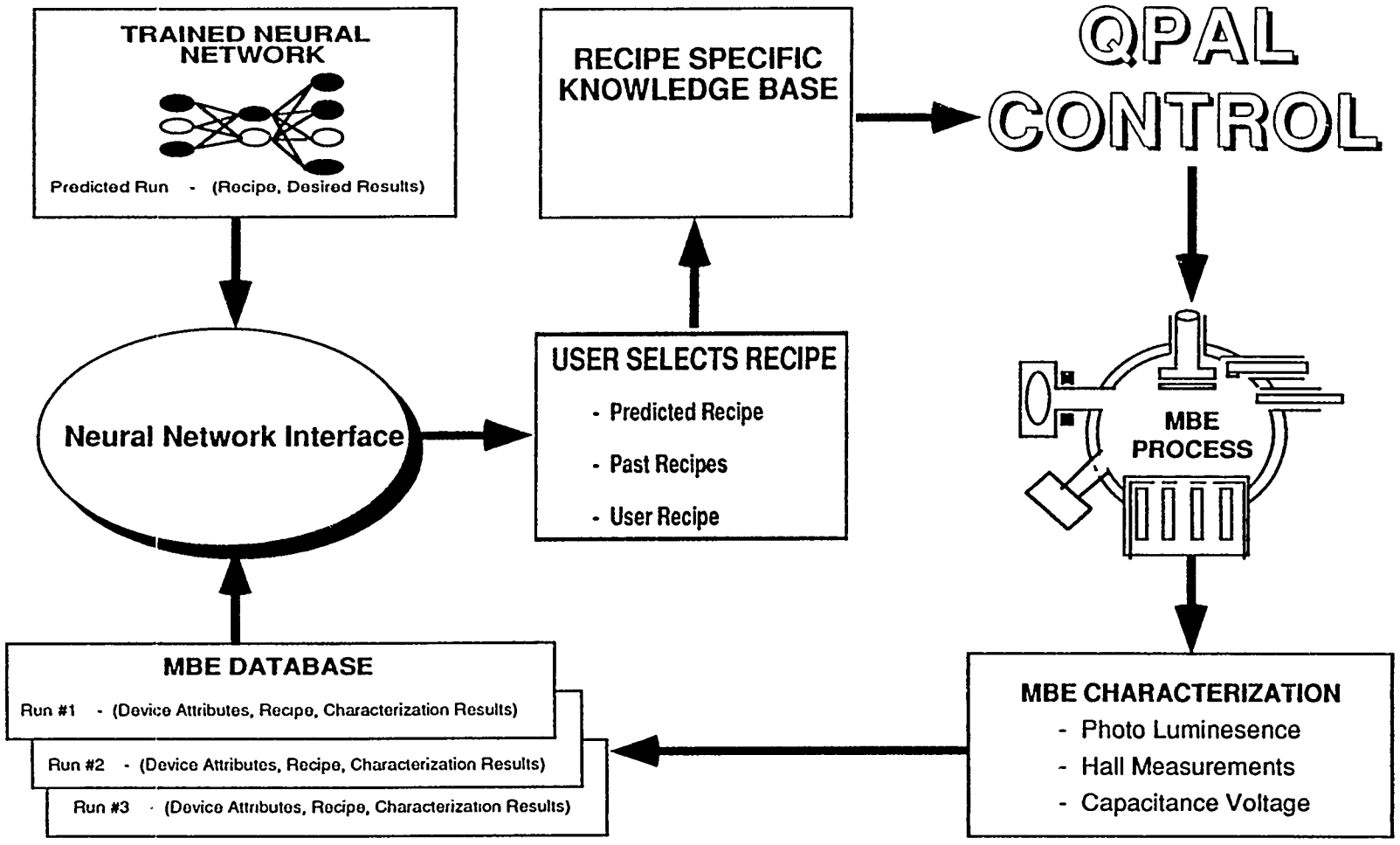


FIGURE 3. Self-Directed, Self-Improving MBE Process Control

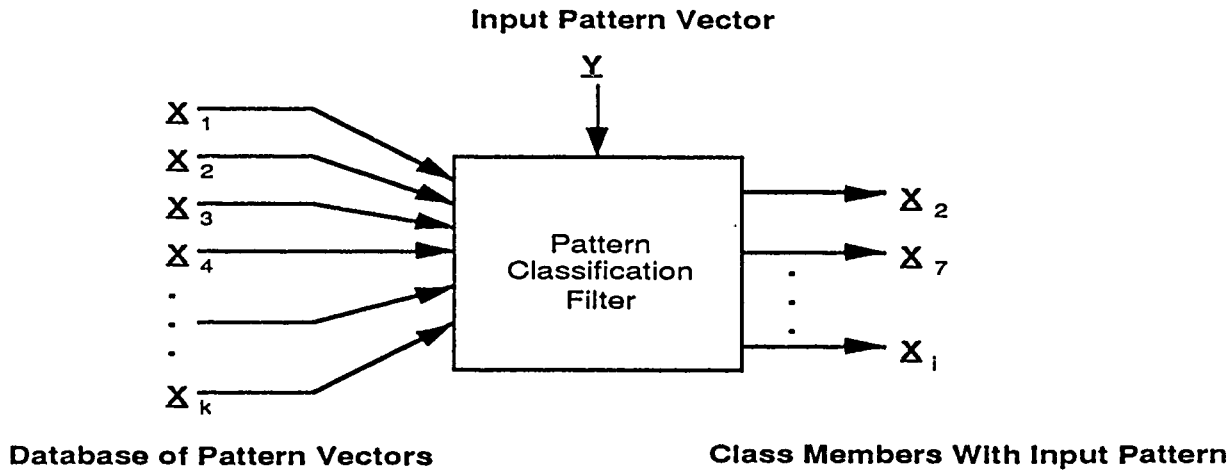


Figure 4(a). Classification for Training Pattern Set

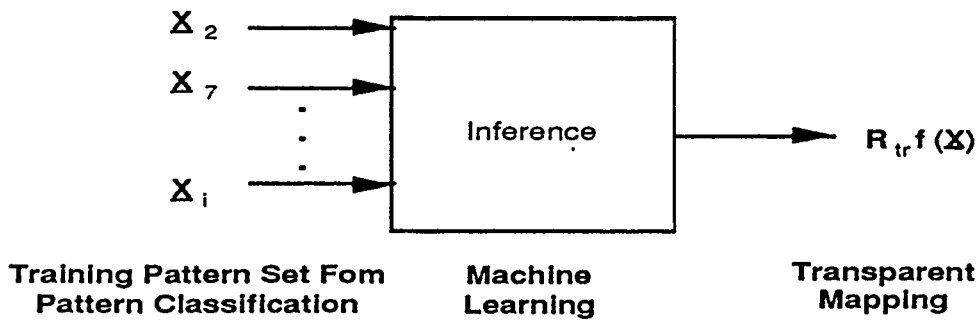


Figure 4(b). Creation of Transparent Mapping [1]

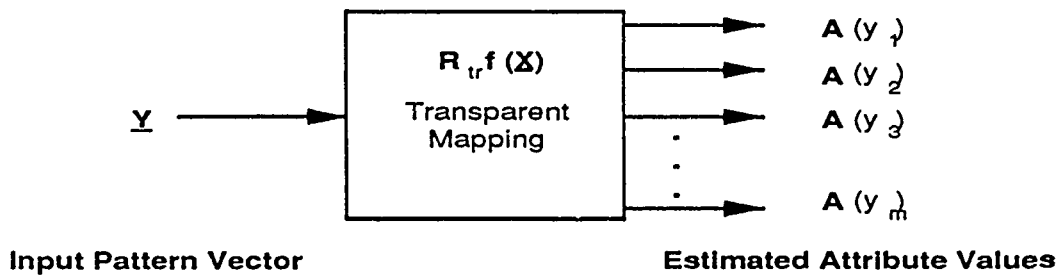


Figure 4(c). Estimation of Attribute Values [1]

improved due to the reduced variability of the input features. The final step (Figure 4(c)) is to use the transparent mapping formed in Figure 4(b) to estimate the appropriate attribute values given a specific input pattern vector.

VI. RECOMMENDATIONS:

To utilize neural networks in intelligently characterizing the MBE process it is imperative that data be collected on any and all variables that have a significant role in mapping the input to output patterns. The minute amount of historical data available during this project, demonstrated that critical information about the process is lacking. Therefore, it is suggested that an automated data acquisition system be developed to monitor process variables throughout the run. By automating this function the critical role of the operator to monitor the process can be accomplished without interruption for recording data.

There is also a need to customize a neural network interface between the operator and the QPA Language (QPAL). This will be the focus of a follow-on proposal to enhance the control of the MBE process and create a "self-improving" process control system. Using the NNET 210 software a user interface can be created which will allow for accessing a database in which data from previous runs may be stored and accessed for knowledge acquisition.

REFERENCES

[1] Pao, Yoh-Han, Adaptive Pattern Recognition and Neural Networks, Addison-Wesley Publishing Co., Inc., Reading, MA, 1989.

[2] Anderberg, M. R., Cluster Analysis for Applications, Academic Press, New York, New York, 1973.

[3] Goldstein, M. and W. R. Dillon, Discrete Discriminant Analysis, John Wiley & Sons, New York, New York, 1978.

[4] Dillon, W. R. and M. Goldstein, Multivariate Analysis Methods and Applications, John Wiley & Sons, New York, 1984.

[5] Kandel, A., Fuzzy Techniques in Pattern Recognition, Wiley-Interscience, New York, 1982.

[6] Bezdek, J. C., "A Convergence Theorem for the Fuzzy ISODATA Clustering Algorithms", IEEE Transactions on Pattern Analysis and Machine Intelligence, Vol. 2, 1980, pp. 1-8.

[7] Carpenter, G. A. and S. Grossberg, "Category Learning and Adaptive Pattern Recognition, a Neural Network Model", Proc. Third Army Conference on Applied Mathematics and Computing, ARO Report 86-1, 1985, pp. 37-56.

[8] Kohonen, T., "Adaptive, Associative, and Self-Organization Functions in Neural Computing, Applied Optics, Vol. 26, 1987, pp. 4910-4918.

[9] Lippman, R. P., "An Introduction to Computing With Neural Nets", IEEE ASSP Magazine, Vol. 4, 1987, pp. 4-22.

[10] Rummelhart, D. E., G. E. Hinton, and R. J. Williams, "Learning Internal Representations by Error Propagation" in D. E. Rumelhart and J. L. McClelland (Eds.), Parallel Distributed Processing: Explorations in the Microstructures of Cognition. Vol. 1: Foundations, MIT Press, Cambridge, MA, 1986, pp. 318-362.

[11] Pao, Yoh-Han, "Functional Link Nets: Removing Hidden Layers", AI Expert, April, 1989, pp. 60-68.

[12] Abrams, F. L., T. L. Lagnese, S. R. LeClair, and J. B. Park, "Qualitative Process Automation for Autoclave Curing of Composites", Air Force Wright Aeronautical Laboratories Technical Report 87-4083, November, 1987.

1989 USAF-UES FACULTY RESEARCH PROGRAM/

GRADUATE STUDENT RESEARCH PROGRAM

Sponsored by the

AIR FORCE OFFICE OF SCIENTIFIC RESEARCH

Conducted by the

Universal Energy Systems, Inc.

FINAL REPORT

SCANNING TUNNELING MICROSCOPY AND BALLISTIC-ELECTRON-EMISSION SPECTROSCOPY

Prepared by:	Peter N. Henriksen
Academic Rank:	Professor
Department and University:	Physics The University of Akron
Research Location:	WRDC/MLBM (Bldg. 652) Wright-Patterson AFB WPAFB, OH 45433-6533
USAF Researcher:	T. W. Haas, Ph. D.

Date:	11 Aug 89
Contract No:	F49620-88-C-0053

SCANNING TUNNELING MICROSCOPY AND BALLISTIC-ELECTRON-EMISSION SPECTROSCOPY

by

Peter N. Henriksen

ABSTRACT

A scanning tunneling microscope from the Department of Physics at The University of Akron has been configured to image surfaces and Schottky-barrier heterostructures of electronic devices fabricated in the Materials Laboratory of Wright-Patterson AFB. Computer code has been written in Microsoft C for: a) adjusting the tip-sample distance, b) acquiring data for topographic images of surfaces, c) acquiring ballistic-electron-emission spectra, and d) data processing for image enhancement. Electronic circuits have been designed and fabricated for: a) obtaining images of metal and semiconductor surfaces at constant tunneling current, and b) measurement of collector currents from the base metal electrode into the semiconductor as a function of tip-to-base bias voltage. The latter is a high-sensitivity (gain= 10^{11} V/A), low-impedance current amplifier. Topographical images with atomic resolution of highly oriented pyrolytic graphite have been obtained.

ACKNOWLEDGEMENTS

I wish to thank the Air Force Systems Command and the Air Force Office of Scientific Research for sponsorship of this research, and Universal Energy Systems for guidance in administrative aspects of the program. In particular, I want to thank Col. Claude Cavender, Jr. of AFOSR, and Milton Danishek, Rodney Darrah, and Ross Morgan of UES for their concern and guidance.

Special appreciation is due Dr. T. Walter Haas of the Materials Laboratory Surface Studies Group at WPAFB for suggesting this particular problem and for his encouragement throughout the summer. The technical assistance and support of Larry Grazulis and Jim Hierholzer with electronics, and David Tomich with computer programming has been invaluable to the research. Help from all members of the Surface Studies Group and their willingness to provide space in a crowded laboratory is greatly appreciated.

I. INTRODUCTION

Despite decades of intensive study, a complete understanding of the electronic structure of metal-semiconductor interfaces is still lacking (Henisch 1984). Of particular interest has been the metal-semiconductor Schottky-barrier (SB) interface, because of its importance in determining electrical properties of electronic devices. SB formation is complicated by several parameters such as interface defect formation and reconstruction, electrode interdiffusion, and chemical reaction; all of which may produce structural inhomogeneities affecting the electronic properties of heterojunction structures. These inhomogeneities, and the fact we are dealing with a buried interface, compound the problem when attempting to ascertain band structure information employing conventional surface analytical techniques. When used, conventional methods yield a complicated average of SB properties if structural inhomogeneities exist in the interfacial plane.

Recently, Kaiser and Bell (1988) developed ballistic-electron-emission microscopy (BEEM), which utilizes a scanning tunneling microscope (STM) for investigation of SB systems, semiconductor heterojunctions, and other interfaces. For the first time, this technique allows investigation and imaging of the electronic structure of buried interfaces, and does so with high spatial resolution.

Figure 1 is a schematic illustration of the electron energy levels of a BEEM experiment when the tunnel tip is positioned within tunneling distance of the base metal of a SB heterojunction. When the base electrode is no thicker than 100 Angstrom, some of the tunneling electrons travel ballistically through the metal, reaching the interfacial region with no attenuation and with little lateral divergence. With the base grounded, electrons reaching the semiconductor (collector) can be detected as a collector current which can be measured as a function of tip bias relative to the grounded electrode. The resulting collector current versus tip bias spectrum provides a direct probe of the buried interface electronic structure. From the schematic it can be seen that the collector current remains zero until the tip bias (V) is equal to the SB barrier height (V_b). Thus, the onset of collector current provides a direct measure of S-B height.

High spatial resolution is a result of being able to place the tunnel tip over the surface with great precision, and conservation of transverse momentum of the ballistic electrons upon entering the semiconductor. These effects result in a lateral resolution of 10 Angstroms for a 100 Angstrom thick base layer, and allows one to obtain spatial images of buried interfacial electronic structures while scanning the tunnel tip over the heterostructure. A simultaneous topographic image of the base electrode can be obtained for comparing geometric features of the surface with electronic features of the subsurface.

II. OBJECTIVE OF RESEARCH EFFORT

The overall objective of the SFR program was to develop facilities for BEEM investigations of SB heterojunctions. For this purpose the following equipment and materials were needed: 1) an STM for positioning and scanning the tunnel tip over the surface of the base electrode, 2) an electronic circuit for driving the STM in a constant current mode to obtain topographic images of the base electrode, 3) electronic circuitry for measuring collector currents as low as 1 pA with 0.1 pA resolution, 4) software for driving the STM, for data acquisition, and for displaying both topographic and BEEM images, and 5) techniques for tip and SB heterojunction preparation.

Prior to this project no STM facilities existed in the Materials Laboratory of Wright-Patterson AFB. After ten weeks of effort, considerable progress has been made in both instrumentation and software development. The project will be continued at both The university of Akron and WPAFB. At WPAFB it will be continued under the auspices of a faculty improvement leave from The University of Akron, and the AFOSR University Resident Research Program; at UA with the aid of an AFOSR Mini Grant. The progress made thus far will be delineated in the following section.

III. ACCOMPLISHMENTS

A. SOFTWARE

Eight programs have been written for setting scanning parameters, data collection, image display, and data manipulation. All programs were written in Microsoft C.

1. "ADJUST" is used in positioning the tip within tunneling range. This program is initiated by entering the bias voltage to be used in subsequent scans. The tip-to-sample distance is then adjusted with specified bias voltage applied to tip. During adjustment, two sets of numbers are being displayed: "z-offset" which is proportional to extension of z-piezoelectric tube, and "current" which is proportional to tip-to-surface distance.
2. "SCAN" acquires x-, y-, and z-position data, allows limited data manipulation, displays a topographical image, and allows one to do voltage spectroscopy at a particular point.
3. "SCAN2" allows one to acquire data for two topographic images simultaneously; one image is obtained while the tip is scanning from left-to-right, the other while the tip is scanning in the opposite direction. A comparison of images provides information on tip quality.
4. "LINE SCAN" allows one to retrieve a stored image and obtain a plot of a particular horizontal or vertical line of the image, i.e., a particular row or column of data array.

5. "SEE" recalls and displays any topographical image which has been stored in the data files, and allows on to do data smoothing by weighting each point, its nearests and next nearest neighbors.
6. "BEEM" simultaneously acquires topographic and collector-current images and displays them sequentially. The program addresses two data files, and topographic and collector-current data are acquired at each position of the tip during a scan.
7. "BEEM2" is a routine similar to BEEM, however, in this case both images are displayed side-by-side for simultaneous visual comparison.
8. "SEEBEEM" allows one to recall and display a particular BEEM image in a manner similar to SEE.

B. ELECTRONICS

The original electronics for controlling the STM were designed to provide topographical images while maintaining constant conductance between tip and sample. With this design the STM could be used in an inelastic-electron-tunneling mode for obtaining vibrational spectra of adsorbed molecules. Such a design is not appropriate for BEEM investigations, thus two additional circuits were required which have been designed and fabricated.

1. CONSTANT CURRENT ELECTRONICS consist of a preamplifier with a feedback loop which maintains a constant current from tip to sample, a low pass filter which blocks high frequencies beyond the preamplifier, and an active bias circuit which controls the tip bias.

2. CURRENT PREAMPLIFIER consisting of an electrometer grade operational amplifier, filters, and additional amplification for collector current measurements.

Both circuits have been constructed and tested for optimal performance, and analog noise levels have been reduced by installing shielded cables and improving grounding techniques.

C. TIP PREPARATION

The quality of images obtained with an STM is directly related to the quality of the tip used in scanning the surface. Ideally, one would like a very sharp tip with tunneling always being from one particular atom. All tips used thus far have been prepared by electrochemically etching 0.01 in. diameter tungsten wire in 4 molar solution of KOH using about 30 V ac. Tungsten provides relatively good and inexpensive tips, and etching techniques and parameters are easily varied until one learns to consistently produce satisfactory tips.

D. TOPOGRAPHIC IMAGES OF HIGHLY-ORIENTED PYROLYTIC GRAPHITE

HOPG consists of planes of carbon atoms forming a hexagonal net. The planes are stacked such that every other atom around a

hexagon is located directly above (or below) an atom in adjacent planes, and the remaining atoms are located above (or below) the center of hexagons in adjacent planes. This arrangement causes the electric potential of alternate atoms around the hexagon to be different. Potentially equivalent carbon atoms in the surface plane are separated by 2.456 Angstroms and are clearly visible as the darkest regions in Figs. 2 and 3, which are STM images of HOPG obtained during this appointment. A portion of the hexagonal net is indicated in Fig. 2. The asymmetry of the hexagons is due to lack of symmetry about the cylindrical axis of the piezoelectric scanner which moves the tip across the surface. Lines connecting adjacent equivalent atoms, which are separated by 2.456 Angstrom, are drawn in Fig. 3.

IV. RECOMMENDATIONS

BEEM is a promising new technique for characterizing the electronic structure at metal/semiconductor interfaces. Results of BEEM measurements can depend sensitively on the quality of the interface between the semiconductor and deposited metal. To ensure characterization of quality SB devices, metal deposition should be done in ultrahigh vacuum to keep the interface free of unwanted adsorbates, and measurements made in an inert atmosphere, including liquid nitrogen, to prevent unwanted oxidation and contamination which may cause deterioration.

An STM specifically for BEEM investigations is being designed which includes several feature to reduce noise and sharpen band

edge and barrier height measurements. The design will includes a new tip holder assembly, a Macor body to reduce thermal effects, improved electronics for data acquisition and driving the STM, and a scanning mechanism and preamplifier which can be submerged in liquid nitrogen.

Image quality is directly related to tip characteristics such as sharpness, cleanliness and state of oxidation. In the future, gold tips will be used since they are less susceptible to oxidation and contamination, and will reduce electrical noise at low collector currents. Techniques for etching and preparing gold tips will be of major concern.

In summary, meticulous care in sample preparation, working in an atmosphere of dry nitrogen, and electronics with sensitive low-level signal detection, good filtering and minimal noise levels are necessary for BEEM measurements. These features will be incorporated in continued research.

As mentioned earlier, the project will be continued as parallel efforts at The University of Akron and WPAFB. It is important for scientists at both laboratories to understand all aspects of BEEM measurements and sample preparation using MBE apparatus. Such an effort will result in unique capabilities for characterizing the various surfaces of GaAs, metal adsorbates on these surfaces, and Schottky barriers formed at the interface of such surfaces.

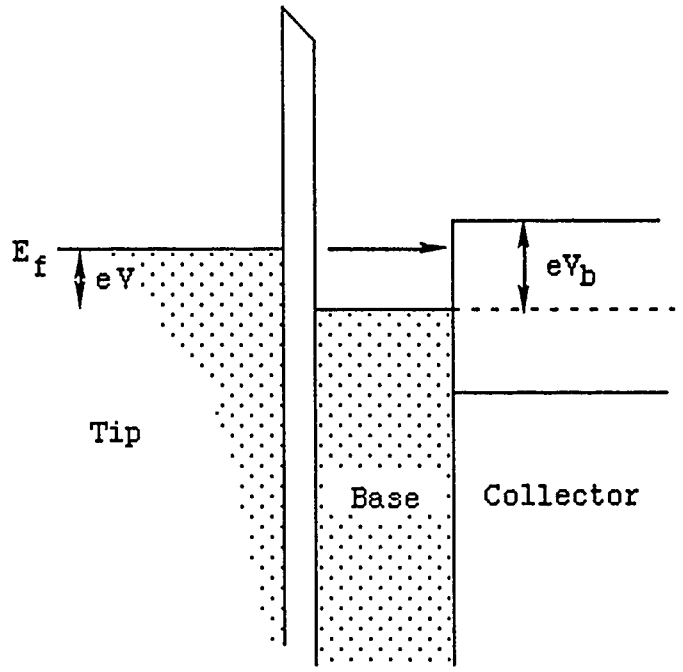


FIGURE 1

Schematic energy-band diagram for three-terminal BEEM measurement. The tip is separated by a vacuum barrier from the base metal. Ohmic contacts are made to the tip, base, and semiconductor collector. Shown is the case for tunnel bias less than the barrier voltage, $eV < eV_b$.

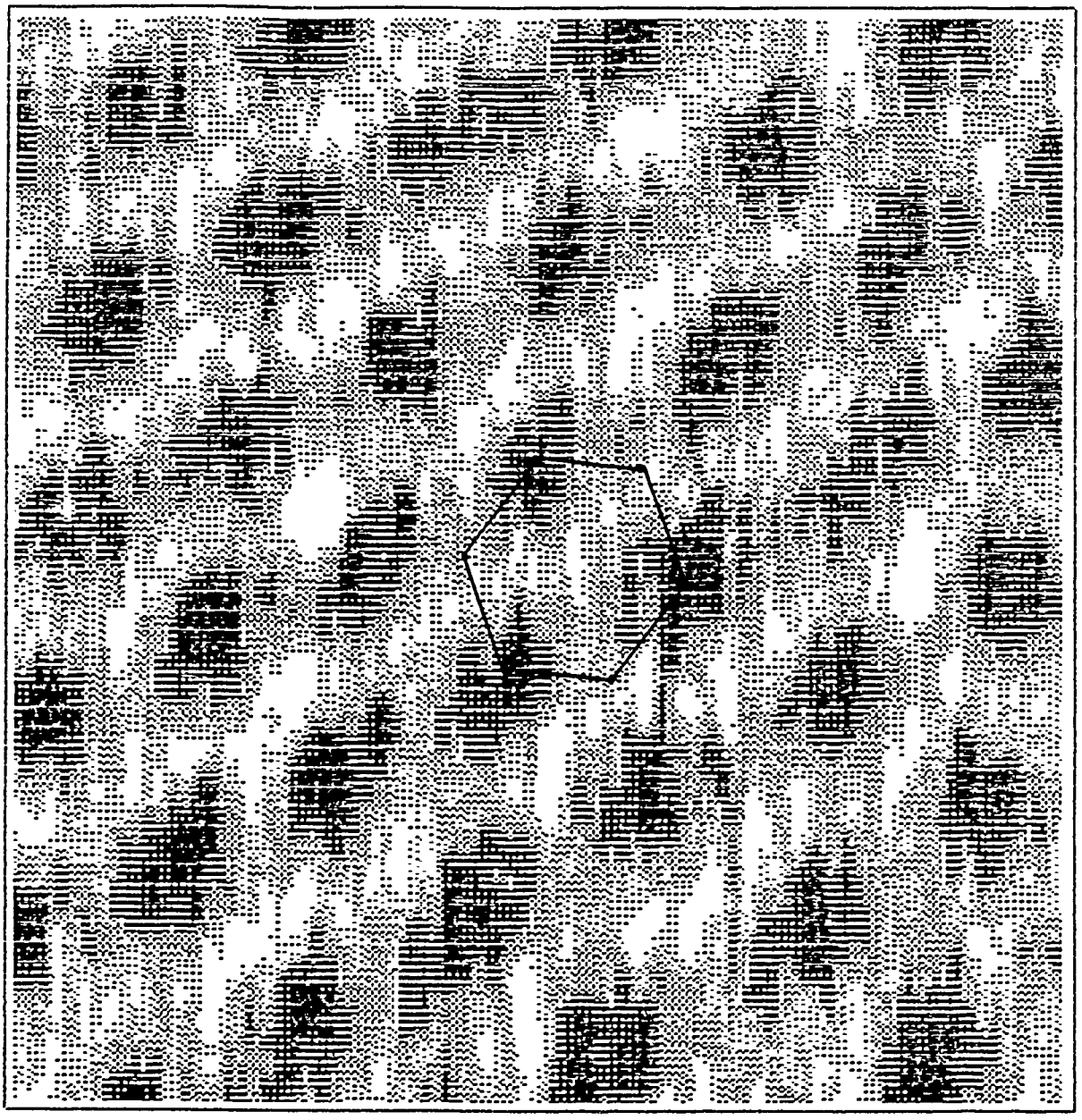


FIGURE 2

Topographical image of HOPG. Dark regions correspond to higher points and white to lower points on surface. In the hexagonal illustration, dark corners represent atoms which are directly above atoms in adjacent planes, while circles indicate atoms located above centers of hexagons in adjacent planes.

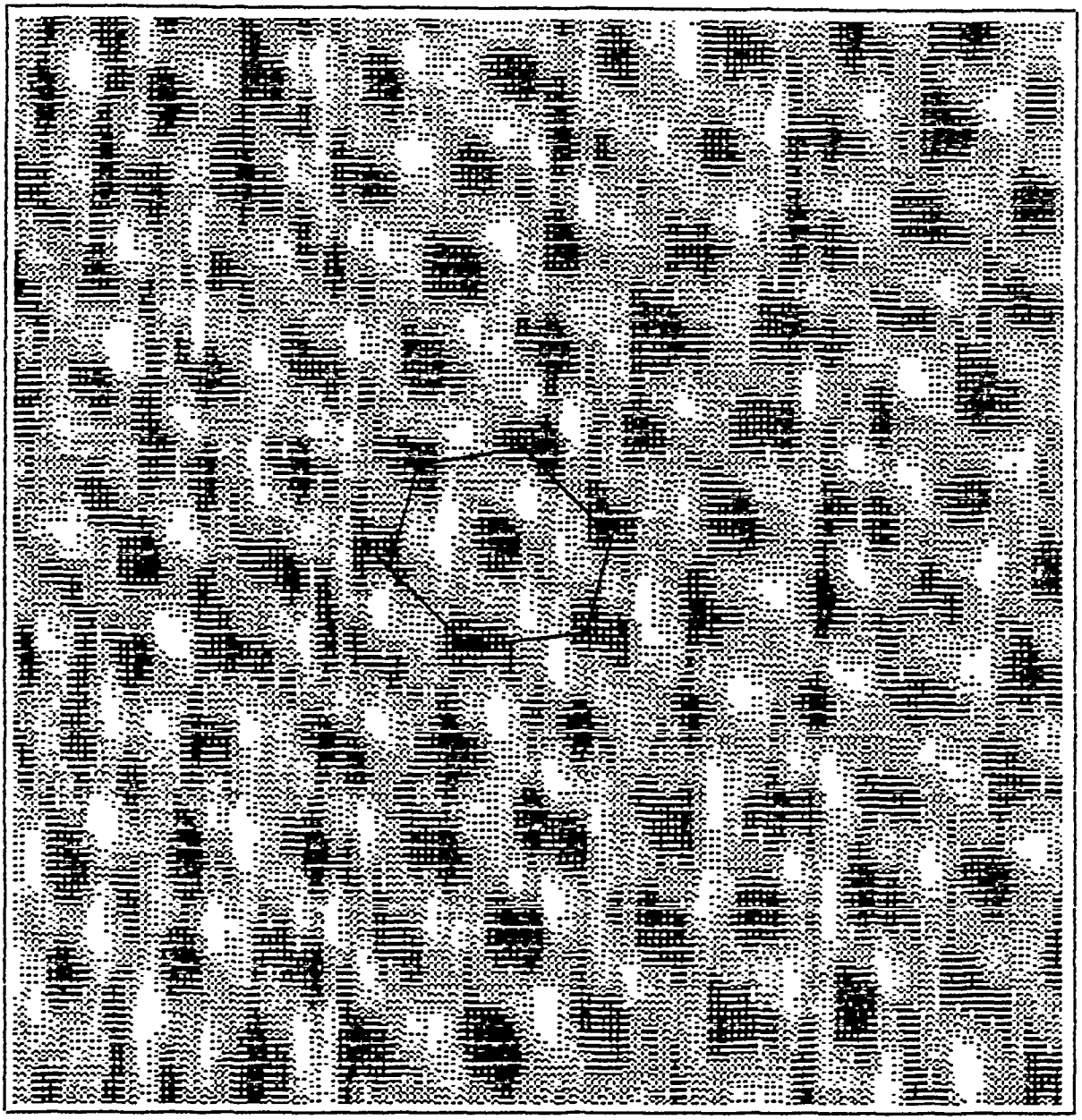


FIGURE 3

Hexagonal array formed by carbon atoms located directly above atoms in adjacent array. The nearest neighbor distance between similar atoms in an array is 2.456 Angstroms. The length of each side of the figure is about 24 Angstroms.

REFERENCES

Journal Publications:

1. W. J. Kaiser and L. D. Bell, "Direct Investigation of Subsurface Interface Electronic Structure by Ballistic-Electron-Emission Microscopy", Physical Review Letters, Vol 60, pp. 1406-1409, 4 April 1988.

2. L. D. Bell and W. J. Kaiser, "Observation of Interface Band Structure by Ballistic-Electron-Emission Microscopy", Physical Review Letters, Vol. 61, pp, 2368-2371, 14 Nov 1988.

Textbooks:

3. Henisch, Heinz K., Semiconductor Contacts: An Approach to Ideas and Models, Oxford, England, Clarendon Press, 1984.

1989 USAF-UES SUMMER FACULTY RESEARCH PROGRAM/

GRADUATE STUDENT RESEARCH PROGRAM

Sponsored by the

AIR FORCE OFFICE OF SCIENTIFIC RESEARCH

Conducted by the

Universal Energy Systems, Inc.

FINAL REPORT

EVALUATION OF CR-SI ALLOYS FOR AEROSPACE STRUCTURAL APPLICATIONS

Prepared by:	Joseph W. Newkirk , James Sago
Academic Rank:	Assistant Professor , Graduate Student
Department and University:	Department of Metallurgical Engineering University of Missouri-Rolla
Research Location:	Wright Research and Development Center High Temperature Materials Branch
USAF Researcher:	Dennis M. Dimiduk
Date:	26 September 1989
Contract No.:	F49620-88-C-0053

EVALUATION OF CR-SI ALLOYS FOR AEROSPACE STRUCTURAL APPLICATIONS

by

Joseph W. Newkirk

James Sago

ABSTRACT

Cr-Si alloys offer important advantages as an aerospace material, including high service temperature and good oxidation resistance. This in-situ composite combines a hard, brittle silicide phase with a softer chromium phase. The silicide phase has a high specific stiffness from room temperature up to 1400C. The soft phase is intended to add damage tolerance by bridging cracks and stopping them from propagating at low temperatures. Different volume percents of the two phases were evaluated and the bend strength measured as a function of temperature. Alloys with high volume percents of the silicide phase had good strength values at temperatures up to 1200C or more. Although toughness tests were not performed during this initial study, microhardness indents were used to demonstrate that the chromium phase could act as a crack bridging material. In addition the microstructural stability of these materials were studied with encouraging results. Finally, further study of these alloys is recommended and specific areas of study are included.

ACKNOWLEDGEMENTS

I wish to thank the many individuals at WRDC who went out of their way to make my work in the Materials Laboratory as productive and rewarding as possible. I especially want to acknowledge the help of Dennis Dimiduk and Dan Miracle at WRDC and Madan Mendiratta and Lou Henrich at Universal Energy Systems. The support of the Air Force Office of Scientific Research, through contract F49620-88-C-0053 with Universal Engery Systems, Inc., is greatfully acknowledged.

I. INTRODUCTION:

The Air Force is very interested in the area of intermetallic alloys for high temperature applications. The strong ordering of these alloys leads to many useful properties of interest for aerospace applications. Included in these properties are high stiffness and good high temperature specific strength. Unfortunately, the strong ordering also tends to make intermetallic alloys extremely brittle at ambient temperatures and give them a correspondingly low damage tolerance. In addition several other problems, such as fabrication and oxidation resistance at elevated temperatures, will have to be solved before this class of materials makes a significant contribution in aerospace applications.

An approach to improving the damage tolerance of these materials, currently receiving a great deal of attention is ductile second-phase toughening(1). Ductile second-phase toughening involves incorporating a dispersed ductile phase in a brittle matrix, in this case an intermetallic alloy. This approach has been used successfully at the Materials Laboratory to dramatically improve the fracture toughness of a Nb-Nb_5Si_3 alloy. Certain alloy compositions of Si in Nb will result in Nb metal dispersed throughout a Nb_5Si_3 matrix after solidification from the melt (2,3). As solidified samples showed an improvement in toughness with a concomitant loss of strength. Samples which were subsequently extruded developed even better properties (4). This improvement in properties was not deleteriously effected by a high temperature anneal.

This past summer, I began a preliminary investigation of the alloy Cr-Cr_3Si in a study similar to that in progress on the Nb-Si alloy. Si is soluble in Cr up to about 7 atomic %, undergoes a eutectic reaction at about 15% Si and 1705 C, and forms Cr_3Si between 22 and 25%. Hypereutectic alloys (Si contents between 15 and 22%) upon solidification from the melt form a dispersed Cr phase in a matrix of Cr_3Si. Such a microstructure may be suitable for ductile second-phase toughening of the Cr_3Si phase. The Cr-Si alloy system offers two significant advantages over the Nb-Si system. First, the specific gravity will be significantly lower than is possible with Nb making it more attractive for aerospace applications and second, Cr is inherently more resistant to oxidation at elevated temperatures. If an alloy based on Cr_3Si can be given sufficient toughness it may be a very attractive material for structural applications.

My research interests have been in the area of high temperature aerospace alloys and particularly intermetallic alloys. My experience with the metallography,

testing and mechanical behavior of other intermetallic systems such as Ti-Al and Co-Al resulted in my being assigned to the high temperature materials group at WRDC to work on this study.

II. OBJECTIVES:

The purpose of the ten week tenure at the Materials Laboratory was to investigate the Cr-Si system in the composition range between 5 and 25% Si. The overall goal of the study was to determine if this system showed promise as a potential structural material and whether further study of this material should be undertaken. In order to accomplish this, three short term goals were decided upon. The three involved the microstructural stability, the high temperature strength and the ability of Cr to provide toughening.

The microstructural stability concerns whether microstructures produced during processing will retain the same sizes and shapes during prolonged high temperature exposures. The temperature at which the microstructure is no longer stable will be a potential limit on the maximum service temperature of the alloy. In order for this system to compete with existing high temperature alloys the maximum service temperature must be well above 1100C, preferably above 1400C.

Chromium, like all refractory metals, is brittle at low temperatures and ductile at high temperatures. The ductile-brittle transformation temperature for chromium depends on its purity and its thermomechanical history(5). Therefore the question arises as to whether chromium will behave in a ductile manner when constrained by a brittle matrix and at what temperature will the chromium, saturated with silicon, revert to brittle behavior. The goal therefore is to determine if the chromium phase would act as a ductile second-phase in the silicide matrix.

The third goal was to measure the strength of the Cr-Si alloys as a function of temperature. In order to compete with existing alloys the Cr-Si system must be capable of producing alloys with a significant specific strength advantage at high temperatures.

III. PROCEDURE:

Samples of Cr-Si with compositions as given in Table 1 were prepared by arc-melting in a argon atmosphere. The argon was gettered by first melting a titanium button before melting the Cr-Si charge. Each sample was flipped over and remelted at least four times to improve the homogeneity. The melt compositions

were chosen so that there would be a hypoeutectic, a eutectic, and a hypereutectic microstructure. In addition a single phase Cr solid solution alloy and a single phase silicide sample were chosen to provide a baseline. Some of the first melts were made accidentally with bad stock and in addition the eutectic sample was off significantly in composition (see Table II). Therefore two more melts (#10 and #11) were added to the original list. A series of small melts which were intended to help determine the eutectic composition were all too low in silicon content to fulfill the intended purpose and are not included in Table I (#3,4,5,9).

Table I

Nominal Composition of Melts Used in This Study

Melt #	Composition (at%)	Geometry	Weight (gm)
1	Cr-5.4Si	cigar	250
2	Cr-12.2Si	cigar	250
6	Cr-15.5Si	button	50
7	Cr-18.6Si	cigar	250
8	Cr-24.6Si	cigar	250
10	Cr-12.2Si	button	250
11	Cr-15.5Si	button	250

The microstructural stability was studied by comparing the as-cast samples to samples that had been annealed at various times and temperatures and furnace cooled. The samples were annealed at 1400C for 1/2, 16 and 100 hours and for 25 hours at 1500 and 1600C. A flowing argon atmosphere which was titanium gettered was used to prevent oxidation. After annealing samples were prepared for examination by grinding and then polishing with 0.5 and 0.25 micron alumina. The samples were final polished with 0.06 micron colloidal silica. This process produced a very flat surface with a slight relief in the two phase alloys. This relief was only visible when using differential interference contrast in the optical metallograph. In addition to optical metallography, the backscattered electron mode of the scanning electron microscope was used to study the microstructure and the compositions measured with an electron microprobe.

Bend strength bars were machined by wire EDM and then ground and final polished with 0.05 alumina. The nominal dimensions were; L-1.25", W-1/4", and T-1/8". The bend bars were tested on an Instron universal test machine equipped

with a vacuum furnace. The samples were allowed to soak for 20 minutes at temperature before being tested. All tests were done with a four point bend fixture at a crosshead speed of 0.01"/min. The proportional limit was used to determine the yield strength. Since only a limited number of test specimens survived the preparation without breaking, the test temperatures depended on the sample composition and the number of each available.

The approach to determining whether chromium could act as a ductile phase toughener was threefold. First, the bend tests of the chromium solid solution alloy determined the temperature dependence of the ductility. The behavior of the chromium phase in the two phase alloys was predicted from this result. Second, the fracture surface of broken bend bars were examined in the scanning electron microscope for evidence of ductile behavior in the chromium phase. Third, a vickers microhardness indenter was used to deliberately crack the surface and provide a toughness comparison of the various alloys. For this purpose a 1 kg load proved suitable. Concurrently, the microhardness of the various phases was measured at lower loads.

IV. RESULTS AND DISCUSSION:

The actual melt compositions are listed in Table II. Several problems occurred in making the alloys. There were very high oxygen contents in some of the alloys due to some contaminated starting material as mentioned in the procedure section. However, even the melts made with pure starting materials had a high total interstitial content, which may alter some of the mechanical properties. In addition, tungsten was found in relatively large quantities in all of the melts for which it was analyzed. Tungsten has been shown to be a strong solid solution strengthener in chromium and could also effect the properties of the alloys (6).

Table II

Actual Melt Compositions as Determined by Chemical Analysis

Melt #	Nominal	Nom.(wt%)	Si	W	O(ppm)	N(ppm)	C(ppm)
1	Cr-5.4Si	Cr-3Si	2.24	-	3510	210	65
2	Cr-12.2Si	Cr-7Si	6.1	-	1300	260	22
6	Cr-15.5Si	Cr-9Si	7.2	-	730	40	56
7	Cr-18.6Si	Cr-11Si	10.7	-	80	180	85
8	Cr-24.6Si	Cr-15Si	12.3*	-	110	190	51
10	Cr-12.2Si	Cr-7Si	6.6	1.6	80	260	-
11	Cr-15.5Si	Cr-9Si	8.7	1.8	40	130	-

- Not analyzed

* Sample Inhomogeneous

There was a large difference in the 250 gram melts as to whether they could be machined into bend bars. After machining, grinding and polishing no bars survived from any melt which had a button shape. However all cigar-shaped melts yielded bend bars. I believe this difference between the two geometries is due to residual stresses developed during cooling on the copper hearth. The cigar melts are finished by running the electrode down the length of the cigar resulting in more even cooling. In contrast the buttons are finished by running the electrode around the outside of the button, causing large stresses to build up in the center of the button. The 100% Cr_3Si alloy broke into many small pieces during cooling from the melt and the routine handling afterwards.

All of the alloys contained inclusions, whose number varied proportionally with the oxygen content. The electron microprobe determined that these inclusions were Cr-Si oxides. The as-cast microstructure of four of the two-phase alloy melts is shown in Figure 1. Figures 1b and 1c illustrate the fine lamellar eutectic structure formed upon solidification. At low volume fractions of the eutectic microconstituent the eutectic divorces as seen in Figures 1a and 1d. The results in the lower volume percent phase having a high degree of connectivity. In all cases the proeutectic matrix has a dendritic structure.

The results of annealing at 1500C for 24 hours are shown in Figure 2. Large blocky precipitates appear in the matrix phase and the fine lamellar structure coarsens. Electron microprobe data of the phases was taken on the as-cast and annealed samples and compared (Table III). The results reveal that in the as-cast

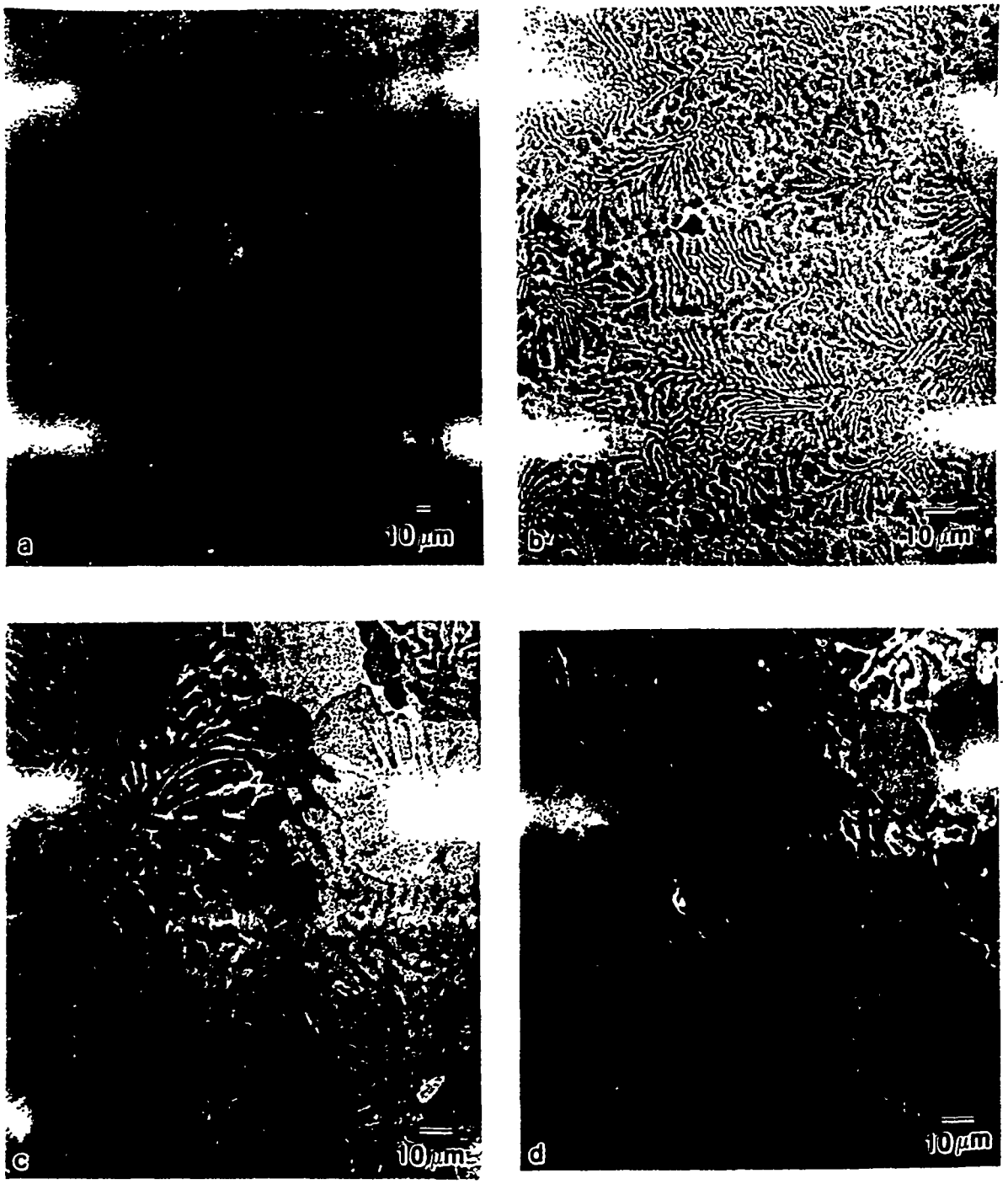


Figure 1. Backscattered images of the as-cast microstructure of the two phase alloys. a) Melt #2, Cr-12.2Si; b) Melt #6, Cr-15.5Si; c) Melt #11, Cr-15.5Si; d) Melt #7, Cr-18.6Si.

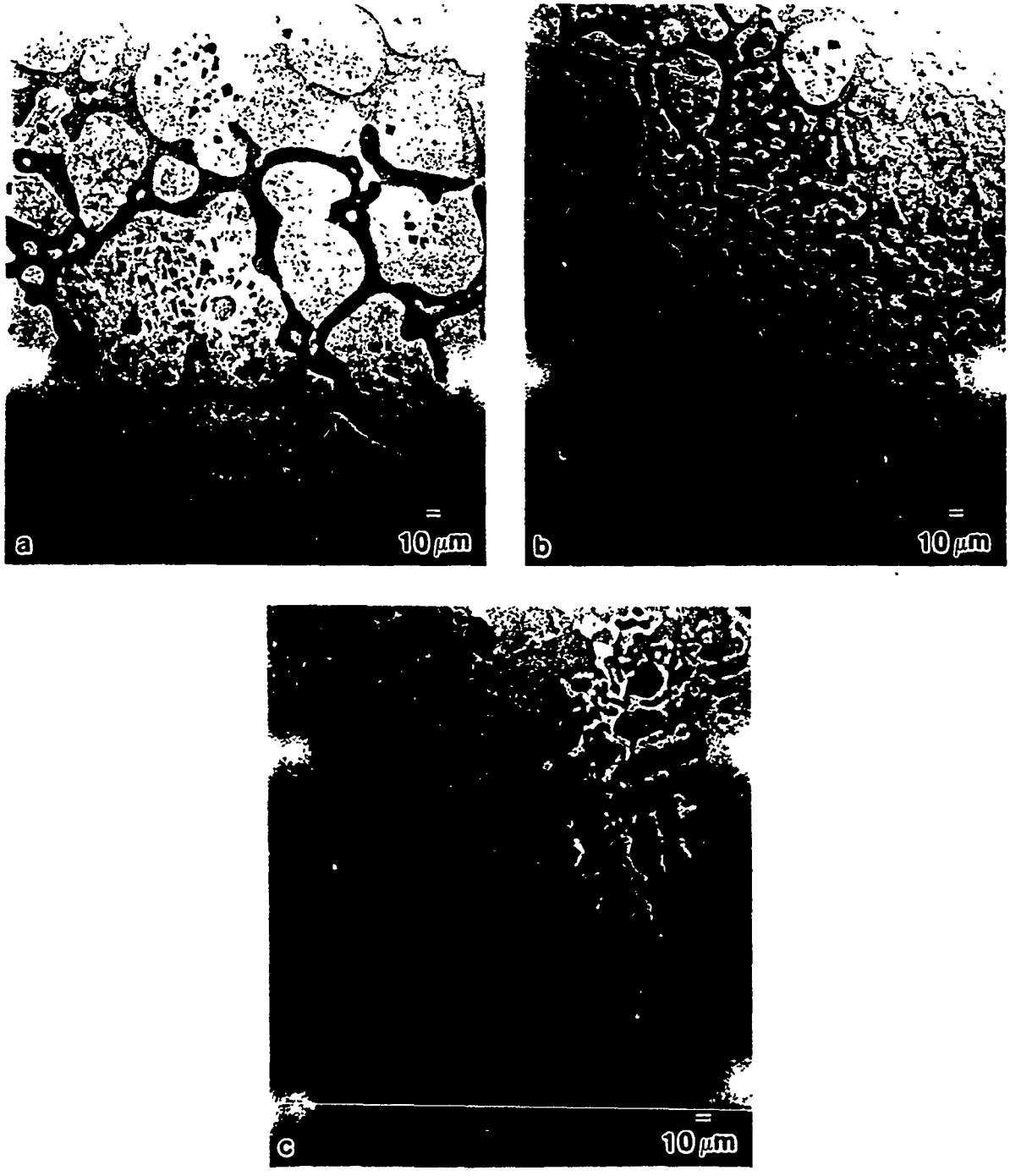


Figure 2. Backscattered images of the two phase alloys annealed at 1500C for 25 hours. a) Melt #2, Cr-12.2Si; b) Melt #11, Cr-15.5Si; c) Melt #7, Cr-18.6Si.

samples the chromium phase has the eutectic composition and is therefore supersaturated at room temperature. During annealing and furnace cooling the supersaturated chromium phase precipitates Cr_3Si particles, which coarsen, and achieves the equilibrium concentration. This precipitation should also occur at the boundaries of the chromium phase lamellae resulting in an apparent thickening of this phase.

Table III

Electron Microprobe Data for High and Low Si Phases

		As-Cast		Annealed(1400C,16hrs)	
Melt #	Nominal	Low Si	High Si	Low Si	High Si
2	Cr-12.2Si	10.64(0.83)	21.99(0.25)	6.90(0.17)	22.31(0.20)
6	Cr-15.5Si	10.37(0.49)	21.33(0.25)	6.79(0.22)	22.40(0.32)
7	Cr-18.6Si	8.33(0.60)	22.60(0.21)	6.68(0.22)	22.42(0.38)
Solubility limits		at 1705C		at RT	
		9.5	22.5	6.5	22.5

The stability of the two-phase alloys was of mixed character at 1400C. For example melt #10 (Cr-15.5Si), which is hypoeutectic, after 1/2 hour had many fine precipitates. After 100 hours at 1400C the precipitates had coarsened extensively, but the as-cast phase sizes and shapes remained nearly constant with only a slight thickening of the silicide phase. This thickening is to be expected as the alloy approaches chemical equilibrium. In contrast, the fine eutectic structure contained in some of the alloys was replaced by a coarser lamellae structure (same as Figure 2b). The proeutectic structure in the hypereutectic alloys was stable (same as Figure 2c).

The microstructure in the two-phase samples annealed at 1500C for 25 hours looked virtually indistinguishable from the 1400C for 100 hours samples. However, at 1600C for 25 hours there was considerable coalescence of the chromium phase. In the hypoeutectic alloy the matrix precipitates disappeared completely. These results suggest that well-annealed microstructures will be stable at temperatures up to 1500C.

Bend strength as a function of temperature is shown in Figure 3. The Cr-5.4Si alloy is of interest because of its similarity to the chromium phase in the two phase alloys. While a small amount of ductility was observed at all test temperatures, significant ductility occurred only at temperatures of 700C and above. The ductile-brittle behavior of chromium is strongly effected by both high interstitial contents, particularly nitrogen, and by tungsten. Improving the melt purity should significantly improve the ductility at lower temperatures.

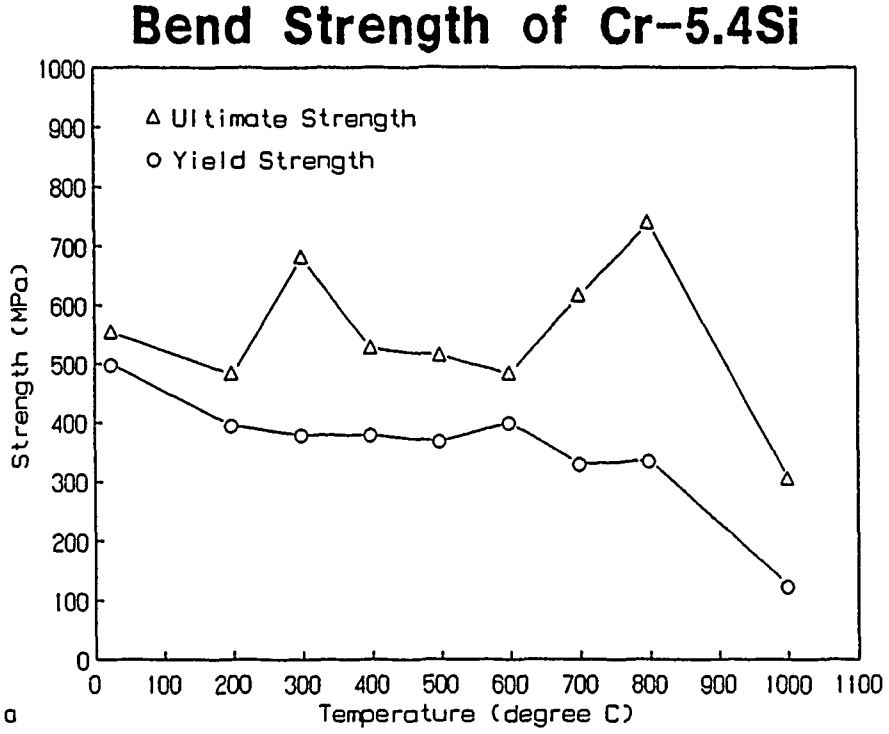
The Cr-12.2Si shows no ductility at temperatures of 800C or lower. The highest yield strength (proportional limit) is 49 ksi at 900C and decreases at higher temperatures. The Cr-18.6Si alloy is brittle at temperatures of 1000C or lower. At 1200C, the yield strength is a promising 52 ksi. Extensive ductility occurs at 1400C.

The 1kg microhardness indents cracked the monolithic Cr_3Si easily as shown in Figure 4a. Using the crack length as a measure of toughness (7) results in a value of 1.8 $MPa*m^{1/2}$. The two phase alloys should be tougher since the chromium phase is effective at blunting cracks (Figure 4b). In Figure 4b the chromium phase stretches across the crack (arrow) indicating significant ductility at room temperature in the hypereutectic alloy. This behavior is exactly what is expected if ductile phase toughening is to occur.

The Cr-18.6Si alloy was not bend tested at room temperature. Examining the fracture surfaces of this alloy after testing at 1000C, shows that the chromium phase has deformed in a ductile fashion. As seen in Figure 5, the chromium has failed with a chisel edge. In addition it can be seen that the chromium has pulled away from the edges of the silicide phase before failing. This is also strong evidence for ductile phase toughening.

V. RECOMMENDATIONS:

This alloy system should be studied further. A yield strength of 52 ksi at 1200C in the Cr-18.6Si alloy without any attempt at optimizing the properties is exceptional. This alloy has not been tested below 1000C to see if the chromium acts as a toughening phase at low temperatures. This experiment should be repeated with melts lower in nitrogen, oxygen and tungsten. Toughness tests as well as bend strength tests need to be performed on as-cast as well as annealed material. The eutectic alloy, which was the most effective at blunting cracks produced by the microhardness indenter, must be included in these tests.



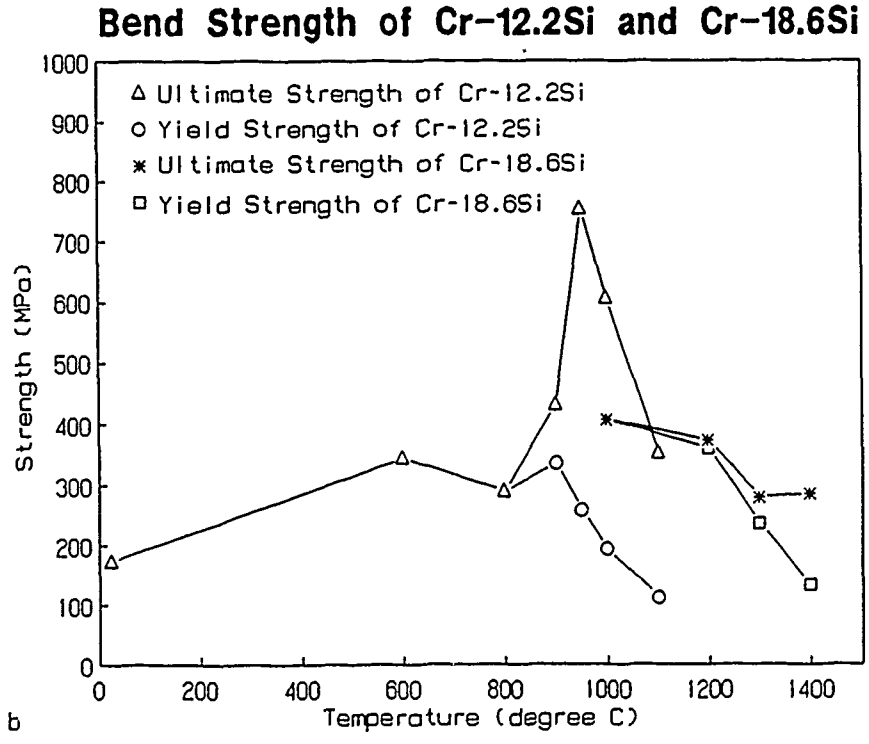


Figure 3. Bend strength versus temperature of as-cast alloys. a) Cr-5.4Si solid solution alloy; b) Hypoeutectic Cr-12.2Si and Hypereutectic Cr-18.6Si.

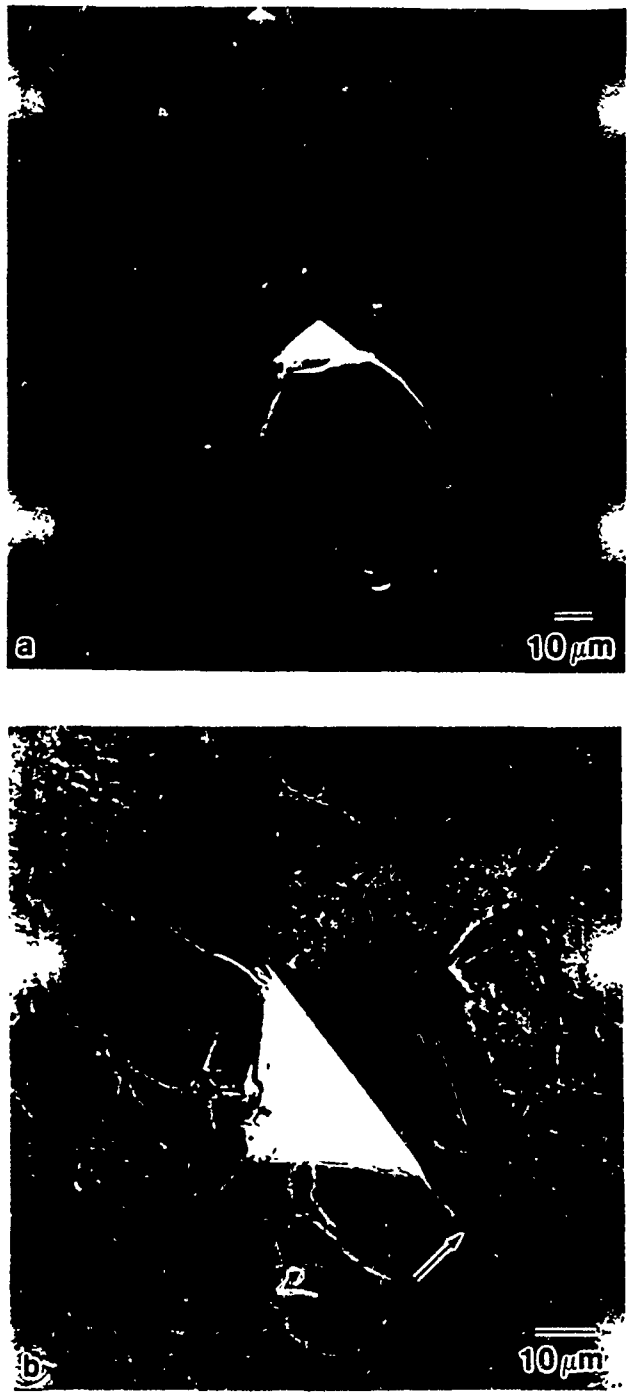


Figure 4. Surface cracking due to 1 kg vickers indent, as-cast. a) Monolithic silicide Cr-24.6Si; b) Hypereutectic Cr-18.6Si. Arrow shows chromium phase bridging surface crack.



Figure 5. Fracture surface of hypereutectic Cr-18.6Si alloy tested at 1000C illustrating chisel edge failure of chromium phase.

The effect of modifying the microstructure through thermomechanical processing should be studied. Alloying routes to improve the low temperature ductility of the chromium (8) may lead to improved properties. Phase stability should be studied on samples that have been allowed to reach chemical equilibrium during a short anneal at a higher temperature and then exposed for long times at a lower temperature. Finally, the inclusion of dispersoids may result in significant improvements in the behavior of the alloys (9).

REFERENCES

1. L. S. Sigl, et al., Acta Metallurgica, Vol. 36, 4, pp. 945-953, 1988.
2. J. J. Lewandowski, D. Dimiduk, W. Kerr, and M. G. Mendiratta, Materials Research Society Sympsosia Proceedings, Vol. 120, pp. 103-109, Materials Research Society, 1988.
3. M. G. Mendiratta and D. M. Dimiduk, "High Temperature Ordered Intermetallic Alloys III", pp. 441-446, Materials Research Society, 1989.
4. M. G. Mendratta, unpublished.
5. A. G. Metcalfe, et al., WADC Technical Report 58-342, July 1958.
6. J. W. Clark, NASA CR-72731, November 1980
7. K. Niihara, R. Morena, and D. P. H. Hasselman, Journal of Materials Science Letters, 1, pp. 13-16, 1982.
8. A. M. Filippi, NASA CR-72883, November 1970.
9. B. A. Wilcox, N. D. Veigel, and A. H. Clauer, Metallurgical Trans., Vol. 3, pp. 273-283, January 1972.

1989 USAF-UES SUMMER FACULTY RESEARCH PROGRAM

GRADUATE STUDENT RESEARCH PROGRAM

Sponsored by the

AIR FORCE OFFICE OF SCIENTIFIC RESEARCH

Conducted by the

Universal Energy Systems, Inc.

FINAL REPORT

Molecular Modeling and Computational Chemistry: Studies of Additives for Fluids and Lubricants

Prepared by:	Harvey L. Paige, Ph.D.
Academic Rank:	Associate Professor
Department and University:	Chemistry Department Alfred University
Research Location:	WRDC/MLBT Wright-Patterson AFB Dayton, OH 45433
USAF Researcher:	Carl E. Snyder, Jr.
Date:	8 September 1989
Contract No:	F49620-88-C-0053

Molecular Modeling and Computational Chemistry: Studies of Additives for Fluids and Lubricants

by

Harvey L. Paige

Molecular modeling and computational chemistry were used to study seven corrosion inhibitors and three anti-wear additives which have been found to be useful in chloro-trifluoroethylene (CTFE) fluids. These compounds were selected because of effectiveness and because their structures did not include proprietary moieties. The geometrical structures of all of the compounds were optimized using molecular mechanics and semi-empirical molecular orbital techniques. These structures were visually compared with the aid of a graphics program. The electronic structures of the molecules were calculated using a semi-empirical molecular orbital program and some of them were displayed as three dimensional maps and were also visually compared.

Acknowledgements

The author thanks the Air Force Systems Command and the Air Force Office of Scientific Research for sponsorship of the program under which this research was accomplished. Thanks are also due to Universal Energy Systems for the well-structured and efficient program.

My work in the Nonstructural Materials Branch, Nonmetallic Materials Division of the Materials Laboratory was made easier by the aid and encouragement of individuals too numerous to list. Mr. Carl E. Snyder, Jr. and Dr. Kent Eisentraut of the Nonstructural Materials Branch and Dr. Charles Lee of the Polymer Branch were particularly helpful in making available essential resources and discussing results. The author is very grateful for their assistance.

I. INTRODUCTION:

The use of additives in fluids and lubricants is essential for resistance to oxidation, appropriate viscosity characteristics, inhibition of corrosion, and minimization of wear. For hydrocarbon-based fluids and lubricants, necessary additives are available although the mode of action is not always well understood. In the case of non-hydrocarbon materials, there is a need for effective additives. The search for new additives using the empirical approach is costly and time-consuming. Therefore, there is an interest in employing the techniques of computational chemistry and molecular modeling as a guide in the search.

The author has previously studied the oxidative and thermal stabilities of model lubricant and fluid molecules using computational as well as experimental methods. In addition, a quantitative structure-property relationship (QSPR) of some of these molecules was studied wherein the structural parameters were based on computed electronic descriptors and the properties were measured viscosities. This earlier work contributed to my assignment to the to the Nonstructural Materials Branch of the Nonmetallic Materials Division.

II. OBJECTIVES OF THE RESEARCH EFFORT

The physical and chemical behavior of molecules are known to depend on the particular geometrical arrangements of atoms in the molecules and on the electronic structures of those molecules. The solubility properties, for example, depend on the relative polarities of the solvents and solutes and on the relative sizes of the solvent and solute molecules. The more the molecules are alike, the greater the mutual solubility. Chemical reactions can also be explained on the basis of the arrangements of atoms and the electrons around those atoms. In the case of anti-wear additives and corrosion inhibitors, however, specific chemical reactions are unknown.

It seems clear that additive molecules react with metal surfaces, but the exact nature of that interaction and the requirements of the surface and the additive molecule are not apparent. Further, because the interaction occurs between molecules in low concentration and the surface, analytical determination of the details of interaction is an extraordinarily difficult task. Consequently, an indirect method for determining the essential features of additive molecules would be valuable. The main objective of this research effort is to determine how the techniques of molecular modeling and computational chemistry can be employed to help select or design effective additives which are soluble in, and compatible with, non-hydrocarbon fluids and lubricants.

The method which was selected to determine essential features of additive molecules resembles that used in pharmaceutical research. Specifically, the arrangements of geometrical entities or of reactive groups in molecules having some biological effect are compared to features of other molecules in a data base. By examining various molecules, each having one of the features of the active molecule, the importance of the many structural features can be assessed. New molecules can then be synthesized which have all of the important features in varying proportions in order to find the optimum structure for the desired reactivity. In the present study, several molecules with some activity as corrosion inhibitors or anti-wear additives were studied to find common features.

III. PROCEDURE, RESULTS, AND DISCUSSION

Structures of the corrosion inhibitors studied are given in Table 1 and those of the anti-wear additives are given in Table 2. Because of limitations on the size of the molecules which could presently be studied using the modeling program, succinic acid (CF) and succinic anhydride (CG) were studied, in addition to the larger molecules containing these functional groups.

The molecular modeling program used was the CHEM-X suite of programs from Chemical Design, Ltd. of Oxford, England. Included in CHEM-X are interfaces to quantum mechanics packages such as MOPAC and Gaussian 80. The size of molecules which can be studied with these programs is severely limited by CHEM-X parameters and by the size of the computer on which CHEM-X runs.

Table 1. Structures of Some Corrosion Inhibitors

Designation	Structure
CA	$C_{18}H_{35}\underset{\displaystyle CH_2\text{--}CO}{\overset{\displaystyle CHCO}{|}}\ \underset{\displaystyle |}{\overset{\displaystyle NCH_2CH_2OCH_2CH_2OH}{|}}$
CB	$C_{12}H_{23}\underset{\displaystyle CH_2\text{--}CO}{\overset{\displaystyle CHCO}{|}}\ \underset{\displaystyle |}{\overset{\displaystyle NCH_2CH_2CH(OH)CH_2OH}{|}}$
CC	$C_{12}H_{23}CH(CH_2COOH)CON\begin{matrix}CH_2CH_2O\\ \diagdown\quad\quad\diagup\\ CH_2\ \text{--}CH_2\end{matrix}$
CD	$CH_3(CH_2)_xCH{=}CH(CH_2)_{9-x}CH(COOH)CH_2COOH$ (x = 4 studied)
CE	$C_8H_{15}\underset{\displaystyle CH_2\text{--}CO}{\overset{\displaystyle CHCO}{|}}\ \underset{\displaystyle |}{\overset{\displaystyle NCH_2CH_2OCH_2CH_2OCOCH(CH_2COOH)C_8H_{15}}{|}}$
CF	$HOOCCH_2CH_2COOH$ (succinic acid)
CG	$\begin{matrix}CH_2CH_2CO\\ \diagdown\quad\diagup\\ C(O)O\end{matrix}$ (succinic anhydride)

Table 2. Structures of Some Anti-Wear Additives

WA	$C_8H_{15}\underset{\displaystyle CH_2\text{--}CO}{\overset{\displaystyle CHCO}{|}}\ \underset{\displaystyle |}{\overset{\displaystyle NCH_2CH_2OCH_2CH_2OH}{|}}$
WB	$C_6H_{13}OCH_2CH_2OCH_2CH_2OH$
WC	2,2-ethylidenebis(4,6-di-tertbutylphenyl)-fluorophosphite

Thus, initial entry of the molecular structure and a preliminary structure optimization were accomplished via CHEM-X. For these procedures, there was not a restriction on the size of a molecule which could be studied, although the computer time required for large molecules was substantial. Following the structure optimization, the program was used to provide a mathematical description of the molecule in terms of a so-called Z matrix. The Z matrix contains the identities of the atoms, the bond lengths, angles, and dihedral angles, and the connectivities. Together these completely define the molecular structures. These files were edited to provide input for a version of the MOPAC semi-empirical molecular orbital program on the CRAY computer which has less severe molecular size restrictions. Finally, these programs were run on MOPAC.

Visualization of the results of quantum mechanical results is accomplished through maps. The electron density map describes the three dimensional surface of the molecule inside of which the computed electron density is, at a minimum, an operator-selected value. Fig. 1a gives an electron density contour map of succinic anhydride with an electron density of 0.1 e/A^3 (blue) and 0.5 e/A^3 (green). Fig. 1b shows the molecule and map rotated 80° around the x-axis.

The electrostatic potential map is a three dimensional surface which represents the attraction or repulsion by the molecule of an operator-selected test charge. Fig. 2a gives the electrostatic potential map of succinic anhydride with a test charge set equal to the charge on an sp^3 carbon of the succinic acid molecule. Note

that in the region of the oxygen, the potential is color coded red for attraction, whereas in the vicinity of carbons and hydrogens the potential is color coded blue for a repulsive force. Fig. 2b shows the molecule and map rotated 80° around the x-axis.

The wavefunction maps differs from the previous two maps in that they each represent single molecular orbitals, and not the entire electronic structure of the molecule. Fig. 3 shows the highest occupied molecular orbital (HOMO) of succinic acid and Fig. 4 shows the lowest unoccupied molecular orbital (LUMO) of the same molecule. The blue and green colors represent the different phases of the wavefunctions. Note that in Fig. 3 there is electron density (proportional to the square of the wavefunction) between some atoms, representing bonding interactions. In the case of Fig. 4, however, the phase alternates between adjacent atoms. Therefore, the orbitals are antibonding and, if filled, would weaken the bonds between the associated atoms.

One could also give representations of other molecular orbitals, but they are generally less useful than the "frontier molecular orbitals", the HOMO and LUMO. This is because interactions between chemical species are unlikely to involve lower energy electrons than those in the MO and they are similarly unlikely to leave an electron in an orbital higher in energy than the LUMO, which would be an electronically excited state. Orbital interactions require that the orbitals have "equivalent" symmetries. For example, the (p-d)pi interaction between carbon monoxide and a transition metal (ie. "back-bonding") occurs because the t_{2g} orbitals on the metal ion have the same symmetry

as the pi* molecular orbital of carbon dioxide. A second requirement for interactions between orbitals is that they be of comparable energy. This can be visualized as similar size so that the orbitals can occupy the same region of space (overlap). Thus, carbon monoxide forms strong bonds with the nickel atom, but not with the larger members of the group, palladium and platinum.

All of the numerical information necessary to graphically present the electron density maps, the potential energy maps, and the wavefunction maps is now available. Also available is the means for finding difference maps, representations of the differences between molecules. Not yet available is the mechanism for reading the numerical information into the CHEM-X graphics program so that results of calculations done outside of the program can visualized and manipulated. Thus, much of the groundwork for evaluating the computational chemistry results has been completed, but the ultimate evaluation of those results remains to be completed.

IV. RECOMMENDATIONS

Molecular modeling and computational chemistry may provide a means by which the mechanism of action of lubricant additives can be understood. It is clear that the project will require insight as well as persistence. It is strongly recommended that means for the visualization of computational chemistry results be pursued further. In addition, it is desirable that a means for providing an objective measure of similarity of the features of interest be sought.

MODEL CORROSION INHIBITOR

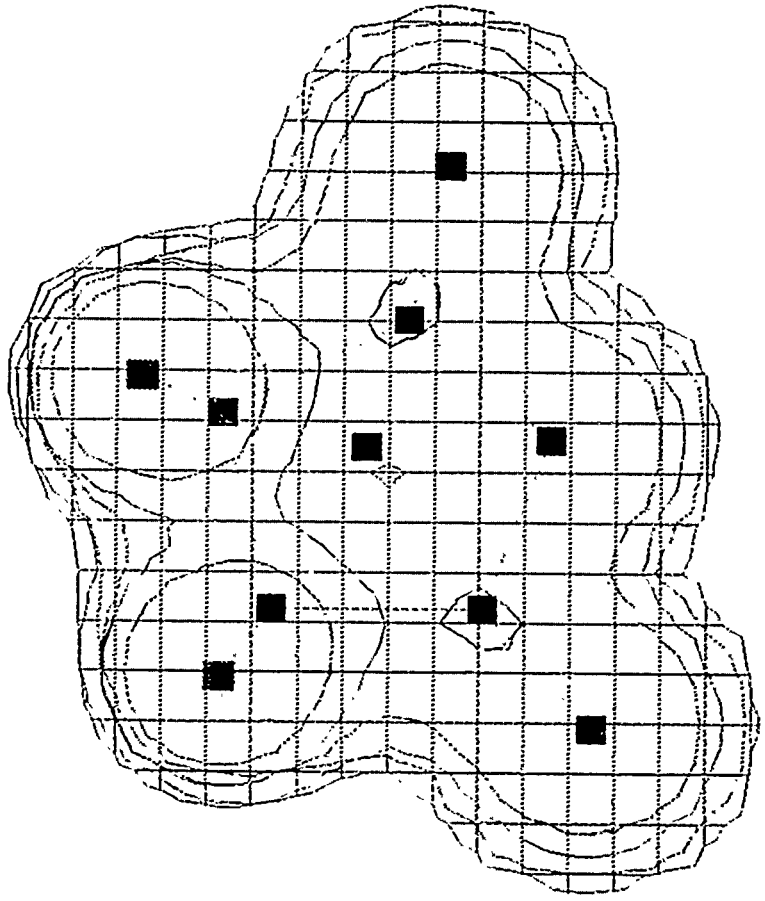


FIGURE 1A. ELECTRON DENSITY MAP OF SUCCINIC ANHYDRIDE

MODEL CORROSION INHIBITOR

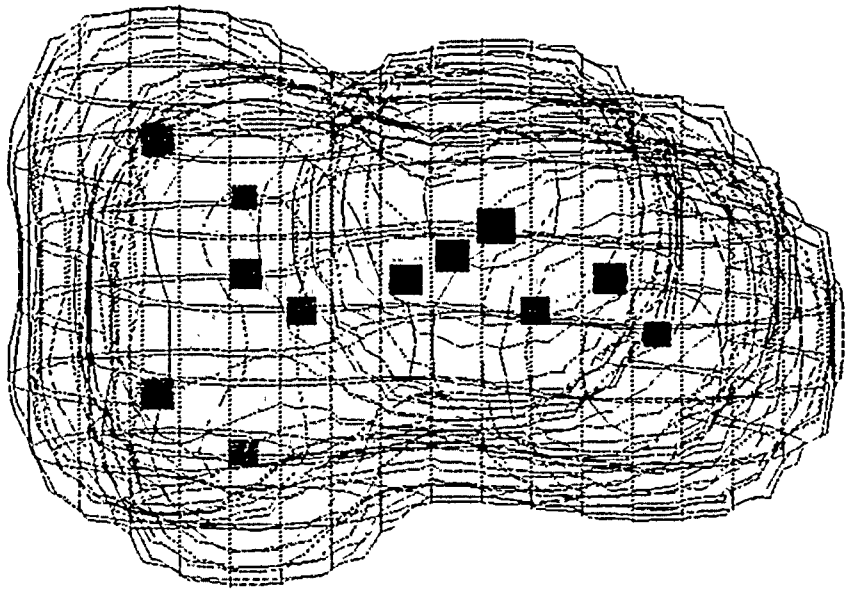


FIGURE 1B. ELECTRON DENSITY MAP OF SUCCINIC ANHYDRIDE

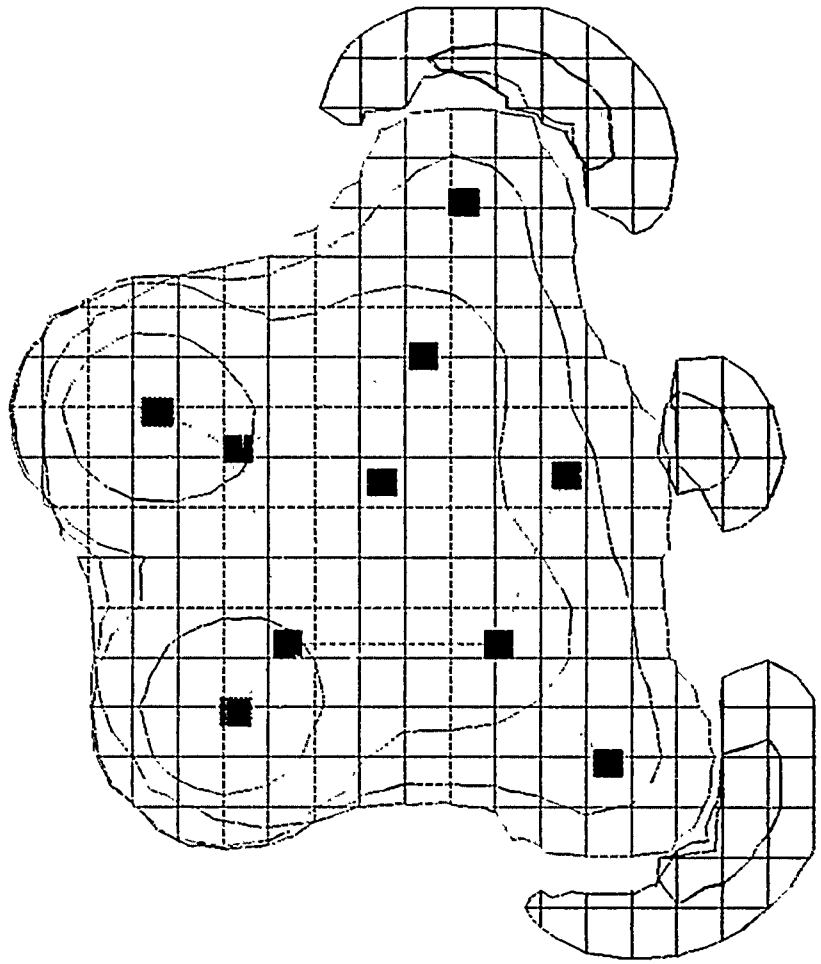


FIGURE 2A. ELECTROSTATIC POTENTIAL MAP OF SUCCINIC ANHYDRIDE

MODEL CORROSION INHIBITOR

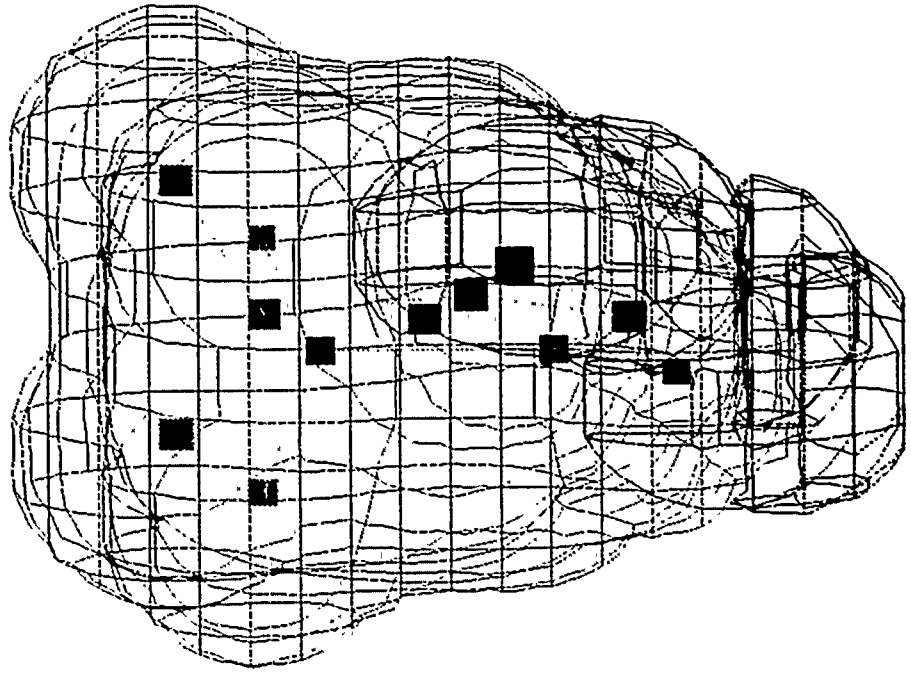


FIGURE 2B. ELECTROSTATIC POTENTIAL MAP OF SUCCINIC ANHYDRIDE

MODEL CORROSION INHIBITOR

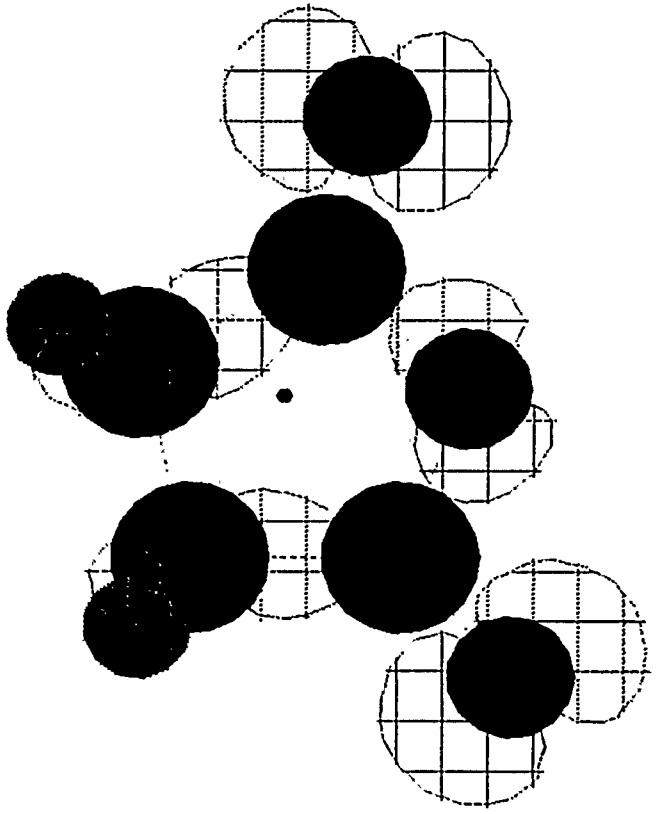


FIGURE 3. HIGHEST OCCUPIED MOLECULAR ORBITAL OF SUCCINIC ANHYDRIDE

MODEL CORROSION INHIBITOR

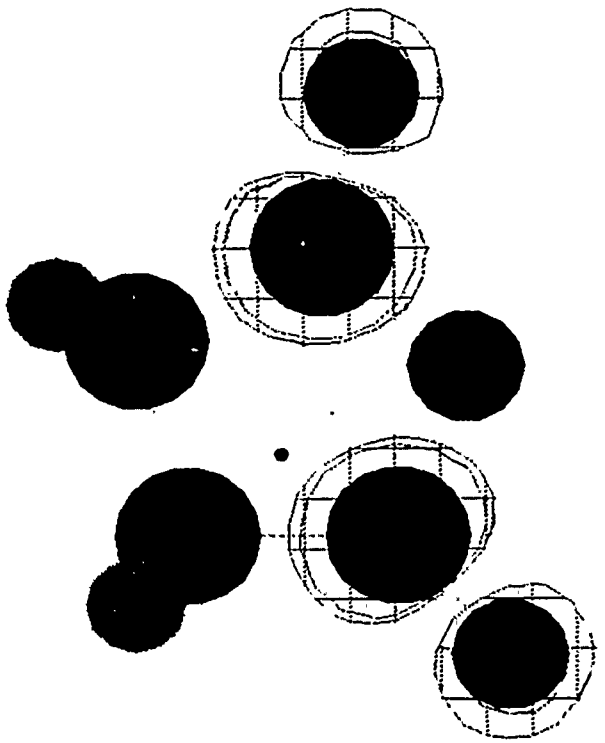


FIGURE 4. LOWEST UNOCCUPIED MOLECULAR ORBITAL OF SUCCINIC ANHYDRIDE

REFERENCES

Clark, Tim, "A Handbook of Computational Chemistry", Wiley, New York, 1985.

Hinchcliffe, Alan, "Computational Quantum Chemistry", Wiley, New York, 1988.

Stewart, James J. P., "MOPAC: A General Molecular Orbital Package, Version 4.0", Quantum Chemistry Program Exchange, Bloomington, IN, 1987.

"The CHEM-X SUITE Reference Manual", Chemical Design Limited, Oxford, England, 1988.

Gustavo, A. A., et al, Shape group studies of molecular similarity: relative shapes of Van der Waals and electrostatic potential surfaces of nicotinic agonists, J. Mol. Graphics, Vol. 6, 45-53, 1988.

Sosa, C., G. W. Trucks, G. D. Purvis III, and R. J. Bartlett, An application of the SCF, MBPT, and CC correlated densities: a graphical display along the potential energy surface of CH_4 ----> CH_3 + H, J. Mol. Graphics, Vol. 7, 28-35, 1989.

1989 USAF-UES SUMMER FACULTY RESEARCH PROGRAM/

GRADUATE STUDENT RESEARCH PROGRAM

sponsored by the

AIR FORCE OFFICE OF SCIENTIFIC RESEARCH

conducted by the

Universal Energy Systems, Inc.

FINAL REPORT

IMPROVEMENT IN THE DETECTION OF MICROCRACK INITIATION AND GROWTH DURING FATIGUE CYCLING BY SURFACE ACOUSTIC WAVE SCATTERING

Prepared by:	Michael T. Resch, Ph.D.
Academic Rank:	Assistant Professor
Department and	Engineering Mechanics
University:	University of Nebraska-Lincoln
Research Location:	WRDC/MLLP Building 655, Room 168 Wright-Patterson AFB, OH 45433
USAF Researcher:	Thomas J. Moran, Ph.D.

Date:	September 30, 1989
Contract No.:	F49620-88-C-0053

IMPROVEMENT IN THE DETECTION OF MICROCRACK INITIATION AND GROWTH DURING FATIGUE CYCLING BY SURFACE ACOUSTIC WAVE SCATTERING

by

Michael T. Resch, Ph.D.

ABSTRACT

A surface acoustic wave non-destructive evaluation technique was used to detect the natural nucleation of surface microcracks in highly stressed regions of hourglass shaped 6061-T651 aluminum specimens during fatigue cycling. The experimental procedure involved excitation of a Rayleigh wave on the surface of each specimen and observation of the presence of a reflected echo from the nucleating crack superimposed on reflections from microstructural features surrounding the flaw. Contacting wedge transducers were used to excite the incident waves and to detect the reflected wave signals. The effectiveness of a split-spectrum processing algorithm to separate specular reflections of isolated cracks from non-specular reflections of microstructural features in the scattering field was demonstrated. Application of compressive stresses normal to the crack faces was observed to degrade the effectiveness of the processing algorithm to distinguish the presence of microcracks from the surrounding microstructural features.

Acknowledgements

I wish to thank the Air Force Systems Command and the Air Force Office of Scientific Research for sponsorship of this research. Universal Energy Systems must be mentioned for their concern and help to me in all administrative and directional aspects of this program.

My experience was rewarding and enriching because of many different influences. Both Don Forney and Tom Moran of WRDC/MLLP went out of their way to ensure that I was supplied with all the instrumentation and technical help necessary to address my stated research goals and objectives. Special thanks are due to Prasanna Karpur who shared his exceptional knowledge of signal processing toward the successful completion of this initial investigation. All split-spectrum processing of the data obtained in these experiments was performed courtesy of Dr. Karpur utilizing his personal software. Additional thanks are due to Ted Nicholas, Jay Jira, and Jim Larsen of WRDC/MLLN for their assistance in procuring access to the servohydraulic testing machines necessary for application of fatigue cycling to the specimens. Finally, I would like to extend a special thanks for the many encouraging discussions with Dr. Nicholas regarding the potential role of surface acoustic wave scattering as a viable tool in small fatigue crack growth research.

I. INTRODUCTION:

Early detection of crack nucleation and growth in metals, ceramics, and polymers has many implications in the design, fabrication, and maintenance of high performance structures. In particular, structural ceramics such as silicon nitride, and advanced metallic alloys such as titanium aluminide are extremely susceptible to premature failure due to the presence of microscopic surface cracks produced by conventional fabrication techniques.

The Nondestructive Evaluation Branch of the Wright Research and Development Center is particularly concerned with the creation of practical techniques to measure damage in materials important to the mission of the Air Force both under laboratory conditions and on structures operating in the field. The expertise of this branch in the development of innovative and useful ultrasonic techniques to characterize damage in metals, ceramics, and composites is well documented in the international literature.

My research interests have been in the area of application of surface acoustic wave scattering techniques to investigate the growth behavior of small surface cracks in metals and ceramics. Up to the present time this work has been successful on relatively simple alloys of aluminum and steel with small cracks in the size range between 50 μm and 250 μm in depth below the surface. Current research interests in the NDE branch relating to the possible effectiveness of split-spectrum

processing of signals to improve the signal-to-noise ratio obtained from a number of quantitative nondestructive evaluation techniques, combined with the possibility that this technique could significantly reduce this minimum detectable crack size for technologically important alloys such as titanium aluminide contributed to my assignment in this branch.

II. OBJECTIVES OF THE RESEARCH EFFORT:

Currently, there is no reliable method for nondestructive evaluation of the nucleation of surface microcracks in hourglass shaped specimens now in use for fatigue crack initiation studies in the High Temperature Metals and Ceramics Branch of the Wright Research and Development Center, except for direct optical scanning at high magnification in a standard metallographic microscope. This process is exceedingly time consuming, requiring periodic inspections of the specimen performed by physically taking the specimen out of the servohydraulic machine, scanning many square millimeters of surface area in the high stress region, and replacing and realigning the specimen in the hydraulically actuated grips before resuming the test. Additionally, during crack mouth opening displacement measurements of already nucleated fatigue microcracks with a laser interference displacement gage, there is considerable uncertainty concerning the exact amount of tensile stress to be applied to the specimen to cause the adjacent crack faces of the microcrack to become traction free. Thus, the adaptation of a proven method for the in-situ measurement of crack size and crack opening behavior [1,2] during cycling in a servohydraulic testing machine would

prove to be an extremely useful addition to current research efforts in both MLLN and MLLP.

The chief physical phenomenon which stands as an obstacle to the utilization of the SAW scattering technique in these experiments is that the metallurgical features in a complex alloy such as titanium aluminide contribute to the scattered signal which also contains the reflected echo from a nucleating fatigue crack. The goal of this program is to determine the effect of split-spectrum processing [3,4] on improving the signal-to-noise ratio of SAW scattering from microscopic surface fatigue cracks, in order to determine whether or not SAW scattering might provide a viable measurement technique in this experimental endeavor.

The proposed investigation was to include, but not be limited to the following experiments:

1) Analysis of transducer insertion loss, and other materials related SAW scattering parameters necessary for quantitative measurement of reflection coefficients on titanium aluminide and aluminum alloy specimens. Design and fabricate appropriate clips for coupling existing transducers to new specimen configurations.

2) SAW scattering from microstructural features in metallic specimens of various titanium aluminides and aluminum alloy specimens. Narrow band gated CW excitation of existing contacting wedge transducers with 50% bandwidth and center frequency of 3 MHz will be utilized for SAW

generation. Purpose of the experiment is to determine the minimum detectable crack size limited by microstructural scattering prior to signal processing.

3) Split-spectrum signal processing of signals obtained by narrow band excitation of SAW transducers. Purpose of the experiment is to determine the effectiveness of split-spectrum processing for reducing the background due to SAW scattering from microstructural features.

4) SAW reflection coefficient measurements from a 150 μm deep half-penny shaped surface crack in an existing hour-glass shaped specimen of 7075-T651 aluminum alloy. Purpose of the experiment is to provide initial experimental focus for set-up and calibration of SAW scattering electronics and computerized data acquisition of scattered signals from a real surface microcrack superimposed on signals due to microstructural features.

5) SAW reflection coefficient measurements from artificially nucleated microcracks in 6061-T651 aluminum. Cracks will be nucleated from microscopic EDM pits on new hour-glass shaped specimens to be designed and fabricated to accomodate existing SAW contacting wedge transducers.

6) Split-spectrum signal processing of reflection coefficient measurements from artificially nucleated cracks. Purpose of the experiment is to evaluate improvement in signal-to-noise ratio of the crack reflection coefficient relative to microstructural background

scattering noise.

7) Develop new numerical model for predicting SAW reflection coefficient of small surface fatigue cracks as a function of crack depth and crack length at the surface. Existing model only rigorously valid for half-penny shaped surface cracks.

8) Comparison of acoustic predictions of crack size utilizing signal processing with post-fracture measurements. Purpose of this experiment is to evaluate any coupling between reductions in background noise with amplitude of reflected signals from the microcracks. True crack size during acoustic measurements will be accomplished through heat-tinting or control of fracture surface topography using the stress history effect on the deformation texture.

9) SAW reflection coefficient measurements from naturally nucleated microcracks. Purpose of the experiment is to evaluate the ability of signal processed scattering measurements to detect natural nucleation of microcracks in selected high stress regions of an hour-glass shaped fatigue specimen.

III. SAW SCATTERING PARAMETERS:

a. Transducer insertion loss is evaluated by placing two wedge transducers face-to-face on a substrate of interest, and measuring the amplitude of the signal incident to the transmitting transducer, then

measuring the amplitude of the signal at the terminals of the receiving transducer. Surface acoustic wave velocity on a sample of titanium aluminide was evaluated by measuring the change in transit time between the transmitting and receiving wedge transducer at several separation distances and performing a linear regression to obtain the slope of distance v. time, and hence velocity from this data.

b. Measured one-way insertion loss for 4 mm wide contacting wedge transducers on titanium aluminide operating at 3 MHz with 3 wavelengths excitation at a repetition rate of 100 Hz was approximately -22 dBV, which compares favorably to a value of -18 dbV on aluminum substrates. The measured Rayleigh wave velocity on the titanium aluminide specimen was V_R = 2663 m/second. This is approximately 10% less then the velocity calculated from material constants of Young's modulus, E=101 GPa, and a density of 3800 kg/m^3, and Poisson's ratio, ν=0.3, yielding a theoretical velocity of 2968 m/sec. Other physical parameters important in scattering measurements which depend only on Poisson's ratio are almost identical to those for aluminum, and are listed in references [1,2].

IV. MINIMUM CRACK SIZE DUE TO MICROSTRUCTURE:

a. The minimum detectable crack size due to microstructural scattering is obtained by placing the transmitting and receiving transducers approximately side by side on a flat, metallographically prepared surface, and illuminating an area on the surface which is in the far

field of the transducers, then measuring the amplitude of the reflected signals from the illuminated area. The crack size is obtained by calculating the equivalent size of half-penny shaped crack which the acoustic scattering theory [1,2] predicts would give the same amplitude of reflection under identical acoustic scattering conditions.

b. Measurements of the acoustic scattering from the microstructure of titanium aluminide demonstrate that the crack depth of a half-penny shaped surface crack which would give the same amplitude exceeds the maximum allowable crack depth required for the validity of the elastostatic assumptions inherent in the scattering theory by at least a factor of two. This correlates to a minimum detectable crack depth of approximately 350 μm for the specimen tested, and under the acoustic scattering conditions existing during the test.

V. SPLIT SPECTRUM FROM NARROW BAND EXCITATION:

a. Split spectrum processing is a digital filtering technique which utilizes a nonlinear algorithm for sorting out specular reflections from nonspecular reflections from a scattered field. Physically, the reflected signal received at the terminals of the receiving transducers is amplified to a convenient magnitude, captured digitally, and then processed [3,4] with appropriate software to remove the nonspecular reflections, and finally the specular reflections are displayed graphically in the time domain. Narrow band excitation utilizes a gated continuous wave signal to excite the transmitting transducer primarily

at its center frequency, and generally results in a more efficient conversion of electrical energy into the desired mode of wave propagation.

b. FFT of the transmitted signal from one transducer to another placed face to face revealed that the bandwidth of these transducers is approximately 50% at a center frequency of 3 MHz. This demonstrated that there was more than enough bandwidth for the existing transducers for the split spectrum algorithm to be effective.

VI. SPLIT SPECTRUM PROCESSING OF 150 μm CRACK:

a. Reflection coefficient measurements of the existing crack in a specimen of 7075-T651 aluminum were made with varying amounts of bending moment applied manually to the specimen. In this way the effect of applied tensile or compressive stress could be studied in the ultrasonics laboratory without resorting to a servohydraulic testing machine to apply the load. Although the exact level of stress was not known, this technique proved extremely convenient to test the sensitivity of the processing algorithm under varied crack closure conditions.

b. Results of split spectrum processing of reflected signals from this crack are virtually identical to processing of the naturally nucleated crack shown in Figures 1 and 2. The specular reflections from the crack were most evident with an applied bending moment on the specimen to

cause the adjacent crack faces to be completely traction free, as evidenced by a 'saturation' of the reflection amplitude with increasing tensile stress. With no applied load the signal was less robust, showing fewer cycles of specular reflection, and with compressive stress, the algorithm was no longer able to discern any specular scattering from the closed crack with respect to microstructural scattering. Instead the algorithm has a tendency to 'key' on the strongest microstructural scatterer, and display single positive-going or negative going 'spikes' in the processed time domain signal.

VII. ARTIFICIALLY NUCLEATED MICROCRACKS IN 6061-T651:

a. Microscopic pits were produced at the surface of metallographically prepared specimens of 6061-T651 aluminum alloy by sharpening ordinary sewing needles with an extremely fine ceramic hone equivalent to 1000 grit carborundum paper. The tips of the needles sharpened in this way were only approximately 10 μm across. A 60 v. spark applied for a few seconds using the edge-finder feature of a conventional electric discharge machine (EDM) device produced extremely reproducible pits approximately 30-50 μm in diameter and approximately half this amount in depth as measured by conventional metallographic methods. All spark machining was performed with the specimen and needle tip submerged in kerosene. Specimens prepared in this way were cycled at a stress ratio of R=+0.05 ($R=\sigma_{min}/\sigma_{max}$) with σ_{max}=90% σ_y for this material. Specimens were cycled in fatigue at approximately 10 Hz until a crack was detected, or until specimen failure, whichever came first.

b. In all, six small hourglass shaped specimens were manufactured by machine shop personnel back at the University of Nebraska-Lincoln, due to the inability to obtain shop time within the constraints of the WRDC machine shop schedule. Close monitoring of the region surrounding the tiny EDM pits in all six specimens failed to reveal microcrack initiation at any of the artificial nucleation sites. Optical microscopy also failed to reveal nucleation at any of the sites. It was felt that compressive residual stresses produced by the metallographic preparation of the surfaces contributed to prevention of nucleation at these sites. However, natural nucleation of an isolated microcrack on Specimen #1 was noted at a cycle life of approximately 150,000 cycles from the SAW reflection coefficient, as well as nucleation at the root of the side notch in the reduced section of three out of six specimens.

VIII. SPLIT SPECTRUM PROCESSING FROM MICROCRACKS IN 6061-T651:

a. In order to facilitate computerized data acquisition of the reflected signals obtained during cycling in a servohydraulic testing machine, a remote data acquisition system was constructed from a spare PDP-11 computer combined with a spare LeCroy digitizer from the precision ultrasonics laboratory in MLLP. Although this system was not connected to the VAX computer system in real time, data could be transferred to the VAX by obtaining a scan from the cycling specimen, then hand carrying a transfer diskette from the fatigue testing laboratory to the precision ultrasonics laboratory where the split-

spectrum processing algorithm was installed. The procedure was to periodically obtain an A-scan of the reflected signals from the vicinity of the EDM starter pit. Then, once the crack was observed acoustically to grow larger than the minimum detectable crack size, we would be able to work back through the previously obtained signals to determine when detectable nucleation had occurred.

b. Although numerous A-scans were obtained during fatigue cycling, since none of the cracks nucleated at the EDM starter pit, the goal of observing nucleation at an artificial defect was not achieved. However, the system still proved extremely valuable in that microcrack initiation on the sides of the specimen was easily detected in the real-time reflected signal being obtained continuously during cycling. Limitations of depth of field for light optical microscopy on the curved sides of these specimens made it impossible to visibly locate the position of the nucleated cracks. However, the locations of these cracks were easily detected by passing a Q-tip swab dipped in methanol over the surface until the reflected signal from the crack was momentarily dampened from the methanol entering the volume of the crack.

IX. NEW NUMERICAL MODEL:

a. The scattering model reported in references [1,2] was obtained using simplifying approximations concerning the mode I stress intensity factor distribution around the crack edge beneath the surface for a semi-elliptical crack residing in the stress field of a surface acoustic

wave with acoustic wavelength much larger than the crack depth. Subsequent to the publication of these articles, a numerical solution for semi-elliptical surface cracks in a plate in pure bending was discovered in the literature [5] which lends itself to construction of a more rigorous numerical prediction of the relationship between crack depth below the surface, a, crack length at the surface, 2c, and the magnitude of the reflected echo from the crack. Briefly stated, this analysis is comprised of performing a line integral of the stress intensity factor distribution obtained from [5] around the crack edge for cracks with varying values of crack aspect ratio, a/c, and crack depth a, along the lines of the analysis previosly reported in [1,2].

b. The experiments concerning the nucleation of microcracks from the EDM starter notches ended up consuming over half of the summer visit at MLLP laboratories. It was decided during these experiments, in conjunction with the supporting experiments required to produce the EDM nucleation sites, that the improvements in the acoustic theory would be proposed as future work for this researcher's mini grant.

X. ACOUSTIC PREDICTIONS V. POST-FRACTURE MEASUREMENTS:

a. The basic procedure to accomplish a valid relationship between acoustic predictions of crack size, a_p, and post-fracture measurements of crack size, a_m, is to produce isolated microcracks using the EDM technique described previously to nucleate a microcrack on a specimen in

a position away from any other major reflectors such as the edge of the specimen or a hole. Then after acoustic measurement of the amplitude of the reflected echo, the specimen is either placed in an elevated temperature environment to grow an oxide coating of known thickness on the fracture surface (this works well with steel and titanium alloys), or additional fatigue cycling is performed after the acoustic measurements at a variety of stress amplitudes in order to produce a deformation pattern which will be visible around the periphery of the acoustically measured crack once the specimen has fractured. The central theme of this experiment is to determine whether or not the signal processing algorithm is capable of removing the nonspecular reflections from the signal without distorting the amplitude information contained in the specular reflection from the crack.

b. Currently, the split-spectrum processing algorithm is designed to normalize the reflection amplitude from specular reflectors in the scattered field. Therefore, it is not possible to perform this experiment with the processing algorithm in its present form. However, development of the algorithm to remove the normalization of signal amplitudes is being contemplated as a joint project between Karpur and Resch to be proposed in the near future. Additionally, creation of a number of calibrated specimens with varying microstructures and containing a number of cracks of known sizes is still important to the success of the project. Therefore, manufacture of a number of calibrated standards will be proposed shortly in this researchers mini-grant proposal.

XI. NATURALLY NUCLEATED MICROCRACKS:

a. As stated previously, unforseen problems in getting the fatigue cracks to nucleate at artificial defects took up a lot more time than originally scheduled. However, on the first specimen tested in fatigue an isolated crack nucleated naturally on the transducer side of the specimen, but within several millimeters of one edge. The reflected echo from this crack was detected in real time from the continuously monitored reflection amplitude of signals illuminating the high stress region of the specimen, and although it subsequently grew to millimeter size, the surface was planed down by metallographic techniques until an acoustically perceived crack depth of approximately 50 μm was achieved.

b. Figure 1. shows the specular reflection from this crack after metallographic techniques reduced its depth to the final size, as it resides in a field of nonspecularly reflected signals from microstructural features surrounding the crack. Figure 2 shows the elimination of all nonspecular reflections from this signal, providing a dramatic example of the effectiveness of the processing algorithm to achieve the stated goal.

XII. RECOMMENDATIONS:

a. The efficacy of the SAW scattering technique to provide useful information concerning the size and opening behavior of surface

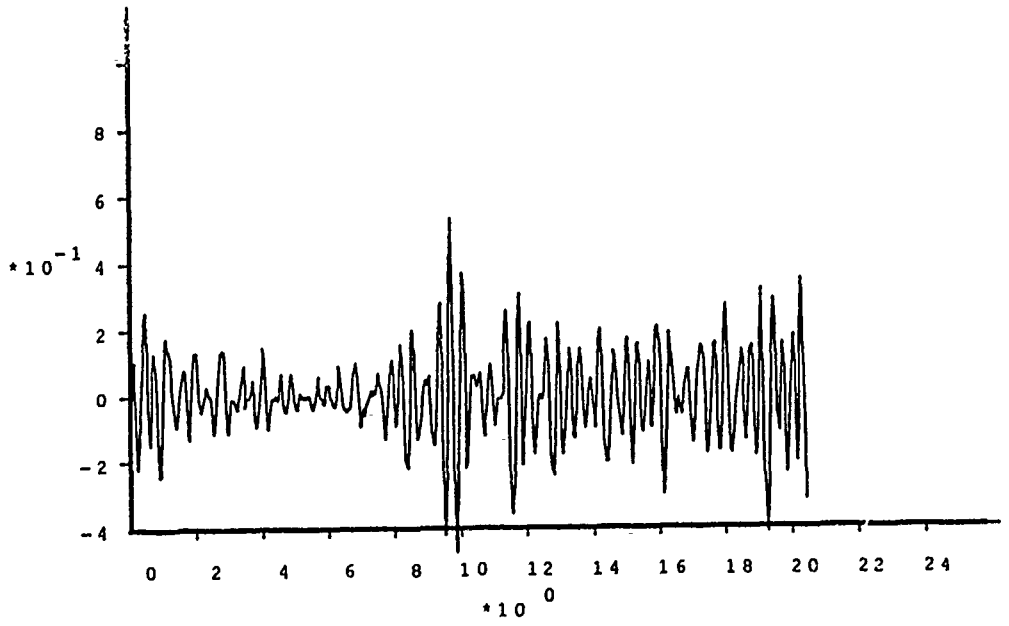


Figure 1. Time averaged signal from the vicinity of the surface microcrack containing the reflected signal from the crack superimposed on the reflections from microstructural features.

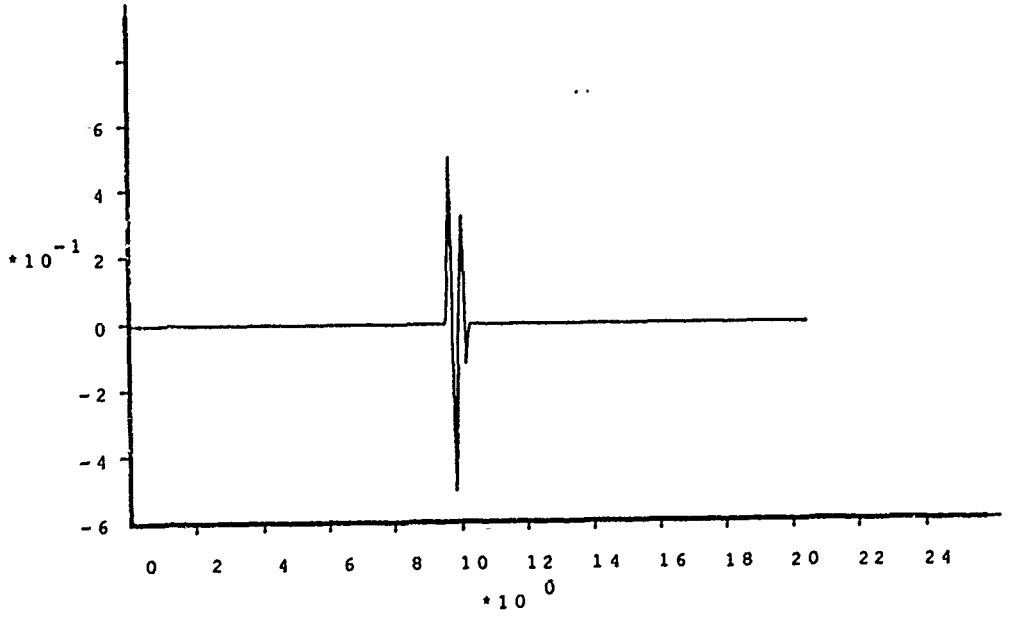


Figure 2. Split-spectrum processing of the previous signal showing the elimination of nonspecular reflections and the location of the reflected signal in the time domain.

microcracks in metals during fatigue is well documented. However, its usefulness as a viable tool in fatigue research is currently limited by; 1) the inability of split-spectrum processing software to retain amplitude information from the specular reflector, 2) the lack of contacting wedge transducers small enough to transmit and receive surface acoustic waves on extremely small hourglass shaped specimens now in use in MLLN and 3) the lack of a rigorous scattering model to predict the reflection coefficient from semi-elliptical shaped surface cracks.

b. Two of the three previously stated limitations are easily rectified. A cursory examination of the limitations of physical acoustics demonstrates that contacting wedge transducers should be able to be produced at a size small enough to fit two transducers side-by-side on a specimen which is approximately 5 mm wide. The improvements in the scattering model can be obtained utilizing ordinary numerical analysis techniques in addition to the results available in reference [5]. Implementation of this model into the software component of the feedback loop during fatigue cycling is also easily accomplished. The only limitation which is not easily overcome is the uncertainty in developments to the signal processing algorithm. However, the production of a number of calibrated standards will be necessary to test the utility of any improvements in the algorithm, in order to evaluate the accuracy of the acoustic predictions.

REFERENCES

1 Resch, M.T., Nelson, D.V., Yuce, H.H., and Ramusat, G.F., "A Surface Acoustic Wave Technique for Monitoring the Growth Behavior of Small Surface Fatigue Cracks", Journal of Nondestructive Evaluation, Vol. 5, No. 1, 1985, pp. 1-7.

2 Resch, M.T., Nelson, D.V., Yuce, H.H. and London, B.D., "Use of Nondestructive Evaluation Techniques in Studies of Small Fatigue Cracks", Basic Questions in Fatigue: Volume I, ASTM STP 924, J.T. Fong and R.J. Fields, eds., American Society for Testing and Materials, Philadelphia, 1988, pp. 323-336.

3 Karpur P., Shankar, P.M., Rose, J.L. and Newhouse, V.L., "Split Spectrum Processing: Optimizing the Processing Parameters Using Minimization", Ultrasonics, Butterworth Scientific, Vol. 25, July 1987, pp. 204-208.

4 Karpur P., Shankar, J.L., Rose, J.L. and Newhouse, V.L., "Split Spectrum Processing: Determination of the Available Bandwidth for Spectral Splitting", Ultrasonics, Butterworth Scientific, Vol. 26, July 1988, pp. 204-209.

5 Newman, J.C., Jr., and Raju, I.S., "Analysis of Surface Cracks in Finite Plates under Tension or Bending Loads", NASA Technical Paper 1578, Dec. 1979.

1989 USAF-UES SUMMER FACULTY RESEARCH PROGRAM/

GRADUATE STUDENT RESEARCH PROGRAM

Sponsored by the

AIR FORCE OFFICE OF SCIENTIFIC RESEARCH

Conducted by the

Universal Energy Systems, Inc.

FINAL REPORT

INVESTIGATION OF THE THERMOMECHANICAL RESPONSE OF A TITANIUM ALUMINIDE METAL MATRIX COMPOSITE USING A VISCOPLASTIC CONSTITUTIVE THEORY

Prepared by:	James A. Sherwood, Ph.D.
Academic Rank:	Assistant Professor
Prepared by:	Marcia J. Boyle
Academic Rank:	Graduate Student
Department and University:	Mechanical Engineering University of New Hampshire
Research Location:	WRDC/MLLN Wright-Patterson AFB, OH 45433
USAF Researcher:	Theodore Nicholas, Ph.D.
Date:	22 September 89
Contract No:	F49620-88-C-0053

INVESTIGATION OF THE THERMOMECHANICAL RESPONSE OF A TITANIUM ALUMINIDE METAL MATRIX COMPOSITE USING A VISCOPLASTIC CONSTITUTIVE THEORY

by

James A. Sherwood

Marcia J. Boyle

ABSTRACT

A research program has been initiated to investigate the stress distribution in a fiber-reinforced metal matrix composite resulting from thermomechanical loads. A detailed three-dimensional finite-element model of a unit cell of the composite was generated for evaluation via the ADINA finite-element code using the ADINA-IN preprocessor. Investigations of the thermomechanical response have been initiated using a classical temperature-dependent bilinear elastoplastic material model and a temperature-dependent viscoplastic unified state variable theory which includes drag stress and back stress state variables.

ACKNOWLEDGEMENTS

We wish to thank the Materials Behavior Branch of the WRDC Materials Laboratory and the Air Force Office of Scientific Research for sponsorship of this research. We also wish to thank Universal Energy Systems for their assistance in finding a research topic of mutual interest to the Air Force and us.

Our research experience was enhanced by many individuals. We wish to thank Dr. Ted Nicholas for his suggestion of this research topic and for providing us with an enjoyable work environment. We are also indebted to Jay Jira and Bill Teal for helping us to take full advantage of the excellent computing facilities at WPAFB and to Joe Kroupa of UDRI for initiating us to the CRAY-XMP. We are also grateful for the experimental data furnished to us by Capt. Steve Balsone and Kathy Williams of WRDC/MLLN, Dr. Donald C. Stouffer of the University of Cincinnati and Dr. M. Khobaib of the University of Dayton.

I. INTRODUCTION

Ever since man has been using gas turbines to power aircraft, the performance of these engines has been limited by the thermomechanical behavior of the materials used in their construction. Complicating this dilemma is the potentially conflicting requirement of reduced weight to increase flight range. Today's alloys based upon titanium, iron, nickel and cobalt are approaching their developmental limit with respect to achieving increased temperature capabilities while maintaining structural integrity. Thus, with the dual requirement of increased temperature performance while maintaining structural integrity with reduced weight, research efforts for the development of ceramics and intermetallics, many of which exhibit low density, high strength and inertness up to relatively high temperatures have been initiated.

In response to the need of maintaining structural integrity while increasing turbine operating temperatures, the Materials Behavior Branch of the Materials Laboratory at Wright-Patterson Air Force Base is supporting research and development of titanium aluminide composites. To date, this support has primarily been for mechanical testing of the macroscopic behaviors of the titanium aluminide matrix materials and the macroscopic behaviors of the metal matrix/fiber systems. While these experimental efforts are informative in characterizing the thermomechanical behavior of the composite and its individual constituents, they do not provide a thorough understanding of the associated stress field throughout the composite system.

One of the initial issues of importance with respect to these composites is the residual stress field associated with the manufacturing process. During the manufacturing process, the silicon carbide fibers are bonded to the metal matrix at 950°C, and the fiber-matrix system is then cooled to room temperature. However, the coefficients of thermal expansion (CTE) differ significantly between the fiber material and the matrix material. As a consequence, significant residual stresses are present in the matrix material as evidenced by the radial cracks originating at the fiber-matrix interface which have been observed following the manufacturing process. The presence of these cracks verifies that the matrix demonstrates nonlinear material behavior during the manufacturing process which will subsequently affect the material's service life response. Complicating the understanding of the residual stress situation is a lack of knowledge about the bonding mechanism between the fiber and the matrix, i.e. mechanical, chemical or some combination of the two. If the bond is such that slippage between the fiber and the matrix is possible, then the values of the static and dynamic coefficients of friction will also influence the resulting stress field. Parametric studies using finite element methods can provide some qualitative information concerning these stress fields and plausible boundary conditions at the fiber-matrix interface.

To date, only a small amount of support has been toward investigating the thermomechanical behavior and, hence, the associated resulting stress distribution of the composite system using analytical techniques. Although these analytical investigations have proven informative, none have included time-dependent material models. While time-independent

material models are sufficient for the silicon-carbide fibers which remain essentially elastic throughout the deformation process until they fracture, the metal matrix exhibits time-dependent behaviors, i.e. creep, relaxation, strain-rate dependence and recovery. Thus, to fully understand the thermomechanical response of the titanium-aluminide matrix with the silicon-carbide fiber using analytical techniques, it is essential that a robust viscoplastic material model be used.

Dr. Sherwood's research interests include the complimentary areas of constitutive modelling of high-temperature materials and nonlinear finite element techniques. Dr. Sherwood's work on the development of a phenomenologically based constitutive model using drag stress, back stress and damage state variables is directly applicable to his research assignment within the Materials Laboratory at WPAFB. His knowledge of nonlinear finite element techniques and the incorporation of material models in finite element codes make the analytical investigation of the thermomechanical response of the metal-matrix composite possible.

II. OBJECTIVES OF THE RESEARCH EFFORT

Currently, there is no reliable analytical tool for investigating the time-dependent thermomechanical response of metal matrix composites. As a consequence, analytical investigations of the mechanical behavior of these materials are generally conducted using time-independent plasticity models. An improvement upon these classical plasticity analyses can be achieved by using a creep model in conjunction with the

plasticity models. The advantage of such analyses is that they can be readily handled with commercially available finite element codes such as ADINA, MARC and ABACUS. However, the disadvantage of such analyses is that they ignore the time-dependent deformation history of the composite and, thus, do not fully reflect the response of the material in service.

Our assignment as participants in the 1989 Summer Faculty Research Program/Graduate Student Research Program was to incorporate a form of the Bodner constitutive model into a nonlinear finite element program and to use this program to investigate the composite's response to various thermomechanical loads. The finite element code selected for this work was ADINA. The ADINA code was selected because it is one of the best commercially available nonlinear finite element codes and it is licensed for use at both WPAFB and the University of New Hampshire (UNH).

III. CONSTITUTIVE MODELS

Currently, there are two general classes of constitutive models available for investigating the thermomechanical response of metal-matrix composites. Of these two classes, the classical viscoplasticity models are widely used within commercially available finite element codes and give reasonably accurate material behavior responses. However, the second important class of models, the unified constitutive models, are not as widely available even though they are in general

better capable in capturing the material response than the classical viscoplasticity models.

There are essentially two primary reasons for the limited availability of the unified models in commercially available codes. First, the unified models are relatively new, while the classical viscoplasticity models have been in use for over four decades. Thus, knowledge of the capabilities of the unified models is just now trickling into the general engineering population. The second reason is the mathematical complexity of the unified models in comparison to the classical viscoplastic models makes the implementation of these models into finite element codes rather tedious.

III.A. Classical Viscoplasticity

In classical viscoplasticity, the strain is separated into four distinct components. The compatibility equation relating these components is written as

$$\varepsilon_{ij}^{TOT} = \varepsilon_{ij}^{E} + \varepsilon_{ij}^{P} + \varepsilon_{ij}^{C} + \varepsilon_{ij}^{TH} \qquad (1)$$

In Equation (1), ε_{ij}^{TOT} is the total strain, ε_{ij}^{E} is the elastic strain, ε_{ij}^{P} is the plastic strain, ε_{ij}^{C} is the creep strain and ε_{ij}^{TH} is the thermal strain. The expression relating the elastic strains to the

stresses is well known and is written as

$$\varepsilon^{E}_{ij} = \frac{1+\nu}{E}\sigma_{ij} - \nu(\sigma_{kk}\delta_{ij}) \tag{2}$$

The thermal strains are expressed as

$$\varepsilon^{TH}_{ij} = \alpha(T - T_{ref})\delta_{ij} \tag{3}$$

where α is the secant coefficient of thermal expansion at the temperature T with respect to the reference temperature T_{ref}. The variability among the classical models is as to how the nonlinear material behavior, i.e. the plastic and creep strains, are represented.

In these models, the plastic strains are the time-independent nonlinear strains. One of the most commonly used techniques for modelling this strain contribution is a piecewise continuous stress-strain curve. Other common representations are curve fits such as a simple power relation, e.g.

$$\varepsilon^{P} = A\sigma^{m} \tag{4}$$

where A and m are material constants.

The creep strains denote the time-dependent contribution to the overall strain response. Some commonly used creep laws are:

Baily-Norton Law

$$\varepsilon^{C} = A\sigma^{m}t^{n} \tag{5}$$

where A, m and n are thermally dependent material constants

Logarithmic Law

$$\varepsilon^c = a + b(\log(ct^{1/3})) \tag{6}$$

where a, b and c are material constants which depend upon stress and temperature

Marin-Pao Law

$$\varepsilon^c = k\sigma^m(1-ae^{-kt}) + B\sigma^m t \tag{7}$$

where k, m, a and B are temperature dependent constants

Andrade 1/3 Law

$$\varepsilon^c = \varepsilon_0^c(1+\beta t^{1/3})e^{-kt} \tag{8}$$

where e_0^c is the initial creep strain and β and k are material constants which depend upon stress and temperature

Sinh Law

$$\varepsilon^c = a + b\sinh(ct^{1/3}) \tag{9}$$

where a, b and c are material constants which depend upon stress and temperature

The material behavior creep regions over which these time-dependent laws are applicable are limited to primary and secondary creep. To capture tertiary creep, an additional law is required along with a criterion for switching from one governing equation to another. Yet another compromise in the accuracy of these laws is introduced when they are used to capture multistep creep responses since no variable exists to denote the deformation history of the sample.

III.B. Unified State Variable Constitutive Theory

In contrast to the classical viscoplasticity models where the nonlinear strain response is separated into time-independent plastic strain and time-dependent creep strain, unified state variable constitutive theories denote all nonlinear strains in one term, ε_{ij}^{I}. Thus, the associated strain compatibility equation is written as

$$\varepsilon_{ij}^{TOT} = \varepsilon_{ij}^{E} + \varepsilon_{ij}^{I} + \varepsilon_{ij}^{TH} \tag{10}$$

where ε_{ij}^{E} and ε_{ij}^{TH} are the same as give in Equations (2) and (3), respectively, and

$$\varepsilon_{ij}^{I} = \varepsilon_{ij}^{P} + \varepsilon_{ij}^{C} \tag{11}$$

The advantages of using one term to denote nonlinear strain over the classical approach are significant. With using ε_{ij}^{I}, the modeller does not have to differentiate as to what portion of the nonlinear strain response is due to plasticity and what portion is due to creep. Furthermore, it is very important that constitutive models demonstrate coupling between the creep and plastic strains. This coupling has proved to be extremely difficult when using separate creep and plastic strains. Collapsing these two strains into one term facilitates the coupling requirement.

Complimenting the strain compatibility equation and, hence, completing the constitutive model are the associated flow rule which relates the applied stresses to the resulting strain rates and evolution equations for the state variables. These phenomenologically based internal state

variables characterize microstructural changes in an average sense to describe the macrostructural behavior of the material. For this research, the flow rule proposed by Ramaswamy and Stouffer [1] has been chosen. This flow rule is a modification of the inelastic flow equation originally developed by Bodner et. al. [2,3] and includes two state variables, i.e. drag stress and back stress, Z and Ω_{ij}, respectively.

IV. PHYSICAL BASIS OF THE UNIFIED CONSTITUTIVE MODEL

It has been well established that the shear stress needed to cause the dislocation slip associated with inelastic deformation increases with increasing shear strain. This increase in the required stress has been identified as strain hardening and is the result of the multiplication of dislocations and the interaction of these numerous dislocations with each other and barriers which inhibit dislocation glide through the crystal lattice. As a consequence, hardening is a complex process, and it is not easy to describe this material behavior in a straightforward mathematical manner. Hence, overly simplified isotropic and kinematic hardening rules are commonly used to consider strain hardening when investigating plastic deformation with commercially available finite element codes.

In addition to material hardening, material softening may occur due to material recrystallization and damage accumulation. Due to the nature of the formulation of the general isotropic and kinematic hardening rules, these mechanisms cannot be described explicitly, i.e. separately,

in the material model but rather as an inherent piece of the overall hardening rule.

With the advent of state variable constitutive models, the combined effect of strain hardening and damage accumulation can be mathematically described, while at the same time the individual contributions of each of these mechanisms can be quantified. This separation is accomplished by assigning an individual or set of state variables to each deformation "mechanism", i.e. directional hardening, isotropic hardening and damage accumulation. The combination of these effects is accomplished through the inclusion of these state variables in the associated flow equation.

IV.A. Back Stress

Long-range internal stresses that vary as a function of the direction arise from small groups of stray dislocations piling up on slip planes in the immediate region of barriers, e.g. microscopic precipitates, cell walls, grain boundaries and foreign atoms. As a consequence, a "back stress" which effectively counteracts the applied stress in the slip plane is created. Thus, nonzero strain rates can occur even at zero applied stress. Furthermore, since these pile-ups occur over long distances, they are relatively independent of temperature and strain rate. Due to the directional dependence of the back stress, it is associated with kinematic hardening.

Since the piled-up groups of stray dislocations are not strongly bound to the barrier, they can be easily moved under a reversed stress. When

deformation in one direction is followed by deformation in the opposite direction, a yield stress of lower magnitude for the latter deformation than was observed in the first deformation occurs--the Bauschinger effect. The saturation of the Bauschinger effect at plastic strains greater than 0.05 suggests that the back stress resulting from the dislocation pile-ups does not increase indefinitely throughout the deformation process. Thus, the back stress does possess a limiting upper bound [4].

IV.B. Drag Stress

During the inelastic deformation process, numerous isotropic effects which impede the glide of mobile dislocations are present in the microstructure. These effects include the presence of second-phase precipitates and the reciprocating interactions of the dislocations. These effects exhibit a uniform resistance, i.e. drag stress, on a mobile dislocation and are best described as contributing to isotropic hardening.

The presence of second-phase particles in the metal matrix may act in two distinct ways to inhibit the glide of mobile dislocations. If the precipitates are small and/or soft, the mobile dislocations cut and deform them. Since the cutting process arises from short-range forces occurring over distances less than 5 to 10 interatomic distances [5], this type of hardening can be overcome at finite temperatures with the aid of thermal fluctuations. Hence, in contrast to the "back stress"

contribution to hardening, the drag stress is dependent upon temperature and strain rate. If cutting of the precipitate is not feasible, then the dislocations must overcome the precipitate by moving around it. This process can be achieved by the process of Orowon looping. These loops increase the resistance to dislocation motion equally in all directions.

V. THE UNIFIED CONSTITUTIVE MODEL

One of the major advantages of a constitutive model which includes back stress is its capability to model anelastic recovery. It has been observed in materials at high temperature that when a specimen is loaded into the inelastic regime and then unloaded, there is a time-dependent recovery of the residual inelastic strain [6]. The resulting inelastic strain rate is a function of the difference of the applied stress and the current value of the back stress. Hence, anelastic strains can be modeled whenever this difference is nonzero.

One such constitutive model, which is based on the metallurgical considerations of back stress and drag stress, has been proposed by Ramaswamy and Stouffer. In this proposed model, the drag stress scalar, Z, simulates long term cyclic hardening or softening, while the back stress tensor, Ω_{ij}, models the short-term strain hardening. This constitutive model was the result of a detailed review of the Bodner model, other back stress models and a generic back stress/drag stress model [7]. The accuracy of this model has been verified extensively

through the comparisons of experimental and calculated responses of René 80 over a range of temperatures and for tensile, cyclic and creep loadings. However, the model does not include a state variable for calculating fatigue failure or tertiary creep deformation due to damage accumulation. A modification in the model to accommodate damage accumulation has been achieved by Sherwood [8].

V.A. Associated Flow Equation

Using dislocation dynamics, Bodner proposed an inelastic flow equation that included a drag stress state variable. Based upon Bodner's equation, Ramawamy and Stouffer have proposed a variation of the original Bodner equation to include a backstress term. The proposed inelastic flow equation is given by

$$\dot{\varepsilon}^{I}_{ij} = D_0 \exp\left\{-\frac{1}{2}\left(\frac{Z^2}{3K_2}\right)\right\}^n \frac{S_{ij}-\Omega_{ij}}{\sqrt{K_2}} \tag{12}$$

where

$$K_2 = \frac{1}{2}(S_{ij}-\Omega_{ij})(S_{ij}-\Omega_{ij}) \tag{13.a}$$

and

$$S_{ij} = \sigma_{ij} - \sigma_{kk}\delta_{ij} \tag{13.b}$$

In Equation (12), D_0 is a temperature-dependent material constant denoting the limiting inelastic-strain rate, and n is a temperature-dependent material constant controlling the strain-rate sensitivity.

The modification of the Bodner flow law from using σ_{ij} as the driving stress to the use of $(S_{ij}-\Omega_{ij})$ is based upon the argument that the combination of the externally applied load and the internal stress, i.e. the back stress generated by the dislocation substructure, determine the effective stress experienced by the microstructure. Thus, an inelastic flow equation that ignores the contribution of the back stress would not fully describe the effective stress state experienced by the material, and, hence, the flow equation would improperly describe the mechanical behavior of the material.

V.B. State Variable Evolution Equations

The energy imparted to a ductile material by a dynamic load is either stored as an elastic strain energy or dissipated through one of the mechanisms of microstructural rearrangement. These rearrangement mechanisms include damage accumulation and cold work. The observed nonlinear material response, i.e. the inelastic strain rate, is greatly influenced by the mode of energy dissipation. If the material work hardens, then the resistance to inelastic flow is increased; an opposite response is observed if the material work softens. If the energy is dissipated through damage accumulation, then the resistance to inelastic flow is diminished.

The rate of inelastic flow, $\dot{\varepsilon}^{I}_{ij}$, is a function of the state variables, i.e. Z and Ω_{ij}, the stress, σ_{ij}, and the temperature, T. Although the

temperature is a state variable, its effect on the inelastic strain is not explicitly shown, but is introduced through the thermal- and material-dependent constants D_0 and n. However, the state variables, Z and Ω_{ij}, are functions of the thermomechanical history of the material. Consequently, evolution equations for the state variables are required to describe their variation.

Just as the current values of the state variables are functions of the current physical state of the material, the rates of change of these state variables at any given time are dependent upon the current physical state of the material. This current state is assumed to be fully described by the state of stress, temperature and the internal variables. Hence, the evolution equations are of the general form

$$\dot{\Omega}_{ij} = \dot{\Omega}_{ij}(\sigma_{ij}, T, \Omega_{ij}, Z) \tag{14}$$

and

$$\dot{Z} = \dot{Z}(\sigma_{ij}, T, \Omega_{ij}, Z) \tag{15}$$

Physically, these rate equations are interpreted to be macroscopic representations of the microscopic-rearrangement rates within the material. These rearrangements may include the nucleation and growth of microcracks, dislocation pile-ups, the mutual interaction, multiplication and annihilation of dislocations, the looping and shearing of precipitates by dislocations, grain boundary sliding and twinning.

X. REFERENCES

1. Ramaswamy, V.G., Stouffer, D.C., and Laflen, J.H., "A Unified Constitutive Model for the Inelastic Uniaxial Response of Rene 80 at Temperatures between 538°C and 982°C," to appear in ASME Journal of Engineering Materials and Technology.

2. Bodner, S.R., and Partom, Y., "Constitutive Equations for Elastic Viscoplastic Strain Hardening Materials," ASME Journal of Applied Mechanics, Vol. 42, pp. 385-389, 1975.

3. Bodner, S.R., and Kim, S.S., "Plastic Fracturing Theory for Concrete," J. Eng. Mech. Div., ASCE, Vol. 105, pp. 429-446.

4. Embury, J.D., "Strengthening by Dislocation Structures," Strengthening Methods in Crystals, ed. A. Kelly and R.B. Nicholson, p.354, 1971.

5. Dieter, G.E., Mechanical Metallurgy, McGraw-Hill, New York, 1976.

6. McKnight, R.L., Laflen, J.H., and Spamer, G.T., "Turbine Blade Tip Durability Analysis," NASA CR165268, February 1982.

7. Ramaswamy, V.G., Van Stone, R.H., Dame, L.T., and Laflen, J.H., "Constitutive Modelling for Isotropic Materials," NASA Conference Pulication 2339, October 1984.

8. Sherwood, J.A., "A Constitutive Model with Damage for High Temperature Superalloys," Ph.D. Dissertation, University of Cincinnati, 1987.

9. Bathe, K.J., "Usage of the User-Supplied Material Model," ADINA Users Manual, Vol. 2, pp. G1-G25, 1987.

10. Press, W.H., Flannery, B.P, Teukolsky, S.A., and Vetterling, W.T., Numerical Recipes, The Art of Scientific Computing, pp. 24-29, 1986.

11. Stouffer, D.C., Final Report on Inelastic Deformation Modeling of Titanium Aluminide Matrix Material, General Electric Contract No. 201-LS-L1P15231, 1988.

APPENDIX MAY BE OBTAINED FROM
AUTHOR OR
UES

1989 USAF-UES FACULTY RESEARCH PROGRAM/

GRADUATE STUDENT RESEARCH PROGRAM

Sponsored by the

AIR FORCE OFFICE OF SCIENTIFIC RESEARCH

Conducted by the

Universal Energy Systems, Inc.

FINAL REPORT

PHOTOREFLECTANCE OF AlGaAs/GaAs INTERFACES

Prepared by:	Michael Sydor
Academic Rank:	Professor
Department and	Physics Dept.
University:	Univ. of Mn. Duluth
Research Location:	WRDC/MLPO
	Wright-Patterson AFB
	Dayton Ohio 45433
USAF Researcher:	William Mitchel
Date:	12 Aug 89
Contract No:	F49620-88-C-0053

PHOTOREFLECTANCE OF AlGaAs/GaAs INTERFACES

by

Michael Sydor

ABSTRACT

A detailed examination of modulated photoreflectance spectrum from high electron mobility transistor materials, and other layered structures, reveals a distinct signal which can be attributed to the sharp AlGaAs/GaAs interfaces, essential in manufacture of high quality electronic devices. The characteristic photoreflectance appears as a broad signal originating from the laser illuminated GaAs/AlGaAs heterojunction. The signal occurs under the conditions when two-dimensional electron gas was detected or was expected to form in the potential well at the junction of the two materials.

ACKNOWLEDGEMENTS

I wish to thank the Air Force Systems Command and the Air Force Office of Scientific Research for sponsorship of this research. I would also like to thank the Materials Laboratory for allowing me to use their facilities for my research. Universal Energy Systems also deserves mention for their help with the administrative aspects of the program.

I would like to thank Dr. P.M. Hemenger for his efficient supervision of this program, and his diligence in ensuring that all the necessary facilities were at our disposal. We had a lot of equipment to put together in a very short time. My thanks to Dr. William Mitchel for selection of the samples and the Hall data, both were crucial to this experiment. I would like to thank my colleague Dr. Ming-Yuan Yen for collaboration on the research, and his enthusiasm for the experiment. My thanks to Dr. Chris Mudare for collaboration with the PL measurements, and special thanks to Dr. Tim Peterson, Dr Dave Zelmon, Dr. Chris Mudare, and Dr. Omar Manasreh for their support and loan of equipment. My thanks to Ron Perrin, Tom Kensky, and Laura Rae for help with computers and electronic work. My appreciation to Gerald Landis for his assistance with sample etching and for being a friendly scrounge. Last but not least, my thanks to Neal Jahren, my student, for the support, the enthusiasm, and the friendship as well as hard and devoted work on this project.

I. INTRODUCTION:

The Materials Laboratory of the Wright Research and Development Center at Wright-Patterson Air Force Base is interested in devising a quick, inexpensive, and nondestructive method for testing of materials before they are processed into electronic or electro-optic devices. Photoreflectance (PR) is ideally suited for this task.

My research task was to set up an operational PR apparatus, and to make a series of measurements designed to isolate and characterize the PR signature from doped GaAs/AlGaAs heterojunctions. Physical sharpness and the electronic integrity of material junctions are the essential features of high-performance layered electronic structures.

II. OBJECTIVES OF THE RESEARCH EFFORT:

Manufacture of electronic devices is a tedious and an expensive process. The ability to select high-quality material before it is used in fabrication of devices is important in the economics of the electronics industry, in progress of scientific research in the field of new materials growth, and in design of electronic systems. The ultimate aim of this project is the construction of a prototype PR system which can be used on-line in a molecular beam materials growing process.

III.

The use of photoreflectance (PR) in determination of quality of layered GaAs/AlGaAs structures depends largely on one's ability to identify the signal from individual surfaces. In structures such as high electron mobility transistors (HEMT), one observes at the same time a sum of signals from several layers of material. Often, layers as deep as 3 μm from the illuminated surface contribute to the total PR signal. A demonstration of this can be seen from Fig. 1 which shows a distinct GaAs signature from a layer of GaAs overgrown by 3.2 μm epilayer of heavily doped AlGaAs.

The signal from each layer depends on its location in the structure, the layer thickness, its doping level, the unintentional impurity concentration, the layer's band-gap energy relative to the adjacent layers, and the sharpness of its interfaces with the neighboring layers.

In order to learn how to interpret the PR from HEMT structures, we have performed a series of measurements designed to isolate the PR signature from individual junctions. Some 25 distinct samples were examined in this experiment in an excess of 150 individual measurements.

In an attempt to isolate the effects of unintentional impurities[1], we have made a series of PR measurements as a function of sample temperature and laser pump intensity Impurity effects generally show a PR which behaves differently with temperature and laser intensity from the electric field modulated PR that one normally observes for pure, high-quality material. Fig. 2 shows an example of PR from a HEMT at two different laser intensities. The results in Fig. 2 indicate that the broad signal observed in this sample is not an impurity-related signal. Fig. 3 shows the behavior of PR with

temperature. Notice that the AlGaAs band edge peak at 1.82 eV, and the GaAs oscillations above 1.42 eV, shift and sharpen as the temperature drops to 200 K. The sample in Fig. 3 shows a PR indicative of sharp interfaces and good device material. We will return to this sample again when we discuss the differences in PR between good and diffused GaAs/AlGaAs interfaces.

We have indicated above that interference effects are important in the interpretation of PR data from layered structures. Even a readily identifiable feature, such as the band edge PR from AlGaAs, may often appear in a distorted form and give an erroneous indication of the AlGaAs composition. An example of such distortion can be seen in Fig. 1. The AlGaAs peak in Fig. 1 seems to appear at ~1.82 eV. Low temperature PR measurements resolve the structure and show that the band edge for this sample actually lies at the inflection on the high energy side of the peak observed at room temperature, at 1.85 eV. This band edge energy corresponds to an $Al_XGa_{1-X}As$ composition of 27.5% Al, a value which was verified by Photoluminescence measurements. Similarly, in Fig. 3, the AlGaAs band edge for a capped HEMT structure is located at the high energy side of the main AlGaAs peak.

A particularly interesting interference effect[2] comes from a HEMT type structure G513 grown using $In_{.1}Ga_{.9}As$ and $Al_{.15}Ga_{.85}As$. The PR from this structure is shown in Fig. 4. In this sample, the peak at ~1.66 eV is due to the $Al_{.15}Ga_{.85}As$ band edge. Notice that the sample in Fig. 4 shows an additional oscillatory PR in the 1.32 eV region. This signal was absent in HEMTs shown in Figs. 2 and 3. It comes from the buried InGaAs layer, which has a band gap lower than GaAs. The PR from InGaAs behaves differently from the PR due to the adjacent GaAs layer. The InGaAs signal appears to depend on interference with the signal reflected from the front surface[2]. This can be seen from Fig. 5 which

shows that after the GaAs cap has been etched off, the signal from InGaAs increased and shifted relative to the PR from the underlying GaAs layer .

One of the most important properties which affects the quality of HEMT structures is the sharpness or the integrity of the GaAs/AlGaAs junctions. PR is well suited for the investigation of sharpness of heterojunctions, because it responds to the electric field uniformity within the depletion layer, the doping of material through its effect on the thickness of the depletion layer, and the the built-in electric potential difference at the interface between the two materials. Thus, the PR signal from an abrupt, uniform interface, will be relatively high, and will show narrow GaAs FKO riding on top of a broad signal extending from the GaAs band edge energy to the main PR peak for the AlGaAs. The GaAs FKO come from the active, undoped GaAs layer.[3] An example of the lack of high quality heterojunction can be seen from a comparison of the PR in Fig. 6 with the PR shown in Fig. 3. The HEMT structures in both figures are nearly the same, however, the HEMT in Fig. 6 shows dopant diffusion across the interface boundaries. The contamination of the active GaAs layer is exemplified in Fig. 6 by the widely spaced FKO which appear above the GaAs band edge energy, and the simultaneous absence of the broad PR signal between the two band edges.

We close by saying that PR technique appears ideal for quick and nondestructive testing of HEMTs and electronic materials.

IV. RECOMMENDATIONS

a. Identifiable PR features from GaAs/AlGaAs interfaces show that PR is ideally suited as an on-line method for monitoring of materials growth.

b. Further research should directed toward PR measurements at elevated temperatures.

c. The diagnostic ability of PR for impurities has not been tested, although many reports of impurity effects have been reported in the scientific literature. Further research in this area could enhance the viability of the technique as a diagnostic tool for layer by layer analysis of materials during the growth process.

REFERENCES

1. Huang, D. G. Ji, U. K. Reddy, H. Morkoc, F. Xiong, and T. A. Tombrello, J. Appl. Phys. 63(11), 5447 (1988).

2. Huang, D., D. Mui, and H. Morkoc, J. Appl. Phys. 66(1), 358 (1989).

3. Snow, E. S., O. J. Glembocki, and B. V. Shanabrook, Phys. Rev. B38(17), 12485, (1988-1).

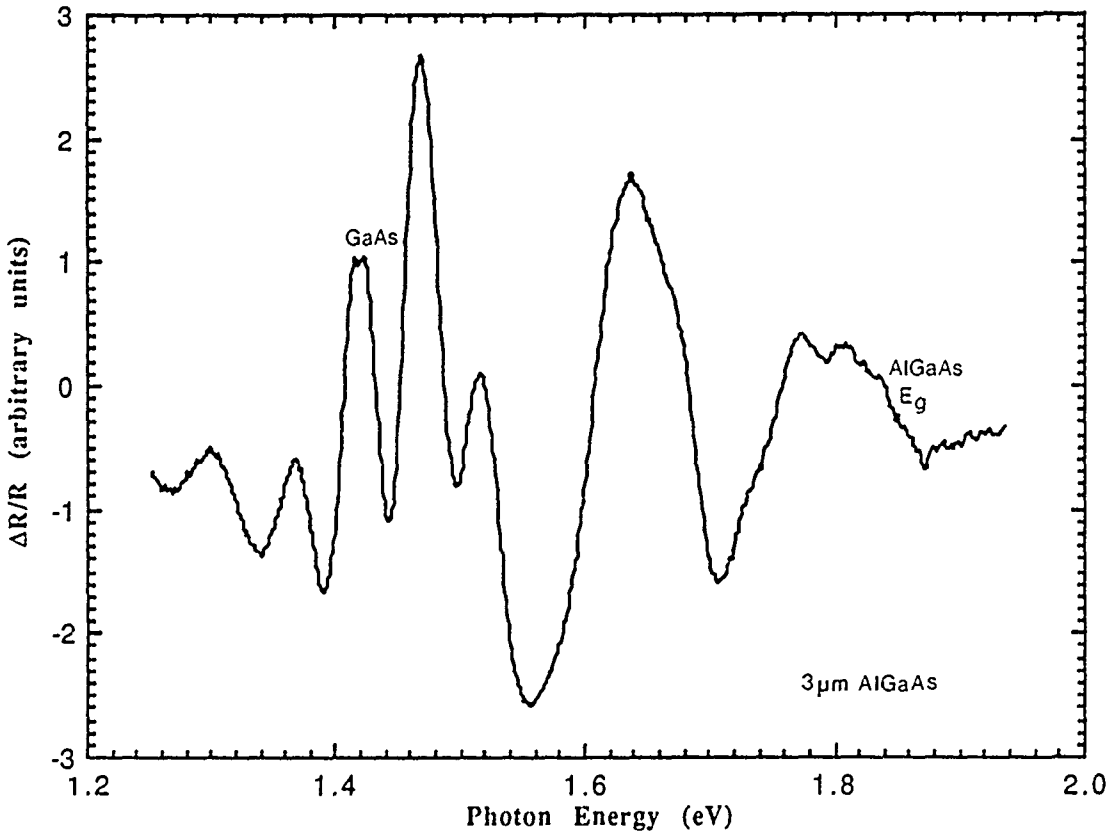


Figure 1: PR trace from a capped Si doped 3.2 μm layer of AlGaAs. Notice the distorted AlGaAs PR at ~1.8 eV, and the characteristic oscillatory GaAs signature above 1.42 eV.

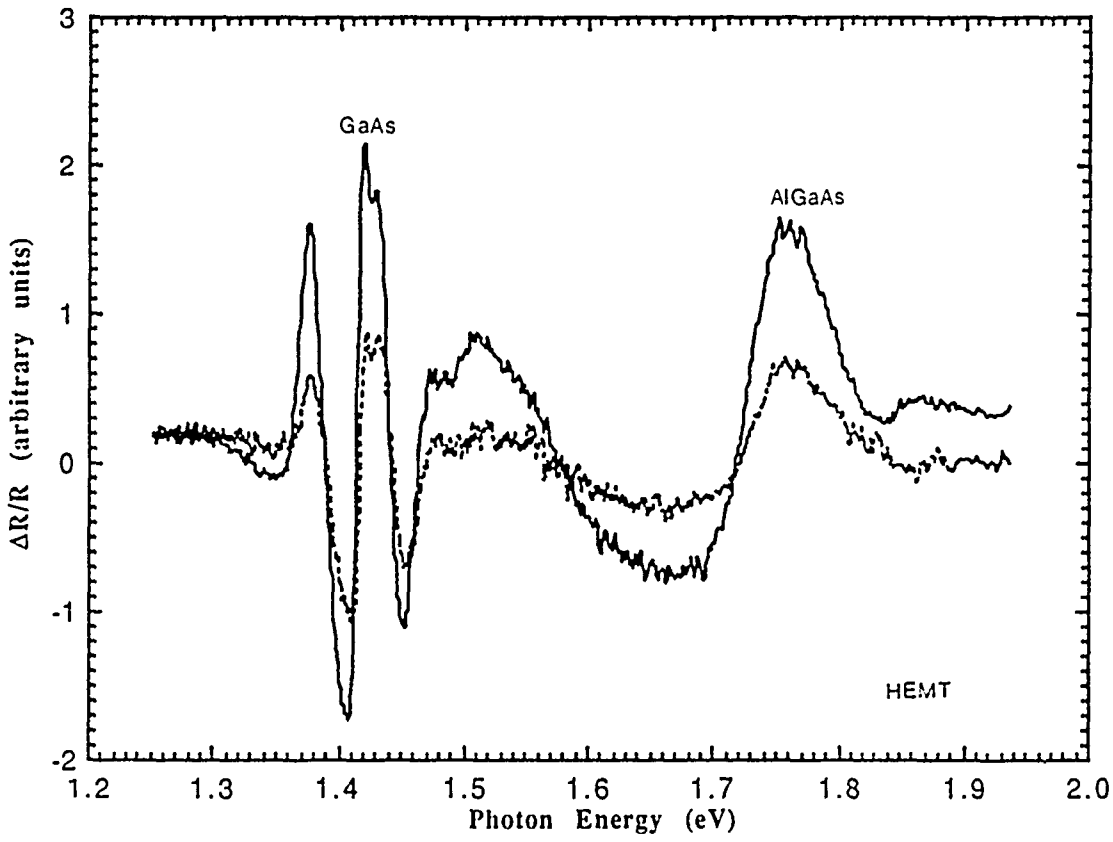


Figure 2: A trace of PR for a HEMT structure at 20 mW/cm^2, shown by the solid line, and at 2 mW/cm^2 indicates that the broad PR structure between 1.42 eV and 1.76 eV is not due to impurities.

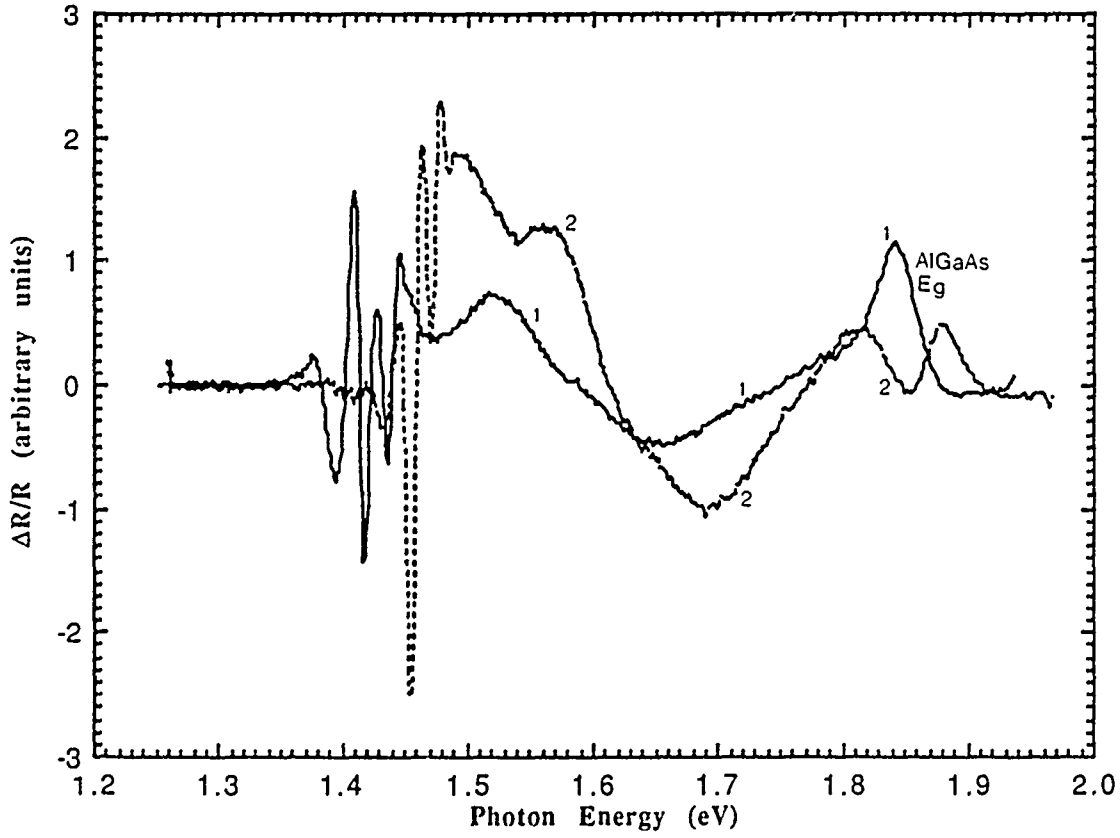


Figure 3: Solid line shows HEMT G2-510 at room temperature. As the temperature is lowered to 200 K the AlGaAs PR at ~1.84 eV becomes resolved from interference effects into two peaks, showing that the actual band edge PR for the AlGaAs was at 1.86 eV.

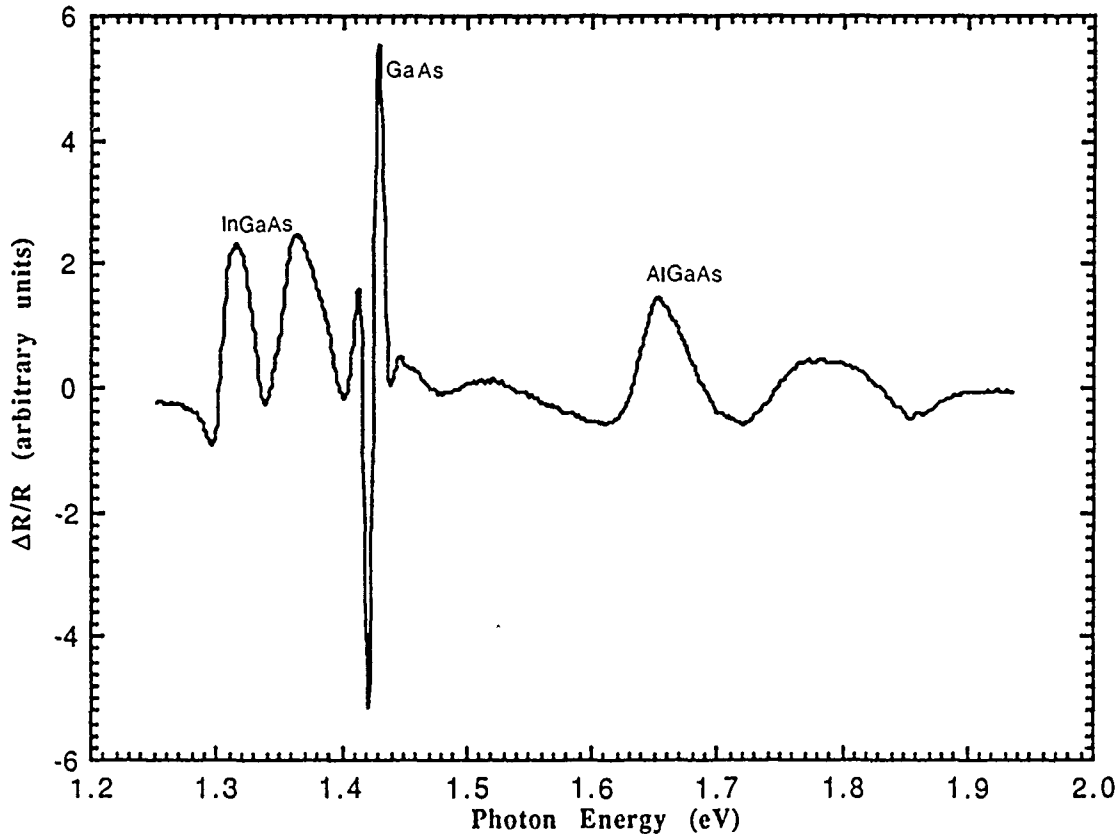


Figure 4: A HEMT structure grown with $In_{.1}Ga_{.9}As$ and $Al_{.15}Ga_{.85}As$ shows low energy oscillations below 1.42 eV. The oscillations are attributable to the InGaAs layer.

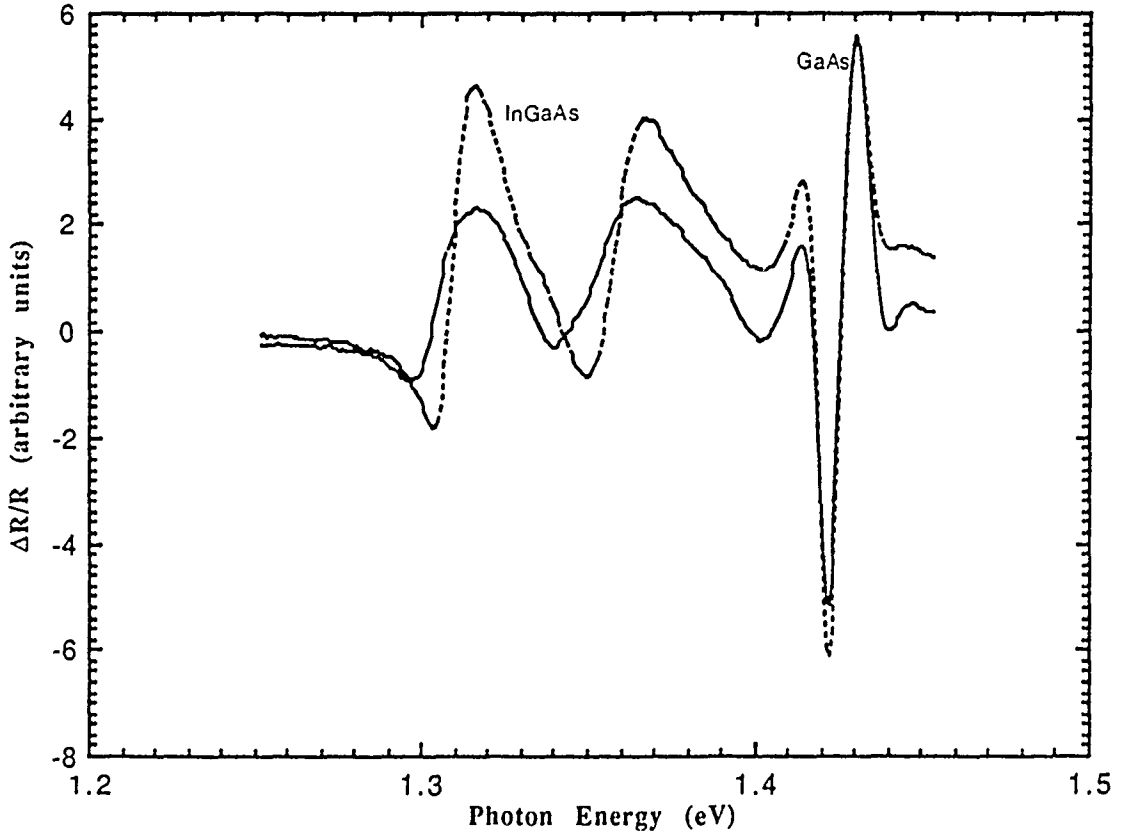


Figure 5: As the GaAs cap is etched off, the structure from InGaAs grows while the GaAs signal at 1.42 eV remains relatively unchanged.

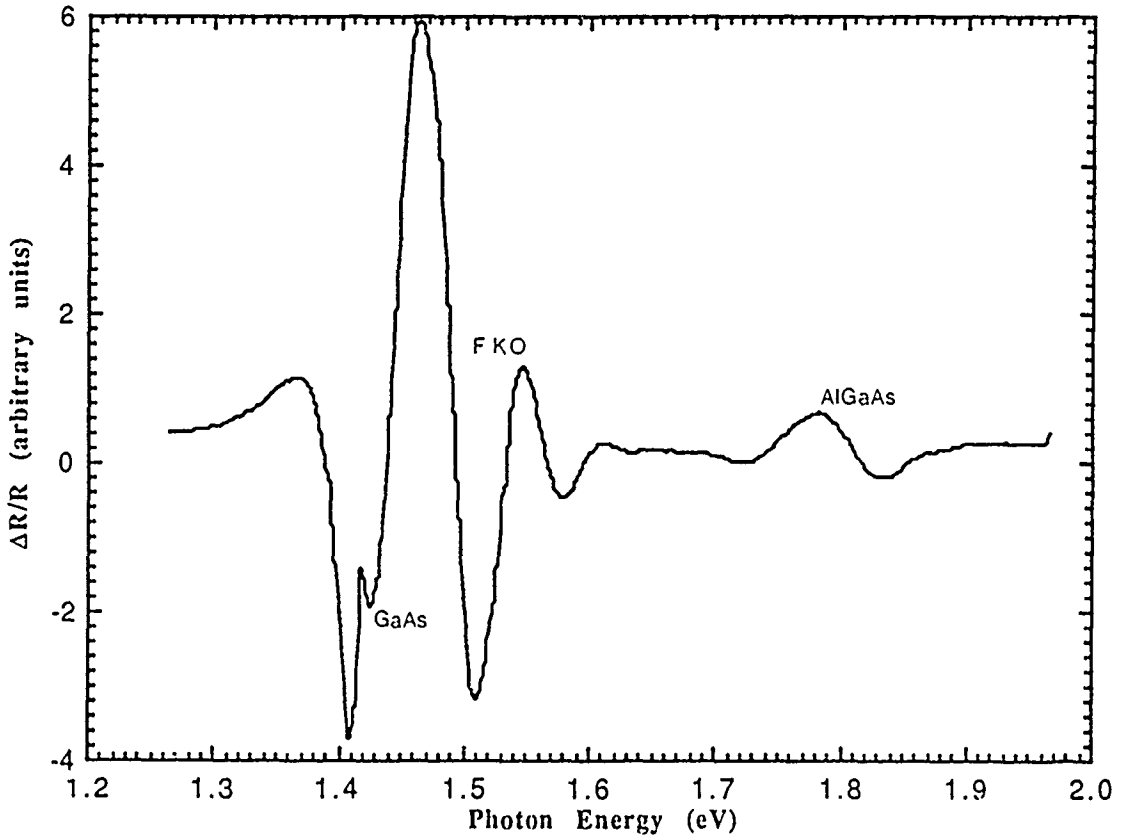


Figure 6: A comparable but poor HEMT structure, with dopant diffusion across the AlGaAs spacer lacks the sharp GaAs signature observed in figures 2 and 3.